

Carbon dots-loaded layer-by-layer capsules as multifunctional nanotheranostic delivery systems to treat osteosarcoma.

A thesis presented for the degree of

Doctor of Philosophy

Thomas Christopher Wareing

Ву

School of Engineering,

Newcastle University, United Kingdom

February 2025

Abstract

Nanotheranostics, an emerging field which encompasses nanotechnology used theranostically, is the combination of diagnostics and therapeutic techniques. It exploits the unique properties of nanoparticles, particularly large surface area to volume ratio, optical and magnetic properties, low melting point and mechanical strength. Theranostic strategies have shown potential in monitoring targeted delivery of drugs. In this thesis, carbon dots were combined with the layer-by-layer (LBL) technique to create a platform for drug delivery that could be easily tracked via fluorescent imaging. This type of treatment has the potential to be less harsh and more effective than current treatments, such as chemo and radiotherapy which have very extreme side effects including pain, nausea, and hair loss. Specifically, carbon dots (synthesised from renewable and sustainable sources e.g. spent coffee ground, a food waste) are nanoparticles that have interesting physical and optical properties that make them a good candidate for fluorescent bioimaging, replacing conventional toxic, metal-based nanomaterials, whereas the LBL technique applies layers of alternately charged polyelectrolytes by self-assembly to create a thin film or nanocapsules. The technique is cheap, simple and has a high degree of control over layer size.

Carbon dot (CD) syntheses were performed using hydrothermal processes with conventional and microwave assisted heating approaches. Hydrothermal processes are simple and nonhazardous using water as a process medium at subcritical conditions (180 and 300 °C, with corresponding pressures 10-88 bar) to synthesise CDs as they are simple to operate and do not require further modification steps. The effects of synthesising conditions such as pH, types of catalysts, ratio of feedstock material and water, reaction time and temperature on properties of CDs were examined. The surface properties of CDs were characterised with Fourier transform infrared (FT-IR) spectroscopy and X-Ray photoelectron spectroscopy (XPS). The results showed that the CDs had an increased ratio of oxygen (40-70%) against carbon and nitrogen, when compared to starting spent coffee grounds (~10%). This is due to the introduction of oxygen-containing functional groups to the surface of the carbon dots such as carboxylic acid and alcohol. The size of the CDs was between 1 and 14nm and was correlated with reaction conditions such as retention time and catalyst choice. Regardless of synthesising conditions, the CDs showed blue emissions between 300 and 450nm with UV (ultraviolet) excitation energies 250-300nm and quantum yields up to 13%. The CDs that were synthesised in tannic acid and aqueous conditions were chosen for biocompatibility testing (PrestoBlue),

using fibroblast cells. The dots synthesised using aqueous conditions showed at least 80% cell viability with the highest concentration of 1mg/ml. These CDs are suitable for application in this work as imaging agents due to their optical properties and biocompatibility.

For the development of the nanocapsule, calcium phosphate nanoparticles were chosen as a template because they are simple to synthesise and have a charged surface, meaning that they are easy to functionalise with a LBL technique (involving stacking layers of polyelectrolytes with alternating charges). This technique can be done in aqueous conditions at atmospheric temperature and pressure. The dipping technique was applied because it is fast and requires no specialised equipment. Initially LBL capsules were created using polyethyleneimine as the first layer followed by the main polyelectrolytes using renewable, non-toxic chitosan and alginate. The transmission electron microscopy (TEM), FT-IR and XPS showed the use of sodium acetate buffer partially dissolved the calcium phosphate core and destabilised the layers. Cell tests against Saos-2 and U2OS cell lines showed little therapeutic effect and encapsulation efficiency tests showed that drug encapsulation was unsuccessful, however incorporation of carbon dots into the layers showed potential in photoluminescence spectroscopy with a 380% increase in photoluminescence intensity when compared against nanoparticles with no carbon dots. A second LBL synthesis was attempted on poly(allylamine hydrochloride) (PAH) functionalised calcium phosphate nanoparticles using aqueous conditions and chitosan and chondroitin sulphate as the polyelectrolyte layers. These devices performed well in terms of drug encapsulation, release, and in-vitro cell tests against Saos-2 and U2OS cell lines where the nanoparticles showed particular therapeutic effect against Saos-2 cells. Incorporation of carbon dots had little detrimental effect on the performance of the particles further suggesting that the combination of carbon dots and the LBL technique should be a candidate for future research for the nanotheranostic treatment of osteosarcoma.

Acknowledgements

I would like to take this opportunity to express my immeasurable gratitude to my supervisors Professor Anh Phan and Dr Piergiorgio Gentile for their exemplary supervision, support, and guidance over the last 4 years of this project, which without I would not have been able to complete this. It was truly an honour to work under their supervision and wish them the best of luck with their future research.

I would also like to highlight the work completed by Masters students under my supervision and express appreciation. Their work was excellent and greatly expanded the scope of this project. I highly recommend them for their work in research and wish them the best of luck with their future careers.

- Simone Margini, from Politecnico di Torino for his assistance in the LBL capsule formation.
- Thomas James, from Newcastle university, for his assistance in the tannic acid ultrasonic pretreatment of coffee grounds for the synthesis of carbon dots.

I also express extreme gratitude to the array of institutes, departments and fellow students that aided me with my work, which without, the completion of this work would not have been possible. These are:

- The Engineering and Physical Sciences Research Council (EPSRC) for funding my PhD over the last 3 and a half years.
- Merz court, Newcastle University, and all the technical staff that work in this building that
 have helped in many ways over the years, whether that be by booking equipment for me
 to use, helping with use of machines, as well as countless other roles that, without them,
 would not be possible for me to carry out the work.
- The Biolab/Biofab department here at Newcastle University, for providing support and equipment that aided in the completion of my LBL experiments.
- The Process Intensification group, Newcastle University, for providing access to laboratories and resources that facilitated the completion of the completion of my carbon dot syntheses.
- Dr Tracey Davey and Ross Laws for their assistance in TEM and SEM analysis at Newcastle University.
- EPSRC National Facility for XPS (HarwellXPS) at Cardiff University for XPS data analysis.
- Dr Leon Bowen at Durham University for his support in acquiring HRTEM analysis.

- Lawrence Bruce, a fellow PhD student and Dr Fabio Cucinotta for their assistance with photoluminescence spectroscopy and quantum yield measurements.
- Ha Phan, a fellow PhD student, for his assistance with the analysis of XPS data and introduction to HTC.

I would also like to thank the members of Team SUGAR: Kitty Crompton, Alex Stokes, Koren Murphy and Annachiara Scalzone, supported by Dr. Adam Wollman and the European Space Agency for their work and investment on the Fly Your Thesis project that was completed alongside this PhD project. It was an experience I will never forget.

To the fellow members of The Newcastle Trebles and the Newcastle Acapella Society as a whole, I thank you for providing your support via friendship and an outlet for my musical inclinations.

To my friends, both longstanding and the ones I've met during my time at Newcastle University. Thank you for your encouraging words and emotional support you have given me for the duration of this project.

To my Family, most specifically my parents Alan and Sharon; You have supported me and have provided for me continuously throughout this project and beyond, I cannot thank you enough.

I dedicate this thesis to my paternal grandparents, whom unfortunately, both lost their lives to cancer. Their fights inspired me to pursue a career in furthering the research against cancer, I hope this project serves as a good start to this career and I make them proud.

Contents

Ch	apter	1. Introduction1
1.1	Back	ground1
1.2	Imp	act5
1.3	Aim	s and objectives 5
1.4	The	sis layout6
Ch	apter	2. Literature review7
2.1	Back	ground of Osteosarcoma and the current treatment strategies
2.2	Nan	otheranostics and cancer treatment9
2.2	1	Nanoparticle-based imaging
2.2	2	Nanoparticle-based therapy
2.2	3	Examples of nanotheranostics for cancer treatment
2.2	.4	Challenges and future directions
2.3	Carb	on dots25
2.3	.1	Photoluminescence mechanisms
2.3	.2	Synthesis methods
2.3	.3	Functionalization
2.3	.4	Applications
2.3	.5	Limitations 41
2.3	.6	Future perspectives
2.4	Laye	er-by-layer
2.4	.1	Fabrication methods
2.4	.2	Materials
2.4	.3	Properties
2.4	.4	Applications53
2.4	.5	Layer by layer micro/nanocapsules for drug delivery 55
2.4	.6	Limitations and future perspectives 57
2.5	Com	bination of techniques59
2.6	Sum	mary 61
Ch	napter	3. Materials and Experimental Methods63
3.1	Synt	hesis of Carbon dots 63
3.1	1	Materials
3.1 nit		Acid catalysed Hydrothermal carbonisation (HTC) of spent coffee grounds and oxidation (Synthesis 1)

3.1.3 hydrother	Ultrasonic pretreatment of spent coffee grounds and tannic acid catalysed rmal carbonisation (synthesis 2)	.68
3.1.4	Microwave assisted aqueous hydrothermal carbonisation of SCG (synthesis 71	3)
3.2 Laye	r-by-layer techniques	.73
3.2.1	Materials	.73
3.2.2	Flowrate and drying methods investigation	.74
3.2.3	Calcium phosphate template functionalisation with first layer	.76
3.2.4 PEI- funct	Layer by layer deposition of chitosan and alginate polyelectrolyte solutions ionalised CaP NP, drug encapsulation and release	
• •	Deposition of aqueous solutions of chondroitin sulphate and chitosan olytes on PAH calcium phosphate nanoparticles, functionalisation with carb encapsulation and release	
3.2.6	Drug encapsulation efficiency methods	.83
3.3 Anal	ytical techniques	.85
3.3.1	Physiochemical analysis	.85
3.3.2	Optical spectroscopy	.86
3.3.3	Biological	.87
3.3.4	Microscopy	.89
Chapter	4. Carbon Dots from Spent Coffee Grounds: Results and	
		92
	Catalysed Hydrothermal Carbonisation of Spent Coffee Grounds and Nitric on (synthesis 1)	.93
	Effect of reaction time, catalyst types and concentration on properties of s obtained from HTC for producing carbon dots	.94
4.1.2 synthesis	Carbon dots produced via nitric acid oxidation and the effect of precursor parameters	102
4.1.3	Summary	115
	asonic pretreatment of spent coffee grounds and tannic acid catalysed al carbonisation (synthesis 2)	115
4.2.1	Effect of Ultrasonic pretreatment on spent coffee grounds	116
4.2.2 ultrasonio	Properties of carbon dots after hydrothermal carbonisation and effect of pretreatment	123
4.2.3	Summary	135
	owave assisted aqueous hydrothermal carbonisation of spent coffee ground	
4.3.1	Properties of carbon dots and the effect of temperature and retention time	

4.3.2	2	Summary	. 152
Cha 5.1	•	r 5. layer by layer capsules: Results and Discussion	153
nanop	articl	es	153
5.1.: met		Peristaltic pump method for the preparation of CPNPs, effect of drying and flow rate	. 153
5.1.2	2	Initial layer deposition, comparison between PEI and PDADMAC	. 158
5.2 and ca		osan and alginate layer by layer capsules functionalised with anticancer drudots	•
5.2.	1	Initial layer-by-layer deposition without drugs	. 161
5.2.2	2	Effect of drug loading on the layer-by-layer process	173
5.2.3	3	In-vitro drug release tests	. 181
5.2.4	4	In-vitro cell tests	184
5.2.	5	Functionalization with carbon dots	. 186
5.2.0	6	Summary	189
5.3 antica		osan and chondroitin sulphate layer by layer capsules functionalised with drugs and carbon dots	. 190
5.3.	1	Physio-chemical characterisation of PAH-coated calcium phosphate cores.	190
5.3.2	2	Layer-by-layer functionalisation	. 198
5.3.3	3	In-vitro cell tests	206
5.3.4	4	Summary	213
Cha	apte	r 6. General discussion, Conclusions and Future Work	214
6.1	Gen	eral discussion	214
6.2	Con	clusions	. 217
6.3	Futu	ure work	. 220

List of Figures

Figure 2.1 - A) MRI Image of osteosarcoma in a knee - Case courtesy of Dr Frank Gaillard, Radiopaedia.org, rID: 7527 (Gaillard, 2023), B) Image of a knee with osteosarcoma digital removed to simulate "healthy knee" for comparison	lly 8 ; in g,). 10 ts –
Society	
Figure 2.4 - Examples of carbon dot functionalisation - Adapted from (Yan et al., 2018)	35
Figure 2.5 - Advantages of the layer-by-layer technique for drug delivery adapted from	
(Shende et al., 2020)	
Figure 2.6 - Outline of the steps of the layer-by-layer process - Adapted from (Guzmán et	
2017)	
Figure 2.7 - The process of layer-by-layer capsule formation — adapted from (Shende et a	
2020)	
Figure 3.1 - Dried spent coffee grounds	64
Figure 3.2 - The reaction schematic of two step carbon dot synthesis; hydrothermal	
carbonisation of coffee grounds followed by a nitric acid oxidation	
Figure 3.3 - Schematic of the hydrothermal reactor and heating apparatus	
Figure 3.4 - Experimental configuration for 1 – ultrasonic pre-treatment, 2 - hydrotherma	
carbonisation, and 3 - dialysis of carbon dots	
Figure 3.5 - Microwave reaction set up for the hydrothermal carbonisation of spent coffe	
grounds	
Figure 3.6 - Reaction schematic of the flowrate and drying method tests	75
Figure 3.7 - Reaction schematic for calcium phosphate nanoparticle synthesis and first lay	-
depositiondeposition	
Figure 3.8 - Reaction schematic for the layer-by-layer deposition of chitosan and alginate	
onto PEI functionalised calcium phosphate nanoparticles	
Figure 3.9 - The layer-by-layer deposition process used to deposit chitosan and chondroit	
sulphate into PAH functionalised calcium phosphate nanoparticles	
Figure 3.10 - Newcastle University's Hitachi HT7800 120kV Cryo TEM	
Figure 3.11 - Left; sample grid with droplet of sample, Right; sample grid in sample holde	r.90
Figure 4.1 - FT-IR analysis of precursors obtained from spent coffee grounds after HTC	95
Figure 4.2 - XPS wide survey scan of the precursors synthesised by a 2 hour hydrotherma	l
pretreatment with a concentration of 0.01g/ml sulphuric acid catalyst (TT-2H-P/AT-0.01-	•
Figure 4.3 - XPS C 1s scan of the precursors synthesised by a 2 hour hydrothermal	97
pretreatment with a concentration of 0.01/g/ml sulphuric acid catalyst (TT-2H-P/AT-0.01	-P1
	•
Figure 4.4 - TEM image of the precursor synthesised for 2 Hours with 0.01g/ml Sulphuric	
(TT-2H-P/AT-0 01-P) — Scale Bar 100nm	100

Figure 4.5 - TEM image of the precursor synthesised for 2 Hours with 0.02g/ml Sulphur (AT-0.02-P) – Scale bar 100nm	
Figure 4.6 - TEM image of the precursor synthesised for 2 Hours with 0.005g/ml tannic	acid
(TA-0.005-P) – Scale bar 100nm	
Figure 4.7 - Reaction schematic of the nitric acid oxidation from precursor to carbon do	t. 102
Figure 4.8 - FT-IR of carbon dot samples obtained after nitric acid oxidation	103
Figure 4.9 - XPS wide survey scan of the carbon dot sample TT-2H-CD/AT-0.01-CD	106
Figure 4.10 - XPS C 1s survey scan of the carbon dot sample TT-2H-CD/AT-0.01-CD	106
Figure 4.11 - TEM image of carbon dots (TT-2H-CD/AT-0.01-CD) synthesised from precu	irsor
TT-2H-P/AT-0.01-P (2 Hours with 0.01g/ml Sulphuric acid) - Scale Bar 20nm	108
Figure 4.12 - TEM image of carbon dots (AT-0-CD) synthesised from precursor (AT-0-CD) (2
Hours with water) - Scale Bar 20nm	-
Figure 4.13 - Size distributions of the carbon dots samples as analysed with ImageJ	
Figure 4.14 - TEM image of carbon dots (TA-0.05-CD) synthesised from precursor (TA-0.	
CD) (2 Hours with 0.05g/mL Tannic acid) - Scale Bar 20nm	
Figure 4.15 - Solutions of carbon dots under visible lights (1) and under UV-Light (2); A)	
left to right; TT-2H-CD, TT-3H-CD, TT-4H-CD, B) from left to right; AT-0-CD, AT-0.005-CD	
0.01-CD, AT-0.02-CD, C) from left to right; TA-0.005-CD, TA-0.01-CD, TA-0.05	
Figure 4.16 - Comparison in photoluminescence intensity when excited at 300nm	112
wavelength according to reaction parameters	112
Figure 4.17 - Images left to right of a) Raw SCGs, b) Dried solids following 90-minute pro	
treatment with tannic acid c) Dried solids following pre-treatment and 3-hour HTC at 20	
and d) Freeze dried solids following separation by dialysis	
Figure 4.18 - FT-IR analysis of raw SCGs and SCGs pre-treated via ultrasonication for 90	
with a 50ml of 0.05g/ml tannic acid solution, with no heating (std-cnd-PT) and heating	
40°C, 60°C and 80°C. Peaks are labelled with their corresponding wavelength and funct	
groups (Merek, 2023)	
Figure 4.19 - FT-IR analysis of raw SCGs, Std-cnd-PT, Conc-0-01-PT and Conc-0.1-PT for	
purposes of analysing the effect of changing concentration. Peaks are labelled with the	
corresponding wavelength and functional groups (Merek, 2023)	
Figure 4.20 - FT-IR analysis of raw SCGs, Std-cnd-PT, Ratio.2.5-PT and Ratio-10-PT for th	
purposes of analysing the effect of changing biomass and tannic acid solution ratio. Pea	
are labelled with their corresponding wavelength and functional groups (Merek, 2023)	
Figure 4.21 - FT-IR analysis of raw SCGs and samples taken from thre reaction of Std-cn	
every fifthteen minutes during the reaction progression for the purposes of analysing t	
effect of time. Peaks are labelled with their corresponding wavelength and functional g	-
(Merek, 2023)	121
Figure 4.22 - XPS wide survey scan of the precursor sample Std-Cnd-PT	122
Figure 4.23 - XPS C 1s scan of the precursor sample Std-Cnd-PT	122
Figure 4.24 - FT-IR of Carbon dot samples synthesised from 3 hour HTC from the precur	sors
obtained from the ultrasonic pretreatment	124
Figure 4.25 - TEM image of carbon dots (Std-Cnd-CD) synthesised from pre-treated coff	ee
grounds (Std-Cnd-PT) (~20°C, 0.05/mL TA, 10/50 biomass ratio) - Scale Bar 100nm	126
Figure 4.26 - TEM image of carbon dots (Temp-80-CD) synthesised from pretreated cof	fee
grounds (Temp-80-PT) (80°C, 0.05g/mL TA, 10/50 biomass ratio) - Scale Bar 50nm	126

Figure 4.27 - TEM image of carbon dots (Ratio-20-CD) synthesised from precursor (Ratio-20-
PT) (~20°C, 0.05/mL TA, 10/20 biomass ratio) - Scale Bar 20nm127
Figure 4.28 - Size distribution of carbon dots according to reaction parameters from TEM
analysis with ImageJ
Figure 4.29 - Graph to show the photoluminescence intensity of different carbon dots at
excitation 230nm
Figure 4.30 - Samples of solution of CDs with tannic acid following 90-minute ultrasonic
pretreatment at varying conditions and 3 hours high temperature carbonisation at 200°C,
left to right: a) No-PT-CD, b) Conc-0.0-CD, c) Std-Cnd-CD, d) Temp-40-CD, e) Temp-60-CD f)
Ratio-25-CD, g) Ratio-100-CD, h) Conc-0.01-CD, i) Conc-0.1-CD
Figure 4.31 - Samples of solution of CDs with tannic acid following 90-minute ultrasonic pre-
treatment without heating and 3 hours high temperature carbonisation at 200°C, with
concentration of tannic acid increasing from left to right. Tannic acid concentrations:
0.00g/ml, 0.01g/ml, 0.05g/ml and 0.1g/ml133
Figure 4.32 - Cell viability, given in (%), for all samples following freeze drying after 24 (A)
and 48 (B) hours
Figure 4.33 - Comparison of the FT-IR of microwave carbon dots synthesised at different
temperature (150-200°C) and retention times (30-120 mins)137
Figure 4.34 - XPS wide surface scan of carbon dots synthesised at 150°C and 120 minutes
(150-120-CD)
Figure 4.35 - XPS C 1s scan of carbon dots synthesised at 150°C and 120 minutes (150-120-
CD)139
Figure 4.36 - Comparison of the ζ -potential of microwave carbon dot samples synthesised at
different reaction temperatures (150-200°C) and time (30-120 mins)141
Figure 4.37 - Photoluminescence intensity of carbon dots synthesised at 150°C at excitation
wavelength 300nm143
Figure 4.38 - Photoluminescence intensity of carbon dots synthesised at 175°C at excitation
wavelength 300nm143
Figure 4.39 - Photoluminescence intensity of carbon dots synthesised at 200°C at excitation
wavelength 300nm144
Figure 4.40 - Photoluminescence emission spectra of the dots synthesised at 200-120 at
increasing levels of excitation
Figure 4.41 - Photos of carbon dot solutions showing photoluminescence under a UV lamp.
147
Figure 4.42 - TEM image of the carbon dots 150-30, right: TEM images of the carbon dots
175-60
Figure 4.43 - Graph to show the relationship between carbon dot size and reaction
parameters
Figure 4.44 - HRTEM image of the carbon dots synthesised at 200°C with a retention time of
90 minutes with the layered structure highlighted. Right; Layer lengths of all carbon dots at
200°C as measured with ImageJ from HR-TEM images150
Figure 4.45 - Viability of cells when exposed to different concentrations of carbon dots for 24
(A) and 48 (B) hours as measured with PrestoBlue™ cell viability reagent and procedure151
Figure 5.1 - SEM images of calcium phosphate nanoparticles washed with water and dried in
air, synthesised at different flow rates; a) – 0.5mL/min, b) – 3mL/min, c) - 6mL/min, d) –
9mL/min 9mL/min

Figure 5.2 - SEM images of calcium phosphate nanoparticles washed with water and freeze
dried, synthesised at different flow rates; a) – 0.5mL/min, b) – 3mL/min, c) - 6mL/min, d) -
9mL/min
Figure 5.3 - SEM images of calcium phosphate nanoparticles washed with isopropanol and
dried in air, synthesised at different flow rates; a) – 0.5mL/min, b) – 3mL/min, c) - 6mL/min,
d) - 9mL/min
Figure 5.4 - TEM images of PEI functionalised particles (10mg/mL)
Figure 5.5 - TEM images of PDADMAC functionalised particles (10mg/mL)
Figure 5.6 - ζ-potential for each layer of the layer-by-layer process deposited on CaP 161
Figure 5.7 - FT-IR of each layer deposited on CaP nanoparticles in the initial layer by layer
process
·
Figure 5.8 - XPS scans of sodium alginate raw material – Top C1s scan, bottom O1s scan. 164
Figure 5.9 - XPS scan of chitosan raw material – Top C1s scan, bottom O1s scan
Figure 5.10 - XPS scans of the first layer deposition (CaP nanoparticle + PEI) – left C1s scan,
right O1s scan
Figure 5.11 - XPS scan of the second layer deposition (CaP nanoparticle + PEI + Alginate) –
left C1s scan, right O1s scan. 168
Figure 5.12 - XPS scan of the third layer deposition (CaP nanoparticle + PEI + alginate +
chitosan) – left C1s scan, right O1s scan.
Figure 5.13 - TEM images of each layer of the layer-by-layer process
Figure 5.14 - ζ-potential of the LBL process for each drug loading conditions: a) both DAX and
DOXO, b) DOXO only and c) DAX only
Figure 5.15 - FT-IR of the layer-by-layer process for each drug loading experiment; a) Both
drugs, b) DOXO and c) DAX
Figure 5.16 - TEM images of each layer of the layer-by-layer process with DOXO 178
Figure 5.17 - TEM images of each layer of the layer-by-layer process with DAX 179
Figure 5.18 - TEM images of each layer of the layer-by-layer process both drugs 180
Figure 5.19 - Drug release curves for the DOXO release data - a) DOXO only sample, b) both
drug sample
Figure 5.20 - Drug release curves for the DAX release data – a) DAX only sample, b) both drug
sample
Figure 5.21 - UV-Vis calibration curves of different materials at different wavelengths – a)
480nm b) 230nm
Figure 5.22 - PrestoBlue results of all samples using U2OS cells
Figure 5.23 - PrestoBlue essay of all samples using SAOS-2 cells
Figure 5.24 - ζ-potential data of the layer-by-layer formation of nanoparticles – left: without
carbon dots, right: with carbon dots
Figure 5.25 - Photoluminescence data for bare carbon dots - emission data at increasing
excitation wavelengths
Figure 5.26 - Photoluminescence data for unfunctionalised particles - emission at increasing
excitation wavelengths
Figure 5.27 - Photoluminescence data for nanoparticles functionalised with carbon dots –
emission data at increasing excitation wavelengths
Figure 5.28 - FT-IR data for calcium phosphate nanoparticles pre and post dialysis: A)
Unfunctionalised, B) Functionalised with PAH

Figure 5.29 - Cumulative release of DOXO from CaP(DOXO)_PAH (A) and study of burst
release rate (B)195
Figure 5.30 - DLS measurements: Hydrodynamic diameter (A) and PDI (B) of CAP_PAH and CaP(DOXO) PAH196
Figure 5.31 – TEM analysis from literature of unfunctionalized particles a) reprinted from
Urch et al. (Urch et al., 2009) b) reprinted from Šupová et al. (Šupová et al., 2018)196
Figure 5.32 - TEM analysis of CaP PAH (A-B), CaP(DOXO) PAH (C-D)197
Figure 5.33 - TEM measurements of CaP PAH and CaP(DOXO) PAH197
Figure 5.35 - ζ-potential graph of the LBL of CaP_PAH_7DC199
Figure 5.34 - ζ-potential graph of the LBL of CaP_PAH_7L (A) and CaP_PAH_7D (B)199
Figure 5.36 - NPs colour after deposition of CS or CH (A), CH/DOXO (B) and CS/DOXO (C)200
Figure 5.37 - Excitation of CaP_PAH_7DC by a wavelength of 365nm201
Figure 5.38 - DLS measurements: hydrodynamic diameter (A) and PDI (B) of CaP_7L and
CaP_7DC
Figure 5.40 - Efficiency of DOXO encapsulation by layers of CaP_7D and CaP_7DC in different
units: μg (A) and percentage (B)203
Figure 5.41 - DOXO cumulative release profiles and the study of burst release from CaP_7D
(A-B) and CaP_7DC (C-D)205
Figure 5.42 - PrestoBlue assay of Saos-2 (A) and U2OS (B) seeded with CaP_7L207
Figure 5.43 - PrestoBlue assay of Saos-2 (A) and U2OS (B) seeded with CaP_7DC at different
concentrations and free DOXO at 10µg/mL concentration208
Figure 5.44 - Live/Dead images of Saos-2 (left) and U2OS (right) with or without free DOXO at
10μg/mL concentration210
Figure 5.45 - Live/Dead images of Saos-2 (up) and U2OS (bottom) with or without CaP_7L at
different concentrations210
Figure 5.46 - Live/Dead images of Saos-2 (up) and U2OS (bottom) with or without CaP_7DC
at different concentrations211
Figure 5.47 - TEM images of Saos-2 cells treated with a concentration of 500 $\mu g/mL$ CaP_7DC
(M – Mitochondria, N – Nucleus, Vac – Vacuole)212
Figure A.6.1 - XPS O 1s scan of the precursors synthesised by a 2 hour hydrothermal
pretreatment with a concentration of 0.01/g/ml sulphuric acid catalyst (TT-2H-P/AT-0.01-P).
224
Figure A.6.2 - XPS O 1s scan of the precursors synthesised by a 2 hour hydrothermal
pretreatment with a concentration of 0.01/g/ml sulphuric acid catalyst (TT-2H-P/AT-0.01-P).
Figure A.6.3 - TEM images of precursors obtained though HTC carbonisation225
Figure A.6.4 - Figure A4 - XPS O 1s scan of the carbon dot sample TT-2H-P/AT-0.01-P225
Figure A.6.5 - XPS N 1s scan of the carbon dot sample TT-2H-P/AT-0.01-P226
Figure A.6.6 - FT-IR data for the ultrasonication treatment of spent coffee grounds227
Figure A.6.7 - XPS O 1s scan of the precursor sample Std-Cnd-PT228
Figure A.6.8 - XPS N 1s scan of the precursor sample Std-Cnd-PT228
Figure A.6.9 - XPS O 1s scan of carbon dots synthesised at 150°C and 120 minutes (150-120-
CD)
Figure A.6.10 - XPS N 1s scan of carbon dots synthesised at 150°C and 120 minutes (150-120-
CD)

Figure A.6.11 - XPS N 1s scan of the first layer deposition (CaP nanoparticle + PEI)	230
Figure A.6.12 - XPS N 1s scan of the second layer deposition (CaP nanoparticle + PEI +	
alginate)	230
Figure A.6.13 - XPS N 1s scan of the third layer deposition (CaP nanoparticle + PEI + algir	nate
+ chitosan)	231

List of Tables

Table 2.1 - Advantages and disadvantages of different imaging techniques (Arms et al., 2018	
Chang Xu, 2021; Pham et al., 2015)1	
Table 2.2 - Summary of the advantages and disadvantages to nanoparticles used in imaging.	
Table 2.3 - The advantages and disadvantages of different nanoparticles used in	
therapeutics2	1
Table 2.4 - A comparison between biomass derived carbon dots, chemical carbon dots, and	
semiconductor quantum dots - Adapted from Radnia et al., 20203	8
Table 2.5 - Outline of the most used LBL fabrication methods along with their advantages	
and disadvantages:4	6
Table 2.6 - Examples of common polyelectrolytes used in the layer-by-layer technique5	
Table 3.1 - Outline of the concentrations of acid catalysts and corresponding pH used in the	-
following experiments	4
Table 3.2 - Experimental conditions on hydrothermal synthesis of the graphitic precursor	
using SCG at a fixed temperature of 200oC and ratio of spent ground coffee to water of 1:30	
wt/vol6	
Γable 3.3 - Pre-treatment conditions applied during ultrasonic pre-treatment of SCGs over 90	
minutes pre-treatment time6	
Table 3.4 - Sample codes of each microwave carbonisation according to temperature (prefix	
and time (suffix)7	
Table 3.5 - Conditions of the polyelectrolyte solutions used in the CaP template	
functionalisation7	7
Table 3.6 - Outline of the different chitosan/alginate layer-by-layer test conducted7	9
Table 3.7 - Measurement times of drug release8	O
Table 3.8 - Outline of particles investigated with the acid recovery method8	4
Table 3.9 - Outline of particles investigated with the supernatant recovery method8	5
Table 4.1 - Summary of the XPS results of the precursors synthesised by a hydrothermal	
oretreatment9	6
Table 4.2 - Outline of all XPS results from each carbon dots sample obtained after nitric acid	
oxidation10	5
Table 4.3 - Quantum yield of each carbon dot sample11	4
Table 4.4 - The XPS results of the ultrasonic pretreatment for each sample obtained after 90	
minutes12	
Table 4.5 - Average size of carbon dots summariesd from TEM analysis12	8
Table 4.6 - Mass yield of carbon dots obtained after purification with dialysis and freeze-	
drying129	
Table 4.7 - QY data for all carbon dot samples13	1
Table 4.8 - Outline of all XPS results from each carbon dot sample obtained after HTC13	3
Table 4.9 - The emission wavelengths and corresponding intensity (WL - I) at various	
excitation wavelengths for each carbon dot reaction parameter tested14	
Table 4.10 - Table to outline the Quantum yield against the reaction parameters14	
Table 5.1 - ζ-potential and size values of the nanoparticles obtained using a peristaltic pump	
with different drying methods15-	4

Table 5.2 - SEM ImageJ analysis of the size of the nanoparticles obtained with the peristal	ltic
pump and using different drying methods	157
Table 5.3 - ζ-potential and DLS measurement of functionalised calcium phosphate	
nanoparticles with polyelectrolyte solutions of different concentrations	158
Table 5.4 - XPS data for raw alginate and chitosan for comparison to deposited layers. Toլ	p –
wide survey scan, bottom – C 1s, N 1s, O 1s	163
Table 5.5 - Summary of the XPS data for all scans of each layer of the sample containing n	10
drugs. Top – wide survey scan, bottom – C 1s, N 1s, O 1s	166
Table 5.6 - TEM average particle of the layer-by-layer process with no drugs size as measu	ured
by ImageJ	172
Table 5.7 - Summary of the XPS data for each layer sample of the DOXO loaded sample. T	ор
– wide survey scan, bottom – C 1s, N 1s, O 1s	176
Table 5.8 - Summary of the XPS data for each layer sample of the DAX loaded sample. Top	p –
wide survey scan, bottom – C 1s, N 1s, O 1s	176
Table 5.9 - Summary of the XPS data for each layer sample of the loaded sample loaded v	vith
DOXO and DAX. Top – wide survey scan, bottom – C 1s, N 1s, O 1s	177
Table 5.10 - Average particle size per layer of each sample as measured using ImageJ fron	n
the TEM images	181
Table 5.11 - Encapsulation efficiency for each individual drug in all the different sample ty	
	181
Table 5.12 - Summary of ζ-potential data of calcium phosphate nanoparticles with differe	ent
synthesis	193

Abbreviations

AA – Alginate
ACD – Amorphous Carbon Dot
AT – Acid Test
CaP - Calcium Phosphate
CD – Carbon dot
CH – Chitosan
CNTs – Carbon Nano Tubes
CS - Chondroitin Sulphate
CT – Computed Tomography
CTC – Circulating Tumour Clusters
DAX - Docetaxel
DI – Deionised
DMEM - Dulbecco's Modified Eagle Medium
DNA – Deoxyribonucleic acid
DOXO – Doxorubicin
EDT - Ethanedithiol
EGFR Ab - Epidermal growth factor receptor monoclonal antibodies
EPR – Enhanced permeability and retention
EPSRC – Engineering and Physical Sciences Research Council
FBS – Foetal Bovine Solution
FT-IR – Fourier Transform Infrared
GOx - Glucose Oxidase
GCD – Graphene carbon Dots
GQD - Graphene quantum dots
HA – Hyaluronic Acid
HTC – Hydrothermal Carbonisation
HR-TEM – High Resolution Transmission Electron Microscopy
LBL – Layer-by-layer
MCE – Mixed cellulose ester
MRI – Magnetic Resonance Imaging
MW -Molecular Weight

MWCO - Molecular weight cut off NIR - Near Infrared NMP - Nanomagnetic Hydrogel ND – Nano Dumbbell NC - Nanocapsule NP - Nanoparticle OS - Osteosarcoma P - Precursor PA - Photoacoustic PAA - Polyacrylic acid PAH - Poly(allylamine hydrochloride) PBS - Phosphate-buffered saline PDADMAC - Poly(diallyldimethylammonium chloride) PDT- Photodynamic Therapy PEG - Polyethylene glycol PEI - Polyelethylenimine PET – Positron Emission Tomography PGA - Polyglycolide PGG - Poly(l-γ-glutamylglutamine) PLL - Poly-L-Lysine PRP- Platelet-rich plasma PSS - Poly(sodium 4-styrenesulfonate) PT – Pretreatment PTT - Photothermal Therapy PVP - Polyvinylpyrrolidone PVS - PolyVinyl Sulphate QD/SCQD - Quantum dot/Semiconductor quantum dot QLED - Quantum dot light-emitting diode

QY - Quantum yield

RNA - Ribonucleic acid

RPM – rotations per minute

SA - Sulphuric acid

SCG - Spent coffee grounds

SAB - Sodium acetate buffer

SEM - Scanning Electron Microscope

SMX - Sulfamethoxazole

SPIO – Superparamagnetic iron oxide

SWCNT – Single walled carbon nanotubes

SWNH – Single walled nanohorn

TA - Tannic acid

TEM - Transmission Electron Microscope

TT – Time test

US – Ultrasound

UCNP – Up-conversion nanoparticles

UV – Ultraviolet

UV-Vis – Ultraviolet and visible (spectroscopy)

XPS – X-Ray Photoelectron Spectroscopy

ZNP – Zien nanoparticles

List of Publications

Biomass-Based Carbon Dots: Current Development and Future Perspectives

Thomas C. Wareing, Piergiorgio Gentile, and Anh N. Phan ACS Nano 2021, 15, 10, 15471–15501, Publication Date: September 24, 2021 https://doi.org/10.1021/acsnano.1c03886

Characterization of the Shells in Layer-By-Layer Nanofunctionalized Particles: A Computational Study

Emillio Barchiesi, Thomas Wareing, Liam Desmond, Anh N. Phan, Piegorgio Gentile, and Giuseppe Pontrelli

Frontiers in Bioengineering and Biotechnology 2022, 10:888944. Publication date: June 30, 2022

https://doi.org/10.3389/fbioe.2022.888944

Effect of Operating Parameters on the Properties of Carbon Dots from Spent Coffee Grounds

Thomas C. Wareing, Anh N. Phan, Piergiorgio Gentile, and Fabio Cucinotta Journal of Technical Education Science 2023., (74), 56–64. Publication date January 16, 2023 https://doi.org/10.54644/jte.74.2023.1336

In production

research paper based on chapter 4 – Three different synthesis of carbon dots from spent coffee grounds.

research paper based on chapter 5 – Synthesis of carbon dot functionalised layer-by-layer capsules on calcium phosphate templates for drug delivery and imaging.

Research paper based on the European space agency fly your thesis project - Gravityscope: microscopy with microfluidics in microgravity.

List of conferences/lectures

SagE PGR conference, Newcastle University, June 2020 - Poster

SagE PGR conference "From the Faculty, For the Future" Newcastle University, July 2021, internal conference - Presentation

Insights public lecture "New voices on science, agriculture and engineering", Newcastle University May 2022, Presentation – Team SUGAR fly your thesis project.

SagE PGR conference, Newcastle University, July 2022, - Poster

GTSD 2022 - The 6th international conference on green technology & sustainable development, July 2022 - Presentation

Chapter 1. Introduction

1.1 Background

Osteosarcoma is a type of bone cancer that most commonly effects children and teenagers. Prognosis and treatment options of osteosarcoma depends upon the timeframe of diagnosis, tumour placement and age of patient (ACS, 2020). The main treatment options include surgery, radiotherapy and chemotherapy. Most treatments are used in combination and have significant side effects and life altering consequences, for example surgery can include amputation (MayoClinic, 2023). The biggest challenges in treating osteosarcoma are resistance to chemotherapy and lung metastasis (Gaspar et al., 2018; Mohr et al., 2024). New and more targeted treatments may help to address these issues. Such as, immunotherapy which uses the body's immune system to fight primary osteosarcoma and its metastasis (Yifan et al., 2020) that can work alongside or without chemotherapy, examples of which are immunomodulation, vaccination, and precision medicine (Rajiv Supra, 2023).

Nanotheranostics is relatively new research area that has potential for developing treatments for cancer. Nanotheranostics involves the use of nanoparticles to deliver imaging and therapeutic agents directly to cancer cells (Ladju RB, 2022). This allows for earlier and more accurate diagnosis of cancer and allows treatments to be targeted to specific cancer cells and could minimise the side effects on healthy tissues (Chavda et al., 2023). One major challenge in the field of nanotheranostics is the development of nanoparticles that can be safely used in humans. These nanoparticles need to be non-toxic and bypass biological barriers, so they aren't cleared from the body before they have had a therapeutic effect. (Kievit and Zhang 2011). Some of the most promising nanoparticles being developed for cancer nanotheranostics include liposomes, dendrimers, gold nanoparticles, and iron oxide nanoparticles (Mitchell et al., 2021).

There a few examples of research being conducted for the treatment of osteosarcoma using nanotheranostic methods. For example, Kong et al (Kong et al., 2022) developed multifunctional nanotheranostic device for diagnosing and treating osteosarcoma and associated osteolysis. The device was a dual peptide-engineered gadolinium-doped polydopamine particle. The peptides used were the D8 peptide, which facilitated bone targeting, and the RGD2 peptide which enabled inhibition of osteoclasts and tumour targeting. Additionally, the Gd doped polydopamine particle scaffold allowed for tumour

imaging via a combination of magnetic resonance and photo acoustic imaging modalities. The device effectively suppressed the growth of bone tumours and associated osteolysis in an osteosarcoma model. These findings present a promising nanoplatform for the treatment of malignant bone tumours and tumour-induced osteolysis. However, the use of gadolinium ions is concerning since they are highly toxic within mammals (Davies et al., 2022). It was shown in this research that the device and some larger components are biocompatible and do not show a toxic effect in mice models. This is positive; however, it is not outlined by the researchers how this system is expected to be metabolised and cleared from the body, or how stable these nanoparticles are. These concerns would need to be fully addressed before clinical use as release of gadolinium ions into the body could cause toxicity and other health problems. Creating a device from non-toxic and biocompatible materials would mitigate these kinds of issues.

Stability and release of metal ions was analysed by Cipreste et al. (Cipreste et al., 2018) when they developed hydroxyapatite/tenorite (CuO) nanocomposites as a potential theranostic system for osteosarcoma. They found that CuO crystallites can grow with hydroxyapatite crystallites to form a bi-phase nanocomposite with theranostic properties. XPS analysis and stability assays revealed that hydroxyapatite-CuO is stable, with no release of copper or CuO from the matrix. Functionalisation with folic acid resulted in a stable interaction, enhancing its potential for targeted osteosarcoma treatment. It was shown that neutron activation enabled production of ⁶⁴Cu suggesting that the activated and folic acid functionalised device could be used for the theranostic treatment of osteosarcoma and diagnosis through the release of radiation and drugs. This is a good premise for a nanotheranostic device to treat osteosarcoma, however this paper does not outline any evaluation of this, just a detailed suggestion of application for the material. To validate this potential, cell tests, evaluating the effectiveness of both the drug and radiation release for imaging and therapeutic effect need to be conducted.

A more thorough investigation was conducted by Martins et al. (Martins et al., 2024), they outlined the synthesis of multifunctional platforms that combined polymetric nanoparticles with a superparamagnetic iron oxide nanoparticles and curcumin. The synthesised devices exhibited superparamagnetic behaviour at room temperature and were capable of magnetic hyperthermia applications. These devices also demonstrated a high fluorescence intensity in

the blue/green region, which persisted with internalisation in human osteosarcoma cells (OSAS2). They also show remarkable biocompatibility, with no observed cell toxicity. Given their demonstrated superparamagnetic behaviour, high fluorescence intensity, and excellent biocompatibility, the devices hold promising potential as versatile tools for cell tracking and as platforms in nanotheranostics. This paper is a great example of a nanotheranostic device to treat and diagnose osteosarcoma. The authors were very thorough in analysing both the optical and magnetic properties of the device, both are which are needed to properly investigate the potential for use in application, this is the sort of investigation that will be conducted in this thesis. However, some of materials used in fabrication have some toxicity and could potentially cause harm once the device is metabolised by the body. For example, it was found that superparamagnetic iron oxide nanoparticles have the potential for toxicity (Singh et al., 2010). To properly negotiate the limitations of nanotheranostics in relation to potential toxicity, it is best to use components that are biocompatible to minimise this risk.

This project investigates the use of carbon dots produced from biomass, e.g. from spent coffee grounds, in conjunction with a LBL capsule fabricated from natural polymers and calcium phosphate nanoparticle templates chosen for their biocompatibility (Elizarova & Luckham, 2016; Urch et al., 2009). Synthesised CDs will be incorporated into the nanocapsules along with anticancer drugs to create a device which will be tested against osteosarcoma cell lines to investigate its efficiency as a nanotheranostic agent. Currently there is no literature on using CDs in conjunction with the LBL technique to create a nanotheranostic device for cancer imaging and treatment.

Carbon dots (CDs) have potential in nanotheranostics as an imaging agent. They are carbon nanoparticles that are smaller than 10nm and have either a graphitic or amorphous structure (Das et al., 2018). They have strong photoluminescence, tuneable emission wavelength, high solubility, and biocompatibility, making them suitable for application in bioimaging (Namdari et al., 2017; Zuo et al., 2016). The mechanism for their photoluminescence is not fully understood but it has been suggested that it originates from the quantum confinement effect, edge effects, surface defects and passivation of emissive traps (Namdari et al., 2017).

CDs can be synthesised via "top-down" and "bottom-up" approaches. Top-down methods involve reducing a larger material down to a nanoparticle using harsh chemicals but result in

higher yield, while bottom-up methods use smaller building blocks to create a nanoparticle (Zuo et al., 2016) and offer more control over size and morphology but can be more complex and time-consuming (Abbas et al., 2018). There have been numerous studies outlining the synthesis of CDs using biomass as a carbon source because of its advantages over lab bought chemicals such as reduced cost, greener synthesis, and increased biocompatibility (Tejwan et al., 2019) (Radnia et al., 2020). Although CDs have great potential for application in imaging there are still limitations to address including low quantum yield (QY) (Song et al., 2019) low production yield (Park et al., 2014) and lack of understanding of photoluminescent mechanisms (Namdari et al., 2017).

The layer-by-layer (LBL) technique has potential for use in nanotheranostics as a drug delivery method. The technique is a method for building up thin films with precise control over their thickness and composition by alternately depositing oppositely charged materials onto a substrate forming a thin film by self-assembly (Lipton et al., 2020). The technique is simple and inexpensive and can be carried out in ambient temperature and pressure (Díez-Pascual & Rahdar, 2022). A wide range of materials can be used in LBL films and different materials will impart different properties onto films and can be tuned by adjusting the number of layers, concentration of solutions, or other fabrication conditions (Elizarova & Luckham, 2018). Polyelectrolytes are one of the most used materials in LBL films. They are macromolecules with charged groups along their chains, making them suitable for electrostatic interactions. Choosing polyelectrolytes that are derived from nature is advantageous because they are renewable and biocompatible and have application in biomedical application (Criado-Gonzalez et al., 2021; Wohl & Engbersen, 2012). However, selection of polymers must be done carefully, as even though naturally occurring polyelectrolytes are biocompatible, they can still invoke immune responses from cell systems (Tripathi et al., 2023).

The LBL deposition method offers a diverse range of drug delivery. LBL coatings improve the colloidal stability of nanoparticles, making them suitable for *in-vivo* administration. Core-shell nanocapsules for drug delivery are created by depositing layers onto particulate template cores (Caruso, 2004; Peyratout & Dähne, 2004). The choice between templates depends on the desired properties for loading and releasing cargo in various applications (Parakhonskiy et al., 2014). Although the LBL technique is widely used, there are still gaps that need to be addressed such as limited scalability, compatibility issues and limited control over therapeutic release.

1.2 Impact

The impact of this research is wide reaching and touches several areas of research, as outlined above. This project has significant impact on the field of nanotheranostics because it is such a rapidly expanding field, and this thesis will be a significant addition to the current research with a device utilizing the functionalisation of natural polymer LBL capsules with biomass-based CDs. A combination of materials that has not been extensively researched previously.

The project overall will have an impact on scientists working within the fields of CDs and the LBL technique as this project provides perspectives and valuable insight in the suitability and refinement of these techniques for the purposes of nanotheranostics.

This project is intended to assist future scientists develop carbon dots that are more easily tuned to application by investigating the effect of changing synthesis parameters on the properties of the resulting CD. This type of investigation is not always outlined in literature, as teams usually focus on the application of the carbon dots produced by using specific conditions.

Lastly, this project could indirectly impact the public, especially cancer patients and doctors, because this research provides a starting point that can be further investigated in the future. The result of this future research may allow the simultaneous diagnosis and treatment of different tumours using nanoparticles, which would be another weapon in the arsenal that we can use to fight cancer.

1.3 Aims and objectives.

This PhD project aims to produce a nanotheranostic device capable of drug delivery and imaging of osteosarcoma with the combination of biomass-based CDs and the LBL technique. The following objectives are to be carried out to achieve this goal:

- 1. To synthesise biomass-based CDs and investigate how changing synthesis parameters affects the properties of CDs.
- 2. To investigate the fabrication of a LBL capsule using different combinations of biocompatible polymers.

3. To create a device, using the combination of CD and the LBL technique, specifically tailored to deliver drugs to, and image, osteosarcoma.

1.4 Thesis layout

Chapter 1 – Presents a brief background and the motivation behind this research. This chapter also outlines the aims and impact of the research.

Chapter 2 – An in-depth review of the background literature; Osteosarcoma, the treatment of cancer using nanotheranostics, synthesis methods, properties, and applications of CDs and the LBL process.

Chapter 3 – The methodology related to the synthesis of CDs, LBL capsules and the analysis of the products.

Chapter 4 – Results and discussion of the investigation of CD synthesis.

Chapter 5 – Results and discussion of the investigation of the LBL capsule synthesis on calcium phosphate nanoparticle templates.

Chapter 6 – General discussion, conclusions of the findings of this work and a proposal of future work related to this project.

Chapter 2. Literature review

Osteosarcoma (OS) poses a significant challenge in the realm of oncology. As researchers strive to enhance therapeutic strategies, the intersection of nanotechnology and medicine has paved the way for innovative approaches in the form of nanotheranostics. This burgeoning field focuses on the development of nanoscale therapeutic and diagnostic agents, allowing for targeted drug delivery and real-time monitoring of treatment responses. In the context of OS, nanotheranostics holds promise for improving treatment outcomes by providing a platform for precision medicine and minimising off-target effects.

This review introduces osteosarcoma and the current treatment methods. Then, it outlines the field of nanotheranostics delving into how both the drug delivery and imaging sides of the field are currently pursued paying close attention to cancer therapeutics and diagnosis, after which the combination of techniques is investigated, and several examples are outlined and reviewed.

Next the field of CDs is outlined. This section focuses on their photoluminescent mechanisms, synthesis methods, functionalisation and application, paying close attention to how biomass-based carbon dots might address some limitations currently seen in the field especially with application of bioimaging with potential future work.

This review then focuses on the field of the LBL technique, exploring different fabrication methods, materials and the application of the LBL technique in the context of drug delivery with micro and nanocapsules.

Finally, this review investigates the potential for a combination of the techniques as seen in current literature to show that there is a gap for a nanotheranostic device based on a biomass CD functionalised LBL nanocapsule.

2.1 Background of Osteosarcoma and the current treatment strategies

Each year, 3.4 million people are diagnosed with OS (Misaghi et al., 2018) (Figure 2.1). OS is a form of bone cancer that is particularly common in young people (NHS, 2021). Prognosis of an OS diagnosis depends on factors such as tumour placement, stage, and the age of the patient (ACS, 2020). The development of bone cancer is still unknown. However risk factors include;

previous exposure to radiotherapy, Paget's bone disease (which disrupts the normal cycle of bone renewal) and Li-Fraumeni (A rare genetic condition which presents as a fault in a gene that prevents cancerous cell growth) (NHS, 2021).

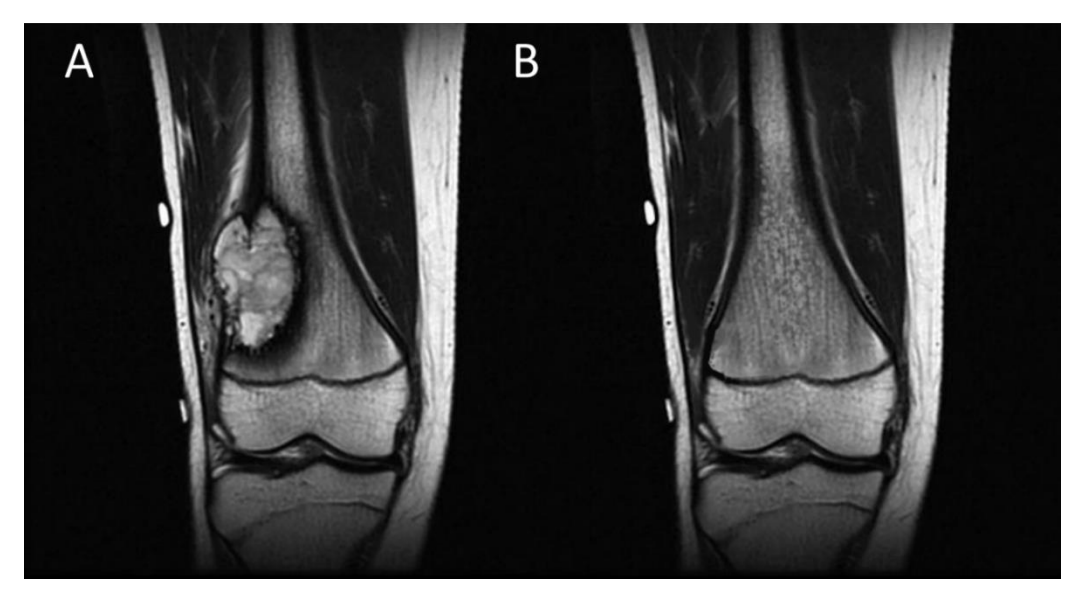


Figure 2.1 - A) MRI Image of osteosarcoma in a knee - Case courtesy of Dr Frank Gaillard, <u>Radiopaedia.ora</u>, rID: <u>7527</u> (Gaillard, 2023), B) Image of a knee with osteosarcoma digitally removed to simulate "healthy knee" for comparison.

Treatment options for bone cancer depend on the type and stage of the cancer and other factors such as age and health. The main treatment options include (MayoClinic, 2023);

- Surgery is used to remove the entire tumour; amputation is sometimes required since
 the fact that bone cancers can get very large or are in a complicated area. Surgery can
 cause pain, swelling, and numbness in the affected area, and may require a long recovery
 period.
- Radiation therapy uses high-powered beams of energy, such as X-rays, to kill cancer cells
 prior to, after, or instead of surgery. For people with advanced bone cancer, radiation
 therapy may help control signs and symptoms, such as pain.
- Chemotherapy uses strong anti-cancer drugs to kill cancer cells. It is generally not very
 effective for chondrosarcoma, but it is an important part of treatment for OS and Ewing
 sarcoma.

Treatment options often include a combination of techniques. Although, while effective, they can also have significant side effects. Research is ongoing to develop new and more targeted treatments e.g. immunotherapy (immunomodulation, vaccination and precision medicine),

which uses the body's immune system to fight cancer (Rajiv Supra, 2023). Immunomodulation involves activating components of the innate immune system, leading to the enhancement of natural killer cells, monocytes, and macrophages to target tumour cells, which have been clinically trialled (Yoshida et al., 2020). The utilisation of cancer vaccines (peptides, deoxyribonucleic acid (DNA), ribonucleic acid (RNA), and tumour antigens) has been explored extensively to induce anti-tumour effects by stimulating the immune response within patients. (Pollack et al., 2017). However, the effectiveness of this therapy is low due to the presence of immunosuppressive molecules within the tumour microenvironment. Multiple approaches need to be developed to overcome this resistance (Liu et al., 2022).

Precision medicine uses sequencing techniques to improve the understanding of OS, allowing for comprehensive genomic analysis that can reveal crucial prognostic biomarkers and inform personalised treatment strategies. (Morganti et al., 2019; Tirtei E, 2021). The application of this approach to rare cancers like OS is still in its early stages with many challenges to overcome, such as the rarity of the disease, unique technical issues related to bone tissue, complex genomic landscape, and age distribution (Tirtei E, 2021).

Bone cancer is rare but affects children more than adults with potentially life changing or deadly consequences. While these treatments can have significant side effects, they are generally well-tolerated and can be effective in treating bone cancer. Ongoing research is focused on developing new and more targeted treatments, which may further improve outcomes for patients. One such field that may help in the treatment and diagnosis of OS is nanotheranostics (Ravichandran & Rengan, 2020).

2.2 Nanotheranostics and cancer treatment

Nanotheranostics is an emerging field of medicine that combines the use of NPs (delivering imaging agents) with diagnostic and therapeutic drugs for the simultaneous diagnosis and treatment of diseases (Ladju RB, 2022). It is important in cancer treatment because (i) it allows for earlier and more accurate diagnosis of cancer; (ii) it can improve the effectiveness of current cancer treatments while minimizing side effects and drug usage and (iii) it can be used to monitor the response of cancer cells to treatment (Chavda et al., 2023). The field of nanotheranostics has been rapidly growing in recent years focusing on the development of new NP-based diagnostic and therapeutic agents for a wide range of diseases including cancer

(Alshehri S, 2021). Some of the most promising NPs being developed for cancer nanotheranostics include liposomes, dendrimers, gold NPs, and iron oxide NPs (Mitchell et al., 2021).

2.2.1 Nanoparticle-based imaging

The utilisation of NPs in imaging applications holds significant promise for advancing cancer diagnostics, therapeutics, and treatment management. In both biomedical research and clinical settings, NPs can function as labels or carriers, facilitating the monitoring of drug delivery and serving as imaging agents to enhance contrast. They contribute to improved signal sensitivity and specificity for *in-vivo* imaging of molecular and cellular processes (Liu & Grodzinski, 2021). Figure 2.2 demonstrates some imaging techniques that can utilise NPs for the imaging of cancer. Table 2.1 compares the advantages and disadvantages.

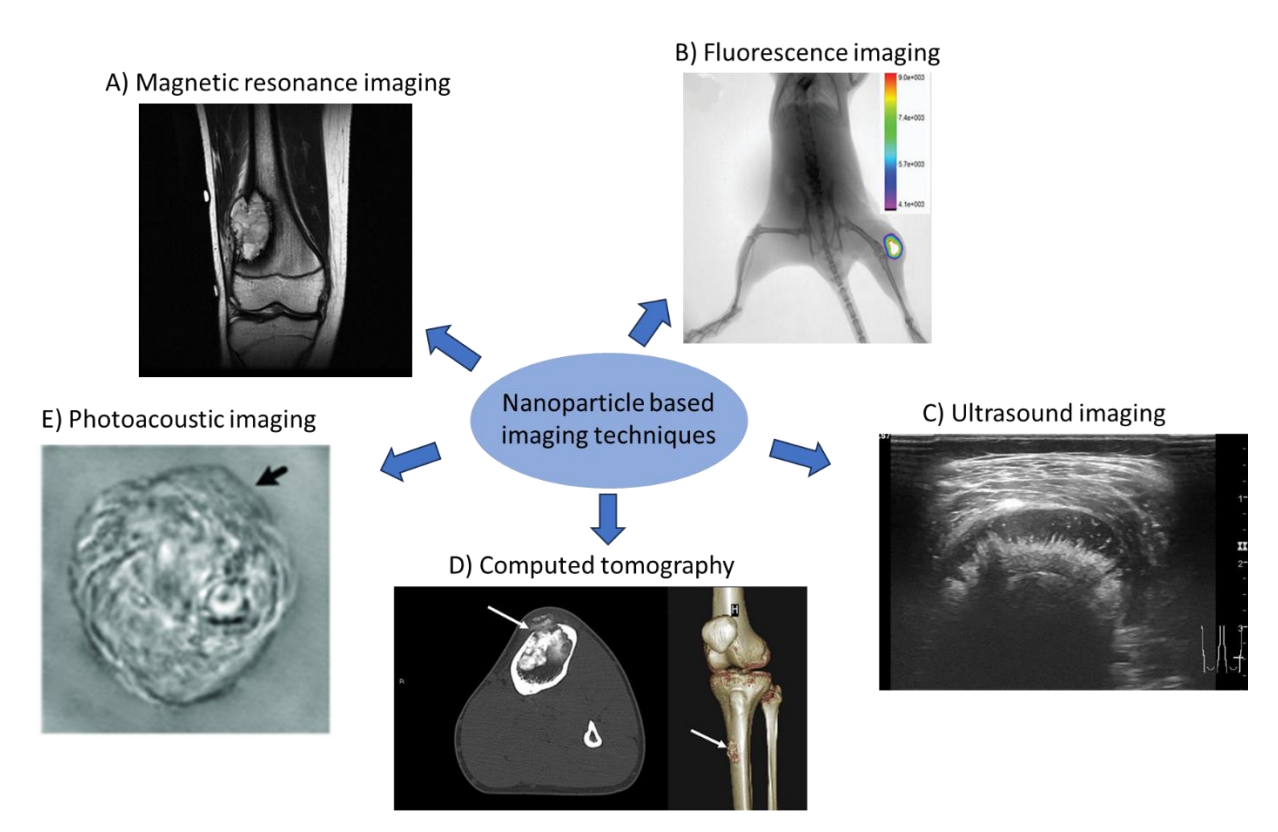


Figure 2.2 - Examples of nanoparticle-based imaging for osteosarcoma and other cancers in tissues. Adapted from references A) - Case courtesy of Dr Frank Gaillard, <u>Radiopaedia.org</u>, rID: <u>7527</u> (Gaillard, 2023), B) - (Zhou et al., 2020), C) - Case courtesy of Dr Maulik Patel, <u>Radiopaedia.org</u>, rID: <u>67572</u> (Patel, 2019), D) - (Kantzos et al., 2024), E) - (Jun et al., 2011).

Fluorescence imaging is a popular technique used for imaging cells and tissues. Fluorescent NPs such as quantum dots are often used for fluorescence imaging as they emit bright and

stable fluorescence when excited with light. The fluorescence can be detected using a fluorescence microscope or a confocal microscope. Fluorescence imaging is widely used in biology and medicine for applications such as tracking cells, monitoring drug delivery, and studying biological processes (Wolfbeis, 2015). NPs offer valuable advantages in overcoming the potential limitations of fluorescence imaging, both by improving the properties of currently used fluorescent dye molecules such as boosting local concentrations or fully replacing the dyes by being engineered to minimise issues like blinking and photobleaching effects. Consequently, there has been considerable effort invested in developing fluorescent NP platforms (Han et al., 2019).

Magnetic resonance imaging (MRI) is a non-invasive imaging technique that provides high-resolution images of internal structures (Dominguez, 2021) using iron oxide NPs as contrast agents for MRI. MRI is a powerful tool in clinical medicine for diagnosing various diseases, including cancer, cardiovascular diseases, and neurological disorders (Haris et al., 2015).

Ultrasound (US) imaging utilises sound wave to produce images of structures within the body (Mayo-Clinic, 2023). Nano and microparticle contrast agents have enabled the diagnosis and monitoring of pathological processes at the molecular level. Common contrast agents include micron-sized, gas-containing microbubbles that are functionalised to selectively bind to molecules expressed on inflamed or angiogenic vascular endothelial cells (Abou-Elkacem et al., 2015).

Computed tomography (CT) imaging is a medical imaging technique that uses X-rays to produce high-resolution images of internal structures using gold NPs due to their high X-ray absorption. CT imaging is widely used in clinical medicine for diagnosing diseases such as cancer, cardiovascular diseases, and neurological disorders (Cormode et al., 2014; Griffeth, 2005).

Photoacoustic (PA) imaging is a non-invasive imaging technique that combines the benefits of optical and US imaging using a laser to illuminate nanoparticles, such as gold NP and carbon nano tubes (CNTs), inside tissue, which causes the tissue to emit US waves. These waves can be detected by an US detector and used to create an image (Lemaster & Jokerst, 2017; L. Li et al., 2020).

Table 2.1 - Advantages and disadvantages of different imaging techniques (Arms et al., 2018; Chang Xu, 2021; Pham et al., 2015)

Imaging Modality	Magnetic Resonance Imaging	Fluorescence Imaging	Ultrasound Imaging	Photoacoust ic Imaging	Computed Tomography
Advantages	Deep penetration,	High sensitivity/ resolution,	Safe, Deep	High resolution,	High contrast resolution,
	High spatial resolution,	Non-invasive	penetration, Real-time	3D imaging	3D dataset,
	Safety	Low cost	dynamic imaging		
Disadvantages	Signal decays as the material degrades,	Light bleaching, Limited	Short life and large size of contrast agents	Interference from signals in the blood,	Patient exposed to ionising radiation,
	Signal intensity not linearly proportional to its concentration.	optical penetration - Superficial imaging,		Imaging only available where the laser can penetrate	Expensive equipment required,
	Long acquisition time and claustrophobic				Iodinated contrast material

NPs (size ranging from 1 to 100 nm), have unique physical, chemical, and optical properties that make them attractive for various biomedical applications including imaging (Nune et al., 2009). There have been many examples of NPs used in the diagnosis of cancer:

Quantum Dots (QDs) are semiconductor metal (CdSe, CdTe, ZnSe and InAs (Chan et al., 2002)) based nanomaterials that emit bright and stable fluorescence when excited with light with a narrow emission spectrum, lending them ideally for multiplex imaging (Singh et al., 2020). An example of QDs used in cancer detection was outlined by Yang et al. (Yang et al., 2011). QDs were incorporated with epidermal growth factor receptor monoclonal antibodies (EGFR Ab) to develop a probe (QD800-EGFR Ab) for *in-situ* and *in-vivo* imaging of head and neck cancer using this QD800-EGFR Ab probe. Quantum dots have limitations in terms of both solubility and toxicity (Gidwani et al., 2021), to address this Mansur et al (Mansur et al., 2017) used a carboxymethylcelluose surface modifier on ZnCdS quantum dots to improve biocompatibility and solubility. These nanoconjugates were used to bioimage OS cancer cells.

Quantum dots offer numerous advantages over conventional fluorophores like organic dyes, fluorescent proteins, and lanthanide chelates. One major advantage is their wide excitation spectrum, allowing excitation to occur over a broad range of wavelengths. Additionally, quantum dots exhibit a narrow emission spectrum, and their emission wavelength can be precisely controlled by adjusting the size, composition, and surface coating of the NPs. This control allows for tuneable emission wavelengths across a wide range, from ultraviolet to infrared (Naseri et al., 2018).

Magnetic nanoparticles are nanoparticles which can be manipulated by a magnetic field. Iron oxide NP, which have a size between 1 and 100nm (Buzea et al., 2007), are used for MRI, which is a non-invasive imaging technique that provides high-resolution images of tissues. They are commonly coated with biocompatible materials such as dextran or polyethylene glycol (PEG) to make them stable and reduce toxicity (Gul et al., 2019). Iron oxide NPs coated with PEG were used intravenously for iron deficiency treatment while possessing contrast agent properties for MRI by Lazaro-Carrillo et al. (Lazaro-Carrillo et al., 2020). Iron oxide NPs coated with PEG are suitable for biomedical application due to their biocompatibility. The effective uptake of these NPs by tumour cells and mouse leukaemia virus transformed macrophages confirms their potential as valuable tools for cancer treatment, including magnetic hyperthermia and drug delivery, as well as for longitudinal imaging studies. Considering the growing interest in non-invasive diagnostic assays that rely on real-time and long-term tracking and monitoring of labelled cells such as tumour-associated macrophages, these biocompatible NPs serve as a powerful tool for various biomedical applications. Chen et al. (L. Chen et al., 2019) developed a bispecific molecular nanoprobe with a magnetic iron oxide core (22.17 nm) and a biocompatible shell. The nanoprobe exhibited favourable magnetic properties and demonstrated long-term stability during use and in storage. This combined strategy led to remarkable contrast enhancement, highlighting its potential for enhanced cancer diagnosis and treatment.

In comparison to current contrast agents such as gadolinium ions, superparamagnetic iron oxide (SPIO) NPs offer several advantages, such as tuneable size and shape, potential for surface modification, and high sensitivity and effectiveness at low concentrations due to their superparamagnetic property. (Naseri et al., 2018).

Gold Nanoparticles have unique optical properties that make them ideal for imaging applications. They can absorb and scatter light very efficiently, making them useful for various

imaging modalities, such as PA imaging and CT. Gold NPs can also be functionalised with biomolecules such as antibodies or peptides, which allow them to target specific cells or tissues (Wu et al., 2019). Gold NPs have specific advantages owing to their excellent photothermal conversion efficiency, stable imaging ability, and biosafety. The inert characteristic of gold NPs has a minimal side-effect on cell function (Chang Xu, 2021).

Doxorubicin (DOXO) conjugated radiolabelled gold NPs using citraconic anhydride were used for positron emission tomography (PET) tumour imaging. Under the acidic conditions found in tumour cells, the citraconic anhydride linkage in DOXO-AuNP was cleaved releasing DOXO. This research offers valuable insights for the development of drug delivery systems and sheds light on the potential use of radioligands for tumour detection through PET imaging (Yim et al., 2021). Zhang et al. (Zhang et al., 2009) evaluated the ability of systemically administered PEGylated gold NPs as a contrast agent for *in-vivo* tumour imaging with PA imaging. This treatment has potential applications in the image guided therapy of superficial tumours such as breast cancer, melanoma, and Merkel cell carcinoma.

Carbon Nanotubes are tubular structures synthesised from a graphite source using synthesis techniques such as laser ablation (Jha et al., 2020) and arc discharge (Kaur et al., 2019). They have diameters between 0.7 and 3nm and have lengths of up to several centimetres (Naief et al., 2024). They have high surface area to volume ratio and unique electrical and optical properties that make them suitable for various imaging applications. CNTs can be functionalised with biomolecules to target specific cells or tissues, and they can also be used for fluorescence imaging and PA imaging (Secchi et al., 2016). Avti et al. (Avti PK, 2012) investigated the efficiency of multiscale PA microscopy of tissues using single walled carbon nanotubes (SWCNTs). It was found to be an effective method with a detection sensitivity of picogram levels of SWCNTs with scalable penetration and resolution. In 2019 Ceppi et al. (Ceppi et al., 2019) reported the real time fluorescent imaging of ovarian tumours in mice during resection surgery using SWCNTs, which increased post operative survival rates which shows potential future application in humans. In 2020 Moreno-lanceta et al. (Moreno-Lanceta et al., 2020) reported single walled carbon nanohorns-based (SWNH) smart nanotheranostic: From phototherapy to enzyme-activated fluorescence imaging-guided photodynamic therapy. Single walled nanohorns are conelike graphene sheets similar to other carbon NPs such as nanotubes and fullerenes (lijima et al., 1999). The nanosystem is SWNH loaded with the fluorescent dye (IR-808) conjugated with Hyaluronic acid (HA) (HA-IR808). It takes advantage of the mediated endocytosis of a multifunctional cell surface adhesion receptor (CD44), that is a regulator of progression and metastasis of cancer cells (Senbanjo & Chellaiah, 2017), and the enhanced permeability and retention (EPR) effect, resulting in the accumulation of the SWNHs predominantly in tumour tissue. Within cancer cells, the overexpressed endogenous hyaluronidase disassembles the device release the dye which exhibits a strong fluorescent signal, serving as an indicator of viable tumour cells. Subsequent laser exposure effectively kills the remaining tumour cells. This research is a great use of the intracellular enzyme response to create a nanotheranostic system using fluorescence imaging guided photodynamic therapy, the findings lay the groundwork for the future development of smart and highly efficient nanotheranostics for tumour ablation.

Upconversion Nanoparticles (UCNPs) are made of rare-earth elements such as ytterbium and erbium, which can convert low-energy photons into high-energy photons. This property allows them to emit light in the visible and near-infrared regions of the electromagnetic spectrum, which makes them ideal for imaging applications. UCNPs can also be functionalised with biomolecules to target specific cells or tissues (Chen et al., 2014). Core-shell structured UCNPs were used to guide cancer treatment by converting near-infrared (NIR) light into UV light to activate a trans-platinum (IV) pro-drug with simultaneous trimodality imaging (Dai et al., 2013).

NP-based imaging has emerged as a promising approach for various biomedical applications. Table 2.2. summarises the advantages and limitations of each NP listed above. The efficacy of NP-assisted imaging is contingent on factors such as penetration depth and the photothermal conversion efficiency of contrast nanoagents. Therefore, advancing the development of nanomaterials with improved near-infrared responsiveness and enhanced biocompatibility represents a prospective avenue for NP-based imaging (Alrushaid et al., 2023; Chang Xu, 2021; Chapman et al., 2013; Naseri et al., 2018).

Table 2.2 - Summary of the advantages and disadvantages to nanoparticles used in imaging.

Nanoparticle	Imaging type used	Advantages	Limitations	refs
Semiconductor Quantum Dots	Fluorescence	 highly sensitive excellent contrast in-vitro and in-vivo convenience of use photostable deep tissue penetration 	- Slow elimination from the body causes accumulation - heavy metals are cytotoxic	(Mohammadi et al., 2022; Radenkovic et al., 2016)
Magnetic NPs	MRI	 chemical inertness high compatibility to living tissues excellent stability ease of surface modification physiochemical and magnetic characteristics 	 high surface energy causes aggregation interact with serum proteins 	(Dongsar et al., 2023)
Gold NPs	PA Fluorescent CT	 provide bioconjugation chemistry tuneable NIR region resonances high biocompatibility used for photo thermal therapy 	- retention of the AuNPs in important organs	(Dheyab et al., 2023)
Carbon nanotubes	Fluorescence PA Raman imaging	- strong Raman scattering resonance - semiconducting due to their small band gap - high-resolution intravital microscopic image	-150µm penetration depth -low QY	(Chary et al., 2023; Hong et al., 2015)
Up conversion NPs	Fluorescence MRI CT PET	 extremely high imaging contrast deep tissue fluorescence imaging NIR photoluminescence 	- synthesised in organic solvents - unstable without surface modification	(Dubey & Chandra, 2022; Naher et al., 2023)

2.2.2 Nanoparticle-based therapy.

NP-based therapy is a promising approach for cancer treatment due to its ability to deliver drugs, radiation, or other therapeutic agents to targeted cells or tissues. Here are some of the mechanisms of NP-based therapy (Yao et al., 2020):

Passive targeting involves the accumulation of NPs in tumour tissues due to the EPR effect. Tumour tissues have leaky blood vessels and impaired lymphatic drainage, leading to the accumulation of NPs in tumour tissues. Passive targeting can improve the efficacy of chemotherapy or radiotherapy by increasing the concentration of therapeutic agents in tumour tissues and reducing systemic toxicity (Bazak et al., 2014).

Active targeting involves the functionalisation of NPs with targeting ligands such as antibodies, peptides, or aptamers. These ligands can bind to specific receptors or antigens overexpressed on cancer cells, leading to the accumulation of NPs in cancer cells. (Bazak et al., 2015). Active targeting plays a crucial role in delivering theranostics to specific locations of interest while minimizing exposure to normal tissues, thus enhancing therapeutic efficacy, and reducing side effects. By actively targeting specific cells or tissues, the amount of drug delivered can be significantly increased compared to free drug or passively targeted nanosystems (Attia et al., 2019).

Controlled release: NPs can be engineered to release therapeutic agents in a controlled manner. This can improve the pharmacokinetics and pharmacodynamics of therapeutic agents, reducing the frequency of administration and enhancing drug efficacy. Controlled release can be achieved through various combinations of mechanisms such as pH-responsive, temperature-responsive, or enzyme-responsive drug release (Dang & Guan, 2020).

Phototherapy: Is a non-invasive, and highly effective method for the treatment of cancer and includes both photodynamic therapy (PDT) and photothermal therapy (PTT)(J. Yang et al., 2022). PTT involves the use of NPs that can absorb near-infrared (NIR) light and convert it into heat. This can cause hyperthermia in tumour tissues, leading to cancer cell death. PTT can be used as a standalone therapy or in combination with chemotherapy or radiotherapy to enhance therapeutic efficacy (Alamdari et al., 2022). PDT relies on the use of photosensitizers which, excited by light at a specific wavelength, react with molecular oxygen to generate reactive oxygen species in target tissues, ultimately leading to cancer cell death (Zhi et al., 2024).

Immunotherapy: NPs can be functionalised with immunostimulatory molecules such as toll-like receptor agonists, cytokines, or antigens. These NPs can activate the immune system and enhance the anti-tumour immune response. Immunotherapy can be used as a standalone therapy or in combination with chemotherapy or radiotherapy to enhance therapeutic efficacy (Debele et al., 2020).

NPs have been used as a promising approach for cancer therapy due to their unique properties such as high surface area to volume ratio, biocompatibility, and the ability to target specific cells or tissues with functionalisation. Here are some of the types of NPs used for cancer therapy (Gavas et al., 2021):

Liposomes are spherical NPs composed of a phospholipid bilayer. They can encapsulate hydrophilic or hydrophobic drugs and target cancer cells through surface modifications. Liposomes have been used in cancer therapy to improve drug delivery, reduce toxicity, and enhance drug efficacy (Park, 2002; Tian et al., 2022). In 2001, A study was conducted by Harrington et al. (Harrington et al., 2001) on 17 patients with locally advanced cancers to of investigate the biodistribution and pharmacokinetics Indiumdiethylenetriaminepentaacetic acid-d-phenylalanine-labelled pegylated liposomes. Positive tumour images were obtained in 15 out of 17 studies, with breast, head and neck, bronchus, glioma, and cervix cancer showing nanoparticle uptake and correlated with the estimated tumour volumes for each tumour type. Furthermore, significant localisation of the liposomes was observed in the tissues of the reticuloendothelial system, including the liver, spleen, and bone marrow. These findings strongly support the potential of pegylated liposomal agents for the treatment of solid tumours and highlighted the promising role of pegylated liposomes as a targeted therapeutic approach for cancer treatment.

Gold nanoparticles have unique optical properties that can be exploited for cancer therapy. They can absorb and scatter light, allowing for PTT or PDT. Gold NPs can also be functionalised with drugs or antibodies for targeted drug delivery or immunotherapy (Jain et al., 2012). Yeom et al. (Yeom et al., 2023) present an intracellular antibody delivery system based on gold NPs conjugated with DNA aptamers against the crystallisable constant fragment region of immunoglobulin G. The resulting platform demonstrated a remarkable ability to load various antibodies and effectively deliver them to the cytosol of different human cancer cell types. Furthermore, the researchers demonstrated the platform's capability to specifically target and

selectively inhibit disease-associated mutant proteins, thereby showing its potential for therapeutic applications for various diseases. A great example of gold NPs combined with lipids was demonstrated by Granja et al. (Granja et al., 2023) where they produced solid lipid NPs co-loaded with gold nanorods and mitoxantrone using an economical method. The particles demonstrated non-haemolytic properties and were not cytotoxic to healthy cells at high concentrations. It was shown that the active targeting strategy using folic acid was successful and the chemotherapy, light-induced drug release, and photothermal therapy significantly enhanced cell death in breast cancer cells.

Iron oxide nanoparticles have magnetic properties that can be exploited for cancer therapy. They can be guided to tumour sites using a magnetic field for the application of magnetic hyperthermia therapy or MRI. Magnetic hyperthermia therapy uses magnetic NPs to generate heat in tumours, killing cancer cells. MRI using iron oxide NPs as contrast agents can also help diagnose and monitor cancer (Alphandéry, 2020). Quinto et al. (Quinto et al., 2015) used PEG SPIO NPs to generating heat and deliver DOXO to cancer cells. The phospholipid-PEG coated SPIOs effectively raised the local temperature to apoptotic levels and showed sustained DOXO release without affecting drug activity. Combining hyperthermia and DOXO treatment resulted in more effective cell death compared to individual modalities. These particles also offer imaging capabilities by providing T2 contrast for MRI, or can be used in fluorescence imaging by loading a lipophilic dye in the coating layer.

Carbon-based nanoparticles, such as carbon nanotubes and graphene oxide, have been used for cancer therapy due to their unique properties. They can be functionalised with drugs or antibodies for targeted drug delivery or immunotherapy. Carbon nanotubes can also be used for PTT and/or drug release under laser irradiation. Graphene oxide can also be used for PDT, drug delivery, and cancer imaging (Seyed Mohammad Hosseini et al., 2023). Khoshoei et al. (Khoshoei et al., 2020) developed a smart and responsive drug carrier capable of delivering DOXO and Paclitaxel for effective therapeutic application by utilising pH-sensitive functionalised single-walled carbon nanotube (SWCNTs) and graphene carriers with chitosan and carboxyl groups. This proved to be a smart drug system with pH responsive behaviour and controllable drug release, making it promising for cancer therapy.

Polymeric nanoparticles are often biodegradable and can be engineered to have various properties for cancer therapy. They can be functionalised with drugs or antibodies for targeted drug delivery or immunotherapy. Polymeric NPs can also be used for sustained drug release,

reducing the frequency of drug administration, and improving drug efficacy (Xiao et al., 2022). Peng et al. (Peng et al., 2016) investigated a novel polymer-based drug delivery system called poly (I-γ-glutamylglutamine)-DOXO (PGG-DOXO) conjugate. The study showed that the nanoparticle entered tumour cells primarily through the pinocytosis pathway, forming vesicles that entered the cells. The study highlights the potential of both polymer-drug conjugates and unconjugated complexes as promising strategies to overcome drug resistance in anti-tumour treatments. The findings suggest that PGG-DOXO conjugate holds promise for enhancing drug efficacy in multidrug-resistant cancer cells.

Azimijou et al. (Azimijou et al., 2023) created tumour-targeting nanodevices through the self-assembly of amphiphilic chondroitin sulphate-palmitoyl copolymers with varying amounts of hydrophobic groups. These redox-sensitive NPs demonstrated promising potential as efficient chemotherapeutic drug carriers for combating breast cancer using tamoxifen, exhibiting favourable behaviour both *in-vitro* and *in-vivo*.

Asghar et al. (Asghar et al., 2023) developed a controllable release device be exploring the potential of cross-linked quaternised chitosan NPs and applied it to the delivery, and pH-dependent release of olive phenolic extract in liver and colon cancers as an effective and safe approach for the controlled delivery of natural bioactive extracts in long-term cancer therapy. However, the researchers indicated that further research is needed to investigate the efficacy and safety of these nanoplatforms for various cancer treatments.

Jiang et al. (Jiang et al., 2023) presented a pH-responsive NP to deliver programmed death ligand 1 silence gene combined with a natural polycationic macromolecule called protamine which is used as the carrier to construct an antigen and adjuvant co-packaged nano-vaccine. This novel combinational approach enhances oncotherapy efficiency by simultaneously stimulating antitumor immune responses and reducing immune escape. This study offers promising insights into the future of cancer immunotherapy research.

NP-based cancer therapy can offer several advantages over currently used therapeutic methods such as targeted delivery to specific cells, improved pharmacokinetics, and pharmacodynamics, reduced systemic toxicity, versatility in combination therapy, and potential for personalised medicine based on individual needs. However, their use faces challenges such as manufacturing complexities, regulatory approval hurdles, potential toxicity

concerns, slow clearance leading to accumulation in vital organs, and limited efficacy across all cancer types and patients. These considerations highlight the need for careful evaluation and further research to harness the full potential of NP-based therapies in clinical settings (Xin et al., 2017). Some of the advantages and limitations of each NP listed above are outlined in Table 2.3.

Table 2.3 - The advantages and disadvantages of different nanoparticles used in therapeutics.

Nanoparticle	Therapy modalities	Advantages	Limitations	refs
Liposomes	Drug delivery	 biocompatibility reduced drug clearance several clinically approved examples easily functionalised 	 low reliability with batch to batch synthesis variation complex large-scale manufacturing high fabrication costs 	(Nel et al., 2023)
Gold	Photothermal, Photodynamic, Drug delivery, Gene therapy,	 easily functionalised for biocompatibility and targeting multimodal therapy 	- toxicity - Limited diffusion within tissues	(Nejabat et al., 2023)
Iron oxide	Photothermal, Drug delivery	 multimodal therapy high variety and research for overcoming limitations 	agglomeration,toxicity concernsbioaccumulation	(Yang et al., 2023)
Carbon based	Drug delivery, Photodynamic therapy	 high chemical stability tuneable surface unique thermal and electrical properties 	agglomerationlow solubilitybioaccumulation	(Nitheesh et al., 2021)
Polymeric	Drug delivery	naturally derivedbiocompatiblehighly solublehigh drug loadingcapabilities	- mostly <i>in-vitro</i> studies - early stage research	(S. M. Hosseini et al., 2023; Nitheesh et al., 2021)

2.2.3 Examples of nanotheranostics for cancer treatment

Below are some examples of how these imaging and therapeutic techniques are combined into a single system for the purposes of nanotheranostics.

Circulating tumour clusters (CTC) disseminating from the primary tumour are responsible for secondary tumour formation. Conventional treatments such as chemotherapy and radiotherapy do not prevent the metastasis at locally advanced stage of breast cancer (Paoletti et al., 2019). Dhandapani et al. (Dhandapani et al., 2023) developed a nanotheranostic system to track and eliminate the CTCs before they can colonise at a new site. The team used targeted multi-responsive nanomicelles incorporated with NIR fluorescent self-assembly superparamagnetic iron oxide NPs for dual modal imaging (NIR and MRI) and dual therapeutics for spontaneous killing of CTCs by the release of DOXO and magnetic hyperthermia. It was shown that the treatment was biocompatible and reduced CTCs in blood stream and distant organ metastasis demonstrating its potential to attach to, and kill, the CTCs that minimise the secondary tumour formation at distant sites.

In 2014 Ferber et al. (Ferber et al., 2014) presented the design, synthesis, and characterisation of a theranostic nanomedicine based on N-(2-hydroxypropyl) methacrylamide copolymer for PTX release. The nanomedicine incorporates a self-quenched near-infrared fluorescence (NIRF) probe, enabling fluorescence-based monitoring of site-specific drug release. In animal experiments using mice with cathepsin B-overexpressing mammary adenocarcinoma, the N-(2-hydroxypropyl) methacrylamide copolymer-SQ-Cy5 exhibited preferable body distribution and drug release compared to the free drug and probe when administered. This co-delivery approach of two complementary systems serves as a proof-of-concept for real-time deep tissue intravital orthotopic monitoring and may hold potential for clinical applications as a theranostic nanomedicine.

Afraz et al. (Afraz et al., 2022) described a novel nanomagnetic hydrogel (NMH) platform with dual functionality as a nanomedicine and MRI contrast agent. The pH-responsive hydrogel was created by crosslinking chitosan (CH) with hyaluronic acid (HA) using carbodiimide hydrochloride and N-Hydroxysuccinimide. Simultaneously, glucose oxidase (GOx) was immobilised within the hydrogel matrix. Fe₃O₄ NPs were incorporated into the GOx-loaded hydrogel using the co-precipitation method. It was found that the NMH-CHHA-GOx system had low cytotoxicity and was biocompatible due to the presence of biopolymers. The device

also had a significant therapeutic effect with the controlled release of hydroxyl radical in a tumour microenvironment. These results indicated the high potential of the designed platform for application as a nanotheranostic platform in cancer therapy.

Zhang et al. (Zhang et al., 2020) proposed a programmable method for the plasmonic modulation of gold nanotheranostics in the NIR-II window. The team prepared gold nanodumbbells (AuNDs) which possessed good thermal stability, strong PA signals as well as high photothermal conversion efficiency (84.9 %). The AuNDs were then conjugated with nucleolin-targeted DNA aptamer AS1411. The obtained AP-AuN could perform effective NIR-II PA imaging-guided PTT for subcutaneous 4T1 tumours. When combined with an anti-programmed death ligand 1 antibody, the AP-AuNDs significantly suppressed tumour growth and stimulated potent host anti-tumour immunity, resulting in significant inhibition of both distant tumour growth and whole-body spreading of tumour cells.

Yue et al. (Yue et al., 2017) developed a pH-responsive, self-sacrificial nanotheranostic agent for potential multimodal imaging and real-time MRI and CT monitoring of cancer therapy and tested it both *in-vivo* and *in-vitro*. FePt NPs were synthesised and loaded onto PEGylated graphene oxide (GO) sheets. In therapy experiments on tumour cells, the FePt/GO nanocomposites demonstrated promising potential as a theranostic agent for cancer inhibition.

2.2.4 Challenges and future directions

The development of nanotheranostics for cancer treatment faces several challenges that need to be addressed for successful clinical translation (Aminolroayaei et al., 2021; Ang et al., 2021; Chen et al., 2017; Kievit & Zhang, 2011; Melancon et al., 2012; Sonali et al., 2018). Some of the major challenges are:

1. Biocompatibility and toxicity: NPs used for cancer treatment should be biocompatible and non-toxic to avoid adverse effects on healthy cells and tissues. The toxicity of NPs depends on their size, shape, surface charge, and composition, which can affect their pharmacokinetics and pharmacodynamics. Therefore, it is essential to evaluate the toxicity of NPs *in-vitro* and *in-vivo* before their clinical use (Kievit & Zhang, 2011). This can be done by focusing on the rational design of NPs which involves optimizing the

- properties of NPs to improve their biocompatibility. This can be further enhanced by focusing on personalised nanotheranostics, which involves tailoring the design and formulation of NPs based on the individual's tumour characteristics, such as the genetic profile and the tumour microenvironment (Mura & Couvreur, 2012).
- 2. Specificity and efficacy: NPs used for cancer treatment should be specific and efficacious in targeting cancer cells and delivering drugs or contrast agents. The specificity of NPs can be improved by functionalising them with targeting ligands such as antibodies, peptides, or aptamers. The use of stimuli-responsive materials such as pH-sensitive polymers or temperature-responsive hydrogels can enhance the release of drugs in response to specific stimuli (Wicki et al., 2015). However, the efficacy of NPs can be affected by various factors such as tumour heterogeneity, drug resistance, and the tumour microenvironment (Chen et al., 2017; Mendes et al., 2018). Further improvements can be made by utilising a combination of therapies by targeting cancer cells from multiple angles, reducing the likelihood of resistance and improving treatment outcomes (Peng et al., 2020), using nanotheranostics alongside other techniques such as chemotherapy, radiation therapy, and immunotherapy to enhance their efficacy and reduce toxicity. The integration of different imaging modalities such as MRI, PET, and optical imaging can improve the sensitivity and specificity of nanotheranostics.
- 3. Regulatory approval: Nanotheranostics for cancer treatment must undergo rigorous preclinical and clinical testing, The approval process involves evaluating the safety, efficacy, and quality of nanotheranostics, which can be time-consuming and expensive. Therefore, it is essential to develop standardised protocols for the preclinical and clinical evaluation of different nanotheranostic method and treatments to facilitate their regulatory approval (Chen et al., 2017). Clinic translation is becoming more feasible as clinical trials continue to demonstrate the safety and efficacy of nanotheranostics, and their application in cancer treatment will likely become more widespread (Hua et al., 2018).
- 4. Scalability and reproducibility: Is needed for the large-scale production of NPs for clinical use. The synthesis of NPs is often complex and involves several steps, which can affect the reproducibility and cost of nanoparticles (Kievit & Zhang, 2011). The high cost of nanotheranostics can limit their accessibility and affordability for patients,

particularly in developing countries. Therefore, it is essential to develop cost-effective and scalable methods for the synthesis and production of NPs by focusing on the use of microfluidic techniques, continuous-flow synthesis, and high-throughput screening that could facilitate the large-scale production of NPs (Chen et al., 2017; Roy et al., 2023).

Overall, the prospects for the field of nanotheranostics in cancer treatment are promising. As technology continues to advance and clinical trials demonstrate their efficacy, nanotheranostics have the potential to revolutionise cancer treatment by enabling more precise, effective, and personalised therapies.

2.3 Carbon dots

This section has been adapted from the literature review; Biomass-Based Carbon Dots: Current Development and Future Perspectives with permission from (Wareing et al., 2021) Copyright 2021, American Chemical Society.

Carbon dots (CDs) are carbon NPs that can have either a graphitic or amorphous structure, are smaller than 10nm (Das et al., 2018) and have many attractive properties, including strong photoluminescence emission and optical properties, good conductivity, broadband optical absorption, high chemical stability, and broad excitation wavelength. They also have a tuneable emission wavelength through modification of synthesis parameters such as size, shape, composition, internal structure, and surface chemistry. They are also environmentally friendly, non-toxic, non-blinking, and resistant to photobleaching (Namdari et al., 2017; Zuo et al., 2016). The mechanisms behind the photoluminescent properties of CDs are not yet fully understood, (Namdari et al., 2017) but the main hypotheses are the quantum confinement effect and surface structure.

CDs were discovered by accident in 2004 during a purification of single-walled carbon nanotubes by electrophoresis, (Xu et al., 2004) and since then, they have received a lot of attention as a potential replacement for conventional semiconductor quantum dots in various applications (Lim et al., 2015). Briefly, semiconductor quantum dots (SCQDs) are fluorescent nanocrystals made up of a semiconductor material with unique optical and electrical

properties that are determined by their size and structure, typically ranging from 1 to 20nm and containing 200 to 10,000 atoms (Geszke-Moritz & Moritz, 2013; Lommens et al., 2007). SCQDs are usually composed of a core and a shell, with the core semiconductor having a narrow bandgap, which represents the minimum energy required to excite an electron from its ground state to the next energy level. The core is enclosed by a shell semiconductor with a higher bandgap, which confines emission and excitation to the core and protects it from photo bleaching while improving its QY (Walling et al., 2009). The performance of SCQDs is evaluated based on their QY, which is the efficiency of photon emission relative to the number of photons absorbed and is commonly used in reactive species detection in biology. SCQDs have many applications including quantum dot light emitting diodes (QLEDs) (He et al., 2019), and fluorescence cellular imaging (Caires et al., 2020; Sarma & Mohanta, 2015; N. Xu et al., 2019). However, there are several drawbacks to using SCQDs that hinder their suitability for application such as their strong blinking effect which may limit use in single molecule fluorescence (Rombach-Riegraf et al., 2013), cytoxicity (Reshma & Mohanan, 2019) of their component heavy metals, bioaccumulation in the liver, to which they are particularly toxic (Reshma & Mohanan, 2019), poor solubility (Tian et al., 2017) and environmental impacts (Lim et al., 2015; Wang & Tang, 2021).

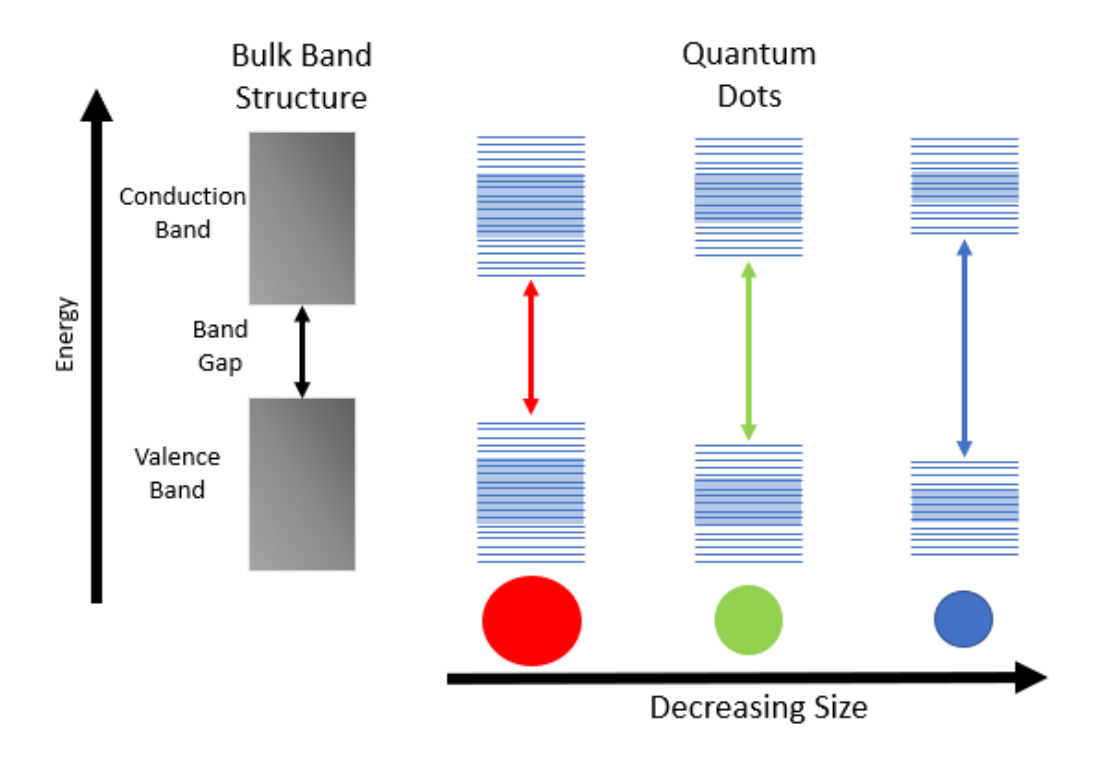
CDs can be synthesised through large-scale, one-step processes at a lower cost compared to SCQDs. They are highly suitable for biomedical applications due to their chemical inertness, high biocompatibility, and low cytotoxicity. The precursor materials used to make CDs, such as chemicals (i.e., ethanol, citrate, glucosamine, and ascorbic acid) or biomass (i.e., pomelo peels, orange juice, and strawberry juice) (Lim et al., 2015) contribute to these desirable properties. CDs are easy to functionalise and highly soluble in water because they have multiple and varied functional groups, such as amine or carboxylic groups and polar moieties, on their surface (Zuo et al., 2016).

2.3.1 Photoluminescence mechanisms

As mentioned above a complete theory of the mechanisms behind the photoluminescence of these particles has not fully described, but attempts have been made to suggest the origin for some of the particles and the mechanisms change depending on the structure of the CDs. Graphene CDs (GCDs) are thought to express their photoluminescence due to the quantum

confinement effect and edge effects. While amorphous CDs (ACDs) photoluminescence originates from surface defects and the passivation of emissive traps (Abbas et al., 2018).

The quantum confinement effect (Figure 2.3) occurs when energy from light is absorbed and causes an electron in the valence band to move to the conductance band, leaving behind a positive "hole" in the valence band. When the electron recombines with the hole, a photon is emitted. In bulk materials, electrons and holes move around in the material within the timescale of light absorption, forming an "exciton" pairing. The distance between the electron and the hole within the exciton is called the Bohr radius (Reshma & Mohanan, 2019). In quantum dots, the dimensions are reduced to the nanometre scale, smaller than the Bohr radius, causing quantum confinement and squeezing of the excitons. The smaller the quantum dot, the greater the quantum confinement and the more energy it takes to excite an electron away from the positively charged hole. When the hole and electron recombine, the energy is



emitted as a photon. The smaller the QD, the larger the band gap and the higher the energy of light emitted when the QD is deactivated (Rosenthal et al., 2011).

Figure 2.3 - Quantum confinement effect photoluminescence mechanism in quantum dots – Reprinted with permission from (Wareing et al., 2021). Copyright 2025

American Chemical Society.

Photoluminescence can originate from the band gap zig zag edge effects on GCDs. The emission can be controlled with pyrrolic doping and chemical functionalities (Sk et al., 2014). Surface modification can also provide fluorescence (Liu et al., 2019), for example a triplet excited state of aromatic carbonyls (Deng et al., 2013) or fluorophores such as citrazinic acids derivatives on the surface of CDs (Ehrat et al., 2017).

2.3.2 Synthesis methods

CD synthesis methods can be classified into two groups: "top-down" and "bottom-up". Top-down methods involve reducing a larger material down to a NP, while bottom-up methods use smaller building blocks to create a NP (Zuo et al., 2016). Top-down methods often result in higher yields but may use harsh chemicals like H₂SO₄ for oxidation. On the other hand, bottom-up methods allow for more control over the size and morphology but can be more complex and time-consuming (Abbas et al., 2018).

Below are some protocols for CD synthesis that use both top-down and bottom-up approaches. Examples are provided that report technical details of each process as well as the advantages and disadvantages of each method. The most environmentally friendly method described is the hydrothermal method, the microwave method is included within this. The least green method is chemical ablation due to the use of strong acids. Chemical ablation is like the hydrothermal method because it uses similar equipment, and heat, to carbonise the carbon source.

The hydrothermal method is a cost-effective, convenient, and eco-friendly approach to produce quantum dots under high temperature and pressure in aqueous conditions. This method offers simplicity, controllability, and non-toxicity due to the materials used, eliminating the need for passivation for photoluminescence. However, it suffers from limited control over size and the presence of impurities (Atchudan et al., 2016; Liu et al., 2012; Sahu et al., 2012; N. Wang et al., 2016). In a 2016 study by Wang et al. (N. Wang et al., 2016) a green synthesis of CDs was achieved through hydrothermal carbonisation of papaya. These dots were used in the imaging of HeLa cells and fluorescence sensing of E. coli bacterial strain. Atchudan et al. (Atchudan et al., 2016) described a hydrothermal method for producing nitrogen-doped dots from unripe peach using aqueous ammonia as a nitrogen source. While

this method yields dots with favourable properties such as bright fluorescence emission, excellent biocompatibility and good water dispersity, the use of ammonia as a nitrogen source is environmentally harmful, and alternative auto-doping biomass selection is recommended. The microwave method is an efficient and environmentally friendly approach to synthesising CDs, which can be applied to both small molecules and biomass without acid catalysts. Water can be used as a reaction medium, and the method is fast, economic, and scalable. However, the size control of the resulting CDs may be poor (Guan et al., 2014; Liu et al., 2018; Namdari et al., 2017; Pajewska-Szmyt et al., 2020). Pajewska-Szmyt et al. (Pajewska-Szmyt et al., 2020) reported a microwave-assisted method for synthesising of high QY (26%) sulphur and nitrogen doped dots using citric acid as the main carbon source, and L-glutathione and thiourea as the nitrogen and sulphur source respectively. Liu et al. (Liu et al., 2018) also demonstrated a onestep microwave method for synthesising CDs from citric acid, L-cysteine and dextrin precursors in water. Bajpai et al. (Bajpai et al., 2019) presented another example of a microwave reaction, utilizing the milk protein casein as the carbon source. This method stands out for its eco-friendliness, as it avoids the use of harsh chemicals and involves only a few steps. Notably, these casein-derived dots displayed a high QY of 18.7% and exhibited blue photoluminescence.

Pyrolysis, a bottom-up process, involves carbonizing organic substances at elevated temperatures (350-750°C) in inert atmospheric conditions, such as nitrogen, offering a simple and eco-friendly approach to produce CDs. However, this method requires further passivation for photoluminescence (Sun et al., 2013) (Teng et al., 2014; Y.-P. Zhang et al., 2019). In a study by Teng et al. (Teng et al., 2014) 1 g of konjac flour was pyrolyzed in air at 470°C for 90 minutes to produce nitrogen-doped CDs. To achieve photoluminescence, further passivation with PEG was required for photoluminescence. Zhang et al. (Y.-P. Zhang et al., 2019) also outlined a pyrolysis synthesis for CDs for Fe³⁺ sensing, using marigold as a carbon source. This method involved compression, fermentation, pyrolysis, and subsequent reduction with sulphuric and nitric acid, followed by nitrogen doping using ethylenediamine. Compared to the previous method, this approach requires more steps involving harsh chemicals, making it less eco-friendly.

The chemical ablation method relies on strong acids to carbonise small organic molecules, resulting in the need for purification, neutralisation steps, and wastewater treatment. This

method also provides poor control over the size of the produced dots (Amer Ridha et al., 2020; Fang et al., 2012; Shen et al., 2013). In 2012, Fang et al. (Fang et al., 2012) utilised acetic acid, water, and a phosphorus pentoxide (P_2O_5) catalyst to synthesise fluorescent CDs without the need for an external heat source due to an exothermic reaction. Although the self-heating aspect of this method makes it cost-effective for further scale-up, the use of P_2O_5 incurs a high processing cost. Additional drawbacks include large particle size 105nm and low reaction yield (0.06%). Shen et al. (Shen et al., 2013) synthesised CDs by chemically ablating polyethylenimine (PEI) with the reflux of PEI and nitric acid at 120°C. Although the dots had an excitation-dependent emission, their QY was low at 2%, and they were relatively large (12nm). This synthesis exemplifies why chemical ablation is used less frequently in recent years. The best methods for size control are template and reverse micelle, which, while less harsh, add complexity to the process due to increased number of steps and increased number of materials.

The template method involves using a mesoporous structure as a template, with the CDs synthesised through calcination inside the structure and then removing the template to obtain the dots. This approach eliminates the need for passivation, and the dots produced have a narrow size distribution. However, the method is complex due to the number of steps and challenging to purify (Amer Ridha et al., 2020; Y. Yang et al., 2013; Zong et al., 2011). One example of the template method is described by Liu et al. (Liu et al., 2009) who used silica spheres as carriers for the aqueous synthesis of CDs. Acid treatment was used to passivate the surface, yielding water-soluble, multicolour photoluminescent CDs with a QY of around 14.7%. The photoluminescence is suggested to be due to the presence of surface energy traps that become emissive upon stabilisation as a result of surface passivation. Another example of the template method is provided by Wang et al., (Wang et al., 2019) who prepared CDs@zeolites in hydrothermal conditions using three templates: Mn-Levyne, Zn-Chabazite, and Zn-Levyne. These systems displayed different photoluminescence properties, with the CDs@Zn-Chabazite exhibiting green photoluminescence and CDs@Zn-Levyne and CDs@Mn-Levyne exhibiting red photoluminescence.

The reverse micelle method involves using a reverse micelle as a nano-reactor to carbonise carbon sources, resulting in dots with a narrow size distribution. The dots can be adjusted in size by modifying the water-surfactant molar ratio, and the method prevents aggregation,

allowing for large-scale production with a high product yield (Amer Ridha et al., 2020; Kwon & Rhee, 2012). However, this method is complicated due to the number of steps. Kwon et al. (Kwon & Rhee, 2012) used the reverse micelle method to create graphene CDs with sugar as the carbon source. The method was highly customisable in terms of size, with water-surfactant molar ratios used to control the size. The use of micelles prevented particle aggregation and resulting in high product yields.

Laser ablation is a method that utilises a laser to irradiate a carbon target to produce CDs. Although it is fast, efficient, and highly customisable, it has drawbacks such as low production yield, poor size control, low QY and passivation may be necessary for photoluminescence (Abbas et al., 2018; Calabro et al., 2018). In a study by Calabro et al. (Calabro et al., 2018), liquid-phase laser ablation was used to generate graphene quantum dots from carbon nano-onions, and the results were compared to those of a chemical oxidation approach. The researchers demonstrated that their liquid-phase laser ablation method was a fast, clean, and straightforward single-step process. In another study, Kang et al. (Kang et al., 2020) described a technique for synthesising nitrogen-doped graphene dots from graphene flakes using pulsed laser ablation. Diethylenetriamine was used as the nitrogen source, and high-power sonication was applied during the laser ablation process.

To produce CDs using the **arc discharge method**, a positive anode is placed a few millimetres away from a graphite rod, which is then evaporated by an electric arc. The resulting products are deposited on the chamber walls as a soot, which can be purified to obtain CDs. However, this method suffers from the presence of impurities in the soot, which are difficult to remove, and the requirement for expensive equipment (Amer Ridha et al., 2020; Dey et al., 2014; Yang, 2015). Dey et al. (Dey et al., 2014) used a two-step chemical route to synthesise B- and N-doped graphene quantum dots (GQD). In the first step, gas phase arc discharge was used in the presence of a Boron/Nitrogen source to prepare B- and N-doped graphene. In the second step, the B/N-doped graphene was chemically scissored to yield B/N-GQDs using the Hummers method, and then thermally deoxidised by heating at 300°C for 3 hours in a nitrogen atmosphere. The resulting dots had great properties; however, this protocol has several drawbacks, including the use of several different gases and expensive equipment making it difficult to scale up production.

The electrochemical method involves the use of high purity graphite anodes and electrolysis to produce CDs. The size and nanostructure of the dots can be controlled by adjusting the water content in the ionic liquid electrolyte. While this approach has a low cost and high output, it has limitations in terms of carbon source choice and doping options (Amer Ridha et al., 2020; Zuo et al., 2016). An et al. (An et al., 2021) synthesised dots using ophenylenediamine via electrolysis for the sensing of Fe³⁺ and ascorbic acid. The simplicity and absence of harsh chemicals are the advantages of this method, but the dots have a very low QY of 0.47%. Higher QY dots were produced by Hou et al. (Hou et al., 2015) using an electrolyte of sodium citrate and urea in aqueous solution with platinum sheets as electrodes. However, the cost of platinum electrodes limits the scalability of this synthesis.

Ultrasonication is a top-down process that involves biomass undergoing dehydration reactions, polymerisation, and carbonisation to synthesise CDs. This method fully synthesises the CDs through a short single nuclear burst, eliminating the need for passivation. While the process is straightforward and promotes crystal structure, it suffers from poor control over size (Liu et al., 2019; Park et al., 2014). An example of ultrasonication synthesis was demonstrated by Huang et al. (H. Huang et al., 2018) using cigarette ash as the biomass source with Dimethylformamide and PEG-Thiol. This method is intriguing as the dots are automatically functionalised with PEG, requiring no further reaction. The dots demonstrated potential application in cell imaging. Notably, this method is environmentally friendly, as the precursor of cigarette ash is a recycled material easily obtainable for scale-up.

The extraction method does not involve the synthesis of dots itself; rather, it utilises simple centrifugation and filtration to extract CDs produced in nature or through processes like cooking or brewing. The advantage of this approach is the avoidance of complicated treatment methods and synthesis processes, resulting in a low-cost method. However, it comes with the drawback of poor control over the properties of the extracted CDs (Dhandapani et al., 2022; Jiang et al., 2014; Z. Wang et al., 2015). Wang et al. (Z. Wang et al., 2015) reported the extraction of CDs from beer for imaging and drug delivery purposes. The process involved stirring, rotary evaporation, filtration, and chromatography. The dots were functionalised with DOXO for potential applications as imaging and anti-cancer agents in nanotheranostics. Similarly, Dhandapani et al. (Dhandapani et al., 2022) also described the extraction of green CDs from fried food waste residue. The method involved stirring, filtration, centrifugation.

These extracted dots were found to emit green wavelength emission, exhibit outstanding dispersibility, constant emission, and relative long-life emission time, and up-converted emission. However, crucial properties such as size, QY, and production yield were not reported in the paper, leaving important information missing for scale-up and application purposes. Including these details could significantly enhance the paper's findings.

The methods above show the large number of materials that can be used but they can usually be separated into two broad categories: purified chemicals that are often bought from a laboratory, or biomass, usually gained from a waste stream. There are advantages and disadvantages for both; biomass derived carbon sources contain impurities that could influence the synthesis in terms of both reproducibility and purification methods used, which would affect the economics and scalability of the synthesis. Lab bought chemicals are usually pure, do not contain impurities and are unaffected by these disadvantages. However, biomass-based CDs have clear advantages in the fact that they are obtained from waste streams at zero/limited cost and provide a use for material that could have ended up in landfill or as pollution, making their synthesis very green. Their synthesis methods tend to be simpler without the use of expensive equipment and extreme conditions which increases the likelihood of a scalable and economical synthesis. Because they are derived from biomass, which tends to be biocompatible by their very nature, and more likely to be biocompatible than their chemically derived counterparts. This means they have greater potential for application in biomedical applications such as imaging and drug delivery.

2.3.3 Functionalisation

Modifying the properties of CDs through functionalisation is crucial for their application. This can be achieved through either surface modification or doping.

Doping refers to the incorporation of heteroatoms into the structure of CDs, (Hu et al., 2017; Shan et al., 2014; Zhou et al., 2014) and it is a common practice to enhance their emissions. Doping with heteroatoms has been demonstrated to improve the properties and surface defects of CDs, which can eliminate or inhibit original O-states and promote radiative recombination, resulting in higher QYs and emissions that are independent of excitation, making the CDs suitable for different applications. Heteroatoms embedded into the carbon

structure of CDs can regulate the initial band gap and form new energy levels. For instance, nitrogen doping is a prevalent method to alter the fluorescent properties of CDs due to its 5 valence electrons and similar size to carbon. Similarly, boron, which has fewer valence electrons than carbon but has a similar radius, can introduce some chemical disorder since the bond between carbon and boron is slightly longer (0.5%) than a carbon-carbon bond (Liu et al., 2019; L. Zhang et al., 2014).

When high electronegative atoms such as nitrogen and sulphur are used for doping, a blue-shifted emission is usually observed. Conversely, doping with low electronegative atoms such as phosphorus and boron results in a red-shifted emission (L. Zhang et al., 2014). Compared to nitrogen doped CDs (N-CD), sulphur doped CDs (S-CD) are more challenging to synthesise due to the difficulty in forming C–S bonds. S and C have similar electronegativities and the bond does not significantly transfer charge. S-doping can modify the chemical properties of CDs and lead to an uneven distribution of the spin density, increase surface reactivity, catalytic effects (Kou et al., 2020), and cause a blue shift in emission (Y. Hu et al., 2014). These properties could make S-CDs useful for various applications such as catalysis or surface functionalisation (L. Zhang et al., 2014).

One approach involves a microplasma process using citric acid and ethylene diamine for nitrogen-doped CDs (N-CDs) (Ma et al., 2020). Another method utilises phosphoric acid and formamide as dopants for phosphorus and nitrogen, respectively, in a solvothermal process (N. Li et al., 2021). Additionally, a hydrothermal synthesis protocol has been developed for N and S self-doped CDs using fungus fibres as a biomass source rich in nitrogen and sulphur. This biomass-derived approach eliminates the need for an additional doping source (C. Shi et al., 2019).

The advantages of the biomass-derived method include its self-doping nature, high QY, biocompatibility, and photostability. The hydrothermal technique offers mild conditions and a simple work-up process without dialysis, making it advantageous for large-scale production. Another example involves a green synthesis for phosphorus-doped CDs using dextrose as the carbon source and disodium hydrogen phosphate as the phosphorus source (Molkenova & Atabaev, 2019). These phosphorus-doped CDs show promise for selective monitoring of ferric ions in drinking water, suggesting potential environmental applications.

Surface modification can alter the properties of CDs by functionalising their surface with a variety of materials including ions, organic molecules, polymers, DNA, and proteins. Due to the abundance of surface groups on CDs, functional ligands can easily bind to them (B. B. Chen et al., 2019). Functionalisation reactions can be categorised as covalent and non-covalent bonding. Covalent modification involves the reduction of functional molecules and groups on the surface, allowing for better control of the size, shape, and physical properties of CDs. The introduction of groups to the surface of CDs can increase the electron cloud density. On the other hand, non-covalent modification utilises π interaction or Van Der Walls forces and has less of an impact on the structure of CDs compared to covalent modification since the surface is not chemically altered (Yan et al., 2018). Additional details on these reactions are briefly discussed in the following paragraphs, and Figure 2.4 provides a visualisation of each method.

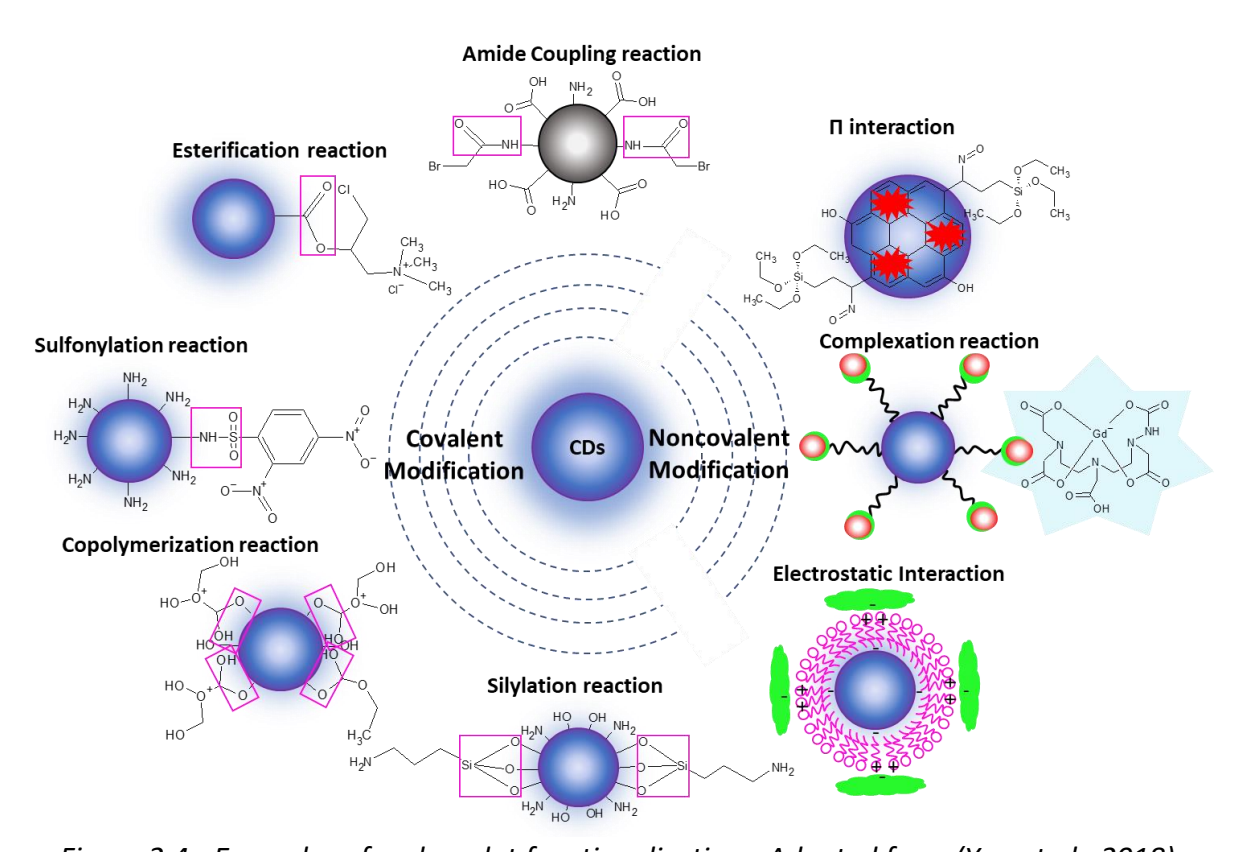


Figure 2.4 - Examples of carbon dot functionalisation - Adapted from (Yan et al., 2018)

Amide coupling is a method of functionalisation that involves the reaction of amino compounds with acylating reagents such as acyl chloride or carboxylic acid. This is a commonly used technique to modify the surface of CDs since they are rich in amino or carboxyl groups. The benefits of amide functionalisation include an increase in the CDs' selectivity and QY, as

well as the introduction of hydrophobicity to make them more accessible in a solvent environment. The amide bond's lack of rotational freedom imparts a partial double character and causes a kink in the CD, resulting in a hydrophobic nature known as a "beta-turn" (Dong et al., 2015).

Esterification is a chemical reaction that involves a carboxylic acid and an alcohol in the presence of an acid catalyst to produce an ester and water. This method is commonly used to functionalise CDs that possess numerous carboxyl or hydroxyl groups on their surface, allowing for the introduction of diverse functional groups to interact with these sites. CDs modified through esterification exhibit remarkable selectivity and reversibility towards targets, which is particularly significant for applications in detection and cell imaging fields. Furthermore, esterification can alter the hydrophilic and oleophobic properties of CDs to impart lipophilic hydrophobicity (Algarra et al., 2014).

Sulphonylation reaction can be used to functionalise CDs that contain amino groups by reacting them with sulfonyl chloride compounds. This introduces sulphur atoms and ligands to the surface of the CDs, which results in increased energy or emissive trap states. Consequently, the rate of photoexcited electron capture is improved, leading to enhanced photoluminescence (Ye et al., 2014).

Copolymerisation - functional groups on the surface of CDs that contain active hydrogen can undergo copolymerisation reactions with cyclic or double bond compounds to create large molecular weight CDs suitable for biological applications (Li et al., 2017).

Similar to copolymerisation, **silylation reactions** utilise the active hydrogen present within functional groups on surface of CDs for functionalisation with silane groups. CDs functionalised with silane are commonly used in sensors and probes due to the ease of chemical modification enabled by the two types of silane functional groups. Silane is also non-toxic and biocompatible, improves dispersion and water solubility, and reduces the cytotoxicity of CDs, (Rao et al., 2016) making it an ideal material for applications in ion detection and temperature sensing (Lei et al., 2015).

 π -interactions: CDs possessing extended π systems can undergo modification through π interactions with small aromatic molecules, which extends conjugation domains and improves QY, photostability, and biocompatibility (Jiang et al., 2016).

The surface of CDs can be modified by **complexation**, which involves coordination bonds formed between the metal ion and functional groups on the CDs surface. Complexation can be used to functionalise CDs with molecules or ions, which can alter their interfacial properties and broaden their applications. When an amphiphilic molecule is complexed with the CD surface, the hydrophobic part can enhance the stability of CDs in organic solvents. Complexation has been applied in various fields, such as desalination of sea water (Guo et al., 2014).

Electrostatic interaction: The charge on the surface groups of CDs can make them amenable to modification through electrostatic interaction with charged reagents. This approach is commonly employed to functionalise CDs with targeting molecules or other fluorophores (Jin et al., 2017).

2.3.4 Applications

CDs demonstrate physical and optical properties comparable to semiconductor-based quantum dots, enabling their use in a wide range of applications. Previous studies have highlighted their potential in luminescent ink (Ge, Han, et al., 2021), enhancing photosynthesis (Xiao et al., 2021), ion sensors (Hg²⁺,(Hou et al., 2015; Lu et al., 2012) Cu²⁺,(Jin et al., 2017; Liu et al., 2018; Rao et al., 2016; Ye et al., 2014) Fe³⁺,(Q. Huang et al., 2018; Molkenova & Atabaev, 2019) Ag⁺(Algarra et al., 2014; Jiang et al., 2016)), bioimaging(Kwon & Rhee, 2012; Li et al., 2017; N. Li et al., 2021), photoelectronics (Kwon & Rhee, 2012), drug release (Li et al., 2017), and seawater desalination (Guo et al., 2014).

Chemical CDs and biomass-derived CDs both exhibit promising applications in various fields, but they differ in some key respects. While both types of CDs possess exceptional photoluminescent properties that make them valuable for diverse applications, the superiority of biomass-derived CDs lies in their enhanced biocompatibility and reduced toxicity, which can be attributed to their source material. This advantage makes them

particularly well-suited for biomedical applications such as bioimaging, drug delivery, and sensors, both within and outside the body. Moreover, their straightforward synthesis methods and environmentally friendly nature make them suitable for large-scale production with a positive environmental impact.

Although chemical CDs offer diverse functionalities, their biocompatibility and environmental impact might not be as favourable as those of biomass-derived CDs. Biomass-derived CDs, due to their low toxicity and eco-friendly synthesis, appear to be more suitable for biomedical applications and could have a positive impact on healthcare and environmental sustainability. Examples of applications for chemical and biomass derived CDs are outlined below. Table 2.4 compares the dots made from chemical, biomass and semiconductor sources in general (Radnia et al., 2020).

Table 2.4 - A comparison between biomass derived carbon dots, chemical carbon dots, and semiconductor quantum dots - Adapted from Radnia et al., 2020.

Biomass derived carbon dots	Chemical dots	Semiconductor quantum dots	
Use of naturally occurring, eco-friendly, safe precursors as a source of carbon for CD synthesis <i>via</i> biological techniques	Inorganic and metallic precursors are mainly used.	Semiconductor sources do not use recycled materials and are toxic	
Environmentally friendly, use of non-toxic and safe reagents, resulting dots are non-toxic	High use of strong acids such as HNO_3 and H_2SO_4 and chemical stabilising agents. The resulting dots can have unwanted reactivity and potential toxicity, uncertainty of composition.	Require long and harsh synthesis with organic solvents. Resulting dots are toxic, especially to the liver	
Self-passivated (reducing chemical exposure)	Extra passivation step required, often with chemicals	Core-shell relationship requires a multistep process.	
Cost-effective, single-step synthesis, consume less energy and is easy to scale-up	Mostly complex synthesis steps we equipment, costly chemicals, and	•	
Availability and affordability/renewable and facilitate waste management	Generating risky products/by-products for the environment and human health, made form non-renewable precursors		
Photoluminescence requires mo Thought to originate with surface confinement effect	Photoluminescence well understood and defined by the quantum confinement effect		

Sensors: Davi et al. (Davi et al., 2021) utilised a hydrothermal technique to synthesise CDs from dansyl chloride, which were used as a radiometric thermal sensor, pH sensor, and for reactive oxygen generation. The fluorescence intensity of the dots increased with increasing temperature, which is opposite to the typical behaviour of CDs and could be used as a "turn-on" temperature sensor. The fluorescence intensity also increased with an increase in pH and changed the colour of the emitted light. The team demonstrated that the generation of reactive oxygen species upon photoexcitation showed a moderate singlet oxygen QY, reaching 11% for excitation intensities above 10 mW/cm². However, the authors did not provide specific examples of applications for these CDs. Biomass-derived CD can also serve as sensors for detecting various materials such as anions, metals, and molecules (Zhang & Yu, 2016). For instance, Lu et al. (Lu et al., 2012) demonstrated a hydrothermal treatment of pomelo peel to produce fluorescent CDs for highly sensitive and selective detection of Hg²+. These dots act as effective fluorescent probes with a low detection limit, making them valuable in detecting even trace amounts of mercury, which can be harmful to human health.

Bioimaging: Li et al. (L.-p. Li et al., 2021) developed near infrared-emitting CDs for bioimaging by subjecting tetraphenyl porphyrin to solvothermal treatment in sulphuric and hydrochloric acid. The fluorescence was attributed to aggregated molecular states of the CDs and exhibited a strong NIR emission at 692nm with a high QY of 23.8%. The CDs had good dispersibility in water, were biocompatible, showed minimal toxicity, and enhanced labelling capability in bioimaging. However, the use of tetraphenylporphyrin, sulphuric acid and hydrochloric acid means that this synthesis cannot be considered environmentally friendly. To increase the sustainability of this reaction and further decrease the minimal toxicity seen in the resulting dots, a greener alternative for both the carbon source and reactants should be used. Biomassderived CDs exhibit better biocompatibility compared to chemically derived counterparts, making them ideal for bioimaging applications (Tejwan et al., 2019). For example, CDs obtained from coffee powder have been shown to be effective in imaging carcinoma cells in small fish. (Jiang et al., 2014) Moreover, CDs synthesised from ginkgo leaves have been used to detect salazosulfapyridine in mouse plasma, essential for managing inflammatory bowel disease. However, further research is needed to improve synthesis efficiency and eliminate the use of non-green solvents (Jiang et al., 2019).

Drug Carriers: The properties that make biomass-derived CDs suitable for bioimaging also render them excellent candidates for drug delivery, including large surface area to volume ratio, enhanced cellular uptake, and easy conjugation with therapeutics (Radnia et al., 2020). For instance, CDs derived from milk have been used as drug carriers for DOXO with pH-dependent release behaviour, demonstrating significant toxicity to carcinoma cells while being less toxic to healthy cells (Yuan et al., 2017).

Electrical Applications: Chang et al. (Chang et al., 2021) developed a solvothermal method using triammonium citrate to synthesise CDs for cell imaging and white LEDs. The choice of triammonium citrate was due to its higher nitrogen content for doping, environmental friendliness, and the lower work up required. The CDs produced were highly stable and had low toxicity. By adjusting the reaction temperature, the emission colour of the CDs was tuneable to wavelengths across the visible spectrum. The CDs' emission mechanism was attributed to the degree of graphitisation, which was controlled by the number of functional groups on the surface. The red, green, and blue emissive dots had QYs of 24.4%, 17.2%, and 12.1%, respectively. The CDs were successfully used for HeLa cell imaging, and CD/polymer composite films were employed to create white LEDs. However, this synthesis method cannot be considered green, as urea and triammonium citrate are not green chemicals. Biomassderived CDs have shown promise in energy applications, such as photovoltaic devices, batteries, and supercapacitors, due to their unique properties (Abbas et al., 2018). For instance, CDs synthesised from waste zucchini were used in supercapacitors, showing good specific capacitance retention. Additionally, CDs derived from gingko leaves were used as an alternative to expensive Pt catalysts in electrocatalysis (Hoang & Gomes, 2019).

Catalysis: Li et al. (Y. Li et al., 2020) demonstrated the use of modified CDs with γ -Fe₂O₃ as a catalyst to efficiently degrade sulfamethoxazole (SMX) by activating persulphate. The CDs@ γ -Fe₂O₃ were synthesised using glucose as a carbon source through a solvothermal method. The researchers showed that the formation of heterojunction structure between CDs and γ -Fe₂O₃ reduced the catalyst band gap, leading to remarkable efficient SMX degradation compared to other systems. The breakdown of SMX is particularly useful for municipal wastewater plants, where residual SMX in waters could potentially cause negative effects on human health and the environment. While glucose and ethanol are renewable and mild chemicals, using raw biomass could further improve the greenness of this method.

2.3.5 Limitations

CDs have a few drawbacks compared to semiconductor quantum dots, as their low QY can limit their range of applications (Song et al., 2019). While the QY of semiconductor quantum dots can reach 40-90% (Z. Yang et al., 2019), CDs typically only reach up to 30%. However, Yang et al. (Yang et al., 2020) achieved a high QY of up to 62.8% by doping the dots with nitrogen and synthesising them via microwave methods from resorcinol, o-Phenylenediamine, and hydrochloric acid. The high QY was due to the dots containing many N atoms from nitrogen doping, few vacancies in the carbon framework, and a large sp²-domain within the core. The presence of HCl acted as a "promoter" to facilitate the reaction, resulting in a bright fluorescence and high production yield. Nevertheless, applying this method to waste biomass instead of raw chemicals could make it more environmentally friendly.

In addition, a significant challenge associated with CDs is their low production yield, which limits their practical applications. While some studies have reported yields in gram and kilogram scales, many studies do not provide yield values. To address this limitation, Park et al. (Park et al., 2014) developed a method for large-scale production of water-soluble, green CDs from food waste. The researchers used a solution of 10% ethanol with 100 kg of food waste and treated it with US for 45 minutes. The resulting mixture was then centrifuged and filtered twice to remove large particles, producing 120 g of CDs from 100 kg of food waste, representing a yield of 0.12%. The resulting CDs, which were 2-4 nm in size, showed excellent water solubility and demonstrated potential for biomedical applications, including imaging HepG2 cells with low cytotoxicity and excellent photostability. The method is environmentally friendly and cost-effective due to the use of waste biomass as a cheap precursor and the possibility of selling the by-products as fertiliser. Despite its low efficiency and yield, the method is promising for scale-up due to its low cost, use of inexpensive materials, and lack of expensive chemicals or heating processes.

Li et al. (Li et al., 2019) developed a simple, environmentally friendly, and high-yield method to synthesise fluorescent CDs using a one-step hydrothermal treatment of poplar leaves. The technique involved heating 5 kg of poplar leaves with 19 L of deionised water in a 30 L autoclave for 24 hours at 200°C. The dots were obtained by vacuum filtration and rotary evaporation. The researchers were able to obtain 1.498 kg of dots with a yield of 30% from

dry biomass. The dots had a photoluminescent QY of 10.64% and were highly stable in aqueous media and photostable. The dots' surface was rich with functional groups, and they showed consistent photoluminescence and low cytotoxicity within a biological pH range. The dots showed potential applications in electrocatalytic water splitting, Fe³⁺ sensing, and bioimaging, exhibiting remarkable electrocatalytic activity, Fe³⁺ sensitivity, and good biocompatibility.

Ge et al. (Ge, Huang, et al., 2021) reported the highest yield of CDs to date, with near 100% yield obtained through a synthesis method that used dehydroabietic acid and ethanolamine mixed with deionised water heated to 200°C for 300 mins. However, no explanation was provided for the high yield, which could be due to the dots being mixed with impurities or the high purity of the initial reagents used. Further research is needed to investigate the difference in yield and other properties between dots made from raw biomass and those made from purified chemicals, as well as the cost-effectiveness of each approach. The methods proposed by Park, Li, and Ge represent a promising starting point for developing environmentally friendly, high-yield methods for synthesising CDs from biomass.

2.3.6 Future perspectives

Future perspectives in the field of biomass-derived CDs hold immense potential for advancements in various applications. However, several challenges need to be addressed to fully exploit their capabilities.

One significant challenge is the low or unreported production yield, which hinders the isolation of solid dots. Researchers should diligently report yield data, even if it is very low, along with the reasons behind it, allowing for improvement in synthesis methods. Increasing yield will enhance the viability of biomass-derived CDs for various applications. Besides, the focus should also be on achieving high-quality dots with uniform size and high QY. Uniform size ensures consistent emission properties, while a high QY boosts the brightness of the dots, making them more suitable for bioimaging applications.

Another hurdle is the lack of a comprehensive understanding of the optical properties of different types of CDs, including the effect of size, surface defects, and doping. Periodic sampling during synthesis and analysis can provide valuable insights into the

photoluminescence mechanisms, enabling researchers to propose effective mechanisms. Describing the impact of changing synthesis parameters on physical and optical properties will further elucidate the relationship between these properties, facilitating the tunability of dots for specific applications.

In the quest for greener synthesis methods, researchers should strive to incorporate principles that minimise environmental impact. Utilising biomass from waste streams and employing efficient and low-waste reactions are crucial steps. Non-hazardous and benign chemistry should be adopted to ensure safer processes and products. Green synthesis will enhance the practicality of biomass-derived CDs in various applications over an extended period.

For potential application in nanotheranostics, more in-depth assessment of different therapeutic agents loaded on CDs and their performance *in-vivo* is needed. Additionally, precise, and efficient targeting of cellular organelles, such as the nucleus, Golgi body, and mitochondria, will expand the feasibility of biomass-derived CDs in various nanomedicine streams. However, further development and improvement in fluorescent imaging technology are required for *in-vivo* human applications.

Moreover, extensive research around photo-catalysis can shed light on the involvement of CDs in catalytic processes, leading to increased efficiency and positive economic and environmental impacts. Selectivity of the dots should be emphasised to make them more viable as sensors in critical areas like global security, radiation prevention, disease detection, and public utility safety.

While challenges remain, biomass-derived CDs show tremendous promise among carbon structures and are poised to be the next-generation material in various applications. Advancements in understanding and engineering these nanomaterials will drive innovation and bring forth transformative breakthroughs in diverse fields.

2.4 Layer-by-layer

The Layer-by-Layer (LBL) technique is a method for building up thin films layer-by-layer. This technique involves the alternate deposition of oppositely charged materials onto a substrate which forms a layer by self-assembly facilitated by electrostatic attraction. The thickness of the film can be precisely controlled by adjusting the number of deposition cycles (Lipton et al.,

2020). LBL technique was first introduced in 1991 by Decher et al. (Decher & Hong, 1991). Since then, it has gained increasing popularity in various fields such as electronics, optics, sensing, biomedical, and nanotechnology. For example, there are several advantages the LBL process has over uncoated systems when it comes to drug delivery. (Figure 2.5)

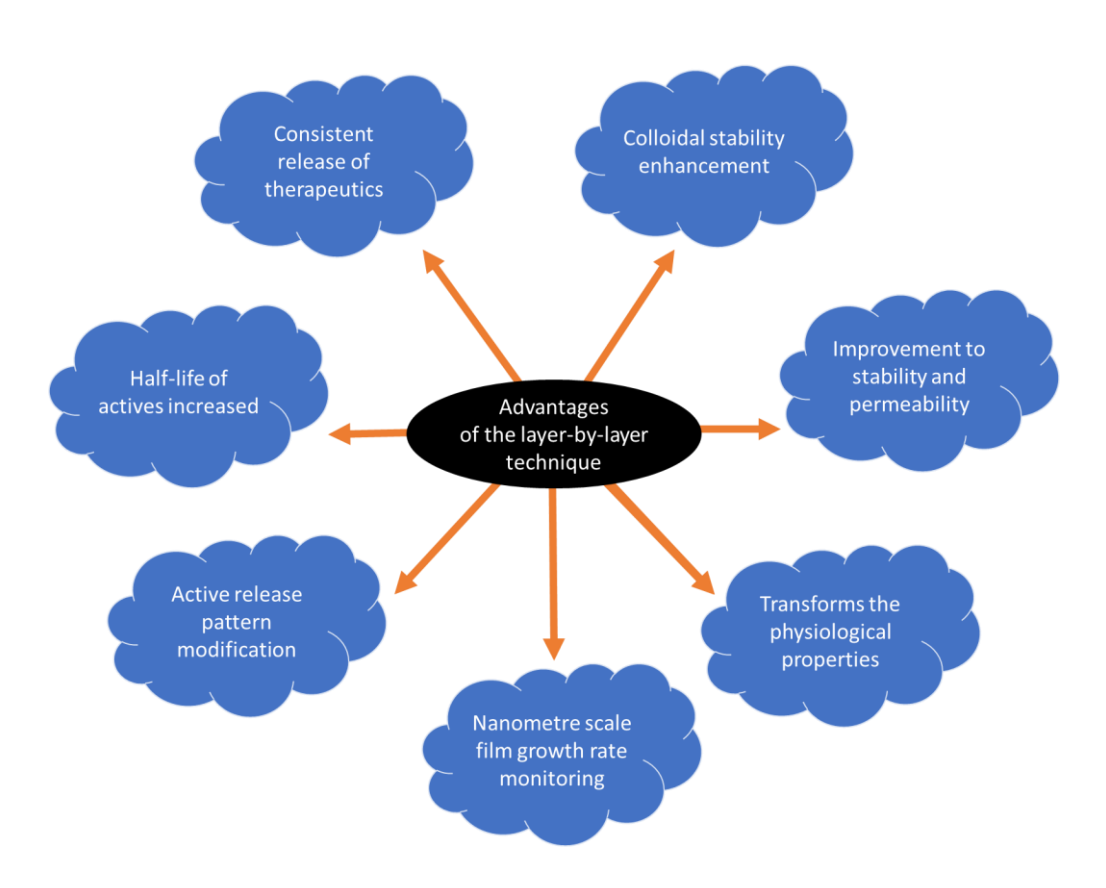


Figure 2.5 - Advantages of the layer-by-layer technique for drug delivery adapted from (Shende et al., 2020)

The LBL technique also has several advantages over other thin-film deposition methods. The technique is also relatively simple and inexpensive and can be carried out in a wide range of conditions, including ambient temperature and pressure. The technique is also being explored for its potential in energy storage, catalysis, and tissue engineering (Díez-Pascual & Rahdar, 2022).

The reasons above outline why the LBL technique is a powerful method for building up thin films; its versatility and simplicity make it an attractive option for a wide range of applications in various fields, especially biomedical applications such as drug delivery, which is a crucial aspect of modern medical research that promises to open the door for new and current pharmaceutical treatments. The development of advanced drug delivery systems with

enhanced therapeutic efficacy and reduced toxicity has been a topic of intense research in recent years. The LBL technique has emerged as a promising method for the development of advanced drug delivery systems or thin films containing other functional molecules such as polymers. (Kurapati et al., 2019).

2.4.1 Fabrication methods

There are several variations of the LBL technique (Table 2.5) that can be used for biomedical applications depending on the materials and the desired properties of the film. The main ones are dip coating, spin coating and spray coating methods. The basis of these methods is the same and starts with the preparation of the substrate with cleaning and modification to increase surface charge density (Li et al., 2012; Shende et al., 2020). The formation of the film involves the following steps (Figure 2.6)(Guzmán et al., 2017):

- Deposition of the first layer: A dispersion of charged particles is deposited onto the oppositely charged substrate. The particles adhere to the substrate due to electrostatic attraction.
- Rinsing: The substrate is rinsed with a solvent to remove any unbound particles; this
 step is very important since unbound material can cause undesirable interpolyelectrolyte complexes which can modify the structure and composition of the final
 material.
- Deposition of the second layer: A solution containing oppositely charged to the first layer's particles is deposited onto the first layer. The second layer adheres to the first layer due to electrostatic attraction.
- 4. Rinsing: The substrate is rinsed with a solvent to remove any unbound particles.
- 5. Repeat: Steps 4 and 5 are repeated to build up the desired number of layers.

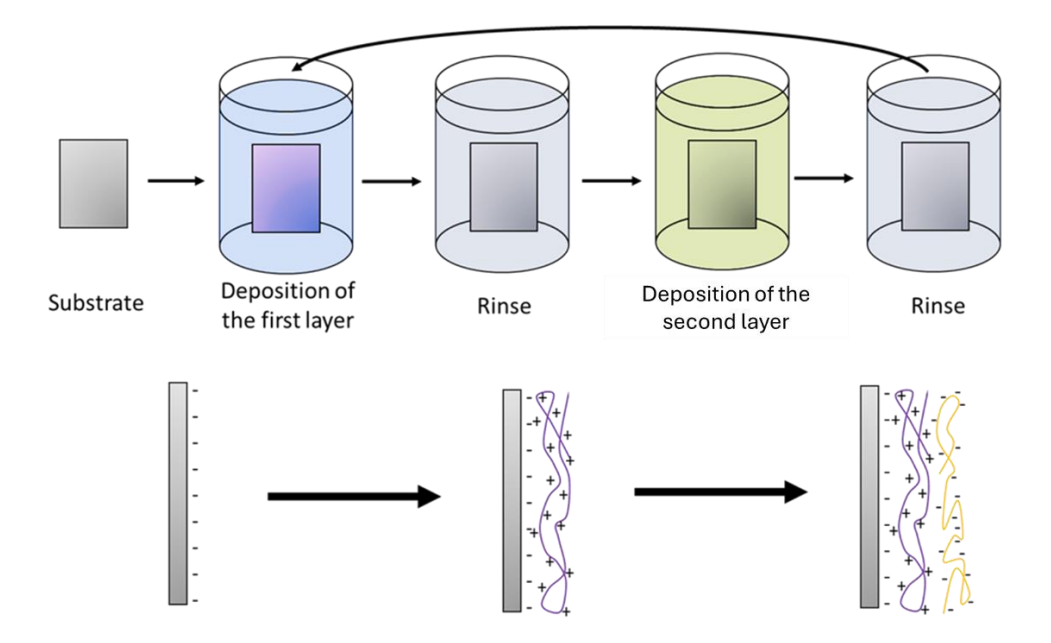


Figure 2.6 - Outline of the steps of the layer-by-layer process - Adapted from (Guzmán et al., 2017).

Table 2.5 - Outline of the most used LBL fabrication methods along with their advantages and disadvantages:

Method	Outline	Advantages	Disadvantages	refs
Spray method	a spray gun to deposit the oppositely charged materials onto the substrate, resulting in a more homogeneous film	Rapid and efficient deposition process. Suitable for large-area coatings. Uniform film deposition. Capable of coating complex geometries.	Limited control over film thickness compared to other LBL methods. Potential loss of material during the spraying process. May require specialised	(Li et al., 2012; Mayilswam y et al., 2022)
Dip coating	the deposition of a	Simple and cost-	equipment for large- scale production. Limited control over	(Shiratori
Dip Coating	thin layer by dipping the substrate into a solution of charged material.	effective method. Suitable for coating various substrates, including porous materials. Capable of producing uniform films. Relatively fast deposition process.	film thickness. May lead to uneven coatings on complex geometries. The deposition rate may vary depending on the solution's properties.	et al., 2002)
Spin coating	The substrate is spun rapidly to evenly distribute a charge material solution on its surface	Precise control over film thickness with subnanometer resolution. Fast and efficient deposition process. Uniform and smooth films. Compatible with a wide range of materials.	Suitable for planar substrates only. May lead to edge effects or non-uniform coatings at the substrate's edge. Limited scalability for large-area coatings.	(Li et al., 2012; Mayilswam y et al., 2022)

The selection of the method depends on the specific application and the materials used. There are many different systems and devices that can be fabricated with the different methods in the LBL technique. However. The method that is most often used be used to synthesise nano or microcapsules is the dip method. This is because spin and spray methods are usually used for creating thin films on larger areas in the macroscale (Fadhillah & Alghamdi, 2023; Matsushita et al., 2023; Vishwakarma et al., 2022; F. Yang et al., 2024).

The dip method is sometimes unsuitable for use cases outside the formation of nano and microcapsules as outlined by Zhao et al. (Zhao et al., 2018) who prepared a LBL assembly composite coating with a polyvinylpyrrolidone (PVP)/polyacrylic acid (PAA) for corrosion protection of AZ31 magnesium alloy. Spin coating was used because the "air shear force and the centrifugal force caused by a high-speed spinning process could rapidly remove the adsorbed water molecules from the coating suspension". With the dip method, these water molecules are not removed and leave pin holes in the surface of the deposited layer making it unsuitable for this application. The microstructure and composition of the coating were investigated using SEM, X-Ray diffraction, and FT-IR measurements and the corrosion performance was tested with electrochemical, immersion, and scratch tests. The results demonstrated that the (PVP/PAA)10 composite coating exhibiting no defects, high density dense, and uniform morphology, was successfully deposited on the surface of the magnesium alloy. This coating demonstrated excellent corrosion resistance and adhesion strength which is a concern with the use of magnesium in biomedical applications (Cui et al., 2016).

For an example of the spray method, Xu et al. (Xu et al., 2021) proposed a simple method for preparing a Tannic acid (TA) contained anti-bacterial coating using the spray LBL method. By controlling the pH and Fe³⁺ ions concentration, they adjusted the complexation states of TA and Fe³⁺. Subsequently, TA-Fe³⁺ complexes and PEI were alternately sprayed onto substrates to form the (TA-Fe³⁺/PEI) coating. Through surface modification using low surface energy silane, they achieved a super-hydrophobic coating with distinct microstructural features. The freshly prepared (TA-Fe³⁺/PEI) coating exhibited inherent contact-killing antibacterial properties. To further enhance the antibacterial effectiveness, in-situ reduction of Ag⁺ ions was performed, resulting in the Ag-loaded (TA-Fe³⁺/PEI) coating that continuously released Ag+ ions in ambient environments. The (TA-Fe³⁺/PEI) coating was successfully coated onto a commercial nonwoven mask, demonstrating its potential practical application in the medical protection field.

Traditionally, layer by layer capsules are created by depositing layers onto particulate cores and then removing the cores to form hollow capsules (Caruso, 2004; Peyratout & Dähne, 2004) (Figure 2.7).

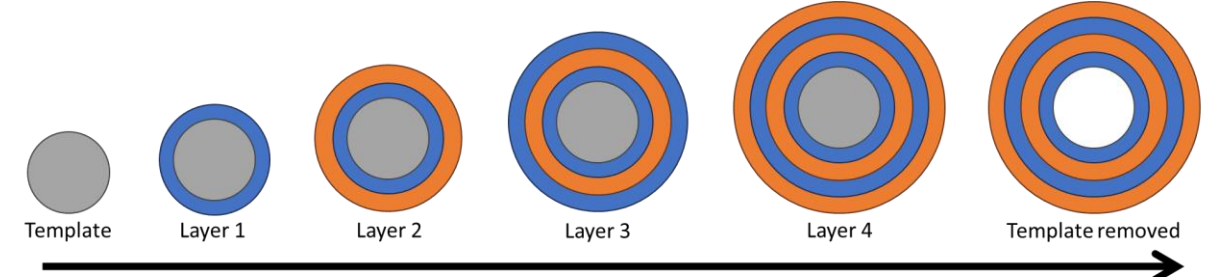


Figure 2.7 - The process of layer-by-layer capsule formation — adapted from (Shende et al., 2020)

There are two essential classes of templates for polyelectrolyte multilayer capsules: smooth surfaces and porous surfaces. The surface porosity influences key parameters such as preparation ease, polymer shell thickness, and loading efficiency. Smooth particles have thinner shells which requires the addition of more layers, while porous cores have a thicker shell because the polyelectrolytes penetrate the matrix, resembling sponges after dissolution. Capsules based on porous particles utilise pores for loading, offering a larger capacity, while those based on smooth particles have a larger inner volume and can easily encapsulate substances through surface shrinking. The choice between these templates depends on the desired properties for loading and releasing cargo in various applications (Parakhonskiy et al., 2014).

An example of nanoparticles being used as a template to create a nanocapsule was outlined by Belbekhouche et al. (Belbekhouche et al., 2020) they designed tailor-made N6L-nanomaterials to treat pancreatic cancer by combining a templating method and a LBL dipping method onto colloidal gold NPs with diameters of 20 nm and 60 nm as a core, capsules were formed with the removal of the templates. The outer layer of the nanomaterial was carefully functionalised with N6L, a synthetic agent that is non-toxic to normal mammalian cells, targets surface nucleolin and induces tumour cell death by apoptosis. A pancreatic cancer model was issued to show that these N6L-based nanostructures targeted cancer cells and inhibited cell survival in a dose-dependent manner highlighting the potential antitumor activity of the developed nanostructures.

A template doesn't always need to be used when creating nanocapsules. Milosavljevic et al. (Milosavljevic et al., 2020) fabricated a nanocapsule encapsulating doxorubicin with layers of furcellaran and chitosan by applying the first furcellaran layer to the free drug. The

nanoparticle showed excellent stability with a pH dependant release. This device showed good anticancer effects in cell tests and entered the cells via endocytosis. Surface modification with homing peptides was used for targeted delivery, which increased the speed of internalisation. This method is a great example reducing steps in the fabrication. Normally nanoparticle templates are first prepared and often later removed to form a nanocapsule. In this instance these steps are completely avoided, speeding up the fabrication time, which in turn would reduce costs, making this method a potential candidate for scale up in future research.

2.4.2 Materials

A wide range of materials can be used in LBL films, including polymers, NPs, biological molecules, and metals. Different material will impart different properties onto films and can be tuned by adjusting the number of layers, concentration of solutions or other synthesis conditions such as solvents, temperatures, time, salt concentrations and pH. The choice of material depends on the functionality of the synthesised device (Elizarova & Luckham, 2018).

Polyelectrolytes (Table 2.6) are one of the most used materials in LBL films. They are macromolecules with charged groups along their chains, making them suitable for electrostatic interactions. They fall into two broad categories: Natural and synthetic. (Wohl & Engbersen, 2012)

- Natural polyelectrolytes consist of DNA, RNA, proteins, peptides, and polysaccharides.
 They have the advantage of being renewable and biocompatible as they are derived from nature which means that layer by layer devices synthesised from these electrolytes have application in the biomedical field. Examples of natural polymers are bovine serum albumin, fibrinogen, and collagen.
- Synthetic polymers used in LBL films include poly(styrenesulfonate), poly(allylamine hydrochloride).

Table 2.6 - Examples of common polyelectrolytes used in the layer-by-layer technique

Polymer	Abbreviation	Origins	References			
Cationic						
Poly(allylamine hydrochloride)	PAH	Synthetic	(Correia et al., 2021; Deligöz et al., 2009; Jiang et al., 2004)			
Poly(diallyldimethy lammonium chloride)	PDADMAC	Synthetic	(Su et al., 2012)			
Polyethylenimine	PEI	Synthetic	(Deng et al., 2021; Ganas et al., 2014)			
Chitosan	CH	Natural	(Hu et al., 2021; Lu et al., 2019; M. Xie et al., 2019)			
Anionic						
Poly(sodium 4- styrenesulfonate)	PSS	Synthetic	(Deligöz et al., 2009; Jiang et al., 2006)			
Poly(vinyl sulfate)	PVS	Synthetic	(Cogo et al., 2006; Xue & Chan, 2015)			
Poly(acrylic acid)	PAA	Synthetic	(Y. Huang et al., 2018; M. Yan et al., 2023)			
Hyaluronic acid	НА	Natural	(Lu et al., 2019; Urbaniak et al., 2023)			
Alginic acid (sodium alginate)	AA	Natural	(Elizarova & Luckham, 2018; Li et al., 2023; Lu et al., 2019; Sun et al., 2021; M. Xie et al., 2019)			

An example of a LBL technique being used with natural polymers was outlined by Ibrahim et al. (Ibrahim et al., 2023). They aimed to enhance DOXO's cytotoxicity while reducing side effects by including metformin in drug delivery using platelet-rich plasma (PRP) mimicking nanocapsules (NC) fabricated via LBL deposition of biodegradable CH and AA on synthesised polystyrene NPs (PS NPs). It was found that the PRP-mimicking NCs have a higher drug loading capacity and smaller size than natural PRP. *In-vitro* and *in-vivo* studies show that metformin enhances the anticancer activity of DOX against breast cancer, and the LBL NCs improve the drugs' biological efficiency compared to free drugs.

Nanoparticles can be used as building blocks in LBL films due to their unique properties, such as high surface area and tuneable optical and electronic properties. Examples of NPs used in LBL films include gold, silica, and magnetic NPs (Silva, 2019; L. Xu et al., 2019). Liu et al. (Liu et al., 2023) used hydrophobic protein (Zein) NPs (ZNP) in a LBL assembly alongside pectin to encapsulate probiotics via the dipping method. The choice of outermost layer significantly impacts cell viability during different conditions. Pectin as the outer layer enhances cell

viability during heating, while ZNP is advantageous during storage. Moreover, the number of coating layers affects cell viability during gastrointestinal digestion. Microcapsules with fewer layers may expose cells to harsh conditions due to pectin dissolution, but consistent coating can mitigate this by leveraging the insolubility of ZNP.

Microcapsules have also been fabricated from gold and silver NPs for application in enhanced Raman scattering active bacterial detection (Li et al., 2022). This was an unconventional synthesis method involving the adsorption of gold NPs and the in-situ synthesis of silver NPs as layers. Notably, the microcapsules exhibited remarkable potential as surface-enhanced Raman scattering substrates for the label-free detection of Rhodamine 6G. It was also demonstrated the practicality of utilising these capsules for microorganism detection by immobilizing bacteria on the particle surfaces.

Lipids are a class of amphipathic molecules that serve as fundamental building blocks of cell membranes. They are widely distributed throughout living organisms (Xuan et al., 2017). Heath et al. (Heath et al., 2015) developed a simple LBL method to create lipid multilayers using vesicle rupture onto existing supported lipid bilayers with the help of an electrostatic polymer linker, poly I-lysine (PLL). Then it was found that adjusting the buffer pH and PLL chain length achieved different thicknesses and close-packed layers in the multilayers. Lipids and membrane proteins within the multilayered membranes could diffuse freely independently of lipid slack and membrane separation. These findings offer new possibilities in various applications, such as energy production and biosensing, and contribute to a better understanding of biological processes.

lonic liquids are salts that are liquid at room temperature and have unique properties, such as high conductivity and low volatility. They can be used as building blocks in LBL films due to their charged nature (Szot et al., 2008; C. Zhang et al., 2014). Li et al. (Li et al., 2024) fabricated novel high-temperature resistant ionic liquid SiO₂ nanocapsules using a combination of the template method and subsequent impregnation method. The capsules had a high loading capacity of 47.7 wt% and an initial thermal decomposition temperature up to 340 °C, which is suitable for the moulding and processing temperatures of various self-lubricating polymers, including polyether ether ketone, polyimide, polytetrafluoroethylene, and polyamide. Friction tests demonstrated that incorporating 3 wt% nanocapsules into nylon significantly increased performance. These results offer valuable insights into the

preparation of high-temperature resistant nanocapsules and promote their industrial application in other self-lubricating polymers.

2.4.3 Properties

The LBL technique enables the precise control of the structure and composition of thin films, resulting in films with unique properties that can be tailored for specific applications. Here are some of the properties of LBL NPs and films (Ai, 2011; Yuan et al., 2020):

Controlled thickness: One of the most significant advantages of LBL films is the ability to control their thickness. The thickness of the film can be precisely controlled by adjusting the number of layers deposited, allowing for films with sub-nanometer to micrometer thickness (Kandjou et al., 2019; Mouhtadi et al., 2023).

Multilayered structure: LBL films have a multilayered structure that can be tailored to provide specific functionalities. The ability to incorporate different materials into each layer enables the creation of films with unique properties, such as mechanical strength, optical properties, and drug release characteristics (Hamdalla et al., 2019; Johansson & Wågberg, 2012; Wohl & Engbersen, 2012).

High surface area to volume ratio: This property is advantageous for applications such as catalysis, sensing, and drug delivery, as it increases the number of active sites available for interaction with the environment (Díez-Pascual & Rahdar, 2022; Rodriguez-Mendez, 2023).

Biocompatibility: LBL films can be designed to be biocompatible by incorporating biocompatible materials, such as natural polymers, peptides, and proteins. This property makes LBL films suitable for biomedical applications such as drug delivery, tissue engineering, and wound healing (Criado-Gonzalez et al., 2021; dos Santos et al., 2024; Mishra et al., 2023; Zeng & Matsusaki, 2019).

Stability: LBL films can exhibit excellent stability due to the strong electrostatic interactions between the layers. This property is beneficial for applications such as sensors and catalysis, where the stability of the film is critical (Erkmen et al., 2022; Zeng & Matsusaki, 2019).

These are just some of the properties of LBL NPs and films. The specific properties of LBL films depend on the materials used, the film thickness, and the order of deposition.

2.4.4 Applications

LBL films in general have many applications that address challenges in various fields, for example

LBL technology offers a surface coating technique to address the challenges facing orthopaedic implants such as insufficient osseointegration, bacterial infection, oxidative stress, immune rejection, and lack of individualised treatment, impacting treatment outcomes and patients' lives. Drugs or biological agents can be loaded onto LBL functionalised implants, and the releases can be controlled at the bone defect site, thereby addressing these challenges and greatly improve patients' lives (Ma et al., 2023).

Food safety is a global concern and antibacterial preservation techniques is a high priority within the field. LBL self-assembly technology offers a promising approach for solutions in food quality inspection and antibacterial preservation such as modifications that enhances the sensitivity, accuracy, and stability of sensors in food quality detection. Additionally, active packaging that exhibits excellent antibacterial preservation properties can effectively extend the shelf life of food (C. Zhang et al., 2022).

One of the most promising applications of LBL assembled systems is in water purification. Two main strategies are used in this context: enhancing the barrier properties of separation membranes and constructing core-shell organic/inorganic sorbents. These systems have specific applications in desalination and the removal of heavy metal ions or organic pollutants from water (Ghiorghita & Mihai, 2021).

LBL micro and nanocapsules fill a slightly different niche in application as compared to the LBL technique in general.

Micro- and nanocapsules hold great promise for applications in sensing. Micro-sized sensing devices allows for the detection of low concentrations of molecules in situ (Johnston et al., 2006). LBL capsules use different techniques for sensing such as immobilizing fluorescent indicators inside the capsules to sense small ions and oxygen (McShane et al., 2002).

Biomolecules such as DNA can be sensed by immobilizing a molecular beacon, which fluoresces upon binding to complementary DNA, within the capsules. This method protects labile species, such as RNA, from degradation prior to analysis (Johnston & Caruso, 2005). This has previously been outlined by Johnston et al. They immobilised a molecular beacon within

a mesoporous silica particle functionalised with a PEI/PAH film deposited with the LBL technique. This device was used to determine the size of DNA that can permeate through the film. This is useful for applications in controlled drug and gene delivery where determining the permeability of films is crucial.

The permeability of the capsule wall is crucial for the sensing process and can be adjusted by varying the film thickness, assembly conditions, and composition (Dubas & Schlenoff, 1999). This ensures that the capsule wall prevents the sensing molecules from diffusing out while acting as a selective barrier for the target molecules (Johnston et al., 2006).

Furthermore, capsules loaded with low molecular weight fluorescent compounds have been utilised in immunoassays (Johnston et al., 2006). This was demonstrated by Trau et al. with their novel class of particulate labels based on nanoencapsulated organic microcrystals. They were fabricated by encapsulating microcrystalline fluorescein diacetate within ultrathin polyelectrolyte layers of PAH and PSS using the LBL technique. This polyelectrolyte coating served as a platform for the attachment of anti-mouse antibodies through adsorption. The applicability of the microcrystal-based label system was demonstrated in a model sandwich immunoassay for mouse immunoglobulin G detection. Following biospecific binding of the capsules to the analyte, exposure to ethanol solubilises the encapsulated fluorophore, allowing it to diffuse out of the capsules and emit a highly fluorescent signal. This method significantly enhances the sensitivity of immunoassays, increasing it up to 2000-fold. This approach provides a general and facile means to prepare a novel class of biochemical assay labelling systems. The technology has the potential to compete with enzyme-based labels as it does not require long incubation times, thus speeding up bioaffinity tests.

To achieve optimal therapeutic effects in medical applications, it is essential to release the appropriate amount of drug for effective treatment. Micro and nanocapsules are used to control drug release at a specific rate and time, preventing drug loss during transport and improving drug utilisation efficiency while reducing toxicity. LBL self-assembly technology allows the synthesis of capsules with customizable properties (X. Zhang et al., 2019). The section below highlights the use of LBL capsules for the delivery of therapeutics.

2.4.5 Layer by layer micro/nanocapsules for drug delivery

The LBL deposition method offers a diverse range of drug delivery vehicles using various organic and inorganic colloids as templates. It has been used to create core-shell NPs and multilayer capsules for drug delivery. The LBL coatings improve the colloidal stability of the NPs, making them suitable for *in-vivo* administration.

Drug release from polyelectrolyte multilayer capsules is done by one of two ways: burst release and sustained release. Burst release is the instantaneous release of the drug and is suitable for intracellular uptake scenarios such as chemotherapy or gene transfection. Sustained release is slow release of the therapeutics over a long period of time; this is preferable when capsules need to remain extracellular, and constant drug levels are necessary such as schizophrenia treatment (Harrison & Goa, 2004; Johnston et al., 2006). Capsules remain extracellular by being too large to enter cells (Horisawa et al., 2002) and gather at the required cells by targeting or passive accumulation (Marin et al., 2022).

Burst release of the therapeutic payload can be achieved by utilising internal or external stimuli to trigger capsule degradation. For instance, light-addressable capsules have been created by incorporating metal NPs into the capsule wall (Angelatos et al., 2005; Radt et al., 2004; Skirtach et al., 2004). These capsules rupture when exposed to short near-infrared laser pulses due to gold NP-mediated heating of the capsule shell (Angelatos et al., 2005; Radt et al., 2004). This approach is viable for releasing various biomaterials, including high molecular weight substances like DNA (Angelatos et al., 2005; Johnston et al., 2006). An example of internal stimuli was outlined by Marin et al. (Marin et al., 2021). They designed their polymer capsules to a have a pH dependant release. The fabricated polymer capsules acted as antioxidant microreactors thanks to the encapsulation of catalase in their core and were able to release DOXO in response to an acidic pH due to the incorporation of functionalised dendritic polyglycerols in their shell.

Alternatively, capsule degradation and burst release can be triggered by the intracellular uptake process itself. This potential is demonstrated through hydrogen-bonded multilayers cross-linked with disulfide linkages (Zelikin et al., 2006), which remain stable in the bloodstream's oxidizing conditions but release their contents in the reducing environment of the cell (Johnston et al., 2006).

For sustained release, therapeutic molecules can slowly diffuse through an intact yet increasingly permeable capsule wall (Park et al., 2005), or they can be gradually released through a slowly degrading capsule wall (Johnston et al., 2006). Environmental stimuli such as pH and ionic strength may trigger changes in the capsule wall necessary for sustained release (Johnston et al., 2006) (Antipov et al., 2003). Antipov et al. (Antipov et al., 2003) explored the impact of ionic strength and pH on fluorescein anion permeation through PSS/PAH multilayer capsules. They observed that fluorescein permeability increases with ionic strength (due to enhanced destruction of the interpolyelectrolyte complex) but decreases with pH (due to increased repulsion between fluorescein molecules and polyelectrolyte multilayers).

Ge et al. (Ge et al., 2022) presented a straightforward and efficient approach for creating large polyelectrolyte microcapsules (Figure 2.22) designed for encapsulating both hydrophilic and hydrophobic substances, with potential applications in drug delivery systems. Microbubbles were used as a template and the capsules had a diameter of $100.4 \pm 14.2 \,\mu m$ and a thickness close to $100 \, nm$. The capsules were shown to encapsulate paclitaxel with high loading capacities and sustained drug release. The capsules offer advantages over conventional methods by eliminating issues associated with template removal, such as template residues, harsh decomposition conditions, and elevated internal osmotic pressure. However, because of their large size these capsules cannot be internalised within a cell which might limit application (Zhang et al., 2023).

A comprehensive investigation into the reaction conditions for the formation of nanosized CaCO₃ cores and LBL capsules was conducted by Elbaz et al. (Elbaz et al., 2020). The synthesised nanocapsules showed stimuli-responsive properties and were designed to offer protection and enable selective drug delivery in the colon. It was found that with the modification of the composition of the layers, distinct drug release behaviours could be achieved.

Shu et al. (Shu et al., 2010) presented the synthesis of biodegradable hollow LBL nanocapsules for the encapsulation of protein drugs. The polyelectrolytes, CH, and dextran sulphate were deposited on protein entrapping amino-functionalised silica particle templates. Cell viability studies indicated good biocompatibility of the nanocapsules, and the drug release kinetics mechanism was identified as Fickian diffusion. These innovative composite nanocapsules hold promise as a delivery system for water-soluble proteins and peptides.

Another example of LBL microcapsules used for drug delivery was reported by Kazemi-Andalib et al. they prepared multilayered pH-responsive hollow microcapsules using two types of polymers: chitosan (CH) and poly(ethylene glycol dimethacrylate-co-methacrylic acid) via the LBL method onto a silica core which was removed once the layer deposition was complete. These microcapsules were designed to carry gemcitabine and curcumin. The drugs were loaded into the microcapsules either during or after the synthesis procedure. Although both methods achieved acceptable loading efficiencies, the drug amount loaded during synthesis was higher. The microcapsules demonstrated high potential for drug delivery. The variation in the amount of drug released in acidic versus neutral pH confirmed the pH-responsivity of the microcapsules. Furthermore, the prepared microcapsules exhibited a dose-dependent high cytotoxicity effect on HCT116 colorectal carcinoma cells.

2.4.6 Limitations and future perspectives

The LBL technique has been widely used for the synthesis of thin films and NPs with controlled properties. However, there are still gaps and limitations in the field that need to be addressed for further development and optimisation of LBL-based materials. Here are some of the major gaps and limitations in the LBL field:

- Limited scalability: The LBL technique is typically performed on a small scale. Scaling up the process for large-scale production can be challenging and will require further research into specialised equipment and processes that can handle an increase in magnitude of production or is much more efficient than current laborious small-scale protocols (Joseph J. Richardson, 2015). Advances in automation will help in the reproducibility and streamlining of these processes (Zhao et al., 2019).
- 2 Problems with compatibility and stability of LBL materials: The LBL technique is not compatible with all materials, and some materials may not adhere well to the surface of the substrate or to other layers in the multilayer structure. LBL films and NPs may be prone to delamination or dissociation under certain conditions, such as changes in pH (Liu, 2014) or temperature, or charged organic materials (Wang et al., 2022). This can limit the range of materials that can be used for LBL-based materials and the stability and longevity of

LBL-based materials and may require additional coatings or modifications to improve their stability, such as cross linking (Liu, 2014). This problem will need to be solved with further research into the how common materials used in the LBL process interact with each other to find optimal combinations and analyse them for their stability in application. A database of research outlining the properties of these materials could help to give researcher better insight into where the research is needed most (Wang et al., 2022).

- Limited understanding of the biological response to LBL-based materials: While LBL-based materials have shown promise in various biomedical applications, there is still limited understanding of the biological response to these materials. This includes their interactions with cells, tissues, and the immune system, as well as their potential toxicity and long-term effects (Zhao et al., 2019). This problem can be mitigated with the use of materials that are derived from biomass which have much more favourable biocompatibility over chemical-based polyelectrolytes. Research should be focused on materials that have the most potential for the highest biocompatibility and with minimal impact in terms of toxicity and long-term effects both inside the body but also in the environment. An example of this is CH, which has been extensively researched in LBL assemblies due to its unique material and biological properties (Hu et al., 2021).
- 4 Limited control over therapeutic release: LBL assemblies are semipermeable by nature which can be tuned with the number of layers and their thickness; however, degradation and unintentional release is still a problem that has yet to be fully solved (Zhao et al., 2019). The problem could be aided by computational works increasing our understanding of how drugs diffuse and release from the layers. This is done by creating models that can accurately predict the drug release curve of individual layer by layer devices, (Jain et al., 2022) allowing for a better understanding of the underlying mechanisms of the drug diffusion. This in turn, would allow researchers to specialise the LBL processes for the required release profile required for application.

In conclusion, the LBL technique has shown great potential for the synthesis of thin films and NPs with controlled properties, but there are still gaps and limitations that need to be addressed for further development and optimisation of LBL-based materials. Addressing these

gaps and limitations will be critical for advancing the field and realizing the full potential of LBL-based materials in various applications.

2.5 Combination of techniques

The research in this project combines both CDs and LBL capsules for the development of a nanotheranostic device that is capable of the imaging and treatment of cancer. There is very little research in the combination of these techniques for any application adding to the novelty of this project, however some examples of current research have already been published is outlined below.

Yang et al. (X. Yang et al., 2013) prepared two types of CDs-embedded polyelectrolyte microcapsules using the LBL technique. The first type, CDs/(PAH/PSS)5PAH microcapsules, were fabricated by alternately adsorbing PSS and PAH onto the CDs/MS composites. The second type, (PAH/CDs)4PAH/PSS/PAH microcapsules, were produced by alternately depositing PAH and CDs onto a sacrificial SiO₂ template. Both resulting CDs-embedded microcapsules emitted blue fluorescence upon UV-light irradiation and exhibited excitationdependent photoluminescence behaviour, like that of CDs in aqueous solution. Furthermore, for the (PAH/CDs)4PAH/PSS/PAH microcapsules, the CDs loading on the shells could be adjusted by varying the CDs concentration or layers, allowing control over the photoluminescence intensity of the microcapsules. Additionally, photo-induced CDs demonstrated electron transfer and redox properties, and other biocompatible materials could replace PAH and PSS. Therefore, the CDs-embedded microcapsules have potential applications in a wide range of fields, including imaging, drug delivery, biosensors, and microreactors for photocatalysis. This one of the only papers that combines the technique of LBL and carbon dots in a way that might be suitable for imaging and drug delivery, however, the capsules that are fabricated in this method are micro-sized, this would limit their application in drug delivery, nanosized particles are internalised much more readily by cells than their micro-sized counterparts (Murugan et al., 2015).

The LBL technique was used by Gonçalves et al. (Gonçalves et al., 2012) to immobilise CDs to a glass optical fibre to create a fluorescence sensor for the detecting sub micromolar concentrations of Hg(II). The CDs used were synthesised by the laser ablation of a carbon target and functionalised with PEG200 and N-acetyl-L-cysteine to make them anionic, PEI was

used as the cation. The author describes that the use of the LBL process allowed the immobilisation of an optimal number of layers which both minimised the background noise due to imperfections on the fibre surface, as well as, leading to an increase in sensor sensibility due to the availability of the CDs to interact with the analyte.

Pinto et al. (da S. Pinto et al., 2017) used oxidised CDs, derived from cellulose acid dehydration, in the creation of self-assembled films in conjunction with the biopolymer CH for potential application in the development of immunosensors, functional coatings, and surface films for photoactivity and UV protection. It was found that film structure, including morphology and thickness, can be effectively controlled, and replicated by managing the conditions of the biopolymer and CD solutions, in addition to the conventional number of dips.

Tuan Nguyen et al. (Tuan Nguyen et al., 2023) introduced a novel approach for fabricating high-performance Quantum Dot Light-Emitting Diode (QLED) devices by utilising layer by layer spin-coating of multi-Quantum Dot (QD) layers along with Ethanedithiol (EDT) treatment. This showed a remarkable 23-fold in increase luminous efficiency for the QLED with double-QD layers compared to a control device featuring a single-QD layer without EDT treatment. This technique is a promising platform for the straightforward realisation of high-performance multi-coloured QLEDs.

There have been a couple of examples of the LBL technique being combined with semiconductor quantum dots for the treatment of cancer, for example.

Adamczak et al. (Adamczak et al., 2012) outlined polyelectrolyte multilayer capsules with quantum dots for biomedical applications in 2012. CdTe quantum dots were encapsulated within layers of biocompatible polyelectrolytes (PLL, Polyglycolide (PGA)) led to a reduction in cytotoxicity. However, the cytotoxicity of CdTe-labelled capsules with PLL/PGA layers was higher than that of plain PLL/PGA capsules. The authors proposed replacing the quantum dots for further research.

Dang et al. (Dang et al., 2016) compared theranostic NIR-II fluorescent probes synthesised from different imaging agents incorporated into biocompatible NPs using the LBL technique. The particles used were; down-conversion NPs, quantum dots, single-walled carbon nanotubes, and organic dyes. The experiments examined their biodistribution, pharmacokinetics, and toxicities and it was found that rare-earth-based down-conversion NPs

emerge as optimal in terms of both biological and optical performance. The QD based platform showed severe toxicities in both the liver and kidneys in tested mouse models which was attributed to QDs leaking out of the capsules.

These studies show the limitations of SCQDs, CDs could be used as a replacement in these applications due to their similar optical properties and better biocompatibility (Desmond et al., 2021). No example of a combination of the LBL technique and biomass-based CDs with application in nanotheranostics were found. This shows that there is novelty in combining these techniques for the nanotheranostic treatment of cancer.

2.6 Summary

The information above serves to outline the current understanding of the field of nanotheranostics and its amazing potential in the medical field, especially cancer treatment, due to its promise of increased efficiency of existing techniques and the discovery of new ones. Comparisons were made between the different techniques used for both bioimaging and therapeutics and different strategies of combining these techniques were investigated. Nanotheranostics allows for multimodal techniques to provide greater range in application and a greater chance that treatments are effective. There are many ways nanotheranostics can be implemented using a variety of drug delivery and imaging techniques meaning that the scope for treatments is extremely wide.

CDs are fluorescent carbon-based NPs that have fantastic potential as a bioimaging agent due to their optical and mechanical properties. They are of particular interest because of their simple synthesis low cost and great biocompatibility, especially when compared to semiconductor quantum dots which are toxic due to their source material. CDs do have some limitations in the fact that their photoluminescence mechanism is not fully understood, and their QY is comparatively low, which will need to be addressed before widespread use in application. Mass yield of CDs is also low, but this is to be expected, especially when they are derived from biomass as the source material contains impurities, this is offset however by the low cost of obtaining the biomass, the lesser environmental impact and the greater biocompatibility shown in biomass derived CDs. research has outlined their potential as fluorescent imaging agents, and some researchers have demonstrated as such in cell and animal models.

The LBL technique is the self-assembly of multilayer films through electrostatic attraction They can be synthesised in many ways and the fabrication method is usually chosen because of application and materials used. For example, nanocapsules are usually fabricated with the dip method. The highly tuneable films can be made up from many charged materials, such as polyelectrolytes, and they derive their properties from the materials they are formed from. This gives them a wide range of applications, especially in the medical field for drug delivery. Drug delivery is often achieved with LBL capsules which are formed around a NP template. Limitations of the LBL technique include scalability, compatibility and uncontrolled drug release. Natural polymers such as CH and AA are often used to increase biocompatibility, and their synthesis is inexpensive and simple. Drug released can be tuned by the number of layers and materials used. Further improvements could be made in the future with more research into drug release from LBL nanoparticles and the use of computational models to improve understanding of release mechanisms.

Currently there is potential for a nanotheranostic technique that uses both LBL capsules and CDs in combination for cancer therapy and imaging. More investigation into these techniques alone and in combination is needed to achieve a fully capable system that can be used in the human body to treat cancer.

Chapter 3. Materials and Experimental Methods

This chapter outlines the methodologies used in this project; this includes the reaction series and the subsequent analysis. Three syntheses of CDs were conducted, two hydrothermal-based using different catalysts such as tannic acid and SA, and a microwave-based reaction using aqueous conditions. The resulting dots were analysed to discover their physical and optical properties.

Several fabrications were conducted to investigate the formation of a LBL nanocapsule and the resulting particles were analysed to investigate their size and surface chemistry.

Discussion of the results from each method can be found in the dedicated chapters for those experiments.

3.1 Synthesis of Carbon dots

The leftover material from coffee brewing is called spent coffee grounds (SCG) and around 6 million tons are generated globally each year, most of which goes to landfill and contributes to potential ecological damage by the leaching of chemicals such as caffeine, tannins and chlorogenic acid into the environment (Janissen & Huynh, 2018). Recent efforts have focused on converting SCGs into high-value products, including fluorescent nanoprobes such as CDs. For example Hsu et al. (Hsu et al., 2012) synthesised CDs from SCGs through heating and a simple separation process which demonstrated efficient fluorescence, making them suitable for cell and matrix imaging. Other groups, Hong et al. (Hong & Yang, 2021) and Xu et al. (Xu et al., 2017), also successfully synthesised CDs from SCGs using a hydrothermal process yielding fluorescent CDs with potential applications in anti-counterfeiting and sensing probes for metal ions in water. While these studies showcased the potential of SCGs as green precursors for CD synthesis, there remains a challenge to establish easily scalable, non-hazardous, and quality-controllable processes that meet both industrial and environmental standards.

To that end, this section outlines the main methodologies for synthesising CDs from SCG. This is split into 3 main syntheses.

Synthesis 1 - A two-step process: acid catalysed hydrothermal carbonisation of coffee grounds followed by a nitric acid oxidation.

Synthesis 2 – An investigation into an ultrasonic pretreatment, followed by a hydrothermal carbonisation.

Synthesis 3 – A microwave-assisted aqueous hydrothermal carbonisation.

3.1.1 Materials

Spent coffee grounds (SCG) (Figure 3.1) were obtained in café shops in Newcastle city, the UK. The SCG were dried before use in an oven at 80°C for 2 hours and analysed using X-ray photoelectron spectroscopy (XPS), Fourier transform infrared spectroscopy (FT-IR), and transmission electron microscopy (TEM).



Figure 3.1 - Dried spent coffee grounds

Other chemicals (tannic acid (TA) (99.9%), sulphuric acid (SA) (99.9%) and nitric acid (70%)) were obtained from Sigma Aldrich. These chemicals were prepared to desired concentrations depending upon experiments (Table 3.1).

Table 3.1 - Outline of the concentrations of acid catalysts and corresponding pH used in the following experiments.

Acid	Concentration a used in experiments	concentration in Mol/dm ³	рН
Sulphuric	0.005 g/ml	0.051	1.22
acid	0.01 g/ml	0.102	0.96
	0.02 g/ml	0.204	0.68
Tannic acid	0.005 g/ml	0.0029	4.27
	0.01 g/ml	0.0058	4.12
	0.02 g/ml	0.012	3.96
	0.05 g/ml	0.029	3.77
	0.1 g/ml	0.059	3.61
Nitric acid	0.2 g/ml (20%	6) 3.17	-0.5

3.1.2 Acid catalysed Hydrothermal carbonisation (HTC) of spent coffee grounds and nitric acid oxidation (Synthesis 1)

This method was adapted from the microwave-assisted method outlined by Xu et al. (Xu et al., 2017) because of the high yields and good fluorescent properties. Their method used a microwave-assisted HTC with a SA catalyst to synthesise a graphitic precursor, which was then subjected to a nitric acid oxidation to form the CDs. The SA catalyst assisted with the decomposition of the cellulose within the SCG by catalysing the depolymerisation reaction (Shrotri et al., 2018). Carbonisation of the glucose followed, synthesising a precursor made up of fine carbon sheets. The dilute nitric acid oxidation cut and exfoliated the precursor to CDs which had a graphitic structure of a few layers. This acid cutting oxidation has also been described previously (Peng et al., 2012). The method used in this project used an oven-assisted hydrothermal process and is outlined in Figure 3.2.



Figure 3.2 - The reaction schematic of two step carbon dot synthesis; hydrothermal carbonisation of coffee grounds followed by a nitric acid oxidation

Step 1 proceeded as such; approximately 0.5g of dry coffee (particle size - 0.05-0.2mm) grounds were mixed with 15ml of water/acid catalyst (ratio - 1:30 wt/vol, conc – 0.005-0.05g/mL) and placed into a 125mL Parr acid digestion vessel, which featured a polytetrafluoroethylene cup (Figure 3.3) and sealed. This sample ratio was chosen due to suggested operation of the vessel. This vessel was then heated to 200°C for a specified amount

of time (between 2-4 hours). This temperature was chosen because effective carbonisation of cellulose occurs above 180°C (Bevan et al., 2023). higher temperatures were not investigated with variations due to limitations with the oven.

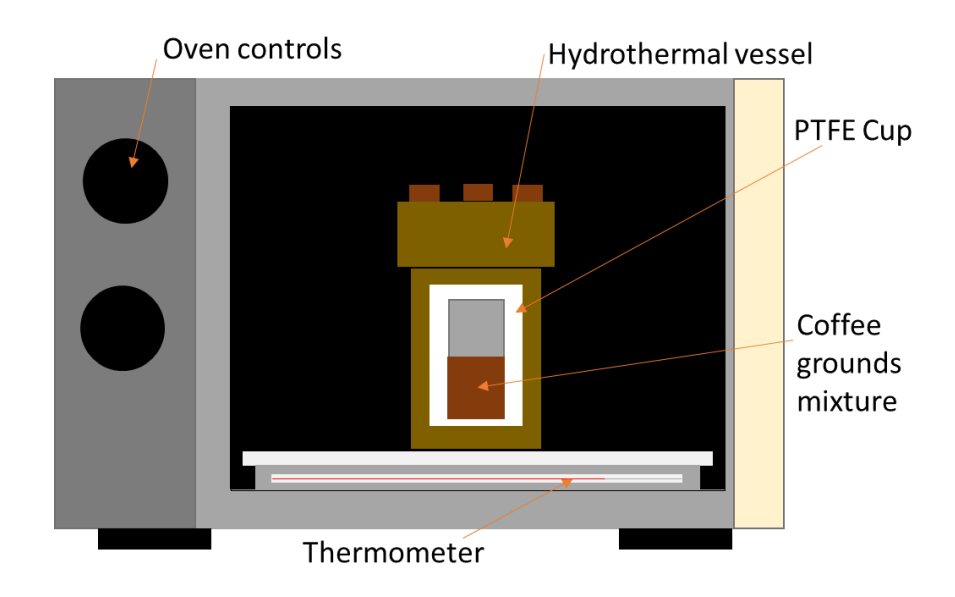


Figure 3.3 - Schematic of the hydrothermal reactor and heating apparatus

The vessel was then left to cool overnight, and the mixture was then filtered via vacuum filtration through a 0.1µm Merck Millipore mixed cellulose ester (MCE) filter to obtain a solid precursor. This small pore size filter was used because using a larger size might have meant loss of precursor in the washing process. The precursor was dried in an oven at 70°C for 24 hours to completely remove any excess water and then was stored for further analysis. This temperature was selected so that the precursor would not burn, and the time was to ensure that it was completely dry.

This synthesis was run 10 times, and the parameters were varied according to Table 3.2. The standard conditions were a SA catalyst solution of 0.01g/mL reacted for 2 hours at 200°C. The time tests investigate the effect of increasing reaction time on the synthesis of the precursor and resulting dots. 2-4 hours were chosen because these are standard times that are used in the carbonisation of biomass, although some studies have been conducted up to 8 hours (Bevan et al., 2023). The acid tests investigate the effect of SA concentration and TA tests investigate the effect of TA as a HTC catalyst.

The sample codes outline the step 1 synthesis parameters used for the sample. The prefix indicates which test the sample is a part of (time test (TT), sulphuric acid tests (AT) or tannic acid tests (TA)). The middle indicates the variable reaction parameter (retention time or

concentration in g/mL) used the suffix indicates the reaction step (Step 1 - precursor synthesis (P), Step 2 - CD synthesis (CD)).

Table 3.2 - Experimental conditions on hydrothermal synthesis of the graphitic precursor using SCG at a fixed temperature of 200oC and ratio of spent ground coffee to water of 1:30 wt/vol.

	Catalyst		Holding
Sample code	Catalyst type	Concentration	time
		(g/mL)	(Hours)
	Time Tests (T	T)	
TT-2H-P/AT-0.01-P	Sulphuric acid	0.01	2
TT-3H-P	Sulphuric acid	0.01	3
TT-4H-P	Sulphuric acid	0.01	4
	Acid Tests (A	Τ)	
AT-0-P	None	0.0	2
AT-0.005-P	Sulphuric acid	0.005	2
AT-0.01-P/TT-2H-P	Sulphuric acid	0.01	2
AT-0.02-P	Sulphuric acid	0.02	2
Tannic Acid Tests (TA)			
TA-0.005-P	Tannic acid	0.005	2
TA-0.01-P	Tannic acid	0.01	2
TA-0.02-P	Tannic acid	0.02	2
TA-0.05-P	Tannic acid	0.05	2

Step 2 proceeded as such; approximately 50mg of each precursor was mixed with 15ml of 20%wt of nitric acid and ultrasonicated at 60°C for half an hour. The mixture was then refluxed at 90°C for half an hour for the oxidation. The reaction proceeds by the degradation-oxidation cutting down the precursor to carbon dots. Ultrasonication was used to disaggregate the particles for a more efficient oxidation by increasing the surface area to volume ratio of the precursor. The temperature was at 60°C so that oxidation would not occur prematurely. Nitric acid is chosen for its powerful oxidising capabilities and have been shown to have worked in previous experiments. However, other oxidisers such as hydrogen peroxide (Mittal et al., 2023) or oxidation methods such as ozonolysis (Osorio-González et al., 2020) could be investigated in the future. Different oxidisers have different oxidising strengths so it would be expected that the size of the carbon dots would change depending on how efficient the oxidation reaction would be. Wang et al produced dots from nitric and sulphuric acid oxidation degradation of carbon black with a size less than 10nm with a reaction time of 60 mins (Wang & Lu, 2015). Roy et al. reported a size of 30-40 nm with a hydrogen peroxide oxidation

degradation of teak leaves (Roy et al., 2024). Jeong et al reported a size of 5-15nm with a oxidation degradation of dried mango pulp with phosphoric acid (Jeong et al., 2014).

The 90°C temperature was needed to achieve reflux as it is above the boiling point of nitric acid. It has been found that the efficiency of the oxidation reaction is proportional the temperature (Hecker et al., 1991). After cooling, the mixture was then filtered to through a 0.1µm Merck Millipore MCE filter to separate solid and liquid containing CDs. The CD analysed with Ultraviolet-visible spectroscopy dispersions were photoluminescence (PL) spectroscopy to investigate the optical properties, absorbance and excitation, emission and QY. The solid fraction was obtained through rotary evaporation and dialysis for 72 hours with a dialysis membrane with a molecular weight cut off (MWCO) of 3500 Da, keeping the CDs within the membrane. The resulting solid was then analysed with XPS and FT-IR to study surface chemistry, and TEM to analyse morphology and size. The reaction conditions for this step were consistent across all samples, for this reason, the CD samples will retain their step 1 parameter code but will change their suffix from -P to -CD (E.g. - TT2H-P ->TT2H-CD).

3.1.3 Ultrasonic pretreatment of spent coffee grounds and tannic acid catalysed hydrothermal carbonisation (synthesis 2)

This synthesis is a two-step ultrasonic pretreatment and TA catalysed HTC of CDs followed by a dialysis purification (Figure 3.4). This was for the investigation of reaction parameters' effect on the properties of CDs and to compare the effect of the ultrasonication pretreatment as later described. The practical work for this investigation was completed by Master's student Thomas James under the supervision of Thomas Wareing and Anh Phan.

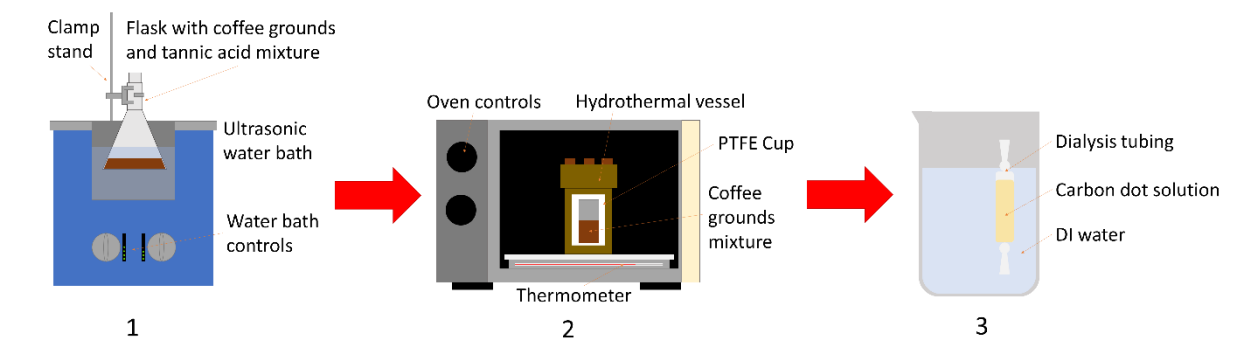


Figure 3.4 - Experimental configuration for 1 – ultrasonic pre-treatment, 2 - hydrothermal carbonisation, and 3 - dialysis of carbon dots.

Pretreatment proceeded as such; Around 10g of dried SCGs was placed into a conical flask and mixed with 50ml of 0.05g/mL TA solution. This 1:5 wt/vol ratio of biomass to catalytic solution is standard for HTC (Heidari et al., 2019; Volpe et al., 2020). This SCG and TA mixture was then placed in a FB15053 ultrasonic water bath (frequency – 37kHz) at room temperature (~20°C) for 90 minutes to allow for proper breaking up and de-clumping of the SCG, which could be seen visually, and allow for multiple samples to be taken to analyse the effect of time. The water in the bath was replaced to maintain a stable temperature. The top of the conical flask was sealed to prevent evaporation. Approximately 1mL aliquots were taken using a pipette at a 15-minute interval for the duration of the pretreatment, for FT-IR surface analysis for functional group analysis. These aliquots contained both the solid and liquid phases aiming at preserving the ratio between these phases for the whole duration of the experiment. The collected aliquots were centrifuged to separate the liquid and solid, the solid samples were then dried at 70°C for 48 hours to remove the water for analysis. Table 3.3 illustrates the conditions used in the pretreatment. These were ratio of biomass to catalytic solution (prefix; Ratio-), concentration of TA catalytic solution (prefix; Conc-) and temperature (prefix; Temp-). The middle part of the sample code denotes the change in condition. The suffix denotes the step of the reaction (either PT or CD).

Table 3.3 - Pre-treatment conditions applied during ultrasonic pre-treatment of SCGs over 90 minutes pre-treatment time.

Sample Code	Temperature (°C)	Ratio of biomass / catalyst solution (wt/vol)	Concentration of tannic acid (g/mL)
Standard cond	itions		
Std-Cnd-PT	~20	1/5	0.05
Ratio Tests			
Ratio-25-PT	~20	1/2.5	0.05
Ratio-100-PT	~20	1/10	0.05
Concentration tests			
Conc-0.01-PT	~20	1/5	0.01
Conc-0.1-PT	~20	1/5	0.1
Conc-0.0-PT	~20	1/5	0.0
Temperature tests			
Temp-40-PT	40	1/5	0.05
Temp-60-PT	60	1/5	0.05
Temp-80-PT	80	1/5	0.05

Hydrothermal Carbonisation (HTC) proceeded as such; each mixture from the ultrasonication pre-treatment was placed into a 125mL Parr reactor, which was heated to 200°C and kept at that temperature for 3 hours. The vessel was then removed and allowed to cool before the reaction mixture was centrifuged to separate solid and liquid. The liquid containing the CDs was stored for purification. All liquid samples were additionally filtered using a 0.1μm Merek Millipore (MCE) membrane filter and vacuum pump to remove residual solids prior to separation of the CDs. The sample codes for this step retain their previous prefix and condition codes and the suffix is changed from -PT to -CD. A dispersion of 10g spent coffee grounds without pre-treatment was added in 50mL of 0.05g/mL TA solution to serve as a control to investigate the effect of the pretreatment against no pretreatment and will be referred to as NO-PT.

Purification of Carbon Dots was done by dialysis, which is a standard practice for the purification of carbon dots (Ullal et al., 2024). In this case, the dialysis was against deionised water using 3500Da then 2000Da membranes, which were each carried out continuously over 3 days. The 3500Da membrane was used to remove particles larger than the CDs as they made their way through this membrane. The 2000Da membrane was used to remove any leftover TA, the dots were retained by this membrane and the TA, with a MW of 1,701Da passes through. The dialysed dispersions were then rotary evaporated to remove excess water, leaving concentrated CD/TA solution for analysis and final separation. The samples were then frozen to -80°C for 3 days before entering a freeze dryer for 48 hours to remove all residual water. The solid dots are then analysed using FT-IR, TEM and XPS for morphological and surface analysis, UV-Vis and photoluminescence spectroscopy for optical properties and cell toxicity against U2OS and Saos-2 cells using PrestoBlue cell viability. Saos-2 is a cell line with epithelial morphology that was isolated from the bone of an 11 year old female osteosarcoma patient (UKHealthSecurityAgency). U2OS Cell line derived in 1964 from a moderately differentiated sarcoma of the tibia of a 15 year old girl (UKHealthSecurityAgency)

3.1.4 Microwave assisted aqueous hydrothermal carbonisation of SCG (synthesis 3)

This synthesis builds upon the results of the previous synthesis, i.e. synthesis 2, and serves as a comparison of the microwave and hydrothermal methods. This is a two-step aqueous HTC of coffee grounds to investigate the effect of retention time and reaction temperature.

A typical synthesis progressed by mixing dried 10g of SCG with 50mL DI water and was subject to ultrasonication for 90 minutes at a temperature of 60°C. This ratio of 1:5 wt/vol (biomass:water) was as used in previous experiments and was found to be the most effective. This mixture was then transferred to a microwave reaction vessel and placed into a microwave for an hour at 200°C (Figure 3.5).

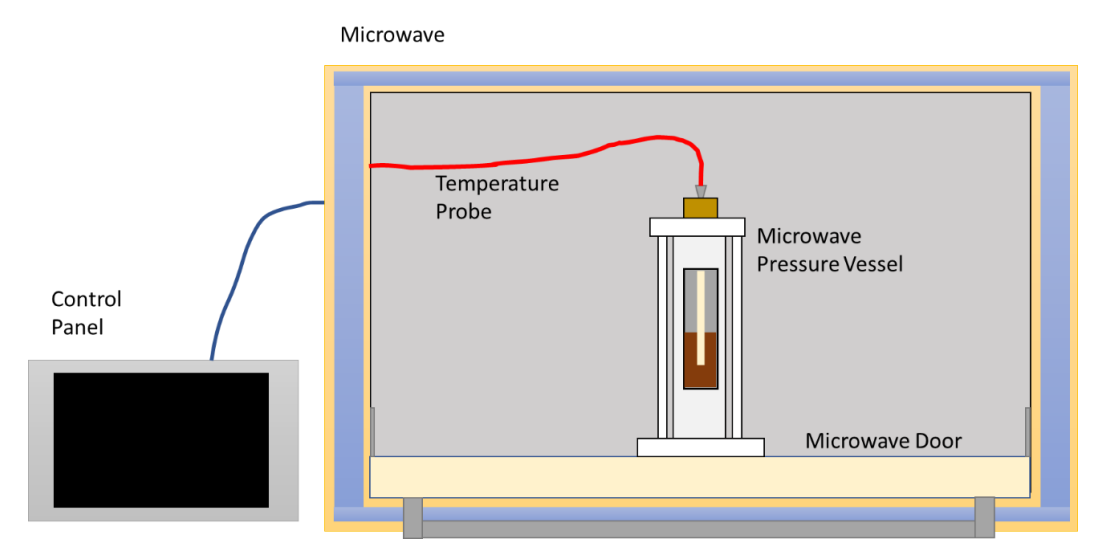


Figure 3.5 - Microwave reaction set up for the hydrothermal carbonisation of spent coffee grounds.

The resulting mixture was then centrifuged 3 times (4400 Rotations per minute (RPM), 15mins) to remove a dispersion containing the CDs from the large solid waste. The dispersion was then filtered through three subsequently smaller Buchner funnel filters. 0.44µm, then a 100nm Millipore MCE filter then a 50nm Millipore MCE filter. This filtration method was to ensure the removal of larger particles. Multiple rounds of filtration were performed as to not clog the smaller filters. The mixture was then concentrated using rotary evaporation to remove excess water. The liquid was then frozen at -80°C for 24 hours and then freeze dried for 48 hours to recover solid CDs. The solid dots were then analysed using FT-IR, TEM and XPS for morphological and surface analysis, UV-Vis and photoluminescence spectroscopy for

optical properties and cell toxicity against U2OS and SAOS-2 cells using PrestoBlue cell viability for toxicity testing.

The parameters adjusted in this synthesis are reaction temperature (150-200°C) and time (30-120 minutes). These are outlined in

Table 3.4 below. This range of retention times is consistent with literature. Previous

Sample	Temperature of microwave (°C)	Retention time (mins)			
	150°C tests				
150-30	150	30			
150-60	150	60			
150-90	150	90			
150-120	150	120			
	175°C tests				
175-30	175	30			
175-60	175	60			
175-90	175	90			
175-120	175	120			
	200°C tests				
200-30	200	30			
200-60	200	60			
200-90	200	90			
200-120	200	120			

experiments are between 2 minutes (Shibata et al., 2022) and two hours (Xu et al., 2017). Due to pressure limitations on the microwave vessel, temperatures above 200°C could not be investigated. Moreover, it has been shown in literature that carbonisation does not efficiently occur below 180°C. Therefore, the temperatures of 150 and 175°C were chosen to investigate the effect of less effective carbonisation on the synthesis of CDs.

Sample	Temperature of microwave (°C)	Retention time (mins)		
	150°C tests			
150-30	150	30		
150-60	150	60		
150-90	150	90		
150-120	150	120		
175°C tests				
175-30	175	30		
175-60	175	60		
175-90	175	90		
175-120	175	120		
	200°C tests			
200-30	200	30		

200-60	200	60
200-90	200	90
200-120	200	120

Table 3.4 -Sample codes of each

microwave carbonisation according to temperature (prefix) and time (suffix).

3.2 Layer-by-layer techniques

Similarly to various other types of inorganic NPs like gold, magnetite and silica, calcium phosphate (CaP) nanocarriers have become particularly attractive in nanomedicine. This heightened interest is attributed to their excellent biocompatibility and biodegradability. The appeal of CaP arises from its status as the inorganic mineral found in human bones and teeth. CaP NPs fulfil crucial criteria for an effective delivery system. These include their capacity to encapsulate drugs or biomolecules and their inherent biodegradation which results in the formation of harmless compounds, namely calcium and phosphate ions. (Qiu et al., 2022) For these reasons, CaP NPs make great templates for a LBL polyelectrolyte nanocarrier as

demonstrated by Elizarova et al. (Elizarova & Luckham, 2016). They utilised a peristaltic pump continuous process to create multilayer polymer capsules. Also, Verma et al. (Verma et al., 2016) also used CaP NPs functionalised with vitamin B12 to create an oral insulin delivery device.

Building upon this research, the fabrication of CD-functionalised LBL capsules on CaP NPs for application in nanotheranostics was conducted. The various procedures that are related to this LBL capsule formation includes.

- Effect off flowrate and drying methods on NP templates
- First layer functionalisation of calcium phosphate templates
- First LBL capsule fabrication chitosan and alginate, functionalisation with anticancer drugs and CDs
- Second LBL Capsule fabrication chitosan and chondroitin sulphate, functionalisation with anticancer drugs and CDs

3.2.1 Materials

Calcium lactate - was obtained from sigma Aldrich as a white powder and was mixed with deionised (DI) water to form a solution with a concentration of 24mM. NaOH and HCl was used to correct the pH to 10.

Ammonium phosphate (di-basic) - was obtained from sigma Aldrich as a white powder and was mixed with DI water to form a solution with a concentration of 15mM. NaOH and HCl was used to correct the pH to 10.

Polyethylenimine (PEI) – had a MW of 800 Da and was obtained from Sigma Aldrich and mixed with water to form solutions of 3 different concentrations: 3, 5 and 10mg/mL. NaOH and HCl was used to correct the pH to 10.

PolydiallyIdimethylammonium chloride (PDADMAC) – had an average MW of 100,000 Da and was obtained from Sigma Aldrich and mixed with DI water to form solutions of different concentrations; 0.5, 1, 2.5 and 5 mg/mL, NaOH and HCl was used to correct the pH to 10.

Poly(allylamine Hydrochloride) (PAH) – had a MW of 15,000 Da was obtained from Sigma Aldrich and mixed with DI water to form solutions of 3 different concentrations; 3, 5 and 10g/mL, NaOH and HCl was used to correct the pH to 10.

Chitosan (CH) - was obtained from Sigma Aldrich and mixed with DI water to form solutions of different concentrations; 0.5, 1, 2.5 and 5mg/mL, NaOH and HCl was used to correct the pH to 5. Solutions of 0.5 and 1mg/mL solutions were also created using a 5.5 pH sodium acetate buffer.

Sodium alginate (AA) - was obtained from sigma Aldrich and mixed 5.5 pH sodium acetate buffer to form a solution of 1mg/ml.

Chondroitin sulphate (CS) - was obtained from sigma Aldrich and mixed with DI water to form a solution of 1mg/ml.

Sodium acetate buffer (SAB) - was synthesised by making a solution with DI water that contained 0.07M sodium acetate and 0.03M acetic acid. the pH is then corrected to 5.5 using HCl and NaOH.

Doxorubicin (DOXO) - was acquired from sigma Aldrich and was dispersed in a solution (1:1 % v/v) Dimethyl sulfoxide (DMSO): phosphate buffered saline (PBS) at a concentration of 1mg/ml.

Docetaxel (DAX) - was acquired from sigma Aldrich and was dispersed in a solution of (1:1 % v/v) DMSO: PBS at a concentration of 600 μ g/ml.

3.2.2 Flowrate and drying methods investigation

This investigation was used to evaluate the effect of flow rate and drying methods on the properties of the CaP NPs.

The templates were synthesised with a peristaltic pump (Pharmacia fine chemicals) reactor at 4 specified flow rates to combine 40mL of 24mM calcium lactate and 15mM ammonium phosphate. The newly synthesised nanoparticles were collected in a beaker with continuous stirring (Figure 3.6). A P-3 peristaltic pump (Pharmacia fine chemicals) was used because it has very precise control with flow rate. The flow rates used are 0.5, 3, 6 and 9mL/min. The resulting solution from each flow rate was then split into three fractions and centrifugation was used to separate the NPs from the supernatant. Once separated all three sets of particles were washed in DI water. One set was left to dry in air, another was frozen at -80°C for 24 hours and then freeze dried for 48 hours. The third fraction was centrifuged once more to

separate the particles from the water, then the particles are washed with isopropanol then left to dry in air.

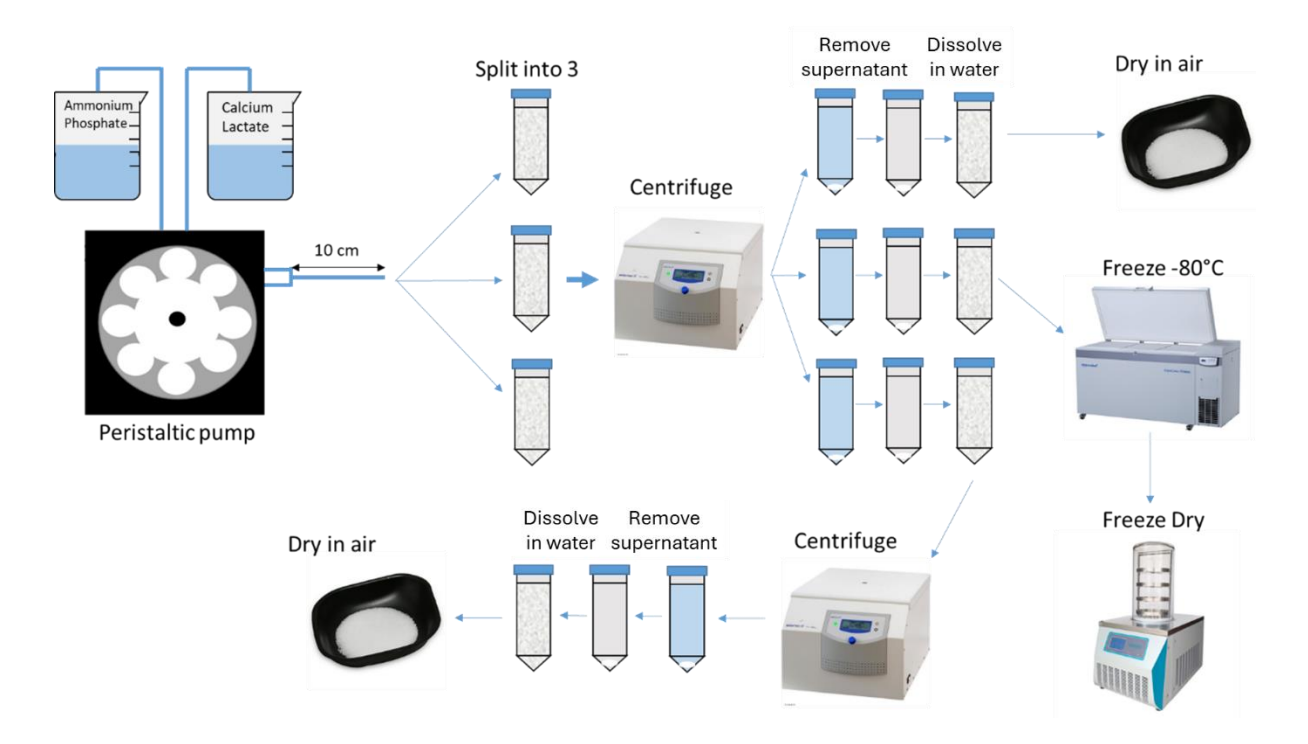


Figure 3.6 - Reaction schematic of the flowrate and drying method tests

3.2.3 Calcium phosphate template functionalisation with first layer

This method was used to investigate the effects of immediate functionalisation of the templates, the saturation level of the polyelectrolyte functionalisation, and the properties of the templates with different polyelectrolyte layers.

The reactions progressed first with the crystallisation of CaP to form NPs and, subsequent stabilisation by functionalisation with a cationic polymer to obtain a precipitate of NPs, as reported by H. Urch et al. (2009) (Urch et al., 2009).

The CaP NPs were synthesised (Figure 3.7) by combining 40mL ammonium phosphate and 40mL calcium lactate solutions using a P-3 peristaltic pump (Pharmacia fine chemicals) in a 10cm silicone tubing reactor (3mm diameter). The resulting particles immediately enter the 100cm tube reactor and were mixed with 40ml of polyelectrolyte solution. The particles and supernatant were collected in a beaker and stirred for 24 hours. The mixture is then dialysed for 12 hours using dialysis tubing with a 14,000 MWCO. After dialysis, the dispersion of NPs is separated using centrifugation at 4400rpm for 20 minutes and the supernatant is removed. The pellets of NPs are then dispersed in DI water and washed again, separating once more with another round of centrifugation. The final products were then either suspended in a NaCl solution or DI water at 4°C for further use or freeze dried for analysis. three polyelectrolyte solutions were tested: PEI, pDADMAC, and PAH in different experiments.

Table 3.5 outlines the concentrations of polyelectrolyte solutions tested with their corresponding pH.

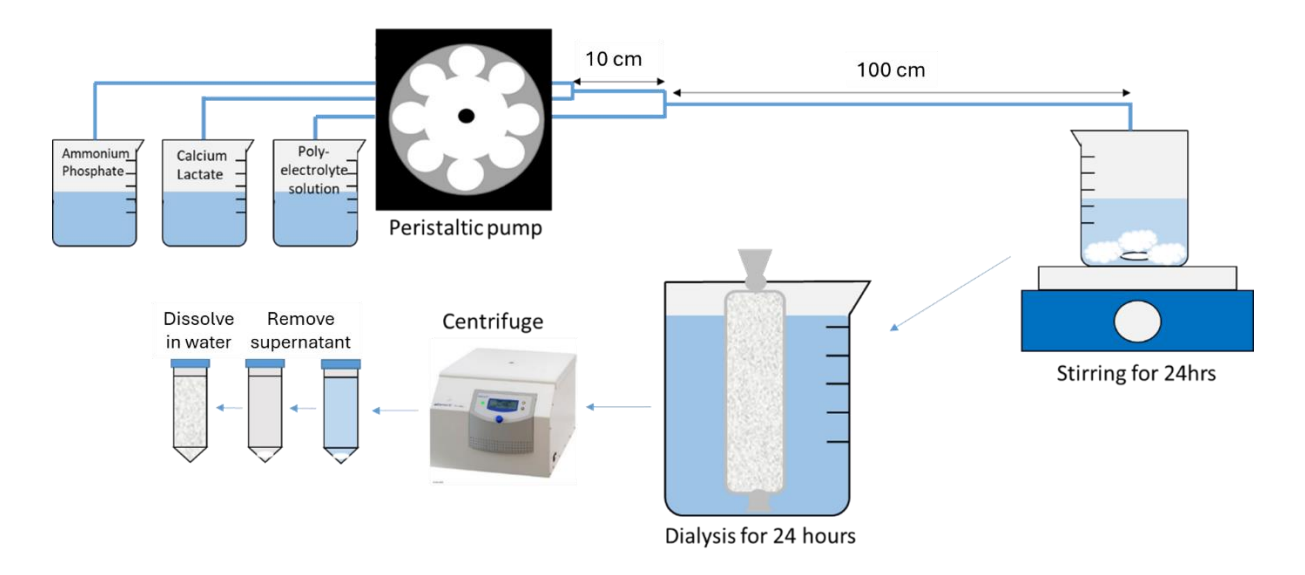


Figure 3.7 - Reaction schematic for calcium phosphate nanoparticle synthesis and first layer deposition.

Table 3.5 - Conditions of the polyelectrolyte solutions used in the CaP template functionalisation.

LBL capsule fabrication method	Polyelectrolyte	Concentrations (mg/mL)	рН
Chitosan and Alginate	PEI	3, 5 and 10	10
Chitosan and Alginate	pDADMAc	3, 5 and 10	10
Chitosan and chondroitin Sulphate	PAH	0.5, 1, 2.5 and 5	10

The different concentrations were used to find the saturation point of the polyelectrolyte. The reaction to synthesise CaP NPs occurs at pH 10 because pH above 9 increases the dissociation of the ammonium phosphate facilitating the reaction (Kim et al., 2018). For this reason, all the polyelectrolyte solutions were adjusted to pH 10.

The drug loading of these particles was investigated. The tests were replicated as described above with the inclusion of solution of anticancer drugs PBS:DMSO (1:1 % v/v) with the ammonium phosphate solution. In the first fabrication method, 3 different drug solution combinations were included (400 μ L of 10mM DOXO,400 μ L of 600nM DAX and 400 μ L of both solutions). In the second fabrication method 135 μ L of 10mM DOXO was included.

3.2.4 Layer by layer deposition of chitosan and alginate polyelectrolyte solutions on PEIfunctionalised CaP NP, drug encapsulation and release

This fabrication was used to investigate the properties and effects caused by polyelectrolyte LBL functionalisation and subsequent drug encapsulation and release.

This fabrication uses the NP templates functionalised with PEI as described in section 3.2.4. (Figure 3.8) This was done by separating the nanoparticles from the supernatant with centrifugation at 4400rpm for 20 minutes and removing the supernatant. The pellet of particles is then fully dispersed in 20 mL of buffer solution. A 1mL aliquot for analysis for the previous layer is then taken. 20 mL of polyelectrolyte solution is added to the particles in the buffer solution to reach the desired concentration polyelectrolyte solution. It was done this way to reduce the number of centrifugation steps and to ensure the proper dispersal of NPs prior to adding the polyelectrolyte solution. the particles were intubated in this solution for 15 minutes with mechanical mixing (95 rpm, Orbital shaker SSM1 (Cole Parmer/Stuart.) The polyelectrolyte solution was then removed by centrifugation. The particles were then redispersed and washed with buffer. This process was repeated for as many layers as was needed.

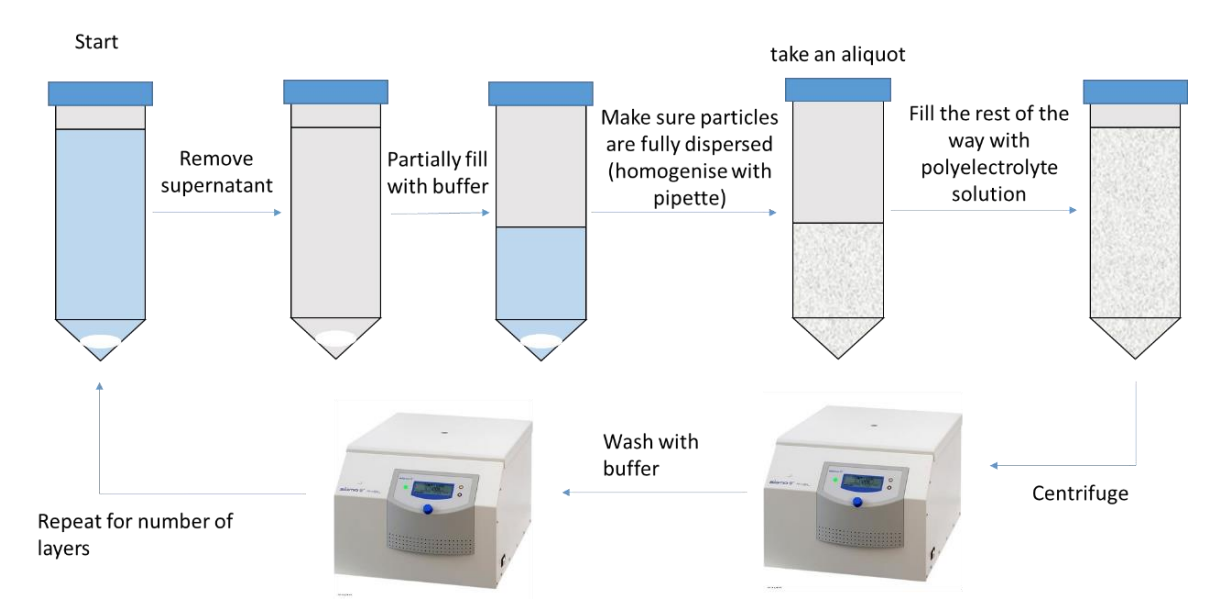


Figure 3.8 - Reaction schematic for the layer-by-layer deposition of chitosan and alginate onto PEI functionalised calcium phosphate nanoparticles.

The particles functionalised with PEI were tested with AA and CH polyelectrolytes to provide the negative and positive layers respectively and were applied alternatively thrice each. For a total of 7 layers with a layer pattern of:

- 1. PEI
- 2. Alginate
- 3. Chitosan
- 4. Alginate
- 5. Chitosan
- 6. Alginate
- 7. Chitosan

1mL Aliquots were taken at each layer for analysis with zeta potential for surface charge, DLS and TEM for size a morphology.

To test the encapsulation and release of anticancer drugs, and functionalisation with CDs, the experiments were repeated with modifications to the protocol. Table 3.6 outlines all the tests that were conducted.

For drug release testing, first layer particles that were also loaded with drugs were used as outlined at the end of section 3.2.4 above. The fabrication continued as above except that drug solutions were included with the CH solutions during the 3^{rd} , 5^{th} and 7^{th} layer depositions. (400µL of 10mM DOXO,400µL of 600nM DAX and 400µL of both solutions). These particles

were tested for drug release and cell tests to analyse their functionality as drug delivery devices.

For the inclusion of CDs, 50mg of CDs were added to the AA solution during the deposition of the 2nd, 4th and 6th layers. This layer was chosen because this is the anionic polyelectrolyte, and the CDs had a negative surface charge (Milkova, 2023). Because of the negative charge, the carbon dots would be attracted to the positive polyelectrolyte layers chitosan and PEI, the negative charge would also prevent the AA from adsorbing to the surface of the carbon dots (Spalla, 2002). These NPs were subject to photoluminescent testing using UV-Vis and Photoluminescence spectroscopy to analyse optical properties.

Table 3.6 - Outline of the different chitosan/alginate layer-by-layer test conducted.

Test	Template + first	Anionic layer	Cationic solution
	layer	solution	
Standard conditions	Plain CaP + PEI	2mg/mL AA	1mg/mL CH
DOXO encapsulation	CaP + PEI and DOXO	2mg/mL AA	1mg/mL CH
			400μL of 10mM DOXO
DAX encapsulation	CaP + PEI and DAX	2mg/mL AA	1mg/mL CH
			400μL of 600nM DAX
Both drugs	CaP + PEI, DOXO and	2mg/mL AA	1mg/mL CH
encapsulation	DAX		400μL of 600nM DAX
			400μL of 10mM DOXO
DOXO Layer only	CaP + PEI	2mg/mL AA	1mg/mL CH
encapsulation			400μL of 10mM DOXO
DAX layer only	CaP + PEI	2mg/mL AA	1mg/mL CH
encapsulation			400μL of 600nM DAX
Both drugs layer	CaP + PEI	2mg/mL AA	1mg/mL CH
only encapsulation			400μL of 600nM DAX
			400μL of 10mM DOXO
With CDs	CaP + PEI	2mg/mL AA	1mg/mL CH
		50mg CDs	

Drug release proceeded by separating the supernatant by centrifugation and removing, the precipitated capsules were washed with PBS once then recentrifuged and separated before resuspending in PBS. This was only done once to minimise the release of the encapsulated drugs (Zhaparova, 2012). 2mg of drug-loaded capsules were then mixed with 2 mL PBS (pH ~7.4) and incubated at 37°C. At specific time intervals the sample was removed from incubation and centrifuged at 13,000 RPM to separate the particles and PBS and a 1.9 mL aliquot of supernatant was removed at the specified time steps (Table 3.7) and replaced. A speed of 13,000 RPM was used to speed up separation, so the experiments could be quickly

returned to incubation. The samples were analysed using UV-Vis multiplate reader at an absorption at 480nm for DOXO and 230nm for DAX. The samples were blanked against pure PBS and the concentration and mass of released at each step was calculated using a previously obtained calibration curve.

Table 3.7 - Measurement times of drug release.

Measuremen	Time
t	
0	0
1	10 mins
2	40 mins
3	1 hour 10 mins
4	2 hours 30 mins
5	4 hours
6	6 hours
7	8 hours
8	22 hours
9	29 hours
10	48 hours
11	72 hours
12	144 hours
13	240 hours

3.2.5 Deposition of aqueous solutions of chondroitin sulphate and chitosan polyelectrolytes on PAH calcium phosphate nanoparticles, functionalisation with carbon dots, drug encapsulation and release

This section outlines the methods used in the second LBL application of polyelectrolytes on PAH functionalised CaP templates. The polyelectrolytes chosen were CS and CH, this was because of their biocompatibility and previous usage in this area of research. The practical work for this investigation was completed by Master's student Simone Margini under the supervision of Thomas Wareing and Piergiorgio Gentile.

The LBL-assembly procedure (Figure 3.9) was conducted using CH and CS as deposition polyelectrolytes. The concentrations of the polyelectrolytes were ranged between 1, 2.5 and 5 mg/mL to find the saturation point of polyelectrolyte deposition on the NPs surface. CH was prepared in a solution of 1 % (v/v) of acetic acid, whereas CS was dissolved only in DI water. The washing steps were carried out in DI water. The pH of all aqueous solutions was adjusted to 6 by adding NaOH and HCl.

10 mg of freeze-dried PAH functionalised CaP nanoparticles, as prepared in according to method outlined in section 3.2.3, were dispersed in 10 mL of CS solution and then sonicated for 15 seconds. The NP dispersion was then shaken at 95 rpm for 15 minutes using an Orbital shaker SSM1 (Cole Parmer/Stuart).

Next, a first centrifugation was performed for 10 minutes at 4400 rpm, followed by two washing steps in DI water to remove excess polyelectrolyte. For the first washing step, the supernatant was removed and replaced with 10 mL of DI water; the NPs were then sonicated for 15 seconds and shaken again for 10 minutes at 95 rpm. This was followed by a second centrifugation for 5 minutes at 4400 rpm. For the second washing step, the procedure was repeated by replacing the supernatant with 3 mL of DI water, sonicating the NPs for 15 seconds, and shaking them again for 3 minutes at 95 rpm. Finally, the NPs were centrifuged again at 4400 rpm for 10 minutes to prepare for the deposition of the next CH layer in the same manner as previously described.

Before the last centrifugation step, $100~\mu L$ of functionalised NPs was removed to measure the corresponding ζ -potential. This process was repeated until 7 layers, alternating in charge, were created consecutively. After the LBL procedure, the final product was freeze-dried and stored in a vacuum desiccator for further testing.

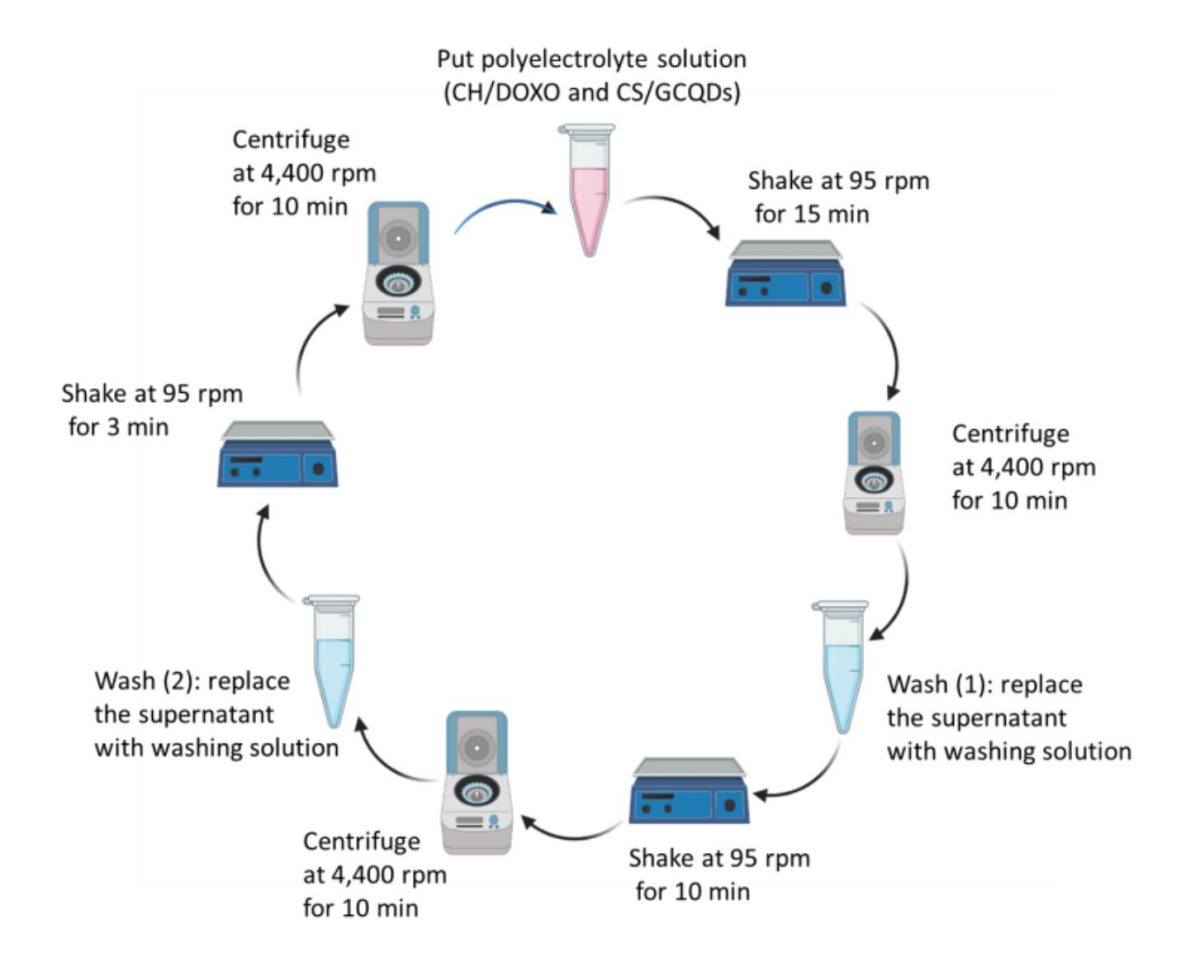


Figure 3.9 - The layer-by-layer deposition process used to deposit chitosan and chondroitin sulphate into PAH functionalised calcium phosphate nanoparticles

Modifications were made for the repeat fabrications to test the encapsulation of both DOXO and CDs. The procedure of LBL was the same as previously stated with changes only occurring in the preparation of the starting solutions. DOXO solution was prepared in PBS:DMSO (1:1) with a concentration of 10mM, this was done because DOXO is not soluble in aqueous buffers (Yamada, 2020). Then, an aliquot of $34\mu L$ of DOXO solution was added for every 10mL of cationic polyelectrolyte solution to create a CH/DOXO solution to incorporate the drug within the positive layers.

Similarly, CDs were added to CS aqueous solution, resulting in a concentration of CD of 0.33mg/mL. This was done so the CDs will be integrated into the negative layer of the NPs. The last layer deposited will be CH and will not contain the drugs to avoid the burst release effect.

The tests outlined above were originally done in a SAB. The method is identical except the washing steps and polyelectrolyte solution were performed/prepared with SAB rather than DI water as outlined above.

For the determination of **drug release** profiles, 0.4 mg of nanoparticles (PAH-functionalised CPNP cores and LBL-functionalised capsules) were precisely weighed, dispersed in 1 mL of PBS, and incubated at 37 °C for up to 28 days, with PBS serving as the release medium. Drug release measurements were taken every 7 days.

To assess the initial burst release, additional measurements were conducted at 10 minutes and at multiple intervals up to 6 hours on the first day of incubation. At each sampling point, $60~\mu L$ of supernatant was withdrawn and replaced with an equal volume of PBS. The collected supernatant was then diluted with PBS in a 1:10 ratio to a final volume of $600~\mu L$. The solution was subsequently centrifuged at 13,000 rpm for 10 minutes, and the supernatant was carefully transferred to a new Eppendorf tube.

Optical density measurements were performed at 480 nm using a plate reader. For each time point analysed, the effective absorbance was determined by subtracting the average absorbance of blank PBS wells from both the standard and sample readings. A calibration curve of DOXO in PBS was used to calculate the concentration of DOXO released at each time point (in μ g/mL). By multiplying this concentration by the supernatant volume (1 mL), the total amount of released DOXO (in μ g) was obtained.

Since the release process was cumulative, the amount of drug released at each time point was added to the previously measured amounts. The percentage of drug release at each time step was calculated by dividing the total released DOXO or DTX by the initially encapsulated amount, as shown in Equation 1 below, where t = time step, $M_{rel}(t-1) = (previously released mass)$ and $M_{(t)} = mass$ at current time step

(1)
$$\%M_{rel} = \frac{M_{rel}(t-1) + M_{(t)}}{(weight\ of\ encapsulated\ drug)} \times 100$$

3.2.6 Drug encapsulation efficiency methods

Below is an outline of the methods used to investigate the encapsulation efficiency of drugs in the NPs. The first method was used to investigate the cores and layers of the first synthesis

and the cores only in the second. This is outlined in Table 3.8. The second method is used to calculate the encapsulation efficiency of the layers only in the second synthesis. This is outlined in Table 3.8. The supernatant recovery method was used for the layers in the second synthesis for efficiency due to already taking out the effluent as part of the method of LBL fabrication.

Acid solubility method proceeded by dispersing 1mg of freeze-dried nanoparticles in 3mL of HCl and stirring at 120 °C until the acid was completely evaporated and a pellet consisting of drug and polymers was obtained. This is because CaPs dissolves in acid. (De Rooij et al., 1984; Tung, 1998) Next the pellet was dispersed in a 3:1 Ethanol/Water solvent, only the drugs are soluble in this solvent. After stirring the solution for 5 hours, the solvent was withdrawn, centrifuged at 13000 rpm for 10 minutes and 100µL of the eluate for each sample was transferred into a 96-well plate.

The optical density of the solution was measured at 480 nm for DOXO and 230 nm for DAX using a FLUOstar Omega MicroPlate Reader (BMG Labtech). Effective absorbance values were determined by subtracting the average absorbance of blank wells (containing an ethanol/water 3:1 mixture) from each standard and sample. For each absorbance measurement, the corresponding DOXO concentration (µg/mL) was calculated based on a previously established calibration curve. Finally, the encapsulation efficiency of the drug within the CaP cores was determined, equation 2 was used (where the drug supplied is a known amount):

(2)
$$EE (\%) = \frac{(amount of drug in nanoparticles)}{(amount of drug supplied)} \times 100$$

Table 3.8 - Outline of particles investigated with the acid recovery method.

Synthesis	Test	Core	Layers
First	Standard conditions	Plain CaP + PEI	AA, CH
First	DOXO encapsulation	CaP + PEI and DOXO	AA, CH, DOXO
First	DAX encapsulation	CaP + PEI and DAX	AA, CH, DAX
First	Both drugs encapsulation	CaP + PEI, DOXO and DAX	AA, CH, DAX, DOXO
First	DOXO Layer only	Plain CaP + PEI	AA, CH, DOXO
	encapsulation		
First	DAX layer only	Plain CaP + PEI	AA, CH, DAX
	encapsulation		
First	Both drugs layer only	Plain CaP + PEI	AA, CH, DAX, DOXO
	encapsulation		
Second	Core encapsulation	CaP + PAH + DOXO	None

Supernatant recovery method proceeds as such; During the formation of each layer and after each centrifugation step in the NP washing process, the supernatant was collected, and 100 μ L of this solution was transferred in triplicate into a 96-well plate. The samples were then analysed by measuring the absorbance of unencapsulated DOXO at 480 nm. Effective absorbance values were determined by subtracting the average absorbance of blank wells (containing washing solutions or drug-free deposition solutions) from each standard and sample. The corresponding DOXO concentration (μ g/mL) was then calculated based on the obtained absorbance values. Finally, the total μ g of drug encapsulated within the layers was determined, equation 3 was used (where the drug supplied is a known amount):

(3)
$$EE (\%) = \frac{(amount of drug supplied) - (amount of drug NOT in nanoparticles)}{(amount of drug supplied)} \times 100$$

Following freeze-drying of the samples, it was possible to match the amount of drug encapsulated by the NP's layers to the actual weight of the NPs produced. Table 3.9 outlines which particles were investigated using this method.

Table 3.9 - Outline of particles investigated with the supernatant recovery method.

Synthesis	Core	Layers
Second	CaP+ PAH + DOXO	CH + CS, No drugs, No
		CD
Second	CaP + PAH + DOXO	CH + CS, DOCO
Second	CaP + PAH + DOXO	CH + CS, DOXO, CD

3.3 Analytical techniques

3.3.1 Physiochemical analysis

FT-IR analysis was carried out to characterise the functional groups on and chemical make-up of a sample. An Agilent Cary 630 FTIR Spectrometer was used to gather the data, the settings used were 16 scans at a resolution of 4cm⁻¹ with a range between 4000 and 600cm⁻¹. The crystal is cleaned with propanol and a background is taken. A small amount of sample is placed onto the crystal so that it is completely covered, the plunger is lowered, and the sample is squashed against the crystal and any excess sample is extruded. This sample placement method ensures consistency in amount and dimensions between samples. A reading is taken, the spectra are saved, and the crystal is cleaned once again.

XPS samples are sent in a powdered form to Harwell XPS. Their protocol is as follows;

X-ray photoelectron spectroscopy measurements were performed on a Thermo Fisher Scientific NEXSA spectrometer under high vacuum ($P \sim 10^{-8}$ mbar). Samples were analysed using a microfocused monochromatic Aluminium X-ray source (72W) with an oval spot size of approximately $200 \times 100 \mu m^2$. Data were recorded at pass energies of 200eV for survey scans and 50eV for high-resolution scans in increments of 1 and 0.1eV, respectively. Charge neutralisation of the sample was achieved using a combination of both low-energy electrons and argon ions. Wide scan, nitrogen, carbon, and oxygen spectra were taken. CasaXPS software was used, using Shirley background to analyse the data to obtain the ratio of elemental and bond make up.

Dynamic light scattering and Zetapotential (ζ-potential) was conducted on a Zetasizer nanosego (Malvern Instruments, Malvern, UK). This machine was used for several measurements including average size analysis of hydrodynamic diameter, size distribution, polydispersity index and ζ-potential. Standard operating procedures were created for size and ζ-potential measurements using the absorbance and refractive index of the standard polystyrene. The solutions were diluted to 1:10 in DI water and placed into the machine in a folded capillary zeta cell and were run in triplicate in an automatic measurement with a maximum of 100 runs. Conductivity values were consistent and ranged between 1.5 and 2.5 mS/cm.

Percentage (Mass) yield is defined by the percentage of the actual yield of a product verses the theoretical yield (Steen, 2023). The theoretical yield of carbon dots is 100% using the biomass as the limiting reagent. This means that the percentage yield calculation uses the starting amount of biomass as the theoretical yield as shown in equation 4 below. This is consistent with previous works (Hao et al., 2023). The carbon dots are freeze dried before mass yield calculations to remove water.

(4)
$$Mass Yield (Y_M) = \frac{Weight of freeze dried CDs}{Weight of raw SCG} \times 100$$

3.3.2 Optical spectroscopy

UV-Vis analysis was conducted on a Shimadzu UV-1900i by diluting the sample in DI water and placing inside a quartz cuvette and then inside the machine. A cuvette of DI water is also placed inside the machine and used as a background. First the background is analysed using a

resolution of 2nm between wavelengths of 200 and 800nm. The sample absorbance spectra are taken after the background. The solution of sample is diluted further, and the measurement is repeated until the desired maximum absorbance of 0.1 is obtained.

Photoluminescence spectroscopy used a diluted sample with an absorbance of less than 0.1. This is placed inside the machine (Shimadzu RF-6000) and both the emission and excitation spectra are obtained using specified wavelengths as the excitation and target emission data.

Quantum yield (QY) is obtained by analysing the emission data of 5 solutions of a sample with known absorbances between 0 and 0.1. the emission data is plotted against the absorbance data to gain a gradient. This data is compared against the same data given from a photoluminescent standard using equation 5, where S denotes sample, R denotes Reference, n = refractive index and $\Phi = QY$ (Wong et al., 2020). The reference used was quinine sulphate in 0.5 M sulphuric acid with quantum yield of 0.546 (Daniel, 2023) and refractive index of 1.427 (Weast, 1975). pure water was used for the solvent for carbon dots and the refractive index was 1.33 (Eisenberg, 1965).

(5)
$$\Phi_{S} = \Phi_{R} \frac{Grad_{S}}{Grad_{R}} \left(\frac{n_{S}}{n_{R}}\right)^{2}$$

3.3.3 Biological

All biological tests and cell splitting were conducted in a biological laminar hood that was previously decontaminated with a 70% mix of ethanol and water. Cells, media and additives were prewarmed in a water bath to 37°C. All items placed inside the hood were decontaminated also with 70% ethanol solution. Different cells were used for different purposes. For cell tests against carbon dots for biocompatibility testing, fibroblast cells were used. Cell tests against layer-by-layer capsules to were conducted against osteosarcoma cell lines SAOS-2 and U2-OS cells to investigate therapeutic effect. The protocol for the different cell lines remained the same and is outlined below.

Cell thawing and preparation of media solution - Solutions of penicillin, foetal bovine solution (FBS) and L-glutamine were defrosted and prewarmed in a water bath at 37°C and filtered through a $0.22\mu m$ syringe filter. 5ml of penicillin, 50mL of FBS and 5ml of L-glutamine was added to a bottle of Dulbecco's Modified Eagle Medium (DMEM). This media with additives

was used for all further cell culturing and tests and will be referred to as DMEM+ henceforth and is stored in an incubator at 37°C.

A cell sample was removed from liquid nitrogen storage and defrosted. 1mL of cells we added to 9mL of DMEM+. This was then added to a flask and was incubated for 2 days at 37°C.

Subculturing – A previously prepared flask containing cells and DMEM+ was taken out of the incubator, the media was removed and 5mL of phosphate buffered saline (PBS) was added to the flask then removed to wash away any dead cells and remaining DMEM+. To detach the cells from the bottom of the flask, 3mL of trypsin was added to the flask and incubated at 37°C for 5 minutes. Prewarmed fresh media (7mL) was added to the flask to obtain a solution of media, cells, and trypsin. This was then transferred to a falcon tube and centrifuged at 1200rpm for 5 minutes to obtain the cells, this low speed was used to not damage or kill the cells. The supernatant was removed, and fresh media was added to the cells. The cells were then split between two flasks and replaced in the incubator.

Cell counting was conducted just before the cells were used in analysis; the protocol for splitting as outlined above was followed until a pellet of cells was obtained. The pellet of cells was resuspended in 10mL of fresh prewarmed DMEM+. A 10μ L sample of suspended cells was placed into a counting grid slide and observed under a 40x optical microscope. The cells in each grid were counted and this information was inserted into equation 6 to determine the concentration and therefore number of cells obtained by culturing. Where Q_x is the number of cells found in each quadrant and V is the volume of resuspended cells (10mL)

(6)
$$\frac{Q_1 + Q_2 + Q_3 + Q_4}{4} \times 10^4 \times V$$

Presto blue viability tests (Thermofisher); 96 multi-well plates were prepared, solutions were made inside the wells containing 5000 cells and different concentrations of the test samples ranging from 1000μm to 50μm. This was done in triplet for each sample, and for a control. Two plates were fully made up each containing the required samples in triplet and placed in an incubator at 37°C. After 24 hours, one of the 96 well plates were taken out of the incubator and the media was removed. 200μL of PrestoBlue (PrestoBlue™ Cell Viability Reagent, ThermoFisher Scientific) solution (10% PrestoBlue to 90% media) was added to each well of the plates and the plate was returned to the incubator for an hour and a half. This plate was then removed from the incubator and placed into a BMG Labtech FLUOstar Omega for

analysis. This process was repeated with the second plate 24 hours later for the 48hour analysis.

Live and dead tests were used to analyse the effect of materials against the cells by comparing alive cells verses dead cells after exposure. Into a 48 multi-well, solutions were made containing cells and different concentration of samples. This was done in doublet for each sample and for a control. These plates were fully made up and placed in an incubator for 24 and 48 hours.

After 24 hours in the incubator, a 48 well plate was taken out of the incubator and the media was removed. Live and dead dyes were added to PBS (Add 5 μ L calcein AM (Component A) and 20 μ L ethidium homodimer-1 (Component B) to 10mL PBS). This solution was then added to each well of the plate (200 μ L) and incubated for 30 minutes at 37°C. This plate was then placed into a fluorescent microscope for analysis with the green and red filters showing live and dead cells respectively. This was repeated with a second plate for analysis at 48 hours.

3.3.4 Microscopy

Transmission electron microscopy (TEM) was conducted on two different machines using the same procedure.

HRTEM - Durham University - JEOL 2100F FEG TEM

TEM - Newcastle University - Hitachi HT7800 120kV Cryo TEM (Figure 3.10)



Figure 3.10 - Newcastle University's Hitachi HT7800 120kV Cryo TEM

TEM sample grids were prepared by dropping aqueous sample onto a copper grid and were dried under a lamp. The concentration depended on the sample type and was not controlled for when qualitative analysis was being used. The grids used were copper 200 mesh grids supplied by Agar scientific, they were prepared with a pioloform carbon film. All samples were suspended in water. One grid was used for each sample, 10μ l of sample was added to the sample grid and left for 20 seconds. After this, filter paper was used to wick away the liquid from the grid. The grid was then placed 1 inch away from halogen bulb lamp for 1 minute to fully dry the grid. The sample grid was then stored in a sample box ready for analysis, no additional staining was used. For analysis, a sample is placed inside the TEM and a vacuum is established inside the microscope (Figure 3.11). The Z height is set by using the wobble feature and the height is manipulated until the image steady; the wobble is then turned off. 6 images per sample were taken and a macro program is used to burn in the optical information to the image before saving. Images were used for size and morphological analysis.



Figure 3.11 - Left; sample grid with droplet of sample, Right; sample grid in sample holder

Scanning electron microscopy (SEM) utilised a Tescan Vega 3LMU scanning electron microscope. SEM carbon stubs are prepared by placing 10mg of a powdered sample onto sticky carbon tape mounted onto a sample stub. To prevent charge build up, the samples were coated with 5nm of gold from a polaron gold coater for conductivity. Images were used for size and morphological analysis.

ImageJ was used to analyse the size of particles in both the TEM and SEM images; this was done manually for each sample. First, the scale was set using the scale bar, then particles were individually measured. At least two images were used to identify samples and up to 60 particles were measured per sample. The mean and standard deviation of the measured particles was calculated.

Chapter 4. Carbon Dots from Spent Coffee Grounds: Results and Discussion

This chapter focuses on the three different syntheses of CDs from spent coffee grounds (SCG) using various methods to evaluate the effect on synthesis parameters on the properties of CDs. Three different synthetic approaches were applied as described below.

Synthesis one – A two-step hydrothermal and oxidation synthesis of CDs to evaluate the effectiveness of different acid catalysts (SA or TA) and reaction times (2-4 hours). This approach used different synthesis parameters to investigate the effect this has on the resulting dots. This method also uses a hydrothermal reactor rather than a microwave for the first step hydrothermal reaction. This work has been partially published as part of a conference proceedings by the journal of technical education science (Wareing et al., 2023).

The hypotheses were that increasing catalyst concentration would decrease the size of the CDs due to the increased availability of small glucose building blocks (Adolfsson et al., 2015; Hassanzadeh et al., 2015; Wu et al., 2023) made available, by assisting the hydrolysis step (Maniscalco et al., 2020) in the HTC, increasing precursor surface area (Wilk et al., 2023). The dots would also have a higher intensity of photoluminescence due the increase presence of surface groups. However, increasing reaction time is expected to produce large CDs, due to longer residence time leading to larger precursor size due to increased polymerisation (Jain et al., 2015) during intermolecular condensation step (Maniscalco et al., 2020).

Synthesis two - A hydrothermal synthesis to look at the effectiveness of a TA catalysts (0-0.05g/mL) and a ultrasonication pre-treatment with different temperatures for the synthesis of CDs. This is a completely novel experiment due to the investigation of the effect of an ultrasonic pretreatment of the SCG.

The hypothesis was that the ultrasonic treatment would improve the yield and properties of the CDs due to the ultrasonication increasing the surface area to volume ratio of the SCG by breaking down the macro structure of the coffee grounds. This allows the catalyst to penetrate the SCG before the start of the hydrothermal synthesis. This would allow for a better break down of the SCG and more glucose building blocks to become available to build up the CDs (Djellabi et al., 2023; Iskalieva et al., 2012).

Synthesis three - A synthesis that investigates the use of a microwave (30-90mins, 150-200°C) as an energy source using aqueous conditions to synthesise CDs via HTC. This is an original synthesis and does not use a catalyst. This is based on the results of previous experiments that show that a catalyst is not needed to create viable CDs (synthesis 1) and the lack of catalyst produces dots that are superior to dots that used a catalyst in their synthesis (synthesis 2). This synthesis is the only example of a purely aqueous CD synthesis from SCG in the current literature as far as we know. This research is yet to be published.

The hypotheses were that higher temperatures would produce larger CDs (C. Hu et al., 2014) and have a higher intensity of photoluminescence to the increase presence of surface groups (Quaid et al., 2022). Longer reaction retention times were expected to produce CDs with a larger size due to the increase time for the CDs to be built up from the building blocks (Zhang et al., 2012).

4.1 Acid Catalysed Hydrothermal Carbonisation of Spent Coffee Grounds and Nitric Acid Oxidation (synthesis 1)

This section outlines the results and discussion of a two-step hydrothermal oxidation to produce CDs. The focus of this research was to investigate the effects of parameter changes in the hydrothermal step in the resulting CDs. The full methodology, rationale and sample codes can be found in chapter 3, section 3.1.2, however, it is summarised below.

The first step is a hydrothermal synthesis of a solid graphitic precursor from SCG with various conditions to yield a selection of precursors. Physiochemical analysis was conducted with FT-IR and XPS and TEM was used for morphology and size, the results of which are outlined in section 4.1.2. CDs were synthesised from each of these precursors with the nitric acid oxidation using ultrasonication followed by a reflux. The reaction conditions for this step were consistent across all samples. The resulting CDs were analysed with FT-IR and XPS for surface analysis, UV-Vis and fluorescent spectroscopy for optical properties and TEM for size and morphology. These results are outlined in section 4.1.3. An overall summary and conclusions are outlined at the end of this section, in 4.1.4.

4.1.1 Effect of reaction time, catalyst types and concentration on properties of precursors obtained from HTC for producing carbon dots.

Figure 4.1 shows functional groups (via FT-IR analysis) of raw coffee grounds and samples pretreated with a HTC at 200°C with a 1:30 ratio of biomass to catalytic solution at various acid concentrations using two types of acids (SA and TA) and retention times between 2 to 4 hours, as explained in Table 4.1. The raw SCG show several peaks which correspond to several functional groups (Merek, 2023) (Venkatesan et al., 2022; Xu et al., 2017; Yang et al., 2016). The broad peak at ~3280cm⁻¹ corresponds to an -OH alcohol group which comes from residual water left over after the drying process. The peaks at ~2918 and 1459cm⁻¹ correspond to the C-H bond from alkane group. The 2849cm⁻¹ and 1736cm⁻¹ peaks correspond to C-H and C=O aldehyde groups respectively. The peaks at 1634, 931, 864 and 806cm⁻¹ correspond to the C=C bond from an alkene group, this could be derived from the double bond found in caffeic, ferulic and chlorogenic acid (Erskine et al., 2022; Nuhu, 2014) which are major components found in coffee grounds. The peak at 1308cm⁻¹ corresponds to the O-H bond in a phenol group. 1168cm⁻¹ corresponds to a C-O ester group, 1238cm⁻¹ corresponds to the C-O alkyl group and 1023cm⁻¹ corresponds to a C-O-C group.

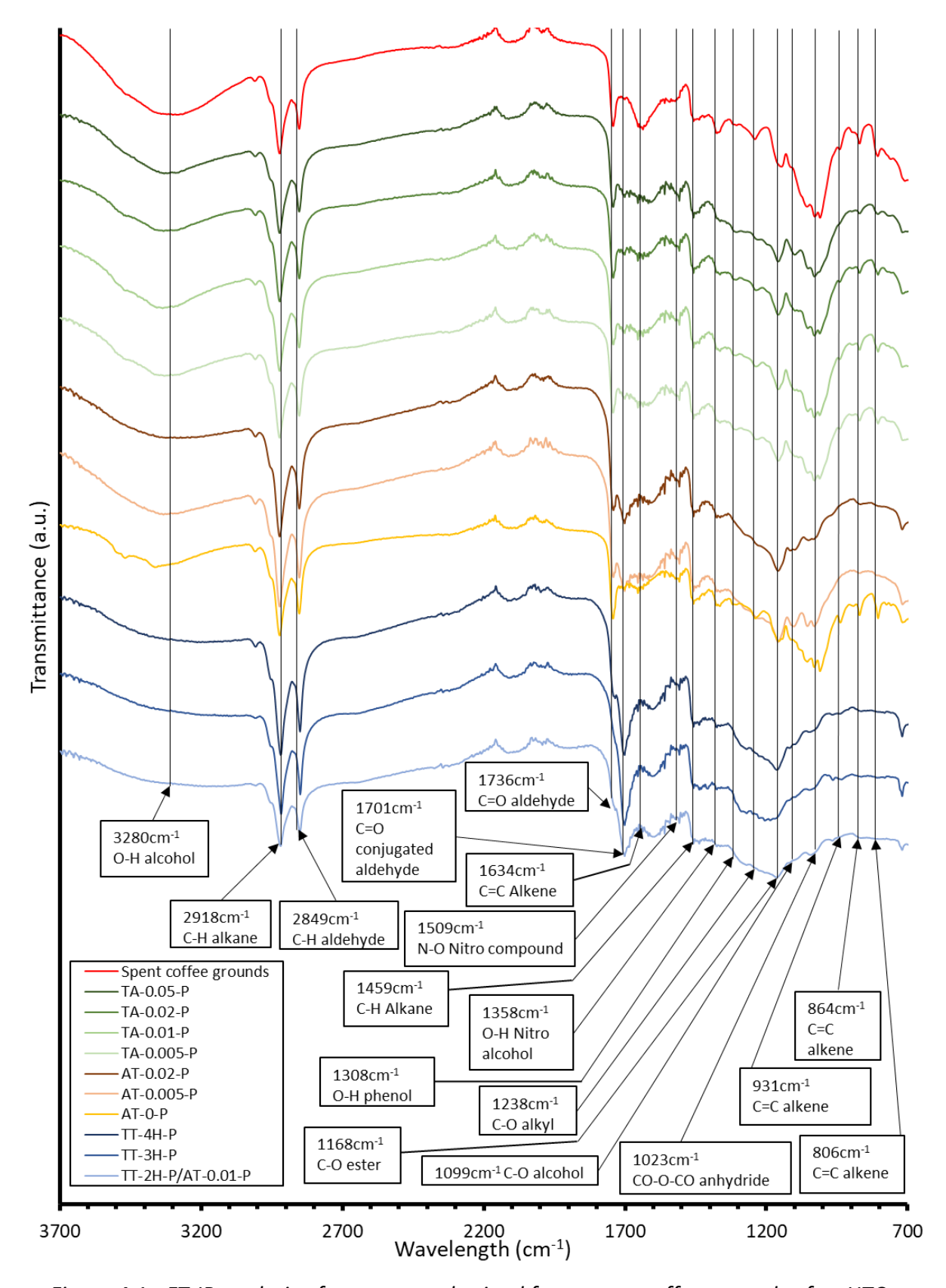


Figure 4.1 - FT-IR analysis of precursors obtained from spent coffee grounds after HTC.

The samples obtained from HTC using SA as catalysts (TT-2H-P, TT-3H-P, TT-4H-P, AT-0.005-P and AT-0.02-P) show a much intense C=O conjugated aldehyde peak at 1701cm⁻¹ when compared to the SCG. This shows that the SA catalyst introduces more oxygen containing groups into the precursor in the form of conjugated aldehyde on the surface of the precursor. However, all samples show aldehydes at 1701cm⁻¹. There is also a drastic reduction in the intensity and width of the peak at 1023cm⁻¹ which corresponds to C-O-C. This could suggest that the SA helps to break down the cellulose structure of SCG by facilitating the hydrolysis of the ester bond between the glucose building blocks (Adolfsson et al., 2015; Hassanzadeh et al., 2015; Wu et al., 2023).

The samples that did not use SA (TA series and AT-0-P) still show this ester bond (1023cm⁻¹) the same as the raw SCG showing that TA does not facilitate this reaction. These samples also lack the peaks at 1634, 931, 864 and 806cm⁻¹ which correspond to the C=C bond from an alkene group. Because of this using TA as a catalyst, or no catalyst, does not generate the same precursor as SA. From FT-IR results, samples pre-treated with TAs at all tested concentrations and without catalysts had similar functional groups; the raw SCG showing that little to no reaction has taken place and TA does not act like a catalyst in the reaction. It was reported by Hassanzadeh et al. (Hassanzadeh et al., 2014) that they did not observe hydrothermal degradation without a catalyst when investigating microwave liquefaction of cellulose. To confirm the effects of acids, XPS analysis was carried out. Table 4.1 outlines the XPS results from the wide survey and the C 1s, O 1s and N 1s scans, and example of peak fitting in the wide and C 1s scan is provided by Figure 4.2 and Figure 4.3. (O 1s – Figure A.6.1, N 1s – Figure A.6.2)

Table 4.1 - Summary of the XPS results of the precursors synthesised by a hydrothermal pretreatment.

Scan	At %											
	Survey			C 1s				N 1s		O 1s		
Element/Bond	Carbon	Nitrogen	Oxygen	sp2/C=C	sp3/C-C	C-O	C=O	C-NH2	NO3	C=O	C-O	Na KLL Auger
Binding energy (eV)	284.95	399.95	532.84	284.46	284.89	283.79	288.64	389.1	406.08	531.99	533.25	541.62
Sample												
spent coffee grounds	70.74	2.93	26.33	17.48	34.84	40.43	7.24	97.29	2.71	38.8	58.72	2.48
TT-2H-P/AT-0.01-P	68.77	4.5	26.73	11.37	24.11	47.46	17.06	80.35	19.65	40.53	53.89	5.58
TT-3H-P	71.65	1.6	26.75	7.69	36.22	42.03	14.06	75.4	24.6	12.44	83.51	4.05
TT-4H-P	68.75	5.24	26.01	8.89	32.06	48.81	10.24	70.55	29.45	9.98	87.81	2.2
AT-0-P	76.44	0.7	22.85	14.96	44.7	33.34	7	73.22	26.78	41.2	40.47	18.33
AT-0.005-P	68.71	1.98	29.31	9.59	39.46	34.22	16.73	63.29	36.71	36.27	40.42	23.31
AT-0.02-P	70.51	2.09	27.4	7.46	62.1	24.41	6.03	96.69	3.31	46.06	46.37	7.59
TA-0.005-P	69.55	1.16	29.3	14.3	66.91	13.62	5.18	99.98	0.02	34.68	65.32	0
TA-0.01-P	70.79	1.87	27.34	9.13	59.75	26.04	5.08	98.89	1.11	27.02	72.98	0
TA-0.05-P	70.69	2.03	27.29	8.96	69.45	18.35	3.24	99.66	0.34	22.62	77.38	0

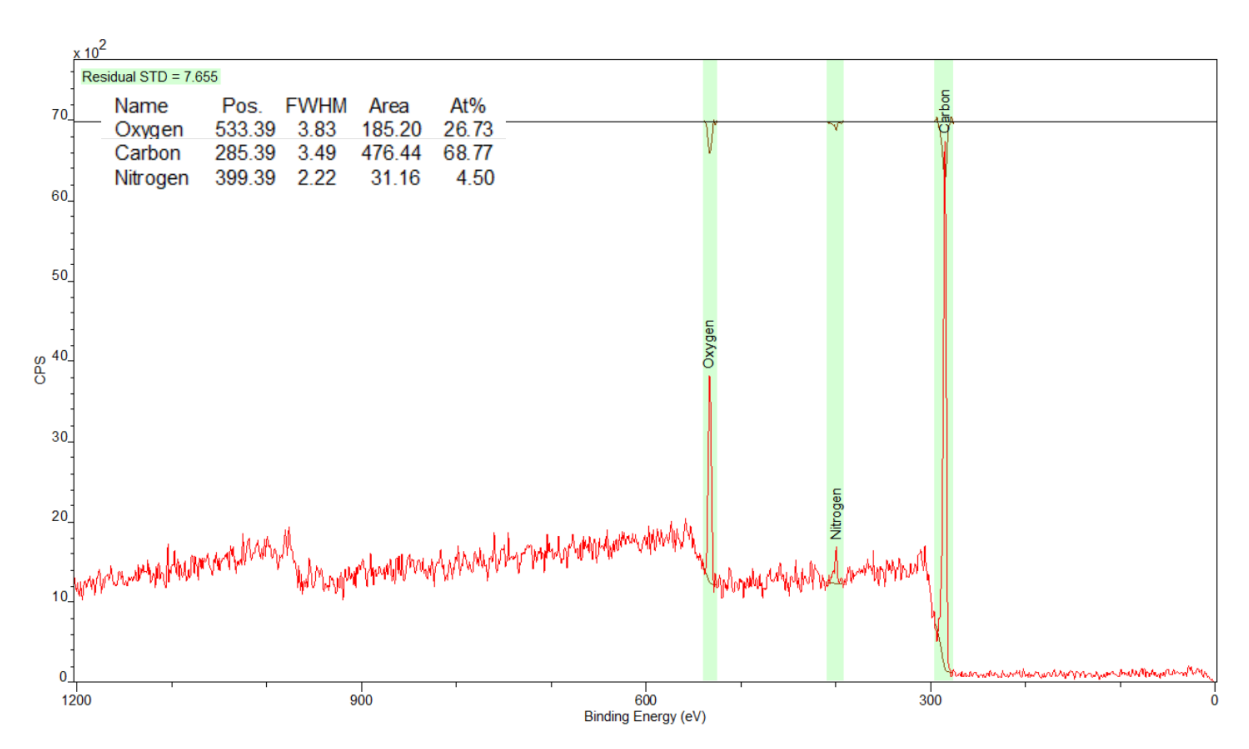


Figure 4.2 - XPS wide survey scan of the precursors synthesised by a 2 hour hydrothermal pretreatment with a concentration of 0.01g/ml sulphuric acid catalyst (TT-2H-P/AT-0.01-P).

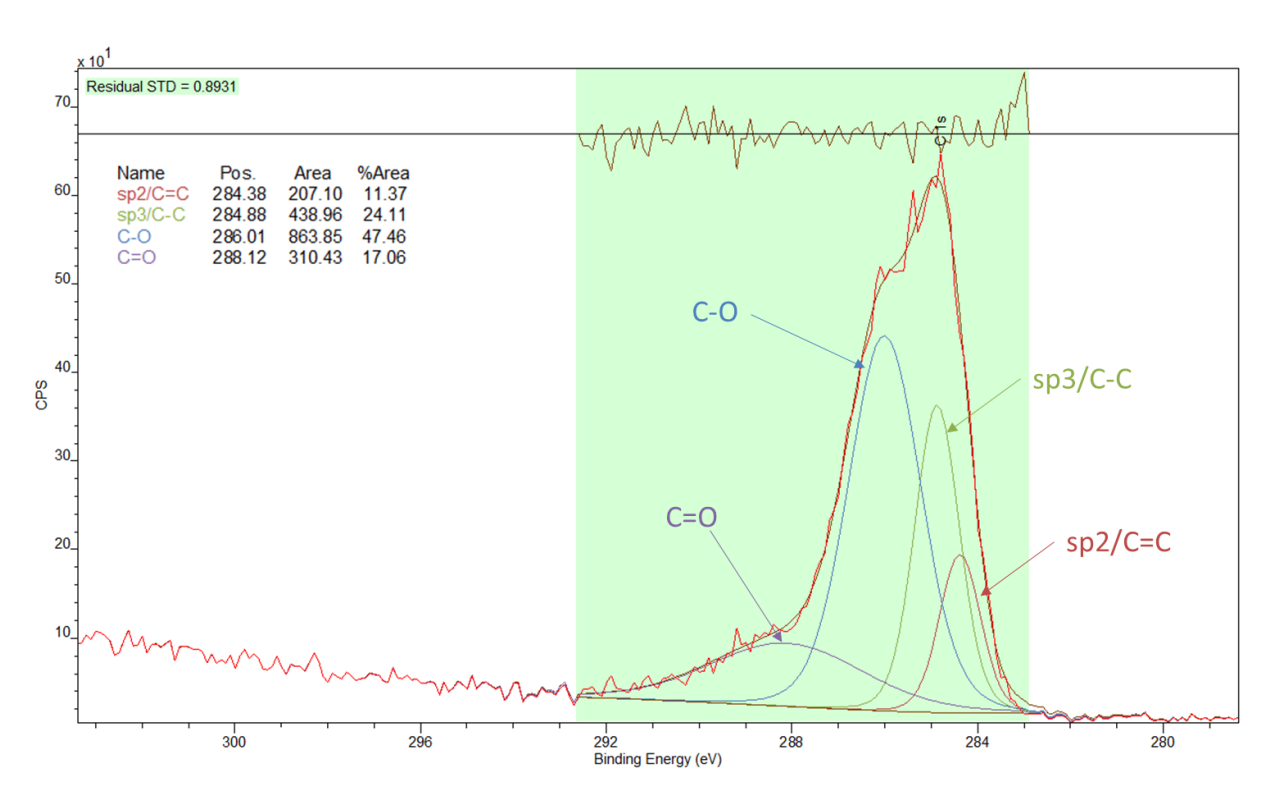


Figure 4.3 - XPS C 1s scan of the precursors synthesised by a 2 hour hydrothermal pretreatment with a concentration of 0.01/g/ml sulphuric acid catalyst (TT-2H-P/AT-0.01-P).

XPS of the SCG and other samples were analysed against Thermofisher materials science learning centre database (Thermofisher, 2023). It was revealed that SCG had a surface chemistry elemental make-up of 70.74 At% carbon, 2.93 At % nitrogen and 26.33 At % oxygen.

The C 1s scan revealed sp^2 area percentage of 17.48%, sp^3 - 34.84%, C-O – 40.43% and C=O – 7.24%. The O 1s scan showed C=O as 38.8% and C-O as 58.72% which is in terms of ratio is inconsistent with the C 1s values for C-O and C=O. The nitrogen scan showed the nitrogen content was mostly due to the presence of amine groups. It has been previously reported that the nitrogen peak can also be associated with intrinsic heteroatom of N (Kim et al., 2020).

The mechanism of HTC initially involves the hydrolysis of cellulose to glucose followed by series of dehydration, decarboxylation and intermolecular condensation reactions to produce the aromatic/graphitic network of hydrochar (Maniscalco et al., 2020). Overall, it could be expected that oxygen content of the precursor would be decreased in relation to carbon when compared to the raw SCG because it would be removed via dehydration in the formation of the precursor, and a decrease in C-O bonds and an increase in C=O which shows the conversion of some of the alcohol and ester groups in cellulose to carboxylic acid, aldehyde, and carbonyl groups (B. Zhu et al., 2013). The C 1s and O 1s scans do not show this increase in C=O bonds in all samples, The C 1s show an increase in samples; TT-2H-P/AT-0.01-P, TT-3H-P, TT-4H-P and AT-0.005-P: samples that all used SA as a catalyst. The O 1s scan shows an increase in TT-2H-P/AT-0.01-P, AT-0-P and AT-0.02-P, the first and last of which used SA as a catalyst. This is in line with the FT-IR and suggests that SA plays a role in the introduction of carbonyl groups. However, there are differences in the ratios between the C 1s and O 1s scans; for example, the ratio between the C-O/C=O on average across all the precursors is 3.9 for C 1s scans and 3.1 for the O 1s scan. It is unclear why this is the case.

The predicted aromatic network structure of the precursor (Xu et al., 2017) would also be shown in the C 1s precursor scans as increase in the sp² carbon and a reduction of sp³ (Tuz Johra et al., 2014). This is not shown in any of the samples as the content of sp² bonds decreases from 17.48% to between 14.96 and 7.49%. This suggests that none of the reactions produced a graphitic precursor because the ratio of sp² against sp³ carbon is not increased - it is decreased, suggesting the presence of aliphatic groups (Liu et al., 2016).

The XPS results do not corroborate the observations and conclusions from the FT-IR analysis. The FT-IR indicated that the SA catalysed precursors (TT-2H-P, TT-3H-P, TT-4H-P, AT-0.005-P and AT-0.02-P) showed an increase in C=O in the form of an aldehyde which was based on the peak at 1701cm⁻¹, this was not shown in the O 1s scans. The other significant difference between

the SA catalysed precursors and not, was the absence of the C=C alkene peaks that are shown in the raw SCG and reactions that did not utilise SA. It would be expected to see the reduction in the percentage of sp2/C=C in the C 1s scan only in the SA catalysed precursors. This reduction is shown across the board and there is no relationship in terms of concentration and catalyst type. These differences are most likely down to the difference in penetration depth of each analysis type (Piwowarczyk et al., 2019).

The FT-IR indicated that no reaction took place in the samples that were not catalysed with SA due to the fact that the spectra were so similar to the raw material. The XPS scans show however that there is a slight increase in the overall ratio of oxygen, which is down to an increase in the ratio of C=O bonds and a significant increase in sp³ carbons. This shows that the precursors underwent a reaction that introduced aliphatic fragments to the surface which can occur under milder conditions (N. Shi et al., 2019).

Size and morphology of the samples obtained from HTC experiments was analysed. Transmission electron microscopy was used to visualise the nanostructures of the precursors. Figure 4.4, Figure 4.5 and Figure 4.6 show how examples of the TEM images of the precursors (samples not shown in main text are in the appendix – Figure A.6.3). Figure 4.4 and Figure 4.5 show examples of SA catalysed precursors (TT-2H-P and AT-0.02-P respectively) which all have similar layered type structure; this is consistent across all the samples that were SA catalysed. AT-0-P also shows this layered structure; this is unexpected because of how similar the FT-IR spectra is to the raw material and TA catalysed samples.

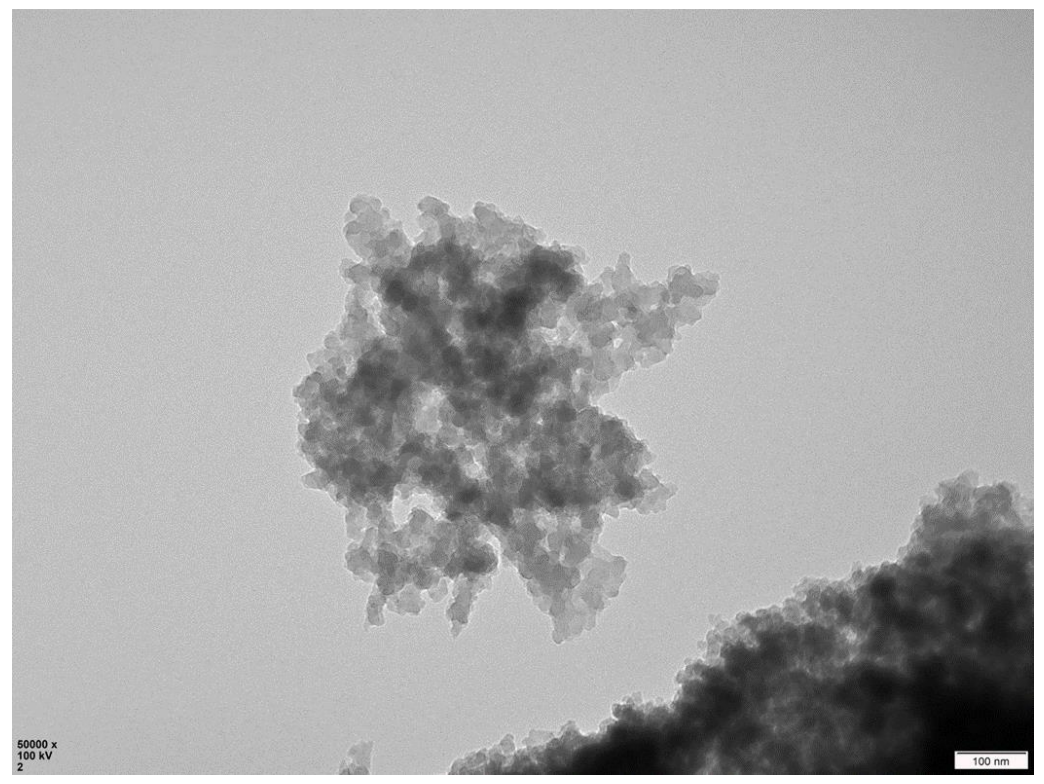


Figure 4.4 - TEM image of the precursor synthesised for 2 Hours with 0.01g/ml Sulphuric acid (TT-2H-P/AT-0.01-P) — Scale Bar 100nm

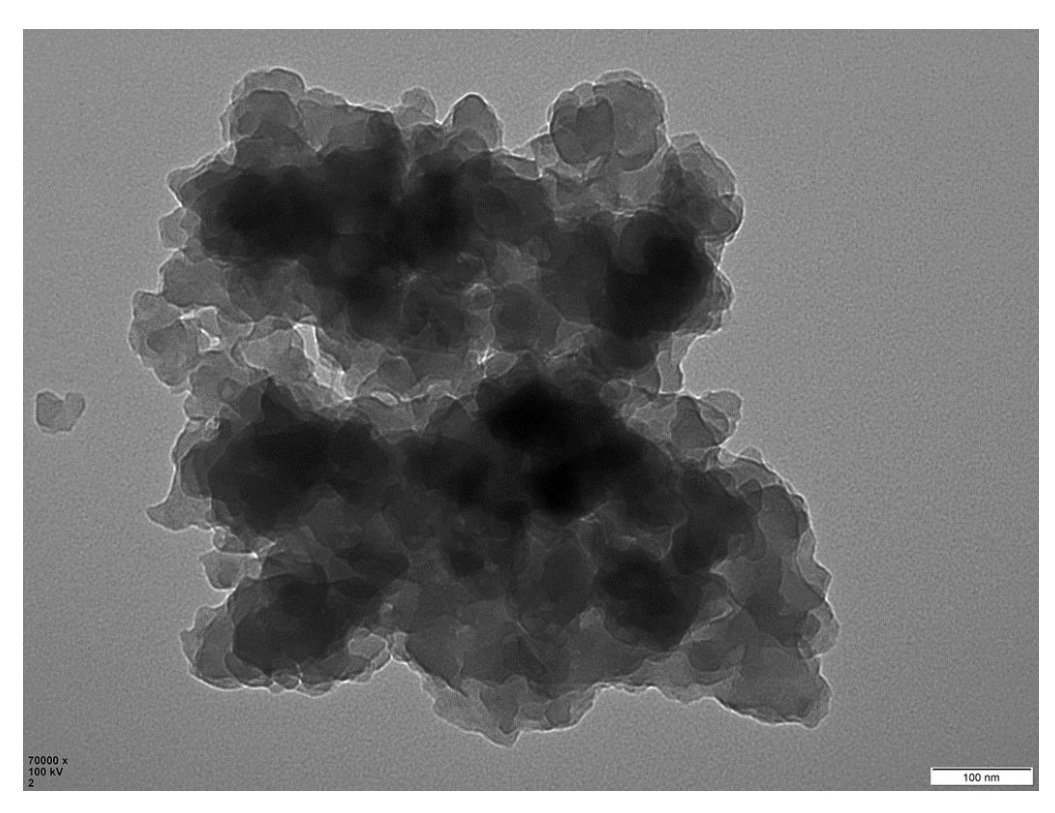


Figure 4.5 - TEM image of the precursor synthesised for 2 Hours with 0.02g/ml Sulphuric acid (AT-0.02-P) – Scale bar 100nm

Comparing all the TEM data, using the SA catalyst leads to the formation of the layered structure. These structures look like hydrochar as previously reported in other works (Lubura et al., 2023; Oumabady et al., 2020; Oumabady et al., 2022). Initially, this was expected to be produced by the HTC of SCG, however the XPS data suggested that this kind of structure was not produced by any of the samples. It is not clear why there is a disconnect between the TEM and XPS, but it could be explained by the fact that XPS only analyses the surface of the samples, specifically a depth of 10nm (Stevie & Donley, 2020). The edges/surface of this structure could have surface and functional groups that contain a high percentage of oxygen and sp³ carbons as indicated in the C 1s scan, such as furans including hydroxymethylfurfural (Massaya et al., 2022), ketones and aliphatics (S. Yan et al., 2023), while the bulk of the material, which was not analysed by the XPS, does indeed have an aromatic structure.

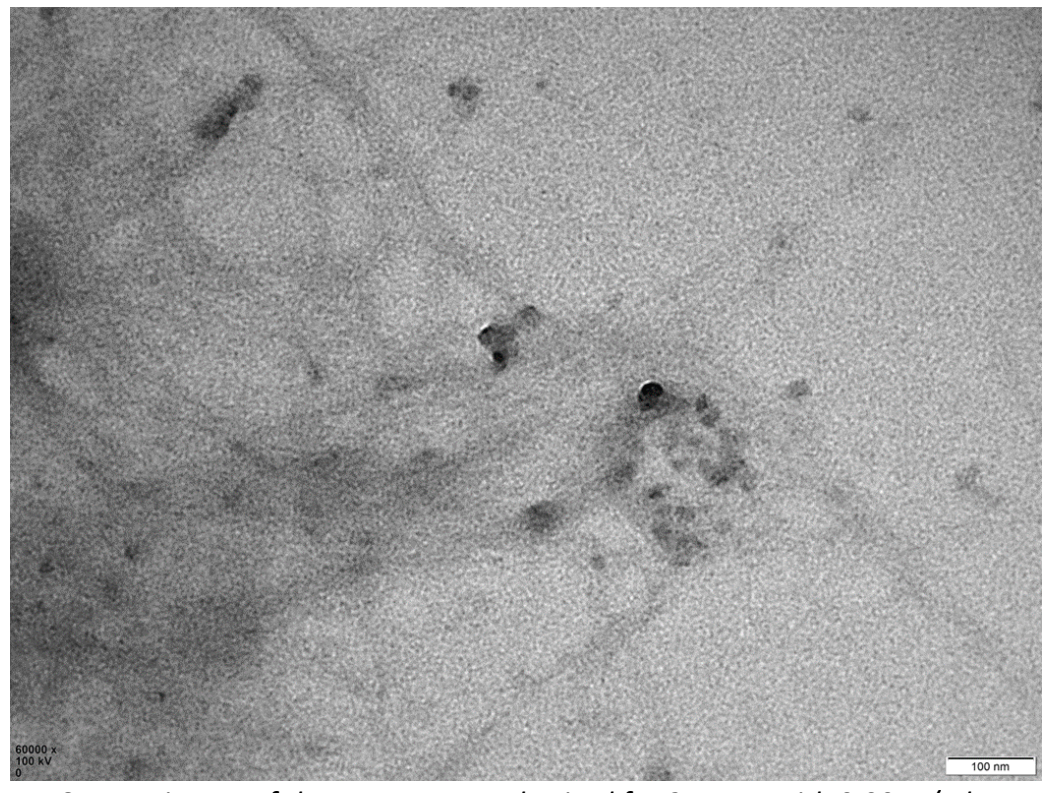


Figure 4.6 - TEM image of the precursor synthesised for 2 Hours with 0.005g/ml tannic acid (TA-0.005-P) — Scale bar 100nm

Figure 4.6 is an image of TA-0.005-P which shows a less ordered structure which does not include as many of the features described above. This image is consistent with all the precursors synthesised using TA as a catalyst. The images of the TA series are consistent with the XPS as it would be expected to see a higher percentage of oxygen containing groups and sp³ carbons.

4.1.2 Carbon dots produced via nitric acid oxidation and the effect of precursor synthesis parameters

Solid samples collected after HTC treatment in section 4.1.2 were further oxidised with 20% nitric acid at 90°C. Rotary evaporation, dialysis and freeze drying were used to obtain solid CDs. Figure 4.7 outlines this reaction in a schematic.

Figure 4.7 - Reaction schematic of the nitric acid oxidation from precursor to carbon dot

Figure 4.8 shows the FT-IR for the CDs produced from each precursor which were analysed using Merek's FT-IR database (Merek, 2023). The structure of carbon dots is made up of sp² and sp³ carbon atoms with large number of polymer chains or functional groups attached to their surface (Jiang, 2015; Mansuriya & Altintas, 2021; Xia et al., 2019).

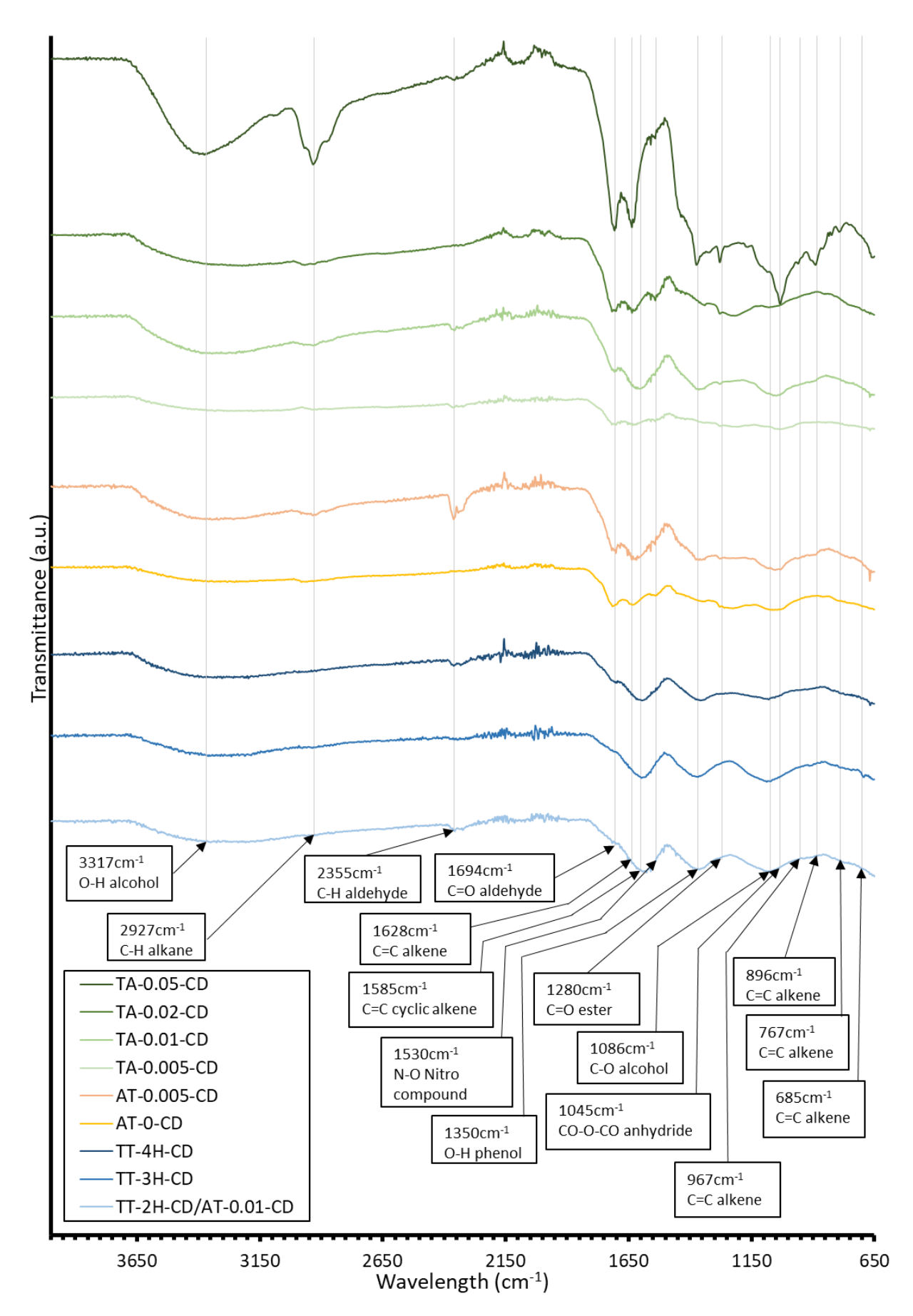


Figure 4.8 - FT-IR of carbon dot samples obtained after nitric acid oxidation.

The broad peak at ~3317cm⁻¹ corresponds to an -OH alcohol group which comes from residual water left over after the drying process and alcohol groups on the surface of the CDs and is present in all samples.

The peak at ~2927cm⁻¹ corresponds to the C-H bond from alkane group (Tungare et al., 2020). This peak is not present in the time tests and is very weakly represented in the other samples aside from TA-0.05-CD in which it is strongly represented. This shows the presence of aliphatic chains on the surface of the CDs. The C 1s XPS scan of precursor TA-0.05-P showed the highest ratio of sp³ carbon bonds in the C 1s XPS scan which suggests that this precursor had the highest concentration of aliphatic groups, which must have been retained through the nitric acid oxidation leading to a greater expression of these groups when compared to other samples.

The peaks at 2355cm⁻¹ and 1694cm⁻¹ correspond to C-H and C=O (González-González et al., 2020; Zhao et al., 2017) from aldehyde groups respectively. The 1694cm⁻¹ peak is present in all samples except TT-3H-CD, AT-0-CD and TA-0.02-CD, and 2355cm⁻¹ peak is present in all samples except TT-3H-CD. This shows that aldehydes are present on the surface of all the dots apart from TT-3H-CD. This could be because TT-3H-P had fewer primary alcohol groups present on its surface causing an under expression of aldehydes in TT-3H-CD, however the XPS and FT-IR of TT-3H-P does not support this, so it is unclear why this is the case. The difference between the aldehyde peaks in AT-0-CD and TA-0.02-CD could be because the oxidation reaction was able to fully convert all the aldehydes to carboxylic acids. The C=O for carboxylic acids also show a peak between 1760-1706cm⁻¹ which is very close to the aldehyde C=O peak. Hu et al. (Hu et al., 2020) also synthesised CDs using a SA catalyst from green tea residue. They also outlined the presence of carboxyl, carbonyl and hydroxyl groups on the surface of their dots; however they did not test the effect of changing the concentration of the catalyst.

The peak at 1628cm⁻¹ corresponds to a conjugated C=C alkene (Mate et al., 2022), which comes from aliphatic surface groups. This peak is present in AT-0-CD, AT-0.02-CD, TA-0.005-CD, TA-0.02-CD and TA-0.05-CD. Samples that do not show this peak (TT-2H-CD, TT-3H-CD, TT-4H-CD and TA-0.01-CD) show a peak at 1585cm⁻¹ which corresponds to C=C bond in a cyclic alkene which corresponds to the bulk material of the CD (Tungare et al., 2020). A hypothesis as to this difference between the samples is that these bonds are present in both samples and the peaks are overlapping each other differently sample to sample.

The peak at 1530cm⁻¹ corresponds to amine groups. (Navidfar et al., 2022)This is barely expressed in these spectra but is most noticeable in AT-0-CD, TA-0.005-CD, TA-0.02-CD and TA-0.05-CD. These groups are present in the raw material (Diana M. A. Crista et al., 2020) and the precursors and would have been brought forward in the nitric acid oxidation.

The peak at 1350cm⁻¹ corresponds to the O-H bond in a phenol group. This could be corresponding to any alcohol group bonded directly to the polyaromatic structure.

The peak at 1280cm⁻¹ corresponds to aromatic esters. The peak at 1080cm⁻¹ correspond to the C-O in alcohol groups (Janpetch et al., 2015) present on the surface of the CDs introduced in the nitric acid oxidation. The peak at 1045cm⁻¹ corresponds to anhydride (Mate et al., 2022) which are expressed in CD functional groups and incorporated into the edge of the bulk material as an aromatic anhydride. Peaks 967, 896, 767 and 685cm⁻¹ correspond to alkenes. These are only shown in TA-0.05-CD and were also shown in the raw material and precursor (TA-0.05-CD) suggest that the nitric acid oxidation wasn't as effective for this sample as the others.

To further analyse the surface of the CDs, XPS was run and analysed. This is summarised in Table 4.2, Figure 4.9 and Figure 4.10 provide an example of the peak fitting in the wide survey scan and C 1s respectively (O 1s – Figure A.6.4, N 1s – Figure A.6.5).

Table 4.2 - Outline of all XPS results from each carbon dots sample obtained after nitric acid oxidation

Scan	At %											
	Survey			C 1s				N 1s		O 1s		
Element/Bond	Carbon	Nitrogen	Oxygen	sp2/C=C	sp3/C-C	C-O	C=O	C-NH2	NO3	C=O	C-O	Na KLL Auger
Binding energy (eV)	285.81	400.86	532.51	284.31	284.88	286.46	288.89	400.52	406.97	531.01	532.84	534.98
Sample												
TT-2H-CD/AT-0.01-CD	30.62	2.04	67.34	12.09	39.11	28.88	19.91	66.56	33.44	31.42	65.01	3.57
TT-3H-CD	29.27	1.89	68.84	10.67	34.78	25.26	29.29	67.6	32.4	30.43	65.53	4.04
TT-4H-CD	35.14	4.54	60.33	6.76	25.94	45.4	21.9	65.85	34.15	34.7	63.03	2.27
AT-0-CD	31.72	3.74	64.54	8.06	24.65	42	25.3	55.26	44.74	30.5	63.85	5.65
AT-0.005-CD	48.49	0	51.51	18.28	39.46	26.46	15.81	100	0	31.43	67.45	1.12
AT-0.02-CD	35.65	1.23	63.12	7.82	19.48	47.38	25.33	88.28	11.72	20.09	78.45	1.46
TA-0.005-CD	26	0.68	73.32	4.2	59.42	20.98	15.4	61.74	38.26	2.52	90.92	6.56
TA-0.01-CD	26.9	1.8	71.3	8.2	23.7	31.24	36.86	96.15	3.85	36.54	60.64	2.82
TA-0.02-CD	20.6	0.2	79.2	7.97	32.68	31.36	27.99	78.61	21.39	6.57	85.87	7.55
TA-0.05-CD	33.62	3.98	62.4	3.72	31.61	43.78	20.89	83.89	16.11	48.69	46.85	4.46

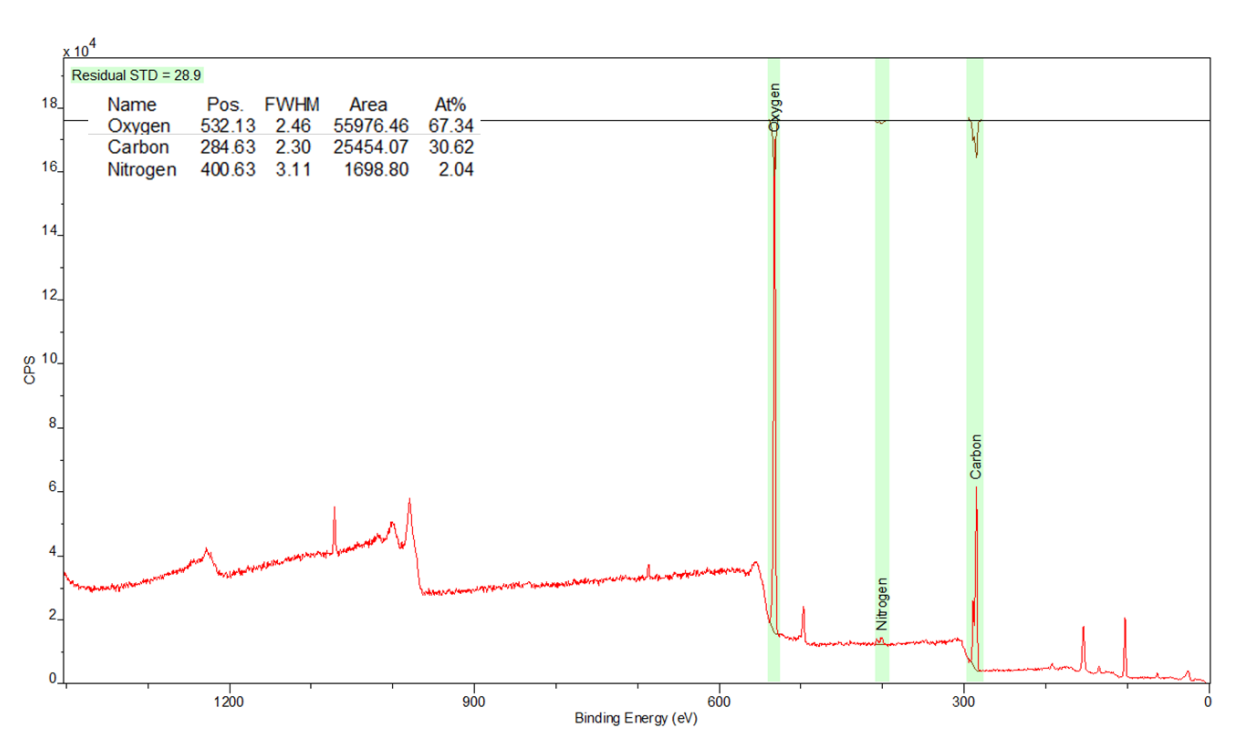


Figure 4.9 - XPS wide survey scan of the carbon dot sample TT-2H-CD/AT-0.01-CD.

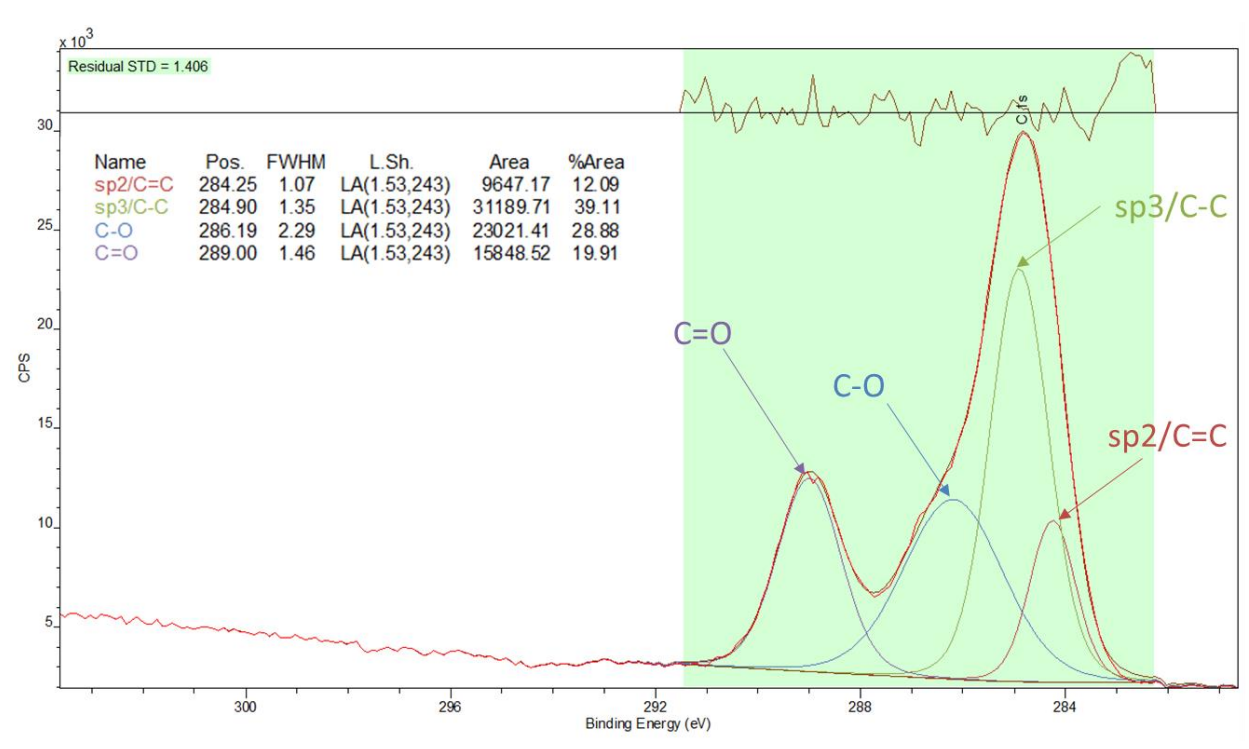


Figure 4.10 - XPS C 1s survey scan of the carbon dot sample TT-2H-CD/AT-0.01-CD.

The wide scan data shows (Table 4.2) a massive (~240% on average across all samples) increase in oxygen content and an insignificant change in nitrogen, in the dots when compared to the precursors. This was to be expected after the nitric acid oxidation. This shows that the purification process of filtration, washing and dialysis does a good job of removing the nitric acid after the oxidation step. The increase in oxygen content shows the success of the

oxidation process with the introduction of oxygen containing groups. There is no trend for the elemental make-up of the CDs in respect to the precursor reaction parameters.

The C 1s data (Table 4.2) shows a decrease in C-C bonds and an increase in both C-O and C=O bonds. This is consistent with the wide scan and further confirms the success of the oxidation step, but it shows a bigger increase in the C=O bonds than the C-O bonds.

The general trend for the O 1s scan is a large increase in the ratio of C=O bonds. This also shows an increase in C=O bonds as SA concentration increases. This could be because the SA catalyst breaks down the coffee grounds by inserting oxygen containing groups into the cellulose fibres to break them down via dehydration and oxidation (Y. Hu et al., 2014; Hu et al., 2020). This in turn leads to the increase of (C=O) groups on the surface on the dots which was shown to increase the intensity of the photoluminescence.

This data (Table 4.2) shows the addition C-NH $_2$ groups on the surface of the dots which would have been exposed during the nitric acid oxidation (Galletti et al., 2018). This is good for application because having a variety of different functional groups allows the dots to be functionalised in more ways (Zhou et al., 2019). The presence of the NO $_3$ can also be explained by left over nitric from the oxidation that had not been fully removed by the dialysis purification. Even though these groups were found in the XPS, they must be in a very low concentration as they are not shown in the FT-IR and nitrogen as a whole is only 0.15 and 4.55 At% of the elemental composition, depending on the sample. This still shows that using harsh chemicals should be avoided because once added they can be hard to remove fully.

The CDs were characterised for their size and morphology using TEM, this is outlined in Figure 4.11, Figure 4.12 and Figure 4.14 which depict examples of TEM images from different samples (TT-2H-CD/AT-0.01-CD, AT-0-CD and TA-0.05-CD). Figure 4.13 outlines the size distribution for each CD sample as analysed from the images using ImageJ.

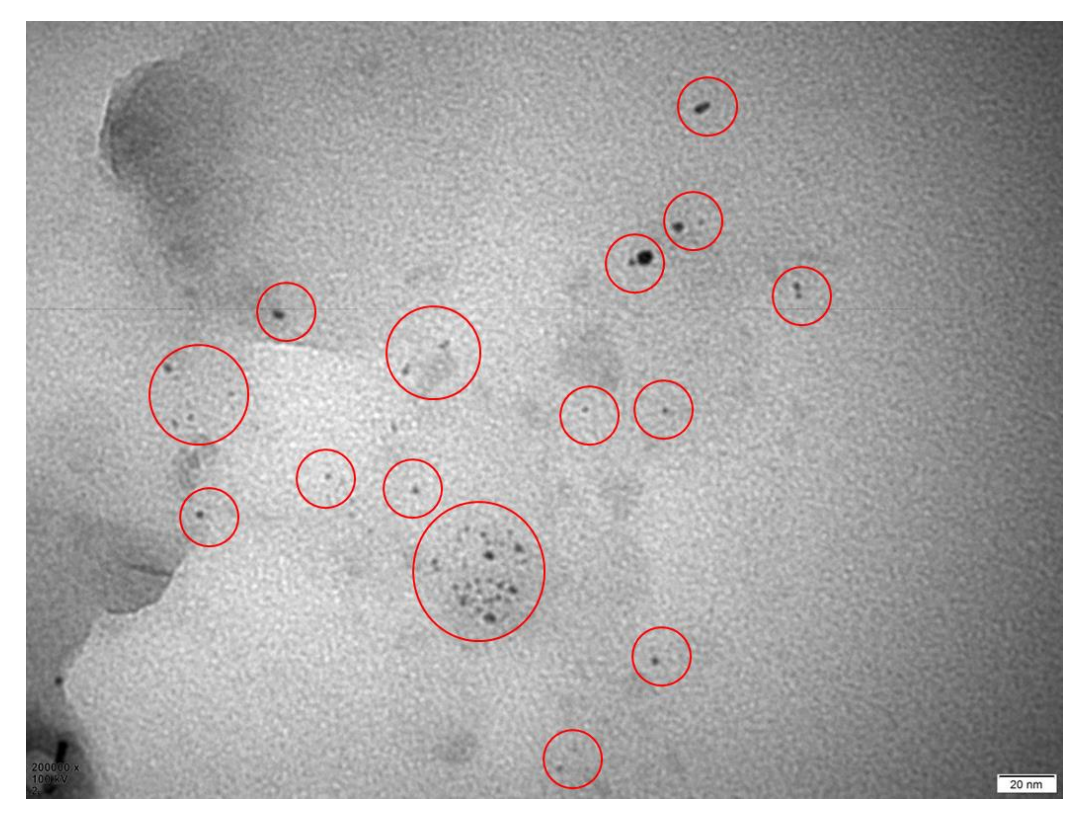


Figure 4.11 - TEM image of carbon dots (TT-2H-CD/AT-0.01-CD) synthesised from precursor TT-2H-P/AT-0.01-P (2 Hours with 0.01g/ml Sulphuric acid) - Scale Bar 20nm

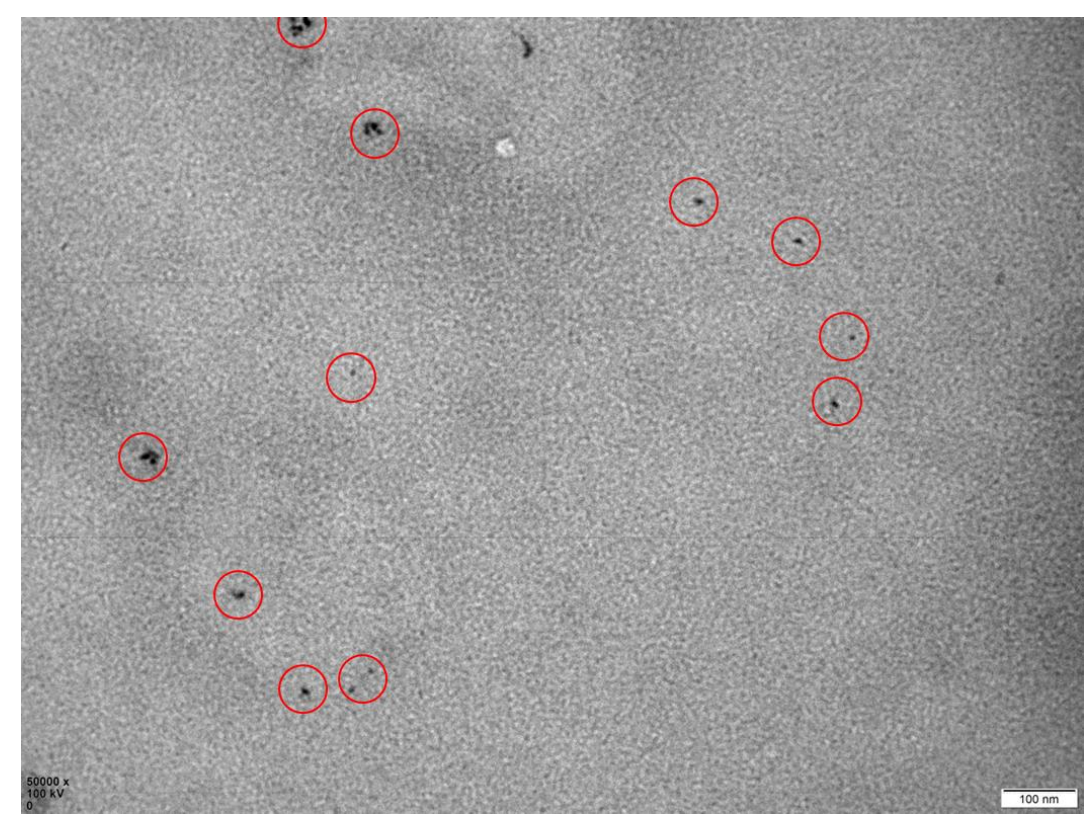


Figure 4.12 - TEM image of carbon dots (AT-0-CD) synthesised from precursor (AT-0-CD) (2 Hours with water) - Scale Bar 20nm

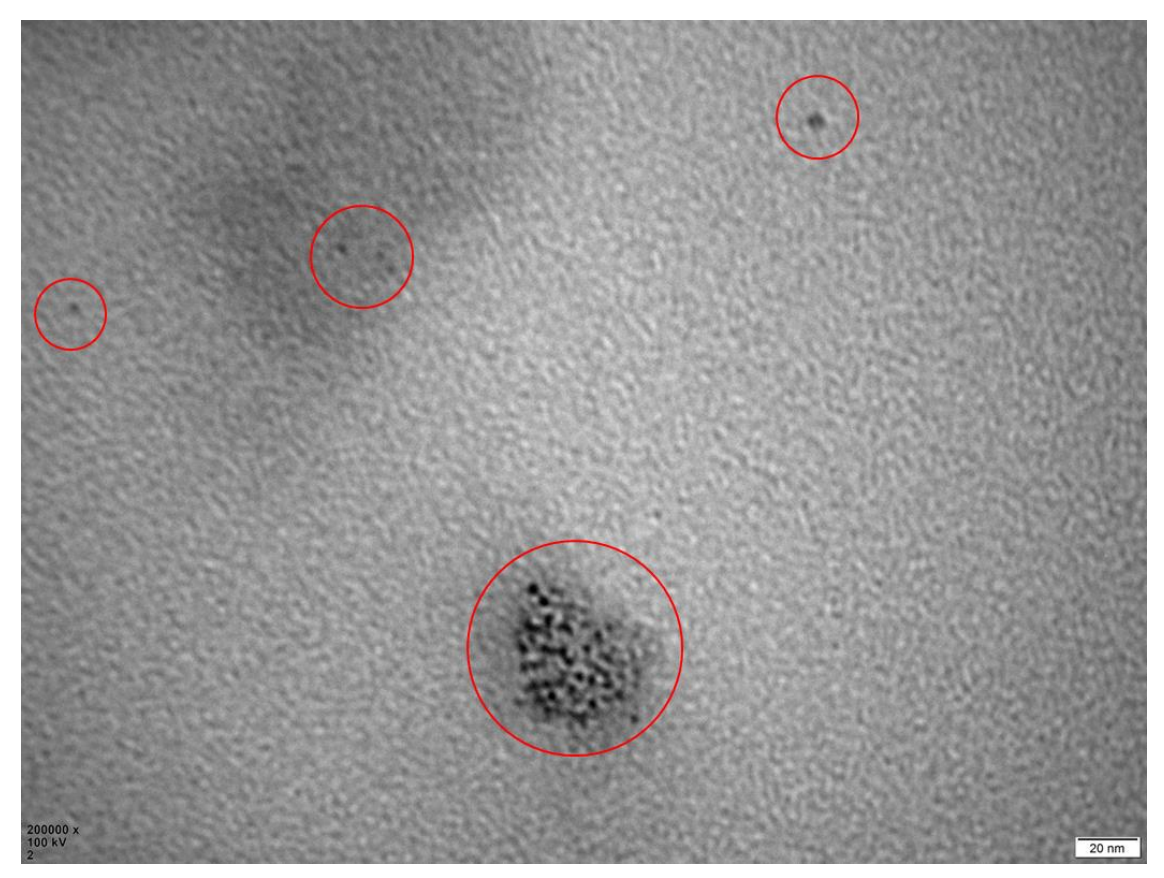


Figure 4.14 - TEM image of carbon dots (TA-0.05-CD) synthesised from precursor (TA-0.05-CD) (2 Hours with 0.05g/mL Tannic acid) - Scale Bar 20nm

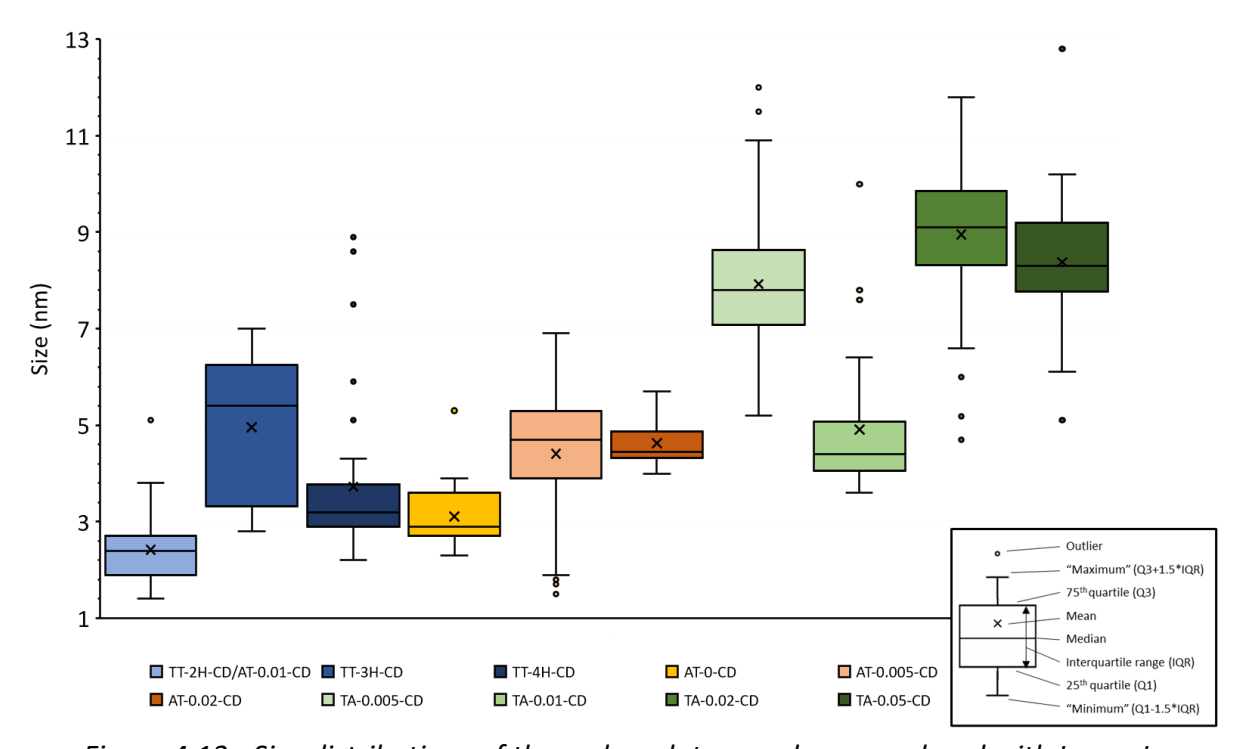


Figure 4.13 - Size distributions of the carbon dots samples as analysed with ImageJ

One way ANOVA testing of the data showed that these results are significant (F > F crit) and (P < 0.05). The results are also significant when comparing the three different catalyst types

with Bonferroni corrected post hoc tests confirming significant differences between each catalyst type. The biggest differences coming from comparing TA catalysed (TA series) dots to the SA catalysed (AT and TT series) and no catalyst tests (AT-0-CD).

It is clear, from these images, the general method in this study produces dots with or without catalyst because the average sizes of the dots are below the 10 nm size that is cited as the upper limit for CDs (Sharma & Das, 2019; Wang & Hu, 2014). However, the size varies greatly depending on precursor synthesis parameters; the dots that were synthesised from precursors that used a TA catalyst were, on average, larger (4.9 – 9.0nm) with much wider distributions when compared to the acid tests (2.4 – 4.6nm). Some recent examples of CD sizes are 1.59-1.64nm (Jeong et al., 2023), 2.1–3.9 nm (D. M. A. Crista et al., 2020) , 1.9 to 5.9 nm (Chen et al., 2021) and 30 nm (Xu et al., 2017). The TA precursor dots are certainly on the upper end of this spectrum, however the SA precursor dots fit perfectly into the ranges presented in previous studies. There is no trend for size of CDs with respect to precursor retention time or catalyst concentration.

The larger size of the TA precursor dots suggests that the oxidation reaction that forms the CDs is less efficient with these precursors. This must be due to the differences in the bulk structure of the precursor. These TA precursors were amorphous in structure while the other precursors (time tests and SA tests - Table 3.2) had a graphitic/polyaromatic structure. The graphitic structure has plenty of aromatic reactive sites that the nitric acid can break open and introduce oxygen containing groups such as alcohol groups, aldehydes and carboxylic acids which are seen in the FT-IR spectra. This effectively cuts downs the precursor, forming smaller CDs with a narrower size distribution (Adolfsson et al., 2015; Xu et al., 2017). The amorphous structure of the TA precursors contains lots of aliphatic chains, and a smaller amount of polyaromatic structures that can be utilised to cut down the precursor, leading to larger CDs. This explains why the TA-0.01-CD has a smaller average size than the rest of the TA series. The FT-IR indicated that there was a higher amount of this graphitic structure with the cyclic amine peak.

At an average size of 3.1 ± 0.7 nm the dots that used a precursor with no acid (AT-0-CD) are one of the smaller sizes produced. This proves that the catalyst is not required to make the

precursor capable of producing smaller CDs. Not using SA makes this synthesis more green, less hazardous, and more viable for scale up in industry (Wareing et al., 2021).

The photoluminescence properties of the CDs were analysed, first this was done with UV-Vis spectroscopy. The UV-Vis was taken to investigate the absorbance of the CD solutions, and it was found that all the solutions had an absorbance between 280 and 300 nm, with most of the values landing between 288 and 294 with no visible trend. This absorption can be attributed to the π - π * transition of the aromatic sp2 domains and the n- π * transition of the C=O bonds (Jeong et al., 2023; Yang et al., 2014; X. Zhang et al., 2018). It was shown that changing the catalyst, catalyst concentration and holding time had little effect on the absorbance wavelength. This shows that absorbance is intrinsic to the dots made using this feedstock process regardless of the changes in the reaction parameters. Absorption values close to this range were found in several other papers that use coffee grounds as a carbon source (Costa et al., 2022; Jeong et al., 2023; Jiang et al., 2014; X. Zhang et al., 2018). The photoluminescence of the dot solutions was shown to be blue when excited by a 365nm UV lamp which is also consistent with the literature (Figure 4.15).

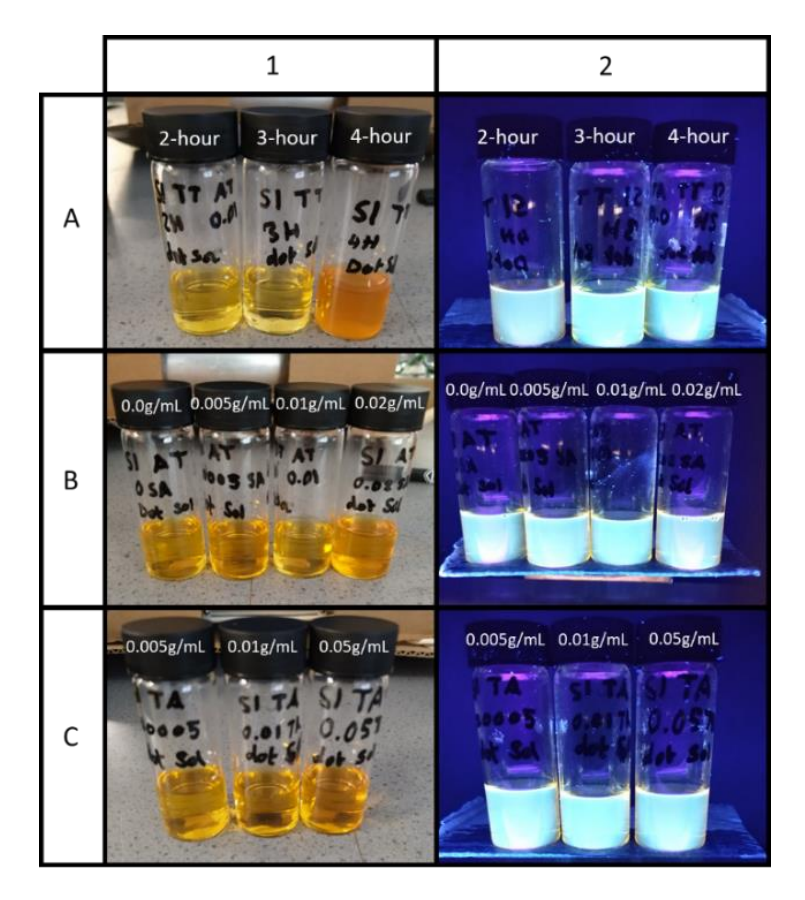


Figure 4.15 - Solutions of carbon dots under visible lights (1) and under UV-Light (2); A) from left to right; TT-2H-CD, TT-3H-CD, TT-4H-CD, B) from left to right; AT-0-CD, AT-0.005-CD, AT-0.01-CD, AT-0.02-CD, C) from left to right; TA-0.005-CD, TA-0.01-CD, TA-0.05

Solutions were then measured with a PL spectrometer at an excitation wavelength of 300nm. This wavelength was chosen due to the absorption maxima that was observed in the UV-Vis data. Figure 4.16 shows that changing the retention time, catalyst concentration and catalyst type for the synthesis of the precursors does not have a drastic effect on the emission wavelengths of the photoluminescence.

The CDs had two photoluminescence maxima: the first between 360-389nm and a second between 420-437nm. Because the second wavelength was consistently the highest for most samples, this was chosen for the QY analysis. The only trend shown for this data is that increasing the concentration of the SA catalyst improves the photoluminescence intensity of the resulting dots. This could be because the SA catalyst breaks down the SCG by inserting oxygen containing groups into the cellulose fibres to break them down. This in turn would lead to an increase of (C=O) groups on the surface on the dots which is indicated by the oxygen XPS. Because =O bonds are responsible for the absorption, the intensity of the photoluminescence is related to the amount of these groups on the surface of the groups. The

tests that used TA, and the test that used no acid provide some of the lowest intensities, showing that using a SA catalyst does produce CDs with superior photoluminescence.

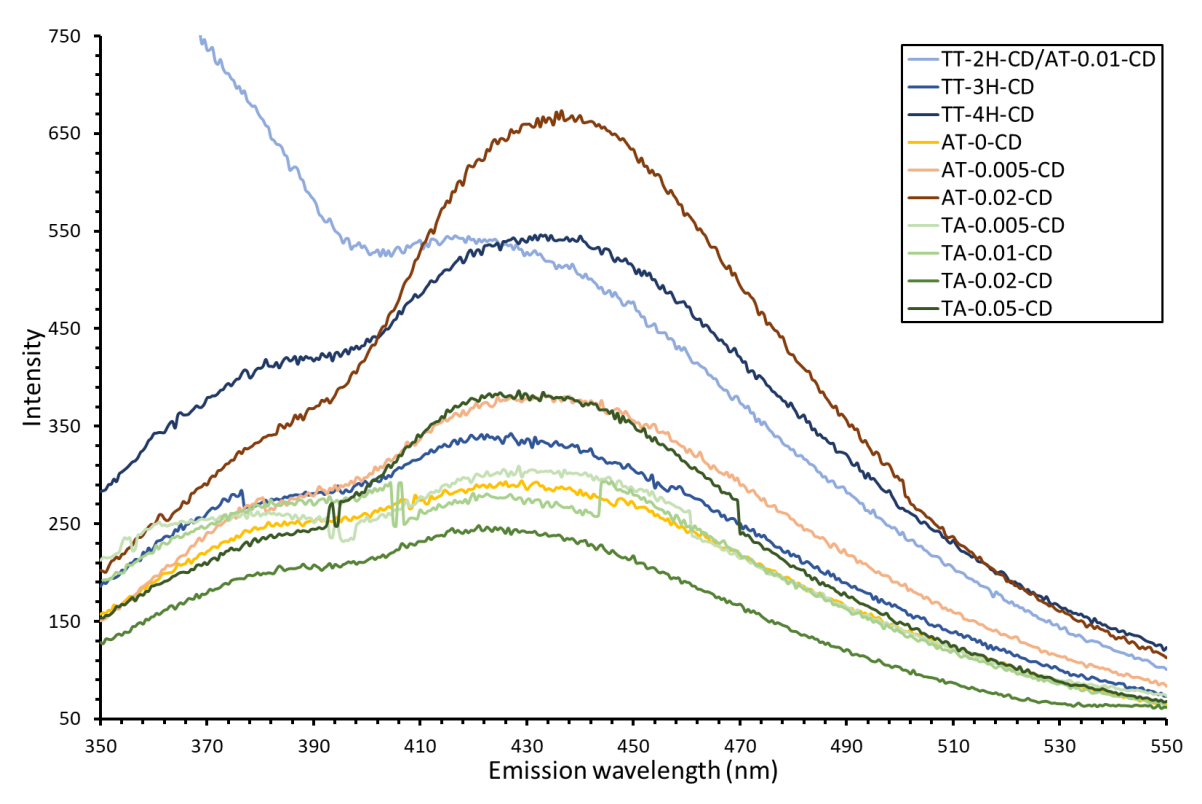


Figure 4.16 - Comparison in photoluminescence intensity when excited at 300nm wavelength according to reaction parameters.

QY analysis allows a direct comparison of the fluorescence of the dots in comparison with dots from other papers and between the samples outlined in this chapter. This data can be compared with that from similar papers synthesising CDs using as biomass as a carbon source. Values over 15% are usually considered high (Cui et al., 2021) for biomass-based CDs with a rare ~80% being the current upper end (Abbas et al., 2020; Palacio-Vergara et al., 2023). There are numerous papers published detailing methods of CD fabrication from SCGs, however few publish QY data with these. This allows for direct comparison of methods and is critical for future research. Previous papers have given QY data based on different experimental conditions. For example, Hsu et al (Hsu et al., 2012) reported a QY of 3.8% in 2012, with a 6-hour HTC at temperatures varied between 100-600°C. This was improved by (Park & Yang, 2022), with a QY of 11% based on a 400°C HTC for a duration between 0.5 and 2 hours. This data indicates that typical QYs from SCGs are quite low. This is something which has been previously noted in research and which utilising pre-treatment is attempting to improve.

Table 4.3 shows that the QY for these CDs is between 3.6 and 6.7% with an average of 4.7 (σ = 1.01), which is mediocre for CDs using SCG as a feedstock (Costa et al., 2022; D. M. A. Crista et al., 2020; Jeong et al., 2023; Jiang et al., 2014).

Table 4.3 - Quantum yield of each carbon dot sample.

Sample	QY %
TT-2H-CD/AT- 0.01-CD	5.99
TT-3H-CD	4.63
TT-4H-CD	5.14
AT-0-CD	4.16
AT-0.005-CD	4.49
AT-0.02-CD	6.7
TA-0.005-CD	4.23
TA-0.01-CD	3.6
TA-0.02-CD	3.44
TA-0.05-CD	4.56

The effect of tuning the concentration of the TA concentration on QY was also investigated, and it was found that there was no significant trend (R² = 0.15) between the two. There is also no significant increase or decrease (-1.2%) in average QY for the samples that used a TA catalyst when compared to the sample using no catalyst at all (AT-0-CD). This shows that a TA precursor synthesis catalyst does not have any effect on the CD synthesis. This is to be expected because the FT-IR of the TA catalysed precursors showed similar spectra to raw SCG which suggests that the TA catalyst does not help to break down the SCG, nor introduces any functional groups to the material that would have a positive effect on the resulting CDs as shown in the XPS and FT-IR.

Comparing the average QY for dots that used SA in their precursor synthesis (TT2H/AT 0.01, TT3H, TT4H, AT 0.005, AT 0.02) against dots that did not (AT 0, TA 0.005, TA 0.01, TA 0.02, TA 0.05) shows a 34.8% increase. There is also a significant trend ($R^2 = 0.98$) between the concentration of the SA precursor catalyst and the QY of the CDs, which is that as concentration of SA increases, the QY increases. Both these pieces of information shows that SA plays an important role in the precursor synthesis for the resulting dots and tuning the

concentration of SA used can affect the QY. This is because it is directly related to the intensity of the photoluminescence: the increased number of emissive sites translates to higher efficiency of the CDs.

4.1.3 *Summary*

CDs were synthesised by a two-step process, a HTC with an acid catalyst followed by an oxidation with nitric acid. Using different catalysts for the HTC precursor synthesis changes the photoluminescence intensity of the dots. It was shown that SA was the superior catalyst as the photoluminescence of the dots is overall more intense than that obtained from the case using TA or no catalyst. No other parameter change, such as the concentration of tannic acid used, makes a significant difference to the properties of the dots. However, the reaction itself is a long two-step process and uses harsh chemicals for the catalyst and an oxidation agent. The mass yield was too low to quantify; this is common for CDs synthesised from biomass as it contains lots of impurities. Further research needs to be completed on a synthesis that does not use harsh chemicals, is a simpler process, and increases the yield of the dots.

4.2 Ultrasonic pretreatment of spent coffee grounds and tannic acid catalysed hydrothermal carbonisation (synthesis 2)

Ultrasonics was used to pre-treat SCG followed by a HTC to produce CDs. Three pre-treatment conditions were examined at a fixed pre-treatment time of 90mins. The contents of the ultrasonic pre-treatment were transferred to the 125ml HTC reactor and reacted for 3 hours at 200°C. The resulting mixture was filtered to obtain a solution containing the CDs which were dialysed to remove impurities using both 3500Da and 2000Da dialysis tubing. The resulting solution was freeze dried to yield solid CDs. The sample codes for this step retain their previous prefix and condition codes and the suffix is changed from -PT to -HTC.

The progression of the carbonisation process can be indicated by the colour of residual solids after each stage of the reaction. Figure 4.17 depicts the solids at different stages. Ultrasonication was intended to break up particles without initiating the reaction. This was seen in the results of the ultrasonic pretreatment with a 'smoothie-like' consistency to the mixture rather than large visible particles. After removal of the water for observation, the materials were compared. The particle size of the solids after pretreatment (Figure 4.17B) was smaller than the untreated SCG. Following HTC, the solids become significantly darker, indicating carbonisation (Park & Yang, 2022). The solution gained from the HTC was purified utilising dialysis and freeze-drying the light-yellow solids show that impurities have been eliminated.



Figure 4.17 - Images left to right of a) Raw SCGs, b) Dried solids following 90-minute pre-treatment with tannic acid c) Dried solids following pre-treatment and 3-hour HTC at 200°C and d) Freeze dried solids following separation by dialysis

4.2.1 Effect of Ultrasonic pretreatment on spent coffee grounds.

During the pre-treatment step, samples were collected at 15-minute intervals. These samples were made up of both liquid (TA/water) and solids (SCGs). After collection, centrifugation was used to separate the two phases, and the solids were subjected to drying for subsequent FT-IR analysis. The composition of the raw SCG was also analysed for comparison. Figure 4.18 displays an FT-IR spectra of raw SCGs, including samples after ultrasonication pre-treatment at different temperatures.

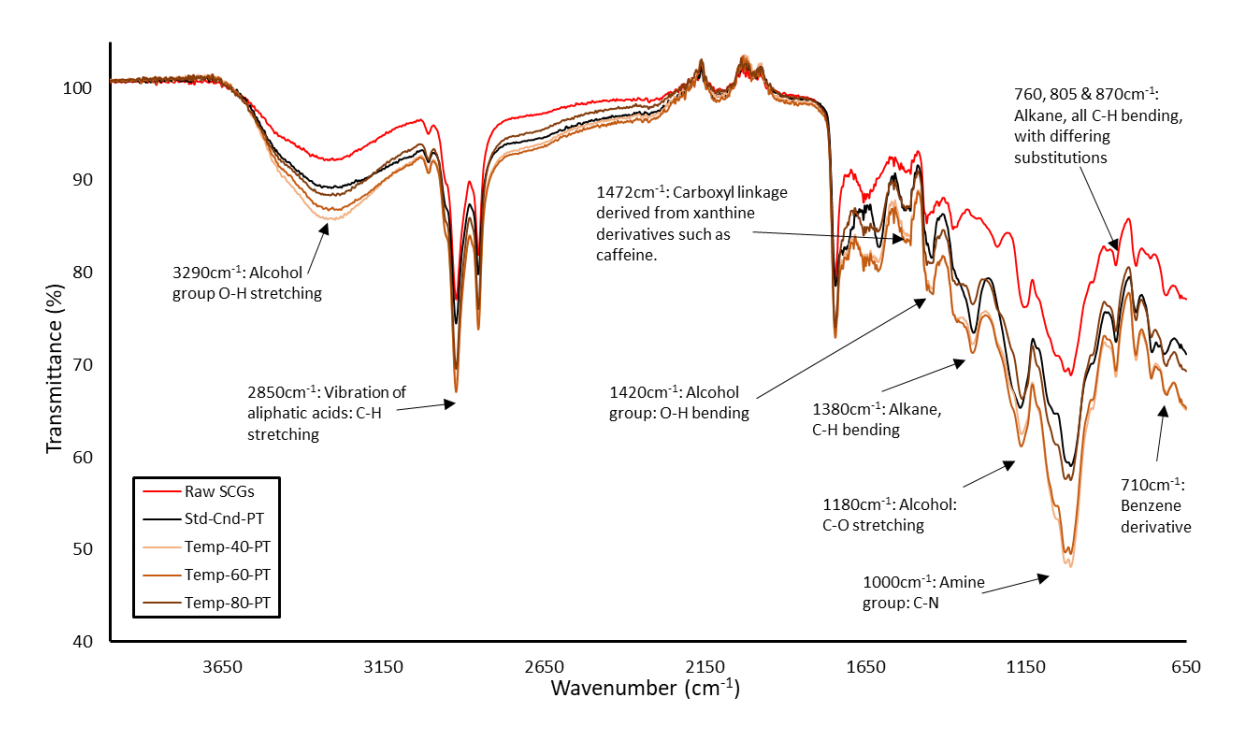


Figure 4.18 - FT-IR analysis of raw SCGs and SCGs pre-treated via ultrasonication for 90 mins with a 50ml of 0.05g/ml tannic acid solution, with no heating (std-cnd-PT) and heating to 40°C, 60°C and 80°C. Peaks are labelled with their corresponding wavelength and functional groups (Merek, 2023)

The "Raw SCG" line in Figure 4.18 provides the composition of the SCGs for comparison. Among the peaks observed, the first three peaks are the most prominent. The peak at 3290cm⁻¹ corresponds to the O-H stretching group, which corresponds to hydrogen bonding in polymeric compounds such as pectin, cellulose, and lignin. These compounds consist of alcohols, phenols, and carboxylic acids, respectively. However, this peak exhibits a broad shape, indicating the presence of both free hydroxyl groups and bonded O-H bands of carboxylic acids (Chou et al., 2012). The identification of aliphatic acids and caffeine in the coffee can be discerned due to the alterations in counter ions associated with carboxylate and hydroxyl groups, which contribute to the uptake of metal ions (Chou et al., 2012).

Effect of Temperature - The impact of pre-treatment temperature was investigated. The data showed that the peaks remain unchanged, which was expected since the reaction is not anticipated to occur in the chemistry at this stage. The temperatures required for hydrothermal carbonisation (HTC) typically falls within the range of 180-250°C (Funke & Ziegler, 2010). However, the intensity of the peaks noticeably increases because of the pre-treatment. The untreated SCGs, represented by the black line, exhibit the least intensity, while greater activity is observed following ultrasonication. This is because ultrasonication induces

cavitation within the mixture. These cavitation bubbles contain liquid vapor and dissolved gas, and collapse of the cavitation generates significant shear forces resulting in cleavage of the lignocellulosic structure of the biomass and exposes more functional groups on the surface of the SCGs (Kassim et al., 2022) and isolation of monomers such as hemicellulose, cellulose and lignin. The influence of temperature on the peaks is also evident. In general, a higher pretreatment temperature results in higher peak intensity, except for the run conducted at 80°C. This could be attributed to the "burning" of coffee grounds when exposed to such high temperatures. Coffee tends to burn at around 85°C or higher (Brown & Diller, 2008), and the ultrasonication bath only provided temperature control within a range of 5°C, which fluctuated during the experiment. Therefore, it is possible that the coffee grounds were exposed to excessively high temperatures during the pre-treatment process, leading to damage to certain organic compounds.

Effect of Tannic Acid Concentration - In addition to temperature, the impact of varying TA concentration during the pre-treatment process was also investigated (Figure 4.19). Previous studies have successfully employed a concentration of 0.02g/ml TA to produce CDs (Achadu & Revaprasadu, 2019). However, the effect of different concentrations has not been explored so far. To examine these effects, FT-IR spectra at different TA concentrations was analysed. The spectra show that the peaks become more intense following ultrasonication with 0.1g/ml TA, the highest concentration tested. This effect is also reflected in the resulting CDs, as TA imparts a fluorescent behaviour on the SCGs (Achadu & Revaprasadu, 2019), suggesting that a more concentrated solution would emit stronger fluorescence. In terms of fluorescence and yield of CDs, based on the FT-IR data indicating improved surface activity, it is proposed that a higher concentration of TA will yield better results.

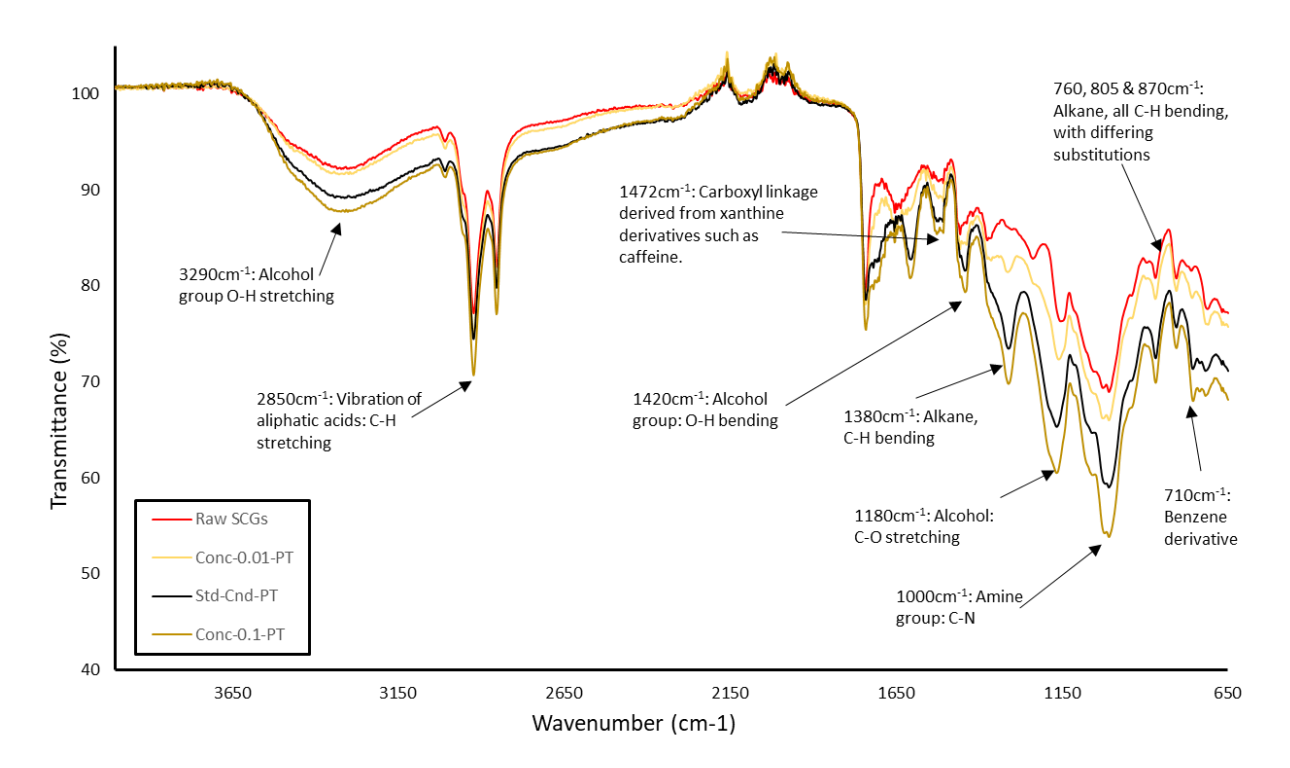


Figure 4.19 - FT-IR analysis of raw SCGs, Std-cnd-PT, Conc-0-01-PT and Conc-0.1-PT for the purposes of analysing the effect of changing concentration. Peaks are labelled with their corresponding wavelength and functional groups (Merek, 2023)

Effect of Ratio of SCGs to Tannic Acid - The next aspect to consider was the impact of the TA solution-to-SCGs ratio on the composition of the CDs (Figure 4.20). The analysis shows that a lower TA to SCGs ratio leads to enhanced surface activation, which is beneficial for the fabrication of CDs. Although there are slight differences between the 25ml and 50ml solutions, both demonstrate significantly better outcomes compared to the 100ml option. Previous studies have utilised ratios of up to 1:100 for the biomass to TA ratio (Achadu & Revaprasadu, 2019), suggesting that these previous findings could potentially be enhanced by adjusting the ratio. Based on these data sets, a recommendation for the most effective method of pretreatment is put forward. The conditions for this are 60°C, 0.1g/ml TA concentration and 25ml TA.

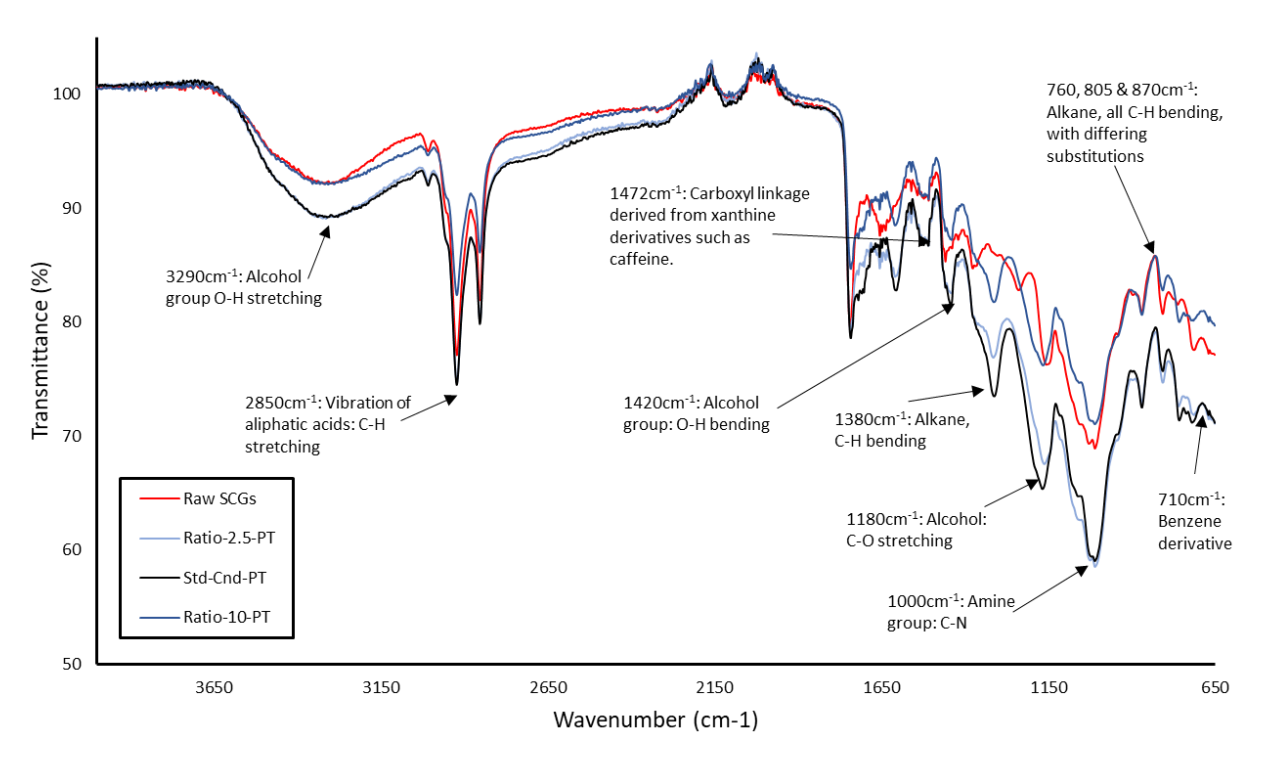


Figure 4.20 - FT-IR analysis of raw SCGs, Std-cnd-PT, Ratio.2.5-PT and Ratio-10-PT for the purposes of analysing the effect of changing biomass and tannic acid solution ratio. Peaks are labelled with their corresponding wavelength and functional groups (Merek, 2023)

Effect of Time - The pre-treatment process was conducted for a duration of 90 minutes, with samples collected every 15 minutes (Figure 4.21). Throughout the 90-minute pre-treatment period, the intensity of the peaks consistently increases, reaching the highest intensity at the end of the 90 minutes. This suggests that completing the full 90-minute duration yields the most successful results in terms of creating a larger surface area for CDs to form. However, this does not necessarily mean that 90 minutes is the optimal choice. It is recommended that in future experiments, longer durations are explored to determine whether further improvements can be achieved with extended pre-treatment. Additionally, it would be valuable to identify the point at which ultrasonication no longer provides any additional benefits.

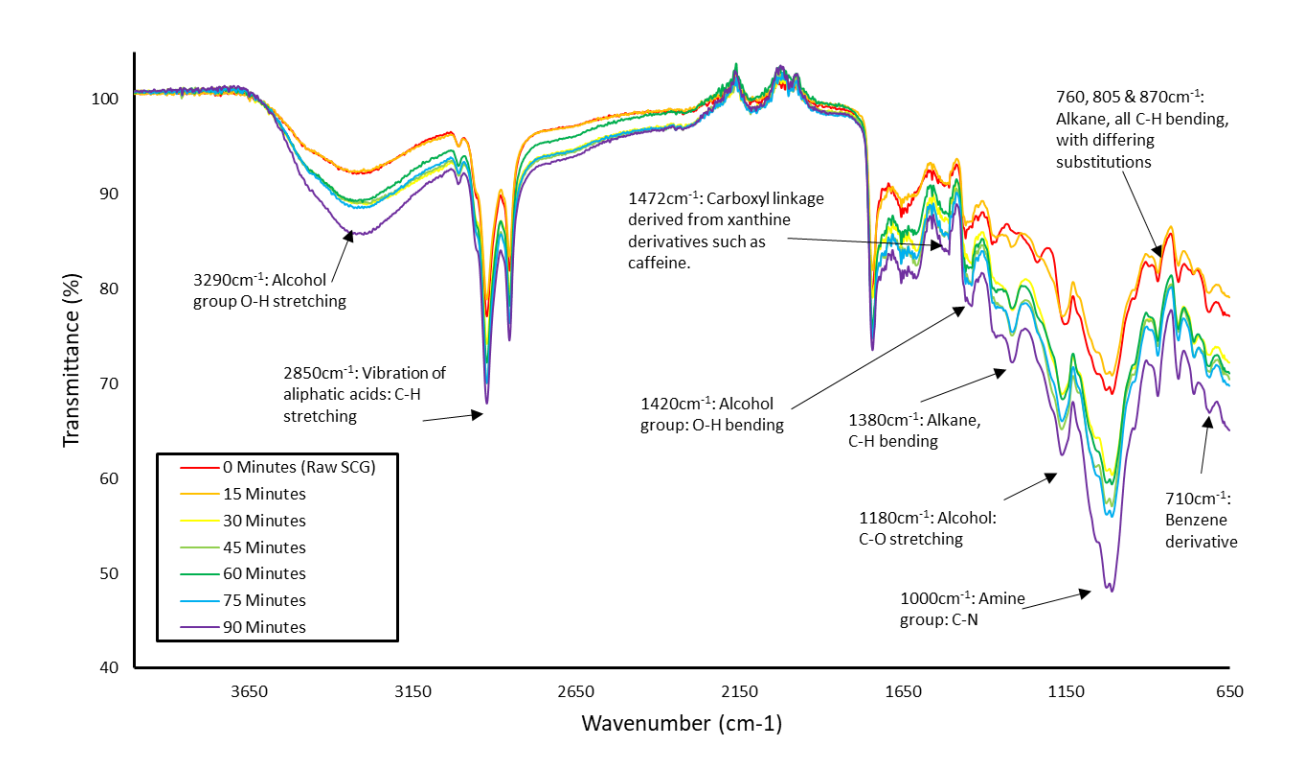


Figure 4.21 - FT-IR analysis of raw SCGs and samples taken from thre reaction of Std-cnd-PT every fifthteen minutes during the reaction progression for the purposes of analysing the effect of time. Peaks are labelled with their corresponding wavelength and functional groups (Merek, 2023)

Samples of each precursor after completion of the pretreatment were analysed with XPS along with a sample of spent coffee grounds for comparison. Table 4.4 outlines the results from each spectrum and Figure 4.22 and Figure 4.23 give examples of peak fitting in the wide and C1s scans in Std-Cnd-PT (O 1s – Figure A7, N 1s Figure - A8).

Table 4.4 - The XPS results of the ultrasonic pretreatment for each sample obtained after 90 minutes.

Scan	At /6											
Scall	Elemental - Wide			Carbon - C 1s				Nitrogen - N 1s		Oxygen - O 1s		
Group	Carbon	Nitrogen	Oxygen	sp2/C=C	sp3/C-C	C-O	C=O	C-NH2	NO3	C=O	C-O	Na KLL Auger
Binding energy (eV)	285.08	399.64	532.75	284.54	284.89	285.91	288.85	399.71	405.19	532.08	533.25	534.93
Sample												
Spent Coffee Grounds	70.74	2.93	26.33	17.48	34.84	40.43	7.24	97.29	2.71	38.8	58.72	2.48
Std-Cnd-PT	69.85	2.27	27.88	21.65	39.06	33.66	5.63	88.93	11.07	23.22	68.05	8.74
Conc-0-PT	71.57	2.13	26.3	6.5	64.17	26.35	2.98	100	0	14.46	85.54	0
Conc-0.01-PT	67.11	0.66	32.23	4.86	67.98	19.23	7.93	96.23	3.77	32.09	67.91	0
Conc-0.1-PT	71.62	1.11	27.27	48.08	36.16	12.28	3.49	100	0	54.53	45.47	0
Ratio-20-PT	70.69	1.33	27.98	54.45	33.66	8.78	3.11	93.13	6.87	54.59	41.94	3.47
Ratio-100-PT	66.23	1.99	31.78	10.62	56.42	28.78	4.18	100	0	30.12	69.88	0
Temp-40-PT	70.08	1.27	28.65	57.81	31.6	7.93	2.66	81.03	18.97	64.81	31.73	3.46
Temp-60-PT	71.44	2.06	26.5	17.18	44.54	34.66	3.62	81.5	18.45	33.74	65	1.26
Temp-80-PT	70.31	0.94	28.75	31.47	29.85	35.9	2.78	100	0	45.97	38.65	15.39

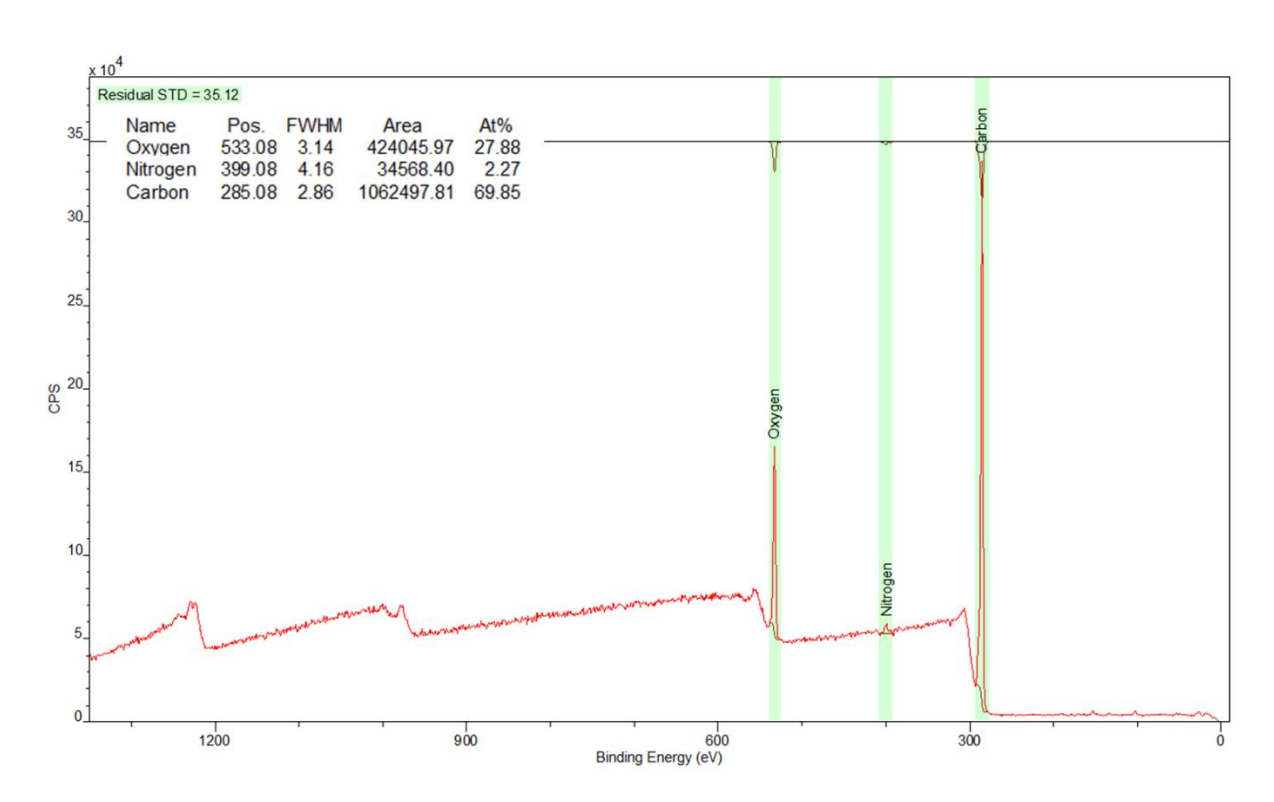


Figure 4.22 - XPS wide survey scan of the precursor sample Std-Cnd-PT

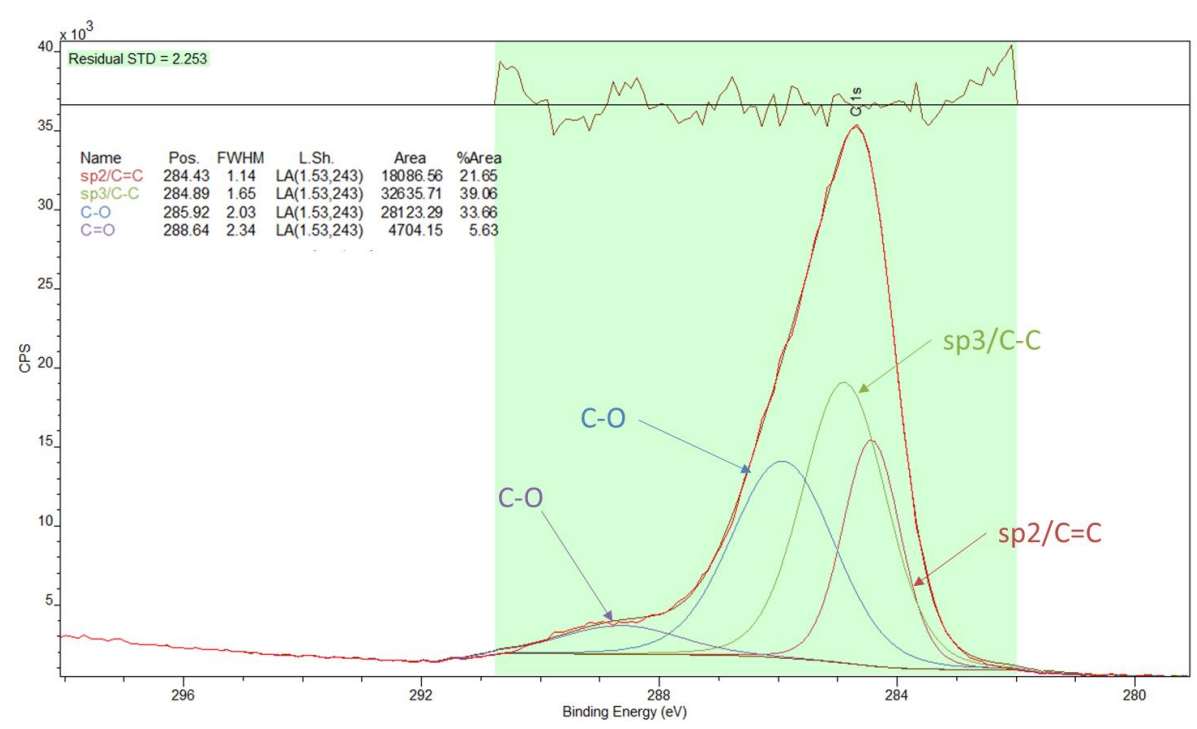


Figure 4.23 - XPS C 1s scan of the precursor sample Std-Cnd-PT

XPS of the raw coffee grounds revealed a surface chemistry elemental make-up of 70.74% carbon, 2.93% nitrogen and 26.33% oxygen. The C1 scan revealed sp^2 percentage of 17.48%, sp^3 - 34.84%, C-O – 40.43% and C=O – 7.24%. The O1 scan showed C=O as 38.8% and C-O as 58.72% which is in terms of ratio is inconsistent with the C1 values for C-O and C=O. The nitrogen scan showed the nitrogen content was mostly due to the presence of amine groups.

It was expected that the ultrasonic pretreatment would not cause significant changes to the XPS scans of the samples because the main purpose was to exfoliate and de-clump to increase the surface area of the coffee grounds, exposing functional groups and allowing the TA solution to soak into the macro structure. The inclusion of TA may have some effect on the XPS (the structure of TA is rich in -OH groups and esters (Guo et al., 2021)) and this should show in the XPS as an increase in the ratio of C-O bonds (Geißler et al., 2016), especially in the sample that used a concentration of 0.1g/mL of TA (Conc-0.1-pt). This is shown in the elemental scan with a slight increase of the ratio of oxygen. Most samples show a slight increase of oxygen; however, this trend is not shown in the individual scans. In the C1 scans, all the samples show a reduction in the radio of C-O bonds. The O 1s scans show a mix of decreases and increases in the C-O bond ratio. Interestingly, The C-O bond ratio in the sample that did not contain TA increased the C-O bond ratio from 58.7 to 85.5 and the sample with the highest concentration saw a reduction in these bonds down to 45.5 which is one of the lowest measurements.

There is no trend in this data to corroborate the findings of the FT-IR data. An explanation for this is that the penetration depth of XPS is shallower (10nm) (Stevie & Donley, 2020) than that of FT-IR up to 60 μ m (Götz et al., 2020). in first 10nm of the outside of the sample, the expression of functional groups could differ wildly giving a large variety of ratios of bonds in each sample as shown in the XPS C 1s, O 1s and N 1s. Because FT-IR penetrates deeper than XPS more material is analysed leading to the more standardised ratio of bonds seen.

4.2.2 Properties of carbon dots after hydrothermal carbonisation and effect of ultrasonic pretreatment

FT-IR analysis was conducted on the CDs obtained after freeze-drying (Figure 4.24). The analysis identified several key bonds, including O-H, C-O, CH₂, and C-O-C. These bonds are consistent with those observed in other FT-IR spectra of CDs (Alarfaj et al., 2018; Andrade et al., 2017; Kurdekar et al., 2016). While the peaks largely resemble those observed in SCGs, some peaks are more pronounced in the CDs. The O-H group remains strong, suggesting the presence of alcohol groups on the surface of the dots.

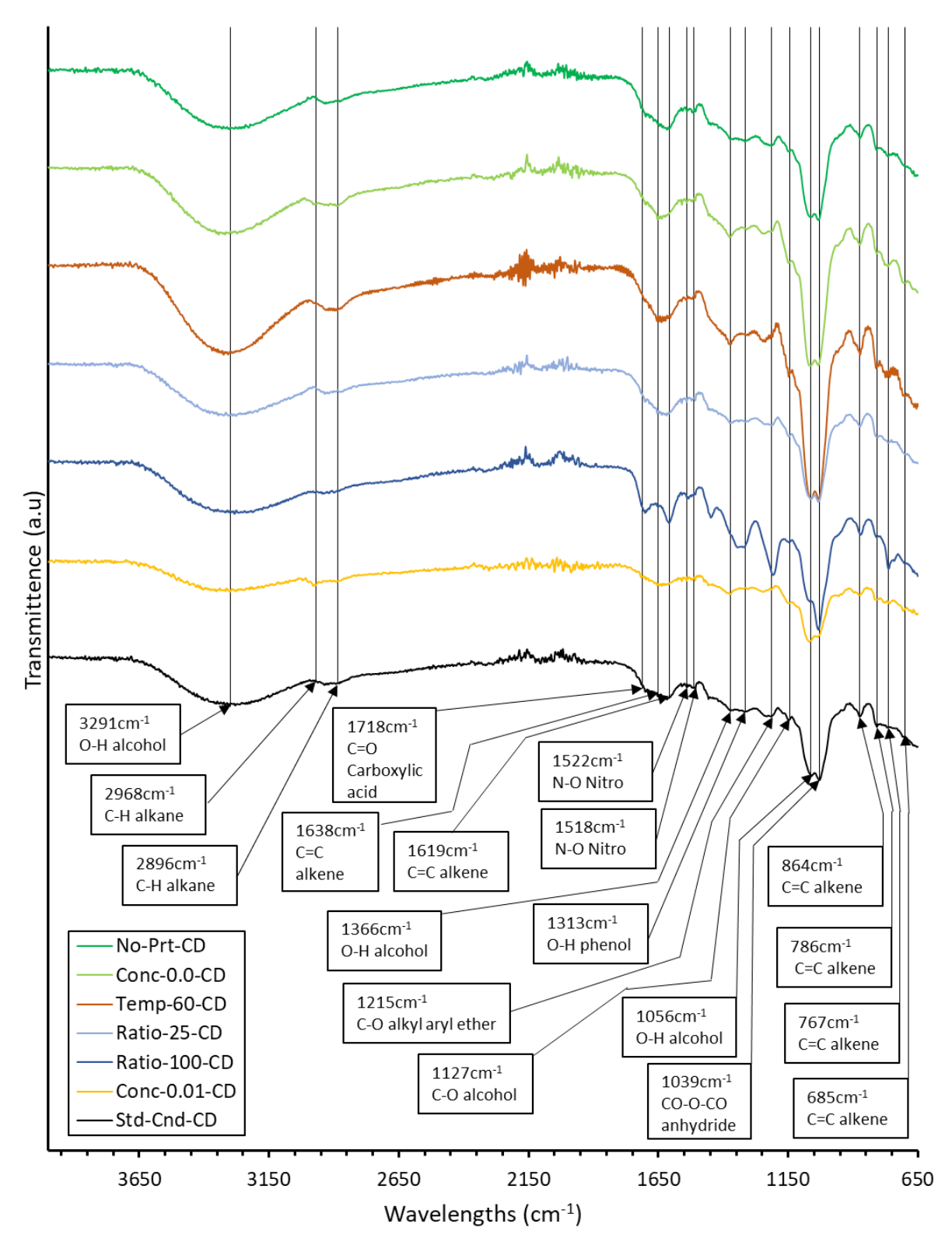


Figure 4.24 - FT-IR of Carbon dot samples synthesised from 3 hour HTC from the precursors obtained from the ultrasonic pretreatment

The peaks at ~2968 and 2896cm⁻¹ correspond to the C-H bond from alkane groups, which shows the presence of aliphatic chains on the surface of the CDs (Tungare et al., 2020). The

peaks at 2355cm⁻¹ corresponds to C=O from carboxylic acid. This group is highly negative, and this led to a negative surface charge which was shown in the ζ -potential (Cheng et al., 2020). The 1638cm⁻¹ corresponds as a conjugated C=C of an alkene (Mate et al., 2022), which comes from aliphatic surface groups. The peak at 1619cm⁻¹ also corresponds to C=C bond in a cyclic alkene which corresponds to the bulk material of the CD (Tungare et al., 2020).

The peak at 1313cm⁻¹ corresponds to the O-H bond in a phenol group. This is often shown in the surface groups and corresponds to any alcohol group bonded directly to the polyaromatic structure.

The peaks at 1056cm⁻¹ corresponds to the C-O (Janpetch et al., 2015) in alcohol groups present on the surface of the CDs. The peak at 1039cm⁻¹ corresponds to cyclic ester (Mate et al., 2022) which are expressed in CD functional groups and incorporated into the edge of the bulk material as an aromatic anhydride.

The differences between each sample are minor. However, the intensity of the samples Conc-0.0-CD and Temp-60-CD at peaks 1056 and 1039cm⁻¹ shows an increase of alcohol and anhydride surface groups when compared to the other samples. The pretreatment at 60°C was found to be optimal in the FT-IR of the precursor due to the expression of surface groups shown in the sample. This high expression has been carried over into the CDs for this sample. High expression of surface groups in Conc-0.0-CD is unexpected because it was found that higher concentrations of TA increased the expression of functional groups found by the FT-IR of the precursors as produced in the ultrasonication step. This result shows that TA could hinder the expression of these functional groups in the formation of CDs during the HTC step as the Conc-0.0-CD sample has such a high expression of functional groups compared to the pretreated material. The sample Ratio-100-CD shows some groups that are not expressed in the other samples, these being the 1718cm⁻¹ carboxylic acid peak, the peak at 1619cm⁻¹ corresponding to an alkene, 1313cm⁻¹ corresponding to a phenol group and a higher intensity in the peak at 1215cm⁻¹ which corresponds to an alkyl aryl ether group. These groups are characteristic of the SCG which shows that a lot of the precursor went unreacted. This higher effluent to biomass ratio is not optimum for HTC and the synthesis of CDs.

TEM imaging was used to provide images of the CDs (Figure 4.25, Figure 4.26 and Figure 4.27) which were analysed to provide the average size of the dots and a distribution (Figure 4.28 and Table 4.5).

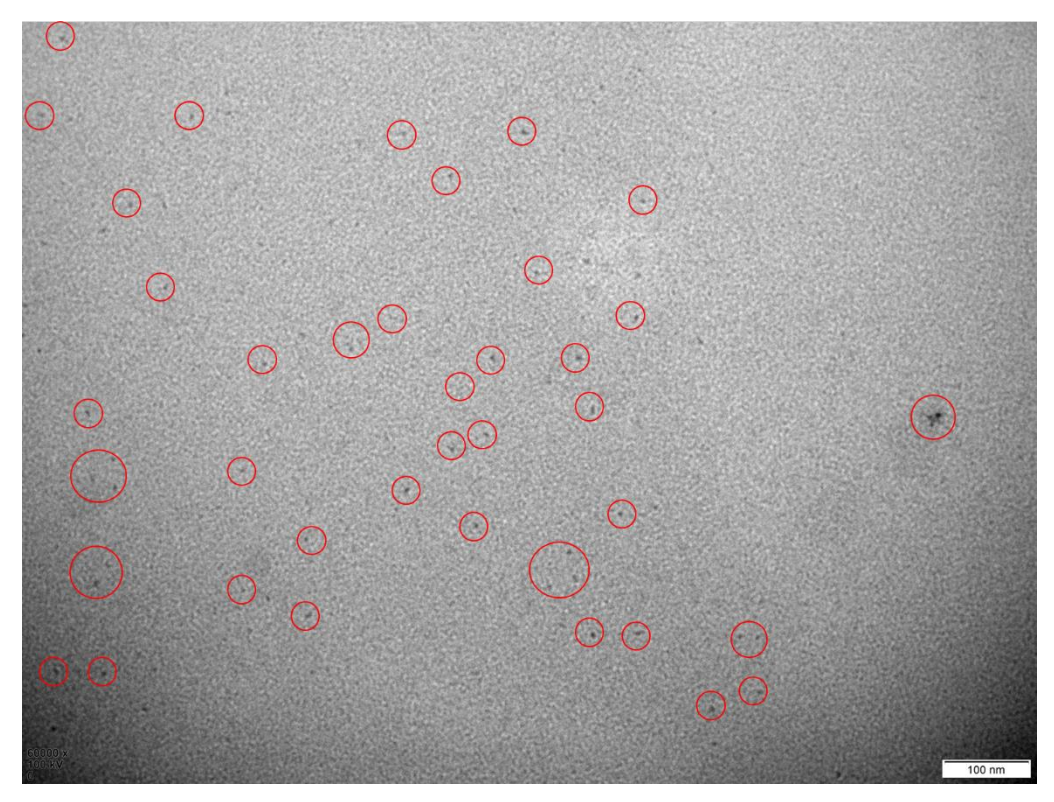


Figure 4.25 - TEM image of carbon dots (Std-Cnd-CD) synthesised from pretreated coffee grounds (Std-Cnd-PT) ($^{\sim}20^{\circ}$ C, 0.05/mL TA, 10/50 biomass ratio) - Scale Bar 100nm

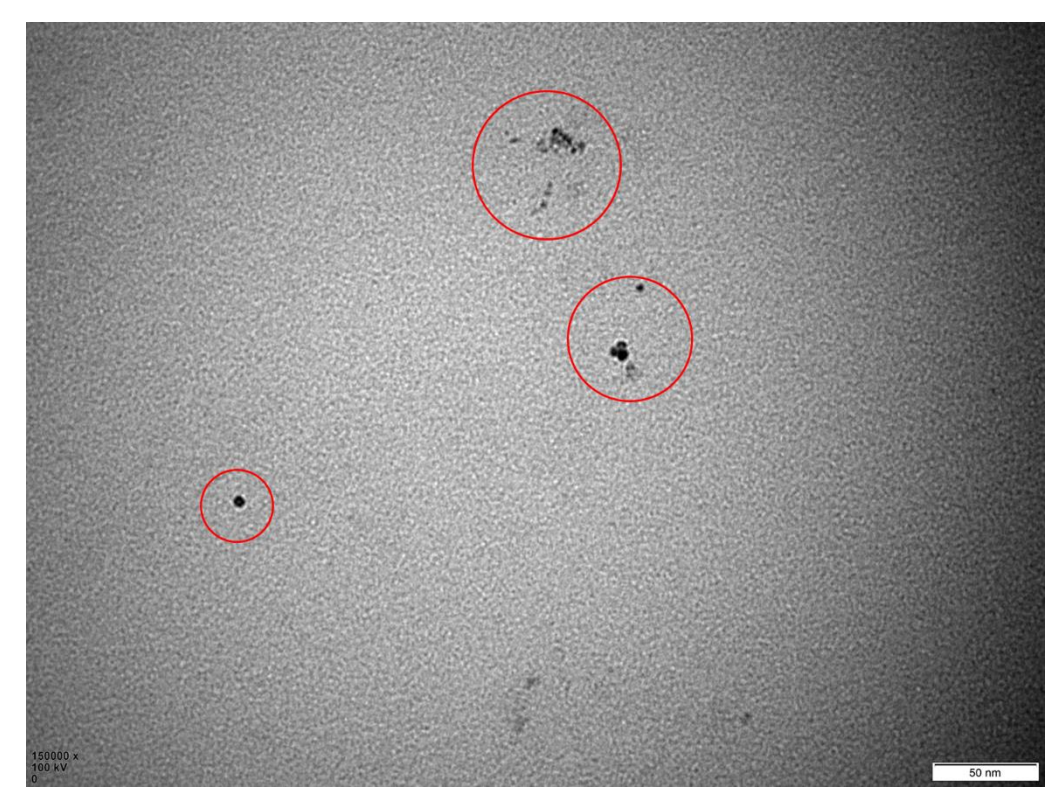


Figure 4.26 - TEM image of carbon dots (Temp-80-CD) synthesised from pretreated coffee grounds (Temp-80-PT) (80°C, 0.05g/mL TA, 10/50 biomass ratio) - Scale Bar 50nm

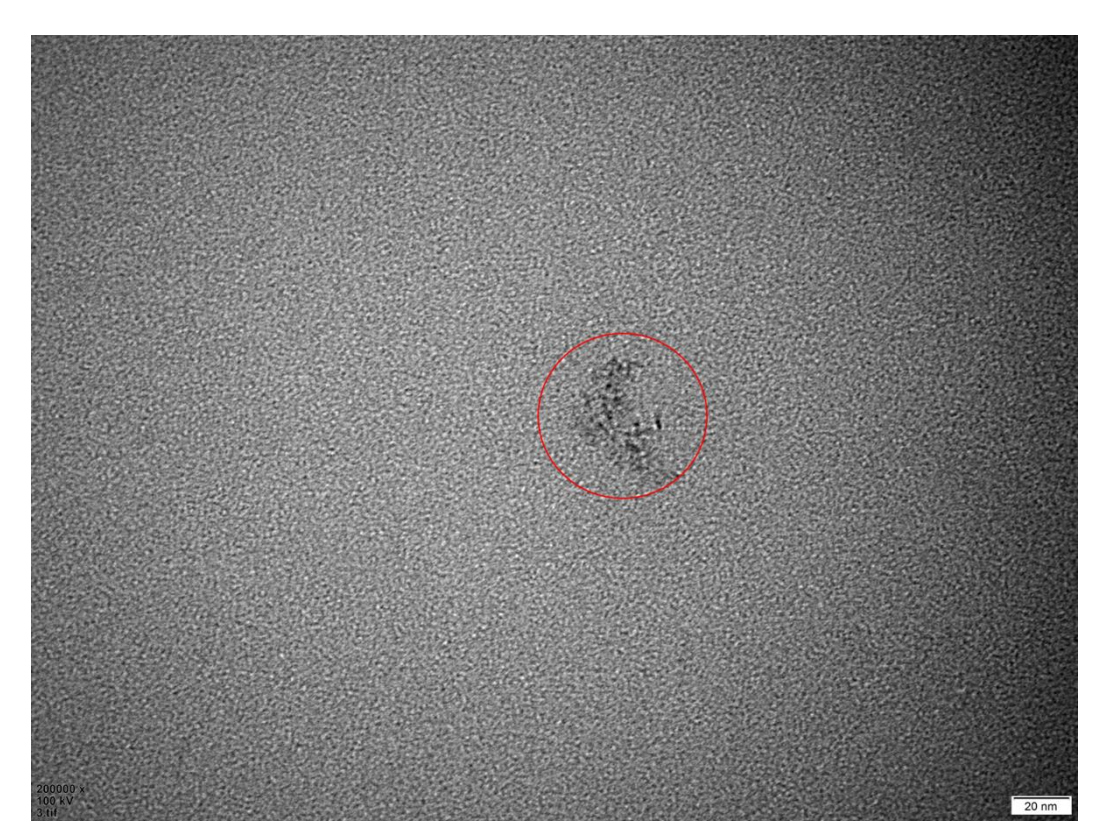


Figure 4.27 - TEM image of carbon dots (Ratio-20-CD) synthesised from precursor (Ratio-20-PT) (~20°C, 0.05/mL TA, 10/20 biomass ratio) - Scale Bar 20nm

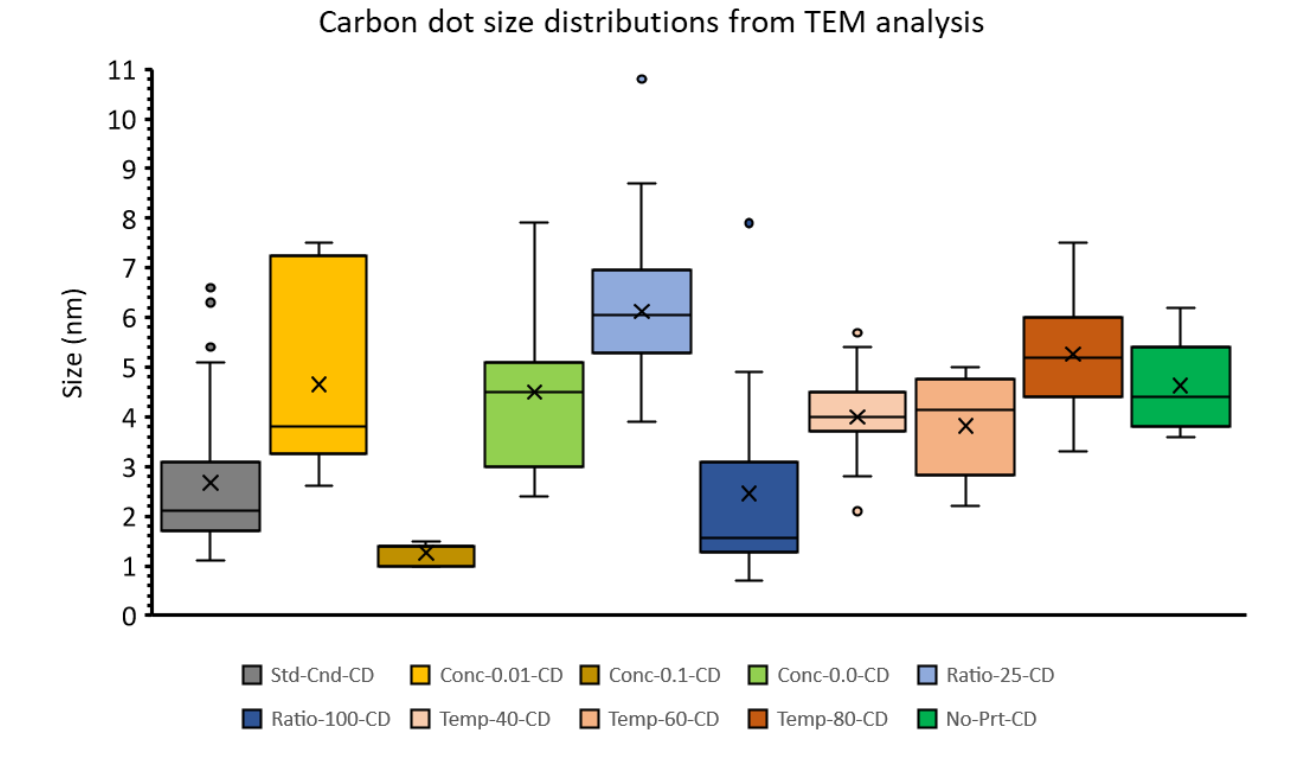


Figure 4.28 - Size distribution of carbon dots according to reaction parameters from TEM analysis with ImageJ.

Table 4.5 - Average size of carbon dots summariesd from TEM analysis

Test	Average size (nm ± STD)
Std-Cnd-CD	2.7 ± 1.4
Conc-0.01-CD	4.7 ± 1.9
Conc-0.1-CD	1.3 ± 0.2
Conc-0.0-CD	4.5 ± 1.5
Ratio-25-CD	6.1 ± 1.5
Ratio-100-CD	2.5 ± 2.2
Temp-40-CD	4 ± 0.9
Temp-60-CD	3.8 ± 1
Temp-80-CD	5.3 ±1
No-Prt-CD	4.6 ± 0.9

One-way ANOVA tests were done on the data as a whole and it was concluded that there are significant differences between the means of the different groups (F>F critical) and (P<0.05). It was shown that as temperature of the pretreatment increased, so did the size of the CDs (R² = 0.86), however there was no statistical difference between Temp 40 and Temp 60. The trend can be explained by the higher energy of the increased temperature, meaning the pretreatment was better at increasing the surface area of the SCG, leading to a more efficient HTC reaction, so more SCG can undergo hydrolysis and dehydration. This leads to a higher concentration of intermediates which can be used during the polymerisation step, thereby leading to larger CDs. Higher temperatures leading to increased sizes has been reported by Hu et al. (C. Hu et al., 2014).

The data also shows the effect that TA volume ratio has on the resulting CDs; a slight decrease in CD size with the increase in TA volume (Ratio-25-CD, Std-Cnd-CD and Ratio-100-CD) ($R^2 = 0.62$), however Std-Cnd-CD and Ratio 100 were not statistically different. This trend has been shown in literature previously that an increase in reaction volume leads to a decrease in CD size due to heterogeneous nucleation (Nammahachak et al., 2022). The concentration of TA also influenced the size of the CDs. The trend shown is that as TA concentration increased the size of the CDs decreased. ($R^2 = 0.97$) However Std-Cnd-CD and Conc-0.1-CD, and Conc-0.01-CD and Conc-0-CD were shown to not be statistically different from one another. All these trends shows that these dots are highly tuneable with reaction parameters which is great for application. The mass yield of each CD sample are presented in Table 4.6

Table 4.6 - Mass yield of carbon dots obtained after purification with dialysis and freezedrying.

Sample	percentage yield of CDs (%)
Std-Cnd-CD	0.63
Conc-0.01-CD	0.50
Conc-0.1-CD	0.91
Conc-0.0-CD	0.65
Ratio-25-CD	0.53
Ratio-100-CD	0.42
Temp-40-CD	0.61
Temp-60-CD	0.53
Temp-80-CD	0.54
NO-PRT-CD	0.26

These mass yields of <1% is lower than others reported, the values are fairly consistent across the samples and the average mass yield is 0.56%. For example, Crista et al (D. M. A. Crista et al., 2020) reported 1.96% mass yield, and Jiang et al (Jiang et al., 2014) 2%, both using SCGs as a biomass source. It is this low mass yield that has inhibited the progress of SCGs for this method, and this research has yielded similar low results. This shows that coffee grounds contain a lot of impurities and material that cannot be converted into CDs and is subsequently removed in the purification process. It noteworthy that the sample without pre-treatment exhibits the lowest mass yield of 0.26% which is 54% lower than the average mass yield. This is likely attributed to ultrasonication, which makes more glucose building blocks available for carbonisation.

The results indicate that, based on mass yield alone, there is not a large difference between using TA and water, as the sample pre-treated with water achieves the second-best mass yield, which suggests that using a TA catalyst does not improve mass yield compared to a control. However, there is evidence suggesting that a higher concentration of TA improves mass yield. Across the experiments with varying TA concentrations (Conc-0.0-CD, Conc-0.01-CD, Std-cnd-CD and Conc-0.1-CD), there is a trend that as TA concentration rises, mass yield increases ($R^2 = 0.71$), However this trend can be explained by contamination of TA that was not removed in the purification process. Together, this shows that the different parameters

tested do not have a large effect on the yield of CDs, but using an ultrasonication pretreatment does. It would be interesting to investigate the impact of a longer pretreatment on the resulting CDs and whether more of the material can be utilised after being manually broken down by ultrasonication, thereby increasing the surface area of the reactants.

The samples underwent testing at excitation wavelengths to identify the wavelength at which the maximum emission occurred. The emission was observed at approximately 335 nm, with the most intense peak occurring at an excitation of 230 nm. This pattern across most samples led to the selection of this wavelength for QY calculations.

The photoluminescence of each CD is shown in Figure 4.29. which emphasises the impact of the temperature of the pre-treatment. This can be explained by the quantum confinement effect (W. Zhang et al., 2014). As these dots were found to be in the size range of 1-6nm, they are of similar size or smaller than many other dots found through research. The wavelengths are also comparatively lower than others, with fluorescence mechanisms due to the surface activity of the dots (Sonsin et al., 2022).

It is worth highlighting that from the literature examined, the lowest excitation and emission wavelengths were seen in the only other study that used an ultrasonication pre-treatment (280nm excitation, 360nm emission, (Z. Wang et al., 2016)). These wavelengths were 50-100nm lower than those reported elsewhere that did not use a pre-treatment on the biomass source, but they were the closest to the results found in this project. This suggests that the pre-treatment process, which deagglomerate the particles and exposes a greater surface area, leads to the formation of smaller CDs. It is important to note that there is a correlation between smaller size and lower excitation/emission wavelengths.

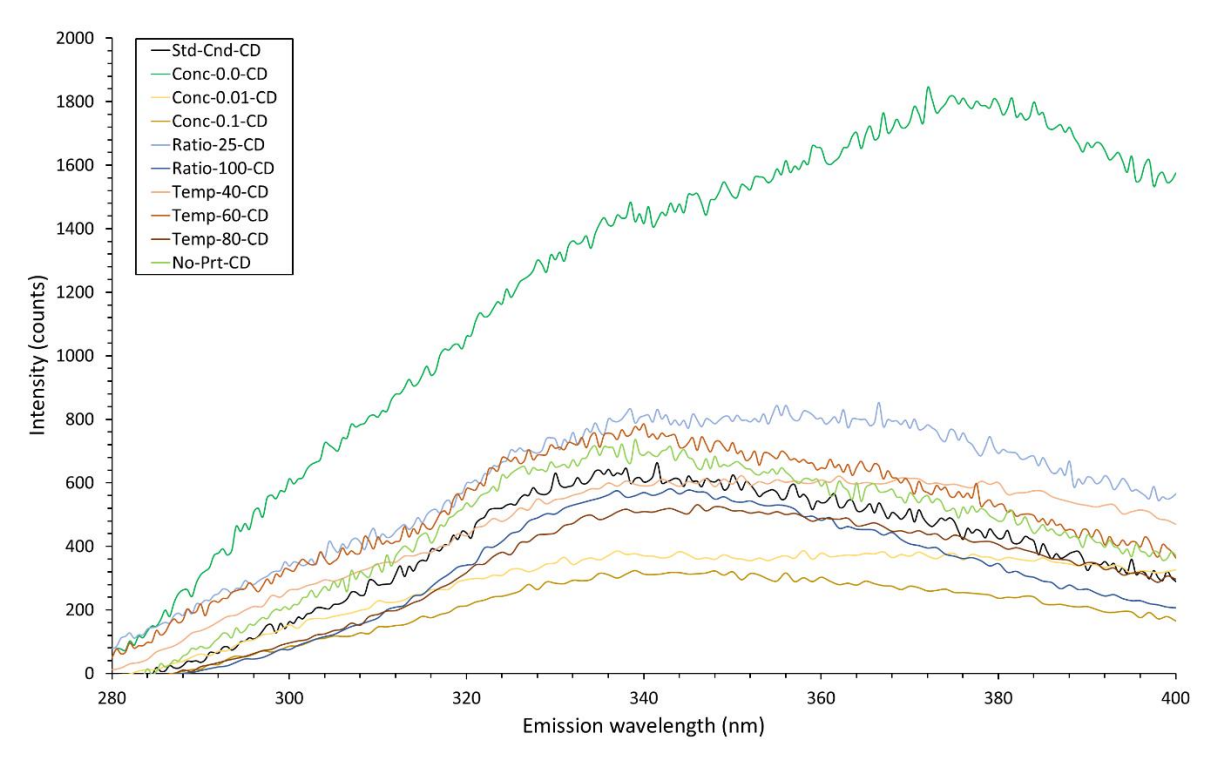


Figure 4.29 - Graph to show the photoluminescence intensity of different carbon dots at excitation 230nm.

The trend between TA concentration and QY (Table 4.7) shows that as TA concentration increases, the QY decreased. This could be explained by the size of the CDs, which follow the same trend with TA concentration. Another reason could be due to TA quenching the fluorescence in the resulting dots as the QY was taken before full purification and freeze drying. Table 4.6 shows the QY data from all samples with varying conditions of pre-treatment from this investigation.

Table 4.7 - QY data for all carbon dot samples

Sample	Quantum yield of CDs
Std-Cnd-CD	7.55
Conc-0.01-CD	7.5
Conc-0.1-CD	3.84
Conc-0.0-CD	13.1
Ratio-25-CD	13
Ratio-100-CD	6.27
Temp-40-CD	6.22
Temp-60-CD	8.43
Temp-80-CD	5.18
NO-PRT-CD	8.87

Overall, this data indicates that the method of pre-treatment which involves the highest QY is that which uses water rather than TA. This high QY indicates that TA may be inhibiting fluorescence of the dots, and that water alone may prove a better catalyst. A caveat to this is that the CDs were not fully separated from TA and as such, the QY of the CDs specifically may be higher than this. This effect has been previously utilised to make TA sensing CDs (H. Yang et al., 2019).

Concerning alternative pre-treatment conditions, the QY values (Table 4.6) align with the most intense peaks identified in FT-IR analysis (Figure 4.24) and mass yield (Table 4.5). Notably, using a smaller ratio of TA yielded higher mass yield and QY compared to higher ratios. Furthermore, heating to 60°C yielded optimal results, likely attributed to coffee grounds burning at higher temperatures and increased activity compared to lower values.

While the mass yield did not vary much based on the concentration of TA, the impact on QY is more pronounced. Lower concentrations resulted in higher QY, reinforcing the fact that just water might be the most favourable for pre-treatment.

The fluorescence can be seen visually, which can be compared with QY data. Figure 4.30 below shows photographs of each sample under UV light (365nm).

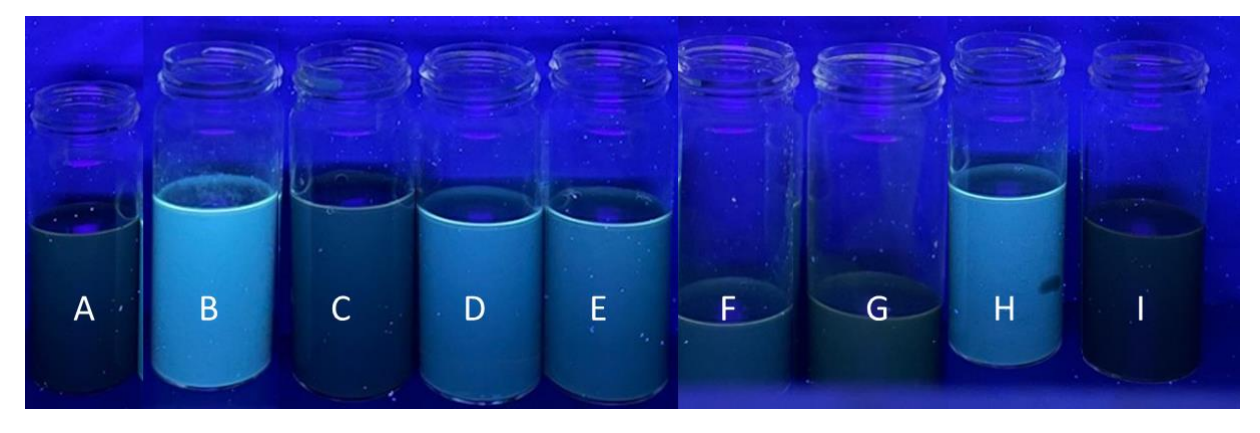


Figure 4.30 - Samples of solution of CDs with tannic acid following 90-minute ultrasonic pretreatment at varying conditions and 3 hours high temperature carbonisation at 200°C, left to right: a) No-PT-CD, b) Conc-0.0-CD, c) Std-Cnd-CD, d) Temp-40-CD, e) Temp-60-CD f) Ratio-25-CD, g) Ratio-100-CD, h) Conc-0.01-CD, i) Conc-0.1-CD.

These images support the QY data, showing the strongest photoluminescence from the sample with no TA (b). This highlights the issues with QY data before the TA is fully separated from the CDs. This can be seen most clearly with the images of the samples that were pretreated with varying TA concentrations. It is clear that increasing the TA concentration reduces the fluorescence (Figure 4.31). The only sample that was not mixed with TA is likely to have an accurate QY (13.1%). This gives further evidence to the idea that the most effective way to synthesise CDs using this method is to do so without using an acid catalyst, especially when aiming for a high QY. This approach allows for a simpler purification process and is less time-consuming.

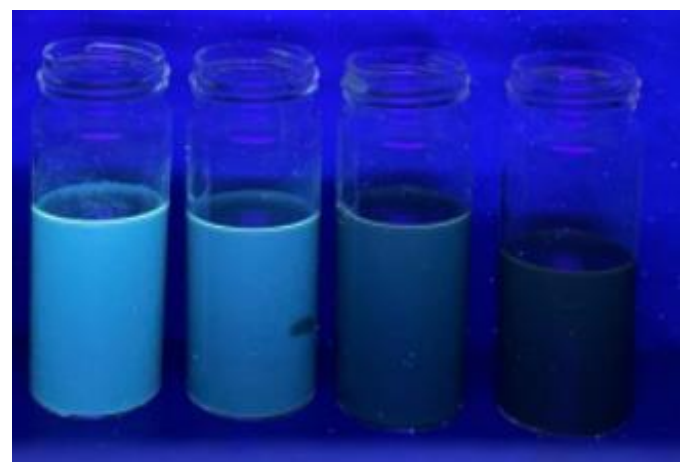
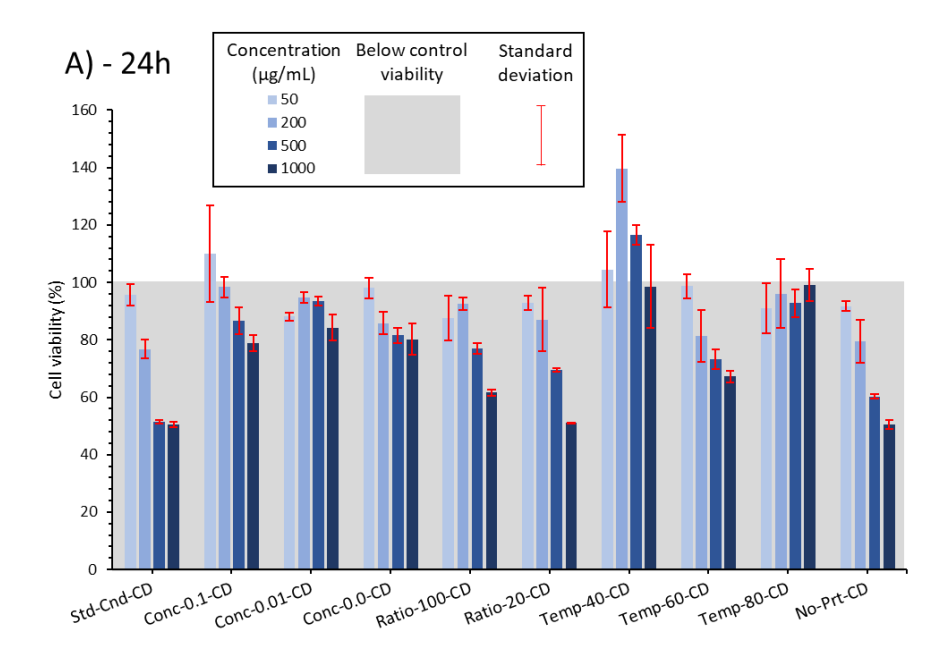


Figure 4.31 - Samples of solution of CDs with tannic acid following 90-minute ultrasonic pre-treatment without heating and 3 hours high temperature carbonisation at 200°C, with concentration of tannic acid increasing from left to right. Tannic acid concentrations: 0.00g/ml, 0.04g/mel, 0.405g/ml/send 0.1g/ml.

Biocompatibility is an important aspect of how effective CDs are for application in the field of imaging. This is one of the reasons why CDs are investigated as a replacement to SCQDs which have been shown previously to exhibit high cytotoxicity (Su et al., 2009), and can cause heavy metal leaching and slow metabolism (Wagner et al., 2019). To determine whether the CDs synthesised in this project are feasible for application cell tests were conducted. Figure 4.32 below gives cell viability data after 24 and 48-hour periods. Higher concentration has been shown to lead to greater toxicity (Lovrić et al., 2005), so different concentrations were tested to see at what level the dots become cytotoxic. Samples are normalised against cells with no treatment, which is indicated by the grey box.



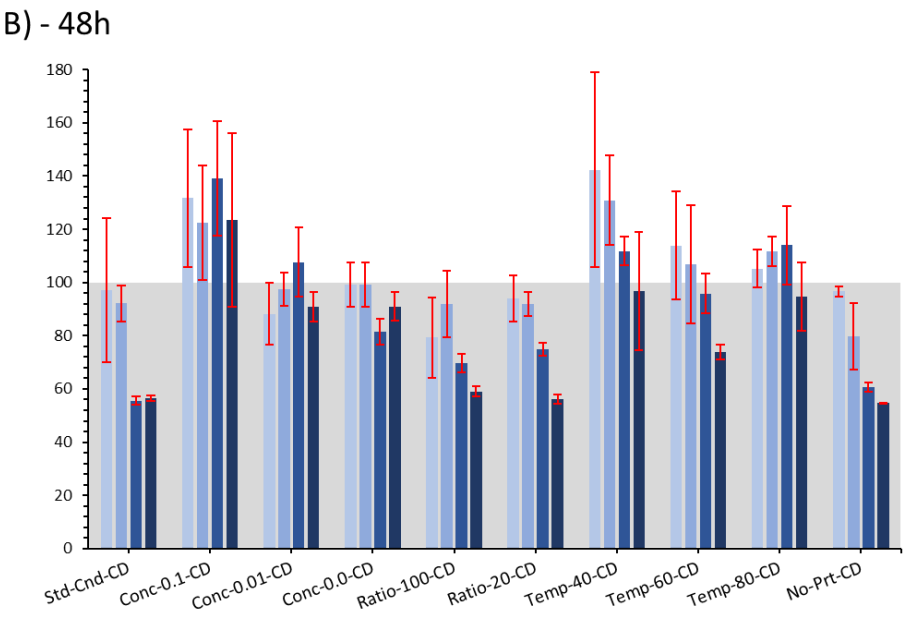


Figure 4.32 - Cell viability, given in (%), for all samples following freeze drying after 24 (A) and 48 (B) hours.

Statistical analysis was run on the data and each concentration set being compared between each sample and the control with a Bonferroni corrected P-value. The concentration of dots affects the viability of the cells. It is shown that for concentrations below 200µg/ml, all samples exhibit robust viability and can be tolerated by cells at time scales between 24 to 48 hours. Statistical analysis showed no significant differences between the samples at these concentrations and the controls. In the context of cancer screening, the dots can remain in the body for more than 48 hours, with dots previously demonstrating stability for up to 100 days (Ballou et al., 2007).

Certain samples demonstrate notably superior results compared to others. These are the samples that do not significantly negatively affect the viability of the cells at higher

concentrations; 0.0, 0.1 and 0.01g/ml TA, and 40, 60 and 80°C ultrasonication temperature. This shows there is no trend between synthesis parameters and toxicity, implying that the inclusion of TA in the synthesis does not have detrimental effects on the toxicity of dots, even though TA has a moderate level of toxicity (Ballou et al., 2007; Robles, 2005).

TA was chosen for this experiment because it is less toxic/hazardous than other catalysts such as H_2SO_4 (Z. Wang et al., 2016), NaOH (X. Zhang et al., 2018), or N_2H_4 (Xu et al., 2017). It was shown to be effective by improving the typical cell viability from 84% after 24 hours for a cadmium-based CD (Zhang et al., 2011) to 94.1% under standard conditions for this sample. The findings indicate that using SCG and TA is a better choice over SCQDs and warrants further investigation.

The sample treated with water alone demonstrated a consistently high cell viability across all conditions. Even at high concentrations, it maintains a viability of 79.1% at the maximum tested concentration of $1000\mu m/ml$. This is promising, because coupling this data with the fact that this sample also achieves the highest QY (13.1%), indicating that pre-treating SCG samples with water is promising for further testing.

4.2.3 *Summary*

The results from the analysis of this synthesis demonstrates that a ultrasonication pretreatment is effective at enhancing the optical properties, toxicity, and mass yield of CD derived from SCGs (spent coffee grounds). This improvement is attributed to the US process, which facilitates particle separation and exposes a larger surface area, thereby enhancing the interaction during hydrothermal carbonisation. The mass yield of the sample without pretreatment was the lowest of all tested, as well as it being one of the most toxic, and achieving an average QY. These results indicate the positive impact of the pre-treatment method.

4.3 Microwave assisted aqueous hydrothermal carbonisation of spent coffee grounds (synthesis 3)

This section outlines the results and discussion for the aqueous microwave HTC for the synthesis of CDs. The focus of this research was to investigate the effects of parameter changes in the HTC on the resulting CDs. The full methodology and rationale can be found in

chapter 3, section 3.14; however, it is summarised here. The synthesis started with an ultrasonic pretreatment of SCG. The resulting mixture was filtered to yield a solution containing the CDs, which was then freeze dried to yield solid CDs. The dots were analysed with FT-IR and XPS for surface analysis, UV-Vis and fluorescent spectroscopy for optical properties and TEM for size and morphology and cell tests for toxicology.

4.3.1 Properties of carbon dots and the effect of temperature and retention time

FT-IR was utilised to survey the surface chemistry of the CDs and the results were analysed against the Merek FT-IR database (Merek, 2023). Figure 4.33 contains the FT-IR spectra for the CDs and compares them. Each spectrum was individually compared, in scale with transmittance values, to the FT-IR of raw coffee grounds as presented previously in Figure 4.1

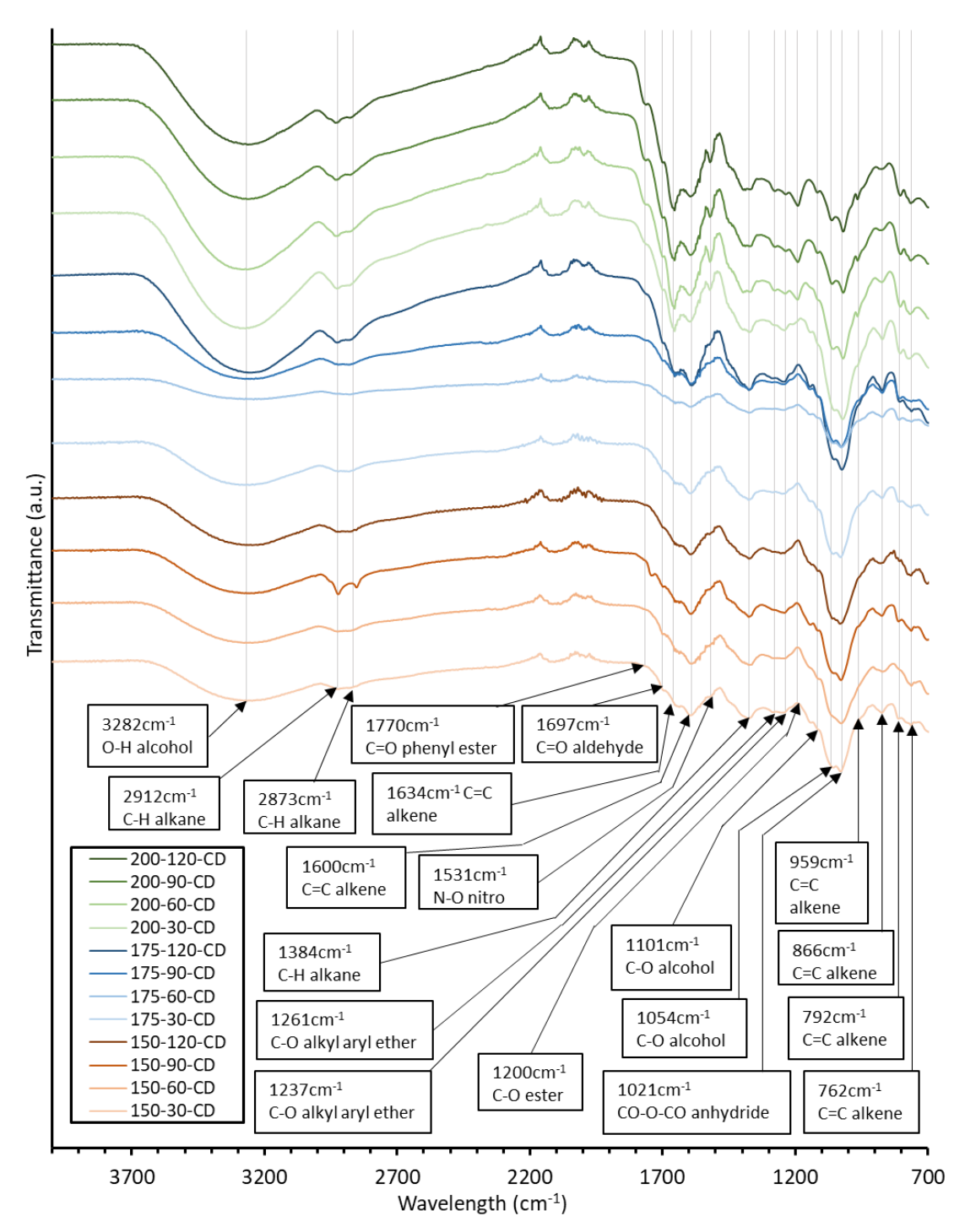


Figure 4.33 - Comparison of the FT-IR of microwave carbon dots synthesised at different temperature (150-200°C) and retention times (30-120 mins)

The CDs especially show a decrease in alkane groups which suggests a reduction of aliphatic surface groups (Tungare et al., 2020) when compared to spent coffee grounds intensity (Figure 4.1). There is also an increase in intensity for alcohol groups with peaks 1100 and 1059cm⁻¹ showing that alcohol groups have been introduced to the surface (Alarfaj et al., 2018; Andrade et al., 2017; Kurdekar et al., 2016). For the 150°C temperature tests, increased retention time slightly increases the intensity of the spectra in the resulting dots. For the 175°C, this effect is

very pronounced, and this leads to the assumption that there is a greater number of functional groups on the CD surface that are introduced with longer retention time. For the 200°C tests increased retention time does not further increase the temperature, leading to the assumption that increased time does not improve functional group expression at this temperature. The 200°C tests also peak that are not expressed in the other spectra, 1770cm⁻¹ and 1200cm⁻¹ which corresponds to a C=O phenyl ester and C-O ester.

XPS of the CDs (Table 4.8) were analysed against Thermofisher materials science learning centre database (Thermofisher, 2023) and compared against the XPS of SCG as perviously outlined in this chapter. Examples of peak fitting in the wide survey scan and C 1s from sample 150-120-CD are provided in Figure 4.34 and Figure 4.35 respectively. (O 1s – Figure A.6.9, N 1s - Figure A.6.10)

Table 4.8 - Outline of all XPS results from each carbon dot sample obtained after HTC.

Scan								At %						
Scall		Survey				С	1 s			N	1s		O 1s	
Element/Bond	Carbon	Nitrogen	Oxygen	sp2/C=C	sp3/C-C	C-O	C=O	pi-pi sat	plas loss	C-NH2	NO3	C=O	C-O	Na KLL Auger
Binding energy (eV)	284.6	399	531.86	284.01	284.85	285.44	286.9	291.45	294.96	399.13	405.64	531.72	532.96	534.95
Sample														
150-30-CD	40.69	3.72	55.59	41.92	17.96	22.34	14.77	1.88	1.14	100	0	69.47	24.91	5.61
150-60-CD	38.7	2.9	58.4	49.64	1.52	26.84	18.48	2.26	1.25	96.63	3.37	95.27	4.73	0
150-90-CD	51.35	2.18	46.46	40.13	0	46.99	12.81	0	0.06	100	0	92.78	7.22	0
150-120-CD	39.38	2.91	57.71	48.01	1.98	30.39	19.04	0.35	0.22	100	0	99.93	0	0.07
175-30-CD	45.52	4.99	49.49	60.67	0	24.03	14.69	0.42	0.19	95.92	4.08	100	0	0
175-60-CD	32.39	3.16	64.45	30.79	2.74	18.53	43.98	3.41	0.54	83.49	16.51	64.09	12.29	23.62
175-90-CD	64.26	1.12	34.62	83.34	2.43	10.47	4.76	0	0	100	0	100	0	0
175-120-CD	39.68	5.79	54.53	60.04	2.52	16.07	21.21	0.15	0	100	0	81.35	10.5	8.15
200-30-CD	46.78	5.54	47.68	70.36	0.99	14.89	13.75	0	0	100	0	100	0	0
200-60-CD	49.24	5.07	45.69	46.83	1.24	13.93	38	0	0	100	0	62.41	34.95	2.64
200-90-CD	45.59	4.72	49.7	78.86	13.07	3.17	4.9	0	0	100	0	98.43	1.57	0
200-120-CD	45.33	5.8	48.87	34.07	31.17	22.22	12.05	0.41	0.08	100	0	47.91	51.92	0.17

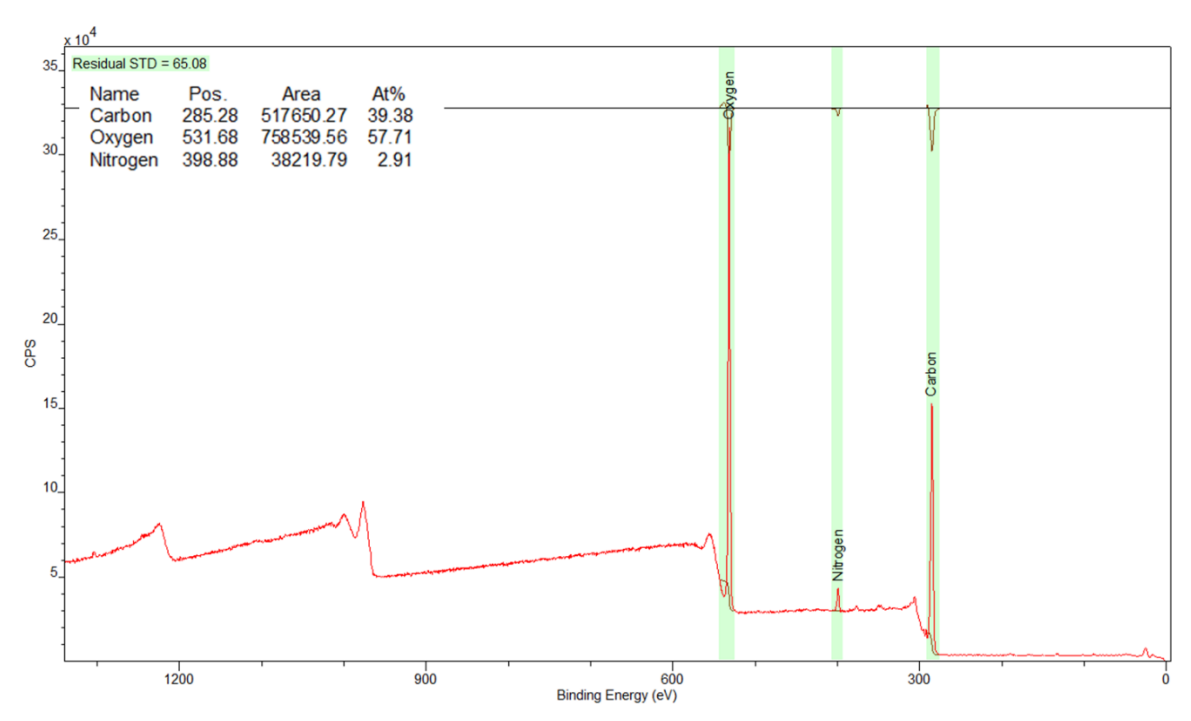


Figure 4.34 - XPS wide surface scan of carbon dots synthesised at 150°C and 120 minutes (150-120-CD)

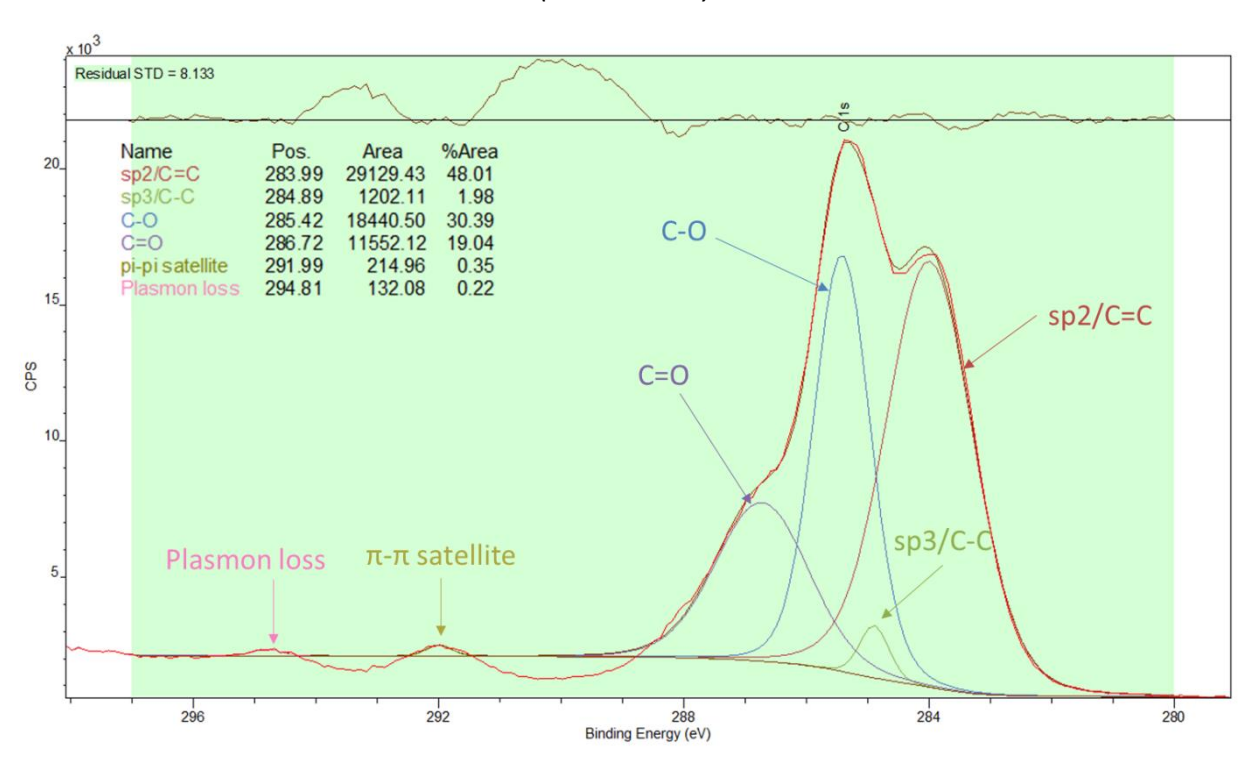


Figure 4.35 - XPS C 1s scan of carbon dots synthesised at 150°C and 120 minutes (150-120-CD)

The XPS elemental scan shows a high ratio of oxygen (average of ~51%) compared to the ~26% of SCG, suggesting a significant presence of oxygen containing functional groups. This is also corrobated by the C 1s and O 1s scans the high percentage of C-O and C=O bonds represent. This is consistant with other works (Hao et al., 2023; Long et al., 2022).

There is a disconnect between the C=O and C-O bond ratio between the C1 and O1 scans. On average, the ratio of the C=O/C-O in the C1 scan is 0.87 and 6.83 in the O1 scan. This makes it very difficult to confirm the true make up of the oxygen groups on the CD surface. The FT-IR suggests that C=O and C-O groups are expressed and the XPS scans confirms this. There are also no trends in the C=O/C-O either the FT-IR or the XPS to suggest any effects the synthesis parameters may have on the structure of these CDs.

The C 1s spectra shows that sp^2 carbons makes up a proportion of the material which suggests a graphitic structure as shown in previous works (Long et al., 2022). This is further suggested by the π - π * satellite peak and plasmon loss peaks which are found in graphitic structures (Thermofisher, 2023).

The FT-IR spectra of the 175°C tests (Figure 4.33) showed increased intensity with longer retention time, and this higher intensity was maintained in the 200°C tests. This sugested that functional groups were expressed in a higher number as retention time increased in the 175°C tests The increased time allows for more groups to be introduced. The temperature of 200°C introduces more energy allowing this reaction to occur faster, to the point where increased reaction time does not increase the number of these groups. There is no trend in any of the XPS scans to corroborate this.

 ζ -potential analysis was conducted to analyse the surface change of the CDs. Figure 4.36 outlines the results of the testing.

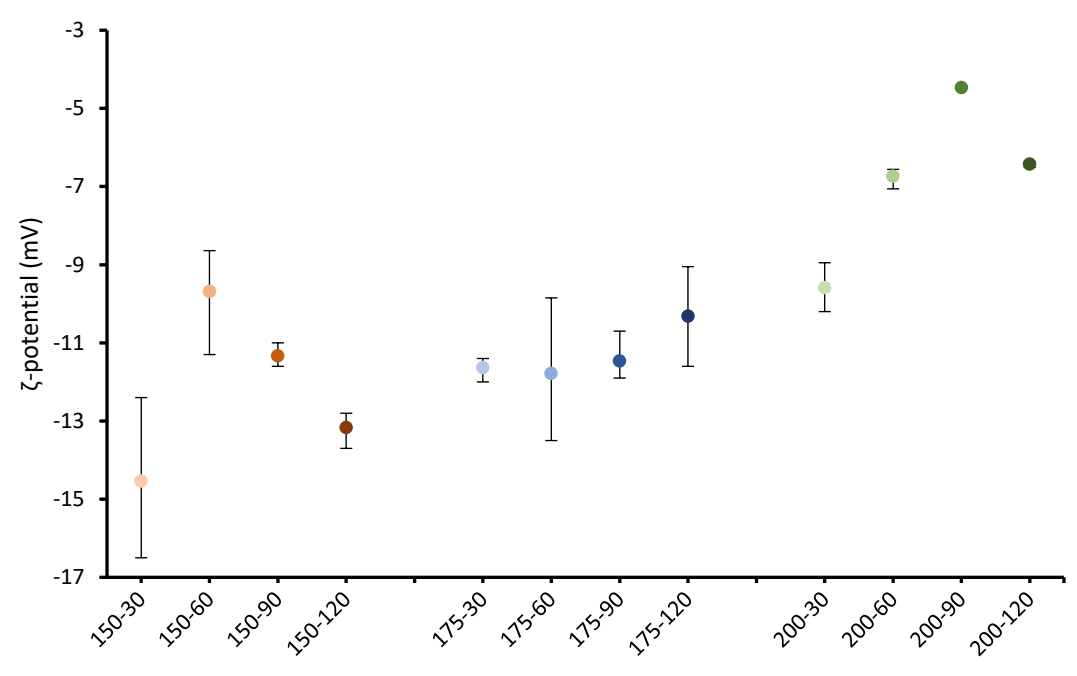


Figure 4.36 - Comparison of the ζ -potential of microwave carbon dot samples synthesised at different reaction temperatures (150-200°C) and time (30-120 mins).

All the dots had a negative surface charge; this indicates that the surface of the CDs contains carboxylic acid functional groups due its highly negative charge. The changes in ζ-potential can be explained by a reduction in the ratio between the carboxylic acid group and other neutral groups such as alcohols, anhydrides, aldehydes and esters (Byrd & Hildreth, 2001; Struyf, 2009). The FT-IR of the CDs produced at 200°C showed a peak indicating the presence of esters. This suggests that an increase in reaction temperature leads to an esterification of some of these carboxyl groups leading to an increase in the surface charge. This has been shown previously by Ding et al (Ding et al., 2012). The graph also shows that increased retention time at 200°C (200-30, 200-60, 200-90, 200-120) leads to an increase in esterification and a further decrease in charge. For esterification to fully explain the results shown in the graph however, more evidence would be needed. This could potentially be done in future research with potentiometric titration. In this technique the electrochemical potential of the analyte solution is measured in the form of pH and a pH titration curve is determined with the addition of acids or bases. The amount of protonable/deprotonable functional groups of the analysed sample is determined from the equivalence point of the titration curve (Charron et al., 2012; Fedin & Talapin, 2014; Geißler et al., 2021).

The negative surface charge and the related surface chemistry is also good for application as this gives the CDs a good platform for surface functionality. A higher negativity also increases stability of the NPs and their propensity to repel one another leads to a resistance to aggregation (Pandey et al., 2020). This trend shows how tuning the reaction time and temperature can select dots with a specific surface potential, which can be useful for surface functionalisation for example, applications in the LBL process like the further experimentation in this project.

The optical properties of the CDs were analysed using UV-Vis and Photoluminescence spectroscopy. The UV-Vis showed an average absorbance wavelength of 288nm +/- 3.8. This narrow range of absorbances shows that absorbance is not affected by changes in synthesis parameters. As with the other dots synthesised above, this absorbance can be attributed to the π - π * transition of the aromatic sp² domains and the n- π * transition of the C=O bonds (Jeong et al., 2023; Yang et al., 2014; X. Zhang et al., 2018).

Figure 4.37, Figure 4.38, Figure 4.39 and Figure 4.40, coupled with Table 4.9, show the photoluminescence data of the CDs which outlines the effect that excitation wavelengths, between 250-370nm, have on the emission of fluorescence of the CDs.

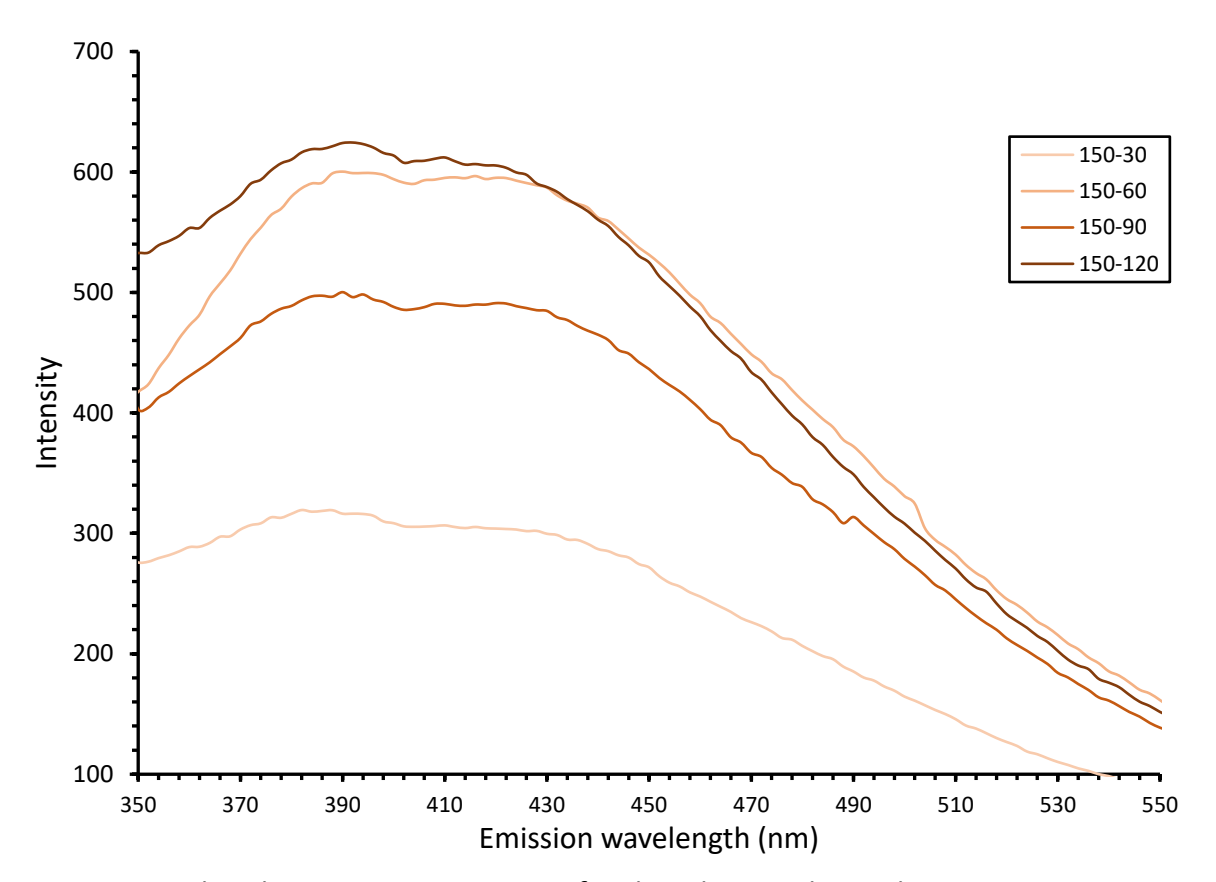


Figure 4.37 - Photoluminescence intensity of carbon dots synthesised at 150°C at excitation wavelength 300nm

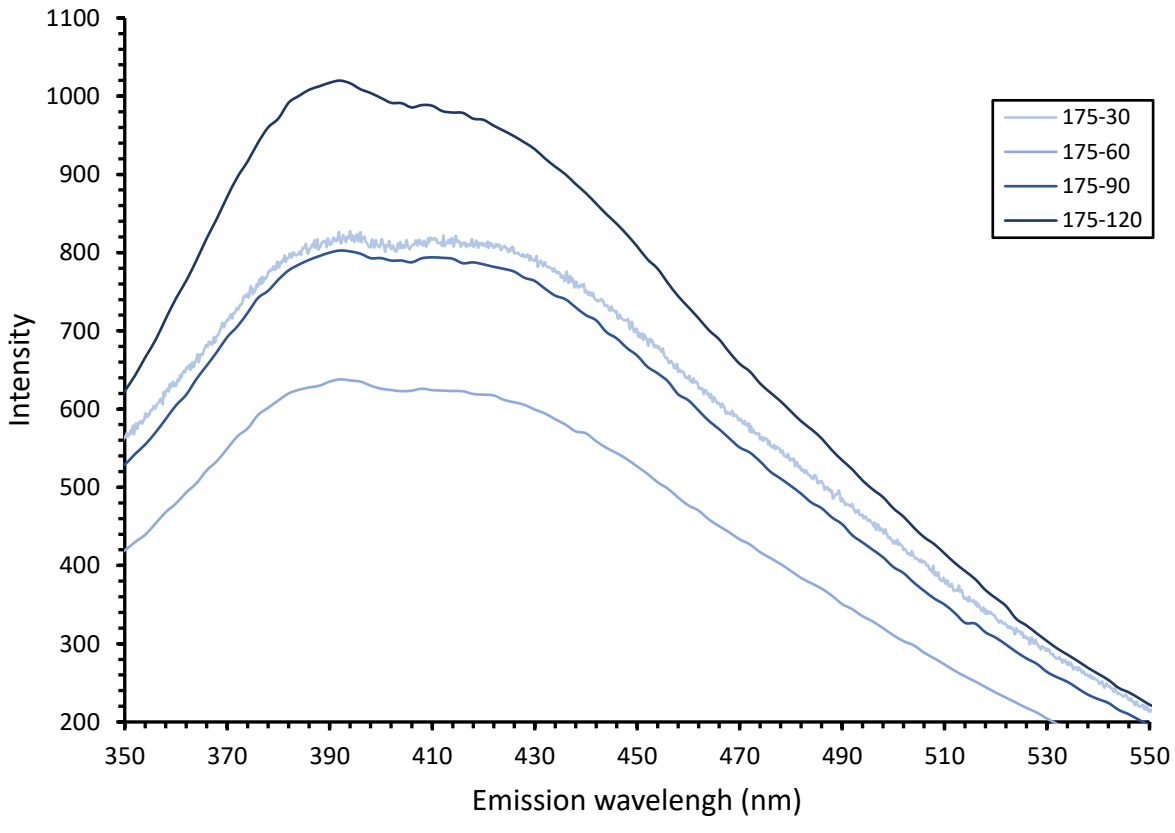


Figure 4.38 - Photoluminescence intensity of carbon dots synthesised at 175°C at excitation wavelength 300nm

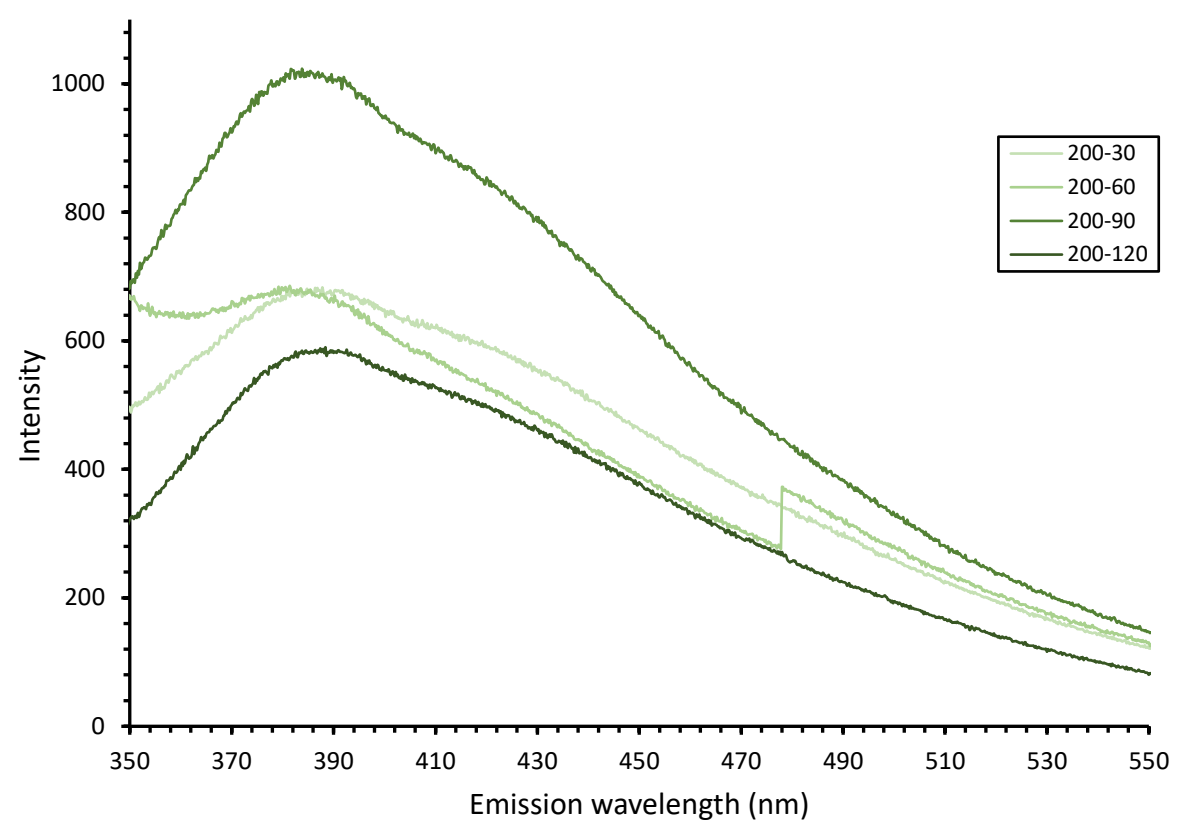


Figure 4.39 - Photoluminescence intensity of carbon dots synthesised at 200 °C at excitation wavelength 300nm.

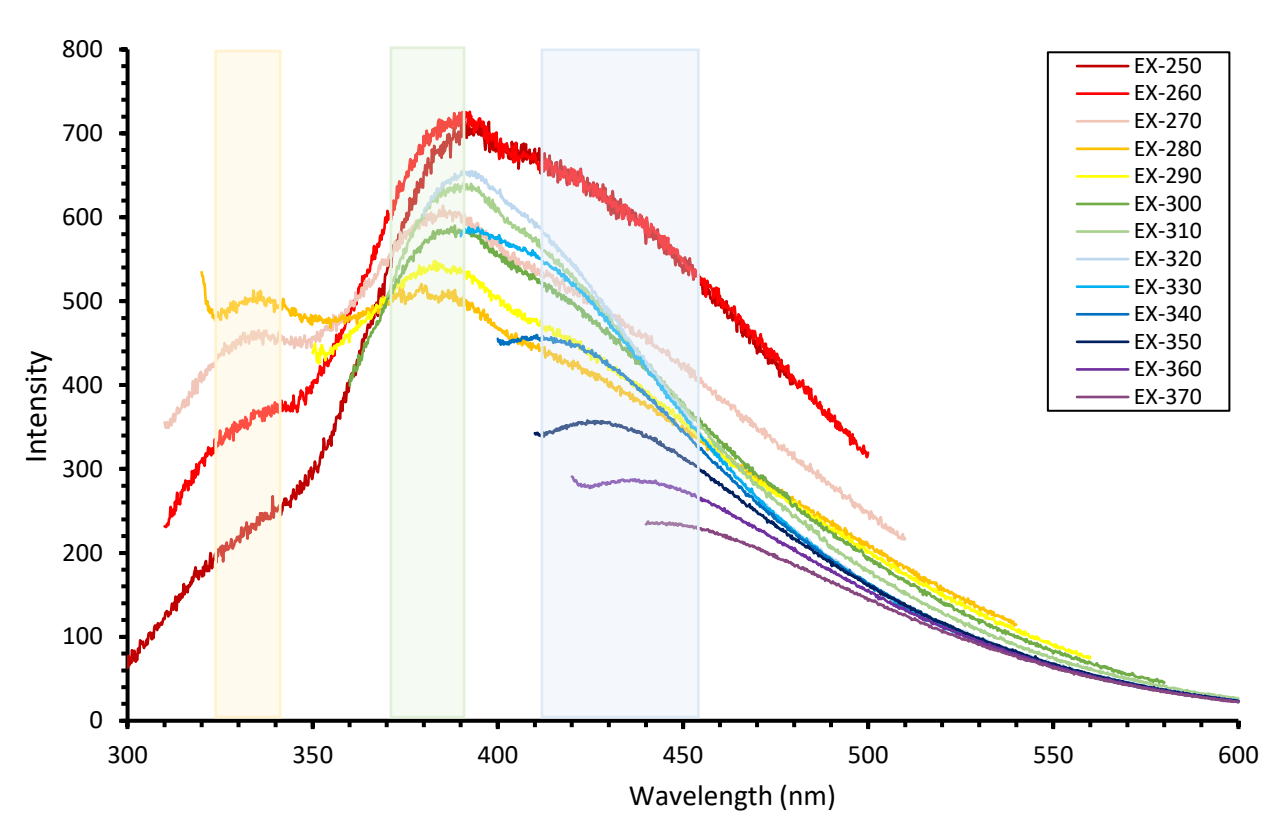


Figure 4.40 - Photoluminescence emission spectra of the dots synthesised at 200-120 at increasing levels of excitation.

Table 4.9 - The emission wavelengths and corresponding intensity (WL - I) at various excitation wavelengths for each carbon dot reaction parameter tested.

	Sample											
	150				175				200			
Excitation	30	60	90	120	30	60	90	120	30	60	90	120
wavelength	WL - I	WL - I	WL - I	WL - I	WL - I	WL - I	WL - I	WL - I	WL - I	WL - I	WL - I	WL - I
EX-250	320 – 376	342 – 454	336 – 532	338 – 879	378 – 613	344 – 448	344 – 614	338 – 597	309 – 609		340 - 337	339 - 268
		398 -710	394 - 607	394 - 819	396 - 907	398 - 733	398 - 913	396 - 1161	395 - 714	387 – 438	392 - 964	390 - 719
	440 - 406	432 - 787	434 - 662	432 - 845	429 - 1021	434 - 804	432 - 982	420 - 1203	417 - 710	428 - 480	411 - 955	408 – 687
EX-260	316 – 652	334 – 715	328 – 879	332 – 1528	333 – 921	336 – 673	336 – 909	336 – 926	312 – 968		341 - 548	340 -377
		390 - 706			392 - 869	394 - 700	382 - 892	392 - 1136	390 – 734	382 - 565	390 - 1060	392 - 725
	442 – 419	440 - 826	442 - 702	442 - 841	444 - 1035	438 - 803	438 – 1011	434 - 1265	422 - 716	419 - 539	401 - 1027	420 - 671
EX-270	324 – 808	332 – 1008	324 – 1213	328 – 2019	320 – 1182	330 – 918	326 – 1158	336 – 1229	315 – 922		341 – 734	336 - 462
								376 - 1017	379 – 654	378 - 611	386 - 969	385 - 614
	434 - 337	444 - 674	434 - 562	426 - 657	436.6 - 845	436 - 645	436 - 817	430 - 1014	424 – 568	410 - 513	412 - 875	410 – 544
EX-280	330 – 779	332 – 1086	330 – 1201	330 – 2007	330 – 1266	330 – 973	330 – 1205	332 – 1343	336 – 80		344 - 834	336 - 512
										375 – 616	376 – 876	380 – 520
	426 - 294	426 - 575	426 - 480	426 - 584	425 - 748	426 - 568	424 - 721	424 - 883			410 - 750	
EX-290								342 – 1003				
		376 – 663			380 - 838	374 - 662	380 - 816	380 - 998	374 – 683		379 – 952	383 - 548
	426 - 293	426 - 579	424 - 477	424 - 601	421 - 776	424 - 587	420 - 755	418 - 916	424 - 546	375 - 669	411 - 815	410 - 474
EX-300	386 - 318	388 - 599	390 - 500	394 - 623	394 - 827	394 – 394	394 - 801	392 - 1020	387 – 678		384 - 1024	388 - 590
	408 – 312	416 - 597	420 - 491	410 - 612	412 - 822	408 - 626	410 - 794	412 - 981	425 - 575	381 - 688	413 - 883	412 - 522
EX-310	394 – 313	394 - 605	392 - 501	396 - 620	394 - 828	396 - 654	396- 820	396 - 1053	392 – 702	387 – 639	386 - 1090	391 - 641
	410 - 307	410 - 608	410 - 505	410 - 618	413 - 830	410 - 653	410 - 820	408 - 1031	425 – 594	407 - 576	410 - 960	412 – 566
EX-320			394 - 492	394 - 610	397 - 821	396 - 658	398 - 809	394 - 1053	394 – 697	392 – 604	392 - 1071	392 – 652
	410 - 324	410 - 324	416 - 508	410 - 625	413 - 842	410 - 666	408 - 815	408 - 1051	408 - 660	409 - 554	410 - 965	409 - 595
EX-330									395 – 628	394 – 525	394 – 929	393 – 584
	416 - 316	416 - 316	420 - 507	414 - 606	419 - 830	416 - 665	418 - 796	410 - 1022	410 - 620	406 - 521	408 - 889	411 - 554
EX-340	428 - 292	428 - 292	426 - 485	422 - 565	426 - 774	426 - 615	422 - 740	420 - 948	417 - 531	417 - 433	410 - 728	410 - 459
EX-350	434 - 265	432 – 496	434 – 441	434 - 505	431 - 699	430 - 550	432 - 653	430 - 836	429 - 430	428 - 350	423 - 566	424 - 358
EX-360	442 - 226	442 - 428	440 - 388	442 - 433	440 - 620	436 - 470	440 - 569	438 - 719	438 - 362	437 - 290	434 - 466	437 - 287
EX-370	444 - 193	444 - 364	444 - 333	448 - 372	444 – 522	444 - 398	442 - 482	444 - 613	445 - 309	447 - 243	443 - 389	441 - 237

Table 4.9 shows the data gathered from the dots synthesised at 200°C with a 2-hour retention time. The graph is typical of all the samples showing photoluminescence curves with up to three peaks within ranges indicated by the coloured regions.

- The first orange region indicates emission peaks that are between 309-342nm. These
 peaks indicate fluorescence from excitation wavelengths between 250-290nm with
 increase in intensity with increasing excitation wavelength.
- The second green region indicates emission peaks that are between 376-398nm. These
 peaks indicate fluorescence from excitation wavelengths between 250-330nm with a
 slight decrease in intensity as the excitation wavelength increases.
- The third blue region indicates emission peaks that are between 401-448nm. These
 peaks indicate fluorescence from excitation wavelengths between 250-330nm with a
 decrease in intensity as the excitation wavelength increases.

This information shows that these dots have three emission maxima for the photoluminescence which are not moved significantly by excitation wavelength. Variation in emission wavelength with variation in excitation wavelength can explained by the dots having a wide size distribution (up to \pm 12nm from the average size) and variation in surface properties indicated by the inverse of the findings outlined by various works (Liu et al., 2014; Nie et al., 2020; Y. Xie et al., 2019). This could indicate why 200-60-CD only shows two emission maxima: it has narrower size distribution as outlined by the TEM.

A particular emission wavelength can be selected for by using a corresponding excitation wavelength. This means that these dots can be used in the best way to fit a particular application. It has been reported that blue fluorescence originates from the presence of surface defect states (sites with non-perfect sp² domains) by forming a series of surface state emissive traps (Mahto et al., 2023; Zhu et al., 2015). There are no trends between emission wavelength and synthesis parameters, but it is typical of dots made from this feedstock material (Costa et al., 2022; Jeong et al., 2023; Jiang et al., 2014; X. Zhang et al., 2018).

Photos of photoluminescence (Figure 4.41) when lit by UV lamp (365nm) the CDs glow blue.

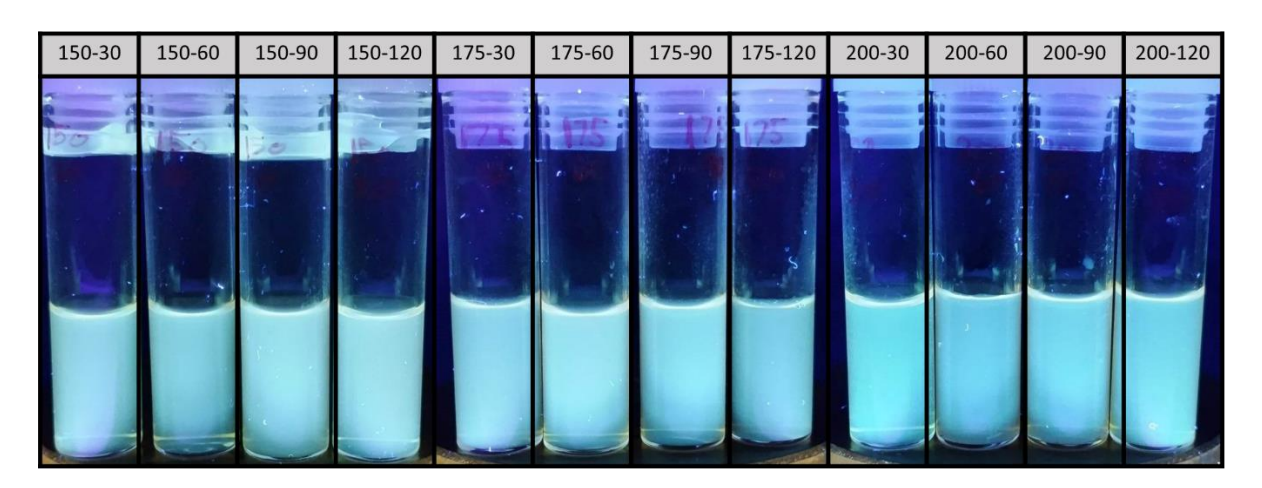


Figure 4.41 - Photos of carbon dot solutions showing photoluminescence under a UV lamp.

Table 4.10 - Table to outline the Quantum yield against the reaction parameters.

Sample	QY (%)
150-30-CD	5.5
150-60-CD	7
150-90-CD	4.8
150-120-CD	7.2
175-30-CD	9.6
175-60-CD	6
175-90-CD	8.1
175-120-CD	11.6
200-30-CD	8.4
200-60-CD	7.2
200-90-CD	11.9
200-120-CD	7

The QYs of the CDs are outlined in Table 4.10 above. The averages QY of these dots is 7.9 with a range of 4.8 to 11.9. This is a moderate QY in comparison to literature as shown in the syntheses above. There is no trend between the QY and retention time. however, the dots synthesised at 150°C have an average QY (6.1) ~30% lower than the dots synthesised at 175°C (average QY = 8.8) and 200°C (average QY = 8.6). This shows that for an optimum QY the reaction temperature needs to be above 175°C. This indicates that QY is linked to the carbonisation of the biomass. It has been shown in literature that carbonisation occurs from ~180°C and above (Zhai et al., 2017). This suggests that the minimum temperature for carbonisation is required to produce CDs with higher QY. This has been shown previously with CDs synthesised at a range of temperatures from citric acid. Zhang et al. (Zhang et al., 2016) used temperatures between 120 and 220°C and found that QY increased from 8.03% at 120°C to 35.4% at 180°C. Temperature increases after this then showed a decrease in QY. They found

that the QY was directly tied to fluorescent polymer chain of the surface of the CD the presence of which is tied to reaction temperature.

TEM was used to visualise the CDs. The images were used to conduct size analysis using ImageJ, Figure 4.42 provides examples of the images gathered and Figure 4.43 outlines the size distributions obtained from the analysis.

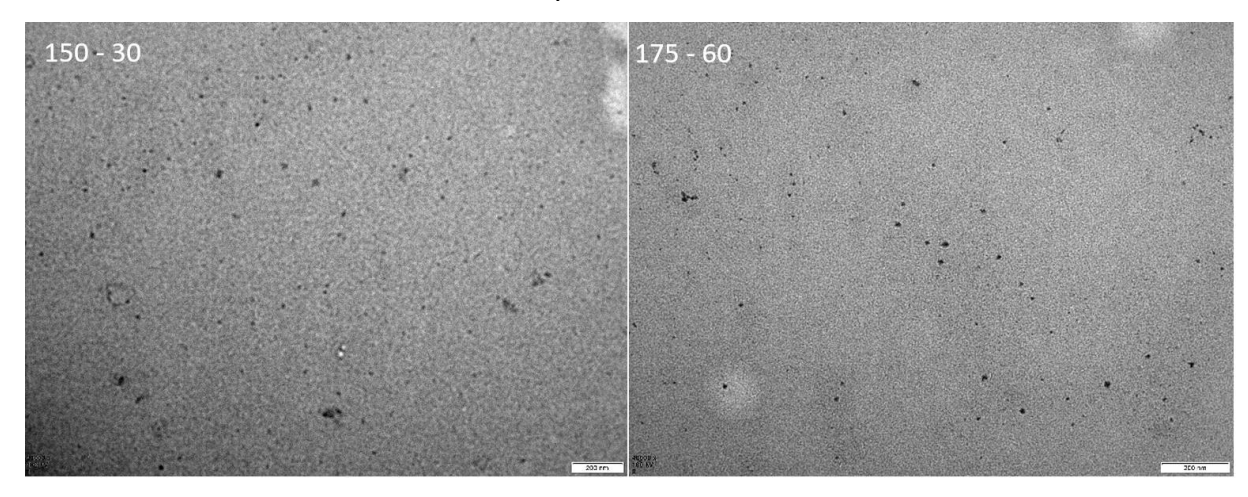


Figure 4.42 - TEM image of the carbon dots 150-30, right: TEM images of the carbon dots 175-60

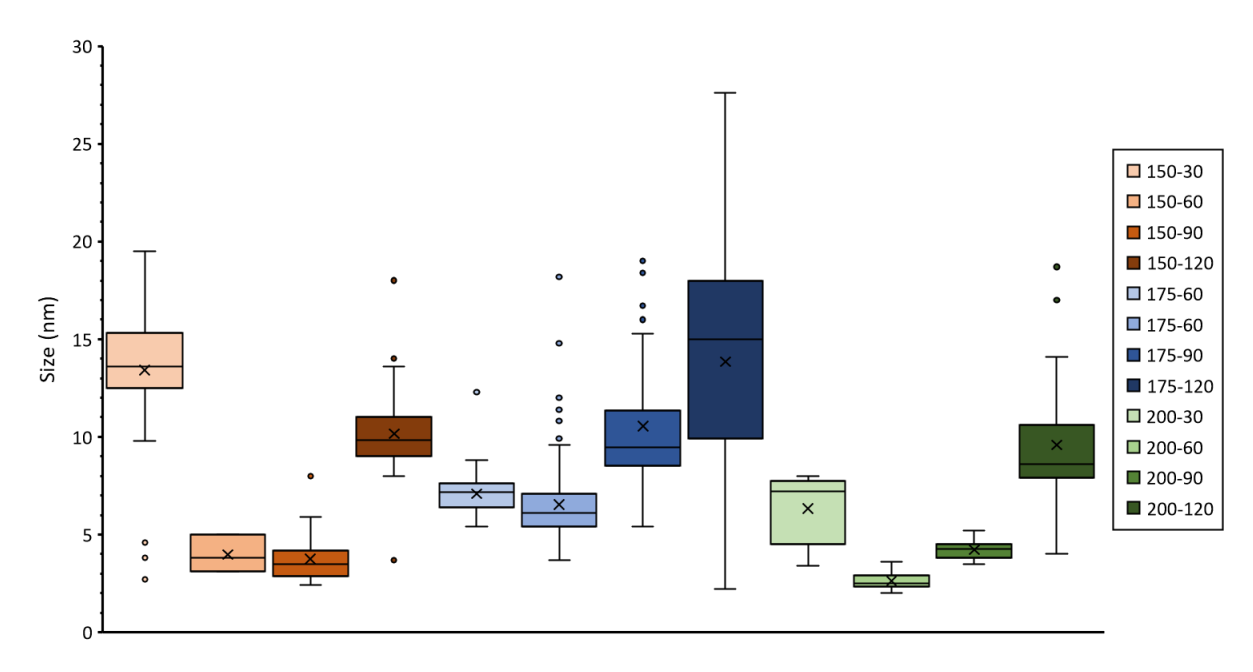


Figure 4.43 - Graph to show the relationship between carbon dot size and reaction parameters.

The graph shows that temperature is not responsible for the differences in the sizes as there is very little trend. Size is clearly determined by reaction retention time; this is shown that as retention time increases the size of the dots initially decreases with the 60- and 90-minute

reactions and then increases again with the longest retention time of 120 minutes. The literature is conflicted on the effect of synthesis parameters on the size of CDs. Hu et al. reported the increase in HTC temperature increases size (C. Hu et al., 2014). Quaid et al. (Quaid et al., 2022) reported the opposite, saying that reaction temperature had only a slight effect on size, but decreased with increase temperature. It has also been reported that a longer retention time increases CD size (Zhang et al., 2012). A study (Zhang et al., 2016) that included lower reaction temperatures similar to this one also found a fluctuation in size relative to reaction temperature consistent with the findings of this experiment "The overall size of NCDs shows a fluctuation of increase (140–160 °C), decrease (160–180 °C) and increase (180–220 °C) as the reaction temperature increases". The team attributed this phenomenon to aggregation.

An alternate explanation, based on the mechanism of HTC (Maniscalco et al., 2020), could be that the initial increase in time allowed for increased break down of the coffee grounds during the hydrolysis stage of the HTC. This allows for greater amount of smaller building blocks for optimum formation of smaller CDs. Increasing the retention further allows more intramolecular condensation to occur increasing the size of CDs. This shows that the size of the CDs can be tuned by manipulating the synthesis parameters for application; for example, nanoparticle size can be optimised to maximise cellular uptake which is beneficial for applications such as bioimaging (Hoshyar et al., 2016). To confirm this, further investigation with analysis of samples to taken at shorter time intervals would be required.

There is no trend between the size of the CDs and the QY of the dot. This shows that the intensity of the photoluminescence is not size-dependent and is most likely due to the structure and surface chemistry of the dots as indicated above.

HRTEM was used to visualise the lattice spacing of the CDs that were reacted at 200°C. Figure 4.44 provides an example of the lattice spacing within the CDs and shows the lattice spacing sizes for each sample in a box plot to analyse the effect of time.

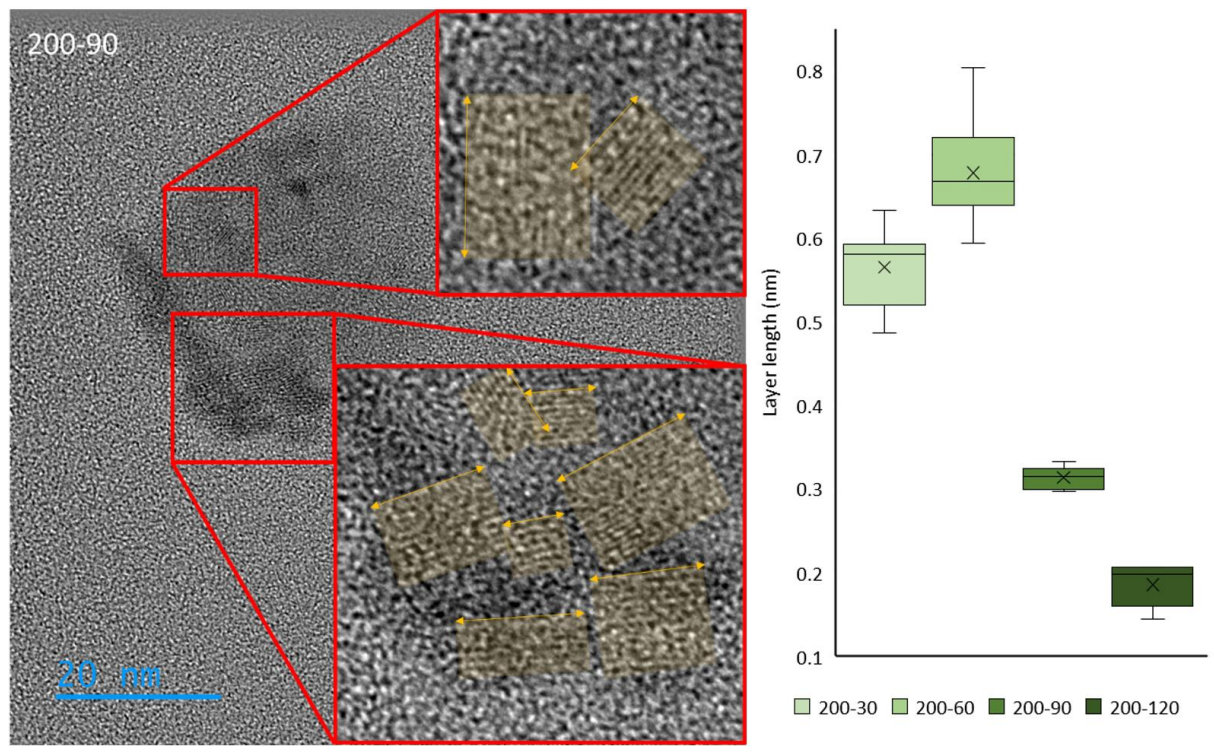


Figure 4.44 - HRTEM image of the carbon dots synthesised at 200°C with a retention time of 90 minutes with the layered structure highlighted. Right; Layer lengths of all carbon dots at 200°C as measured with ImageJ from HR-TEM images

The average lattice spacing of the 200-120 CDs is 0.185nm which is close to the (102) diffraction planes of sp² graphitic carbon (C. Li et al., 2021; Maniscalco et al., 2020; S. Zhu et al., 2013). The lattice spacing 0.314nm in 200-90-CD corresponds to the Z spacing between carbon sheets (Pal et al., 2020). The difference between the samples is the orientation of the CDs imaged. The other lattice spacings shown in CDs 200-60-CD and 200-30-CD are not consistent with other lattice spacings reported in literature. A suggestion of why this might be the case is that the measured single layer was a double layer, effectively doubling the values gained.

Biocompatibility testing was conducted using PrestoBlue cell viability and live/dead assays. The results of the PrestoBlue analysis are outlined in Figure 4.45.

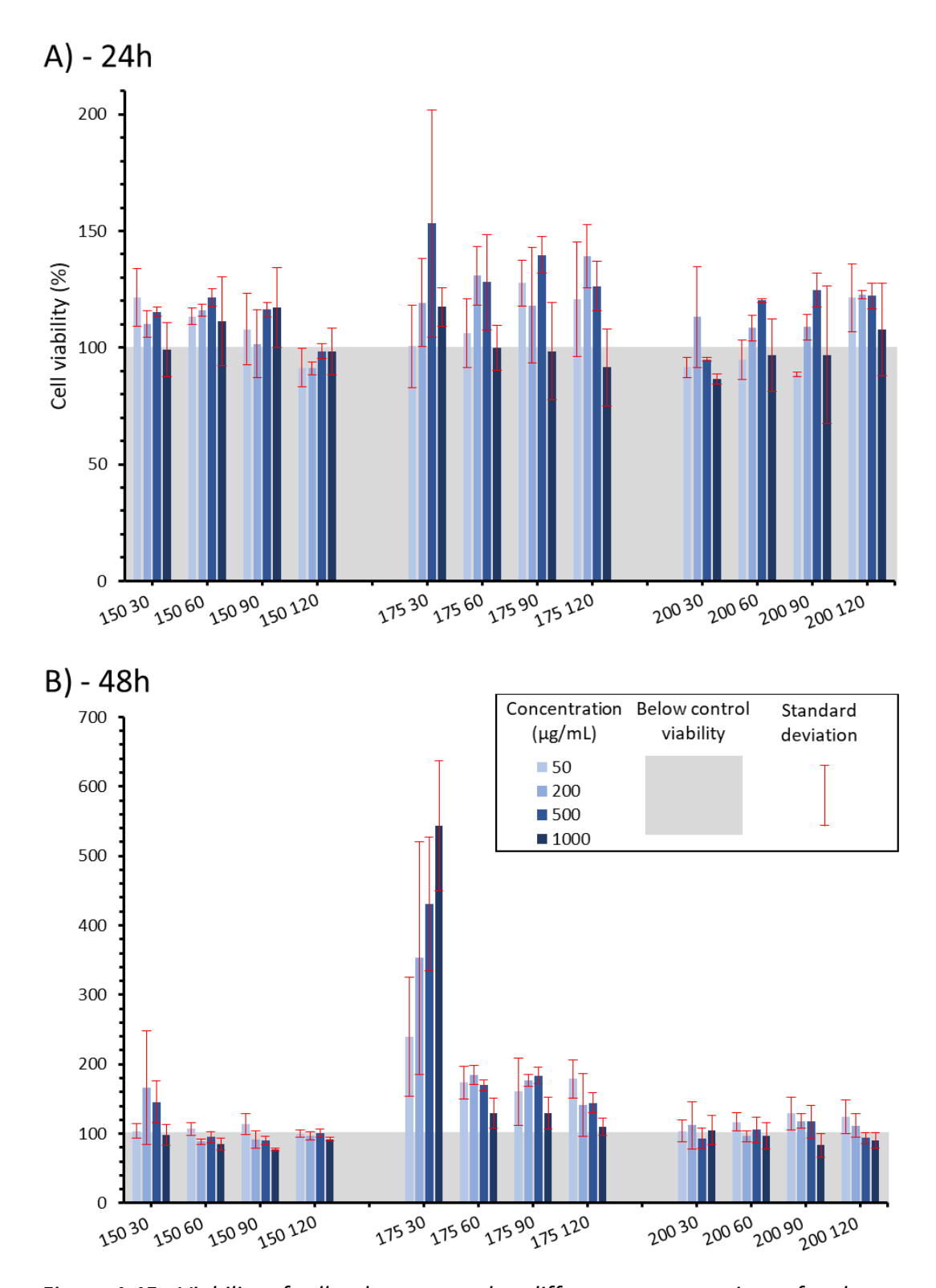


Figure 4.45 - Viability of cells when exposed to different concentrations of carbon dots for 24 (A) and 48 (B) hours as measured with PrestoBlue™ cell viability reagent and procedure.

Statistical analysis was run on the data and each concentration set compared between each sample and the control with a Bonferroni corrected P-value. The PrestoBlue graphs (Figure 4.42) shows that all the dots have very good biocompatibility with most cells 120 and 89%

viability after 24 hours and between 100% and 77% viability after 48 hours when compared to cells not exposed to the CDs, with a trend of a decrease in viability with increased concentration in some of the CDs. At 24h there was statistically no significant difference between the any of the 1000μg/mL samples when compared against the controls. At 48h most 1000μg/mL were statistically insignificant against the control aside from the samples 150 90 and 175 30. The 150 90 sample was 77% viable against the control, which is still fairly biocompatible. This shows that these CDs are overall very biocompatible, leading to the conclusion that these dots have great potential for application

in bioimaging. The values for 175-30 in the 48h tests increase with concentration and reach values above 600%; this is down to contamination in this particular sample.

4.3.2 *Summary*

The above data shows that a green microwave synthesis of CDs that does not require any form of catalyst produces biocompatible, blue fluorescence carbon. Changing the synthesis retention time and temperature parameters does influence some of the other properties of the dots, but not significantly. For example, a longer retention time does slightly increase the size of the dots but has no effect on QY, and a lower temperature increases the negativity of the ζ -potential of the dots by changing the ratio of surface groups.

Chapter 5. layer by layer capsules: Results and Discussion

This chapter outlines the experiments that are most relevant to the LBL capsule formation and the final device which contains both CDs and anticancer drugs.

Section 5.1 - Outlines the initial investigation of the effect of synthesis conditions and drying methods for the formation of CaP NP templates. Initial nanolayer formation was also evaluated, and two different polyelectrolytes were investigated. These results were used as templates for building the LBL capsules in some of the following experiments section.

Section 5.2 - Investigates the formation of LBL capsules on calcium phosphate nanoparticles (CP NPs) templates using PEI, CH and AA. This was followed by loading with anti-cancer drugs and CDs to obtain nanotheranostic systems.

Section 5.3 - Outlines the formation of LBL capsules formed using the CPNP templates with PAH, CH and CS. These were also loaded with anti-cancer drugs and CDs to obtain nanotheranostic systems.

5.1 Optimisation of the processing parameters for the calcium phosphate nanoparticles

This section outlines and discusses the results from the initial testing of CaP NP synthesis including flow rate and drying investigation using a peristaltic pump, and initial layer deposition comparing PEI and PDADMAC.

5.1.1 Peristaltic pump method for the preparation of CPNPs, effect of drying method and flow rate

It was expected that a peristaltic pump would synthesise the particles in a precise method (Mohammed et al., 2004). Table 5.1 summarises the ζ -potential values of the obtained NPs surfaces using different drying methods.

Table 5.1 - ζ -potential and size values of the nanoparticles obtained using a peristaltic pump with different drying methods.

Sample		Measurement		
Drying method	Flow rate (mL/min)	Zetapotential (mV)	Size (nm)	
	0.5	-16.9 ± 0.9	7269 ± 2619	
Water wash and	3	-0.2 ± 0.2	1127 ± 275	
freeze dry	6	-1.4 ± 0.4	4280 ± 1059	
	9	-4.4 ± 0.9	1637 ± 572	
	0.5	-12.2 ± 1.1	884 ± 13	
Isopropanol wash	3	-1.3 ± 0.2	1398 ± 463	
and air dry	6	-13.2 ± 2.8	6877 ± 1232	
	9	-12.7 ± 4.5	1545 ± 111	
	0.5	0.3 ± 0.5	1707 ± 70	
Water wash and	3	-11.7 ± 3.0	2484 ± 621	
air dry	6	-10.5 ± 2.1	543 ± 102	
	9	-10 ± 0.7	1049 ± 253	

This data does not show much of a trend between the different flow rates or drying method; however, the flow rate 9mL/min tends to have a smaller particle size and more negative ζ -potential. The drying methods are difficult to evaluate because there is such a range of values; however, for the surface charge the freeze drying presented the less negative values (-0.2,-1.4) while water washing and air drying showed more negative values (-11.7,-10.5). The effect on the size was not possible to fully analyse because some of the samples did not show any peaks, which means that agglomeration was affecting the results, causing peaks that were off the scale of the zetasizer. The best flow rate was shown to be 9mL/min. This is because of the consistency of the ζ -potential and smaller size across the different drying methods. SEM was also used to analyse the size of the NPs (Figure 5.1, Figure 5.2 Figure 5.3).

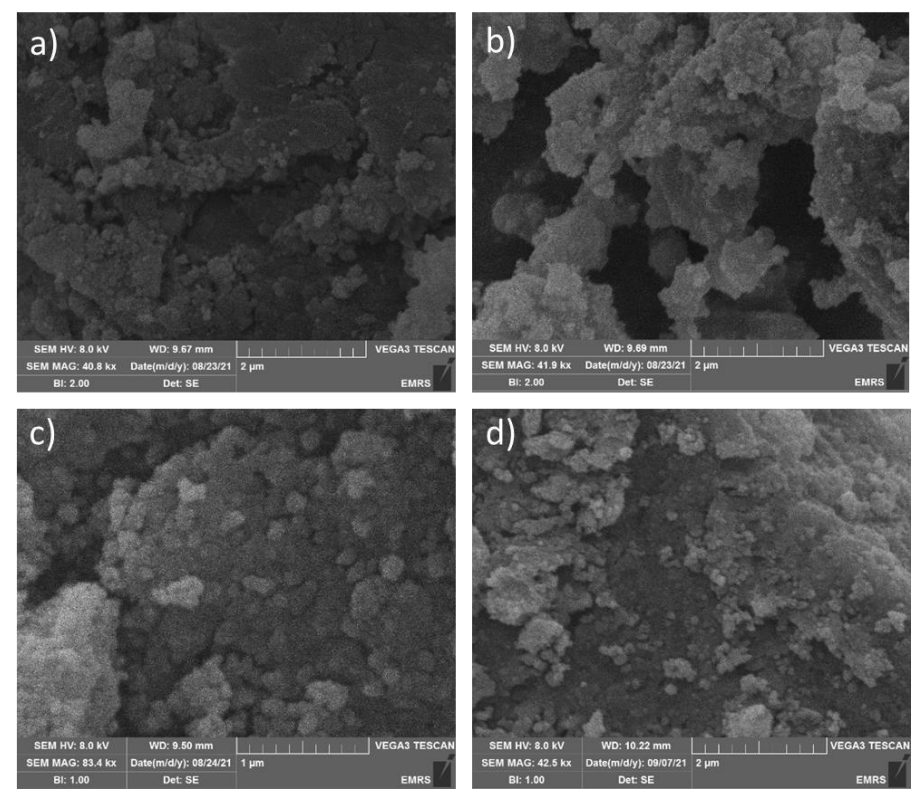


Figure 5.1 - SEM images of calcium phosphate nanoparticles washed with water and dried in air, synthesised at different flow rates; a) – 0.5mL/min, b) – 3mL/min, c) - 6mL/min, d) – 9mL/min 9mL/min

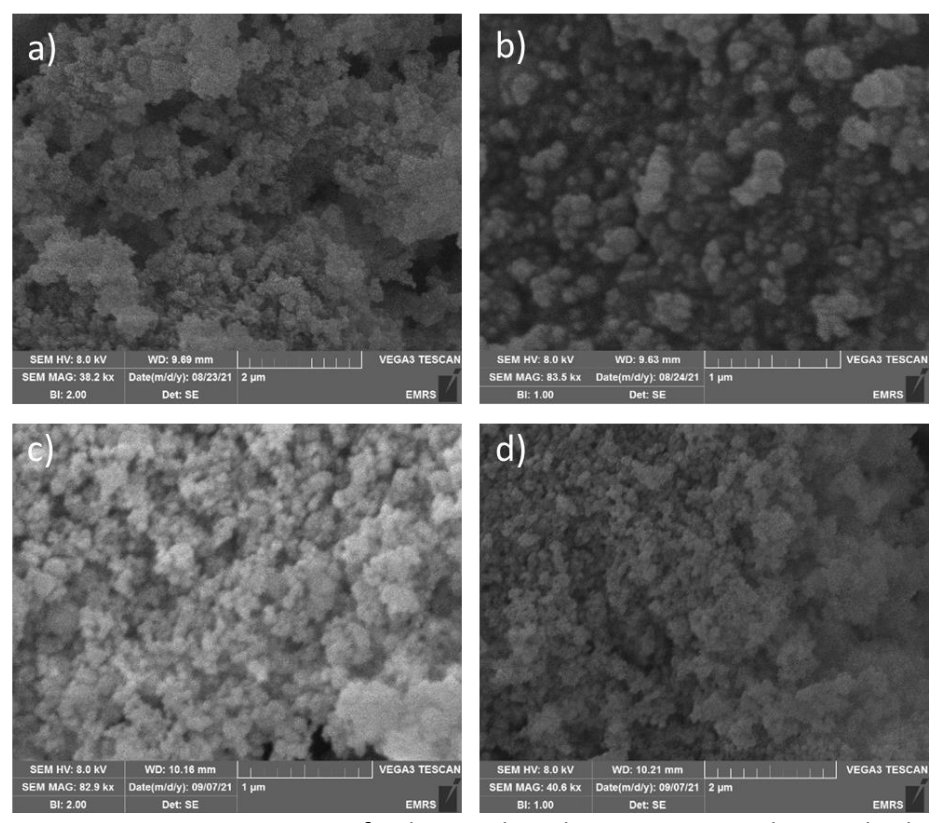


Figure 5.2 - SEM images of calcium phosphate nanoparticles washed with water and freeze dried, synthesised at different flow rates; a) – 0.5mL/min, b) – 3mL/min, c) - 6mL/min, d) - 9mL/min.

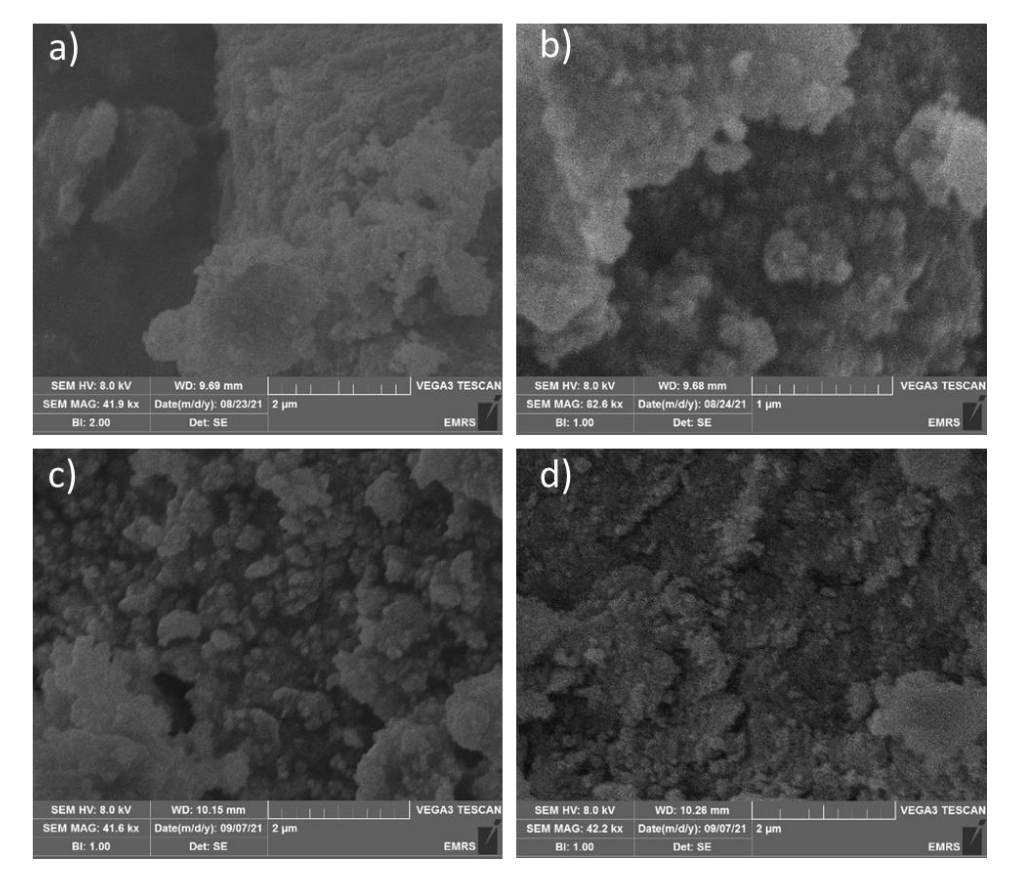


Figure 5.3 - SEM images of calcium phosphate nanoparticles washed with isopropanol and dried in air, synthesised at different flow rates; a) – 0.5mL/min, b) – 3mL/min, c) - 6mL/min, d) - 9mL/min

The images show extremely high agglomeration, confirming the results obtained from the DLS and previous works (Mohammed et al., 2004; Urch et al., 2009). ImageJ software was used to analyse the images to get an estimation of the average sizes. (Table 5.2). The SEM images show high agglomeration of the samples which made it difficult to analyse with ImageJ. However single particles were found and used for size analysis.

Table 5.2 - SEM ImageJ analysis of the size of the nanoparticles obtained with the peristaltic pump and using different drying methods.

Sam	Sample		Average size of			
Drying method	Flow rate (mL/min)	Size (nm)	the drying method			
	0.5	59 ± 9				
Freeze dry	3	62 ± 10	65 ± 14	Average size of each flow rate		
rreezeury	6	55 ± 14	65 ± 14			
	9	85 ± 13				
	0.5	76 ± 22				
Isopropanol wash and	3	67 ± 12	72 - 44			
air dry	6	84 ± 11	72 ± 11			
	9	60 ± 11				
	0.5	85 ± 11		73 ± 13		
Water wash	3	71 ± 6	83 ± 11	67 ± 5		
and air dry	6	97 ± 19	02 111	79 ± 21		
	9	78 ± 13		74 ± 13		

The NPs presented a size between 60 and 90 nm. On average, the flow rate did not have a large effect on the size of the particles and there was no trend between the flowrate and the particle size. This was unexpected as the hypothesis was that the increased reaction time of a lower flow rate would have produced larger particles. Speed of reactant addition is mentioned in literature as a potential control for size (Piazza et al., 2020) along with temperature and pH (Raynaud et al., 2002), stirring and drying process (Afshar et al., 2003). The drying method was shown to have a slight effect on the size of the particles. The freeze dry method produced the smallest particles. The water wash particles are larger, and this is consistent will all four flowrates.

The research above suffers from several limitations in the analysis due to the agglomeration found in the samples. For this reason, these results cannot be used to draw any definitive conclusions. This experiment and its findings were not used directly in the synthesis of the final devices because, in future experiments, the first layer was applied directly onto the CaP particles immediately after formation without drying to help with agglomeration. (Piazza et al., 2020; Raynaud et al., 2002; Urch et al., 2009). For future research, the results of these experiments could potentially be improved by using a lower concentration of the nanoparticles or a different solvent for dispersal for zetapotential and DLS with PDI so that

the suitability of the data can be assessed. TEM should have been used instead of SEM because the magnification is much higher. This would have given images in which single particles could have been more discernible for imageJ analysis.

5.1.2 Initial layer deposition, comparison between PEI and PDADMAC

For the LBL deposition, it was hypothesised that directly applying a layer to the templates during the synthesis using the peristaltic pump would stop the growth of the NPs templates after their nucleation. This could decrease the final size of the particles and reduce the phenomenon of agglomeration. Particle formation occurs at pH 10, so the polyelectrolyte chosen as the first layer needed to be soluble at pH 10. PEI and PDADMAC were chosen for comparison for this reason and have been used in similar experiments previously (Elizarova & Luckham, 2016; Rojas-Sánchez et al., 2020; Urch et al., 2009). Three different concentrations (3, 5, 10mg/mL) were chosen to find the lowest concentration needed for the deposition of the layer to discover the optimal concentration needed to saturate the surface of the NP. Dynamic Light Scattering and ζ -potential (Table 5.3) and TEM (Figure 5.4 and Figure 5.5) were used to analyse the deposition of the first polycationic layer on the surface of the NPs.

Table 5.3 - ζ -potential and DLS measurement of functionalised calcium phosphate nanoparticles with polyelectrolyte solutions of different concentrations

Test	Z-potential (mV)	DLS - Size (nm)		
PEI 3mg/mL	16.2 ± 0.4	5111 ± 778		
PEI 5mg/mL	14.7 ± 0.7	2896 ± 137		
PEI 10mg/mL	17.3 ± 0.3	3222 ± 632		
pDADMac 3mg/mL	37.9 ± 1.0	515 ± 8		
pDADMac 5mg/mL	36.2 ± 0.3	748 ± 19		
pDADMac 10mg/mL	27.5 ± 1.0	540 ± 11		

The ζ -potential showed that for both the polyelectrolytes, the lowest concentration of 3mg/mL was adequate for deposition onto the template, because no changes in the ζ -potential were observed while increasing the concentration. The data also showed that PDADMAC has higher ζ -potential (27.5-37.9mV), which is better for the application of further layers because the particles are more stable through electrostatic repulsion leading to a

decrease in agglomeration (Hanaor et al., 2012). These particles were also much smaller (515-748nm) when compared to the use of PEI (3222-5111nm) tendency to agglomerate. TEM was used to measure the exact size of these NPs without the agglomeration effecting the results.

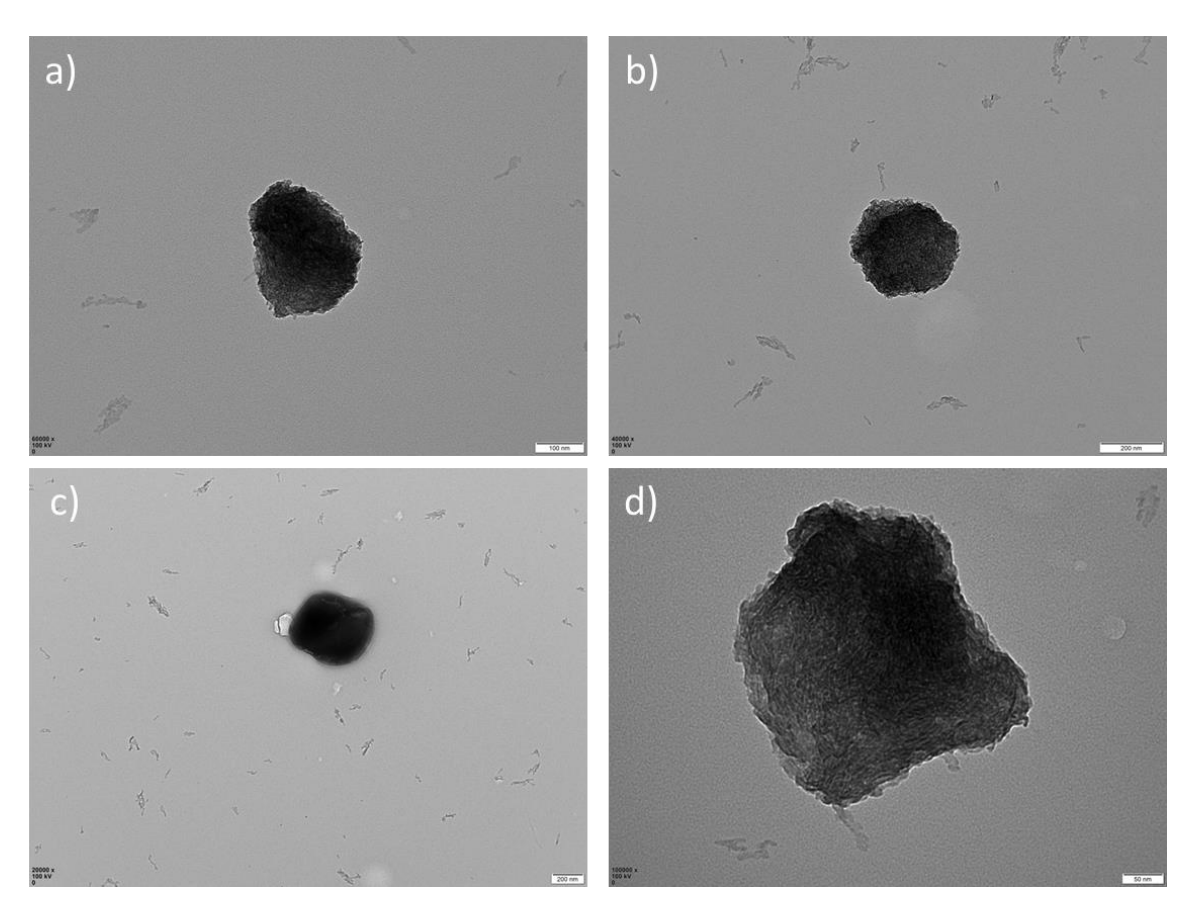


Figure 5.4 - TEM images of PEI functionalised particles (10mg/mL)

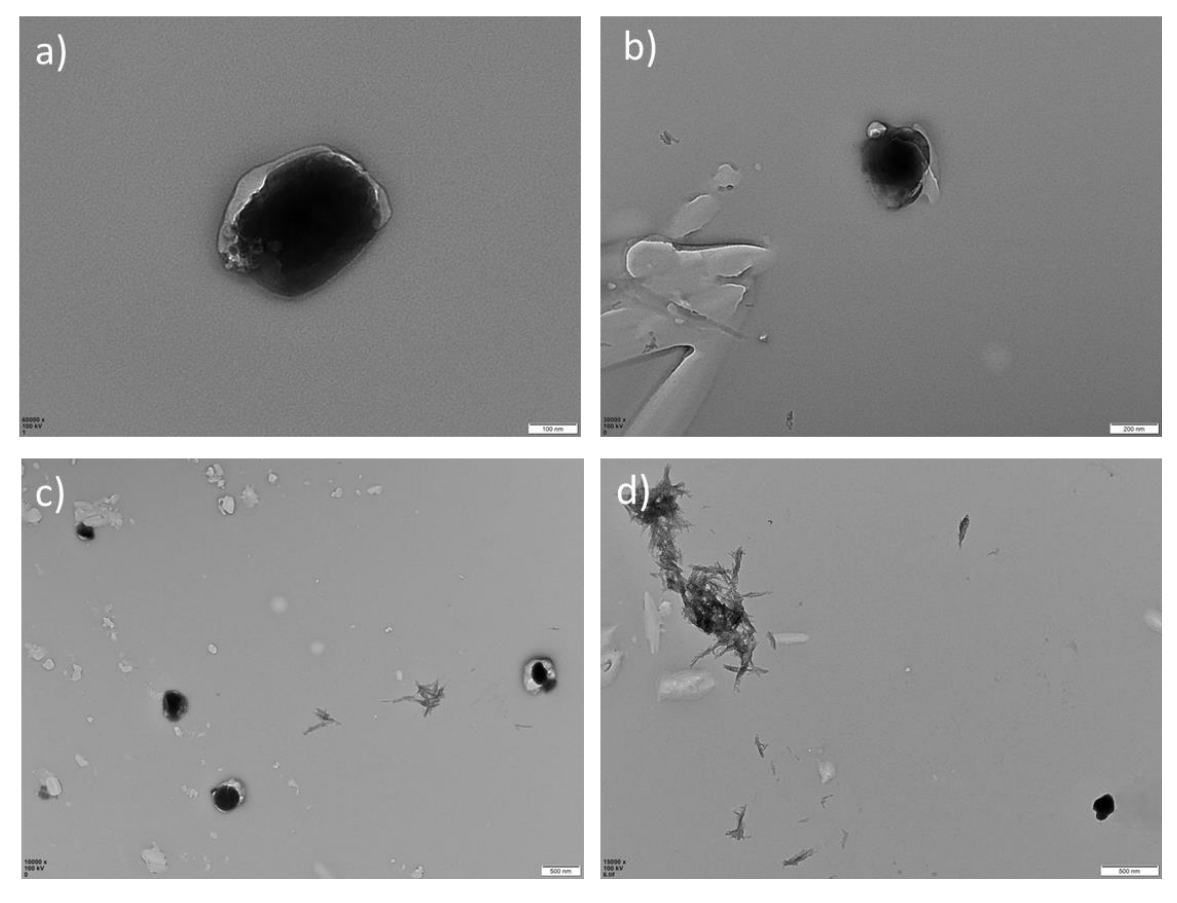


Figure 5.5 - TEM images of PDADMAC functionalised particles (10mg/mL)

The TEM images from Figure 5.4 and Figure 5.5 were analysed with ImageJ and are as follows:

PEI functionalised particles (Figure 5.4) - A - 237nm; B - 349nm; C - 561nm; D - 345nm PDADMAC functionalised particles (Figure 5.5) - A - 303nm; B - 290nm; C - 347nm, 235nm, 204nm, 245nm; D - 193nm.

After this experiment was complete, it was found that the molecular weight of the PDADMAC was 100,000. This is much higher than the molecular weight cut off of the dialysis membrane used in part of the purification process. This would have affected the cleaning process of the PDADMAC tests and is an explanation for the large crystals present in the TEM images.

The average particle size for the PEI coated particles (Figure 5.4) is 373 ± 136 nm and for PDADMAC coated particles (Figure 5.5) is 260 ± 56 nm. The smaller particle size of the PDADMAC is more suitable for cellular internalisation which would facilitate efficient drug release (Mazumdar et al., 2021). However initial tests with the LBL process showed that PDADMAC functionalised particles were difficult to obtain in centrifugation meaning many particles were lost once the layers had been deposited. This was also found by Elizarova et al. (Elizarova & Luckham, 2016): they reported a significant loss of particles after 10-20

centrifugation/redispersal cycles. This meant that PEI was chosen for the first layer despite functionalisation resulting in a larger particle size and a less negative ζ -potential.

5.2 Chitosan and alginate layer by layer capsules functionalised with anticancer drugs and carbon dots

PEI functionalised CaP NPs were subject to the LBL treatment with alternating layers of AA and CH to form nanocapsules. Drug loading with DOXO and DAX was conducted to investigate the drug release capabilities of the capsule. The capsule was also functionalised with CDs and subject to photoluminescence spectroscopy to analyse the photoluminescent properties.

5.2.1 Initial layer-by-layer deposition without drugs

The formation of the core proceeded the same as discussed in section 5.2 using PEI as first layer and then functionalised by LBL assembly using CH as polycation and AA as polyanion. A sample was taken after the completion of each layer and analysed with ζ -potential, XPS, FT-IR for surface chemistry and TEM to characterise the size. The ζ -potential data clearly shows the deposition of the layers (Figure 5.6).

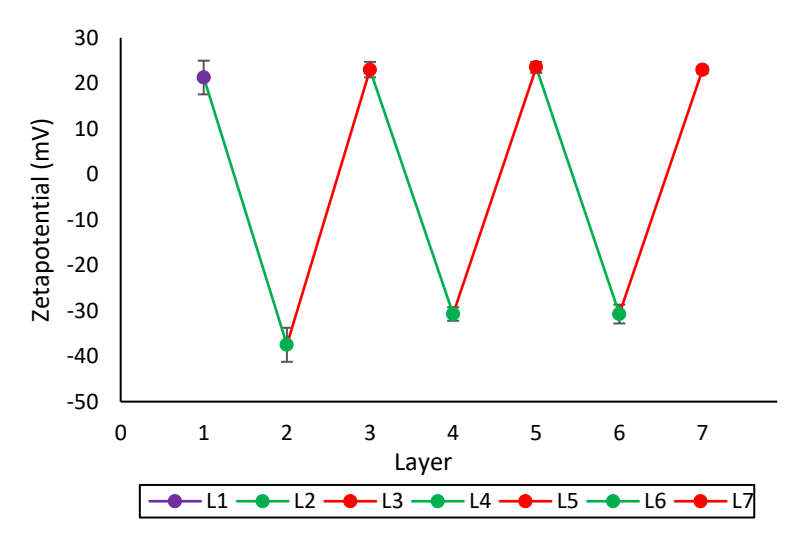


Figure 5.6 - ζ-potential for each layer of the layer-by-layer process deposited on CaP

The results are consistent for each layer ranging between 20 – 25 mV for the positive charged PEI core and CH layers and between -30 - -40mv for the AA layers. This clearly showed the charge reversal for each layer suggesting successful deposition of each layer (Haidar et al., 2008; Jardim et al., 2018). The higher magnitude of charge of the AA layer

compared to the CH layer was to be expected because a higher concentration was used. The saturation concentration ratio between the two polyelectrolytes (2:1 AA/CH) found in this project agrees with previous literature but contrasts with others. Zhao et al. (Zhao et al., 2007) used the exact same concentrations as used in this project to functionalise calcium carbonate microcapsules. However, Pawlak et al. (Pawlak & Belbekhouche, 2021) found in their functionalisation of E.coli bacteria. concentrations of 0.12mg/mL and 0.05mg/mL for CH and AA respectively giving a ratio of 2.4 in favour of CH, a potential reason for this difference is the use of different substrate.

FT-IR is a simple, fast, and non-destructive technique for surface characterisation. For this reason, it was attempted to be used to characterise the surface of the NPs to confirm the deposition of each layer. The data are presented in Figure 5.7.

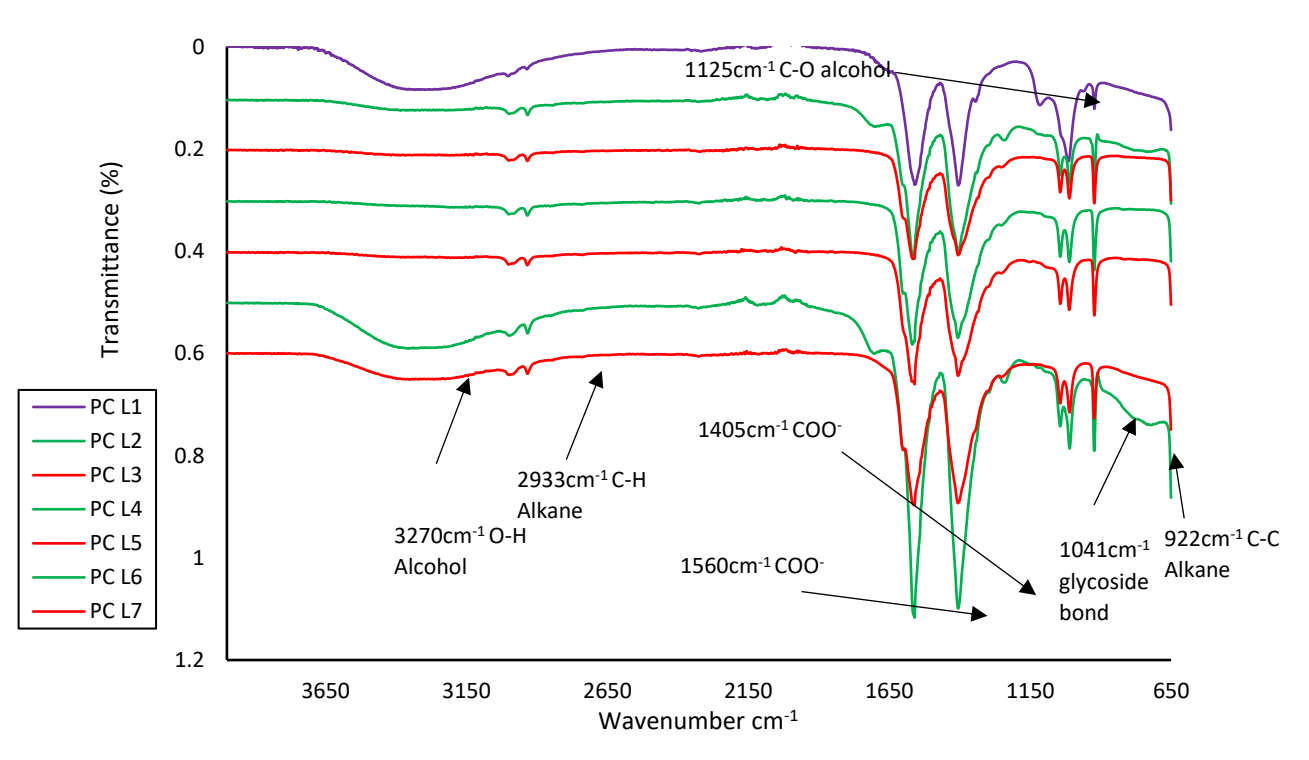


Figure 5.7 - FT-IR of each layer deposited on CaP nanoparticles in the initial layer by layer process.

All the layers showed very distinct peaks at ~1559cm-1, ~1405cm⁻¹, ~1015cm⁻¹, 1010cm⁻¹ and ~922cm⁻¹. These peaks correspond to sodium acetate that was used as a buffer to keep the pH stable. (NIST; Rani et al., 2021) ~1559cm⁻¹ corresponds C=O stretching in the carboxylic acid group. ~1405cm⁻¹ corresponds to the stretching mode of –CH₂ scissoring. ~1015cm⁻¹ and 1010cm⁻¹ corresponds to the CH₃ rocking vibration. The ~922cm⁻¹ corresponds to the O-H

bend in the carboxylic acid group. This sodium acetate contamination overwhelms the PEI, CH and AA in the samples which makes it harder to characterise.

The penetration depth of this technique can also be up to 60 μ m (Götz et al., 2020) which is much larger than any one single NP. This means that this technique is not just analysing the surface of the particle, it is reporting data from the material as a bulk. Therefore, the data from each layer sample is a combination of the new material and all the material deposited in the pervious layers, this makes changes between each layer more subtle and harder to characterise.

According to Lawrie et al. (Lawrie et al., 2007) and their 2007 study on the characterisation of AA-CH polyelectrolyte complexes, FT-IR and XPS must be used in conjunction for the identification of the presence of the AA and CH. They report that a band at 1710cm⁻¹ corresponds to the protonation of the carboxylate group. This peak is shown in Figure 5.13 in samples 2 and 6. For CH, a band at ~1530cm⁻¹ appears due to the partial protonation of the amine group. This is overwhelmed by the 1560cm⁻¹ peak from the COO⁻ but is shown as a shoulder in 2 through 7 partially suggesting the deposition of CH.

XPS was used to help confirm the surface of the NPs. The raw material of AA and CH was analysed for comparison (Table 5.4). Examples of peak picking of the C1s and O1s scans are shown in Figure 5.8 and Figure 5.9.

Table 5.4 - XPS data for raw alginate and chitosan for comparison to deposited layers. Top – wide survey scan, bottom – C 1s, N 1s, O 1s

		At %										
Scan		Survey										
Element/Bond	Phosphorus	Carbon	Calcium	Nitrogen	Oxygen	Sodium						
Binding energy (eV)	137.79	137.79 286.04 346.29 399.79 137.79 532.5										
Sample												
Alginate	0.11	55.79	0.01	0.39	39.24	4.47						
Chitosan	0	63.93	0.09	6.49	29.49	0						

		At %									
Scan	C 1s			N 1s				O 1s			
Element/Bond	sp2/C=C	sp3/C-C	C-O	C=O	C-NH2	CONH2	C-NH3+	Nitrate	C=O	C-O	Na KLL Auger
Binding energy (eV)	284.41	284.9	286.28	287.82	399.48	400.4	401.3	406.5	531.74	532.74	534.86
Sample											
Alginate	3.65	20.03	42.12	34.2	38.66	25.89	5.25	30.2	25.57	67.57	6.86
Chitosan	2.36	21.53	53.08	23.03	84.51	6.53	8.96	0	44.83	54.44	0.73

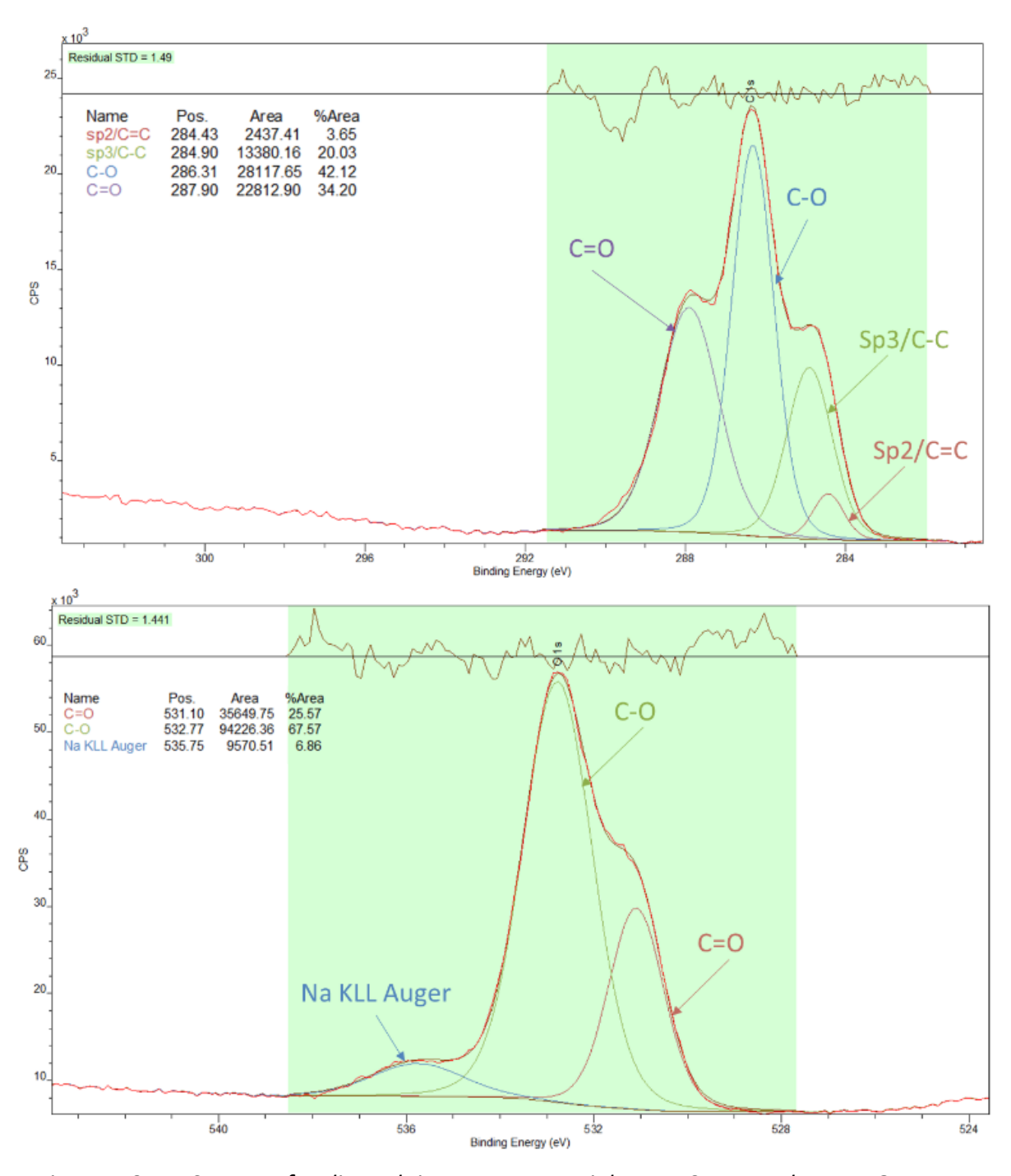


Figure 5.8 - XPS scans of sodium alginate raw material – Top C1s scan, bottom O1s scan.

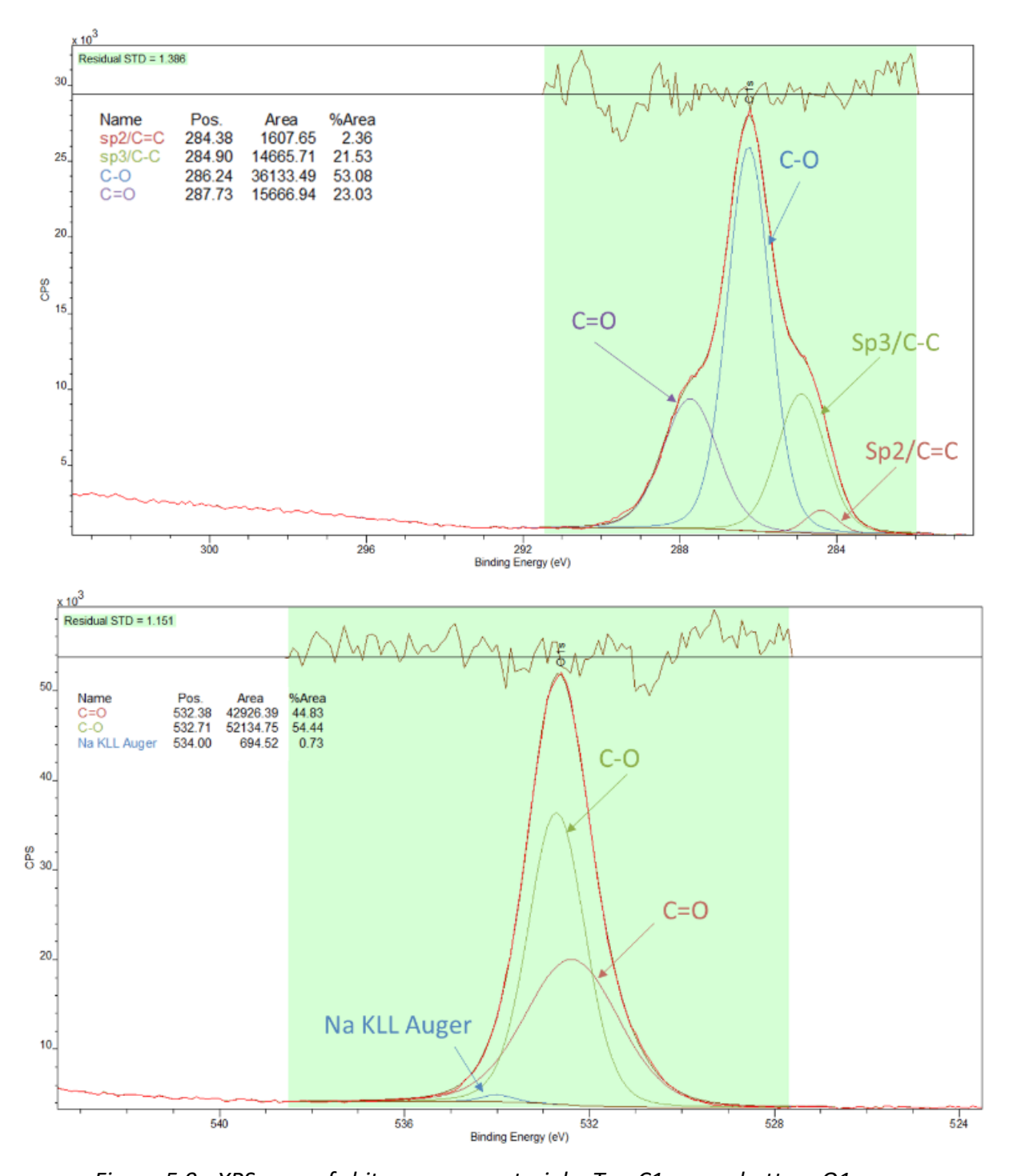


Figure 5.9 - XPS scan of chitosan raw material – Top C1s scan, bottom O1s scan.

The results from the wide elemental scan were as expected with no phosphorus, sodium, and calcium for either sample. A higher ratio of carbon and nitrogen and no sodium was seen for CH, whilst no nitrogen, more equal carbon and oxygen ratio and a small percentage of sodium was seen for AA (Jejurikar et al., 2012). This showed that the telltale sign of a CH layer deposition is an increase in nitrogen and carbon ratios and the sign for AA deposition is an

increase in both oxygen and sodium content. The peak at ~287.87eV is attributed to C=O bonding and is shown in literature (de Godoi et al., 2013; Li et al., 2016; Vieira et al., 2011).

XPS was also used to analyse the surface of the NPs to characterise the layer deposition (Table 5.5, Figure 5.10Figure 5.11Figure 5.12). (N 1s scans - Figure A.6.11Figure A.6.12Figure A.6.13)

Table 5.5 - Summary of the XPS data for all scans of each layer of the sample containing no drugs. Top — wide survey scan, bottom — C 1s, N 1s, O 1s

		At %									
Scan	Survey										
Element/Bond	Phosphorus	Carbon	Calcium	Nitrogen	Oxygen	Sodium					
Binding energy (eV)	134.28	284.71	348.78	399.63	134.28	531.13					
Sample											
ND L1	0.83	55.55	2.43	1.59	31.95	7.64					
ND L2	0.15	1.23	1.23	1.1	32.35	8.3					
ND L3	0.19	56.24	0.62	0.25	33.02	9.68					
ND L4	0	64.91	0.19	1.1	27.67	6.13					
ND L5	0.15	57.46	0	0.44	32.57	9.38					
ND L6	0.09	58.36	0.21	0.6	31.87	8.86					
ND L7	0	56.28	0.17	0.46	33.36	9.73					

		At %										
Scan	C 1s				N 1s				O 1s			
Element/Bond	sp2/C=C	sp3/C-C	C-O	C=O	C-NH2	CONH2	C-NH3+	Nitrate	C=O	C-O	a KLL Auge	
Binding energy (eV)	284.54	284.88	285.6	288.36	399.48	400.4	401.3	406.5	531.17	532.5	535.75	
Sample												
ND L1	12.94	33.88	24.66	28.51	92.33	1.11	6.56	0	87.03	1.94	11.03	
ND L2	11.48	34.36	24.04	30.12	80.45	4.45	15.07	0	80.13	6.54	13.33	
ND L3	11.54	46.75	12.1	29.61	99.53	0.21	0.26	0	82.48	3.01	14.5	
ND L4	11.16	45.95	22.6	20.28	79.2	5.87	14.93	0	67.88	19.25	12.87	
ND L5	15.79	41.48	13.99	28.74	73.79	20.68	3.53	0	78.49	6.9	14.62	
ND L6	14.53	41.27	16.64	27.57	100	0	0	0	78.04	7.16	14.8	
ND L7	11.2	42.01	16.3	30.5	81.77	18.23	0	0	81.59	4.35	14.06	

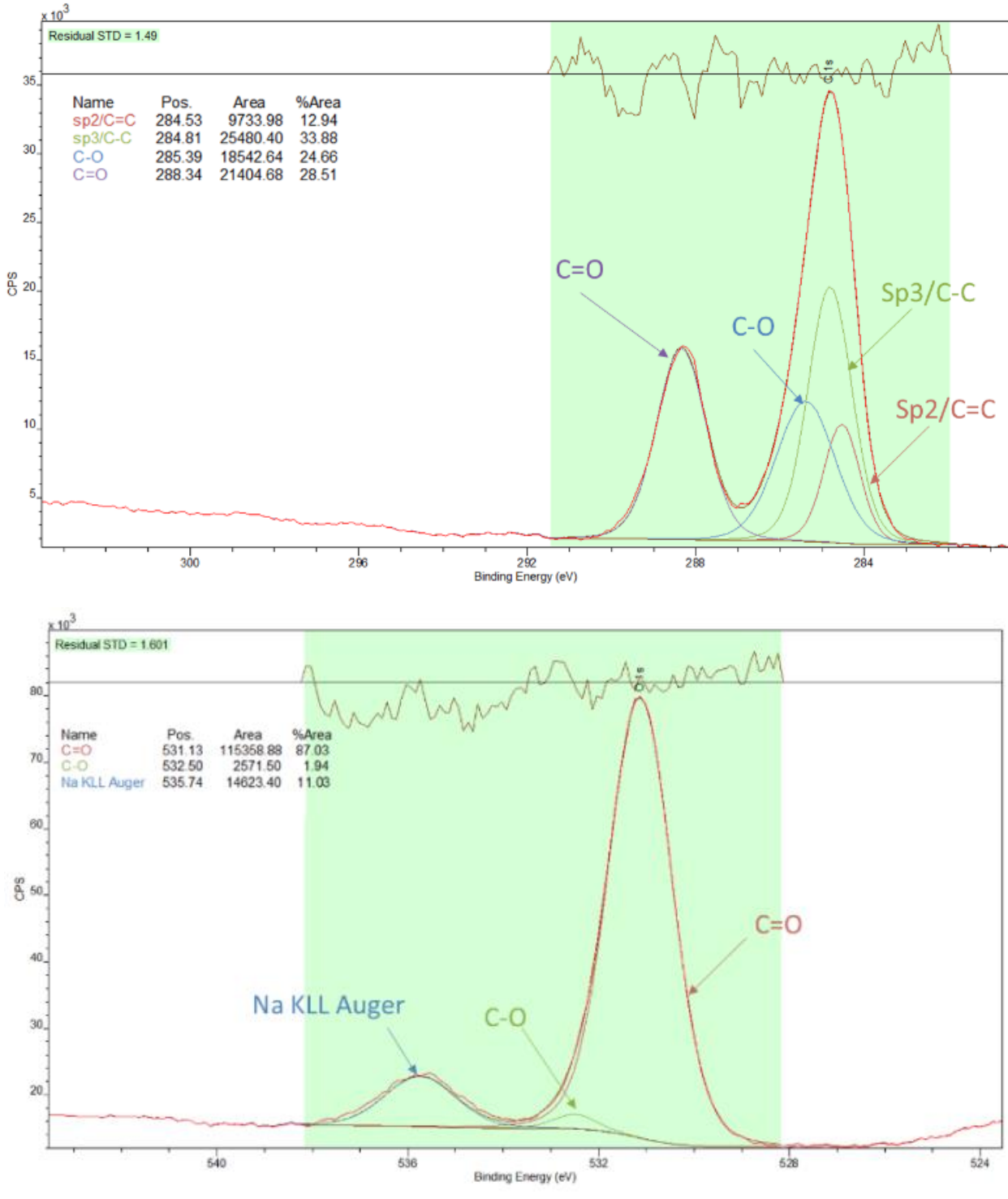


Figure 5.10 - XPS scans of the first layer deposition (CaP nanoparticle + PEI) – left C1s scan, right O1s scan.

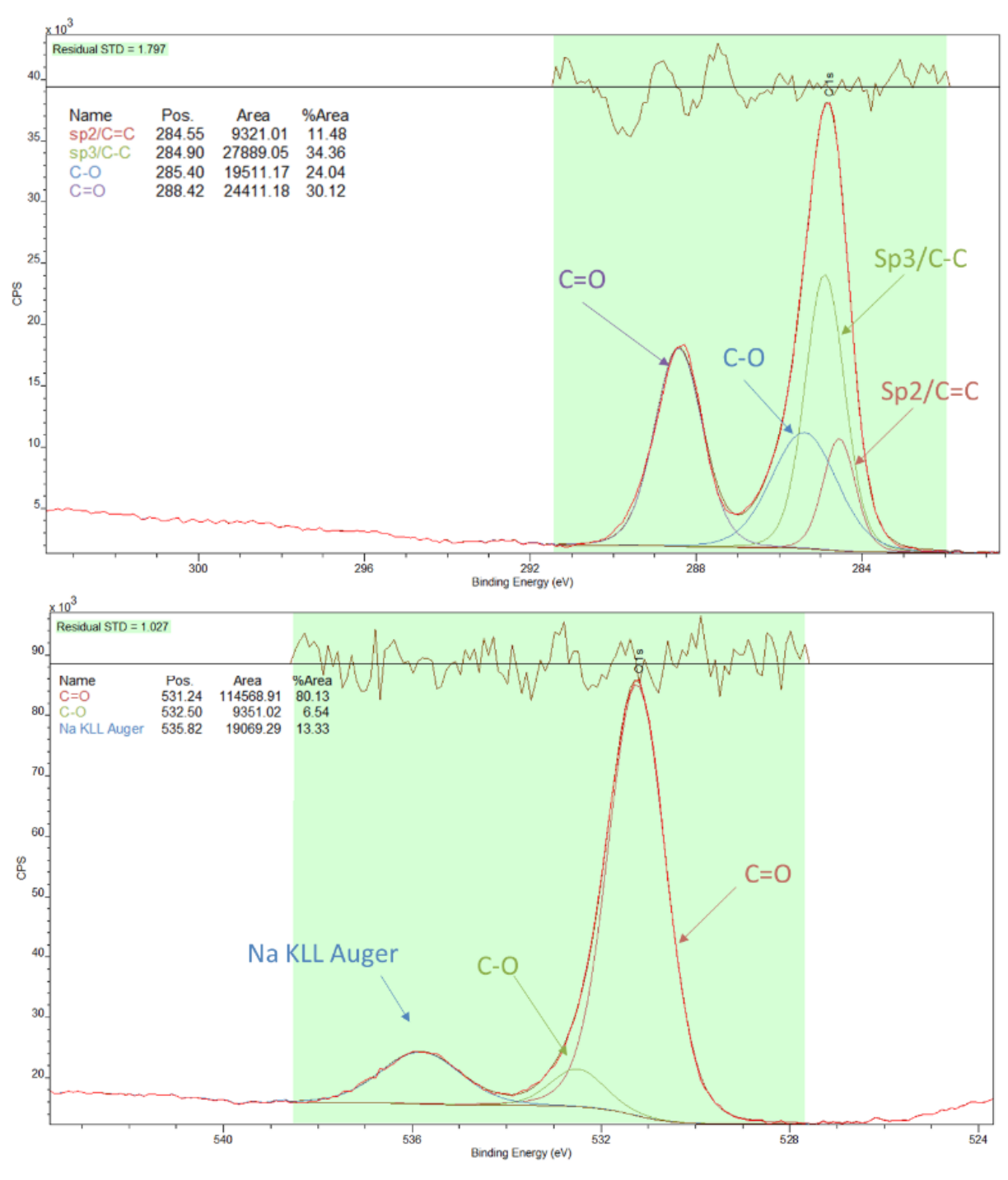


Figure 5.11 - XPS scan of the second layer deposition (CaP nanoparticle + PEI + Alginate) – left C1s scan, right O1s scan.

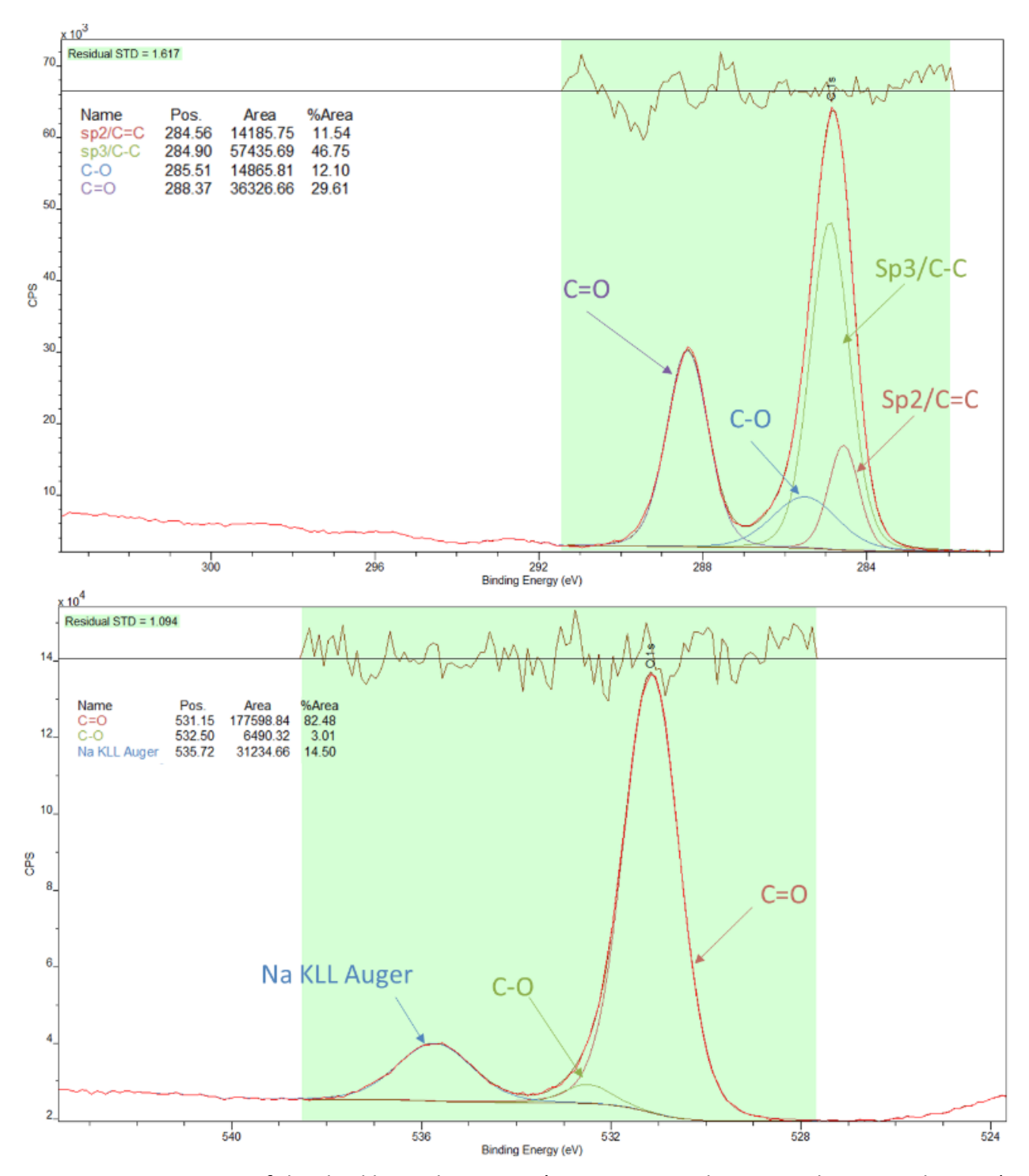


Figure 5.12 - XPS scan of the third layer deposition (CaP nanoparticle + PEI + alginate + chitosan)

— left C1s scan, right O1s scan.

The XPS results for the layers also show contamination from the SAB just like the FT-IR. This is shown most prominently with the high sodium content in the elemental scan and high presence of C=O in the O 1s and C 1s scans and the fact that there is no variation from one sample to the next. The presence of a small amount of phosphorus and calcium from the CaP templates which decreases as the layers increases shows the deposition of each layer and the increase in particle size.

Lawrie et al. (Lawrie et al., 2007) observed that when CH is the outermost layer in an LBL assembly, the amine groups extending into the solution during fabrication become deprotonated (neutral) upon washing and drying. Conversely, when AA is the outermost layer, the amine groups of the underlying CH layer experience a higher degree of protonation due to interaction with the deprotonated carboxylate group of AAs. Consequently, a greater number of protonated amines is expected when AA is the outermost layer. This means that the N 1s peak can be used as evidence of CH and AA deposition depending on the ratio of amine protonation.

The first 5 layers of the deposition follow this trend of increasing with the deposition of AA suggesting that the LBL deposition was somewhat successful, however the ratio of protonation is in the range of 0.26% to 15.07% rather than the 40-60% found by Lawrie et al. Layers 6 and 7 show no amine protonation and therefore chemical composition cannot be confirmed.

Due to the contamination with sodium acetate the ratios of carbon, oxygen and sodium do not significantly change with the different layers making it impossible to fully characterise the layers with this technique. XPS is only used rarely in literature to characterise the chemical composition of each layer deposition of the LBL technique, making a comparison difficult. For example, Xie et al. (Xie et al., 2011) used XPS to characterise their sodium CH microcapsule and provide confirmation of presence of CH and AA in the outer 100 Å of the membrane but provided no further elaboration in regards to the deposition of each layer.

Transmission electron microscopy was used to visualise the particles (Figure 5.13) and perform size analysis. ImageJ was used to measure the particles and produce a distribution (Table 5.6).

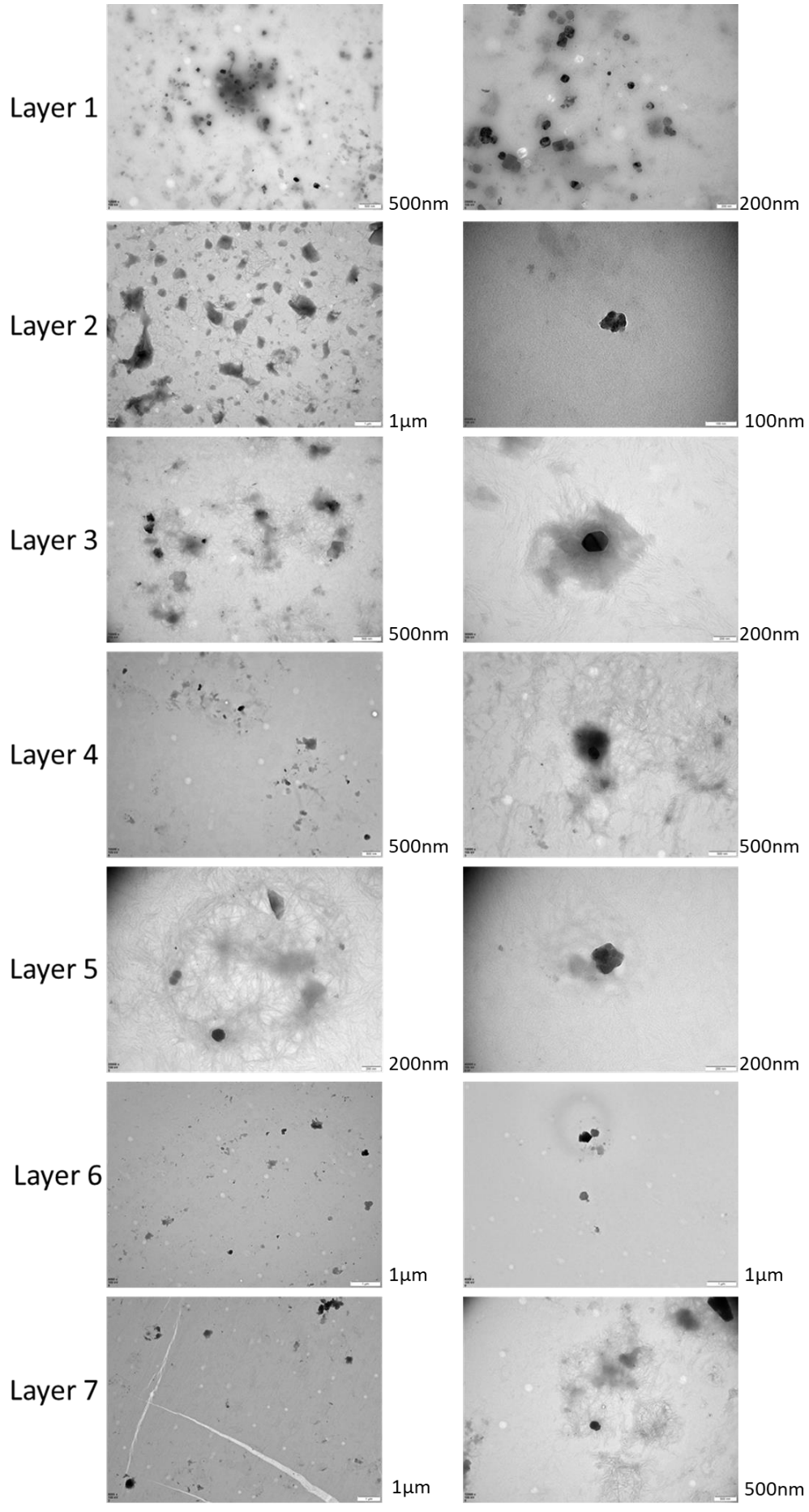


Figure 5.13 - TEM images of each layer of the layer-by-layer process

Table 5.6 - TEM average particle of the layer-by-layer process with no drugs size as measured by ImageJ.

Layer	Average particle size
1	97 ± 22
2	194 ± 71
3	173 ± 45
4	104 ± 51
5	152 ± 48
6	195 ± 91
7	269 ± 86

Overall, the particle size increased with increasing layers. This trend of increasing layer size is shown in literature, for example, Schwiertz et al. (Schwiertz et al., 2008) used CaP templates to create LBL capsule using PAH and PSS as the cationic and anionic layers respectively. They deposited 5 layers in total and saw an increase in particle size in DLS analysis from ~140-165nm in layer 1 to ~200-240nm for layer 5. Their layer deposition consistently increases per layer. This consistent increase in layer size contrasts the data found in this project. For example, Layer 2 presented a massive increase in size which then saw a decrease in layers 3 and 4. This shows poor and inconsistent LBL deposition. This is most likely caused by the SAB infiltrating the deposited layers and partially dissolving the CaP cores (Amjad, 1998) reducing the stability of the layers and causing inconsistent layer deposition. More evidence for this is in the morphology of the particles as this is inconsistent throughout the layers, ranging from smooth spherical particles to angular particles with large polyelectrolyte layering, the latter of which is evidence in the images from the 3rd layer deposition. This is very different from the PEI functionalised particles showcased in the initial layer deposition without the SAB had a rough texture and were spherical. The degradation of calcium phosphates in sodium acetate buffer has previously been documented in literature. Mok et al. (Mok et al., 2021) used acetate buffer to etch the surface of hydroxyapatite disks, a form of calcium phosphate found in teeth, to create fissures to test a remineralising agent. They subjected the disks to the acetate buffer for different time frames between 1 minute and 4 hours. Surface roughness increased from 0.25µm to 1.3µm in 4 hours. Ito et al. (Ito et al., 2011) also used this phenomenon of acidic conditions degrading CaP as a pH dependant release DNA complex carrier. It was shown that acetate buffer would dissolve the CaP layer and release the DNA complex encapsulated inside.

5.2.2 Effect of drug loading on the layer-by-layer process

The synthesis of the CaP NP and LBL process was repeated whist including anti-cancer drugs (DOXO, DAX, and combined). The ζ -potential of the resulting LBL functionalised NPs was analysed. This clearly showed the deposition of the nanolayers in all the samples due to the significant changes in ζ -potential from \sim 0 - 25mV to \sim -15 - -35mV (Figure 5.14).

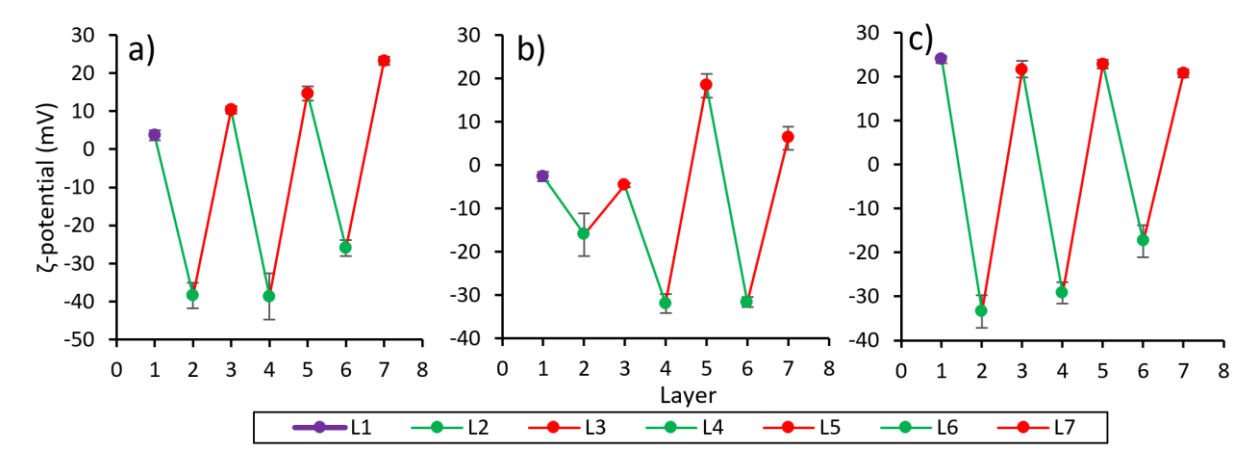


Figure 5.14 - ζ -potential of the LBL process for each drug loading conditions: a) both DAX and DOXO, b) DOXO only and c) DAX only.

However, there was some variation in the ζ-potential for each layer depending on the drug used for loading in the capsules. Indeed, in the sample where both drugs were incorporated in the AA layers and the core of the template NP (Figure 5.14a), the cationic layers increased in ζ-potential as they were deposited: i.e. L1 - 3.7, L3 - 10.3, L5 - 14.7 and L7 -23.2 mV. The AA layers were consistent for layer 2 and 4 at around -38mV, while the 6th layer reached a value of -26mV. This increase is due to the fact that the ζ-potential for the first layer 3.7mV is lower than that of drug free and DAX loaded capsules. This is also shown to a greater extent in the sample with only DOXO (Figure 5.15b) loaded into the template and within the AA layer; the ζ-potential of the template started with a value of -2.66 mV which was significantly lower than the values shown previously with the cores and layer by layer process without drug loading (> 20mV). This shows that the inclusion of the DOXO lowers the surface charge of the first layer deposition, which can then in turn affect the first layer of the AA deposition (layer 2) and the first layer of the CH deposition (Layer 3) which were -16mV and -4mV respectively. These values were significantly higher/lower than the counterparts without drugs (-37.5 mV and 23.0 mV respectively). DOXO has negative ζ-potential (Nguyen et al., 2021). This could have affected the deposition of the PEI as unencapsulated DOXO could lower the ζ-potential of the polyelectrolyte solution in the peristaltic pump, leading to a less effective deposition. The

phenomenon of DOXO lowering ζ -potential in LBL functionalisation contrasts what was reported by Hashemi et al. (Hashemi et al., 2018) as they saw a slight increase with the inclusion of DOXO during their LBL functionalisation of graphene oxide. However, they provided no explanation as to why this occurred. The sample containing only DAX (Figure 5.15c) is consistent with the unfunctionalised particles and does not affect the deposition of the layers.

The FT-IR data for each sample is presented below in Figure 5.16. All of the layers in each sample have very distinct peaks at ~1559cm⁻¹, ~1405cm⁻¹, ~1015cm⁻¹, 1010cm⁻¹ and ~922cm⁻¹ (NIST; Rani et al., 2021). These peaks all correspond to sodium acetate that was used as a buffer to keep the pH stable. ~1559cm-1 corresponds C=O stretching in the carboxylic acid group. ~1405cm⁻¹ corresponds to the stretching mode of –CH₂ scissoring. ~1015cm⁻¹ and 1010cm⁻¹ corresponds to the CH₃ rocking vibration. The ~922cm⁻¹ corresponds to the O-H bend in the carboxylic acid group. This data has the same issues which are outlined in the FT-IR data above for the NPs that did not incorporate drugs and cannot be used for characterisation.

As with the particles without drugs, the characteristic peak at 1710 cm⁻¹ corresponding to the protonation of the carboxylate group with the deposition of AA(Lawrie et al., 2007) can be seen in Figure 5.15 A and B in layers 2 and 4, and in C at layer 6. This provides some evidence towards the fact that AA was deposited onto the surface of these NPs at these layers. For the deposition of CH, a band at ~1530cm⁻¹ appears due to the partial protonation of the amine group. This is shown on the spectra as a shoulder on the peaks at 1560cm⁻¹ peak corresponding to COO⁻ from the sodium acetate and is present in most layers in each of the samples suggesting that that CH has indeed been partially deposited.

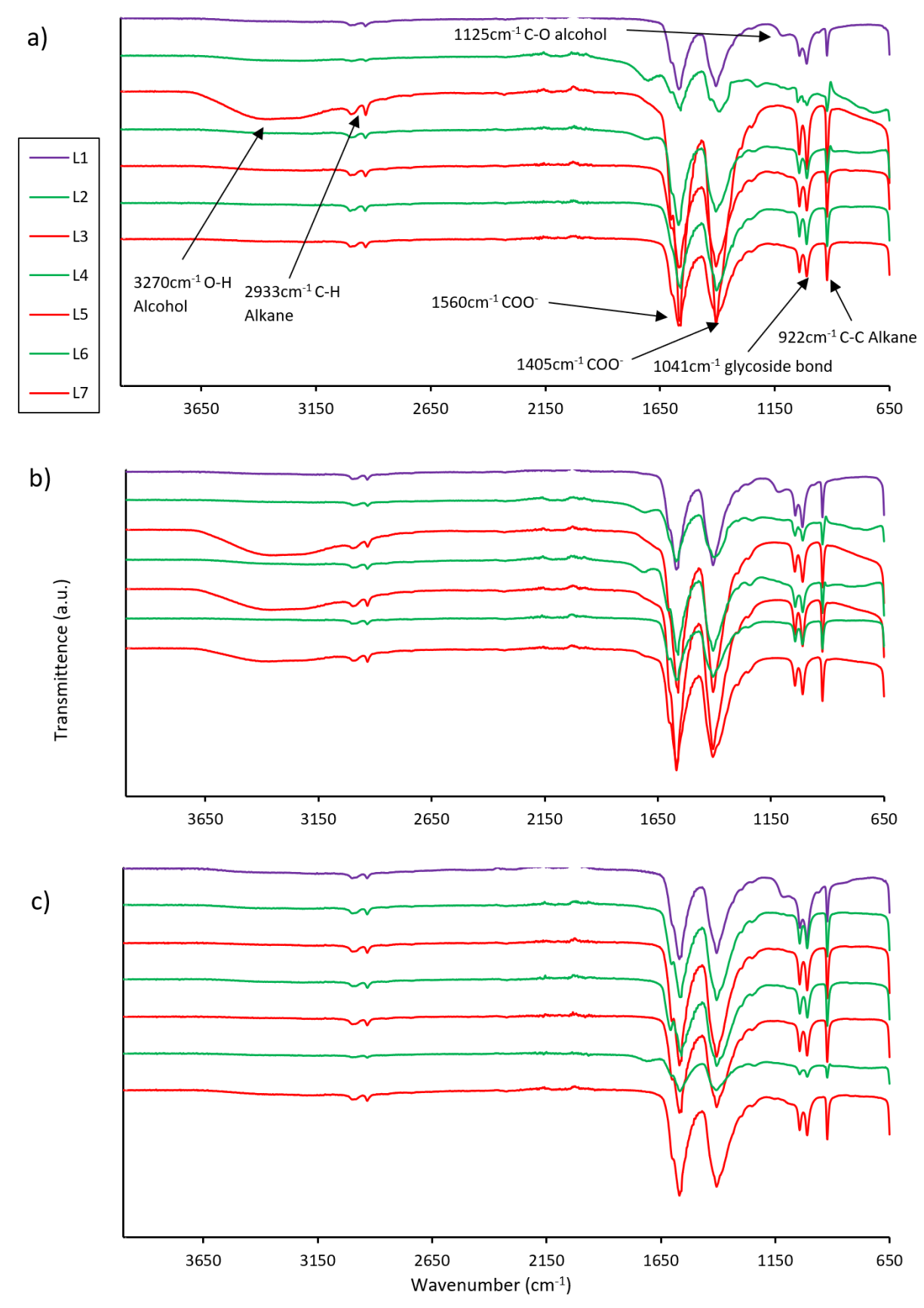


Figure 5.15 - FT-IR of the layer-by-layer process for each drug loading experiment; a) Both drugs, b) DOXO and c) DAX

XPS analysis was undertaken for each freeze-dried samples that were taken after the completion of each layer. The XPS data for each sample is summarised in the tables below (Table 5.7, Table 5.8, Table 5.9).

Table 5.7 - Summary of the XPS data for each layer sample of the DOXO loaded sample. Top – wide survey scan, bottom – C 1s, N 1s, O 1s

		At %										
Scan		Survey										
Element/Bond	Phosphorus	Carbon	Calcium	Nitrogen	Oxygen	Sodium						
Binding energy (eV)	131.69	284.69	348.55	399.48	131.69	531.19						
Sample												
Doxo L1	0.18	70.64	0.87	1.18	23.35	3.79						
Doxo L2	0	63.06	0.37	0.87	29.52	6.17						
Doxo L3	0.07	62.73	0.09	0.07	29.15	7.88						
Doxo L4	0	59.04	0	0.37	31.28	9.31						
Doxo L5	0	56.86	0	0.31	32.7	10.13						
Doxo L6	0.03	59.37	0.12	1.29	30.89	8.31						
Doxo L7	0.07	61.99	0.39	0.4	29.52	7.62						

		At %										
Scan		C 1	ls			N 1s				O 1s		
Element/Bond	sp2/C=C	sp3/C-C	C-O	C=O	C-NH2	CONH2	C-NH3+	Nitrate	C=O	C-O	Na KLL Auger	
Binding energy (eV)	284.53	284.88	286.03	288.34	399.48	400.4	401.3	406.5	531.16	532.5	535.73	
Sample												
Doxo L1	16.69	53.41	15.8	14.1	93.96	6.04	0	0	65.79	24.6	9.61	
Doxo L2	15.79	30.63	33.32	20.26	97.23	0	2.77	0	59.94	27.94	12.11	
Doxo L3	12.66	45.98	20.25	21.12	52.42	47.58	0	0	69.06	17.01	13.94	
Doxo L4	10.02	46.82	15.81	27.34	83.85	13.34	2.8	0	79.57	5.98	14.44	
Doxo L5	10.51	48.95	9.48	31.06	86.24	13.66	0	0	79.54	4.38	16.08	
Doxo L6	3.46	56.6	16.59	23.25	94.86	0.23	4.91	0	71.76	14.76	13.48	
Doxo L7	10.17	57.28	7.3	25.25	91.89	8.11	0	0	79.72	6.19	14.1	

Table 5.8 - Summary of the XPS data for each layer sample of the DAX loaded sample. Top — wide survey scan, bottom — C 1s, N 1s, O 1s

		At %										
Scan		Survey										
Element/Bond	Phosphorus	Carbon	Calcium	Nitrogen	Oxygen	Sodium						
Binding energy (eV)	132.56	284.71	348.06	399.71	132.56	531.14						
Sample												
Dax L1	11.02	54.16	5.65	2.97	30.52	4.79						
Dax L2	0.35	58.46	1.07	1.4	31.24	7.47						
Dax L3	0	60.03	0.22	0	30.99	8.76						
Dax L4	0.06	58.63	0.35	0.63	31.86	8.47						

	At %											
Scan		C 19	5			N 1s				O 1s		
Element/Bond	sp2/C=C	sp3/C-C	C-O	C=0	C-NH2	CONH2	C-NH3+	Nitrate	C=0	C-0	Na KLL Auger	
Binding energy (eV)	284.6	284.89	286.03	288.34	399.48	400.4	401.3	406.5	531.15	532.51	535.74	
Sample												
Dax L1	11.02	52.57	16.27	20.14	78.35	7.93	13.73	0	83.75	7.63	8.62	
Dax L2	5.22	52.37	16.8	25.6	84.45	5.42	10.12	0	72.12	16.07	11.81	
Dax L3	13.88	54.91	3.66	27.55	97.2	1.34	1.46	0	81.79	3.32	14.89	
Dax L4	12.76	52.22	7.5	27.52	85.19	0	14.81	0	79.15	5.77	15.09	
Dax L5	11.57	47	7.07	34.35	79.19	20.81	0	0	81.06	3.3	15.65	
Dax L6	10.01	48.39	19	22.6	95.25	0.8	3.94	0	67.31	20.65	12.04	
Dax L7	14.53	47.68	9.25	28.53	100	0	0	0	79.21	6.57	14.21	

Table 5.9 - Summary of the XPS data for each layer sample of the loaded sample loaded with DOXO and DAX. Top — wide survey scan, bottom — C 1s, N 1s, O 1s

		At %										
Scan		Survey										
Element/Bond	hosphoru	Carbon	Calcium	Nitrogen	Oxygen	Sodium						
Binding energy (eV)	134.77	284.7	346.77	385.34	134.77	531.27						
Sample												
BD L1	0.41	2.26	2.26	0.98	30.85	7.32						
BD L2	0.19	58.84	1.3	0.92	31.18	7.57						
BD L3	0.12	53.32	0.32	0.42	34.93	10.89						
BD L4	0.11	66.65	0.06	1.44	26.24	5.51						
BD L5	0.18	62.09	0.2	0.4	29.42	7.72						
BD L6	0.11	63.52	0.23	0.96	28.91	0.23						
BD L7	0.02	61.94	0.34	0.65	32.29	4.76						

		At %										
Scan		С	1 s			N 1s				O 1s		
Element/Bond	sp2/C=C	sp3/C-C	C-O	C=O	C-NH2	CONH2	C-NH3+	Nitrate	C=O	C-O	Na KLL Auger	
Binding energy (eV)	284.53	284.88	286.01	288.33	399.48	400.4	401.3	406.5	531.16	533.93	535.79	
Sample												
BD L1	11.96	51.66	11.25	25.13	92.11	7.89	0	0	83.76	3.97	12.26	
BD L2	10.2	51.46	12.43	25.91	88.26	0	11.74	0	75.59	11.24	13.17	
BD L3	12.51	48.94	4.41	34.14	79.73	20.27	0	0	83.17	2.06	14.77	
BD L4	9.89	51.31	18.21	20.59	95.11	4.73	0.16	0	62.83	26.31	10.86	
BD L5	13.46	53.11	8.35	25.08	96.96	1.03	2.01	0	76.77	8.17	15.06	
BD L6	16.54	42.02	20.11	21.33	85.62	14.38	0	0	63.39	23.48	12.13	
BD L7	10.99	28.43	34.05	36.54	81.76	18.24	0	0	37.75	51.34	10.91	

As with the particles without drugs, the XPS results for the layers also show contamination from the SAB. However some analysis can still be done using the N 1s peak ratio of amine protonation as before (Lawrie et al., 2007).

In the DAX only and DOXO only samples this change in protonated amine is plain to see in all layers from L2 to L7. I.e. in the DOXO sample the AA layers are the only ones that contain protonated amine. In the sample that contained both drugs this trend is not seen between L4 and L6 with L5 increasing in amine protonation and L6 decreasing which is the opposite of how it should be if the layers were deposited properly. As before, the ratio of amine protonation is much lower than what was shown by Lawrie et al. This shows that the LBL deposition is only partially successful.

Transmission electron microscopy was used to visualise the particles (Figure 5.16, Figure 5.17 and Figure 5.18) and perform size analysis. ImageJ was used to measure the particles and produce a distribution (Table 5.10).

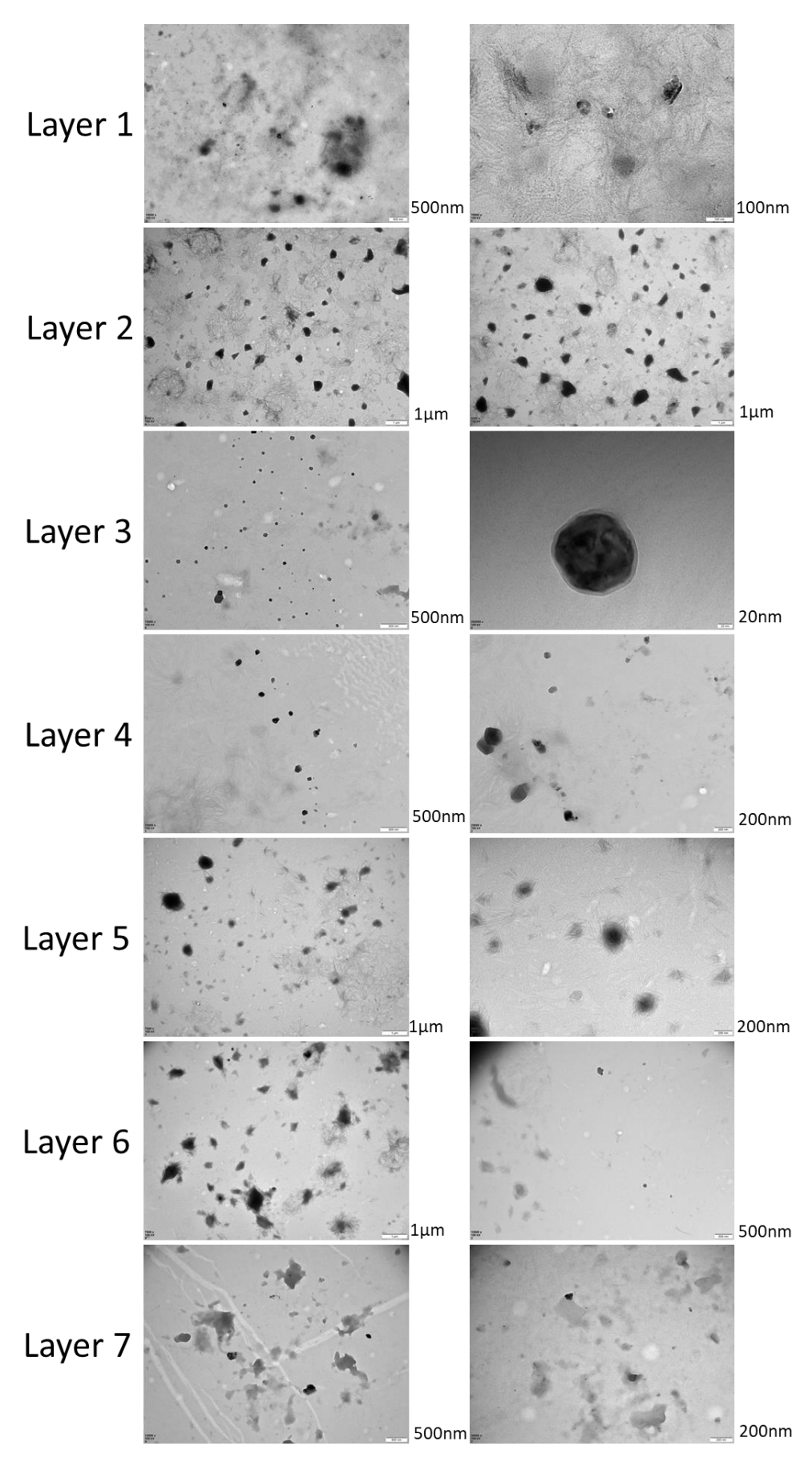


Figure 5.16 - TEM images of each layer of the layer-by-layer process with DOXO

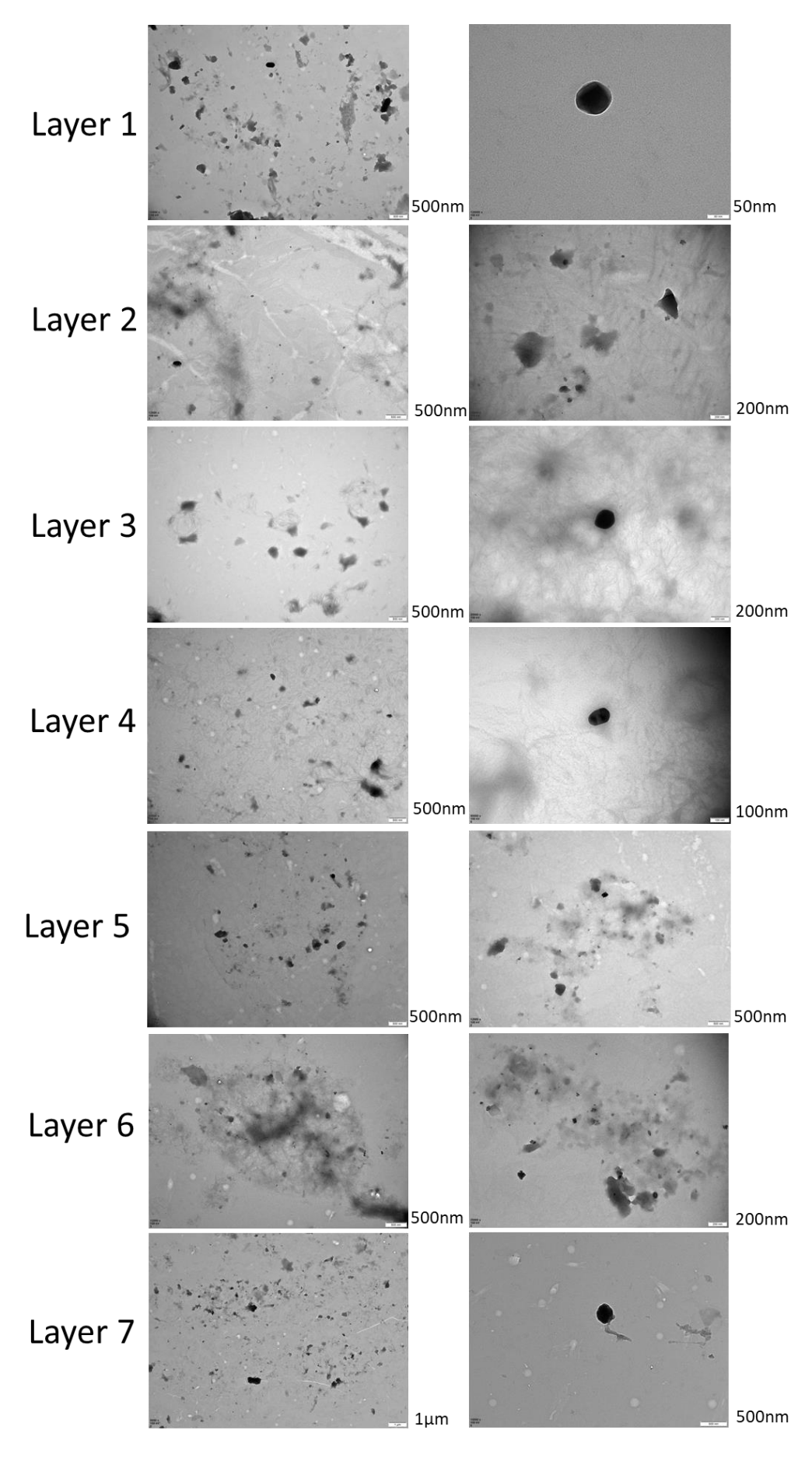


Figure 5.17 - TEM images of each layer of the layer-by-layer process with DAX

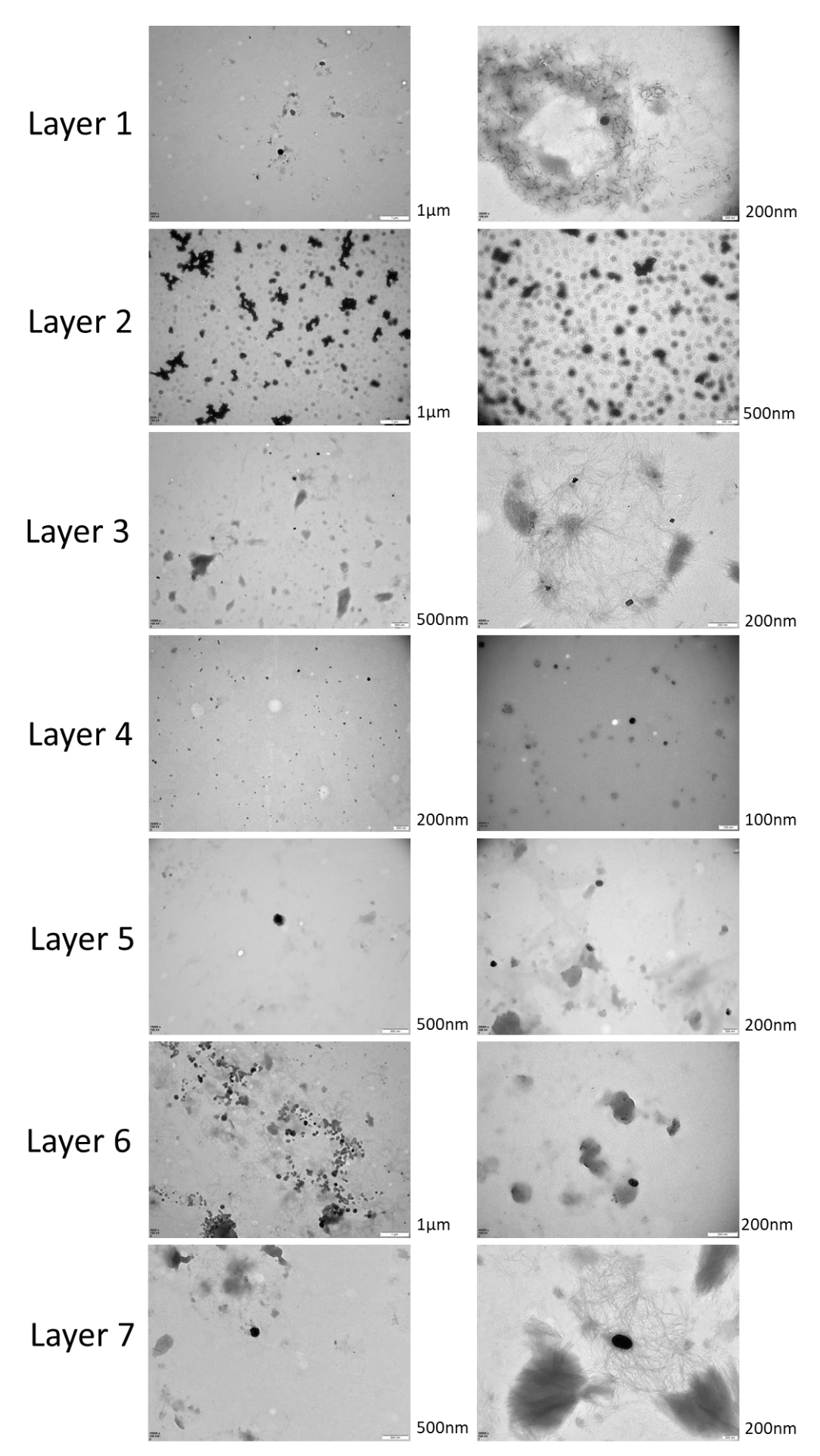


Figure 5.18 - TEM images of each layer of the layer-by-layer process both drugs

Table 5.10 - Average particle size per layer of each sample as measured using ImageJ from the TEM images

Layer	Particle size		
	DOXO only	DAX only	DOXO and DAX
1	135 ± 88	137 ± 52	153 ± 44
2	319 ± 109	113 ± 76	182 ± 40
3	64 ± 26	247 ± 40	57 ± 22
4	93 ± 43	156 ± 60	37 ± 9
5	276 ± 127	125 ± 57	128 ± 63
6	383 ± 167	92 ± 50	129 ± 46
7	200 ± 112	192 ± 81	214 ± 50

Unlike the particles without drugs, no trend was observed in the size of the particles in relation to the layer. The sizes of the particles differed wildly and the distribution of sizes at each layer was wide. This gives further evidence to the fact that the SAB penetrates the layers and causes inconsistent layer deposition. The morphologies of the particles are also consistent with the images of the particles without drugs.

This data also showed that the addition of drugs increased the size of the initial PEI functionalised particles (layer 1) when compared with the particles without drugs. These had an average size of 97 ± 22 , which was smaller than those shown in the table above. Increase in layer size with drug loading has been seen previously (Hashemi et al., 2018) and is likely to be caused by inclusion of drugs in the first layer (Alkekhia et al., 2020) because inclusion of the drugs as CaP NPs has little effect on size (Hashemi et al., 2018; Son & Kim, 2017; Tsikourkitoudi et al., 2020).

5.2.3 In-vitro drug release tests

To test the encapsulation efficiency of the NPs, samples of the cores and the final layer by layer capsules were investigated and reported in Table 5.11.

Table 5.11 - Encapsulation efficiency for each individual drug in all the different sample types

Drug sample type		Ĭ.	per sample (g)	Encapsulation efficiency (%)	
		Core	Capsule	Core	Capsule
Doxorubicin only		1071.27	0	65.64	0
Docetaxel only		87.02	144.52	60.43	16.72
Combined	DOX	1040.38	952.22	63.75	9.72
	DAX	108.27	47.46	75.12	5.49

It is shown that the first layer cores showed a good encapsulation efficiency between ~60 and 75%; for example, the DTX only sample the EE was 60.43% and the DAX EE in the sample that contained both drugs was 75.12%. This can be attributed to the porosity of the CaP NP templates and its great ability to entrap drugs (Yoncheva et al., 2020).

The encapsulation efficiency of the particles with the LBL technique applied was much lower (<17%) for all the samples. DOXO showed a 100% decrease in the overall drug content implying that not only did the LBL technique fail to load any drugs, but the drugs encapsulated in the core were also released. The error in this sample is also very high so this result is not accurate; however, the maximum encapsulation efficiency the standard deviation would allow for this sample would still be lower than the value for the cores, implying that regardless of the actual value, some drug was lost. The reason for this poor encapsulation can be attributed to the SAB effecting the layer deposition as is outlined in the TEM and therefore not protecting the drugs from premature release as the layers should (Yoncheva et al., 2020).

The *in-vitro* drug release of the nanocapsules in PBS was measured using UV-Vis taking measurements over time for 240 hours. The release of DOXO from the samples is outlined in Figure 5.19 and the release of DAX is outlined in Figure 5.20. None of the samples showed a plateau in this time which suggests that not all the drugs had been released completely at the 240-hour mark. The samples transitioned from an initial burst release to a steady release around 6-8 hours.

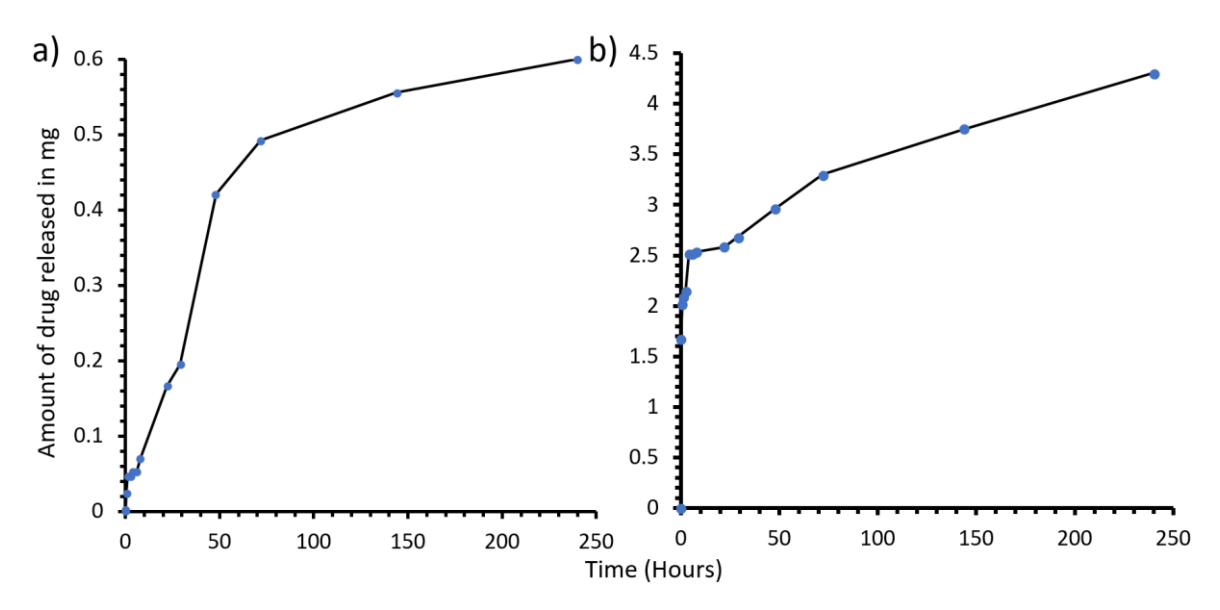


Figure 5.19 - Drug release curves for the DOXO release data - a) DOXO only sample, b) both drug sample

There are some differences between how the DOXO releases when it is by itself when compared to when the drugs are loaded together in the nanocapsule. Firstly, a lot more of the drug is released in the combined sample up to 4.3mg released versus the 0.6mg released in the single drug sample. Both values are much higher than what was found to have been encapsulated in the encapsulation efficiency tests. This suggests that the release is contaminated. This is most likely to be CH as this has been shown previously to have absorbance peaks nearby the wavelengths tested (480nm). A UV-Vis spectra of CH was reported by Akmaz et al. (Akmaz et al., 2013) showing an absorption peak at around between 300 and 500nm with a maxima around 400nm. This suggested CH is releasing from the nanocapsules due to the poor layer adhesion as shown in the TEM. Further analysis of this drug release data could use techniques such as Fluorescence emission of DOXO (White, 2004) or High-pressure liquid chromatography (Tekkeli Evrim Kepekci & Kiziltas Volkan, 2017).

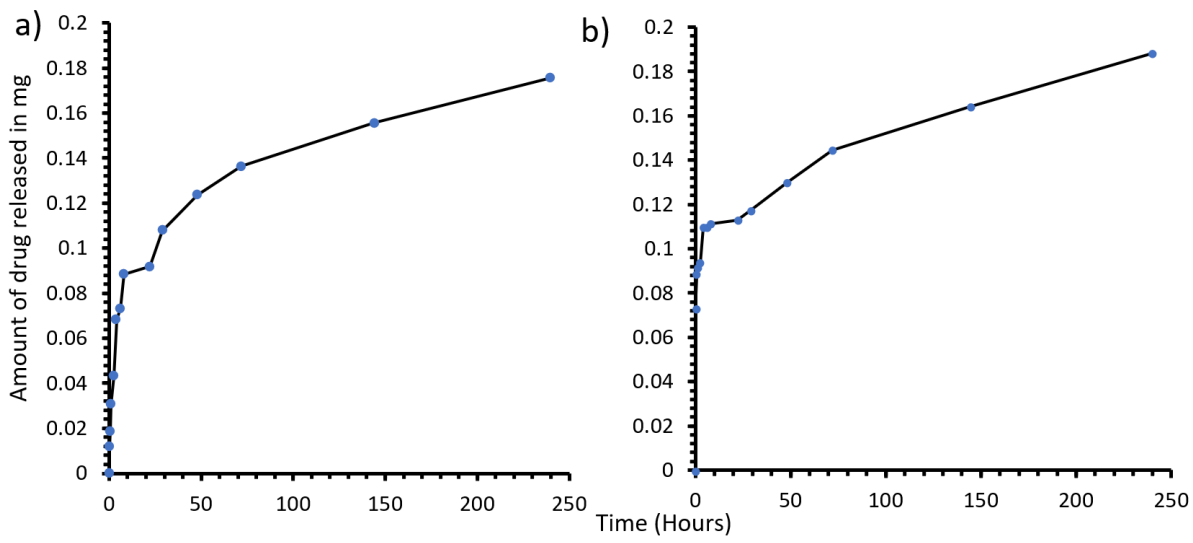


Figure 5.20 - Drug release curves for the DAX release data — a) DAX only sample, b) both drug sample.

The drug release of DAX from both the single drug sample and the combined release were consistent showing a very similar curve and amount of drug released from both sample types. However, the released amount of drug around 0.18mg is double what was found to have been encapsulated in the encapsulation tests. This again shows that the sample is contaminated with CH, which has a characteristic absorption peak at 250nm (Thamilarasan et al., 2018). For confirmation, calibration curves were obtained for the materials used in the synthesis at the wavelengths used for the detection of drugs to show what might have been causing the contamination (Figure 5.21).

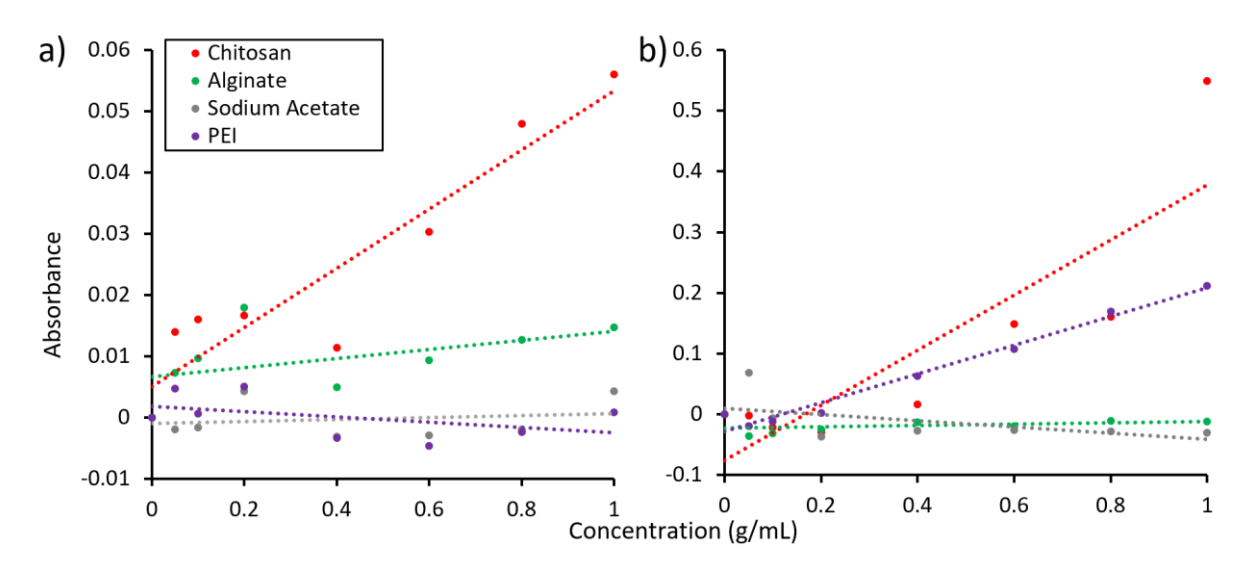


Figure 5.21 - UV-Vis calibration curves of different materials at different wavelengths – a) 480nm b) 230nm

Figure 5.21 A shows the results at 480nm. This shows that the material most likely to affect the DOXO results is CH as this has strong trend of absorbance with concentration. AA might also have some effect as this also have a strong trend but does not absorb as highly as at a concentration of 1mg per mL they have an absorbance of 0.014 against CH's 0.055. The flat trend lines and low absorbance of PEI and Sodium acetate show that these do not affect the results of DOXO drug release.

Figure 5.21 B shows the results at 230nm. This shows that the material most likely to affect the DAX results is CH as this has strong trend of absorbance with concentration. PEI might also have some effect as this also have a strong trend but does not absorb as highly, as at a concentration of 1mg per mL PEI has an absorbance of 0.2 against CH's 0.55. The flat trend lines and low absorbance of AA and sodium acetate show that these do not affect the results of DAX drug release. It was concluded that because the release curve of the DOXO and DAX in the combined sample was the same, just at a different ratio of concentration, the same material was contaminating all the samples, given the data above. This shows that CH is most likely this contaminant. This is due to poor layer adhesion on the NP.

5.2.4 In-vitro cell tests

Cell tests were run to evaluate the nanocapsules drug release effect against cancer cells. Two different OS cell lines, U2OS cells and SAOS-2 were used, as seen in literature previously (Ahmadi et al., 2020; Danışman-Kalındemirtaş et al., 2021; Li et al., 2018; Peng et al., 2014).

PrestoBlue test was used to evaluate the metabolic activity against control cells seeded without the presence of the NPs. Figure 5.22 and Figure 5.23 outline the viability of the cells after being subject to the NPs for 24 hours. Free DOXO and DAX data was also included as a comparison for both cell types.

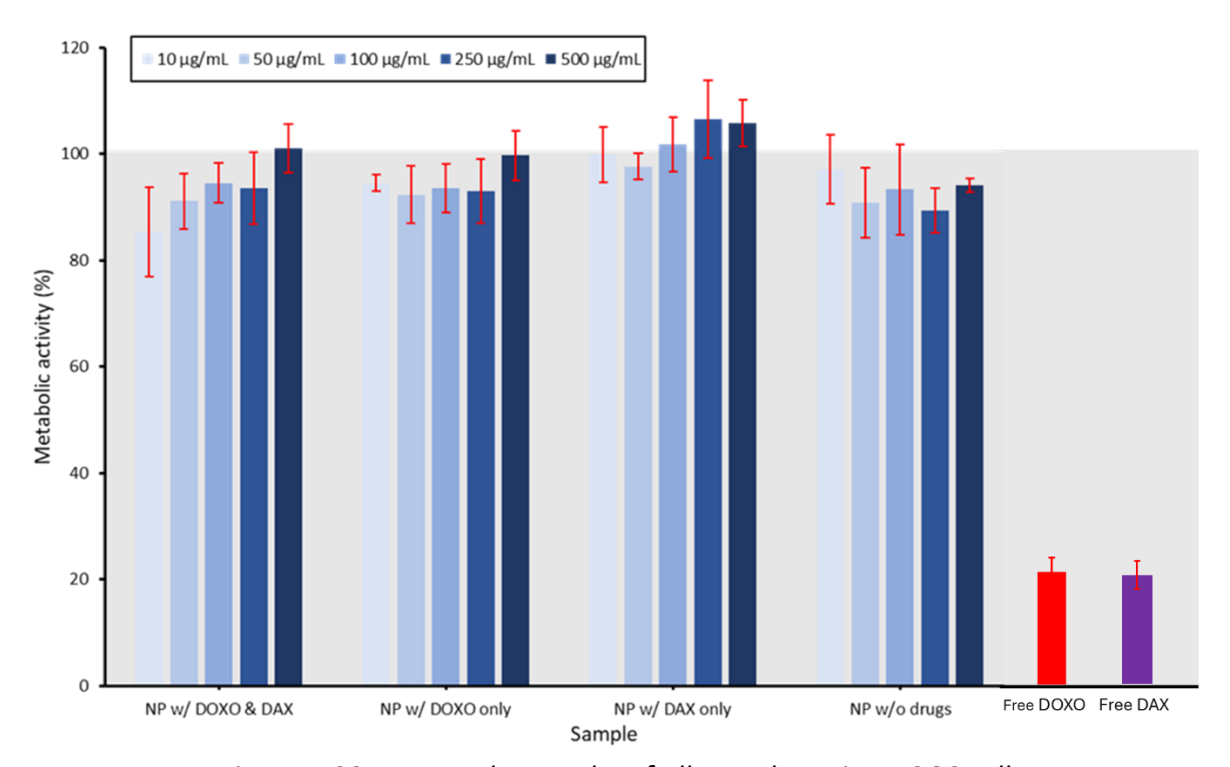


Figure 5.22 - PrestoBlue results of all samples using U2OS cells.

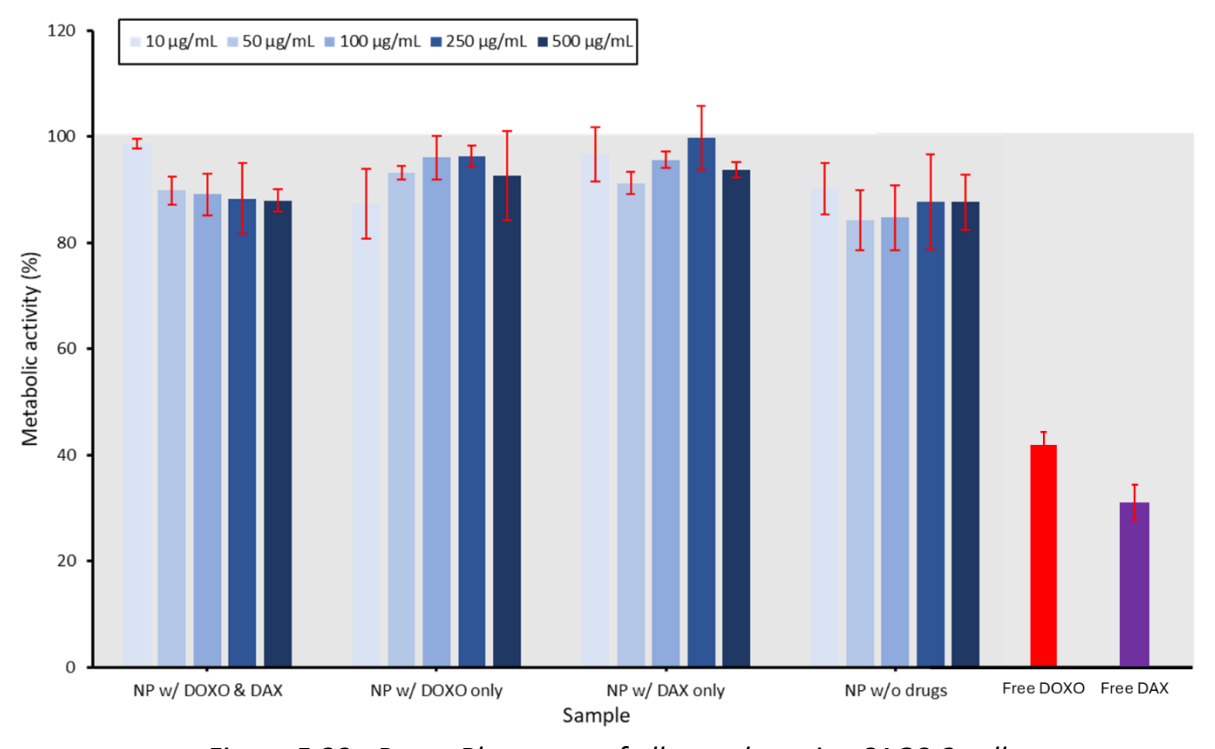


Figure 5.23 - PrestoBlue essay of all samples using SAOS-2 cells.

Statistical analysis was run on the data and each concentration set and was compared between each sample and the control with a Bonferroni corrected P-value. It was found that none of the U2OS cells exposed to the nanoparticle samples had a significant decrease in metabolic activity. Most of the SAOS-2 cells also did not have a significant decrease in metabolic activity aside from NP w/ DOXO & DAX, NP w/ DOXO only and NP w/ DAX only at 50μg/mL and NP w/ DOXO & DAX and NP w/ DAX only at 500μg/mL. Even though these results are significantly different from the control, it does not show that these nanoparticles have a large effect against the cells. This shows that the drugs did not release from the particles, were not encapsulated, or were encapsulated at such a small concentration that once released they were ineffective, corroborating the data found in the encapsulation efficiency and drug release tests. DOXO and DAX are well known for their effectiveness against SAOS-2 (Rudnick-Glick et al., 2016) and U2OS cell lines (Graat et al., 2006; D. Z. Wang et al., 2015). This is also shown in the graphs with the inclusion of free DOXO and DAX at concentrations of 10µg/mL. This shows a significant decrease in the viability of the cells exposed to free drugs as compared to the NP that contained the different combinations of drugs. Docetaxel data used for comparison was taken from a paper by (D. Z. Wang et al., 2015)

5.2.5 Functionalisation with carbon dots

The CDs were included in the AA layers because they were characterised by a negative ζ -potential value. Z-potential analysis was used to investigate the CDs incorporation during the LBL deposition (Figure 5.24).

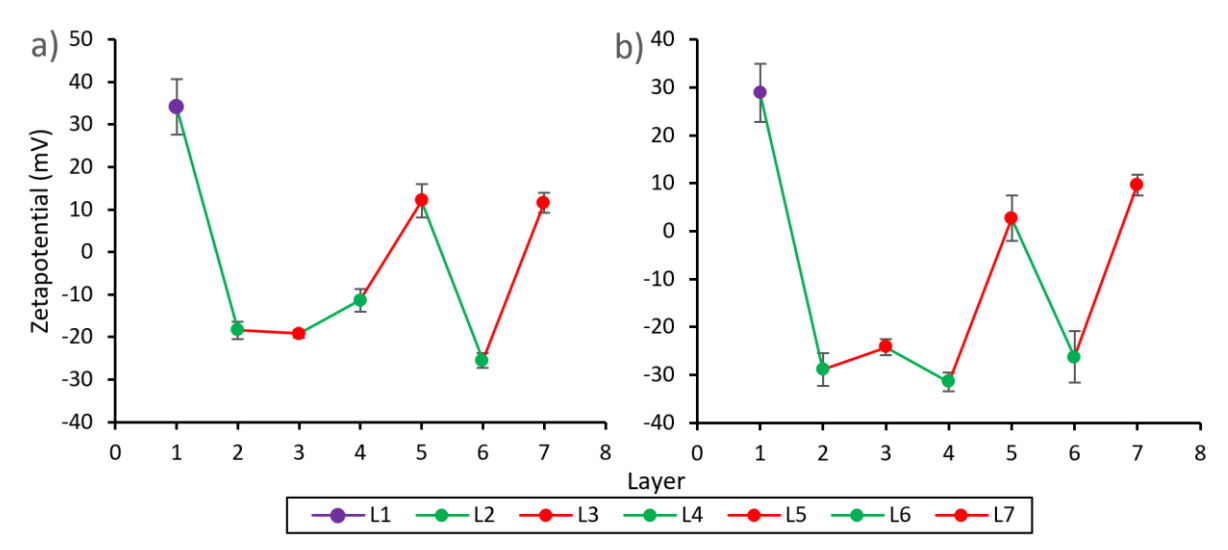


Figure 5.24 - ζ-potential data of the layer-by-layer formation of nanoparticles – left: without carbon dots, right: with carbon dots.

Both conditions evidenced similar ζ -potential values at each layer of the deposition, with a consistent change from positive to negative ζ -potential from the 3^{rd} layer deposition. The 3^{rd} layer deposition in both samples is shown here not to be successful due to the charge not significantly increasing from the alginate deposition for the second layer. The reason for this is most likely user error as a washing step may have been missed. The consistency between the samples showed that the inclusion of the CDs did not affect the deposition of the layers which is the important finding for this particular analysis.

The photoluminescence emission spectra and QY analysis of the plain CDs, unfunctionalised capsules and the CDs functionalised capsules was acquired and shown in Figure 5.25, Figure 5.26 and Figure 5.27 respectively. This process started with the UV-Vis testing of different solutions of the materials to find 5 solutions for each sample with absorbances of around 0.02, 0.04, 0.06, 0.08 and 0.1. These solutions were used for the QY analysis and the 0.1 were used for the photoluminescence emission.

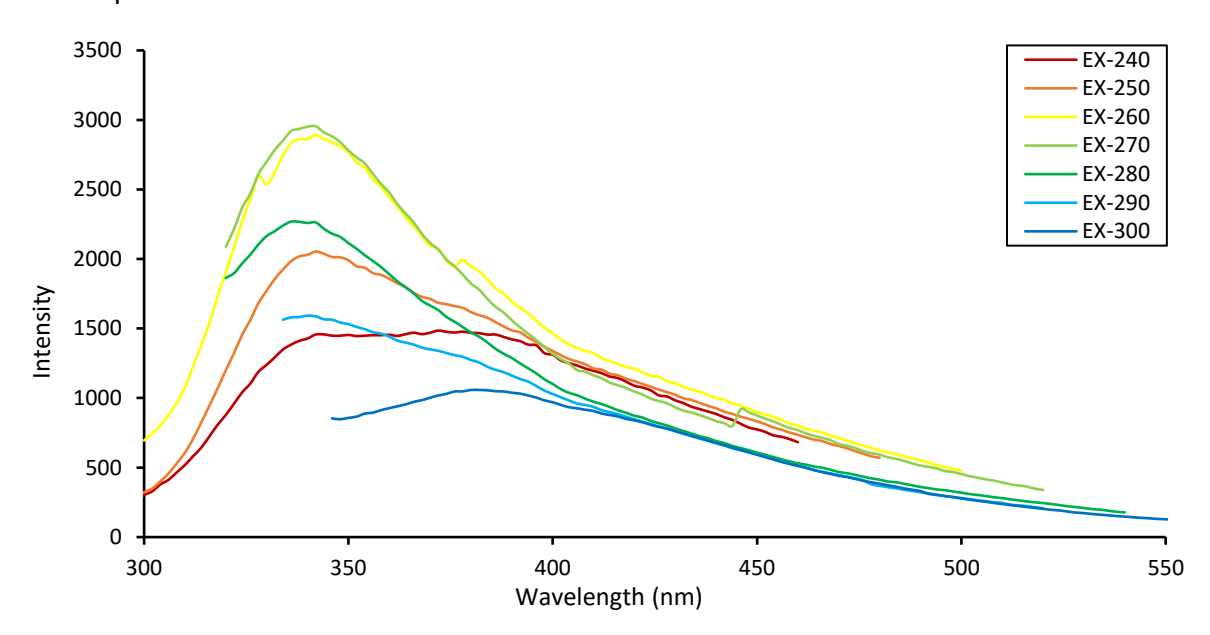


Figure 5.25 - Photoluminescence data for bare carbon dots - emission data at increasing excitation wavelengths.

The CDs were found to have two emission maxima; a stronger emission at 340nm with the most intense emission from an excitation of ~270nm (light green line), and a weaker emission at 380nm, the most intense of which was from an excitation wavelength of ~250nm (orange line). 270nm excitation was used for QY calculations. The QY was found to be 31.7%; this is high for biomass derived CDs (Sadhanala et al., 2021) and much higher than those produced in the previous chapter (7%). This is unexpected because they were produced by the similar

method as previously described; a 2-hour microwave reaction in aqueous conditions at 200°C. However, previously the dots were freeze dried, these carbon dots were dried overnight in an oven. This suggests that drying methods could potentially influence the photoluminescent properties of the carbon dots. This is something that is not currently researched in literature and could be pursued further in future research.

The non functionalised NPs were expected to be non-photoluminescent, but it was shown that they show a similar emission as the CDs (Figure 5.26), a 340nm emission the most intense of which was from an excitation of 280nm. The NPs were half as intense as the CDs at their strongest emissions. This emission must have been caused by the materials used in their synthesis, most likely CH, as this was shown to have some absorbance in the UV-Vis experiments of the materials presented above. The photoluminescence properties have been previously outlined by Motelica et al. in their paper investigating the properties of functionalised CH films. They outline photoluminescence emission at ~395nm at an excitation wavelength of 320nm. Interestingly, CH is a popular choice as a biomass precursor for CDs (Desmond et al., 2021; Mathew et al., 2020; Pawar et al., 2019), so it stands to reason there would be some inherent photoluminescence with this material. The QY was not gained for this sample.

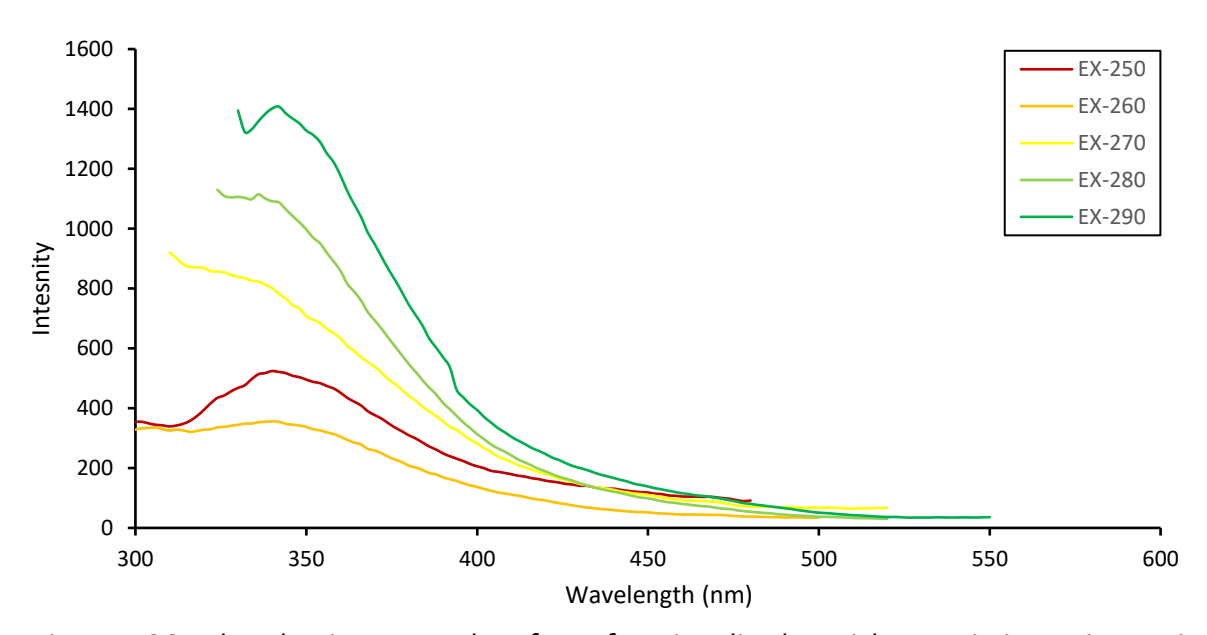


Figure 5.26 - Photoluminescence data for unfunctionalised particles - emission at increasing excitation wavelengths.

The nanocapsules that were functionalised with the CDs (Figure 5.27) were shown to have the most intense emission at \sim 7500, this was at the same 340nm wavelength as the other particles and was caused by an excitation wavelength of 280nm.

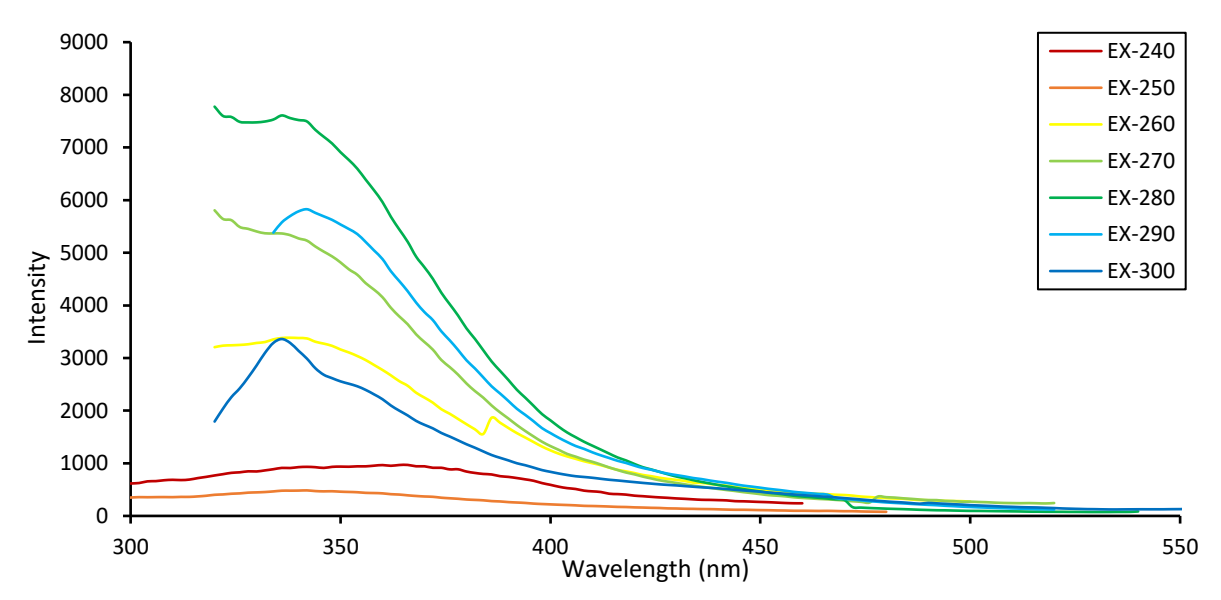


Figure 5.27 - Photoluminescence data for nanoparticles functionalised with carbon dots – emission data at increasing excitation wavelengths.

This clearly shows that the inclusion of CDs does enhance the photoluminescence of the nanocapsules in terms of intensity even past the point the CDs show by themselves. This can be explained that the photoluminescence from the CH within the capsules and the CDs has an additive effect and when combined it shows at a higher intensity than each of the sources by themselves. The QY for these particles is 35.9% as further evidence of this.

5.2.6 Summary

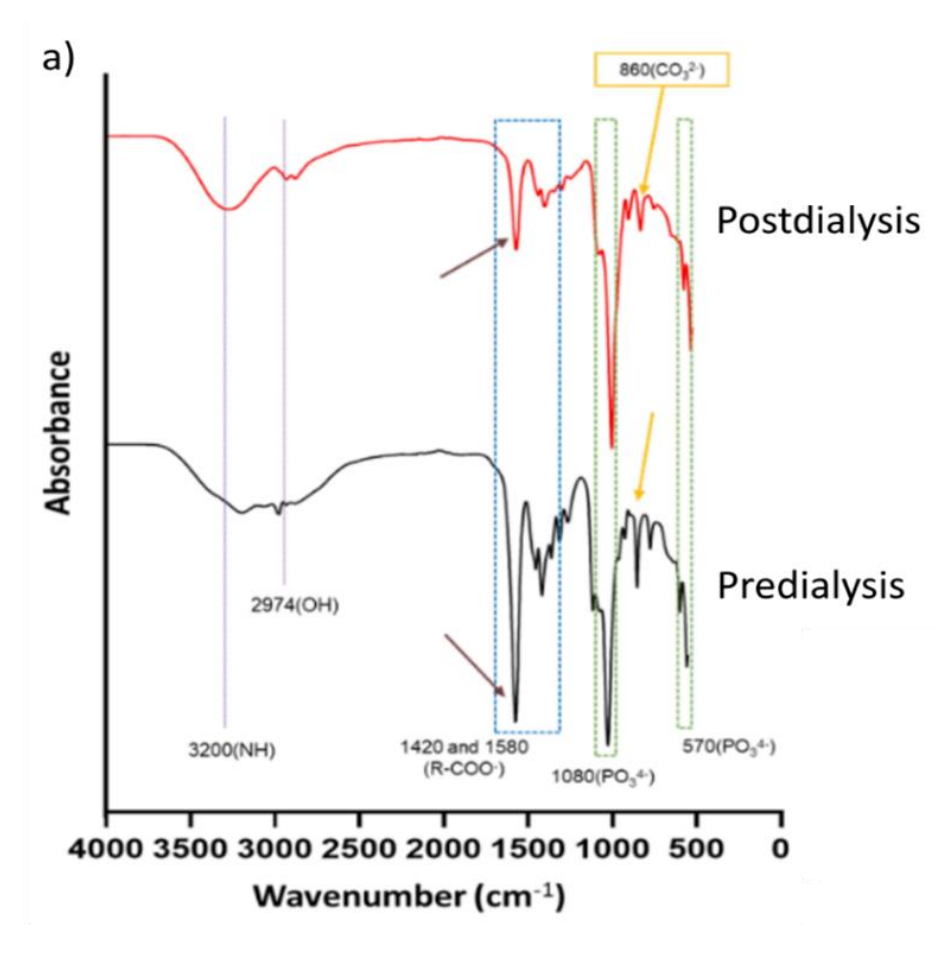
In summary, the synthesis of CH-AA LBL capsules on PEI functionalised LBL capsules for the encapsulation of anticancer drugs and CDs to create a nanotheranostic device was not successful due to the use of a SAB, which penetrated the capsules causing the destabilisation of the layer, confirmed by TEM. This led to loss of encapsulated drugs, causing the particles to be ineffective against OS cell lines according to viability testing. However, the encapsulation of CDs within the layers increased the photoluminescence intensity and QY when compared against plain particles and CDs. This shows potential in combining the techniques for creating a nanotheranostic device.

5.3 Chitosan and chondroitin sulphate layer by layer capsules functionalised with anticancer drugs and carbon dots.

This section investigates the application of the LBL technique on PAH functionalised CaP templates for the encapsulation of anticancer drugs and CDs. First the application of PAH is characterised.

5.3.1 Physio-chemical characterisation of PAH-coated calcium phosphate cores

FT-IR was used to determine the functional groups on the PAH functionalised particles. To this end, unfunctionalised particles were prepared under the same conditions for comparison (Figure 5.28). It was shown that the role of dialysis was fundamental in the removal of carbonate ions from the NPs.



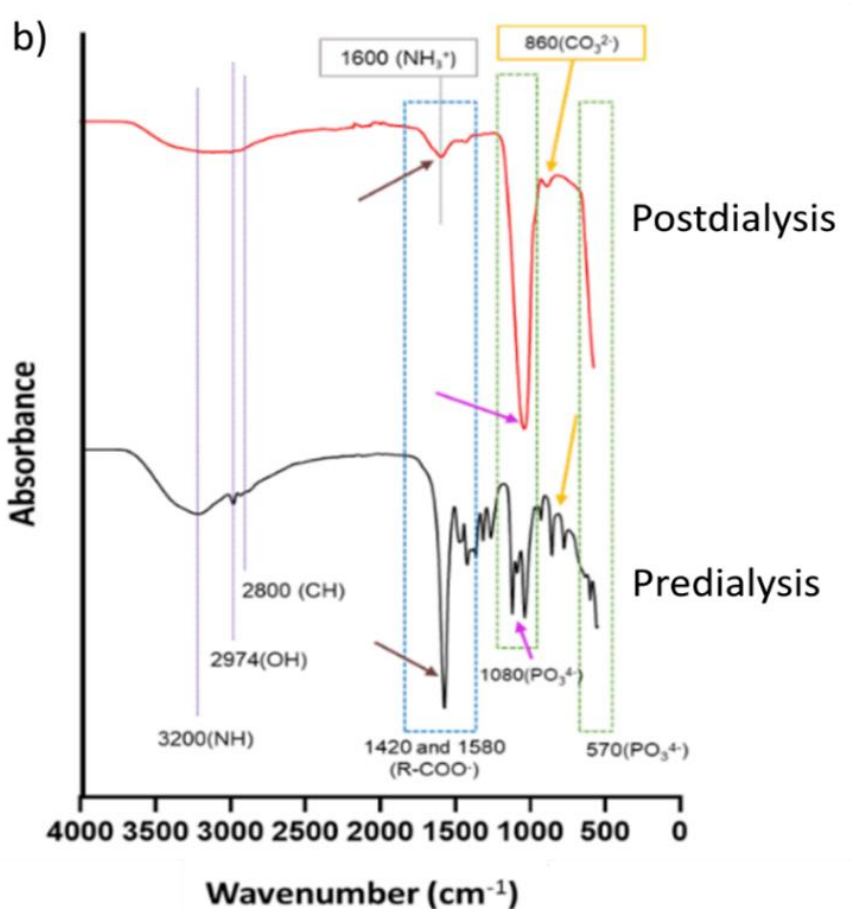


Figure 5.28 - FT-IR data for calcium phosphate nanoparticles pre and post dialysis: A)

Unfunctionalised, B) Functionalised with PAH

FT-IR analysis of CaP (A) and CaP PAH (B) was conducted before (black) and after (red) dialysis. In all samples, carbonate peaks were observed around 1427, 1490 and 860 cm⁻¹. Additionally, phosphate peaks were detected at 570 cm⁻¹ and 1080 cm⁻¹. The region below 1000 cm⁻¹ was interpreted following the findings of Urch et al. (Urch et al., 2009; H. Yang et al., 2019). The peak at 570 cm⁻¹ was attributed to apatite PO₄³⁻, while the peak at 864/868 cm⁻¹ indicated the presence of CO₃²⁻. This specific type of carbonate was the type B carbonate apatite (Pawar et al., 2019), which can be responsible for the surface aggregation of NPs (Urch et al., 2009). Comparing the CaP samples, the freshly precipitated ones exhibited a more intense carbonate peak at 1427-1590 cm⁻¹ than the dialysed sample. The intensity of this peak decreased with dialysis, showing the desorption of excess carbonate anions. This desorption favoured the creation of a hydrated layer from the bulk solution on the NPs' surface. Hence, the dialysis phase was effective in removing carbonate residues. Dialysis is an effective and simple technique for polymeric NP preparation and allows for a narrow size distribution (Krishnamoorthy & Mahalingam, 2015) and removal of excess reagents. This is an advantage over other techniques such as ultracentrifugation, by preventing the need for sonication to disperse the formed pellet. Especially when sensitive biomolecules are present (Barnewitz, 2023).

For the CaP_PAH sample, the carbonate peak at 1427-1490 cm⁻¹ was highly intense upon NP precipitation. However, following dialysis, the peak exhibited a significantly lower intensity, indicating PAH polymer deposition on the CaPs' surface (identified by NH³⁺ deformation vibration and N-H bending groups between 1480 and 1600 cm⁻¹). Dialysis also resulted in a more even and peak-free spectrum below 1000 cm⁻¹, eliminating several harder-to-identify, low-intensity peaks. This emphasised the stabilisation of the particles through polymer deposition (Urch et al., 2009).

After dialysis, the peaks of the phosphate groups showed no changes between the coated and uncoated samples. However, the freshly precipitated CaP_PAH sample displayed a split peak at 1080 cm⁻¹ related to the phosphate group, which was not visible in the CaP sample. this peak showed lower intensity in absorbance than the CaP sample, attributed to PAH polymer deposition on the NPs' surface, which contained an amine group (C-N stretching) around 1020-

1200 cm⁻¹. Following the removal of excess polymer by dialysis and particle stabilisation, the phosphate peak reappeared with similar intensity to the other samples.

Smooth peaks observed between 2950 and 3200 cm $^{-1}$ were associated with the presence of water in the CaP sample since these samples were not freeze-dried. Conversely, the freeze-dried CaP_PAH samples analysed in powder form exhibited this smooth peak, which can be linked to the polymer deposition on the CaP particle, rich in amine groups (N-H stretch 3400 cm $^{-1}$) and C-H stretch groups around 2800 cm $^{-1}$ that imparted a positive charge to the particle. The amine peaks were present before and after dialysis in the CaP_PAH sample. However, the low intensity of the characteristic PAH peaks between 2950 and 3200 cm $^{-1}$ was attributed to the limitations of the technology used. FT-IR allows the analysis of chemical bonds present at a penetration depth of up to 60 μ m (Götz et al., 2020), making it detectable at a size greater than that of the NPs.

Subsequently, the samples underwent ζ -Potential analysis, and the charge of the solutions used was 40.1 ± 0.5 mV for CH and 35.4 ± 1.2 mV for PAH. The ζ -Potential of the NPs was analysed under different conditions: precipitated NPs (only wash), dialyzed NPs (Before NaCl), NPs in the stabilising solution (With NaCl), and 3 and 7 days after their synthesis (Day 3 and Day 7). The results are presented in Table 5.12.

Table 5.12 - Summary of ζ -potential data of calcium phosphate nanoparticles with different synthesis

Materials	Zetapotential ± SD (mV)						
	Only	Before	With NaCl	Day 3	Day 7		
	Wash	NaCl	(15mM)				
CaP	-17.3 ± 0.6	+2.8 ± 0.0	-2.4 ± 0.2	-0.9 ± 0.2	1.9 ± 1.0		
CaP_PAH 0.5mg/mL	32.6 ± 1.2	12.9 ± 1.8	11.1 ± 0.3	9.9 ± 0.8	11.9 ± 0.4		
CaP_PAH 1mg/mL	16.8 ± 0.8	11.9 ± 0.8	13.4 ± 0.3	14.7 ±	18.4 ± 0.5		
				0.4			
CaP_PAH 2.5mg/mL	17.7 ± 0.4	12.9 ± 0.4	14.6 ± 0.3	13.5 ±	14.2 ± 0.8		
				0.3			
CaP_PAH 5mg/mL	14.1 ± 2.2	19.6 ± 0.8	13.3 ± 0.2	14.9 ±	16.1 ± 0.6		
				0.2			
CaP(doxo)_PAH	14.6 ± 0.5	15.6 ± 0.5	/	/	/		
1mg/mL							

The particle combinations exhibited ζ -Potential ranges between +25 mV and -25 mV. Stable colloids are usually shown outside this range (Samimi et al., 2019); thus, a 12-hour stirring

process was necessary to enhance the stability of the produced NPs. Surface charge is not the only factor effecting colloidal stability of these particles, however. Other factors such as concentration (Fuller & Köper, 2018), temperature, pH and ionic strength (García-García et al., 2009) of the solution can also affect the stability. For example, the addition of NaCl to the solution has been shown to increase the ionic strength of a solution of polyelectrolyte which will increase surface charge magnitude (Ngulube et al., 2017). NaCl added to polyelectrolyte solution increases polyelectrolyte adsorption (Scheepers et al., 2021) leading to faster growth of polyelectrolyte multilayers (Tang & Besseling, 2016).

Consistent with the findings of Urch et al. (Urch et al., 2009), CaPs displayed a net negative charge upon precipitation, attributed to the presence of CO_3^{2-} groups on the NPs' surface, as confirmed by FT-IRs. This excess negative charge is crucial for the CaP_PAH system. The charge of the CaPs reduced in magnitude close to zero after dialysis, providing further evidence of successful filtration of the NPs, which facilitated the removal of excess carbonate (the peak between 1427-1490 cm⁻¹ displayed significantly lower intensity). Over the following days, the charge remained stable around zero.

The NPs coated with cationic polymers consistently showed a positive charge, indicating the deposition of the coating. The surface charge of the coated NPs did not undergo significant variations following dialysis. However, even though the ζ -Potential of the PAH-coated NPs was significantly lower than the charge of the PAH solution, the 0.5 mg/mL concentration of PAH was considered the saturation point of the surface. This is because the ζ -Potential of the PAH-coated NPs did not exhibit significant changes with increasing polymer concentration in the solution. As a precaution, a concentration of 1 mg/mL PAH in solution was selected for future NP productions since it fell within the saturation values evaluated.

The NPs encapsulating DOXO displayed no significant difference in terms of charge compared to the CaP_PAH particles. CH-coated CaPs exhibited similar ζ -Potential results to CaP_PAH, both after dialysis and several days after their synthesis.

The encapsulated amount of DOXO within the CaP(DOXO)_PAH core was determined using spectrophotometric analysis. It was found that the encapsulation efficacy was $49.7 \pm 3.9\%$ ($486.9 \pm 38.5 \,\mu g$) relative to the initial amount of drug supplied for CaP synthesis ($979.4 \,\mu g$). This indicates that each milligram of CaP(DOXO) PAH encapsulated approximately 4.9 ± 0.4

μg of DOXO. This is substantial drug encapsulation and clearly shows the porous nature of CaP structures.

The cumulative DOXO release profile for the CaP(DOXO)_PAH configuration was studied over 28 days, revealing a release of $67.5 \pm 2.5\%$ on day 1 and $91.1 \pm 4.6\%$ on day 7 (Figure 5.29A). Following day 1, the drug release was steady until stabilising by day 7, indicating gradual DOXO release from the core. Because of the spacing of the time points it is not possible to predict how gradual the release from day 1 to day 7 was. Extrapolating from the burst release, the maximum 91.1% release could have been achieved by 48 hours, future work should increase time points in this area to get a better understanding of the release curve. From day 7 to day 28, the profile showed a plateau, suggesting minimal DOXO release. This could be attributed to some of the drug being released prior to the release study. Figure 35B outlines the burst release trend line.

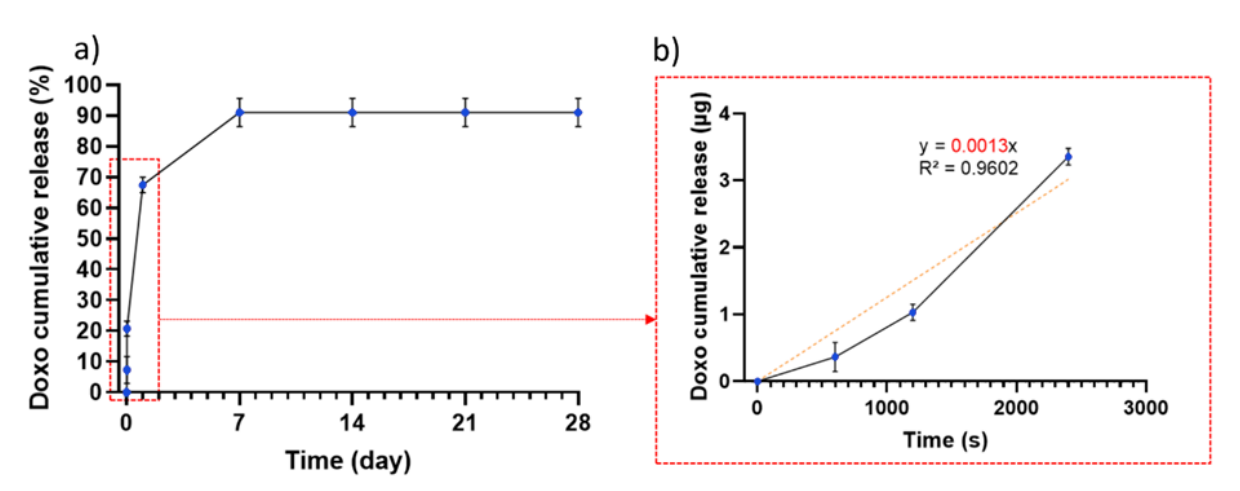


Figure 5.29 - Cumulative release of DOXO from CaP(DOXO)_PAH (A) and study of burst release rate (B)

DLS analyses of the CaPs coated by the cationic polymer and those that encapsulated the drug are shown in Figure 5.30.

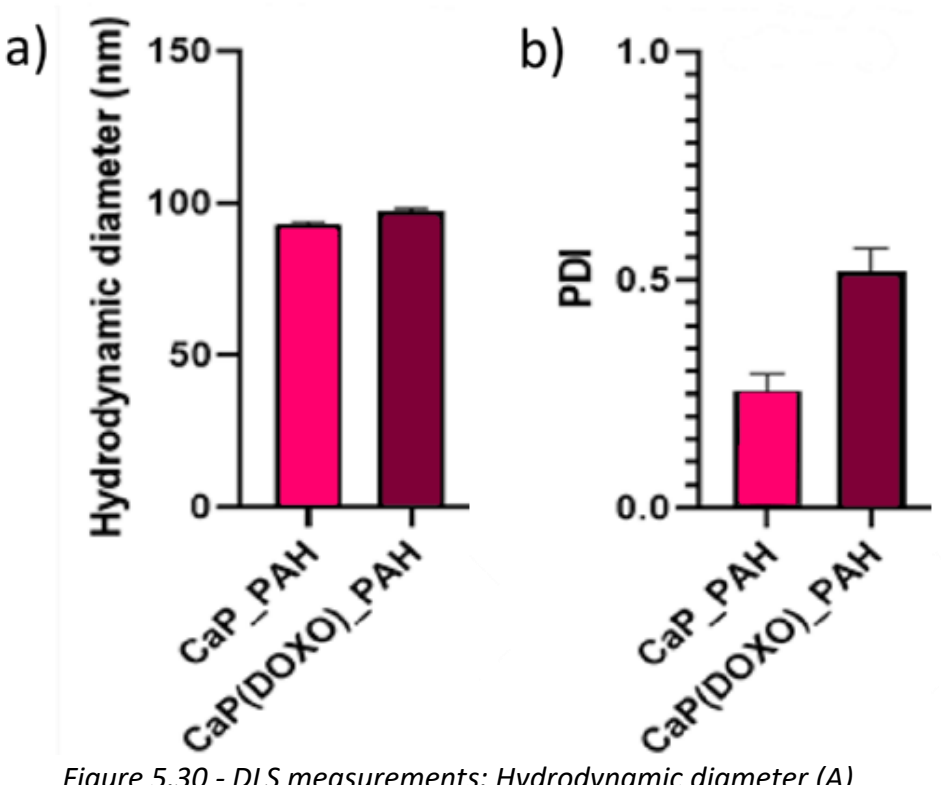


Figure 5.30 - DLS measurements: Hydrodynamic diameter (A) and PDI (B) of CAP_PAH and CaP(DOXO)_PAH

The hydrodynamic diameter of CaP_PAH (Figure 5.30) exhibited the lowest Polydispersity Index (PDI) of 0.25 ± 0.05 compared to the drug loaded sample which had a PDI of 0.5 ± 0.15 . This shows that CaP_PAH has a narrower molecular weight distribution, meaning they are more uniform in size as compared to CaP(DOXO)_PAH. The polydispersity of CaP(DOXO)_PAH might have resulted from the encapsulation of DOXO within the NP core.

To gain deeper insights into the obtained results, TEM analysis was performed on the mentioned structures (Figure 5.32), and compared against unfunctionalised particles, as depicted in Figure 5.31.

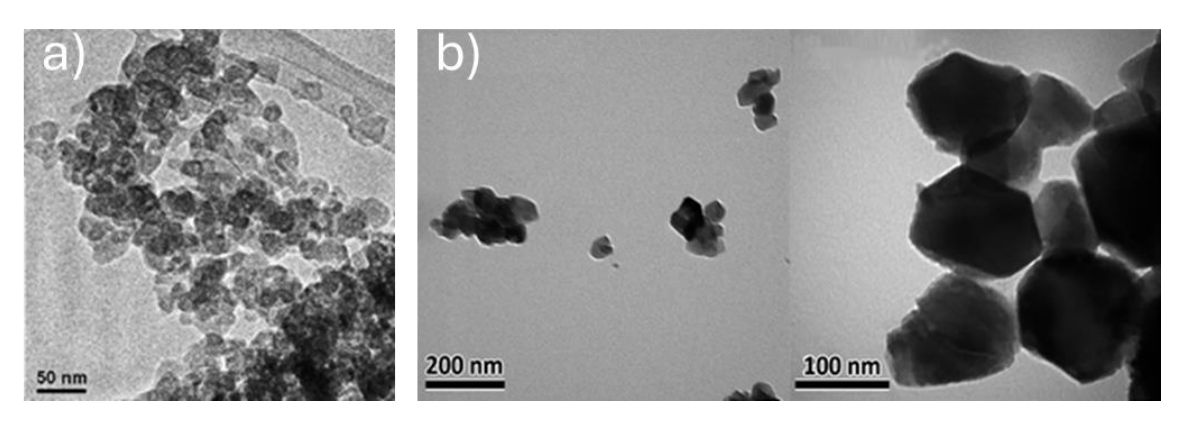


Figure 5.31 – TEM analysis from literature of unfunctionalized particles a) reprinted from Urch et al. (Urch et al., 2009) b) reprinted from Šupová et al. (Šupová et al., 2018)

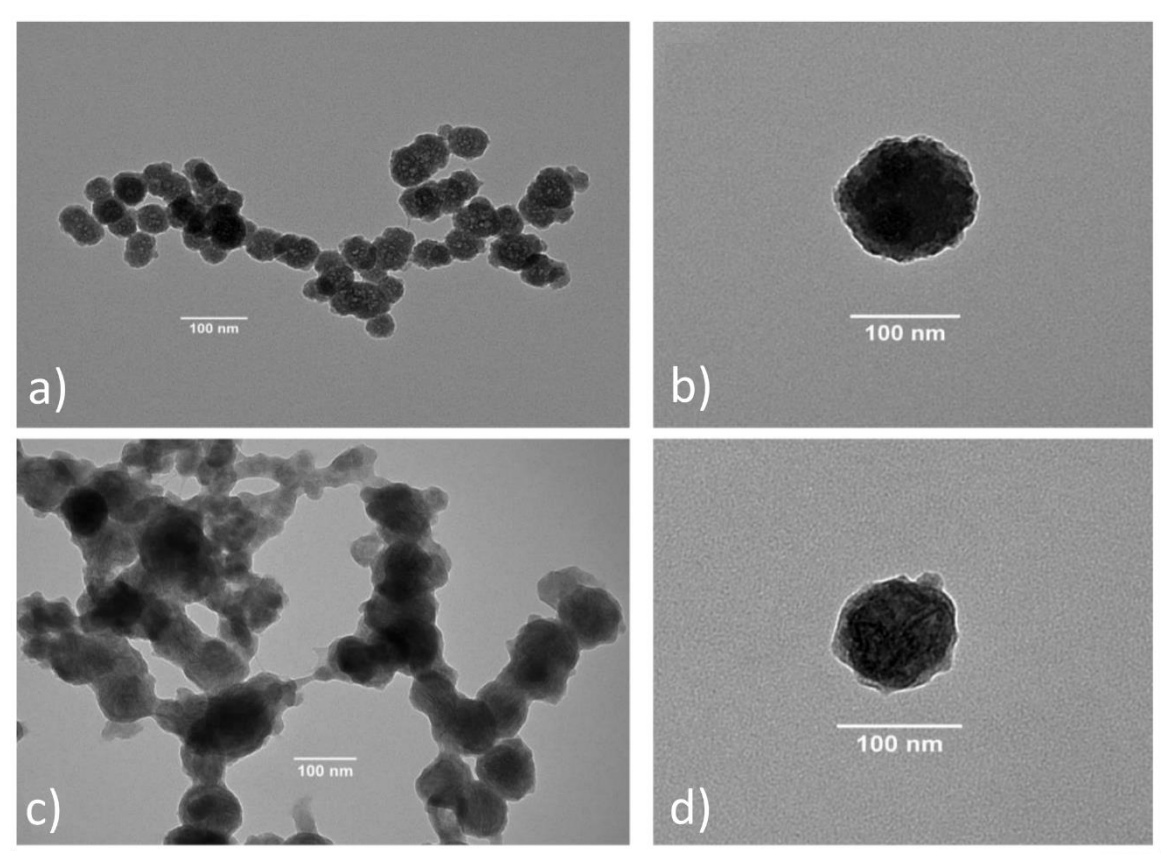


Figure 5.32 - TEM analysis of CaP_PAH (A-B), CaP(DOXO)_PAH (C-D)

Subsequently, the dimensions of the NPs were also calculated using ImageJ software. The results are shown in Figure 5.33.

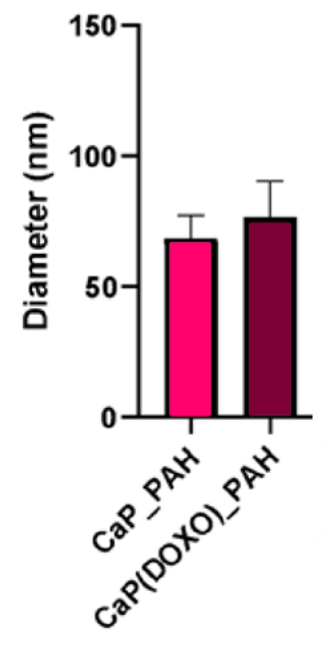


Figure 5.33 - TEM measurements of CaP_PAH and CaP(DOXO)_PAH

The sizes of NPs observed through TEM analysis for CaP_PAH (both with and without DOXO) were smaller than the diameters acquired from DLS measurements. A size increase was observed because of DOXO encapsulation in the core. Because of the wide standard deviations in the CaP(DOXO)_PAH samples, this was not a significant difference. It has been reported previously that drug encapsulation has little effect on CaP size (Son & Kim, 2017). In terms of morphology, both the PAH-coated NPs displayed a uniform, spherical, and rough shape as compared to unfunctionalised particles (Figure 5.31), with the roughness confirming successful cationic polymer deposition.

In conclusion, PAH deposition through polymer dissolution in an aqueous solution at pH 10 did not alter the core morphology or PE deposition, resulting in stable (minimally aggregated), spherical, uniform particles, particularly under 100 nm in size. Considering the combined results, the CaP_PAH and CaP(DOXO)_PAH types were carried forward as templates for subsequent LBL deposition.

5.3.2 Layer-by-layer functionalisation

The LBL process started using a similar process as same as previously described in the chapter. However, to address the issues posed using SAB, a solution was found by employing aqueous solutions of the same polyelectrolytes at a pH of 6 because of the insolubility of CaPs in water (Amjad, 1998). A pH of 6 also aligns with the pH sensitivity properties required for distinct drug release profiles under both neutral and acidic conditions, representing the physiological pH of blood and the internal pH of cancer cells. Ensuring high stability of NPs within the physiological pH range is crucial to prevent non-specific drug release during circulation in the body, thereby facilitating the distribution of the entire drug mass within the acidic cell environment (Hendi et al., 2020).

Initially, the deposition process involved evaluating the deposition of CH and CS polyelectrolytes at a concentration of 1 mg/mL for all layers on the CaP_PAH templates. Subsequently, layers of CH/DOXO with a concentration of 1 mg/mL were deposited, alternating with the deposition of CS at 1 mg/mL. ζ-potential analysis showed these concentration combinations did not lead to complete layer deposition for some of the CS layers. This was because the water had a different polarity and was controlled to a different pH than the previously used SA buffer. These changes affect the ionisation level of

polyelectrolyte chains and their effective charge (Padeste & Neuhaus, 2015) and change the ionic strength of solutions (Guzmán et al., 2020), which in turn impacts the interactions between polyelectrolytes (Guzmán et al., 2020) causing worse deposition of the material.

Taking these factors into account, the concentration of the polyanion was increased to 2.5 mg/mL for CS layers four and six (Figure 5.34A), referred to as CaP_7L configuration. Subsequently, the addition of DOXO (Figure 5.34B) and CDs (Figure 5.35) into the layers deposited on CaP(DOXO)_PAH particles was evaluated while maintaining the PE concentrations of the CaP_7L configuration. This resulted in configurations denoted as CaP_7D and CaP_7DC, respectively.

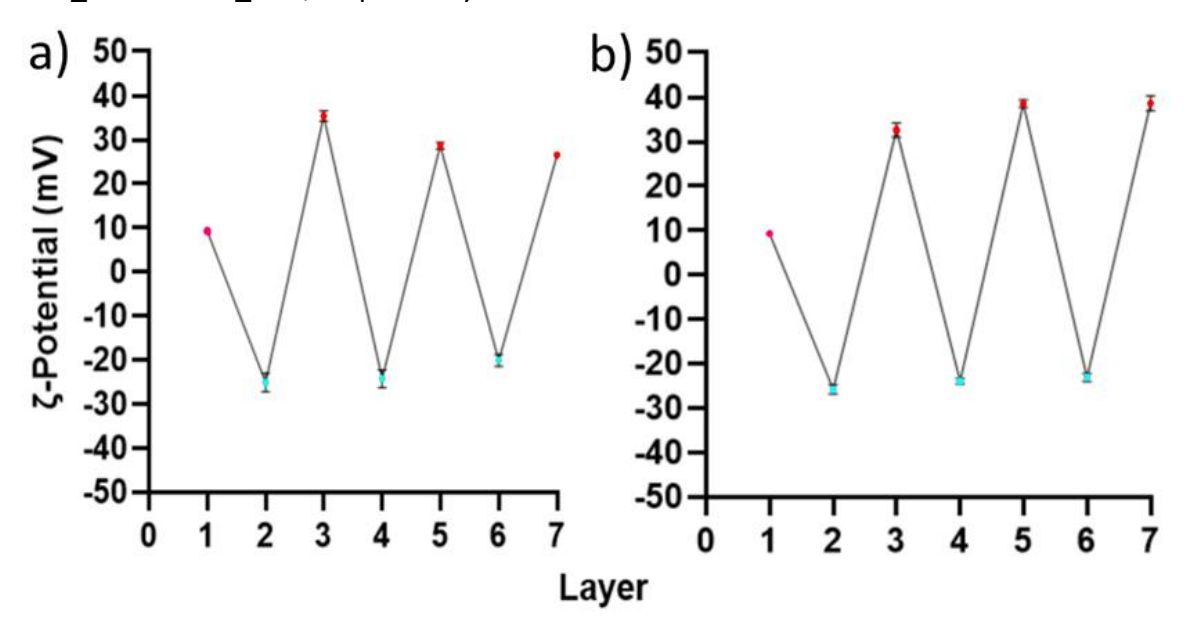


Figure 5.35 - ζ-potential graph of the LBL of CaP_PAH_7L (A) and CaP_PAH_7D (B)

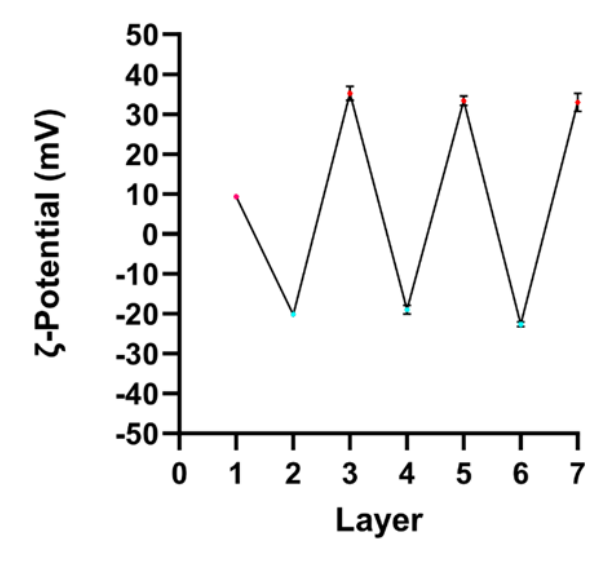


Figure 5.34 - ζ-potential graph of the LBL of CaP_PAH_7DC

The data shows all configurations of NPs exhibited an alternative "zig-zag" trend reaching the saturation values for all layers (±20mV). DOXO encapsulation did not have a significant impact on the surface charge of the layers maintaining saturation values below -20mV and above +30mV for the anionic and cationic layers respectively. However, the inclusion of CDs led to a more uniform trend in terms of alternative charge trend, that could be attributed to the higher negative charge of the CS/CD solution and the presence of the CDs. The charge of the CH layers consistently remained above 25 mV, while most CS layers exhibited a charge below -25 mV. These charge values made it so the NPs had a surface charge of high enough magnitude to repel similar templates during deposition, thereby providing stability of particles in dispersion (Mahobia et al., 2016).

During the LBL assembly process, each deposition step was visually observable (Figure 5.36). The particles exhibited a white colour after CH or CS deposition, a reddish hue following CH/DOXO deposition due to the colour of DOXO, and a brown tint after CH/CDs deposition as the CD solution was brown.







Figure 5.36 - NPs colour after deposition of CS or CH (A), CH/DOXO (B) and CS/DOXO (C)

To verify the encapsulation of CDs in the layers, the CaP_7DC particles were excited with a wavelength of 365 nm, resulting in a characteristic blue photoluminescence from the NPs solution, confirming the presence of the dots within the structure. (Figure 5.37)

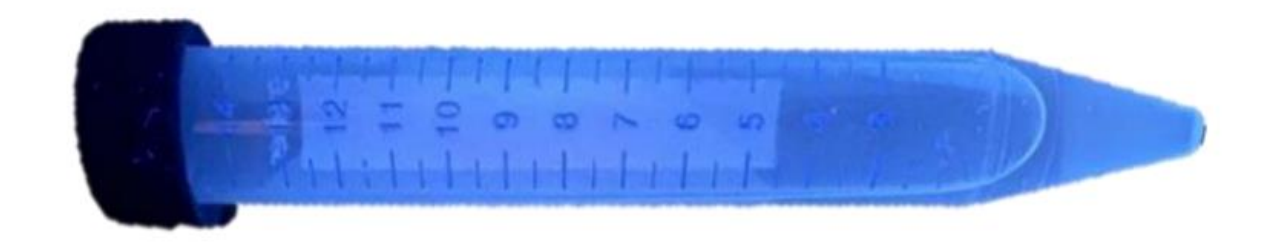


Figure 5.37 - Excitation of CaP_PAH_7DC by a wavelength of 365nm

DLS measurements showed that despite the deposition of seven layers on the CaP templates (Figure 5.38), both types of NPs were just slightly over 100 nm, confirming the nanometric size of the coating by comparing to the hydrodynamic diameter obtained from the first layer particles as outlined in Figure 5.30 above. The difference obtained was divided by 7 for each layer increase in diameter and then again by 2 to obtain the thickness of the layer. This method assumes a linear growth mechanism during deposition. The thickness of each layer was estimated to be ~3 nm for CaP_7L and ~2 nm for CaP_7DC.

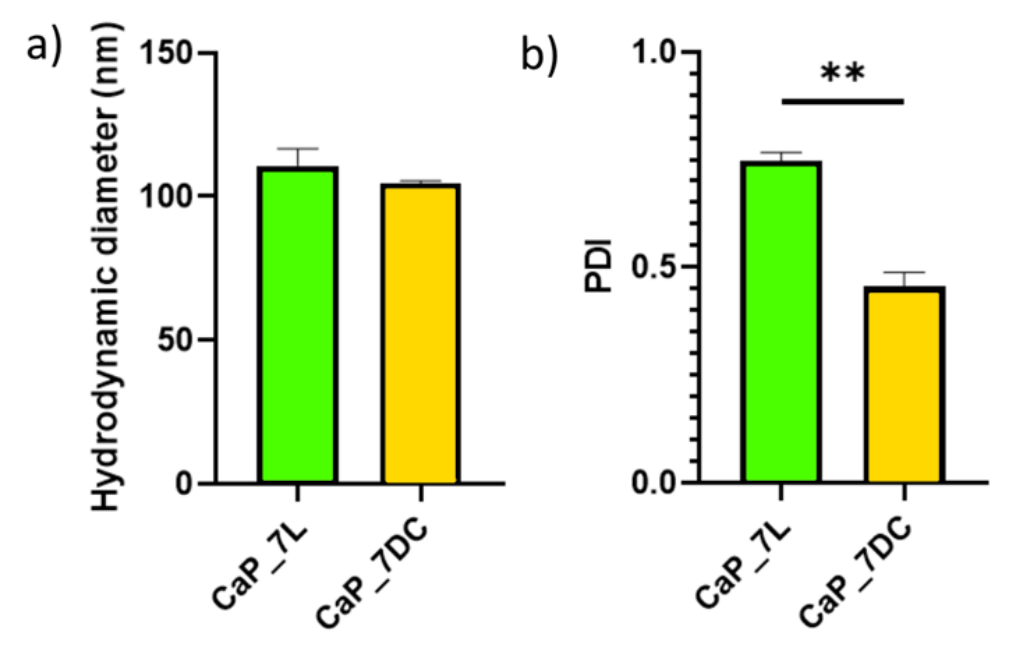


Figure 5.38 - DLS measurements: hydrodynamic diameter (A) and PDI (B) of CaP_7L and CaP_7DC

Despite similar sizes between the two types of NPs, their PDIs were distinct which suggests potential morphological differences between the particles. This could be attributed to improved intercrosslinking of the deposited layers in the case of CaP_7DC, due to the

stabilising effect of CDs in the negative layers leading to a smaller range in particle sizes. Literature shows that crosslinking stabilises the LBL technique (Blacklock et al., 2010).

To better understand the result provided by DLS analysis, CaP_7DC and CaP_7L were visualised by TEM, as shown in Figure 5.39.

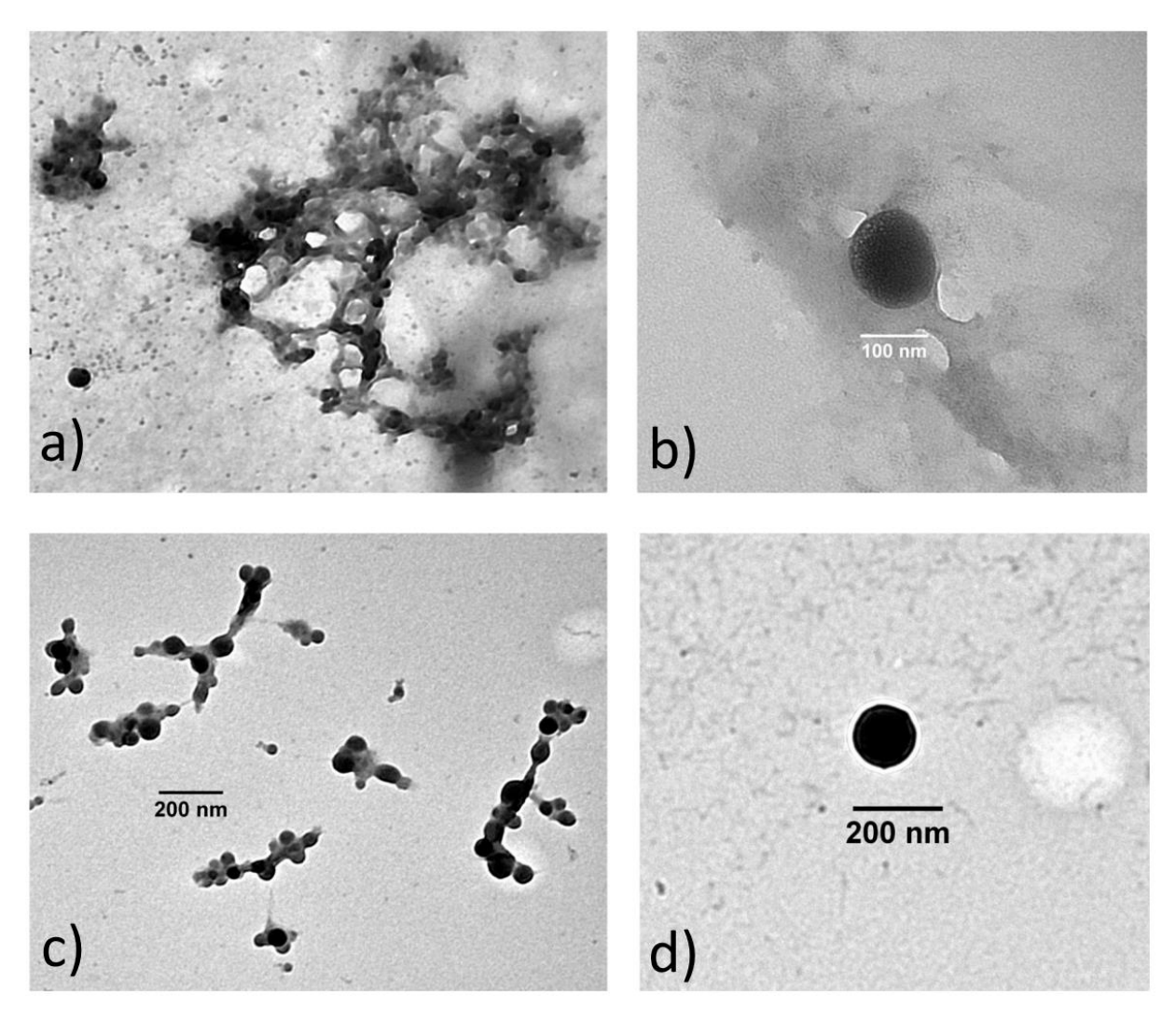


Figure 5.39 - TEM images of CaP_7L (A-B) and CaP_7DC (C-D)

When analysing both types of particles, a higher number of NPs were observed compared to the test performed with CaP_SAB_7L. NPs encapsulating CDs exhibited a more opaque appearance compared to the particles without dots, which appeared rougher and more faded. This is due to the opaque nature of the carbon dots; they appear very dark in TEM images. This observation demonstrated the successful encapsulation of the CDs by the deposited layers. In the case of CaP_7L, aggregates of particles with a different colour could be seen (Fig. A). (Guzmán et al., 2017). Such aggregates were also present in the CaP_7DC sample, but in

smaller size and quantity. These aggregates could account for the PDIs obtained from DLS analysis. Even though the sample contained a high amount of aggregation, there was a high number of individual NPs exhibiting a spherical and uniform morphology, with sizes consistent with DLS measurements. Specifically, CaP_7L had a size of 123.8 \pm 25.4 nm, while CaP_7DCs showed a size of 115.8 \pm 22.1 nm. As a result, the PDI values from DLS analysis were influenced by the composition of the analysis solution. Using a filtering with a 0.1 μ m syringe filter might help with this issue but this might not prove effective as these particle aggregates were generally below 200 nm in size. To further investigate, testing a higher centrifugation speed than 4.4k RPM could provide insight into the effect of this parameter on the formation of these aggregates.

The effectiveness of DOXO encapsulation within the layers of CaP_7D and CaP_7DC systems was assessed (Figure 5.40) and the amount of DOXO released from the NPs' core during the synthesis process was evaluated. To this end, six layers of PEs without CDs and drugs were deposited on the CaP(DOXO)_PAH particles. At each step of deposition and washing, the quantity of DOXO released from the NPs' core was quantified. After the creation of the multilayers, a DOXO release of $45.7 \pm 9.3\%$ ($2.69 \pm 0.54~\mu g$) was observed, and this release originated solely from the NPs' core. This outcome showed a high amount of diffusion of the drug from the core to the outermost layer during the synthesis of the NPs. This release could be because of the continuous stresses experienced by the NPs during the numerous stirring steps involved in deposition and washing solutions, as well as the multiple rounds of centrifugation.

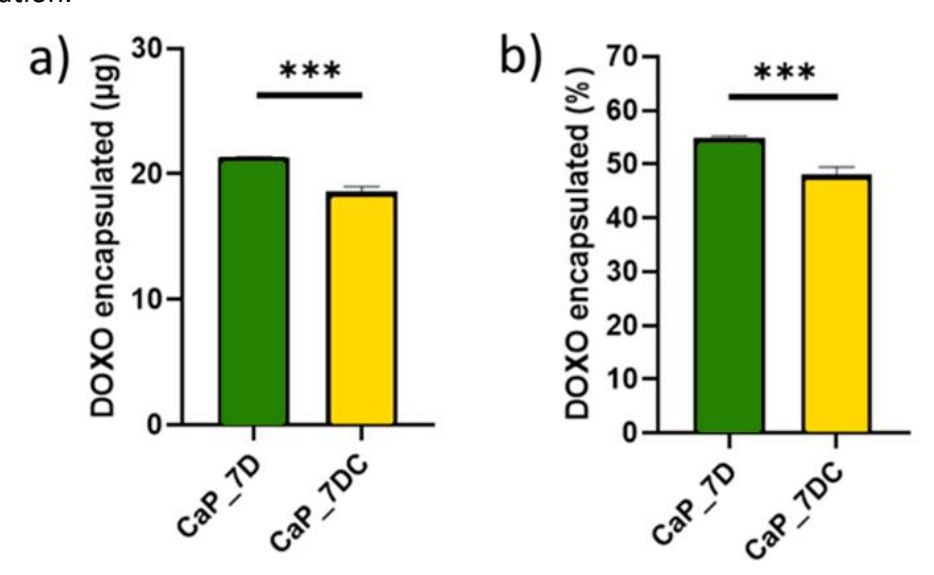


Figure 5.40 - Efficiency of DOXO encapsulation by layers of CaP_7D and CaP_7DC in different units: μg (A) and percentage (B).

The effectiveness of DOXO encapsulation within the layers of the different particle configurations was assessed. The encapsulation efficiency of DOXO in the CaP_7D configuration was measured to be $54.9 \pm 0.4\%$, while CaP_7DC exhibited an encapsulation efficiency of $48.0 \pm 1.5\%$. This discrepancy can be attributed to the presence of CDs in the layers, which might hinder the entrapment of drug molecules within the layers. The lower thickness of layers in the CaP_7DC configuration played a role in the encapsulation of the drug. It is also possible that CDs were able to diffuse during layer deposition (Adamczak et al., 2012), like the behaviour of the drug in the CaP_1L6L configuration. Consequently, CDs could permeate the PE lattices, becoming trapped in adjacent CH and CS layers, which could hinder drug encapsulation. Additionally, due to their negative surface charge and spherical morphology, CDs might help the formation of oppositely charged layers, resulting in thinner CaP_7DC layers compared to CaP_7Ds. This is supported by DLS analysis.

Analysing the obtained data on the DOXO encapsulation efficiency by the layers, the deposition steps allowed an average DOXO entrapment of $70.6 \pm 1.1\%$ for CaP_7D, while for CaP_7DC it was $67.9 \pm 1.0\%$. This confirmed that the deposition steps effectively facilitated high drug encapsulation. These results corroborated the fact that the presence of CDs disrupts DOXO encapsulation, shown by the difference between the two encapsulation values.

However, during the subsequent washing steps, a substantial amount of drug was removed, particularly in the case of CaP_7DC. Consecutive washing steps removed $10.2 \pm 1.1\%$ of the drug trapped in the layers previously deposited on CaP_7DC, while CaP_7Ds exhibited a removal of $5.7 \pm 1.4\%$ of DOXO. For both types of particles, the initial washing step consistently removed the majority of the drug weakly adsorbed on the surface, which is also reported by (Richardson et al., 2015). In conclusion, when considering the amount of DOXO encapsulated in the NP core along with that encapsulated within the layers, CaP_7D encapsulates a total of $26.22 \pm 0.12 \,\mu g$ of DOXO, while CaP_7DC encapsulates $23.53 \pm 0.72 \,\mu g$ of DOXO.

The release profiles of DOXO from the CaP_7D and CaP_7DC systems were examined in PBS solutions at 37°C (Figure 5.41 A and C). Release rate of DOXO from the layers was calculated by establishing a trend line based on the first three time points to analyse burst release (Figure 5.41 B and D).

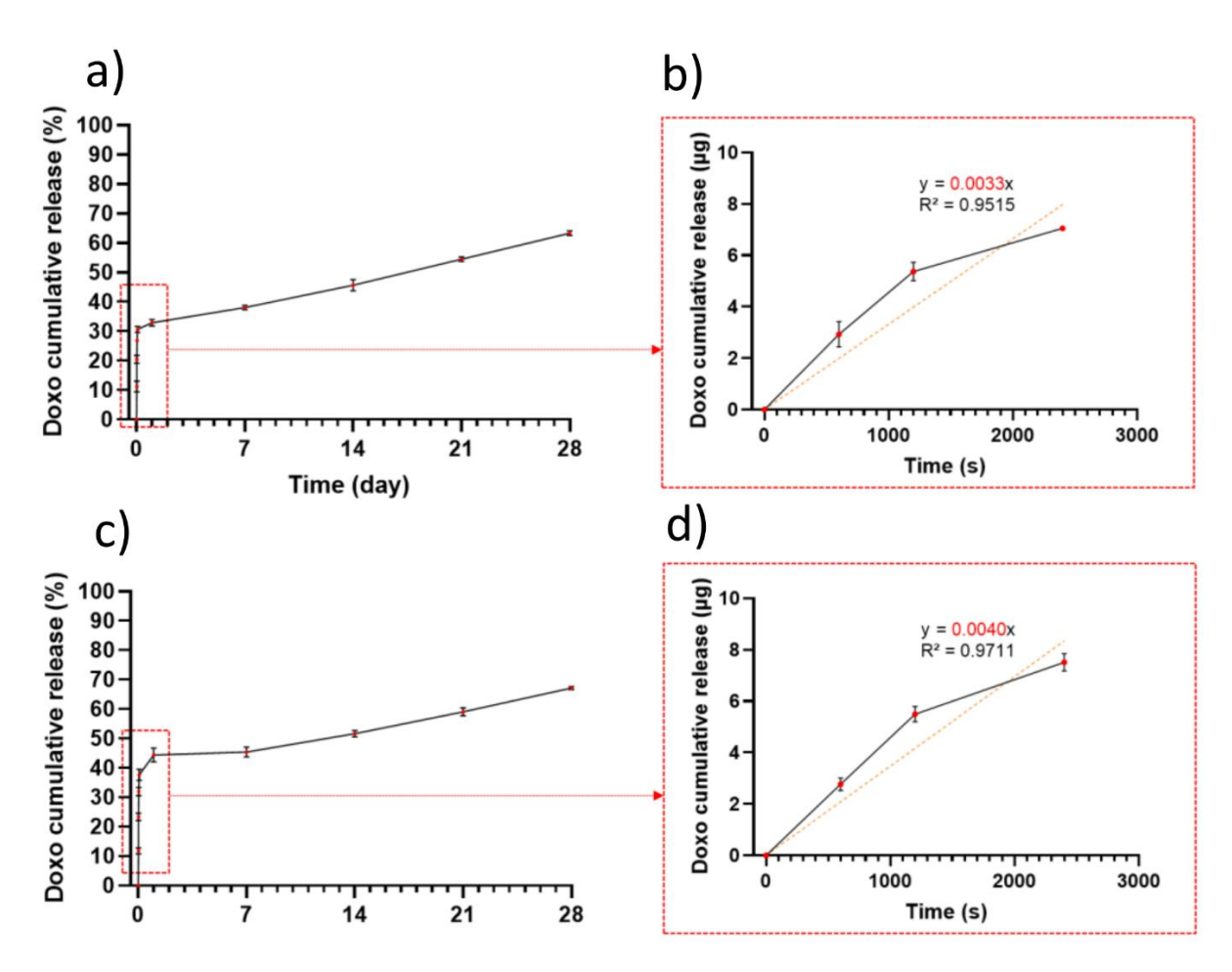


Figure 5.41 - DOXO cumulative release profiles and the study of burst release from CaP_7D (A-B) and CaP_7DC (C-D)

Despite CaP_7D encapsulating the drug both in the layers and core, and though the majority of the drug was located in the outermost layers of the NPs, the burst release was reduced from $67.4 \pm 2.5\%$ to $32.8 \pm 1.1\%$ when compared to CaP(DOXO)_PAH. This shows that using the LBL deposition extends the time half the drug was release from 24 hours to 21 days (54.4 \pm 0.7%). A similar trend was observed with CaP_7DC, but with a slightly more pronounced burst release. For example, within 24 hours, CaP_7DC released 44.3 \pm 2.3% of the drug, resulting in a half release time of 14 days (51.6 \pm 1.1%). This shows these systems exhibited controlled drug release over time due to the surface coatings on the NPs. The LBL technique ensured the drug's stability, preventing premature losses as has been shown previously in literature (Correa et al., 2016; Park et al., 2018).

Despite *in-vitro* studies showing controlled release, the initial drug release profile for both DOXO-loaded NPs is undesirable. The burst release from CaP_7DC was more intense than from CaP_7D, as indicated by the calculated drug release rates of 0.004 and 0.0033,

respectively. Both values are significantly higher than that of CaP(DOXO)_PAH (0.0013), due to higher drug encapsulation in CaP_7D and CaP_7DC. The amount of drug released by CaP_7DC after 24 hours was much greater from the system without CDs. This could be because the presence of dots in the layers. Changes in pH, ionic strength, salinity, and temperature might enable dot diffusion through the polyelectolyte lattices, providing an easier pathway for drug molecules due to their smaller size compared to the CDs. However, this difference diminished over time, disappearing at day 28 (p-value = 0.0765). By day 14, the p-value was below 0.01, and by day 21, below 0.05. The total amount of drug released by CaP_7DC at day 28 was $15.78 \pm 0.13 \,\mu g$.

5.3.3 In-vitro cell tests

Incubating Saos-2 and U2OS cells with CaP_7DC, CaP_7L blank, and free DOXO aimed to test the cytotoxicity of the NPs after 24 hours of seeding. For both cell types treated with CaP_7L, there was no significant change in metabolic activity compared to the untreated control (Figure 5.42). As the concentration of CaP_7L increased, there was a very slight decrease in cell viability observed for both cell types, particularly for U2OS when treated with a concentration of 500 μ g/mL (94.7 \pm 3.9%). However, these decreases in metabolic activity were not statistically significant when compared to concentrations of 250 μ g/mL. It is important to note that the 500 μ g/mL concentration is relatively high. In summary, the results indicate that the presence of CaP_7L NPs did not significantly effect on the metabolic activity of Saos-2 and U2OS cells, and any slight reductions in viability might be because of the known potential effects of CH on certain cancer cell lines, as shown in previous experiments and in literature (Maleki Dana et al., 2021).

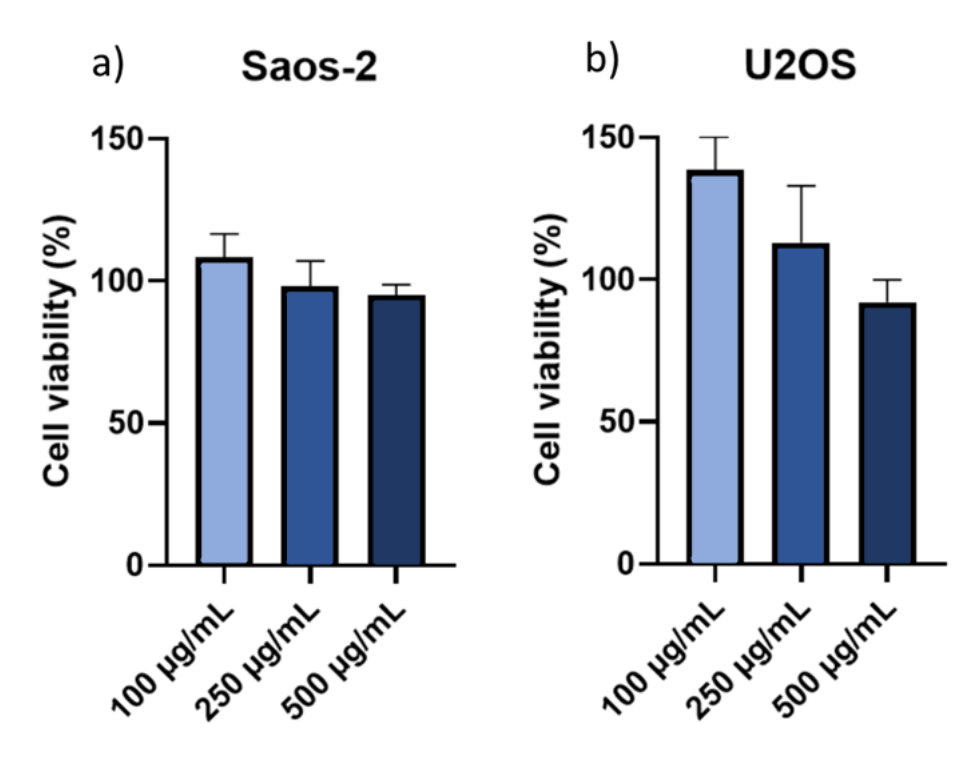


Figure 5.42 - PrestoBlue assay of Saos-2 (A) and U2OS (B) seeded with CaP_7L

The results differed between the two tested cell types when they were exposed to CaP_7DC (Figure 5.43). Both cell types showed a decreasing trend in metabolic activity as the concentration of the tested NPs increased. This suggests that the NPs had a detrimental effect on cancer cells, confirming the therapeutic efficacy of these NPs. For Saos-2 cells, a decline in cell viability was observed starting from the lowest tested concentration of CaP_7DC, which was 5 μ g/mL, resulting in a survival rate of 54.9 \pm 1.5%. For CaP_7DC concentrations above 10 μ g/mL, Saos-2 cells exhibited a survival rate that was half of that in the control (48.5 \pm 4.6%). This finding is important because it suggests significant treatment efficiency at low concentrations and compares very well against free DOXO. Almost complete suppression of metabolic activity was observed in Saos-2 cells treated with concentrations of 250 and 500 μ g/mL CaP_7DC, yielding cell viabilities of 7.4 \pm 3.6% and 1.7 \pm 2.9%, respectively, both results are significantly better than free DOXO alone. It is worth noting that these extreme concentrations may not be suitable for clinical applications.

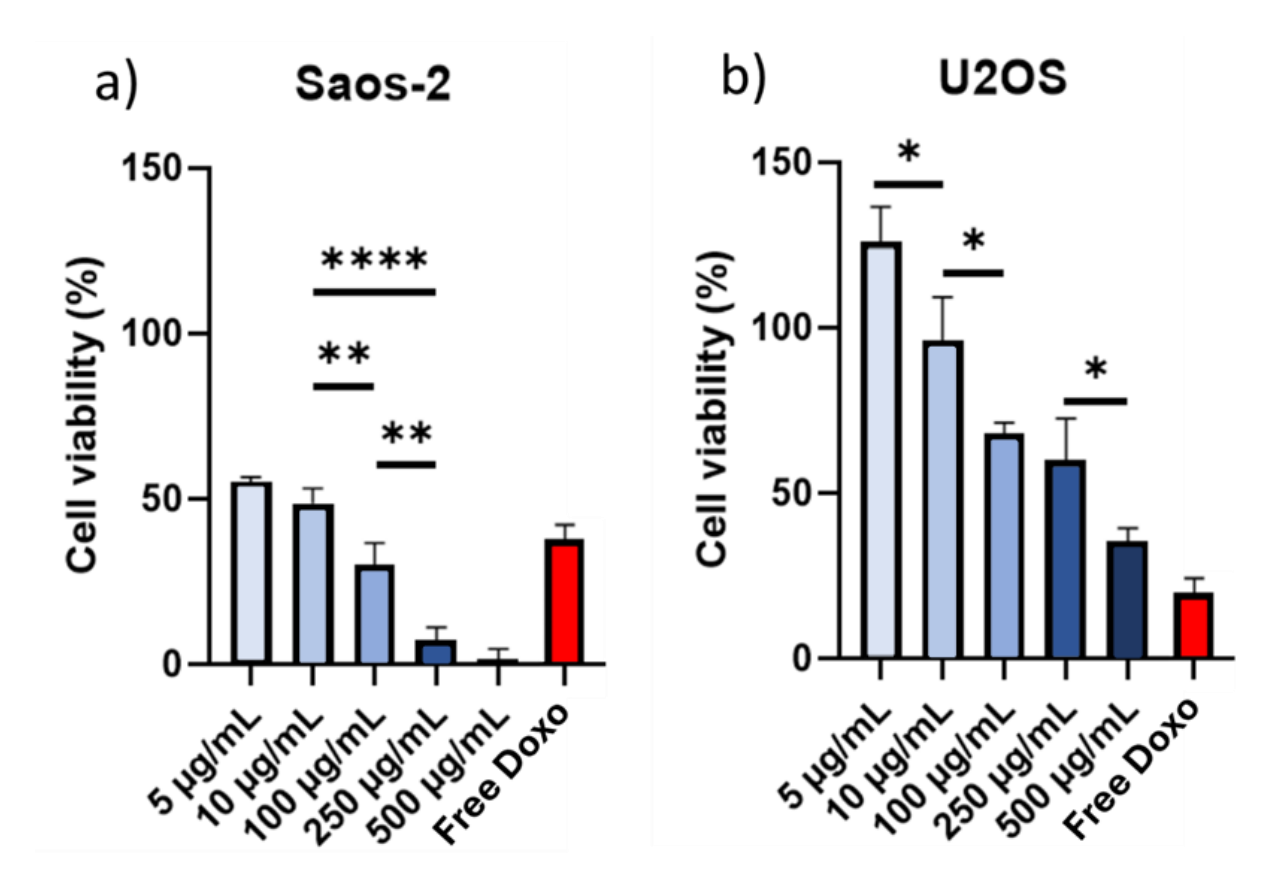


Figure 5.43 - PrestoBlue assay of Saos-2 (A) and U2OS (B) seeded with CaP_7DC at different concentrations and free DOXO at 10μg/mL concentration

U2OS cells showed a higher survival rate than Saos-2 cells when treated with the same concentrations of CaP_7DC. The metabolic activity of U2OS cells decreased below 50% only at the extreme concentration of 500 μ g/mL CaP_7DC, resulting in a survival rate of 35.3 \pm 4.1%. This showed a statistically significant difference compared to the 250 μ g/mL concentration of CaP_7DC (p-value < 0.05). At lower concentrations, the metabolic activity of U2OS cells ranged from 60% to 100% compared to the untreated control, particularly at concentrations of 5 and 10 μ g/mL CaP_7DC. The 100 μ g/mL concentration of CaP_7DC led to a metabolic activity rate of 67.9 \pm 3.3% compared to the control. Every concentration showed a higher metabolic activity than free DOXO showing that, regardless of concentration against U2OS cells, this treatment is less effective than free DOXO.

It is unclear why the nanoparticles performed better against the Saos-2 cells over the U2OS cells when free DOXO performed better against U2OS cells. However, the free DOXO experiments were not performed at the same time as the rest of the results so this could explain these differences seen. Literature suggests that U2OS cells usually perform better against DOXO when compared to Saos-2 cells. For example, that was shown in the MTT essay

in a paper by Zhao et al (Zhao et al., 2014), which shows higher viability for U2OS cells at concentrations of 250 and 500nM. However, this difference was not highlighted or explained. Galembikova et al. (Galembikova & Boichuk, 2021) investigated the expression of the tyrosine kinase signalling profile during chemotherapy in fibrosarcoma and OS cell lines. The research found a positive correlation between the expression of phosphorylated forms of these kinases and the synergistic effect of DOXO with selective inhibitors (crizotinib, BGJ398, MK2206, U0126). Specifically, the activation of the AKT signalling pathway was observed in OS cells. In Saos-2 cells this activation was found to be less pronounced than in U2OS cells, allowing U2OS cells to survive longer than Saos-2 cells.

In summary, the incubation of cells with CaP_7DC NPs resulted in different responses for Saos-2 and U2OS cell lines. Saos-2 cells showed a decline in viability at lower concentrations, suggesting a significant therapeutic effect, while U2OS cells showed a higher survival rate across a wider range of concentrations. The EPR effect seemed to contribute to the therapeutic potential of these NPs, although the optimal concentration for each cell type should be further investigated. Additionally, the extreme concentrations assessed might not be suitable for clinical applications due to potential cytotoxicity.

The Live/Dead assay show the viability (coloured in green) and mortality (coloured in red) of the two cell types after a 24-hour incubation with CaP_7DC, CaP_7L and Free DOXO (Figure 5.44), and their corresponding controls. For all samples, the Live/Dead images show an increasing presence of red stained cells. Samples with cells that show minimal metabolic activity don't adhere as well compared to the controls (CaP_7L and CTRL) due to apoptotic cells losing their adhesion receptors, causing some to detach from the flask and float in the seeding solution. As a result, these cells were removed during the PBS washing steps prior to staining and are therefore less numerous in the sample.

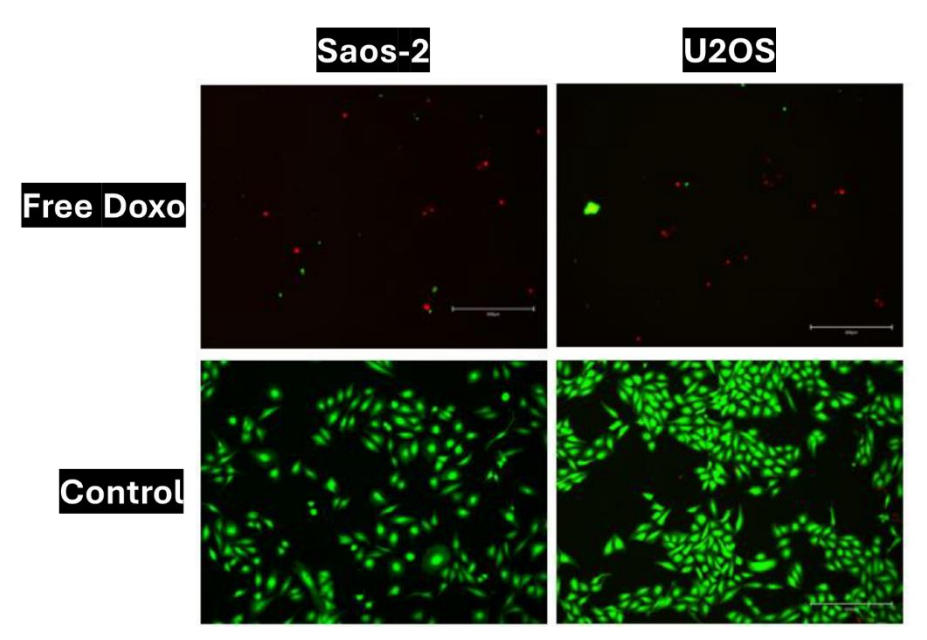


Figure 5.44 - Live/Dead images of Saos-2 (left) and U2OS (right) with or without free DOXO at 10μg/mL concentration

The control groups (Figure 5.45) had a high population of cells and were evenly distributed, showing robust proliferation rates and confluence for both cell types meaning that the was no contamination of the experiment and they provide a good comparison for the cells that were exposed to the NPs. The CaP_7L particles had a green colouration cellular aggregation and spreading in the wells, indicating high biocompatibility of the tested NP. However the number of cells shown in the images decreases as the concentration increases, this suggests that higher concentrations does reduce metabolic activity in both cell lines, the affected cells were removed prior to analysis as explained above. This is in corroboration with the PrestoBlue analysis as this also showed high biocompatibility with a slight decrease in metabolic activity with increased concentration of the nanoparticles.

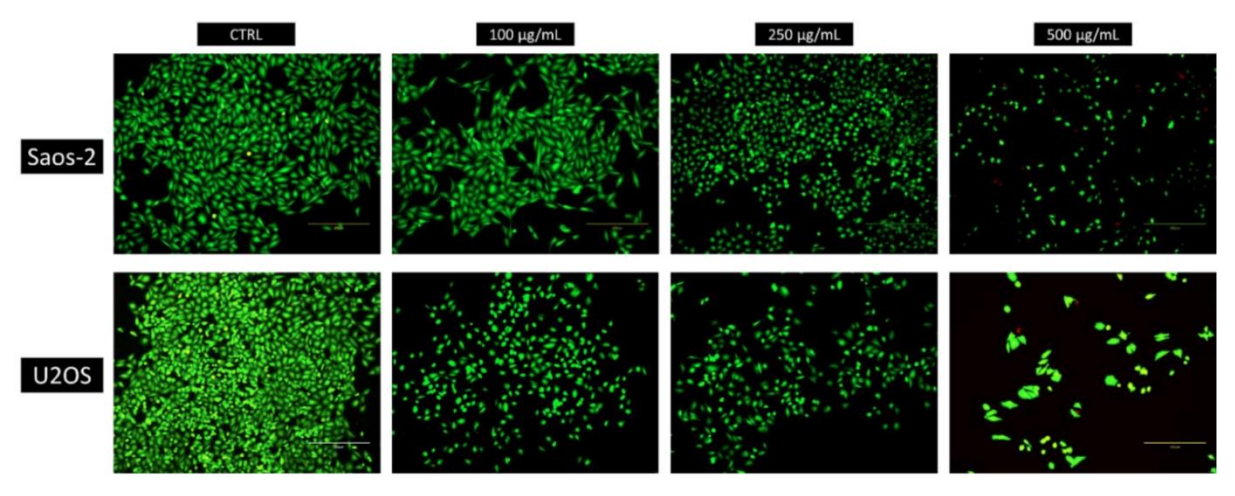


Figure 5.45 - Live/Dead images of Saos-2 (up) and U2OS (bottom) with or without CaP_7L at different concentrations

For the tests analysing CaP_7DC (Figure 5.46). The images depicting the concentrations of 250 and 500 μ g/mL had a high amount of dead cells. Lower concentrations yielded green colourations, indicating that a some of cells had managed to evade the treatment. The U2OS cells displayed a higher proportion of viable cells than Saos-2 cells when subjected to the same concentrations, accompanied by an increased occurrence of cell aggregates. These findings align completely with the PrestoBlue assay.

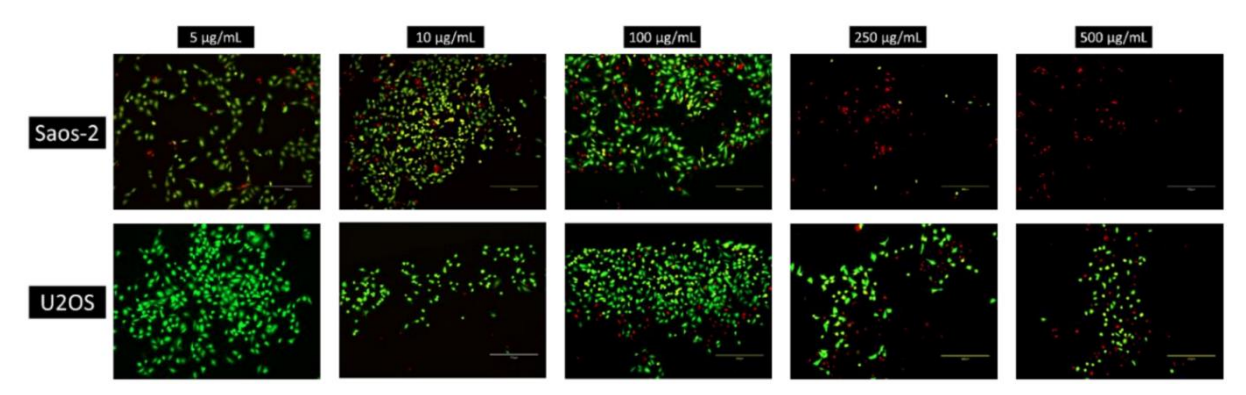


Figure 5.46 - Live/Dead images of Saos-2 (up) and U2OS (bottom) with or without CaP_7DC at different concentrations

It is important to highlight that the surviving Saos-2 and U2OS cells following the CaP_7DC seeding were predominantly located at the edges of the wells. This could be because the cell seeding process might not have been executed accurately, potentially allowing cells at the borders to evade the effects of CaP_7DC treatment. However, another explanation could be that it was possible that the cancer cells might have disrupted their local adhesion domains, facilitated by integrins (Desgrosellier & Cheresh, 2010). This could have led to the detachment of cells from their adhered substrate, causing them to float and collect at the edges of the well.

For a more in-depth assessment of cellular morphology and organelle organisation, Saos-2 cells treated with a 500 μ g/mL concentration of CaP_7DC were subjected to TEM analysis, shown in Figure 5.47. These TEM images facilitated a qualitative evaluation of the encapsulation of CaP_7DC within Saos-2 cells.

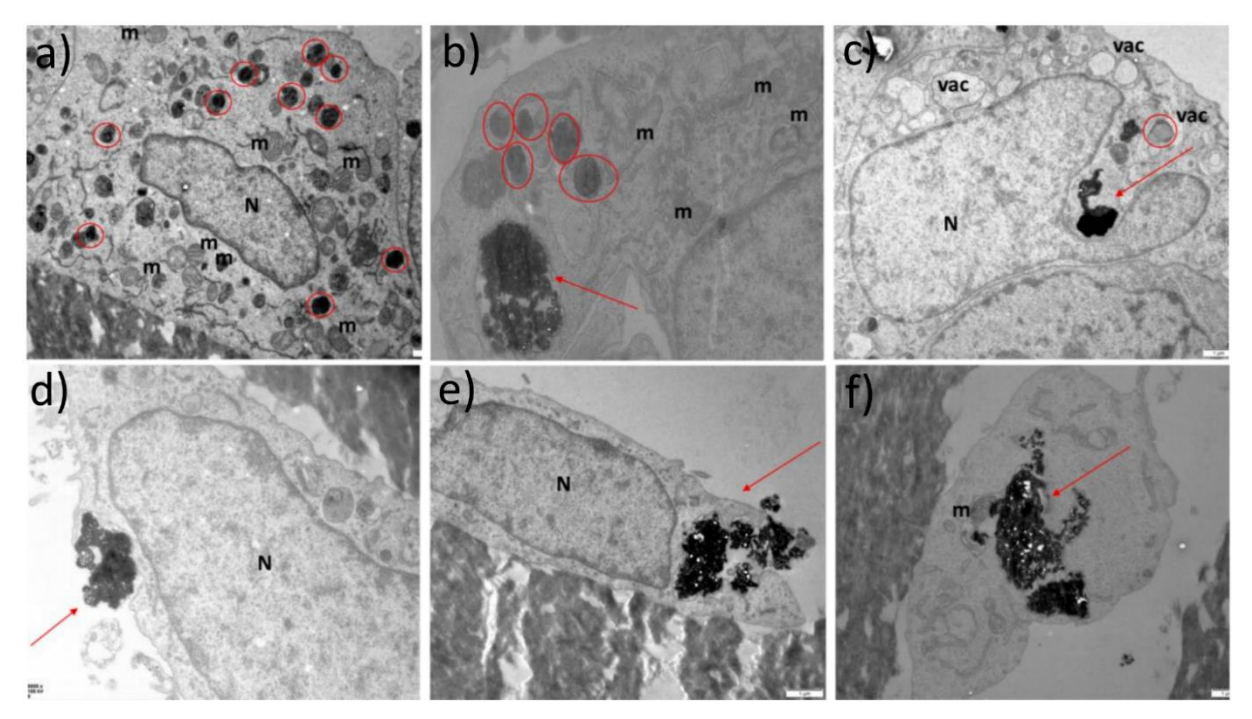


Figure 5.47 - TEM images of Saos-2 cells treated with a concentration of 500 μ g/mL CaP_7DC (M – Mitochondria, N – Nucleus, Vac – Vacuole)

According to Patel et al. in 2019 (Patel et al., 2019) it is a common characteristic of particle systems that they are initially taken up by cells via one or more endocytic mechanisms upon interacting with the cell surface. Such interactions can be governed by specific ligand-receptor interactions or nonspecific interactions like electrostatic and hydrophobic interactions. The images show that CaP_7DC particles do not reach the nucleus and localise within the lysosomes in the cytoplasm. Lysosomes exhibited an opaque black hue due to CaP_7DC internalisation, indicating the presence of CDs. The presence of the Cap 7DC caused changes to cell topography such as changes in cell membrane conformation, nucleus conformation post endocytosis and cytoplasmic organelle arrangement. This indicates that the internalisation mechanism involves several steps: the particles are internalised into early endosomes, which gradually mature into late endosomes showing activation of the endomembrane system in line with Naumenko et al.'s work in 2021. (Naumenko et al., 2021) The luminal pH of these compartments decreases due to proton pumps, leading to fusion with lysosomes (pH 4-5), where lysosomal enzymes degrade the contents, enabling cell survival, as detailed in Siddharth Patel et al.'s work Brief (Patel et al., 2019). for effective therapeutic effect, NPs need to escape the endosomal/lysosomal pathway before being degraded within lysosomes. The process of endosomal escape is inefficient and is not fully understood. Several hypotheses, including the 'proton sponge' hypothesis, membrane destabilisation, disruption, and a budding mechanism, have been put forward to explain this, as detailed by Dehua Pei and Marina Buyanova (Pei & Buyanova, 2019).

The images highlight a potential escape process from the more labile pinocytic vesicles, allowing drug release within the cytosol and contact with the cell nucleus. This mechanism results in changes to cell membrane morphology leading to disruption of the cell nucleus and then apoptosis or cell necrosis. Some TEM images depicted cells undergoing necrosis-induced death mechanisms. The drug's release into the cytosol leads to organelle swelling (endoplasmic reticulum and mitochondria) and the appearance of large vacuoles which leads to in plasma membrane rupture, cell lysis, and cell death.

5.3.4 *Summary*

In summary, the LBL application of CH and sodium CS polyelectrolytes with CDs and DOXO to PAH functionalised CaP NPs created a device capable of delivering drug to OS with a significant therapeutic effect, especially towards SAOS-2 cells. The inclusion of CDs was shown to cause little disruption to the application of the layers and show potential for imaging due to their photoluminescence properties.

Chapter 6. General discussion, Conclusions and Future Work

6.1 General discussion

This PhD project aimed to produce a nanotheranostic device capable of drug delivery and imaging of OS with the combination of biomass-based CDs and the LBL technique. To that end, LBL polyelectrolyte capsules on CaP NP templates functionalised with CDs and DOXO have been successfully produced and initial testing of their effectiveness against the Saos-2 and U2OS OS cell lines has been analysed to show their potential as drug delivery agents. As discussed in chapter two, the combination of CDs and the LBL technique in this way has never been done before for the field of nanotheranostics, so this research gives a completely novel strategy for the treatment of OS and other cancers that could be extensively researched in the future. Current pharmaceutical based treatments for OS are limited to chemotherapy which has harsh side effects such as decrease in bone marrow activity and gastrointestinal reactions, which typically manifest as lower blood, nausea, and vomiting (Y. Zhang et al., 2018). Drug delivery agents such as the one described in this project offer many advantages over the direct administration of bare chemotherapy drugs such as protection from degradation in the bloodstream, better drug solubility, enhanced drug stability, targeted drug delivery, decreased toxic side effects and improved pharmacokinetic and pharmacodynamic drug properties (Senapati et al., 2018).

The work in this PhD has also added to the field of CDs and could influence research conducted in the future. Specifically, all the syntheses explored investigated the effect of different parameters on the properties of the CDs including biomass ratio, catalyst type and concentration, retention time and reaction temperature. This is something that is not always outlined in literature. Most papers that investigate the CDs focus on a single synthesis and how they perform for a specific application (Alhokbany et al., 2023) (Jessy Mercy et al., 2023; M. Yang et al., 2024). The results of this research show how much a small change in synthesis parameters can influence the properties of the resulting CDs. Future research should continue this investigation and outline and publish their experimentation, thus allowing allow other researchers to better tune their syntheses to produce CDs with specific properties.

The first synthesis used a two-step reaction starting with a HTC of spent coffee grounds with an acid catalyst to form a graphitic precursor which was followed by an oxidation with nitric acid to form CDs. The synthesis of the dots was confirmed by photoluminescence spectroscopy and TEM images. It was revealed that the CDs showed UV to blue (360-437nm) photoluminescence with mediocre (3.6 - 6.7%) QY and had average sizes ranging from 4.9nm to 9nm. It was shown that the synthesised dots had a smaller size and more intense photoluminescence when a SA catalyst was used in the precursor synthesis.

This synthesis had numerous limitations due to the harsh chemicals used (H₂SO₄ and NHO₃) and long reaction time, which produced a very small amount of CDs which was too low to quantify. TA was used as a green alternative to the SA. This catalyst was responsible for the lower intensity photoluminescence, lower QY and larger size of the CDs shown in this synthesis. Although the catalyst produced dots of lower quality, it was still shown that a SA catalyst is not required to synthesise the dots using this method and a green alternative can be used. It was decided that further research into CDs without the use of harsh chemicals such as SA and nitric acid was needed, and alternative methods were sought to increase the greenness of the dots. Further research into this method is not recommended without significant changes because of the harsh chemicals used and low production yield which is unsuitable for scale up for industry. More environmentally friendly methods have been previously outlined that produce dots with better properties. For example, li et al. (Z. Li et al., 2021) outlined a synthesis of CDs with a QY of 16% and a size between 1.2 and 3.2nm from corn stalk powered using aqueous conditions and no catalyst.

The effects of a TA catalyst and ultrasonic pretreatment were investigated in the second synthesis outlined in this project. The synthesis used an ultrasonic pretreatment to exfoliate the SCG to increase the surface area ready for the for a hydrothermal treatment. Despite the mass yield improving with the use of an ultrasonic pretreatment, overall, the mass yield of CDs was found in this paper to be low, at a maximum of 0.9%. This is similarly low when compared with other papers which have used SCGs as a biomass source (Andrade et al., 2017; Chen et al., 2021; Costa et al., 2022; D. M. A. Crista et al., 2020; Hong & Yang, 2021; Jiang et al., 2014; Xu et al., 2017; X. Zhang et al., 2018), which are typically below 2%. Further investigation is required to increase this value, as 2% mass yield would not be viable for a commercial scale. The issue of mass yield is important for industrial viability. Until this mass yield can be increased, other carbon sources such as citric acid will be used, for example dots

with a mass yield of 19% were derived from citric acid by Yu et al. (Yu et al., 2023). CDs from SCGs achieve good QY and low toxicity but will not be used on a large scale until research finds a method to improve mass yield. This kind of pretreatment has not been investigated in research for the synthesis of CDs. It has only been described as a method to assist mixing, and these works do not outline the advantages of using it against using unpretreated biomass (Q. Zhang et al., 2022) (Ma et al., 2022). This shows the novelty of this research and how it begins to fill a gap in the current literature.

The use of TA for a catalyst for the synthesis of CDs has not been fully explored in literature. This research shows that the use of a TA catalyst produces CDs with attractive properties with different synthesis parameters explored such as concentration and biomass ratio. Despite the efforts made in this synthesis to completely remove the TA, TA impurities remained as shown in the optical testing which demonstrated lower absorbance in the presence of TA compared to its absence, and QY gradually decreased with increasing TA concentration. There is potential that this phenomenon could be attributed to other properties of the CDs, as there is a weak trend linking the increase in QY to increase in size of the dots. Regardless, if TA is to be utilised as a pre-treatment agent or HTC catalyst, a more effective method of removing the CDs must be developed to ensure their optimal effectiveness.

The third synthesis expanded further on the use of a hydrothermal treatment without using an acid catalyst. The synthesis was a green microwave synthesis of CDs, that produces biocompatible, blue fluorescence CDs with averages sizes between 4 and 13nm. The photoluminescence data shows the dots have 3 distinct, excitation independent, blue emission wavelengths that can be selected for by changing excitation wavelengths. They also have an OK QY between 3.6 and 10%. The photoluminescence is caused by sp² carbon sites in the core of the CDs and the QY can be increased by increasing the ratio of sp² bonds by selecting a retention time of 90 minutes with a temperature above 175°C. The biocompatibility is very high with both live and dead cell tests showing high number of live cells and PrestoBlue cell tests showing above 77% viability after 48-hour exposure to the dots at a concentration of 1000mg/ml.

Comparing the CDs synthesised in this project by various methods, The UV-blue (360-440m) photoluminescence for all the dots is very similar across the different syntheses. The average

QY and size of all the dots synthesised in this project are 6.9% and 5.9nm respectively. A review (Bressi et al., 2023) discussing recent synthesis of CDs from biomass sources outlined the size and QY from different synthesis; the average size and QY from these sources is 4.6nm and 17.9% respectively. Using this as a good sample of the current literature for comparison this shows that the average properties of the dots produced in this project are of lower quality than a good proportion of what is currently being reported. However, some of the dots produced show much more potential. The best examples of each property were a QY of 13.1% and a size of 1.3nm. The dots of this size are very small and are smaller than 93% of the others outlined in the review. 13.1 is middling QY which is higher than 50% of current literature. Further work refining these syntheses parameters could greatly improve the properties of these dots.

The field of LBL has also been impacted by the investigations conducted in this research. Comparing the two main particle syntheses outlined, it is clear to see that the latter produced NPs of much higher quality that were more suitable for application as nanotheranostic agents. it was found that the inclusion of a SAB for the LBL deposition causes the particles to degrade which in turn hinders further LBL functionalisation and drug encapsulation leading to poor release and therapeutic effect against cancer cells. The results of using the SAB are surprising as methods using this buffer did not outline the same issues (Pilicheva et al., 2020). However, most LBL syntheses on CaP NPs do not include the use of a SAB, they used either aqueous conditions with NaCl (Bastos et al., 2023; Verma et al., 2016) or a tris buffer solution (Abdelkebir et al., 2012). The reporting of the findings in this project will ensure that this method is avoided by future researchers.

6.2 Conclusions

The conclusions that can be drawn from the above research are as follows:

• The investigation into varying the synthesis parameters of an acid catalysed HTC followed by a nitric acid oxidation revealed that increasing the concentration of the SA catalyst also increased the intensity of the photoluminescence and the QY when compared to a synthesis without it. SA concentration has previously been shown to affect the photoluminescence properties previously, as outlined by yang et al. (L. Yang et al., 2022). They found that increasing the concentration of the SA increased the

wavelength of the emission of the CDs by varying the degree of carbonisation which affects the amount of surface defects and nitrogen doping which contribute to photoluminescence.

- The investigation into ultrasonic pretreatment concluded that ultrasonic pretreatment increased the mass yield and decreased toxicity of the CDs produced when compared to the control that did not use the pretreatment. This is due to an un-clumping and physical breakdown of the macro structure of the of the SCG which leads to superior increase in solution penetration into the macro structure of the feedstock and an increase surface area. The breakdown of the SCG allows for more carbonisation building blocks to become available for the synthesis of the dots, improving the yield and properties such and size and QY. These CDs are much more suitable for use as an imaging agent and were used in the synthesis of the drug delivery device.
- The effect of temperature on the pre-treatment process was also examined and was shown by the increased intensity in the FT-IR over pretreatment time. When SCGs were treated at 80°C, they burned and yielded weaker QY results. The most favourable outcomes were obtained at 60°C. Other temperatures assessed, namely 40°C and non-heated conditions, resulted in inferior QY values and less surface interaction compared to the pre-treatment at 60°C. This can be attributed to the reduced breaking up of SCGs at lower temperatures, although it was still more effective than the 80°C treatment. Consequently, for future pre-treatment of SCGs to generate CDs, it is recommended to utilise ultrasonication with water at approximately 60°C for a duration of 90 minutes based on the research conducted.
- This investigation also concluded that TA can be used as a catalyst for pre-treatment and CD synthesis as the analyses revealed that utilising TA led to the attainment of good QY (6.2 13.1%) and low toxicity CDs. However, it was also discovered that using just water without a TA catalyst resulted in higher QY and low toxicity in the formed dots. This conclusion was supported by the data obtained by varying the concentrations of TA, which showed varying rates of toxicity and a decrease in QY as the TA concentration rose. Thus, the most recommended pre-treatment method for SCGs involves the use of water alone. it should be acknowledged that the presence of TA may quench the

fluorescence of the dots. This was shown in 2015 by (Ahmed et al., 2015) who used this phenomenon to create a TA detecting probe for applications in the wine industry.

- The investigation into the synthesis parameters of the microwave assisted HTC concluded that changing the synthesis retention time and temperature parameters does influence some of the properties of the dots, but not significantly. For example, A longer retention time does slightly increase the size of the dots but has no effect on QY, and a lower temperature increases the negativity of the zetapotential of the dots by changing the ratio of surface groups.
- Initial CaP template synthesis concluded that that the freeze drying produces particles of a smaller size and flow rate did not have much of an effect on size as confirmed by microscopy, but particles at higher flow rates tended to have a more negative surface charge as confirmed by ζ-potential analysis.
- First layer deposition of polyelectrolyte between PDADMAC and PEI concluded that PDADMC was a superior choice due to smaller size (PEI = 237-561nm, PDADMAC = 193-303nm) and higher magnitude of surface charge (PEI = 14.7-17.3mV, PDADMAC = 27.5-37.9mV) which was found with analysis by TEM and ζ-potential testing. However, it wasn't chosen for further experimentation due to issues with obtaining the product with centrifugation.
- The synthesis of LBL CH and AA capsules using an acetate buffer produced capsules that were not efficient drug delivery devices. This synthesis method does not produce high quality and consistent capsules, and this is shown specifically on the TEM images which indicate a high degree of agglomeration and a high variability of size and shape. The ζ-potential shows good layer deposition with the changes in surface change from layer to layer, but this is not supported by the XPS or FTIR due to SAB contamination, or, in the TEM images due to inconsistent particle size. The drug loading and release of these capsules is poor and is unsuitable for application. This investigation did show however that there is potential with the inclusion of CDs within the layers of the nanocapsules with photoluminescence testing. Photoluminescence analysis revealed that the NPs with CDs showed increased intensity of photoluminescence emission than

both the plain CDs and unfunctionalised particles. This is thought to be caused by an additive effect of the inherent photoluminescence from CH and the photoluminescence from the CDs. The photoluminescent properties of CH have been shown previously by Gurumendi et al. (Gurumendi et al., 2023). This shows that that if the capsule synthesis can be further refined so that the morphology is more consistent and drug release can be enhanced to show a significant therapeutic effect, this combination of imaging technique and therapeutic delivery might have potential in the field of nanotheranostics.

• The formation of CH and CS LBL capsules using aqueous conditions produces high quality capsules that can effectively release anticancer drugs for cancer therapy. The particles showed efficient drug loading and subsequent drug release that was proven using cell tests to be therapeutic against OS cancer cells in terms of both viability and live/dead, especially SAOS-2 cells. It was also shown that the inclusion of CDs within the layers did not significantly hinder this drug loading and release which shows potential of these devices in the field of nanotheranostics.

6.3 Future work

The realms of cancer research and therapy, along with the understanding of the fields of CDs and LBL, are continuously evolving. Further exploration and investigation can be undertaken to advance the findings obtained in this study. Unfortunately, due to time constraints imposed by the COVID pandemic, exhaustive testing of nanocapsule behaviour could not be fully executed. Nevertheless, the research conducted has provided substantial evidence, as outlined above, to affirm that nanotherapy of this nature holds great promise and warrants continued exploration.

- Further research is required to fully explore the use of TA as an HTC catalyst for the synthesis of CDs; however, the results of this project suggest that it does not provide a beneficial property to the resulting CDs.
- Due to limitations of equipment, temperatures higher than 200°C were not tested in this project. Future work on these synthesis methods should test higher temperature as this could yield dots with better quality properties, for example Chauhan et al.

(Chauhan et al., 2021) synthesised CDs with a QY of 62% with the hydrothermal treatment of agarose waste at 450°C.

- Experiments to investigate the use of PDADMAC to functionalise CaP NPs should be conducted due to the promise shown in the initial testing of the first layer depositing. This investigation should include use of higher RPM ultracentrifugation to increase yield and viability of the synthesis. Aqueous conditions should also be evaluated as it is unknown if the yield issues were caused by the SAB. The same LBL processes as outlined above should also be applied to produce functionalised templates for comparison as it could be revealed that they are superior to the PEI or PAH first layer particles.
- Experiments to investigate a continuous process for the synthesis and functionalisation
 of CaP NPs with the LBL should be conducted. As mentioned in chapter 2, difficulty in
 scalability is a limitation often faced by the LBL field (Joseph J. Richardson, 2015; Zhao
 et al., 2019). This has been previously investigated by Elizarova et al. (Elizarova &
 Luckham, 2016); however, different polyelectrolytes and processes are needed for true
 potential for scale up.
- The issue of agglomeration which has been seen to affect the synthesis of the template particles and the formation of the layers in TEM images and DLS measurements should be further investigated. Ultrasonication should be implemented at all stages of synthesis including the formation of the templates and the deposition of the layers. This should reduce agglomeration (Priyadarshi et al., 2021; Vikash & Kumar, 2020) and prevent the layers depositing on multiple particles. This should in turn improve the morphology and layer deposition, which would have a knock-on effect of increasing surface area and could potentially improve drug loading and release. (Hensel et al., 2020)
- Although a process for synthesising a CD functionalised LBL capsule has been outlined, further experiments to find the most optimal combinations of polyelectrolytes and synthesis concentrations should also be run. Choosing the optimal polyelectrolyte and

subsequent concentrations would improve the capsule morphology which would in turn enhance the therapeutic effect and expand applications of the particles.

- Although the CDs have effectively been incorporated into the layers within a LBL capsule and have shown potential for bioimaging, this device has yet to have been shown to be effective at bioimaging. Future works should first focus on single cell scale tests to evaluate the efficiency the device and unfunctionalised CDs as imaging agents and compare against established fluorescent imaging agents used against OS such as indocyanine green (Chen et al., 2022). If these devices show potential, perhaps these particles could be tested in their effectiveness in the imaging of small animals such as mice to evaluate tissue penetration of their emissions and their toxicity. (Luo et al., 2013)
- Better progress was made with evaluating the potential of the synthesised nanotheranostic device for drug delivery, as this was shown to be effective in testing against OS cells. However future research could be taken further to test this in a mouse model (Fu et al., 2021). This would help to evaluate the passive ability of this device and show if increased cellular uptake of OS compared to healthy cells via enhanced permeability retention (Shukla et al., 2019) is enough for the sufficient accumulation of this device for therapeutic drug release. This work could be furthered still by investigating targeting methods specifically for OS, such as functionalisation with the medronate ion, a bone targeting ligand (Wu et al., 2017).
- The drug release of the synthesised capsules could also be investigated computationally, with the data found in this thesis being compared to computational models. This could give further insights into the mechanism of the drug release, similar to the work completed by Barchiesi et al. (Barchiesi et al., 2022). This research could then be used to refine the synthesis process to improve drug release.
- In this project, only DOXO and DAX were tested with particles for their encapsulation and release and the final nanotheranostic device only tested DOXO. Future research should focus on other anticancer drugs and combination of anticancer drugs such as

ifosfamide or cisplatin (Xu et al., 2014) to investigate for the devices ability to encapsulate and release different combinations.

Appendix

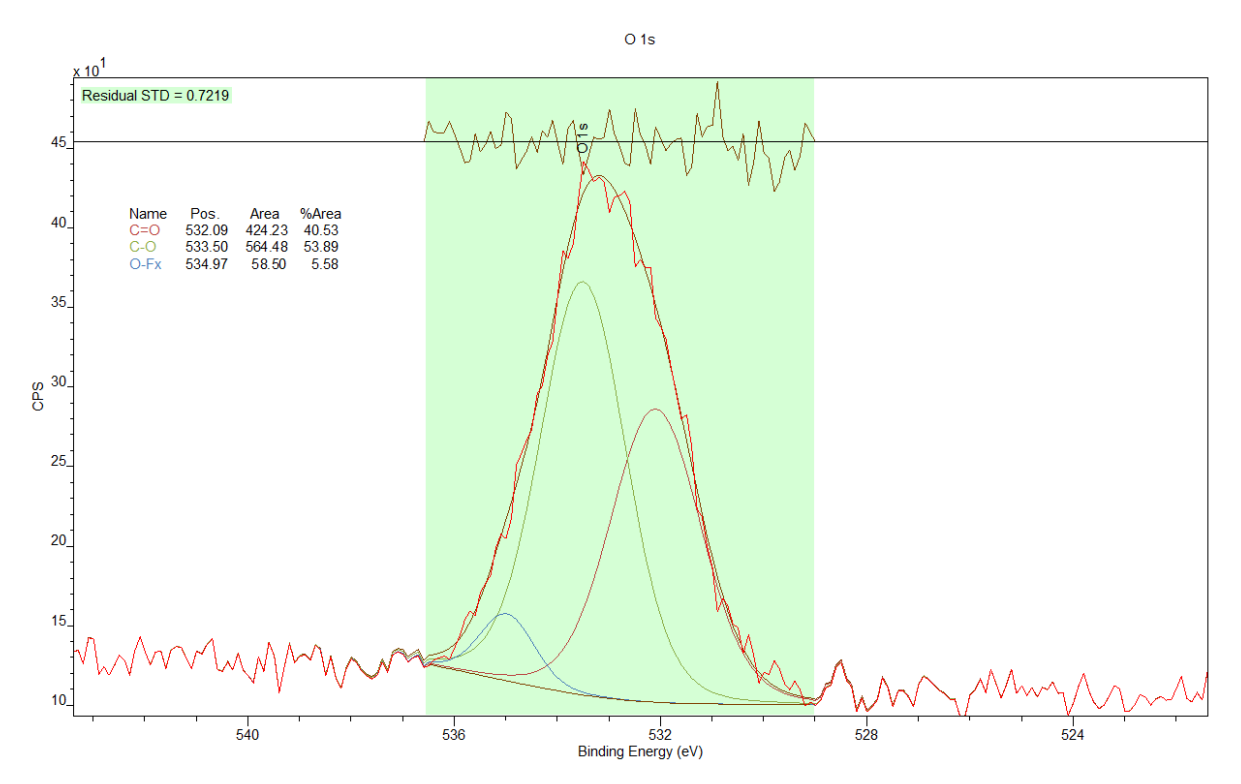


Figure A.6.1 - XPS O 1s scan of the precursors synthesised by a 2 hour hydrothermal pretreatment with a concentration of 0.01/g/ml sulphuric acid catalyst (TT-2H-P/AT-0.01-P).

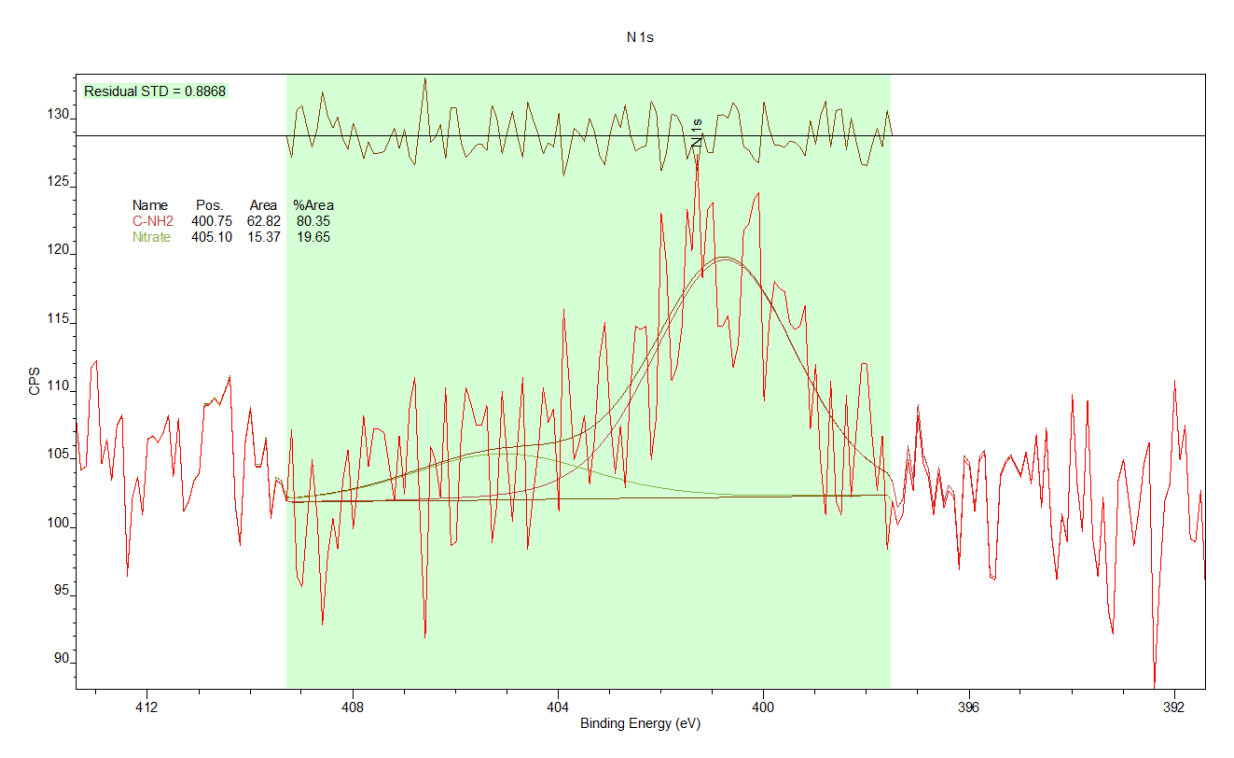


Figure A.6.2 - XPS O 1s scan of the precursors synthesised by a 2 hour hydrothermal pretreatment with a concentration of 0.01/g/ml sulphuric acid catalyst (TT-2H-P/AT-0.01-P).

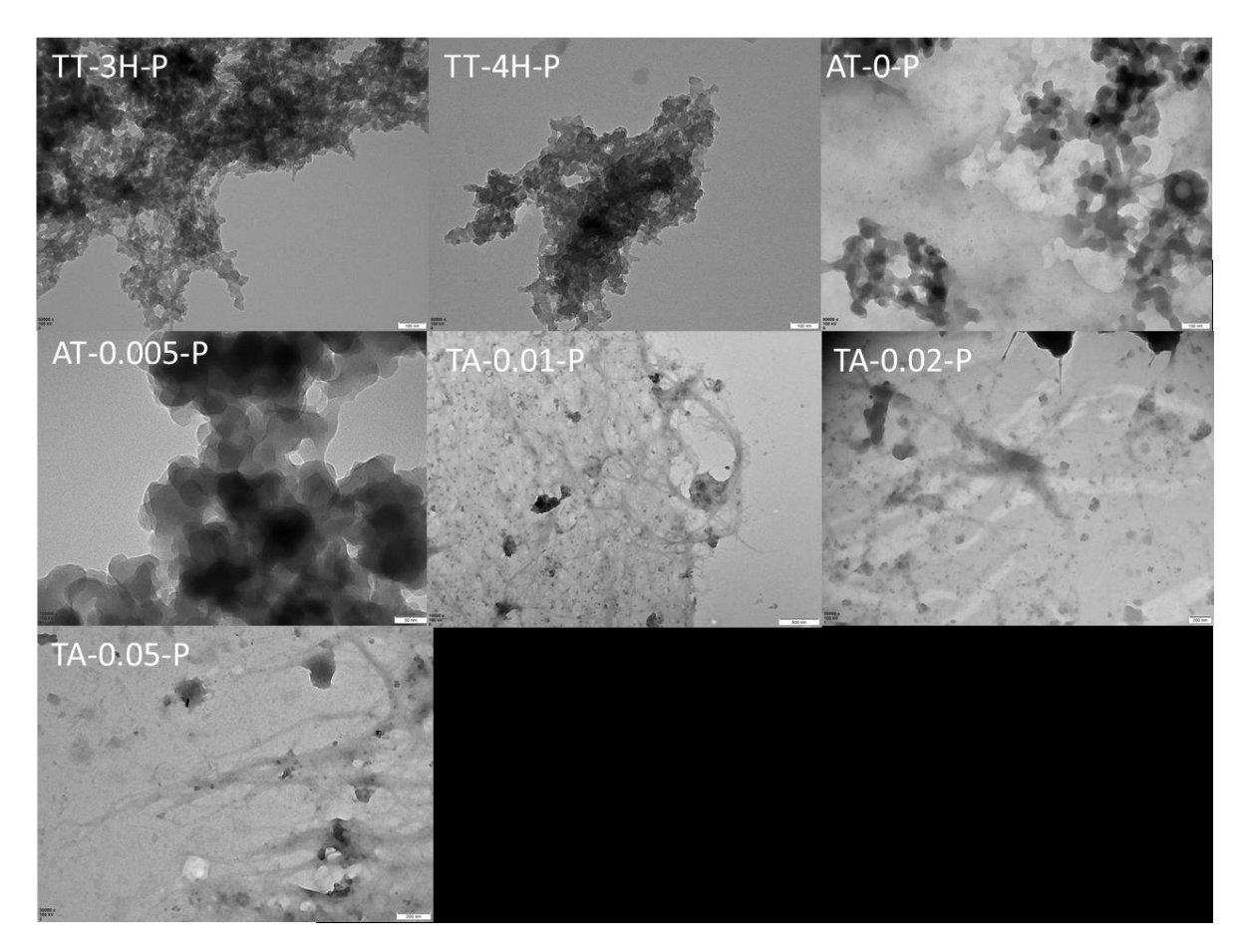


Figure A.6.3 - TEM images of precursors obtained though HTC carbonisation.

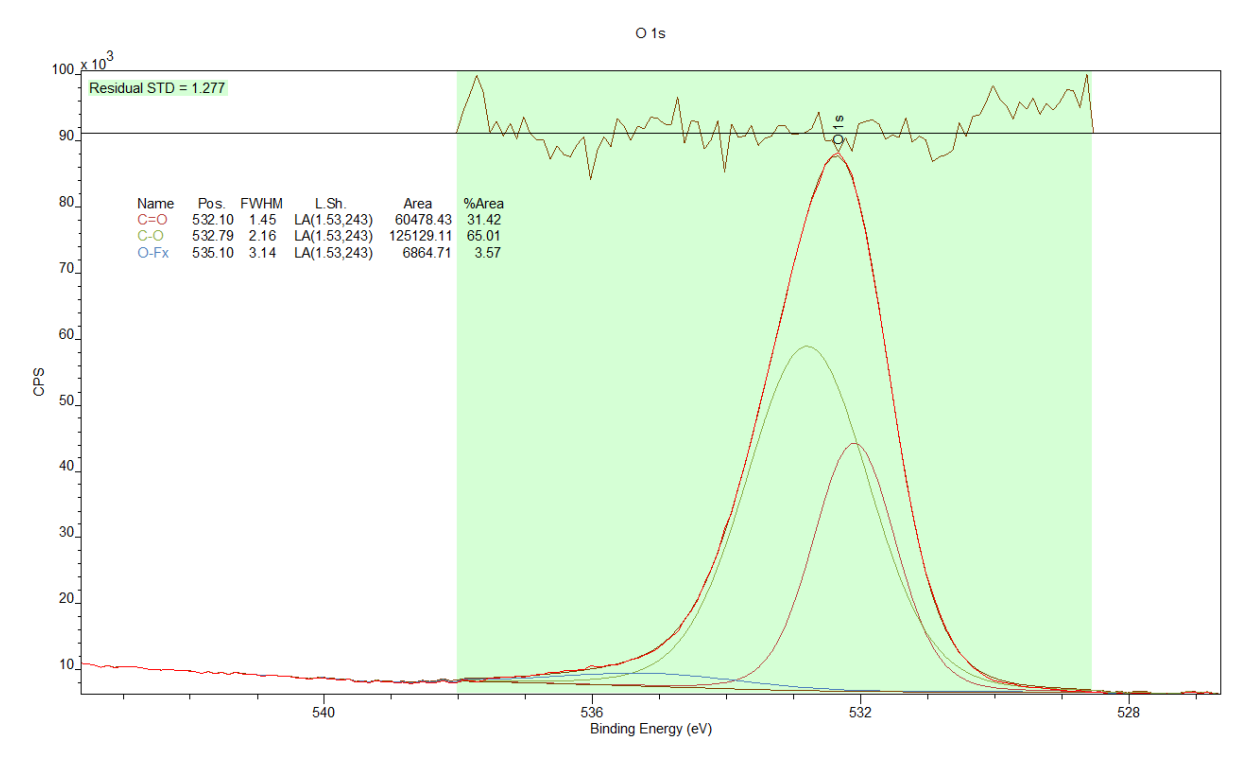


Figure A.6.4 - Figure A4 - XPS O 1s scan of the carbon dot sample TT-2H-P/AT-0.01-P



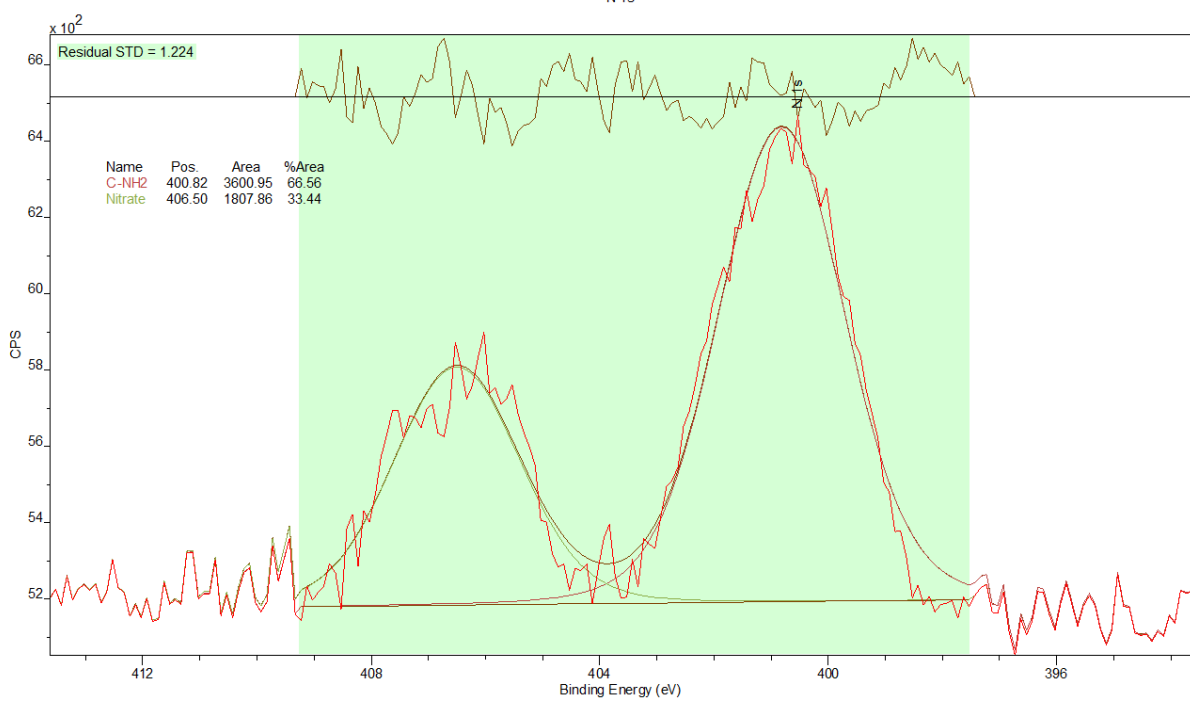


Figure A.6.5 - XPS N 1s scan of the carbon dot sample TT-2H-P/AT-0.01-P

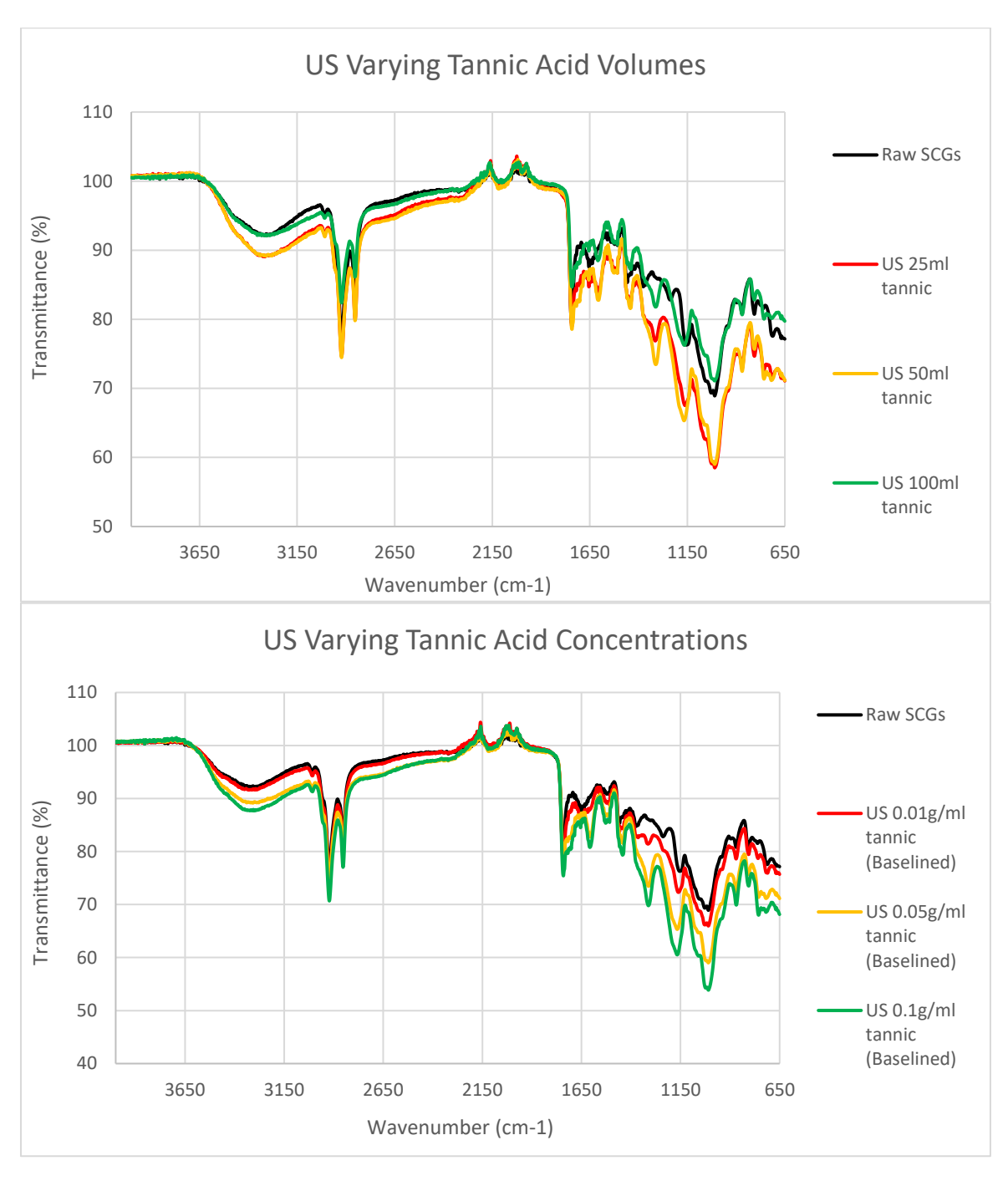


Figure A.6.6 - FT-IR data for the ultrasonication treatment of spent coffee grounds.

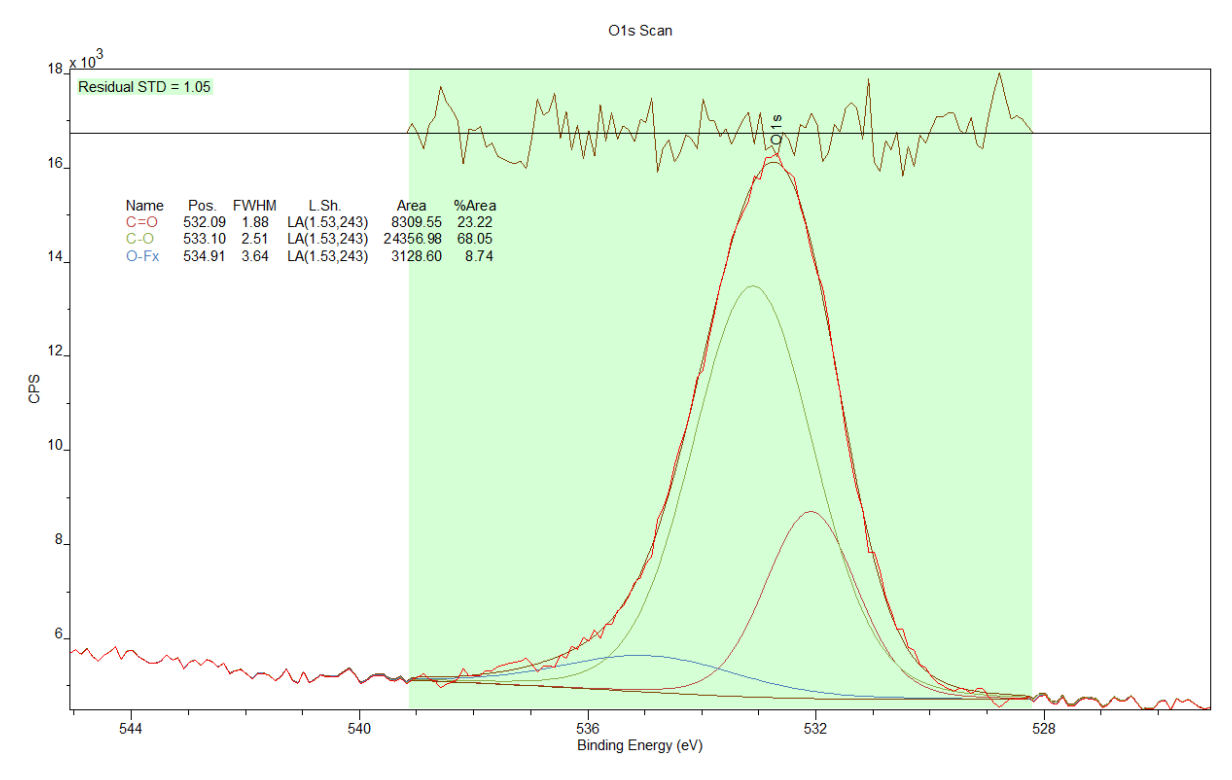


Figure A.6.7 - XPS O 1s scan of the precursor sample Std-Cnd-PT

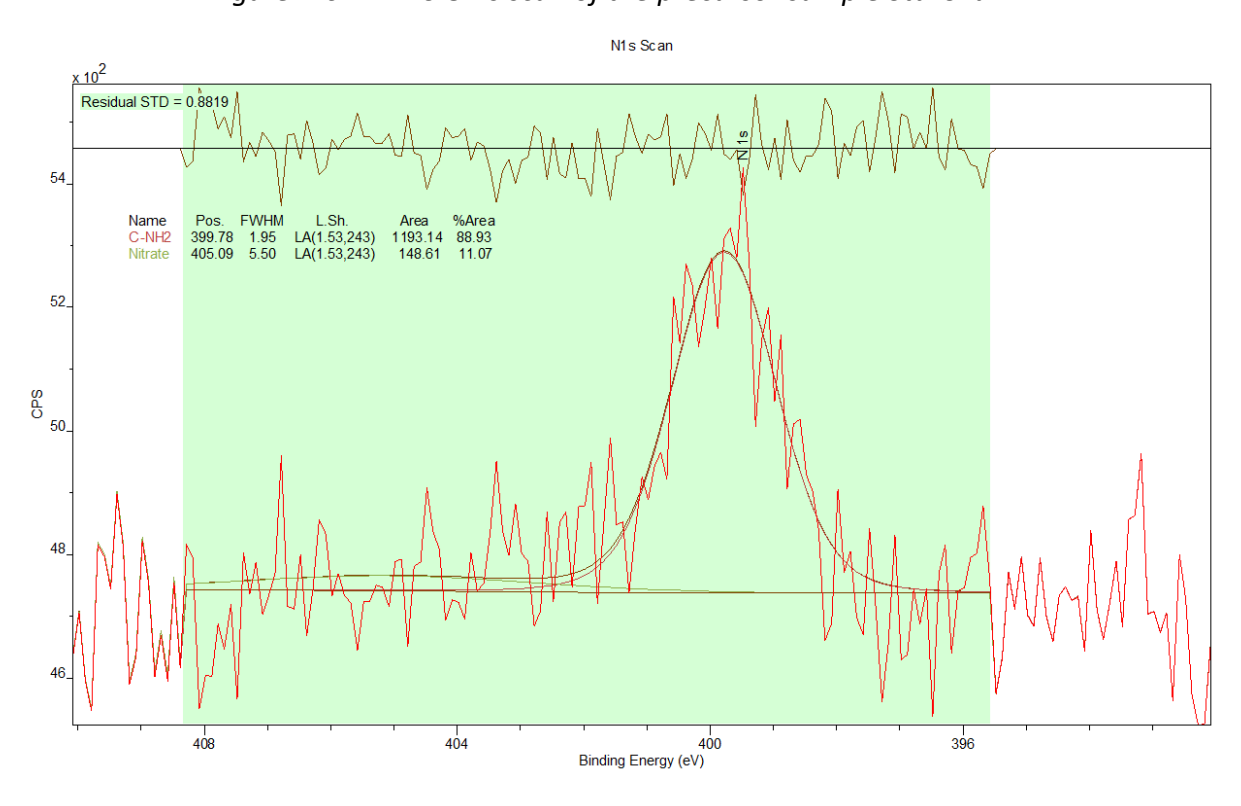


Figure A.6.8 - XPS N 1s scan of the precursor sample Std-Cnd-PT

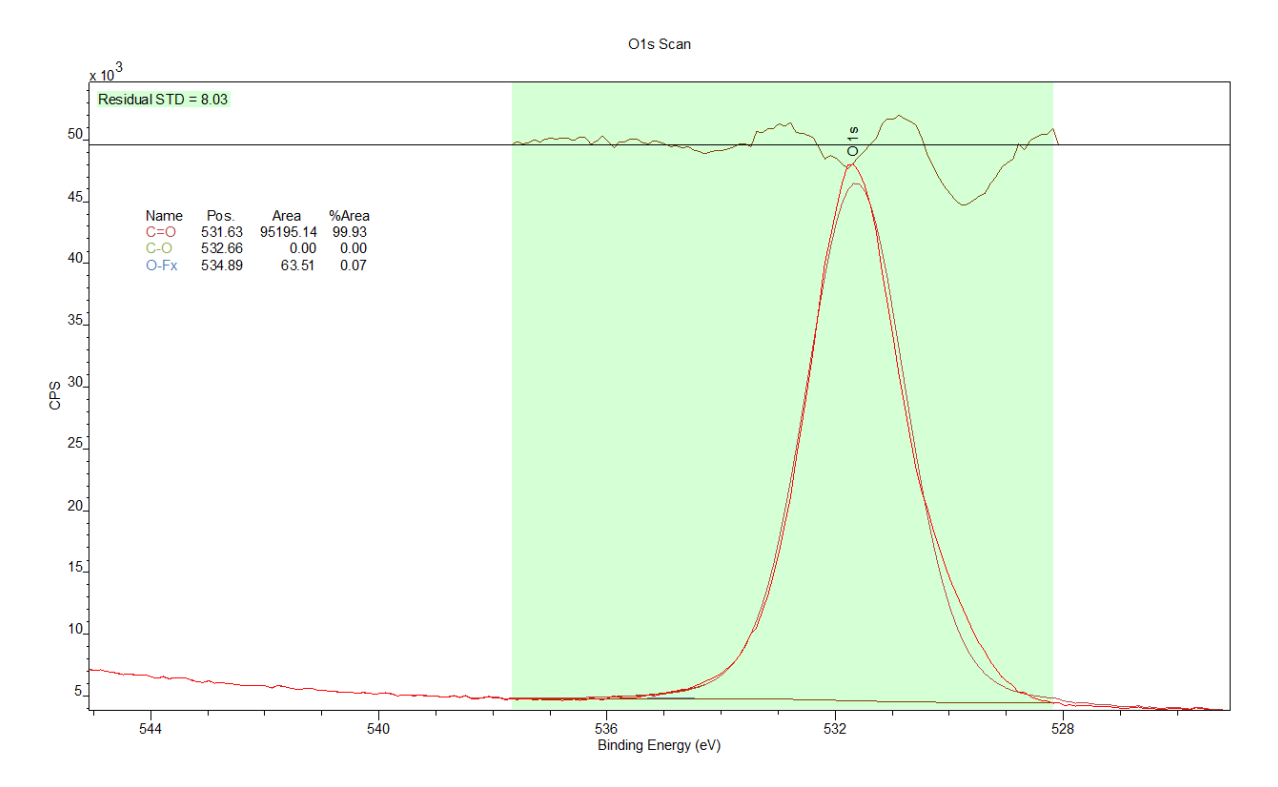


Figure A.6.9 - XPS O 1s scan of carbon dots synthesised at 150° C and 120 minutes (150-120-CD)

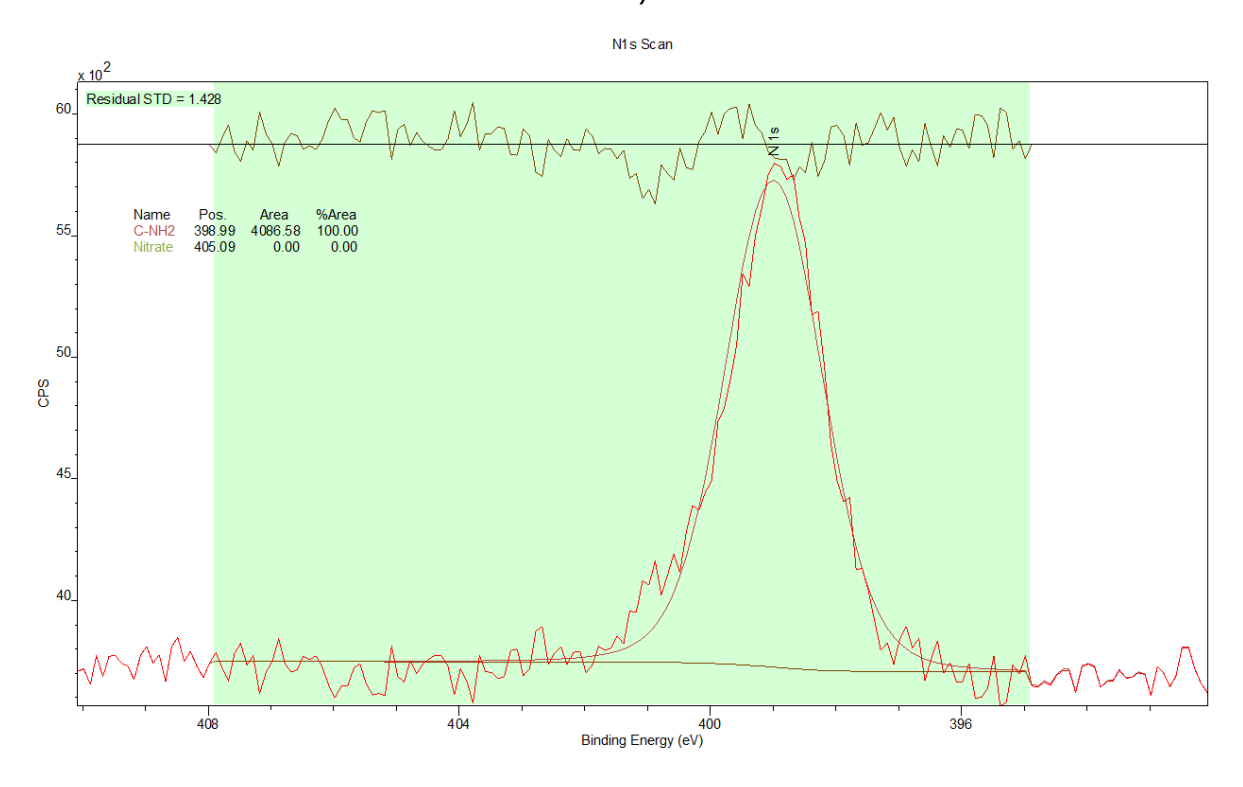


Figure A.6.10 - XPS N 1s scan of carbon dots synthesised at 150° C and 120 minutes (150-120-CD)



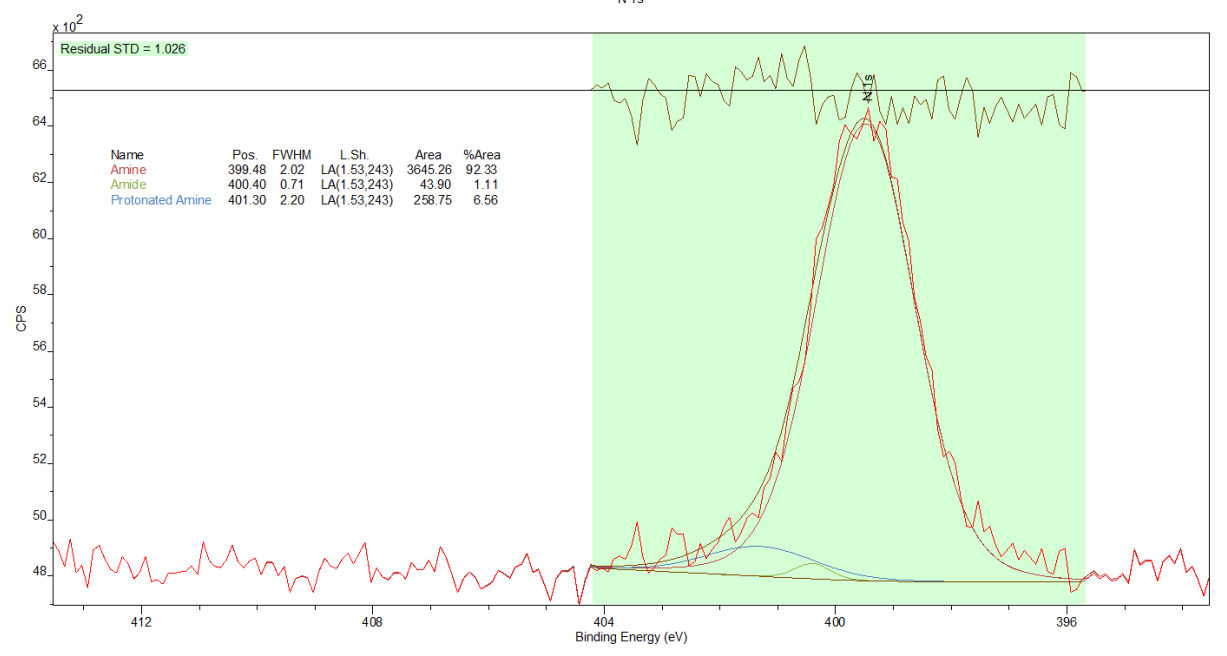


Figure A.6.11 - XPS N 1s scan of the first layer deposition (CaP nanoparticle + PEI)

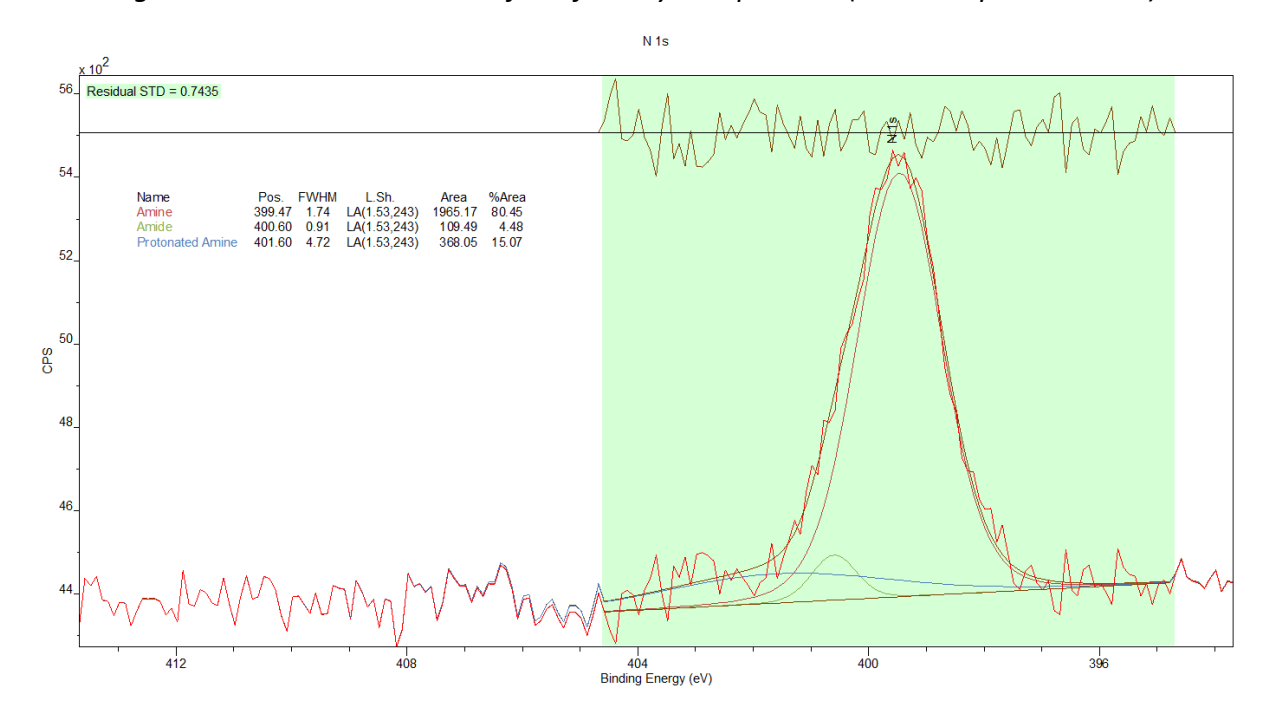


Figure A.6.12 - XPS N 1s scan of the second layer deposition (CaP nanoparticle + PEI + alginate)



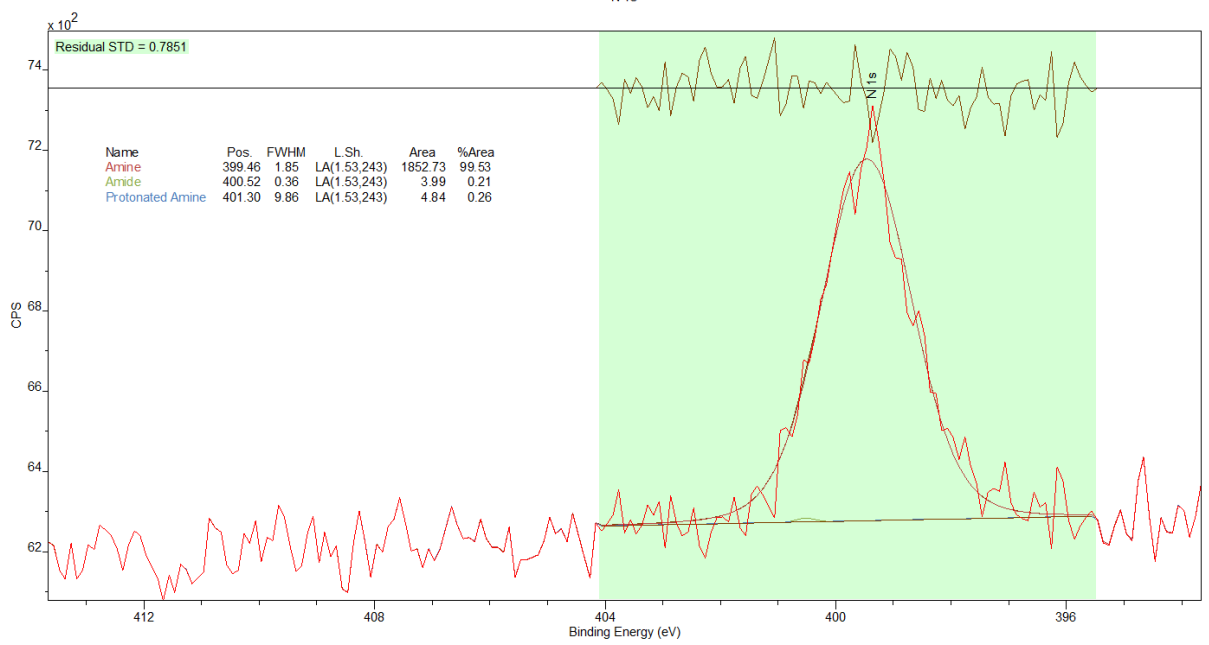


Figure A.6.13 - XPS N 1s scan of the third layer deposition (CaP nanoparticle + PEI + alginate + chitosan)

References

- Abbas, A., Mariana, L. T., & Phan, A. N. (2018). Biomass-waste derived graphene quantum dots and their applications. *Carbon*, *140*, 77-99. https://doi.org/https://doi.org/10.1016/j.carbon.2018.08.016
- Abbas, A., Tabish, T. A., Bull, S. J., Lim, T. M., & Phan, A. N. (2020). High yield synthesis of graphene quantum dots from biomass waste as a highly selective probe for Fe3+ sensing. *Scientific Reports*, 10(1), 21262. https://doi.org/10.1038/s41598-020-78070-2
- Abdelkebir, K., Morin-Grognet, S., Gaudière, F., Coquerel, G., Labat, B., Atmani, H., & Ladam, G. (2012). Biomimetic layer-by-layer templates for calcium phosphate biomineralization. *Acta Biomaterialia*, 8(9), 3419-3428. https://doi.org/https://doi.org/10.1016/j.actbio.2012.05.035
- Abou-Elkacem, L., Bachawal, S. V., & Willmann, J. K. (2015). Ultrasound molecular imaging: Moving toward clinical translation. *European Journal of Radiology*, *84*(9), 1685-1693. https://doi.org/https://doi.org/10.1016/j.ejrad.2015.03.016
- Achadu, O. J., & Revaprasadu, N. (2019). Tannic acid-derivatized graphitic carbon nitride quantum dots as an "on-off-on" fluorescent nanoprobe for ascorbic acid via copper(II) mediation. *Microchimica Acta*, 186(2), 87. https://doi.org/10.1007/s00604-018-3203-x
- ACS. (2020). *Key Statistics for Osteosarcoma*. Retrieved 21/11 from https://www.cancer.org/cancer/types/osteosarcoma/about/key-statistics.html
- Adamczak, M., Hoel, H. J., Gaudernack, G., Barbasz, J., Szczepanowicz, K., & Warszyński, P. (2012). Polyelectrolyte multilayer capsules with quantum dots for biomedical applications. *Colloids and Surfaces B: Biointerfaces, 90,* 211-216. https://doi.org/https://doi.org/10.1016/j.colsurfb.2011.10.028
- Adolfsson, K. H., Hassanzadeh, S., & Hakkarainen, M. (2015). Valorization of cellulose and waste paper to graphene oxide quantum dots [10.1039/C5RA01805F]. *RSC Advances*, *5*(34), 26550-26558. https://doi.org/10.1039/C5RA01805F
- Afraz, S., Ghasemzadeh, H., & Dargahi, M. (2022). Nanomagnetic hydrogel based on chitosan, hyaluronic acid, and glucose oxidase as a nanotheranostic platform for simultaneous therapeutic and imaging applications. *Materials Today Chemistry*, 24, 100807. https://doi.org/https://doi.org/10.1016/j.mtchem.2022.100807
- Afshar, A., Ghorbani, M., Ehsani, N., Saeri, M. R., & Sorrell, C. C. (2003). Some important factors in the wet precipitation process of hydroxyapatite. *Materials & Design*, *24*(3), 197-202. https://doi.org/https://doi.org/10.1016/S0261-3069(03)00003-7
- Ahmadi, D., Zarei, M., Rahimi, M., Khazaie, M., Asemi, Z., Mir, S. M., Sadeghpour, A., Karimian, A., Alemi, F., Rahmati-Yamchi, M., Salehi, R., Jadidi-Niaragh, F., Yousefi, M., Khelgati, N., Majidinia, M., Safa, A., & Yousefi, B. (2020). Preparation and in-vitro evaluation of pHresponsive cationic cyclodextrin coated magnetic nanoparticles for delivery of methotrexate to the Saos-2 bone cancer cells. *Journal of Drug Delivery Science and Technology*, *57*, 101584. https://doi.org/https://doi.org/10.1016/j.jddst.2020.101584
- Ahmed, G. H. G., Laíño, R. B., Calzón, J. A. G., & García, M. E. D. (2015). Fluorescent carbon nanodots for sensitive and selective detection of tannic acid in wines. *Talanta*, *132*, 252-257. https://doi.org/https://doi.org/10.1016/j.talanta.2014.09.028
- Ai, H. (2011). Layer-by-layer capsules for magnetic resonance imaging and drug delivery. *Advanced Drug Delivery Reviews*, *63*(9), 772-788. https://doi.org/https://doi.org/10.1016/j.addr.2011.03.013
- Akmaz, S., Adıgüzel, E., Yasar, M., & Ergüven, O. (2013). The Effect of Ag Content of the Chitosan-Silver Nanoparticle Composite Material on the Structure and Antibacterial Activity. *Advances in Materials Science and Engineering*, 2013, 1-6. https://doi.org/10.1155/2013/690918
- Alamdari, S. G., Amini, M., Jalilzadeh, N., Baradaran, B., Mohammadzadeh, R., Mokhtarzadeh, A., & Oroojalian, F. (2022). Recent advances in nanoparticle-based photothermal therapy for breast cancer. *J Control Release*, 349, 269-303. https://doi.org/10.1016/j.jconrel.2022.06.050

- Alarfaj, N. A., El-Tohamy, M. F., & Oraby, H. F. (2018). CA 19-9 Pancreatic Tumor Marker Fluorescence Immunosensing Detection via Immobilized Carbon Quantum Dots Conjugated Gold Nanocomposite. *International Journal of Molecular Sciences*, 19(4).
- Algarra, M., Campos, B. B., Radotić, K., Mutavdžić, D., Bandosz, T., Jiménez-Jiménez, J., Rodriguez-Castellón, E., & Esteves da Silva, J. C. G. (2014). Luminescent carbon nanoparticles: effects of chemical functionalization, and evaluation of Ag+ sensing properties [10.1039/C4TA00264D]. *Journal of Materials Chemistry A*, 2(22), 8342-8351. https://doi.org/10.1039/C4TA00264D
- Alhokbany, N., Althagafi, H., Ahmed, J., & Alshehri, S. M. (2023). Synthesis and characterization of carbon dots nanoparticles for detection of ascorbic acid. *Materials Letters*, *351*, 134992. https://doi.org/https://doi.org/10.1016/j.matlet.2023.134992
- Alkekhia, D., Hammond, P. T., & Shukla, A. (2020). Layer-by-Layer Biomaterials for Drug Delivery. Annual Review of Biomedical Engineering, 22(1), 1-24. https://doi.org/10.1146/annurev-bioeng-060418-052350
- Alphandéry, E. (2020). Iron oxide nanoparticles for therapeutic applications. *Drug Discovery Today*, 25(1), 141-149. https://doi.org/https://doi.org/10.1016/j.drudis.2019.09.020
- Alrushaid, N., Khan, F. A., Al-Suhaimi, E. A., & Elaissari, A. (2023). Nanotechnology in Cancer Diagnosis and Treatment. *Pharmaceutics*, 15(3).
- Alshehri S, I. S., Rizwanullah M, Akhter S, Mahdi W, Kazi M, Ahmad J. (2021). Progress of Cancer Nanotechnology as Diagnostics, Therapeutics, and Theranostics Nanomedicine: Preclinical Promise and Translational Challenges. *Pharmaceutics*, 13(1), 24. https://doi.org/https://doi.org/10.3390/pharmaceutics13010024
- Amer Ridha, A., Pakravan, P., Hemati Azandaryani, A., & Zhaleh, H. (2020). Carbon dots; the smallest photoresponsive structure of carbon in advanced drug targeting. *Journal of Drug Delivery Science and Technology*, *55*, 101408. https://doi.org/https://doi.org/10.1016/j.jddst.2019.101408
- Aminolroayaei, F., Shahbazi-Gahrouei, D., Shahbazi-Gahrouei, S., & Rasouli, N. (2021). Recent nanotheranostics applications for cancer therapy and diagnosis: A review. *IET Nanobiotechnol*, *15*(3), 247-256. https://doi.org/10.1049/nbt2.12021
- Amjad, Z. (1998). *Calcium Phosphates in Biological and Industrial Systems* (1 ed.). Springer New York, NY. https://doi.org/https://doi.org/10.1007/978-1-4615-5517-9
- An, Q., Lin, Q., Huang, X., Zhou, R., Guo, X., Xu, W., Wang, S., Xu, D., & Chang, H.-T. (2021). Electrochemical synthesis of carbon dots with a Stokes shift of 309 nm for sensing of Fe3+ and ascorbic acid. *Dyes and Pigments*, 185, 108878. https://doi.org/https://doi.org/10.1016/j.dyepig.2020.108878
- Andrade, P. F., Nakazato, G., & Durán, N. (2017). Additive interaction of carbon dots extracted from soluble coffee and biogenic silver nanoparticles against bacteria. *Journal of Physics:*Conference Series, 838(1), 012028. https://doi.org/10.1088/1742-6596/838/1/012028
- Ang, M. J. Y., Chan, S. Y., Goh, Y.-Y., Luo, Z., Lau, J. W., & Liu, X. (2021). Emerging strategies in developing multifunctional nanomaterials for cancer nanotheranostics. *Advanced Drug Delivery Reviews*, 178, 113907. https://doi.org/10.1016/j.addr.2021.113907
- Angelatos, A. S., Radt, B., & Caruso, F. (2005). Light-Responsive Polyelectrolyte/Gold Nanoparticle Microcapsules. *The Journal of Physical Chemistry B*, 109(7), 3071-3076. https://doi.org/10.1021/jp045070x
- Antipov, A. A., Sukhorukov, G. B., & Möhwald, H. (2003). Influence of the Ionic Strength on the Polyelectrolyte Multilayers' Permeability. *Langmuir*, *19*(6), 2444-2448. https://doi.org/10.1021/la026101n
- Arms, L., Smith, D. W., Flynn, J., Palmer, W., Martin, A., Woldu, A., & Hua, S. (2018). Advantages and Limitations of Current Techniques for Analyzing the Biodistribution of Nanoparticles. *Front Pharmacol*, *9*, 802. https://doi.org/10.3389/fphar.2018.00802
- Asghar, B. H., Hassan, R. K. A., Barakat, L. A. A., Alharbi, A., El Behery, M., Elshaarawy, R. F. M., & Hassan, Y. A. (2023). Cross-linked quaternized chitosan nanoparticles for effective delivery and controllable release of O. europaea phenolic extract targeting cancer therapy. *Journal of Drug Delivery Science and Technology*, 83, 104388. https://doi.org/https://doi.org/10.1016/j.jddst.2023.104388

- Atchudan, R., Edison, T. N. J. I., & Lee, Y. R. (2016). Nitrogen-doped carbon dots originating from unripe peach for fluorescent bioimaging and electrocatalytic oxygen reduction reaction. *Journal of Colloid and Interface Science*, 482, 8-18. https://doi.org/https://doi.org/10.1016/j.jcis.2016.07.058
- Attia, M. F., Anton, N., Wallyn, J., Omran, Z., & Vandamme, T. F. (2019). An overview of active and passive targeting strategies to improve the nanocarriers efficiency to tumour sites. *Journal of Pharmacy and Pharmacology*, 71(8), 1185-1198. https://doi.org/https://doi.org/10.1111/jphp.13098
- Avti PK, H. S., Favazza C, Mikos AG, Jansen JA, Shroyer KR, et al. . (2012). Detection, Mapping, and Quantification of Single Walled Carbon Nanotubes in Histological Specimens with Photoacoustic Microscopy. *PLoS ONE*, *7*(4). https://doi.org/https://doi.org/10.1371/journal.pone.0035064
- Azimijou, N., Karimi-Soflou, R., & Karkhaneh, A. (2023). Actively targeted delivery of tamoxifen through stimuli-responsive polymeric nanoparticles for cancer chemotherapy. *Journal of Drug Delivery Science and Technology*, 87, 104779. https://doi.org/https://doi.org/10.1016/j.jddst.2023.104779
- Bajpai, S. K., D'Souza, A., & Suhail, B. (2019). Blue light-emitting carbon dots (CDs) from a milk protein and their interaction with Spinacia oleracea leaf cells. *International Nano Letters*, *9*(3), 203-212. https://doi.org/10.1007/s40089-019-0271-9
- Ballou, B., Ernst, L. A., Andreko, S., Harper, T., Fitzpatrick, J. A., Waggoner, A. S., & Bruchez, M. P. (2007). Sentinel lymph node imaging using quantum dots in mouse tumor models. *Bioconjug Chem*, 18(2), 389-396. https://doi.org/10.1021/bc060261j
- Barchiesi, E., Wareing, T., Desmond, L., Phan, A. N., Gentile, P., & Pontrelli, G. (2022).

 Characterization of the Shells in Layer-By-Layer Nanofunctionalized Particles: A

 Computational Study [Original Research]. Frontiers in Bioengineering and Biotechnology, 10.

 https://doi.org/10.3389/fbioe.2022.888944
- Barnewitz, F. (2023). *Purification of Nanoparticles by dialysis*. Micromod. Retrieved 19/12 from https://fnkprddata.blob.core.windows.net/domestic/download/pdf/MPT-Technote_103_2.pdf
- Bastos, F. R., Soares da Costa, D., Reis, R. L., Alves, N. M., Pashkuleva, I., & Costa, R. R. (2023). Layer-by-layer coated calcium carbonate nanoparticles for targeting breast cancer cells. *Biomaterials Advances*, 153, 213563. https://doi.org/https://doi.org/10.1016/j.bioadv.2023.213563
- Bazak, R., Houri, M., Achy, S. E., Hussein, W., & Refaat, T. (2014). Passive targeting of nanoparticles to cancer: A comprehensive review of the literature. *Mol Clin Oncol*, *2*(6), 904-908. https://doi.org/10.3892/mco.2014.356
- Bazak, R., Houri, M., El Achy, S., Kamel, S., & Refaat, T. (2015). Cancer active targeting by nanoparticles: a comprehensive review of literature. *J Cancer Res Clin Oncol*, 141(5), 769-784. https://doi.org/10.1007/s00432-014-1767-3
- Belbekhouche, S., Cossutta, M., Habert, D., Hamadi, S., Modjinou, T., Cascone, I., & Courty, J. (2020). N6L-functionalized nanoparticles for targeted and inhibited pancreatic cancer cells. *Colloids and Surfaces A: Physicochemical and Engineering Aspects*, 607, 125461. https://doi.org/https://doi.org/10.1016/j.colsurfa.2020.125461
- Bevan, E., Santori, G., & Luberti, M. (2023). Kinetic modelling of the hydrothermal carbonisation of the macromolecular components in lignocellulosic biomass. *Bioresource Technology Reports*, 24, 101643. https://doi.org/https://doi.org/https://doi.org/https://doi.org/10.1016/j.biteb.2023.101643
- Blacklock, J., Sievers, T. K., Handa, H., You, Y. Z., Oupický, D., Mao, G., & Möhwald, H. (2010). Cross-linked bioreducible layer-by-layer films for increased cell adhesion and transgene expression. *J Phys Chem B*, 114(16), 5283-5291. https://doi.org/10.1021/jp100486h
- Bressi, V., Balu, A. M., Iannazzo, D., & Espro, C. (2023). Recent advances in the synthesis of carbon dots from renewable biomass by high-efficient hydrothermal and microwave green approaches. *Current Opinion in Green and Sustainable Chemistry*, 40, 100742. https://doi.org/https://doi.org/10.1016/j.cogsc.2022.100742

- Brown, F., & Diller, K. R. (2008). Calculating the optimum temperature for serving hot beverages. *Burns*, 34(5), 648-654. https://doi.org/10.1016/j.burns.2007.09.012
- Buzea, C., Pacheco, I. I., & Robbie, K. (2007). Nanomaterials and nanoparticles: Sources and toxicity. *Biointerphases*, 2(4), MR17-MR71. https://doi.org/10.1116/1.2815690
- Byrd, S., & Hildreth, D. P. (2001). Learning the Functional Groups: Keys to Success. *Journal of Chemical Education*, 78(10), 1355. https://doi.org/10.1021/ed078p1355
- Caires, A. J., Mansur, A. A. P., Carvalho, I. C., Carvalho, S. M., & Mansur, H. S. (2020). Green synthesis of ZnS quantum dot/biopolymer photoluminescent nanoprobes for bioimaging brain cancer cells. *Materials Chemistry and Physics*, 244, 122716. https://doi.org/https://doi.org/10.1016/j.matchemphys.2020.122716
- Calabro, R. L., Yang, D.-S., & Kim, D. Y. (2018). Liquid-phase laser ablation synthesis of graphene quantum dots from carbon nano-onions: Comparison with chemical oxidation. *Journal of Colloid and Interface Science*, 527, 132-140. https://doi.org/https://doi.org/10.1016/j.jcis.2018.04.113
- Caruso, F. (2004). *Colloids and Colliod Assemblies: Synthesis, Modificaion, Organization and Utilization of Colloid Particles.* WILEY-VCH Verlag GmbH & Co. KGaA.
- Ceppi, L., Bardhan, N. M., Na, Y., Siegel, A., Rajan, N., Fruscio, R., Del Carmen, M. G., Belcher, A. M., & Birrer, M. J. (2019). Real-Time Single-Walled Carbon Nanotube-Based Fluorescence Imaging Improves Survival after Debulking Surgery in an Ovarian Cancer Model. *ACS Nano*, *13*(5), 5356-5365. https://doi.org/10.1021/acsnano.8b09829
- Chan, W. C. W., Maxwell, D. J., Gao, X., Bailey, R. E., Han, M., & Nie, S. (2002). Luminescent quantum dots for multiplexed biological detection and imaging. *Current Opinion in Biotechnology*, 13(1), 40-46. https://doi.org/https://doi.org/https://doi.org/https://doi.org/10.1016/S0958-1669(02)00282-3
- Chang, Q., Zhou, X., Xiang, G., Jiang, S., Li, L., Wang, Y., Li, Y., Cao, Z., Tang, X., Ling, F., & Luo, X. (2021). Full color fluorescent carbon quantum dots synthesized from triammonium citrate for cell imaging and white LEDs. *Dyes and Pigments*, 193, 109478. https://doi.org/https://doi.org/10.1016/j.dyepig.2021.109478
- Chang Xu, Q. F., Peng Ning, Zhenguang Li, Yao Qin, Yu Cheng. (2021). Recent Advances on Nanoparticle-Based Imaging Contrast Agents for in Vivo Stem Cell Tracking. *Material Matters*, 16(2).
- Chapman, S., Dobrovolskaia, M., Farahani, K., Goodwin, A., Joshi, A., Lee, H., Meade, T., Pomper, M., Ptak, K., Rao, J., Singh, R., Sridhar, S., Stern, S., Wang, A., Weaver, J. B., Woloschak, G., & Yang, L. (2013). Nanoparticles for cancer imaging: The good, the bad, and the promise. *Nano Today*, 8(5), 454-460. https://doi.org/10.1016/j.nantod.2013.06.001
- Charron, G., Hühn, D., Perrier, A., Cordier, L., Pickett, C. J., Nann, T., & Parak, W. J. (2012). On the Use of pH Titration to Quantitatively Characterize Colloidal Nanoparticles. *Langmuir*, 28(43), 15141-15149. https://doi.org/10.1021/la302570s
- Chary, P. S., Bhawale, R., Vasave, R., Rajana, N., Singh, P. K., Madan, J., Singh, S. B., & Mehra, N. K. (2023). A review on emerging role of multifunctional carbon nanotubes as an armament in cancer therapy, imaging and biosensing. *Journal of Drug Delivery Science and Technology*, 85, 104588. https://doi.org/https://doi.org/10.1016/j.jddst.2023.104588
- Chauhan, P., Saini, J., Chaudhary, S., & Bhasin, K. K. (2021). Sustainable synthesis of carbon dots from agarose waste and prospective application in sensing of l-aspartic acid. *Materials Research Bulletin*, 134, 111113. https://doi.org/https://doi.org/10.1016/j.materresbull.2020.111113
- Chavda, V. P., Khadela, A., Shah, Y., Postwala, H., Balar, P., & Vora, L. (2023). Current status of Cancer Nanotheranostics: Emerging strategies for cancer management [Review]. *Nanotheranostics*, 7(4), 368-379. https://doi.org/10.7150/ntno.82263
- Chen, B. B., Liu, M. L., Li, C. M., & Huang, C. Z. (2019). Fluorescent carbon dots functionalization. *Advances in Colloid and Interface Science*, *270*, 165-190. https://doi.org/https://doi.org/10.1016/j.cis.2019.06.008
- Chen, G., Qiu, H., Prasad, P. N., & Chen, X. (2014). Upconversion Nanoparticles: Design,
 Nanochemistry, and Applications in Theranostics. *Chemical Reviews*, 114(10), 5161-5214.
 https://doi.org/10.1021/cr400425h

- Chen, H., Zhang, W., Zhu, G., Xie, J., & Chen, X. (2017). Rethinking cancer nanotheranostics. *Nat Rev Mater*, 2. https://doi.org/10.1038/natrevmats.2017.24
- Chen, J., Du, H., Xu, Y., Ma, B., Zheng, Z., Li, P., & Jiang, Y. (2021). A turn-on fluorescent sensor based on coffee-ground carbon dots for the detection of sodium cyclamate. *Journal of Materials Science: Materials in Electronics*, 32(10), 13581-13587. https://doi.org/10.1007/s10854-021-05933-3
- Chen, L., Wu, Y., Wu, H., Li, J., Xie, J., Zang, F., Ma, M., Gu, N., & Zhang, Y. (2019). Magnetic targeting combined with active targeting of dual-ligand iron oxide nanoprobes to promote the penetration depth in tumors for effective magnetic resonance imaging and hyperthermia. *Acta Biomaterialia*, 96, 491-504. https://doi.org/https://doi.org/10.1016/j.actbio.2019.07.017
- Chen, Z., Huang, H., He, S., Wang, Y., Cai, L., & Xie, Y. (2022). Progresses in Fluorescence Imaging Guidance for Bone and Soft Tissue Sarcoma Surgery. *Front Oncol*, *12*, 879697. https://doi.org/10.3389/fonc.2022.879697
- Cheng, L.-C., Hashemnejad, S. M., Zarket, B., Muthukrishnan, S., & Doyle, P. S. (2020). Thermally and pH-responsive gelation of nanoemulsions stabilized by weak acid surfactants. *Journal of Colloid and Interface Science*, *563*, 229-240. https://doi.org/https://doi.org/10.1016/j.jcis.2019.12.054
- Chou, W.-L., Wang, C.-T., Huang, K.-Y., Chang, Y.-C., & Shu, C.-M. (2012). Investigation of indium ions removal from aqueous solutions using spent coffee grounds. *Int. J. Phys. Sci*, 7(16), 2445-2454.
- Cipreste, M. F., Rezende, M. R. d., Hneda, M. L., Peres, A. M., Cotta, A. A. C., Teixeira, V. d. C., Macedo, W. A. d. A., & Sousa, E. M. B. d. (2018). Functionalized-radiolabeled hydroxyapatite/tenorite nanoparticles as theranostic agents for osteosarcoma. *Ceramics International*, 44(15), 17800-17811. https://doi.org/https://doi.org/10.1016/j.ceramint.2018.06.248
- Cogo, L. C., Batisti, M. V., Pereira-da-Silva, M. A., Oliveira, O. N., Nart, F. C., & Huguenin, F. (2006). Layer-by-layer films of chitosan, poly(vinyl sulfonic acid), and platinum for methanol electrooxidation and oxygen electroreduction. *Journal of Power Sources*, *158*(1), 160-163. https://doi.org/https://doi.org/10.1016/j.jpowsour.2005.10.004
- Cormode, D. P., Naha, P. C., & Fayad, Z. A. (2014). Nanoparticle contrast agents for computed tomography: a focus on micelles. *Contrast Media Mol Imaging*, *9*(1), 37-52. https://doi.org/10.1002/cmmi.1551
- Correa, S., Choi, K. Y., Dreaden, E. C., Renggli, K., Shi, A., Gu, L., Shopsowitz, K. E., Quadir, M. A., Ben-Akiva, E., & Hammond, P. T. (2016). Highly scalable, closed-loop synthesis of drug-loaded, layer-by-layer nanoparticles. *Adv Funct Mater*, *26*(7), 991-1003. https://doi.org/10.1002/adfm.201504385
- Correia, A. R., Sampaio, I., Comparetti, E. J., Vieira, N. C. S., & Zucolotto, V. (2021). Optimized PAH/Folic acid layer-by-layer films as an electrochemical biosensor for the detection of folate receptors. *Bioelectrochemistry*, *137*, 107685. https://doi.org/https://doi.org/10.1016/j.bioelechem.2020.107685
- Costa, A. I., Barata, P. D., Moraes, B., & Prata, J. V. (2022). Carbon Dots from Coffee Grounds: Synthesis, Characterization, and Detection of Noxious Nitroanilines. *Chemosensors*, 10(3).
- Criado-Gonzalez, M., Mijangos, C., & Hernández, R. (2021). Polyelectrolyte Multilayer Films Based on Natural Polymers: From Fundamentals to Bio-Applications. *Polymers (Basel)*, *13*(14). https://doi.org/10.3390/polym13142254
- Crista, D. M. A., El Mragui, A., Algarra, M., Esteves da Silva, J. C. G., Luque, R., & Pinto da Silva, L. (2020). Turning Spent Coffee Grounds into Sustainable Precursors for the Fabrication of Carbon Dots. *Nanomaterials (Basel)*, 10(6). https://doi.org/10.3390/nano10061209
- Crista, D. M. A., El Mragui, A., Algarra, M., Esteves da Silva, J. C. G., Luque, R., & Pinto da Silva, L. (2020). Turning Spent Coffee Grounds into Sustainable Precursors for the Fabrication of Carbon Dots. *Nanomaterials*, *10*(6).

- Cui, L.-Y., Zeng, R.-C., Zhu, X.-X., Pang, T.-T., Li, S.-Q., & Zhang, F. (2016). Corrosion resistance of biodegradable polymeric layer-by-layer coatings on magnesium alloy AZ31. *Frontiers of Materials Science*, *10*(2), 134-146. https://doi.org/10.1007/s11706-016-0332-1
- Cui, L., Ren, X., Sun, M., Liu, H., & Xia, L. (2021). Carbon Dots: Synthesis, Properties and Applications. *Nanomaterials*, 11(12).
- da S. Pinto, T., Alves, L. A., de Azevedo Cardozo, G., Munhoz, V. H. O., Verly, R. M., Pereira, F. V., & de Mesquita, J. P. (2017). Layer-by-layer self-assembly for carbon dots/chitosan-based multilayer: Morphology, thickness and molecular interactions. *Materials Chemistry and Physics*, *186*, 81-89. https://doi.org/https://doi.org/10.1016/j.matchemphys.2016.10.032
- Dai, Y., Xiao, H., Liu, J., Yuan, Q., Ma, P. a., Yang, D., Li, C., Cheng, Z., Hou, Z., Yang, P., & Lin, J. (2013). In Vivo Multimodality Imaging and Cancer Therapy by Near-Infrared Light-Triggered trans-Platinum Pro-Drug-Conjugated Upconverison Nanoparticles. *Journal of the American Chemical Society*, 135(50), 18920-18929. https://doi.org/10.1021/ja410028q
- Dang, X., Gu, L., Qi, J., Correa, S., Zhang, G., Belcher, A. M., & Hammond, P. T. (2016). Layer-by-layer assembled fluorescent probes in the second near-infrared window for systemic delivery and detection of ovarian cancer. *Proc Natl Acad Sci U S A, 113*(19), 5179-5184. https://doi.org/10.1073/pnas.1521175113
- Dang, Y., & Guan, J. (2020). Nanoparticle-based drug delivery systems for cancer therapy. *Smart Materials in Medicine*, *1*, 10-19. https://doi.org/https://doi.org/10.1016/j.smaim.2020.04.001
- Daniel, S. (2023). Chapter 4 Characterization of carbon dots. In S. K. Kailasa & C. M. Hussain (Eds.), Carbon Dots in Analytical Chemistry (pp. 43-58). Elsevier. https://doi.org/https://doi.org/10.1016/B978-0-323-98350-1.00015-3
- Danışman-Kalındemirtaş, F., Kariper, İ. A., Hepokur, C., & Erdem-Kuruca, S. (2021). Selective cytotoxicity of paclitaxel bonded silver nanoparticle on different cancer cells. *Journal of Drug Delivery Science and Technology, 61*, 102265. https://doi.org/https://doi.org/10.1016/j.jddst.2020.102265
- Das, R., Bandyopadhyay, R., & Pramanik, P. (2018). Carbon quantum dots from natural resource: A review. *Materials Today Chemistry*, 8, 96-109. https://doi.org/https://doi.org/10.1016/j.mtchem.2018.03.003
- Davi, L. B. O., Silva, M. S., Ferreira, R. L., Muniz, W., Ribeiro, A. S., Lima, D. J. P., de Oliveira, I. N., & Barbosa, C. D. A. E. S. (2021). Multifunctional carbon dots derived from dansyl chloride for ratiometric thermal sensor and reactive oxygen generation. *Dyes and Pigments*, *194*, 109549. https://doi.org/https://doi.org/10.1016/j.dyepig.2021.109549
- Davies, J., Siebenhandl-Wolff, P., Tranquart, F., Jones, P., & Evans, P. (2022). Gadolinium: pharmacokinetics and toxicity in humans and laboratory animals following contrast agent administration. *Archives of Toxicology*, *96*(2), 403-429. https://doi.org/10.1007/s00204-021-03189-8
- de Godoi, F. C., Rodriguez-Castellon, E., Guibal, E., & Beppu, M. M. (2013). An XPS study of chromate and vanadate sorption mechanism by chitosan membrane containing copper nanoparticles. *Chemical Engineering Journal*, 234, 423-429. https://doi.org/https://doi.org/10.1016/j.cej.2013.09.006
- De Rooij, J. F., Heughebaert, J. C., & Nancollas, G. H. (1984). A ph study of calcium phosphate seeded precipitation. *Journal of Colloid and Interface Science*, 100(2), 350-358. https://doi.org/https://doi.org/10.1016/0021-9797(84)90440-5
- Debele, T. A., Yeh, C. F., & Su, W. P. (2020). Cancer Immunotherapy and Application of Nanoparticles in Cancers Immunotherapy as the Delivery of Immunotherapeutic Agents and as the Immunomodulators. *Cancers (Basel)*, 12(12). https://doi.org/10.3390/cancers12123773
- Decher, G., & Hong, J. D. (1991). Buildup of Ultrathin Multilayer Films by a Self-Assembly Process: II. Consecutive Adsorption of Anionic and Cationic Bipolar Amphiphiles and Polyelectrolytes on Charged Surfaces. *Berichte der Bunsengesellschaft für physikalische Chemie*, *95*(11), 1430-1434. https://doi.org/https://doi.org/10.1002/bbpc.19910951122
- Deligöz, H., Yılmaztürk, S., Karaca, T., Özdemir, H., Koç, S. N., Öksüzömer, F., Durmuş, A., & Gürkaynak, M. A. (2009). Self-assembled polyelectrolyte multilayered films on Nafion with

- lowered methanol cross-over for DMFC applications. *Journal of Membrane Science*, *326*(2), 643-649. https://doi.org/https://doi.org/10.1016/j.memsci.2008.10.055
- Deng, Y., Zhao, D., Chen, X., Wang, F., Song, H., & Shen, D. (2013). Long lifetime pure organic phosphorescence based on water soluble carbon dots [10.1039/C3CC42600A]. *Chemical Communications*, 49(51), 5751-5753. https://doi.org/10.1039/C3CC42600A
- Deng, Y. H., Chen, J. H., Yang, Q., & Zhuo, Y. Z. (2021). Carbon quantum dots (CQDs) and polyethyleneimine (PEI) layer-by-layer (LBL) self-assembly PEK-C-based membranes with high forward osmosis performance. *Chemical Engineering Research and Design*, *170*, 423-433. https://doi.org/https://doi.org/10.1016/j.cherd.2021.04.026
- Desgrosellier, J. S., & Cheresh, D. A. (2010). Integrins in cancer: biological implications and therapeutic opportunities. *Nat Rev Cancer*, 10(1), 9-22. https://doi.org/10.1038/nrc2748
- Desmond, L. J., Phan, A. N., & Gentile, P. (2021). Critical overview on the green synthesis of carbon quantum dots and their application for cancer therapy [10.1039/D1EN00017A]. Environmental Science: Nano, 8(4), 848-862. https://doi.org/10.1039/D1EN00017A
- Dey, S., Govindaraj, A., Biswas, K., & Rao, C. N. R. (2014). Luminescence properties of boron and nitrogen doped graphene quantum dots prepared from arc-discharge-generated doped graphene samples. *Chemical Physics Letters*, *595-596*, 203-208. https://doi.org/https://doi.org/10.1016/j.cplett.2014.02.012
- Dhandapani, E., Duraisamy, N., & Mohan Raj, R. (2022). Green synthesis of carbon quantum dots from food waste. *Materials Today: Proceedings*, *51*, 1696-1700. https://doi.org/https://doi.org/10.1016/j.matpr.2020.10.025
- Dhandapani, R., Sethuraman, S., Krishnan, U. M., & Subramanian, A. (2023). Self-assembled multifunctional nanotheranostics against circulating tumor clusters in metastatic breast cancer. *Acta Pharmaceutica Sinica B*, 13(4), 1711-1725. https://doi.org/https://doi.org/10.1016/j.apsb.2022.12.003
- Dheyab, M. A., Aziz, A. A., Khaniabadi, P. M., Jameel, M. S., Oladzadabbasabadi, N., Rahman, A. A., Braim, F. S., & Mehrdel, B. (2023). Gold nanoparticles-based photothermal therapy for breast cancer. *Photodiagnosis and Photodynamic Therapy*, 42, 103312. https://doi.org/https://doi.org/10.1016/j.pdpdt.2023.103312
- Díez-Pascual, A. M., & Rahdar, A. (2022). LbL Nano-Assemblies: A Versatile Tool for Biomedical and Healthcare Applications. *Nanomaterials (Basel)*, *12*(6). https://doi.org/10.3390/nano12060949
- Ding, J., Xia, Z., & Lu, J. (2012). Esterification and Deacidification of a Waste Cooking Oil (TAN 68.81 mg KOH/g) for Biodiesel Production. *Energies*, 5(8), 2683-2691.
- Djellabi, R., Aboagye, D., Galloni, M. G., Vilas Andhalkar, V., Nouacer, S., Nabgan, W., Rtimi, S., Constantí, M., Medina Cabello, F., & Contreras, S. (2023). Combined conversion of lignocellulosic biomass into high-value products with ultrasonic cavitation and photocatalytic produced reactive oxygen species A review. *Bioresource Technology*, 368, 128333. https://doi.org/https://doi.org/10.1016/j.biortech.2022.128333
- Dominguez, M. (2021). *Osteosarcoma* Retrieved 21/11 from https://step2.medbullets.com/oncology/120473/osteosarcoma
- Dong, W., Zhou, S., Dong, Y., Wang, J., Ge, X., & Sui, L. (2015). The preparation of ethylenediamine-modified fluorescent carbon dots and their use in imaging of cells. *Luminescence*, *30*(6), 867-871. https://doi.org/https://doi.org/10.1002/bio.2834
- Dongsar, T. T., Dongsar, T. S., Abourehab, M. A. S., Gupta, N., & Kesharwani, P. (2023). Emerging application of magnetic nanoparticles for breast cancer therapy. *European Polymer Journal*, 187, 111898. https://doi.org/https://doi.org/10.1016/j.eurpolymj.2023.111898
- dos Santos, V. L. S., Araújo, R. C., Lisboa, E. S., Lopes, A. M., de Albuquerque-Júnior, R. L., Cardoso, J. C., Blanco-Llamero, C., Deshpande, T. A., Anderson, H. O. W., Priefer, R., Souto, E. B., & Severino, P. (2024). Layer-by-layer assembly: A versatile approach for tailored biomedical films and drug delivery. *Journal of Drug Delivery Science and Technology*, 91, 105243. https://doi.org/https://doi.org/10.1016/j.jddst.2023.105243
- Dubas, S. T., & Schlenoff, J. B. (1999). Factors Controlling the Growth of Polyelectrolyte Multilayers. *Macromolecules*, 32(24), 8153-8160. https://doi.org/10.1021/ma981927a

- Dubey, N., & Chandra, S. (2022). Upconversion nanoparticles: Recent strategies and mechanism based applications. *Journal of Rare Earths*, 40(9), 1343-1359. https://doi.org/https://doi.org/10.1016/j.jre.2022.04.015
- Ehrat, F., Bhattacharyya, S., Schneider, J., Löf, A., Wyrwich, R., Rogach, A. L., Stolarczyk, J. K., Urban, A. S., & Feldmann, J. (2017). Tracking the Source of Carbon Dot Photoluminescence: Aromatic Domains versus Molecular Fluorophores. *Nano Letters*, *17*(12), 7710-7716. https://doi.org/10.1021/acs.nanolett.7b03863
- Eisenberg, H. (1965). Equation for the Refractive Index of Water. *The Journal of Chemical Physics*, 43(11), 3887-3892. https://doi.org/10.1063/1.1696616
- Elbaz, N. M., Owen, A., Rannard, S., & McDonald, T. O. (2020). Controlled synthesis of calcium carbonate nanoparticles and stimuli-responsive multi-layered nanocapsules for oral drug delivery. *International Journal of Pharmaceutics*, *574*, 118866. https://doi.org/https://doi.org/10.1016/j.ijpharm.2019.118866
- Elizarova, I. S., & Luckham, P. F. (2016). Fabrication of polyelectrolyte multilayered nano-capsules using a continuous layer-by-layer approach. *Journal of Colloid and Interface Science*, *470*, 92-99. https://doi.org/https://doi.org/10.1016/j.jcis.2016.02.052
- Elizarova, I. S., & Luckham, P. F. (2018). Layer-by-layer adsorption: Factors affecting the choice of substrates and polymers. *Advances in Colloid and Interface Science*, *262*, 1-20. https://doi.org/https://doi.org/10.1016/j.cis.2018.11.003
- Erkmen, C., Selcuk, O., Unal, D. N., Kurbanoglu, S., & Uslu, B. (2022). Layer-by-layer modification strategies for electrochemical detection of biomarkers. *Biosensors and Bioelectronics: X, 12,* 100270. https://doi.org/https://doi.org/10.1016/j.biosx.2022.100270
- Erskine, E., Gültekin Subaşı, B., Vahapoglu, B., & Capanoglu, E. (2022). Coffee Phenolics and Their Interaction with Other Food Phenolics: Antagonistic and Synergistic Effects. *ACS Omega*, 7(2), 1595-1601. https://doi.org/10.1021/acsomega.1c06085
- Fadhillah, F., & Alghamdi, A. M. (2023). High-performance thin-film composite membrane consisting of a single layer of m-phenylenediamine/trimesoyl chloride fabricated via spin-assisted molecular layer-by-layer assembly. *Desalination and Water Treatment, 289*, 14-21. https://doi.org/https://doi.org/10.5004/dwt.2023.29321
- Fang, Y., Guo, S., Li, D., Zhu, C., Ren, W., Dong, S., & Wang, E. (2012). Easy Synthesis and Imaging Applications of Cross-Linked Green Fluorescent Hollow Carbon Nanoparticles. *ACS Nano*, 6(1), 400-409. https://doi.org/10.1021/nn2046373
- Fedin, I., & Talapin, D. V. (2014). Probing the Surface of Colloidal Nanomaterials with Potentiometry in Situ. *Journal of the American Chemical Society*, 136(32), 11228-11231. https://doi.org/10.1021/ja503866w
- Ferber, S., Baabur-Cohen, H., Blau, R., Epshtein, Y., Kisin-Finfer, E., Redy, O., Shabat, D., & Satchi-Fainaro, R. (2014). Polymeric nanotheranostics for real-time non-invasive optical imaging of breast cancer progression and drug release. *Cancer Letters*, 352(1), 81-89. https://doi.org/https://doi.org/10.1016/j.canlet.2014.02.022
- Fu, D., Ni, Z., Wu, K., Cheng, P., Ji, X., Li, G., & Shang, X. (2021). A novel redox-responsive ursolic acid polymeric prodrug delivery system for osteosarcoma therapy. *Drug Delivery*, 28(1), 195-205. https://doi.org/10.1080/10717544.2020.1870583
- Fuller, M., & Köper, I. (2018). Polyelectrolyte-Coated Gold Nanoparticles: The Effect of Salt and Polyelectrolyte Concentration on Colloidal Stability. *Polymers*, *10*(12).
- Funke, A., & Ziegler, F. (2010). Hydrothermal carbonization of biomass: A summary and discussion of chemical mechanisms for process engineering. *Biofuels, Bioproducts and Biorefining*, 4(2), 160-177. https://doi.org/10.1002/bbb.198
- Gaillard, F. (2023). Oseosarcoma Distal femur. Radiopaedia.org. Retrieved 11/12 from Galembikova, A., & Boichuk, S. (2021). 64P Tyrosine kinase signaling profile in osteosarcomas: A potential therapeutic target for sensitization to doxorubicin. Annals of Oncology, 32, S1365. https://doi.org/10.1016/j.annonc.2021.08.2060
- Galletti, P., Martelli, G., Prandini, G., Colucci, C., & Giacomini, D. (2018). Sodium periodate/TEMPO as a selective and efficient system for amine oxidation [10.1039/C8RA01365A]. *RSC Advances*, 8(18), 9723-9730. https://doi.org/10.1039/C8RA01365A

- Ganas, C., Weiß, A., Nazarenus, M., Rösler, S., Kissel, T., Rivera_Gil, P., & Parak, W. J. (2014).

 Biodegradable capsules as non-viral vectors for in vitro delivery of PEI/siRNA polyplexes for efficient gene silencing. *Journal of Controlled Release*, 196, 132-138.

 https://doi.org/https://doi.org/10.1016/j.jconrel.2014.10.006
- García-García, S., Wold, S., & Jonsson, M. (2009). Effects of temperature on the stability of colloidal montmorillonite particles at different pH and ionic strength. *Applied Clay Science*, 43(1), 21-26. https://doi.org/https://doi.org/https://doi.org/10.1016/j.clay.2008.07.011
- Gaspar, N., Occean, B.-V., Pacquement, H., Bompas, E., Bouvier, C., Brisse, H. J., Castex, M.-P., Cheurfa, N., Corradini, N., Delaye, J., Entz-Werlé, N., Gentet, J.-C., Italiano, A., Lervat, C., Marec-Berard, P., Mascard, E., Redini, F., Saumet, L., Schmitt, C., . . . Brugieres, L. (2018). Results of methotrexate-etoposide-ifosfamide based regimen (M-EI) in osteosarcoma patients included in the French OS2006/sarcome-09 study. *European Journal of Cancer*, 88, 57-66. https://doi.org/10.1016/j.ejca.2017.09.036
- Gavas, S., Quazi, S., & Karpiński, T. M. (2021). Nanoparticles for Cancer Therapy: Current Progress and Challenges. *Nanoscale Res Lett*, 16(1), 173. https://doi.org/10.1186/s11671-021-03628-6
- Ge, L., Tan, X., Sheng, R., & Xiao, J. (2022). Layer-by-layer self-assembly of giant polyelectrolyte microcapsules templated by microbubbles as potential hydrophilic or hydrophobic drug delivery system. *Colloid and Interface Science Communications*, 47, 100603. https://doi.org/https://doi.org/10.1016/j.colcom.2022.100603
- Ge, M., Han, Y., Ni, J., Li, Y., Han, S., Li, S., Yu, H., Zhang, C., Liu, S., Li, J., & Chen, Z. (2021). Seeking brightness from nature: Sustainable carbon dots-based AlEgens with tunable emission wavelength from natural rosin. *Chemical Engineering Journal*, 413, 127457. https://doi.org/https://doi.org/10.1016/j.cej.2020.127457
- Ge, M., Huang, X., Ni, J., Han, Y., Zhang, C., Li, S., Cao, J., Li, J., Chen, Z., & Han, S. (2021). One-step synthesis of self-quenching-resistant biomass-based solid-state fluorescent carbon dots with high yield for white lighting emitting diodes. *Dyes and Pigments*, 185, 108953. https://doi.org/https://doi.org/10.1016/j.dyepig.2020.108953
- Geißler, D., Nirmalananthan-Budau, N., Scholtz, L., Tavernaro, I., & Resch-Genger, U. (2021).

 Analyzing the surface of functional nanomaterials—how to quantify the total and derivatizable number of functional groups and ligands. *Microchimica Acta*, 188(10), 321. https://doi.org/10.1007/s00604-021-04960-5
- Geißler, S., Barrantes, A., Tengvall, P., Messersmith, P., & Tiainen, H. (2016). Deposition Kinetics of Bioinspired Phenolic Coatings on Titanium Surfaces. *Langmuir*, 32. https://doi.org/10.1021/acs.langmuir.6b01959
- Geszke-Moritz, M., & Moritz, M. (2013). Quantum dots as versatile probes in medical sciences: Synthesis, modification and properties. *Materials Science and Engineering: C, 33*(3), 1008-1021. https://doi.org/https://doi.org/10.1016/j.msec.2013.01.003
- Ghiorghita, C.-A., & Mihai, M. (2021). Recent developments in layer-by-layer assembled systems application in water purification. *Chemosphere*, *270*, 129477. https://doi.org/https://doi.org/10.1016/j.chemosphere.2020.129477
- Gidwani, B., Sahu, V., Shukla, S. S., Pandey, R., Joshi, V., Jain, V. K., & Vyas, A. (2021). Quantum dots: Prospectives, toxicity, advances and applications. *Journal of Drug Delivery Science and Technology*, 61, 102308. https://doi.org/https://doi.org/10.1016/j.jddst.2020.102308
- Gonçalves, H. M. R., Duarte, A. J., Davis, F., Higson, S. P. J., & Esteves da Silva, J. C. G. (2012). Layer-by-layer immobilization of carbon dots fluorescent nanomaterials on single optical fiber. *Analytica Chimica Acta*, 735, 90-95.

 https://doi.org/https://doi.org/10.1016/j.aca.2012.05.015
- González-González, R., González, L., Iglesias, S., Gonzalez, E., Martinez-Chapa, S. O., Madou, M., Alvarez, M., & Mendoza, A. (2020). Characterization of Chemically Activated Pyrolytic Carbon Black Derived from Waste Tires as a Candidate for Nanomaterial Precursor. *Nanomaterials*, 10, 2213. https://doi.org/10.3390/nano10112213
- Götz, A., Nikzad-Langerodi, R., Staedler, Y., Bellaire, A., & Saukel, J. (2020). Apparent penetration depth in attenuated total reflection Fourier-transform infrared (ATR-FTIR) spectroscopy of

- Allium cepa L. epidermis and cuticle. *Spectrochimica Acta Part A: Molecular and Biomolecular Spectroscopy, 224,* 117460. https://doi.org/https://doi.org/10.1016/j.saa.2019.117460
- Graat, H. C. A., Witlox, M. A., Schagen, F. H. E., Kaspers, G. J. L., Helder, M. N., Bras, J., Schaap, G. R., Gerritsen, W. R., Wuisman, P. I. J. M., & van Beusechem, V. W. (2006). Different susceptibility of osteosarcoma cell lines and primary cells to treatment with oncolytic adenovirus and doxorubicin or cisplatin. *British Journal of Cancer*, *94*(12), 1837-1844. https://doi.org/10.1038/sj.bjc.6603189
- Granja, A., Lima-Sousa, R., Alves, C. G., de Melo-Diogo, D., Nunes, C., Sousa, C. T., Correia, I. J., & Reis, S. (2023). Multifunctional targeted solid lipid nanoparticles for combined photothermal therapy and chemotherapy of breast cancer. *Biomaterials Advances*, 151, 213443. https://doi.org/https://doi.org/10.1016/j.bioadv.2023.213443
- Griffeth, L. K. (2005). Use of PET/CT scanning in cancer patients: technical and practical considerations. *Proc (Bayl Univ Med Cent)*, *18*(4), 321-330. https://doi.org/10.1080/08998280.2005.11928089
- Guan, W., Gu, W., Ye, L., Guo, C., Su, S., Xu, P., & Xue, M. (2014). Microwave-assisted polyol synthesis of carbon nitride dots from folic acid for cell imaging. *International journal of nanomedicine*, *9*, 5071-5078. https://doi.org/10.2147/IJN.S68575
- Gul, S., Khan, S. B., Rehman, I. U., Khan, M. A., & Khan, M. I. (2019). A Comprehensive Review of Magnetic Nanomaterials Modern Day Theranostics [Review]. *Frontiers in Materials*, 6. https://doi.org/10.3389/fmats.2019.00179
- Guo, C. X., Zhao, D., Zhao, Q., Wang, P., & Lu, X. (2014). Na+-functionalized carbon quantum dots: a new draw solute in forward osmosis for seawater desalination [10.1039/C4CC01603C]. *Chemical Communications*, *50*(55), 7318-7321. https://doi.org/10.1039/C4CC01603C
- Guo, Z., Xie, W., Lu, J., Guo, X., Xu, J., Xu, W., Chi, Y., Takuya, N., Wu, H., & Zhao, L. (2021). Tannic acid-based metal phenolic networks for bio-applications: a review [10.1039/D1TB00383F]. *Journal of Materials Chemistry B*, 9(20), 4098-4110. https://doi.org/10.1039/D1TB00383F
- Gurumendi, M., López, F., Borrero-González, L. J., Terencio, T., Caetano, M., Reinoso, C., & González, G. (2023). Enhanced Chitosan Photoluminescence by Incorporation of Lithium Perchlorate. *ACS Omega*, 8(15), 13763-13774. https://doi.org/10.1021/acsomega.2c08072
- Guzmán, E., Fernández-Peña, L., Ortega, F., & Rubio, R. G. (2020). Equilibrium and kinetically trapped aggregates in polyelectrolyte—oppositely charged surfactant mixtures. *Current Opinion in Colloid & Interface Science*, 48, 91-108. https://doi.org/https://doi.org/10.1016/j.cocis.2020.04.002
- Guzmán, E., Mateos-Maroto, A., Ruano, M., Ortega, F., & Rubio, R. G. (2017). Layer-by-Layer polyelectrolyte assemblies for encapsulation and release of active compounds. *Advances in Colloid and Interface Science*, 249, 290-307. https://doi.org/https://doi.org/10.1016/j.cis.2017.04.009
- Haidar, Z. S., Hamdy, R. C., & Tabrizian, M. (2008). Protein release kinetics for core—shell hybrid nanoparticles based on the layer-by-layer assembly of alginate and chitosan on liposomes. *Biomaterials*, *29*(9), 1207-1215. https://doi.org/https://doi.org/10.1016/j.biomaterials.2007.11.012
- Hamdalla, T. A., Seleim, S. M., Mohamed, A. K., & Mahmoud, M. E. (2019). Design, characterization and optical properties of assembled nanoscale thin films of copper (II) complex with 5-azo-Phenol-8-Hydroxyquinoline. *Optical Materials*, *95*, 109215. https://doi.org/https://doi.org/10.1016/j.optmat.2019.109215
- Han, X., Xu, K., Taratula, O., & Farsad, K. (2019). Applications of nanoparticles in biomedical imaging. *Nanoscale*, 11(3), 799-819. https://doi.org/10.1039/c8nr07769j
- Hanaor, D., Michelazzi, M., Leonelli, C., & Sorrell, C. C. (2012). The effects of carboxylic acids on the aqueous dispersion and electrophoretic deposition of ZrO2. *Journal of the European Ceramic Society*, 32(1), 235-244. https://doi.org/https://doi.org/https://doi.org/10.1016/j.jeurceramsoc.2011.08.015
- Hao, H.-C., Chen, S., Tan, Z.-X., & Jiang, H. (2023). Preparation of high-yield carbon quantum dots and paper-based sensors from biomass wastes by mechano-chemical method. *Journal of Environmental Chemical Engineering*, *11*(6), 111406. https://doi.org/https://doi.org/10.1016/j.jece.2023.111406

- Haris, M., Yadav, S. K., Rizwan, A., Singh, A., Wang, E., Hariharan, H., Reddy, R., & Marincola, F. M. (2015). Molecular magnetic resonance imaging in cancer. *J Transl Med*, *13*, 313. https://doi.org/10.1186/s12967-015-0659-x
- Harrington, K. J., Mohammadtaghi, S., Uster, P. S., Glass, D., Peters, A. M., Vile, R. G., & Stewart, J. S. W. (2001). Effective Targeting of Solid Tumors in Patients With Locally Advanced Cancers by Radiolabeled Pegylated Liposomes. Clinical Cancer Research, 7(2), 243-254.
- Harrison, T. S., & Goa, K. L. (2004). Long-Acting Risperidone. *CNS Drugs*, *18*(2), 113-132. https://doi.org/10.2165/00023210-200418020-00005
- Hashemi, M., Omidi, M., Muralidharan, B., Tayebi, L., Herpin, M. J., Mohagheghi, M. A., Mohammadi, J., Smyth, H. D. C., & Milner, T. E. (2018). Layer-by-layer assembly of graphene oxide on thermosensitive liposomes for photo-chemotherapy. *Acta Biomaterialia*, *65*, 376-392. https://doi.org/https://doi.org/10.1016/j.actbio.2017.10.040
- Hassanzadeh, S., Aminlashgari, N., & Hakkarainen, M. (2014). Chemo-selective high yield microwave assisted reaction turns cellulose to green chemicals. *Carbohydrate Polymers*, *112*, 448-457. https://doi.org/https://doi.org/10.1016/j.carbpol.2014.06.011
- Hassanzadeh, S., Aminlashgari, N., & Hakkarainen, M. (2015). Microwave-Assisted Recycling of Waste Paper to Green Platform Chemicals and Carbon Nanospheres. *ACS Sustainable Chemistry & Engineering*, 3(1), 177-185. https://doi.org/10.1021/sc500686j
- He, L., Fei, M., Chen, J., Tian, Y., Jiang, Y., Huang, Y., Xu, K., Hu, J., Zhao, Z., Zhang, Q., Ni, H., & Chen, L. (2019). Graphitic C3N4 quantum dots for next-generation QLED displays. *Materials Today*, 22, 76-84. https://doi.org/10.1016/j.mattod.2018.06.008
- Heath, G. R., Li, M., Polignano, I. L., Richens, J. L., Catucci, G., O'Shea, P., Sadeghi, S. J., Gilardi, G., Butt, J. N., & Jeuken, L. J. C. (2015). Layer-by-Layer Assembly of Supported Lipid Bilayer Poly-I-Lysine Multilayers. *Biomacromolecules*, 17(1), 324-335. https://doi.org/https://doi.org/10.1021/acs.biomac.5b01434
- Hecker, W. C., McDonald, K. M., Jackson, C. D., & Cope, R. F. (1991). EFFECTS OF BURNOUT ON CHAR OXIDATION RATES. In L. International Energy Agency Coal Research (Ed.), 1991 International Conference on Coal Science Proceedings (pp. 263-266). Butterworth-Heinemann. https://doi.org/https://doi.org/10.1016/B978-0-7506-0387-4.50068-1
- Heidari, M., Norouzi, O., Salaudeen, S., Acharya, B., & Dutta, A. (2019). Prediction of Hydrothermal Carbonization with Respect to the Biomass Components and Severity Factor. *Energy & Fuels*, 33(10), 9916-9924. https://doi.org/10.1021/acs.energyfuels.9b02291
- Hendi, A., Umair Hassan, M., Elsherif, M., Alqattan, B., Park, S., Yetisen, A. K., & Butt, H. (2020). Healthcare Applications of pH-Sensitive Hydrogel-Based Devices: A Review. *International journal of nanomedicine*, 15, 3887-3901. https://doi.org/10.2147/ijn.S245743
- Hensel, R. C., Moreira, M., Riul, A., Jr., Oliveira, O. N., Jr., Rodrigues, V., & Hillenkamp, M. (2020). Monitoring the dispersion and agglomeration of silver nanoparticles in polymer thin films using localized surface plasmons and Ferrell plasmons. *Applied Physics Letters*, *116*(10), 103105. https://doi.org/10.1063/1.5140247
- Hoang, V. C., & Gomes, V. G. (2019). High performance hybrid supercapacitor based on doped zucchini-derived carbon dots and graphene. *Materials Today Energy*, *12*, 198-207. https://doi.org/https://doi.org/10.1016/j.mtener.2019.01.013
- Hong, G., Diao, S., Antaris, A. L., & Dai, H. (2015). Carbon Nanomaterials for Biological Imaging and Nanomedicinal Therapy. *Chemical Reviews*, *115*(19), 10816-10906. https://doi.org/10.1021/acs.chemrev.5b00008
- Hong, W. T., & Yang, H. K. (2021). Anti-counterfeiting application of fluorescent carbon dots derived from wasted coffee grounds [Article]. *Optik*, *241*, Article 166449. https://doi.org/10.1016/j.ijleo.2021.166449
- Horisawa, E., Kubota, K., Tuboi, I., Sato, K., Yamamoto, H., Takeuchi, H., & Kawashima, Y. (2002). Size-dependency of DL-lactide/glycolide copolymer particulates for intra-articular delivery system on phagocytosis in rat synovium. *Pharm Res*, *19*(2), 132-139. https://doi.org/10.1023/a:1014260513728

- Hoshyar, N., Gray, S., Han, H., & Bao, G. (2016). The effect of nanoparticle size on in vivo pharmacokinetics and cellular interaction. *Nanomedicine (Lond)*, *11*(6), 673-692. https://doi.org/10.2217/nnm.16.5
- Hosseini, S. M., Mohammadnejad, J., Najafi-Taher, R., Zadeh, Z. B., Tanhaei, M., & Ramakrishna, S. (2023). Multifunctional Carbon-Based Nanoparticles: Theranostic Applications in Cancer Therapy and Diagnosis. *ACS Applied Bio Materials*, *6*(4), 1323-1338. https://doi.org/10.1021/acsabm.2c01000
- Hosseini, S. M., Mohammadnejad, J., Salamat, S., Beiram Zadeh, Z., Tanhaei, M., & Ramakrishna, S. (2023). Theranostic polymeric nanoparticles as a new approach in cancer therapy and diagnosis: a review. *Materials Today Chemistry*, *29*, 101400. https://doi.org/https://doi.org/10.1016/j.mtchem.2023.101400
- Hou, Y., Lu, Q., Deng, J., Li, H., & Zhang, Y. (2015). One-pot electrochemical synthesis of functionalized fluorescent carbon dots and their selective sensing for mercury ion. *Analytica Chimica Acta*, *866*, 69-74. https://doi.org/https://doi.org/10.1016/j.aca.2015.01.039
- Hsu, P.-C., Shih, Z.-Y., Lee, C.-H., & Chang, H.-T. (2012). Synthesis and analytical applications of photoluminescent carbon nanodots [10.1039/C2GC16451E]. *Green Chemistry*, 14(4), 917-920. https://doi.org/10.1039/C2GC16451E
- Hu, B., Guo, Y., Li, H., Liu, X., Fu, Y., & Ding, F. (2021). Recent advances in chitosan-based layer-by-layer biomaterials and their biomedical applications. *Carbohydrate Polymers*, *271*, 118427. https://doi.org/https://doi.org/10.1016/j.carbpol.2021.118427
- Hu, C., Yu, C., Li, M., Wang, X., Yang, J., Zhao, Z., Eychmüller, A., Sun, Y. P., & Qiu, J. (2014). Chemically Tailoring Coal to Fluorescent Carbon Dots with Tuned Size and Their Capacity for Cu(II) Detection. *Small*, 10(23), 4926-4933. https://doi.org/https://doi.org/10.1002/smll.201401328
- Hu, R., Li, L., & Jin, W. J. (2017). Controlling speciation of nitrogen in nitrogen-doped carbon dots by ferric ion catalysis for enhancing fluorescence. *Carbon*, *111*, 133-141. https://doi.org/https://doi.org/10.1016/j.carbon.2016.09.038
- Hu, Y., Yang, J., Tian, J., Jia, L., & Yu, J.-S. (2014). Waste frying oil as a precursor for one-step synthesis of sulfur-doped carbon dots with pH-sensitive photoluminescence. *Carbon*, *77*, 775-782. https://doi.org/https://doi.org/10.1016/j.carbon.2014.05.081
- Hu, Z., Jiao, X.-Y., & Xu, L. (2020). The N,S co-doped carbon dots with excellent luminescent properties from green tea leaf residue and its sensing of gefitinib. *Microchemical Journal*, 154, 104588. https://doi.org/https://doi.org/10.1016/j.microc.2019.104588
- Hua, S., de Matos, M. B. C., Metselaar, J. M., & Storm, G. (2018). Current Trends and Challenges in the Clinical Translation of Nanoparticulate Nanomedicines: Pathways for Translational Development and Commercialization. *Front Pharmacol*, *9*, 790. https://doi.org/10.3389/fphar.2018.00790
- Huang, H., Cui, Y., Liu, M., Chen, J., Wan, Q., Wen, Y., Deng, F., Zhou, N., Zhang, X., & Wei, Y. (2018). A one-step ultrasonic irradiation assisted strategy for the preparation of polymer-functionalized carbon quantum dots and their biological imaging. *Journal of Colloid and Interface Science*, 532, 767-773. https://doi.org/https://doi.org/10.1016/j.jcis.2018.07.099
- Huang, Q., Li, Q., Chen, Y., Tong, L., Lin, X., Zhu, J., & Tong, Q. (2018). High quantum yield nitrogen-doped carbon dots: green synthesis and application as "off-on" fluorescent sensors for the determination of Fe3+ and adenosine triphosphate in biological samples. *Sensors and Actuators B: Chemical*, *276*, 82-88. https://doi.org/https://doi.org/10.1016/j.snb.2018.08.089
- Huang, Y., Sun, J., Wu, D., & Feng, X. (2018). Layer-by-layer self-assembled chitosan/PAA nanofiltration membranes. *Separation and Purification Technology*, 207, 142-150. https://doi.org/https://doi.org/10.1016/j.seppur.2018.06.032
- Ibrahim, A., Khalil, I. A., Mahmoud, M. Y., Bakr, A. F., Ghoniem, M. G., Al-Farraj, E. S., & El-Sherbiny, I. M. (2023). Layer-by-layer development of chitosan/alginate-based platelet-mimicking nanocapsules for augmenting doxorubicin cytotoxicity against breast cancer. *International Journal of Biological Macromolecules*, 225, 503-517. https://doi.org/https://doi.org/10.1016/j.ijbiomac.2022.11.107

- lijima, S., Yudasaka, M., Yamada, R., Bandow, S., Suenaga, K., Kokai, F., & Takahashi, K. (1999). Nanoaggregates of single-walled graphitic carbon nano-horns. *Chemical Physics Letters*, 309(3), 165-170. https://doi.org/https://doi.org/10.1016/S0009-2614(99)00642-9
- Iskalieva, A., Yimmou, B. M., Gogate, P. R., Horvath, M., Horvath, P. G., & Csoka, L. (2012). Cavitation assisted delignification of wheat straw: A review. *Ultrasonics Sonochemistry*, *19*(5), 984-993. https://doi.org/https://doi.org/10.1016/j.ultsonch.2012.02.007
- Ito, T., Ibe, K., Uchino, T., Ohshima, H., & Otsuka, M. (2011). Preparation of DNA/Gold Nanoparticle Encapsulated in Calcium Phosphate. *Journal of Drug Delivery*, 2011(1), 647631. https://doi.org/https://doi.org/10.1155/2011/647631
- Jain, A., Balasubramanian, R., & Srinivasan, M. (2015). Hydrothermal Conversion of Biomass Waste to Activated Carbon with High Porosity: A Review. *Chemical Engineering Journal*, 283. https://doi.org/10.1016/j.cej.2015.08.014
- Jain, A., McGinty, S., & Pontrelli, G. (2022). Drug diffusion and release from a bioerodible spherical capsule. *International Journal of Pharmaceutics*, 616, 121442. https://doi.org/https://doi.org/10.1016/j.ijpharm.2021.121442
- Jain, S., Hirst, D. G., & O'Sullivan, J. M. (2012). Gold nanoparticles as novel agents for cancer therapy. *Br J Radiol*, *85*(1010), 101-113. https://doi.org/10.1259/bjr/59448833
- Janissen, B., & Huynh, T. (2018). Chemical composition and value-adding applications of coffee industry by-products: A review. Resources, Conservation and Recycling, 128, 110-117. https://doi.org/https://doi.org/10.1016/j.resconrec.2017.10.001
- Janpetch, N., Vanichvattanadecha, C., & Rujiravanit, R. (2015). Photocatalytic disinfection of water by bacterial cellulose/N–F co-doped TiO2 under fluorescent light. *Cellulose*, 22. https://doi.org/10.1007/s10570-015-0721-0
- Jardim, K. V., Palomec-Garfias, A. F., Andrade, B. Y. G., Chaker, J. A., Báo, S. N., Márquez-Beltrán, C., Moya, S. E., Parize, A. L., & Sousa, M. H. (2018). Novel magneto-responsive nanoplatforms based on MnFe2O4 nanoparticles layer-by-layer functionalized with chitosan and sodium alginate for magnetic controlled release of curcumin. *Materials Science and Engineering: C*, 92, 184-195. https://doi.org/https://doi.org/10.1016/j.msec.2018.06.039
- Jejurikar, A., Seow, X., Lawrie, G., Martin, D., Athipettah, J., & Grøndahl, L. (2012). Degradable alginate hydrogels crosslinked by the macromolecular crosslinker alginate dialdehyde. *J. Mater. Chem.*, 22, 9751-9758. https://doi.org/10.1039/C2JM30564J
- Jeong, C. J., Roy, A. K., Kim, S. H., Lee, J.-E., Jeong, J. H., In, I., & Park, S. Y. (2014). Fluorescent carbon nanoparticles derived from natural materials of mango fruit for bio-imaging probes [10.1039/C4NR04805A]. *Nanoscale*, 6(24), 15196-15202. https://doi.org/10.1039/C4NR04805A
- Jeong, G., Park, C. H., Yi, D., & Yang, H. (2023). Green synthesis of carbon dots from spent coffee grounds via ball-milling: Application in fluorescent chemosensors. *Journal of Cleaner Production*, 392, 136250. https://doi.org/https://doi.org/10.1016/j.jclepro.2023.136250
- Jessy Mercy, D., Kiran, V., Thirumalai, A., Harini, K., Girigoswami, K., & Girigoswami, A. (2023). Rice husk assisted carbon quantum dots synthesis for amoxicillin sensing. *Results in Chemistry*, 6, 101219. https://doi.org/https://doi.org/https://doi.org/10.1016/j.rechem.2023.101219
- Jha, R., Singh, A., Sharma, P. K., & Fuloria, N. K. (2020). Smart carbon nanotubes for drug delivery system: A comprehensive study. *Journal of Drug Delivery Science and Technology*, *58*, 101811. https://doi.org/https://doi.org/https://doi.org/10.1016/j.jddst.2020.101811
- Jiang, C., Wu, H., Song, X., Ma, X., Wang, J., & Tan, M. (2014). Presence of photoluminescent carbon dots in Nescafe® original instant coffee: Applications to bioimaging. *Talanta*, *127*, 68-74. https://doi.org/https://doi.org/10.1016/j.talanta.2014.01.046
- Jiang, K., Sun, S., Zhang, L., Lu, Y., Wu, A., Cai, C., & Lin, H. (2015). Red, Green, and Blue Luminescence by Carbon Dots: Full-Color Emission Tuning and Multicolor Cellular Imaging. Angewandte Chemie: international edition, 127(18), 5450–5453. https://doi.org/https://doi.org/10.1002/ange.201501193
- Jiang, M., Chen, W., Sun, Y., Zeng, J., Ma, L., Gong, J., Guan, X., Lu, K., & Zhang, W. (2023). Synergistically enhanced cancer immunotherapy by combining protamine-based nanovaccine

- with PD-L1 gene silence nanoparticle. *International Journal of Biological Macromolecules*, 242, 125223. https://doi.org/https://doi.org/https://doi.org/https://doi.org/10.1016/j.ijbiomac.2023.125223
- Jiang, S., Chen, X., & Liu, M. (2004). The pH stimulated reversible loading and release of a cationic dye in a layer-by-layer assembled DNA/PAH film. *Journal of Colloid and Interface Science*, 277(2), 396-403. https://doi.org/https://doi.org/10.1016/j.jcis.2004.04.008
- Jiang, S. P., Liu, Z., & Tian, Z. Q. (2006). Layer-by-Layer Self-Assembly of Composite Polyelectrolyte—Nafion Membranes for Direct Methanol Fuel Cells. *Advanced Materials*, *18*(8), 1068-1072. https://doi.org/https://doi.org/10.1002/adma.200502462
- Jiang, X., Qin, D., Mo, G., Feng, J., Yu, C., Mo, W., & Deng, B. (2019). Ginkgo leaf-based synthesis of nitrogen-doped carbon quantum dots for highly sensitive detection of salazosulfapyridine in mouse plasma. *Journal of Pharmaceutical and Biomedical Analysis*, 164, 514-519. https://doi.org/10.1016/j.jpba.2018.11.025
- Jiang, Y., Wang, Z., & Dai, Z. (2016). Preparation of Silicon–Carbon-Based Dots@Dopamine and Its Application in Intracellular Ag+ Detection and Cell Imaging. *ACS Applied Materials & Interfaces*, 8(6), 3644-3650. https://doi.org/10.1021/acsami.5b08089
- Jin, H., Gui, R., Wang, Y., & Sun, J. (2017). Carrot-derived carbon dots modified with polyethyleneimine and nile blue for ratiometric two-photon fluorescence turn-on sensing of sulfide anion in biological fluids. *Talanta*, *169*, 141-148. https://doi.org/https://doi.org/10.1016/j.talanta.2017.03.083
- Johansson, E., & Wågberg, L. (2012). Tailoring the mechanical properties of starch-containing layer-by-layer films. *Colloids and Surfaces A: Physicochemical and Engineering Aspects*, *394*, 14-22. https://doi.org/10.1016/j.colsurfa.2011.11.017
- Johnston, A. P. R., & Caruso, F. (2005). A Molecular Beacon Approach to Measuring the DNA Permeability of Thin Films. *Journal of the American Chemical Society*, 127(28), 10014-10015. https://doi.org/10.1021/ja0527166
- Johnston, A. P. R., Cortez, C., Angelatos, A. S., & Caruso, F. (2006). Layer-by-layer engineered capsules and their applications. *Current Opinion in Colloid & Interface Science*, *11*(4), 203-209. https://doi.org/https://doi.org/10.1016/j.cocis.2006.05.001
- Joseph J. Richardson, M. B., Frank Caruso. (2015). Technology-Driven Layer-by-Layer Assembly of Nanofilms. *Confidential*.
- Jun, H., Menglei, Y., Fei, Y., & Da, X. (2011). *In vivo* photoacoustic imaging of osteosarcoma in a rat model. *Journal of Biomedical Optics*, 16(2), 020503. https://doi.org/10.1117/1.3544502
- Kandjou, V., Hernaez, M., Acevedo, B., & Melendi-Espina, S. (2019). Interfacial crosslinked controlled thickness graphene oxide thin-films through dip-assisted layer-by-layer assembly means. *Progress in Organic Coatings*, 137, 105345. https://doi.org/https://doi.org/10.1016/j.porgcoat.2019.105345
- Kang, S., Jeong, Y. K., Ryu, J. H., Son, Y., Kim, W. R., Lee, B., Jung, K. H., & Kim, K. M. (2020). Pulsed laser ablation based synthetic route for nitrogen-doped graphene quantum dots using graphite flakes. *Applied Surface Science*, 506, 144998. https://doi.org/https://doi.org/10.1016/j.apsusc.2019.144998
- Kantzos, A. J., Fayad, L. M., Abiad, J. E., Ahlawat, S., Sabharwal, S., Vaynrub, M., & Morris, C. D. (2024). The role of imaging in extremity sarcoma surgery. *Skeletal Radiology*, *53*(9), 1937-1953. https://doi.org/10.1007/s00256-024-04586-7
- Kassim, M. A., Meng, T. K., Kamaludin, R., Hussain, A. H., & Bukhari, N. A. (2022). Chapter 9 Bioprocessing of sustainable renewable biomass for bioethanol production. In S. Yusup & N. A. Rashidi (Eds.), *Value-Chain of Biofuels* (pp. 195-234). Elsevier. https://doi.org/https://doi.org/10.1016/B978-0-12-824388-6.00004-X
- Kaur, J., Gill, G. S., & Jeet, K. (2019). Chapter 5 Applications of Carbon Nanotubes in Drug Delivery: A Comprehensive Review. In S. S. Mohapatra, S. Ranjan, N. Dasgupta, R. K. Mishra, & S. Thomas (Eds.), Characterization and Biology of Nanomaterials for Drug Delivery (pp. 113-135). Elsevier. https://doi.org/https://doi.org/10.1016/B978-0-12-814031-4.00005-2
- Khoshoei, A., Ghasemy, E., Poustchi, F., Shahbazi, M.-A., & Maleki, R. (2020). Engineering the pH-Sensitivity of the Graphene and Carbon Nanotube Based Nanomedicines in Smart Cancer

- Therapy by Grafting Trimetyl Chitosan. *Pharmaceutical Research*, *37*(8), 160. https://doi.org/10.1007/s11095-020-02881-1
- Kievit, F. M., & Zhang, M. (2011). Cancer Nanotheranostics: Improving Imaging and Therapy by Targeted Delivery Across Biological Barriers. Advanced Materials, 23(36), H217-H247. https://doi.org/https://doi.org/10.1002/adma.201102313
- Kim, B., Park, J., Baik, S., & Lee, J. W. (2020). Spent coffee derived hierarchical porous carbon and its application for energy storage. *Journal of Porous Materials*, *27*(2), 451-463. https://doi.org/10.1007/s10934-019-00826-7
- Kim, M. H., Park, H., & Park, W. H. (2018). Effect of pH and precursor salts on in situ formation of calcium phosphate nanoparticles in methylcellulose hydrogel. *Carbohydrate Polymers*, 191, 176-182. https://doi.org/https://doi.org/10.1016/j.carbpol.2018.03.032
- Kong, Y., Zhou, L., Liao, S., Wang, C., Chen, J., Cai, X., Zhao, S., Song, D., & Zhang, Y. (2022). Dual peptide-engineered and gadolinium-doped polydopamine particles as targeted nanotheranostics for the treatment of osteosarcoma and related osteolysis. *Chemical Engineering Journal*, 444, 136516. https://doi.org/https://doi.org/10.1016/j.cej.2022.136516
- Kou, X., Jiang, S., Park, S.-J., & Meng, L.-Y. (2020). A review: recent advances in preparations and applications of heteroatom-doped carbon quantum dots [10.1039/D0DT01004A]. *Dalton Transactions*, 49(21), 6915-6938. https://doi.org/10.1039/D0DT01004A
- Krishnamoorthy, K., & Mahalingam, M. (2015). Selection of a suitable method for the preparation of polymeric nanoparticles: multi-criteria decision making approach. *Adv Pharm Bull*, 5(1), 57-67. https://doi.org/10.5681/apb.2015.008
- Kurapati, R., Groth, T. W., & Raichur, A. M. (2019). Recent Developments in Layer-by-Layer Technique for Drug Delivery Applications. *ACS Applied Bio Materials*, *2*(12), 5512-5527. https://doi.org/10.1021/acsabm.9b00703
- Kurdekar, A., Chunduri, L. A. A., Bulagonda, E. P., Haleyurgirisetty, M. K., Kamisetti, V., & Hewlett, I. K. (2016). Comparative performance evaluation of carbon dot-based paper immunoassay on Whatman filter paper and nitrocellulose paper in the detection of HIV infection. *Microfluidics and Nanofluidics*, 20(7), 99. https://doi.org/10.1007/s10404-016-1763-9
- Kwon, W., & Rhee, S.-W. (2012). Facile synthesis of graphitic carbon quantum dots with size tunability and uniformity using reverse micelles [10.1039/C2CC31687K]. *Chemical Communications*, 48(43), 5256-5258. https://doi.org/10.1039/C2CC31687K
- Ladju RB, U. Z., Soraya GV. (2022). Nanotheranostics: A powerful next-generation solution to tackle hepatocellular carcinoma. *World J Gastroenterol*, *28*(2), 176-187. https://doi.org/https://dx.doi.org/10.3748/wjg.v28.i2.176
- Lawrie, G., Keen, I., Drew, B., Chandler-Temple, A., Rintoul, L., Fredericks, P., & Grøndahl, L. (2007). Interactions between Alginate and Chitosan Biopolymers Characterized Using FTIR and XPS. *Biomacromolecules*, 8(8), 2533-2541. https://doi.org/10.1021/bm070014y
- Lazaro-Carrillo, A., Filice, M., Guillén, M. J., Amaro, R., Viñambres, M., Tabero, A., Paredes, K. O., Villanueva, A., Calvo, P., del Puerto Morales, M., & Marciello, M. (2020). Tailor-made PEG coated iron oxide nanoparticles as contrast agents for long lasting magnetic resonance molecular imaging of solid cancers. *Materials Science and Engineering: C, 107*, 110262. https://doi.org/https://doi.org/10.1016/j.msec.2019.110262
- Lei, J., Yang, L., Lu, D., Yan, X., Cheng, C., Liu, Y., Wang, L., & Zhang, J. (2015). Carbon Dot-Incorporated PMO Nanoparticles as Versatile Platforms for the Design of Ratiometric Sensors, Multichannel Traceable Drug Delivery Vehicles, and Efficient Photocatalysts. *Advanced Optical Materials*, 3(1), 57-63. https://doi.org/https://doi.org/10.1002/adom.201400364
- Lemaster, J. E., & Jokerst, J. V. (2017). What is new in nanoparticle-based photoacoustic imaging? Wiley Interdiscip Rev Nanomed Nanobiotechnol, 9(1). https://doi.org/10.1002/wnan.1404
- Li, C., Sun, X., Li, Y., Liu, H., Long, B., Xie, D., Chen, J., & Wang, K. (2021). Rapid and Green Fabrication of Carbon Dots for Cellular Imaging and Anti-Counterfeiting Applications. *ACS Omega*, 6(4), 3232-3237. https://doi.org/10.1021/acsomega.0c05682
- Li, J., Khalenkow, D., Volodkin, D., Lapanje, A., Skirtach, A. G., & Parakhonskiy, B. V. (2022). Surface enhanced Raman scattering (SERS)-active bacterial detection by Layer-by-Layer (LbL)

- assembly all-nanoparticle microcapsules. *Colloids and Surfaces A: Physicochemical and Engineering Aspects*, 650, 129547.
- https://doi.org/https://doi.org/10.1016/j.colsurfa.2022.129547
- Li, J., Liu, J., Xu, L., & Chen, J. (2017). Preparation of thermoresponsive fluorescent carbon dots for cellular imaging. *Polymer International*, *66*(1), 92-97. https://doi.org/https://doi.org/10.1002/pi.5247
- Li, J., Parakhonskiy, B. V., & Skirtach, A. G. (2023). A decade of developing applications exploiting the properties of polyelectrolyte multilayer capsules [10.1039/D2CC04806J]. *Chemical Communications*, *59*(7), 807-835. https://doi.org/10.1039/D2CC04806J
- Li, L.-p., Ren, X.-f., Bai, P.-r., Liu, Y., Xu, W.-y., Xie, J., & Zhang, R.-p. (2021). Near-infrared emission carbon dots for bio-imaging applications. *New Carbon Materials*, *36*(3), 632-638. https://doi.org/https://doi.org/10.1016/S1872-5805(21)60041-0
- Li, L., Guan, Y., Xiong, H., Deng, T., Ji, Q., Xu, Z., Kang, Y., & Pang, J. (2020). Fundamentals and applications of nanoparticles for ultrasound-based imaging and therapy. *Nano Select*, 1(3), 263-284. https://doi.org/10.1002/nano.202000035
- Li, L., Zhang, R., Gu, W., & Xu, Z. P. (2018). Mannose-conjugated layered double hydroxide nanocomposite for targeted siRNA delivery to enhance cancer therapy. *Nanomedicine: Nanotechnology, Biology and Medicine, 14*(7), 2355-2364. https://doi.org/https://doi.org/10.1016/j.nano.2017.06.006
- Li, N., Lei, F., Xu, D., Li, Y., Liu, J., & Shi, Y. (2021). One-step synthesis of N, P Co-doped orange carbon quantum dots with novel optical properties for bio-imaging. *Optical Materials*, *111*, 110618. https://doi.org/https://doi.org/10.1016/j.optmat.2020.110618
- Li, P.-C., Liao, G. M., Kumar, S. R., Shih, C.-M., Yang, C.-C., Wang, D.-M., & Lue, S. J. (2016). Fabrication and Characterization of Chitosan Nanoparticle-Incorporated Quaternized Poly(Vinyl Alcohol) Composite Membranes as Solid Electrolytes for Direct Methanol Alkaline Fuel Cells. *Electrochimica Acta*, 187, 616-628. https://doi.org/https://doi.org/10.1016/j.electacta.2015.11.117
- Li, W., Liu, Y., Wang, B., Song, H., Liu, Z., Lu, S., & Yang, B. (2019). Kilogram-scale synthesis of carbon
- quantum dots for hydrogen evolution, sensing and bioimaging. *Chinese Chemical Letters*, 30(12), 2323-2327. https://doi.org/https://doi.org/10.1016/j.cclet.2019.06.040
- Li, Y., Wang, X., & Sun, J. (2012). Layer-by-layer assembly for rapid fabrication of thick polymeric films [10.1039/C2CS35107B]. *Chemical Society Reviews*, *41*(18), 5998-6009. https://doi.org/10.1039/C2CS35107B
- Li, Y., Xiang, W., Zhou, T., Huang, M., Wang, C., Wu, X., Mao, J., & Wang, P. (2020). Visible light induced efficient activation of persulfate by a carbon quantum dots (CQDs) modified γ-Fe2O3 catalyst. *Chinese Chemical Letters*, *31*(10), 2757-2761. https://doi.org/https://doi.org/10.1016/j.cclet.2020.01.032
- Li, Z., Luo, A., Zhou, R., Li, X., & Li, H. (2024). Preparation of ionic liquid@SiO2 nanocapsules for improving self-lubricating performance of PA6 composites. *Polymer*, *290*, 126537. https://doi.org/https://doi.org/10.1016/j.polymer.2023.126537
- Li, Z., Wang, Q., Zhou, Z., Zhao, S., Zhong, S., Xu, L., Gao, Y., & Cui, X. (2021). Green synthesis of carbon quantum dots from corn stalk shell by hydrothermal approach in near-critical water and applications in detecting and bioimaging. *Microchemical Journal*, *166*, 106250. https://doi.org/https://doi.org/10.1016/j.microc.2021.106250
- Lim, S. Y., Shen, W., & Gao, Z. (2015). Carbon quantum dots and their applications [10.1039/C4CS00269E]. *Chemical Society Reviews*, 44(1), 362-381. https://doi.org/10.1039/C4CS00269E
- Lipton, J., Weng, G.-M., Röhr, J. A., Wang, H., & Taylor, A. D. (2020). Layer-by-Layer Assembly of Two-Dimensional Materials: Meticulous Control on the Nanoscale. *Matter*, *2*(5), 1148-1165. https://doi.org/https://doi.org/10.1016/j.matt.2020.03.012
- Liu, B., Hu, J., Yao, H., Zhang, L., & Liu, H. (2023). Improved viability of probiotics encapsulated by layer-by-layer assembly using zein nanoparticles and pectin. *Food Hydrocolloids*, *143*, 108899. https://doi.org/https://doi.org/10.1016/j.foodhyd.2023.108899

- Liu, C. H., & Grodzinski, P. (2021). Nanotechnology for Cancer Imaging: Advances, Challenges, and Clinical Opportunities. *Radiology: Imaging Cancer*, *3*(3), e200052. https://doi.org/10.1148/rycan.2021200052
- Liu, H., Ding, J., Zhang, K., & Ding, L. (2019). Construction of biomass carbon dots based fluorescence sensors and their applications in chemical and biological analysis. *TrAC Trends in Analytical Chemistry*, 118, 315-337. https://doi.org/https://doi.org/10.1016/j.trac.2019.05.051
- Liu, J., Fu, M., Wang, M., Wan, D., Wei, Y., & Wei, X. (2022). Cancer vaccines as promising immunotherapeutics: platforms and current progress. *J Hematol Oncol*, *15*(1), 28. https://doi.org/10.1186/s13045-022-01247-x
- Liu, P. (2014). Stabilization of layer-by-layer engineered multilayered hollow microspheres. *Advances in Colloid and Interface Science*, 207, 178-188. https://doi.org/https://doi.org/10.1016/j.cis.2013.11.015
- Liu, Q., Zhang, N., Shi, H., Ji, W., Guo, X., Yuan, W., & Hu, Q. (2018). One-step microwave synthesis of carbon dots for highly sensitive and selective detection of copper ions in aqueous solution [10.1039/C7NJ05000C]. New Journal of Chemistry, 42(4), 3097-3101. https://doi.org/10.1039/C7NJ05000C
- Liu, R., Wu, D., Liu, S., Koynov, K., Knoll, W., & Li, Q. (2009). An Aqueous Route to Multicolor Photoluminescent Carbon Dots Using Silica Spheres as Carriers. *Angewandte Chemie International Edition*, *48*(25), 4598-4601. https://doi.org/https://doi.org/10.1002/anie.200900652
- Liu, S., Tian, J., Wang, L., Zhang, Y., Qin, X., Luo, Y., Asiri, A. M., Al-Youbi, A. O., & Sun, X. (2012). Hydrothermal Treatment of Grass: A Low-Cost, Green Route to Nitrogen-Doped, Carbon-Rich, Photoluminescent Polymer Nanodots as an Effective Fluorescent Sensing Platform for Label-Free Detection of Cu(II) Ions. *Advanced Materials*, 24(15), 2037-2041. https://doi.org/10.1002/adma.201200164
- Liu, Y., Song, C., Lv, G., Cao, X., Wang, L., Qiao, Y., & Yang, X. (2016). Surface functional groups and sp3/sp2 hybridization ratios of in-cylinder soot from a diesel engine fueled with n-heptane and n-heptane/toluene. *Fuel*, *179*, 108-113. https://doi.org/https://doi.org/10.1016/j.fuel.2016.03.082
- Liu, Y., Xiao, N., Gong, N., Wang, H., Shi, X., Gu, W., & Ye, L. (2014). One-step microwave-assisted polyol synthesis of green luminescent carbon dots as optical nanoprobes. *Carbon*, *68*, 258-264. https://doi.org/10.1016/j.carbon.2013.10.086
- Lommens, P., Loncke, F., Smet, P. F., Callens, F., Poelman, D., Vrielinck, H., & Hens, Z. (2007). Dopant Incorporation in Colloidal Quantum Dots: A Case Study on Co2+ Doped ZnO. *Chemistry of Materials*, 19(23), 5576-5583. https://doi.org/10.1021/cm071623f
- Long, W.-J., Li, X.-Q., Yu, Y., & He, C. (2022). Green synthesis of biomass-derived carbon dots as an efficient corrosion inhibitor. *Journal of Molecular Liquids*, *360*, 119522. https://doi.org/https://doi.org/10.1016/j.molliq.2022.119522
- Lovrić, J., Bazzi, H. S., Cuie, Y., Fortin, G. R., Winnik, F. M., & Maysinger, D. (2005). Differences in subcellular distribution and toxicity of green and red emitting CdTe quantum dots. *J Mol Med (Berl)*, 83(5), 377-385. https://doi.org/10.1007/s00109-004-0629-x
- Lu, B., Luo, D., Zhao, A., Wang, H., Zhao, Y., Maitz, M. F., Yang, P., & Huang, N. (2019). pH responsive chitosan and hyaluronic acid layer by layer film for drug delivery applications. *Progress in Organic Coatings*, 135, 240-247. https://doi.org/https://doi.org/10.1016/j.porgcoat.2019.06.012
- Lu, W., Qin, X., Liu, S., Chang, G., Zhang, Y., Luo, Y., Asiri, A. M., Al-Youbi, A. O., & Sun, X. (2012). Economical, Green Synthesis of Fluorescent Carbon Nanoparticles and Their Use as Probes for Sensitive and Selective Detection of Mercury(II) Ions. *Analytical Chemistry*, 84(12), 5351-5357. https://doi.org/10.1021/ac3007939
- Lubura, J., Kobera, L., Abbrent, S., Pavlova, E., Strachota, B., Bera, O., Pavličević, J., Ikonić, B., Kojić, P., & Strachota, A. (2023). Natural Rubber Composites Using Hydrothermally Carbonized Hardwood Waste Biomass as a Partial Reinforcing Filler- Part I: Structure, Morphology, and Rheological Effects during Vulcanization. *Polymers*, *15*(5).

- Luo, P. G., Sahu, S., Yang, S.-T., Sonkar, S. K., Wang, J., Wang, H., LeCroy, G. E., Cao, L., & Sun, Y.-P. (2013). Carbon "quantum" dots for optical bioimaging [10.1039/C3TB00018D]. *Journal of Materials Chemistry B*, 1(16), 2116-2127. https://doi.org/10.1039/C3TB00018D
- Ma, X., Li, S., Hessel, V., Lin, L., Meskers, S., & Gallucci, F. (2020). Synthesis of N-doped carbon dots via a microplasma process. *Chemical Engineering Science*, 220, 115648. https://doi.org/https://doi.org/10.1016/j.ces.2020.115648
- Ma, X., Zhao, D., Xiang, Y., Hua, Y., Zhao, W., Cui, Y., & Zhang, Z. (2023). Layer-by-layer self-assembly and clinical application in orthopedics. *Journal of Materials Science & Technology*, 147, 241-268. https://doi.org/https://doi.org/10.1016/j.jmst.2022.11.014
- Ma, Z., Han, Y., Wang, X., Sun, G., & Li, Y. (2022). Lignin-derived hierarchical porous flower-like carbon nanosheets decorated with biomass carbon quantum dots for efficient oxygen reduction. *Colloids and Surfaces A: Physicochemical and Engineering Aspects*, 652, 129818. https://doi.org/https://doi.org/10.1016/j.colsurfa.2022.129818
- Mahobia, S., Bajpai, J., & Bajpai, A. K. (2016). An In-vitro Investigation of Swelling Controlled Delivery of Insulin from Egg Albumin Nanocarriers. *Iran J Pharm Res*, 15(4), 695-711.
- Mahto, M. K., Samanta, D., Shaw, M., Shaik, M. A. S., Basu, R., Mondal, I., Bhattacharya, A., & Pathak, A. (2023). Blue-Emissive Nitrogen-Doped Carbon Dots for Picric Acid Detection: Molecular Fluorescence Quenching Mechanism. *ACS Applied Nano Materials*, *6*(9), 8059-8070. https://doi.org/10.1021/acsanm.3c01523
- Maleki Dana, P., Hallajzadeh, J., Asemi, Z., Mansournia, M. A., & Yousefi, B. (2021). Chitosan applications in studying and managing osteosarcoma. *Int J Biol Macromol*, *169*, 321-329. https://doi.org/10.1016/j.ijbiomac.2020.12.058
- Maniscalco, M. P., Volpe, M., & Messineo, A. (2020). Hydrothermal Carbonization as a Valuable Tool for Energy and Environmental Applications: A Review. *Energies*, *13*(16).
- Mansur, A. A. P., de Carvalho, F. G., Mansur, R. L., Carvalho, S. M., de Oliveira, L. C., & Mansur, H. S. (2017). Carboxymethylcellulose/ZnCdS fluorescent quantum dot nanoconjugates for cancer cell bioimaging. *International Journal of Biological Macromolecules*, *96*, 675-686. https://doi.org/https://doi.org/10.1016/j.ijbiomac.2016.12.078
- Mansuriya, B. D., & Altintas, Z. (2021). Carbon Dots: Classification, Properties, Synthesis, Characterization, and Applications in Health Care-An Updated Review (2018-2021). *Nanomaterials (Basel)*, 11(10). https://doi.org/10.3390/nano11102525
- Marin, E., Tapeinos, C., Sarasua, J. R., & Larrañaga, A. (2022). Exploiting the layer-by-layer nanoarchitectonics for the fabrication of polymer capsules: A toolbox to provide multifunctional properties to target complex pathologies. *Advances in Colloid and Interface Science*, 304, 102680. https://doi.org/https://doi.org/10.1016/j.cis.2022.102680
- Marin, E., Tiwari, N., Calderón, M., Sarasua, J.-R., & Larrañaga, A. (2021). Smart Layer-by-Layer Polymeric Microreactors: pH-Triggered Drug Release and Attenuation of Cellular Oxidative Stress as Prospective Combination Therapy. *ACS Applied Materials & Interfaces*, *13*(16), 18511-18524. https://doi.org/10.1021/acsami.1c01450
- Martins, M. G., Paiva, T. F., Mangia, L. H. R., Santos, E. C. S., Goulart, J. S., Dornelas, J., de França, B. M., Garcia, F., Gemini-Piperni, S., Pinto, J. C., Finotelli, P. V., & Ferraz, H. C. (2024). Development of polymeric nanoparticles associated with SPION and curcumin: a versatile magnetic and fluorescent platform for Life Science applications. *Colloids and Surfaces A: Physicochemical and Engineering Aspects*, 693, 133966. https://doi.org/https://doi.org/10.1016/j.colsurfa.2024.133966
- Massaya, J., Mills-Lamptey, B., & Chuck, C. J. (2022). Soil Amendments and Biostimulants from the Hydrothermal Processing of Spent Coffee Grounds. *Waste and Biomass Valorization*, *13*(6), 2889-2904. https://doi.org/10.1007/s12649-022-01697-x
- Mate, N., Pranav, Nabeela, K., Kaur, N., & Mobin, S. M. (2022). Insight into the Modulation of Carbon-Dot Optical Sensing Attributes through a Reduction Pathway. *ACS Omega*, 7(48), 43759-43769. https://doi.org/10.1021/acsomega.2c04766
- Mathew, S. A., Praveena, P., Dhanavel, S., Manikandan, R., Senthilkumar, S., & Stephen, A. (2020). Luminescent chitosan/carbon dots as an effective nano-drug carrier for neurodegenerative

- diseases [10.1039/D0RA04599C]. *RSC Advances*, *10*(41), 24386-24396. https://doi.org/10.1039/D0RA04599C
- Matsushita, A. F. Y., Nascimento, J. R. V., Leite, J. M. A., Pessoa, C. A., & Garcia, J. R. (2023).

 Incorporation of ZnO/Ag-ZnO nanoparticles into a cotton fiber by the LbL method for Self-Cleaning applications. *Journal of Molecular Liquids*, *375*, 121336.

 https://doi.org/https://doi.org/10.1016/j.molliq.2023.121336
- Mayilswamy, N., Boney, N., & Kandasubramanian, B. (2022). Fabrication and molecular dynamics studies of layer-by-layer polyelectrolytic films. *European Polymer Journal*, *163*, 110945. https://doi.org/https://doi.org/10.1016/j.eurpolymj.2021.110945
- Mayo-Clinic. (2023). *Ultrasound*. https://www.mayoclinic.org/tests-procedures/ultrasound/about/pac-20395177
- MayoClinic. (2023). *Bone Cancer Diagnosis*. https://www.mayoclinic.org/diseases-conditions/bone-cancer/diagnosis-treatment/drc-20350221
- Mazumdar, S., Chitkara, D., & Mittal, A. (2021). Exploration and insights into the cellular internalization and intracellular fate of amphiphilic polymeric nanocarriers. Acta Pharmaceutica Sinica B, 11(4), 903-924. https://doi.org/https://doi.org/10.1016/j.apsb.2021.02.019
- McShane, M. J., Brown, J. Q., Guice, K. B., & Lvov, Y. M. (2002). Polyelectrolyte Microshells as Carriers for Fluorescent Sensors: Loading and Sensing Properties of a Ruthenium-Based Oxygen Indicator. *Journal of Nanoscience and Nanotechnology*, 2(3-4), 411-416. https://doi.org/10.1166/jnn.2002.118
- Melancon, M. P., Stafford, R. J., & Li, C. (2012). Challenges to effective cancer nanotheranostics. *Journal of Controlled Release*, 164(2), 177-182. https://doi.org/https://doi.org/10.1016/j.jconrel.2012.07.045
- Mendes, L. P., Lima, E. M., & Torchilin, V. P. (2018). Chapter 9 Targeted Nanotheranostics for Selective Drug Delivery in Cancer. In J. Conde (Ed.), Handbook of Nanomaterials for Cancer Theranostics (pp. 245-277). Elsevier. https://doi.org/https://doi.org/10.1016/B978-0-12-813339-2.00009-8
- Merek. (2023). *IR Spectrum Table & Chart*. Retrieved 15/09 from https://www.sigmaaldrich.com/GB/en/technical-documents/technical-article/analytical-chemistry/photometry-and-reflectometry/ir-spectrum-table
- Milkova, V. (2023). Polysaccharide/Carbon Quantum Dots Composite Film on Model Colloidal Particles—An Electro-Optical Study. *Polymers*, *15*(18).
- Milosavljevic, V., Jamroz, E., Gagic, M., Haddad, Y., Michalkova, H., Balkova, R., Tesarova, B., Moulick, A., Heger, Z., Richtera, L., Kopel, P., & Adam, V. (2020). Encapsulation of Doxorubicin in Furcellaran/Chitosan Nanocapsules by Layer-by-Layer Technique for Selectively Controlled Drug Delivery. *Biomacromolecules*, 21(2), 418-434. https://doi.org/10.1021/acs.biomac.9b01175
- Misaghi, A., Goldin, A., Awad, M., & Kulidjian, A. A. (2018). Osteosarcoma: a comprehensive review. Sicot j, 4, 12. https://doi.org/10.1051/sicotj/2017028
- Mishra, A., Bhuyan, N. N., Xu, H., & Sharma, G. D. (2023). Advances in layer-by-layer processing for efficient and reliable organic solar cells [10.1039/D3MA00754E]. *Materials Advances*, 4(23), 6031-6063. https://doi.org/10.1039/D3MA00754E
- Mitchell, M. J., Billingsley, M. M., Haley, R. M., Wechsler, M. E., Peppas, N. A., & Langer, R. (2021). Engineering precision nanoparticles for drug delivery. *Nature Reviews Drug Discovery*, 20(2), 101-124. https://doi.org/10.1038/s41573-020-0090-8
- Mittal, N., Kaur, M., & Singh, V. (2023). Mild and selective catalytic oxidation of 5-HMF to 2,5-FDCA over metal loaded biomass derived graphene oxide using hydrogen peroxide in aqueous media. *Molecular Catalysis*, *546*, 113223. https://doi.org/https://doi.org/10.1016/j.mcat.2023.113223
- Mohammadi, R., Naderi-Manesh, H., Farzin, L., Vaezi, Z., Ayarri, N., Samandari, L., & Shamsipur, M. (2022). Fluorescence sensing and imaging with carbon-based quantum dots for early diagnosis of cancer: A review. *Journal of Pharmaceutical and Biomedical Analysis*, 212, 114628. https://doi.org/https://doi.org/10.1016/j.jpba.2022.114628

- Mohammed, B. S., Fields, D. A., Mittendorfer, B., Coggan, A. R., & Klein, S. (2004). Are peristaltic pumps as reliable as syringe pumps for metabolic research? Assessment of accuracy, precision, and metabolic kinetics. *Metabolism*, *53*(7), 875-878. https://doi.org/10.1016/j.metabol.2004.02.008
- Mohr, A., Marques Da Costa, M. E., Fromigue, O., Audinot, B., Balde, T., Droit, R., Abbou, S., Khneisser, P., Berlanga, P., Perez, E., Marchais, A., & Gaspar, N. (2024). From biology to personalized medicine: Recent knowledge in osteosarcoma. *European Journal of Medical Genetics*, 69, 104941. https://doi.org/https://doi.org/10.1016/j.ejmg.2024.104941
- Mok, Z. H., Mylonas, P., Austin, R., Proctor, G., Pitts, N., & Thanou, M. (2021). Calcium phosphate nanoparticles for potential application as enamel remineralising agent tested on hydroxyapatite discs [10.1039/D1NR05378G]. *Nanoscale*, *13*(47), 20002-20012. https://doi.org/10.1039/D1NR05378G
- Molkenova, A., & Atabaev, T. S. (2019). Phosphorus-doped carbon dots (P-CDs) from dextrose for low-concentration ferric ions sensing in water. *Optik*, *187*, 70-73. https://doi.org/https://doi.org/10.1016/j.ijleo.2019.05.013
- Moreno-Lanceta, A., Medrano-Bosch, M., & Melgar-Lesmes, P. (2020). Single-Walled Carbon Nanohorns as Promising Nanotube-Derived Delivery Systems to Treat Cancer. *Pharmaceutics*, 12(9). https://doi.org/10.3390/pharmaceutics12090850
- Morganti, S., Tarantino, P., Ferraro, E., D'Amico, P., Duso, B. A., & Curigliano, G. (2019). Next Generation Sequencing (NGS): A Revolutionary Technology in Pharmacogenomics and Personalized Medicine in Cancer. In E. Ruiz-Garcia & H. Astudillo-de la Vega (Eds.), *Translational Research and Onco-Omics Applications in the Era of Cancer Personal Genomics* (pp. 9-30). Springer International Publishing. https://doi.org/10.1007/978-3-030-24100-1 2
- Mouhtadi, S., Buron, C. C., & Pochard, I. (2023). Thickness-controlled porous NiO films by Ni(OH)2/alginate layer-by-layer assembly. *Surface and Coatings Technology*, *474*, 130110. https://doi.org/https://doi.org/10.1016/j.surfcoat.2023.130110
- Mura, S., & Couvreur, P. (2012). Nanotheranostics for personalized medicine. *Adv Drug Deliv Rev*, 64(13), 1394-1416. https://doi.org/10.1016/j.addr.2012.06.006
- Murugan, K., Choonara, Y. E., Kumar, P., Bijukumar, D., du Toit, L. C., & Pillay, V. (2015). Parameters and characteristics governing cellular internalization and trans-barrier trafficking of nanostructures. *International journal of nanomedicine*, *10*, 2191-2206. https://doi.org/10.2147/ijn.S75615
- Naher, H. S., Al-Turaihi, B. A. H., Mohammed, S. H., Naser, S. M., Albark, M. A., Madlool, H. A., Al-Marzoog, H. A. M., & Turki Jalil, A. (2023). Upconversion nanoparticles (UCNPs): Synthesis methods, imaging and cancer therapy. *Journal of Drug Delivery Science and Technology, 80*, 104175. https://doi.org/https://doi.org/https://doi.org/10.1016/j.jddst.2023.104175
- Naief, M. F., Mohammed, S. N., & Mohammed, A. M. (2024). Carbon nanotubes: A review on synthesis and drug delivery for cancer treatment. *Inorganic Chemistry Communications*, *159*, 111694. https://doi.org/https://doi.org/10.1016/j.inoche.2023.111694
- Namdari, P., Negahdari, B., & Eatemadi, A. (2017). Synthesis, properties and biomedical applications of carbon-based quantum dots: An updated review. *Biomedicine & Pharmacotherapy*, 87, 209-222. https://doi.org/https://doi.org/10.1016/j.biopha.2016.12.108
- Nammahachak, N., Aup-Ngoen, K. K., Asanithi, P., Horpratum, M., Chuangchote, S., Ratanaphan, S., & Surareungchai, W. (2022). Hydrothermal synthesis of carbon quantum dots with size tunability via heterogeneous nucleation [10.1039/D2RA05989D]. *RSC Advances*, *12*(49), 31729-31733. https://doi.org/10.1039/D2RA05989D
- Naseri, N., Ajorlou, E., Asghari, F., & Pilehvar-Soltanahmadi, Y. (2018). An update on nanoparticle-based contrast agents in medical imaging. *Artificial Cells, Nanomedicine, and Biotechnology*, 46(6), 1111-1121. https://doi.org/10.1080/21691401.2017.1379014
- Naumenko, E., Akhatova, F., Rozhina, E., & Fakhrullin, R. (2021). Revisiting the Cytotoxicity of Cationic Polyelectrolytes as a Principal Component in Layer-by-Layer Assembly Fabrication. *Pharmaceutics*, *13*(8).
- Navidfar, A., Peker, M. I., Budak, E., Unlu, C., & Trabzon, L. (2022). Carbon quantum dots enhanced graphene/carbon nanotubes polyurethane hybrid nanocomposites. *Composites Part B:*

- Engineering, 247, 110310. https://doi.org/https://doi.org/10.1016/j.compositesb.2022.110310
- Nejabat, M., Samie, A., Ramezani, M., Alibolandi, M., Abnous, K., & Taghdisi, S. M. (2023). An Overview on Gold Nanorods as Versatile Nanoparticles in Cancer Therapy. *Journal of Controlled Release*, *354*, 221-242. https://doi.org/https://doi.org/10.1016/j.jconrel.2023.01.009
- Nel, J., Elkhoury, K., Velot, É., Bianchi, A., Acherar, S., Francius, G., Tamayol, A., Grandemange, S., & Arab-Tehrany, E. (2023). Functionalized liposomes for targeted breast cancer drug delivery. *Bioactive Materials*, *24*, 401-437. https://doi.org/https://doi.org/10.1016/j.bioactmat.2022.12.027
- Ngulube, T., Gumbo, J. R., Masindi, V., & Maity, A. (2017). An update on synthetic dyes adsorption onto clay based minerals: A state-of-art review. *Journal of Environmental Management*, 191, 35-57. https://doi.org/https://doi.org/10.1016/j.jenvman.2016.12.031
- Nguyen, T. N., Nguyen, T. T., Nghiem, T. H. L., Nguyen, D. T., Tran, T. T. H., Vu, D., Nguyen, T. B. N., Nguyen, T. M. H., Nguyen, V. T., & Nguyen, M. H. (2021). Optical Properties of Doxorubicin Hydrochloride Load and Release on Silica Nanoparticle Platform. *Molecules*, 26(13). https://doi.org/10.3390/molecules26133968
- NHS. (2021). *Overview Bone Cancer* Retrieved 21/11 from https://www.nhs.uk/conditions/bone-cancer/
- Nie, X., Jiang, C., Wu, S., Chen, W., Lv, P., Wang, Q., Liu, J., Narh, C., Cao, X., Ghiladi, R. A., & Wei, Q. (2020). Carbon quantum dots: A bright future as photosensitizers for in vitro antibacterial photodynamic inactivation. *Journal of Photochemistry and Photobiology B: Biology, 206*, 111864. https://doi.org/https://doi.org/10.1016/j.jphotobiol.2020.111864
- NIST. Acetic acid, sodium salt. Retrieved 10/10 from https://webbook.nist.gov/cgi/cbook.cgi?ID=B6008022&Mask=80
- Nitheesh, Y., Pradhan, R., Hejmady, S., Taliyan, R., Singhvi, G., Alexander, A., Kesharwani, P., & Dubey, S. K. (2021). Surface engineered nanocarriers for the management of breast cancer. *Materials Science and Engineering: C, 130,* 112441. https://doi.org/https://doi.org/10.1016/j.msec.2021.112441
- Nuhu, A. A. (2014). Bioactive micronutrients in coffee: recent analytical approaches for characterization and quantification. *ISRN Nutr*, 2014, 384230. https://doi.org/10.1155/2014/384230
- Nune, S. K., Gunda, P., Thallapally, P. K., Lin, Y.-Y., Laird Forrest, M., & Berkland, C. J. (2009).

 Nanoparticles for biomedical imaging. *Expert Opinion on Drug Delivery*, 6(11), 1175-1194. https://doi.org/10.1517/17425240903229031
- Osorio-González, C. S., Hegde, K., Brar, S. K., Vezina, P., Gilbert, D., & Avalos-Ramírez, A. (2020). Pulsed-ozonolysis assisted oxidative treatment of forestry biomass for lignin fractionation. *Bioresource Technology*, *313*, 123638. https://doi.org/https://doi.org/10.1016/j.biortech.2020.123638
- Oumabady, S., S, P. S., Kamaludeen, S. P. B., Ramasamy, M., Kalaiselvi, P., & Parameswari, E. (2020). Preparation and Characterization of Optimized Hydrochar from Paper Board Mill Sludge. *Scientific Reports*, 10(1), 773. https://doi.org/10.1038/s41598-019-57163-7
- Oumabady, S., Selvaraj, P. S., Periasamy, K., Veeraswamy, D., Ramesh, P. T., Palanisami, T., & Ramasamy, S. P. (2022). Kinetic and isotherm insights of Diclofenac removal by sludge derived hydrochar. *Scientific Reports*, *12*(1), 2184. https://doi.org/10.1038/s41598-022-05943-z
- Padeste, C., & Neuhaus, S. (2015). Chapter 1 Functional Polymer Structures. In C. Padeste & S. Neuhaus (Eds.), *Polymer Micro- and Nanografting* (pp. 1-10). William Andrew Publishing. https://doi.org/https://doi.org/10.1016/B978-0-323-35322-9.00001-2
- Pajewska-Szmyt, M., Buszewski, B., & Gadzała-Kopciuch, R. (2020). Sulphur and nitrogen doped carbon dots synthesis by microwave assisted method as quantitative analytical nano-tool for mercury ion sensing. *Materials Chemistry and Physics*, 242, 122484. https://doi.org/https://doi.org/10.1016/j.matchemphys.2019.122484

- Pal, A., Sk, M. P., & Chattopadhyay, A. (2020). Recent advances in crystalline carbon dots for superior application potential [10.1039/D0MA00108B]. *Materials Advances*, 1(4), 525-553. https://doi.org/10.1039/D0MA00108B
- Palacio-Vergara, M., Álvarez-Gómez, M., Gallego, J., & López, D. (2023). Biomass solvothermal treatment methodologies to obtain carbon quantum dots: A systematic review. *Talanta Open*, *8*, 100244. https://doi.org/https://doi.org/10.1016/j.talo.2023.100244
- Pandey, F. P., Rastogi, A., & Singh, S. (2020). Optical properties and zeta potential of carbon quantum dots (CQDs) dispersed nematic liquid crystal 4'- heptyl-4-biphenylcarbonitrile (7CB). *Optical Materials*, 105, 109849. https://doi.org/https://doi.org/10.1016/j.optmat.2020.109849
- Paoletti, C., Miao, J., Dolce, E. M., Darga, E. P., Repollet, M. I., Doyle, G. V., Gralow, J. R., Hortobagyi, G. N., Smerage, J. B., Barlow, W. E., & Hayes, D. F. (2019). Circulating Tumor Cell Clusters in Patients with Metastatic Breast Cancer: a SWOG S0500 Translational Medicine Study. *Clinical Cancer Research*, 25(20), 6089-6097. https://doi.org/10.1158/1078-0432.Ccr-19-0208
- Parakhonskiy, B. V., Yashchenok, A. M., Konrad, M., & Skirtach, A. G. (2014). Colloidal micro- and nano-particles as templates for polyelectrolyte multilayer capsules. *Advances in Colloid and Interface Science*, 207, 253-264. https://doi.org/https://doi.org/10.1016/j.cis.2014.01.022
- Park, J. W. (2002). Liposome-based drug delivery in breast cancer treatment. *Breast Cancer Research*, 4(3), 95. https://doi.org/10.1186/bcr432
- Park, M.-K., Deng, S., & Advincula, R. C. (2005). Sustained Release Control via Photo-Cross-Linking of Polyelectrolyte Layer-by-Layer Hollow Capsules. *Langmuir*, *21*(12), 5272-5277. https://doi.org/10.1021/la047008x
- Park, S., Han, U., Choi, D., & Hong, J. (2018). Layer-by-layer assembled polymeric thin films as prospective drug delivery carriers: design and applications. *Biomaterials Research*, 22(1), 29. https://doi.org/10.1186/s40824-018-0139-5
- Park, S. J., & Yang, H. K. (2022). Ultra-fast synthesis of carbon dots using the wasted coffee residues for environmental remediation. *Current Applied Physics*, *36*, 9-15. https://doi.org/https://doi.org/10.1016/j.cap.2022.01.001
- Park, S. Y., Lee, H. U., Park, E. S., Lee, S. C., Lee, J.-W., Jeong, S. W., Kim, C. H., Lee, Y.-C., Huh, Y. S., & Lee, J. (2014). Photoluminescent Green Carbon Nanodots from Food-Waste-Derived Sources: Large-Scale Synthesis, Properties, and Biomedical Applications. *ACS Applied Materials & Interfaces*, 6(5), 3365-3370. https://doi.org/10.1021/am500159p
- Patel, M. S. (2019). *Sunburst appearance bone (ultrasound)*. Radiopaedia.org. https://radiopaedia.org/cases/67572
- Patel, S., Kim, J., Herrera, M., Mukherjee, A., Kabanov, A. V., & Sahay, G. (2019). Brief update on endocytosis of nanomedicines. *Advanced Drug Delivery Reviews*, 144, 90-111. https://doi.org/https://doi.org/10.1016/j.addr.2019.08.004
- Pawar, S., Togiti, U. K., Bhattacharya, A., & Nag, A. (2019). Functionalized Chitosan—Carbon Dots: A Fluorescent Probe for Detecting Trace Amount of Water in Organic Solvents. *ACS Omega*, 4(6), 11301-11311. https://doi.org/10.1021/acsomega.9b01208
- Pawlak, A., & Belbekhouche, S. (2021). Controlling the growth of Escherichia coli by layer-by-layer encapsulation. *Colloids and Surfaces B: Biointerfaces*, *206*, 111950. https://doi.org/https://doi.org/10.1016/j.colsurfb.2021.111950
- Pei, D., & Buyanova, M. (2019). Overcoming Endosomal Entrapment in Drug Delivery. *Bioconjugate Chemistry*, 30(2), 273-283. https://doi.org/10.1021/acs.bioconjchem.8b00778
- Peng, J., Gao, W., Gupta, B. K., Liu, Z., Romero-Aburto, R., Ge, L., Song, L., Alemany, L. B., Zhan, X., Gao, G., Vithayathil, S. A., Kaipparettu, B. A., Marti, A. A., Hayashi, T., Zhu, J.-J., & Ajayan, P. M. (2012). Graphene Quantum Dots Derived from Carbon Fibers. *Nano Letters*, *12*(2), 844-849. https://doi.org/10.1021/nl2038979
- Peng, S. F., Lee, C. Y., Hour, M. J., Tsai, S. C., Kuo, D. H., Chen, F. A., Shieh, P. C., & Yang, J. S. (2014). Curcumin-loaded nanoparticles enhance apoptotic cell death of U2OS human osteosarcoma cells through the Akt-Bad signaling pathway. *Int J Oncol*, *44*(1), 238-246. https://doi.org/10.3892/ijo.2013.2175
- Peng, S. L., Lai, C. H., Chu, P. Y., Hsieh, J. T., Tseng, Y. C., Chiu, S. C., & Lin, Y. H. (2020).

 Nanotheranostics With the Combination of Improved Targeting, Therapeutic Effects, and

- Molecular Imaging. *Front Bioeng Biotechnol*, *8*, 570490. https://doi.org/10.3389/fbioe.2020.570490
- Peng, T., Liu, K., Gao, L., Gao, L., Chen, J., Wang, J., Liu, Y., Wang, Y., Yan, Z., & Yu, L. (2016). Poly (I-γ-glutamylglutamine) Polymer Enhances Doxorubicin Accumulation in Multidrug Resistant Breast Cancer Cells. *Molecules*, *21*(6). https://doi.org/10.3390/molecules21060720
- Peyratout, C. S., & Dähne, L. (2004). Tailor-Made Polyelectrolyte Microcapsules: From Multilayers to Smart Containers. *Angewandte Chemie International Edition*, *43*(29), 3762-3783. https://doi.org/https://doi.org/10.1002/anie.200300568
- Pham, N., Zaitoun, H., Mohammed, T., Peña-Almaguer, E., Martinez, F., Novaro, G., & Kirsch, J. (2015). *Complications of Aortic Valve Surgery: Manifes- tations at CT and MR Imaging* 1.
- Piazza, R. D., Pelizaro, T. A. G., Rodriguez-Chanfrau, J. E., La Serna, A. A., Veranes-Pantoja, Y., & Guastaldi, A. C. (2020). Calcium phosphates nanoparticles: The effect of freeze-drying on particle size reduction. *Materials Chemistry and Physics*, 239, 122004. https://doi.org/https://doi.org/10.1016/j.matchemphys.2019.122004
- Pilicheva, B., Uzunova, Y., Bodurov, I., Viraneva, A., Exner, G., Sotirov, S., Yovcheva, T., & Marudova, M. (2020). Layer-by-layer self-assembly films for buccal drug delivery: The effect of polymer cross-linking. *Journal of Drug Delivery Science and Technology*, 59, 101897. https://doi.org/https://doi.org/10.1016/j.jddst.2020.101897
- Piwowarczyk, J., Jędrzejewski, R., Moszyński, D., Kwiatkowski, K., Niemczyk, A., & Baranowska, J. (2019). XPS and FTIR Studies of Polytetrafluoroethylene Thin Films Obtained by Physical Methods. *Polymers (Basel)*, 11(10). https://doi.org/10.3390/polym11101629
- Pollack, S. M., Ingham, M., Spraker, M. B., & Schwartz, G. K. (2017). Emerging Targeted and Immune-Based Therapies in Sarcoma. *Journal of Clinical Oncology*, *36*(2), 125-135. https://doi.org/10.1200/JCO.2017.75.1610
- Priyadarshi, A., Khavari, M., Subroto, T., Prentice, P., Pericleous, K., Eskin, D., Durodola, J., & Tzanakis, I. (2021). Mechanisms of ultrasonic de-agglomeration of oxides through in-situ high-speed observations and acoustic measurements. *Ultrasonics Sonochemistry*, *79*, 105792. https://doi.org/https://doi.org/10.1016/j.ultsonch.2021.105792
- Quaid, T., Ghalandari, V., & Reza, T. (2022). Effect of Synthesis Process, Synthesis Temperature, and Reaction Time on Chemical, Morphological, and Quantum Properties of Carbon Dots Derived from Loblolly Pine. *Biomass*, 2(4), 250-263.
- Quinto, C. A., Mohindra, P., Tong, S., & Bao, G. (2015). Multifunctional superparamagnetic iron oxide nanoparticles for combined chemotherapy and hyperthermia cancer treatment [10.1039/C5NR02718G]. *Nanoscale*, 7(29), 12728-12736. https://doi.org/10.1039/C5NR02718G
- Radenkovic, D., Kobayashi, H., Remsey-Semmelweis, E., & Seifalian, A. M. (2016). Quantum dot nanoparticle for optimization of breast cancer diagnostics and therapy in a clinical setting. *Nanomedicine: Nanotechnology, Biology and Medicine*, *12*(6), 1581-1592. https://doi.org/https://doi.org/10.1016/j.nano.2016.02.014
- Radnia, F., Mohajeri, N., & Zarghami, N. (2020). New insight into the engineering of green carbon dots: Possible applications in emerging cancer theranostics. *Talanta*, *209*, 120547. https://doi.org/https://doi.org/10.1016/j.talanta.2019.120547
- Radt, B., Smith, T. A., & Caruso, F. (2004). Optically Addressable Nanostructured Capsules. *Advanced Materials*, 16(23-24), 2184-2189. https://doi.org/https://doi.org/10.1002/adma.200400920
- Rajiv Supra, D. K. A. (2023). Immunotherapeutic Strategies in the Management of Osteosarcoma. Journal of Orthopedics and Sports Medicine, 5, 32-40.
- Rani, M. S. A., Mohammad, M., Sua'it, M. S., Ahmad, A., & Mohamed, N. S. (2021). Novel approach for the utilization of ionic liquid-based cellulose derivative biosourced polymer electrolytes in safe sodium-ion batteries. *Polymer Bulletin*, *78*(9), 5355-5377. https://doi.org/10.1007/s00289-020-03382-2
- Rao, H., Liu, W., Lu, Z., Wang, Y., Ge, H., Zou, P., Wang, X., He, H., Zeng, X., & Wang, Y. (2016). Silicacoated carbon dots conjugated to CdTe quantum dots: a ratiometric fluorescent probe for copper(II). *Microchimica Acta*, 183(2), 581-588. https://doi.org/10.1007/s00604-015-1682-6

- Ravichandran, G., & Rengan, A. K. (2020). Aptamer-Mediated Nanotheranostics for Cancer Treatment: A Review. *ACS Applied Nano Materials*, *3*(10), 9542-9559. https://doi.org/10.1021/acsanm.0c01785
- Raynaud, S., Champion, E., Bernache-Assollant, D., & Thomas, P. (2002). Calcium phosphate apatites with variable Ca/P atomic ratio I. Synthesis, characterisation and thermal stability of powders. *Biomaterials*, 23(4), 1065-1072. https://doi.org/https://doi.org/10.1016/S0142-9612(01)00218-6
- Reshma, V. G., & Mohanan, P. V. (2019). Quantum dots: Applications and safety consequences. *Journal of Luminescence*, 205, 287-298. https://doi.org/https://doi.org/10.1016/j.jlumin.2018.09.015
- Richardson, J. J., Björnmalm, M., & Caruso, F. (2015). Technology-driven layer-by-layer assembly of nanofilms. *Science*, *348*(6233), aaa2491. https://doi.org/10.1126/science.aaa2491
- Robles, S. (2005). Encyclopedia of Toxicology (2nd ed.). Oxford.
- Rodriguez-Mendez, M. L. (2023). Nanostructured thin films as electrochemical sensors and biosensors for milk analysis. *Sensors and Actuators Reports*, *6*, 100179. https://doi.org/https://doi.org/10.1016/j.snr.2023.100179
- Rojas-Sánchez, L., Loza, K., & Epple, M. (2020). Synthesis and intracellular tracing surface-functionalized calcium phosphate nanoparticles by super-resolution microscopy (STORM). *Materialia*, 12, 100773. https://doi.org/https://doi.org/10.1016/j.mtla.2020.100773
- Rombach-Riegraf, V., Oswald, P., Bienert, R., Petersen, J., Domingo, M. P., Pardo, J., Gräber, P., & Galvez, E. M. (2013). Blinking effect and the use of quantum dots in single molecule spectroscopy. *Biochemical and Biophysical Research Communications*, 430(1), 260-264. https://doi.org/https://doi.org/10.1016/j.bbrc.2012.10.140
- Rosenthal, S. J., Chang, J. C., Kovtun, O., McBride, J. R., & Tomlinson, I. D. (2011). Biocompatible Quantum Dots for Biological Applications. *Chemistry & Biology*, *18*(1), 10-24. https://doi.org/https://doi.org/10.1016/j.chembiol.2010.11.013
- Roy, A. K., Ghann, W., Rabi, S., Barua, J., Majumder, S., Amin, R., Ziaul Hyder, M. K. M., & Uddin, J. (2024). Hydrogen peroxide assisted synthesis of fluorescent carbon nanoparticles from teak leaves for dye-sensitized solar cells [10.1039/D3SU00452J]. *RSC Sustainability*, 2(4), 1003-1013. https://doi.org/10.1039/D3SU00452J
- Roy, S., Bag, N., Bardhan, S., Hasan, I., & Guo, B. (2023). Recent progress in NIR-II fluorescence imaging-guided drug delivery for cancer theranostics. *Advanced Drug Delivery Reviews*, 197, 114821. https://doi.org/https://doi.org/10.1016/j.addr.2023.114821
- Rudnick-Glick, S., Corem-Salkmon, E., Grinberg, I., & Margel, S. (2016). Targeted drug delivery of near IR fluorescent doxorubicin-conjugated poly(ethylene glycol) bisphosphonate nanoparticles for diagnosis and therapy of primary and metastatic bone cancer in a mouse model. *J Nanobiotechnology*, 14(1), 80. https://doi.org/10.1186/s12951-016-0233-6
- Sadhanala, H. K., Pagidi, S., & Gedanken, A. (2021). High quantum yield boron-doped carbon dots: a ratiometric fluorescent probe for highly selective and sensitive detection of Mg2+ ions [10.1039/D0TC05081D]. *Journal of Materials Chemistry C, 9*(5), 1632-1640. https://doi.org/10.1039/D0TC05081D
- Sahu, S., Behera, B., Maiti, T. K., & Mohapatra, S. (2012). Simple one-step synthesis of highly luminescent carbon dots from orange juice: application as excellent bio-imaging agents. Chemical communications: Chem comm /, 48(70), 8835-8837. https://doi.org/10.1039/c2cc33796g
- Samimi, S., Maghsoudnia, N., Eftekhari, R. B., & Dorkoosh, F. (2019). Chapter 3 Lipid-Based Nanoparticles for Drug Delivery Systems. In S. S. Mohapatra, S. Ranjan, N. Dasgupta, R. K. Mishra, & S. Thomas (Eds.), *Characterization and Biology of Nanomaterials for Drug Delivery* (pp. 47-76). Elsevier. https://doi.org/https://doi.org/10.1016/B978-0-12-814031-4.00003-9
- Sarma, R., & Mohanta, D. (2015). Luminescence and bio-imaging response of thio-glycolic acid (TGA) and sodium dodecyl sulfate (SDS)-coated fluorescent cadmium selenide quantum dots.

 Journal of Luminescence, 161, 395-402.
 - https://doi.org/https://doi.org/10.1016/j.jlumin.2014.12.060

- Scheepers, D., Chatillon, B., Borneman, Z., & Nijmeijer, K. (2021). Influence of charge density and ionic strength on diallyldimethylammonium chloride (DADMAC)-based polyelectrolyte multilayer membrane formation. *Journal of Membrane Science*, 617, 118619. https://doi.org/https://doi.org/10.1016/j.memsci.2020.118619
- Schwiertz, J., Meyer-Zaika, W., Ruiz-Gonzalez, L., González-Calbet, J. M., Vallet-Regí, M., & Epple, M. (2008). Calcium phosphate nanoparticles as templates for nanocapsules prepared by the layer-by-layer technique [10.1039/B803609H]. *Journal of Materials Chemistry*, 18(32), 3831-3834. https://doi.org/10.1039/B803609H
- Secchi, E., Marbach, S., Niguès, A., Stein, D., Siria, A., & Bocquet, L. (2016). Massive radius-dependent flow slippage in carbon nanotubes. *Nature*, *537*(7619), 210-213. https://doi.org/10.1038/nature19315
- Senapati, S., Mahanta, A. K., Kumar, S., & Maiti, P. (2018). Controlled drug delivery vehicles for cancer treatment and their performance. *Signal Transduct Target Ther*, *3*, 7. https://doi.org/10.1038/s41392-017-0004-3
- Senbanjo, L. T., & Chellaiah, M. A. (2017). CD44: A Multifunctional Cell Surface Adhesion Receptor Is a Regulator of Progression and Metastasis of Cancer Cells [Mini Review]. Frontiers in Cell and Developmental Biology, 5. https://doi.org/10.3389/fcell.2017.00018
- Shan, X., Chai, L., Ma, J., Qian, Z., Chen, J., & Feng, H. (2014). B-doped carbon quantum dots as a sensitive fluorescence probe for hydrogen peroxide and glucose detection [10.1039/C3AN02222F]. *Analyst*, 139(10), 2322-2325. https://doi.org/10.1039/C3AN02222F
- Sharma, A., & Das, J. (2019). Small molecules derived carbon dots: synthesis and applications in sensing, catalysis, imaging, and biomedicine. *Journal of Nanobiotechnology*, *17*(1), 92. https://doi.org/10.1186/s12951-019-0525-8
- Shen, L., Zhang, L., Chen, M., Chen, X., & Wang, J. (2013). The production of pH-sensitive photoluminescent carbon nanoparticles by the carbonization of polyethylenimine and their use for bioimaging. *Carbon*, 55, 343-349. https://doi.org/https://doi.org/10.1016/j.carbon.2012.12.074
- Shende, P., Patil, A., & Prabhakar, B. (2020). Layer-by-layer technique for enhancing physicochemical properties of actives. *Journal of Drug Delivery Science and Technology*, *56*, 101519. https://doi.org/https://doi.org/10.1016/j.jddst.2020.101519
- Shi, C., Qi, H., Ma, R., Sun, Z., Xiao, L., Wei, G., Huang, Z., Liu, S., Li, J., Dong, M., Fan, J., & Guo, Z. (2019). N,S-self-doped carbon quantum dots from fungus fibers for sensing tetracyclines and for bioimaging cancer cells. *Materials Science and Engineering: C, 105,* 110132. https://doi.org/https://doi.org/10.1016/j.msec.2019.110132
- Shi, N., Liu, Q., He, X., Wang, G., Chen, N., Peng, J., & Ma, L. (2019). Molecular Structure and Formation Mechanism of Hydrochar from Hydrothermal Carbonization of Carbohydrates. Energy & Fuels, 33(10), 9904-9915. https://doi.org/10.1021/acs.energyfuels.9b02174
- Shibata, H., Abe, M., Sato, K., Uwai, K., Tokuraku, K., & Iimori, T. (2022). Microwave-assisted synthesis and formation mechanism of fluorescent carbon dots from starch. *Carbohydrate Polymer Technologies and Applications*, *3*, 100218. https://doi.org/https://doi.org/10.1016/j.carpta.2022.100218
- Shiratori, S. S., Ito, T., & Yamada, T. (2002). Automatic film formation system for ultra-thin organic/inorganic hetero-structure by mass-controlled layer-by-layer sequential adsorption method with 'nm' scale accuracy. *Colloids and Surfaces A: Physicochemical and Engineering Aspects*, 198-200, 415-423. https://doi.org/https://doi.org/10.1016/S0927-7757(01)00953-0
- Shrotri, A., Kobayashi, H., & Fukuoka, A. (2018). Cellulose Depolymerization over Heterogeneous Catalysts. *Accounts of Chemical Research*, *51*(3), 761-768. https://doi.org/10.1021/acs.accounts.7b00614
- Shu, S., Sun, C., Zhang, X., Wu, Z., Wang, Z., & Li, C. (2010). Hollow and degradable polyelectrolyte nanocapsules for protein drug delivery. *Acta Biomaterialia*, *6*(1), 210-217. https://doi.org/https://doi.org/10.1016/j.actbio.2009.06.020
- Shukla, T., Upmanyu, N., Pandey, S. P., & Sudheesh, M. S. (2019). Chapter 14 Site-specific drug delivery, targeting, and gene therapy. In A. M. Grumezescu (Ed.), *Nanoarchitectonics in*

- *Biomedicine* (pp. 473-505). William Andrew Publishing. https://doi.org/https://doi.org/10.1016/B978-0-12-816200-2.00013-X
- Silva, D. P. B. M., Celina M; Mascagni, Daniela B. T; Ferreira, Marystela. (2019). Layer-by-Layer Films of Gold Nanoparticles and Carbon Nanotubes for Improved Amperometric Detection of Cholesterol. *Journal of Nanoscience and Nanotechnology*, 19(9), 5483-5488. https://doi.org/https://doi.org/10.1166/jnn.2019.16534
- Singh, N., Jenkins, G. J. S., Asadi, R., & Doak, S. H. (2010). Potential toxicity of superparamagnetic iron oxide nanoparticles (SPION). *Nano Reviews*, 1(1), 5358. https://doi.org/10.3402/nano.v1i0.5358
- Singh, S., Dhawan, A., Karhana, S., Bhat, M., & Dinda, A. K. (2020). Quantum Dots: An Emerging Tool for Point-of-Care Testing. *Micromachines (Basel)*, 11(12). https://doi.org/10.3390/mi11121058
- Sk, M. A., Ananthanarayanan, A., Huang, L., Lim, K. H., & Chen, P. (2014). Revealing the tunable photoluminescence properties of graphene quantum dots [10.1039/C4TC01191K]. *Journal of Materials Chemistry C*, 2(34), 6954-6960. https://doi.org/10.1039/C4TC01191K
- Skirtach, A. G., Antipov, A. A., Shchukin, D. G., & Sukhorukov, G. B. (2004). Remote Activation of Capsules Containing Ag Nanoparticles and IR Dye by Laser Light. *Langmuir*, *20*(17), 6988-6992. https://doi.org/10.1021/la048873k
- Son, K. D., & Kim, Y.-J. (2017). Anticancer activity of drug-loaded calcium phosphate nanocomposites against human osteosarcoma. *Biomaterials Research*, *21*(1), 13. https://doi.org/10.1186/s40824-017-0099-1
- Sonali, Viswanadh, M. K., Singh, R. P., Agrawal, P., Mehata, A. K., Pawde, D. M., Narendra, Sonkar, R., & Muthu, M. S. (2018). Nanotheranostics: Emerging Strategies for Early Diagnosis and Therapy of Brain Cancer. *Nanotheranostics*, 2(1), 70-86. https://doi.org/10.7150/ntno.21638
- Song, J., Liang, X., Ma, Q., An, J., & Feng, F. (2019). Fluorescent boron and nitrogen co-doped carbon dots with high quantum yield for the detection of nimesulide and fluorescence staining. Spectrochimica Acta Part A: Molecular and Biomolecular Spectroscopy, 216, 296-302. https://doi.org/https://doi.org/10.1016/j.saa.2019.03.074
- Sonsin, A. F., Silva, E. C. O., Marques, A. L. X., Silva, L. V. A. T., Nascimento, S. M. S., Souza, S. T., Borbely, A. U., Barbosa, C. D. A. E. S., & Fonseca, E. J. S. (2022). Tuning the photoluminescence by engineering surface states/size of S, N co-doped carbon dots for cellular imaging applications. *Nanotechnology*, *33*(23), 235708. https://doi.org/10.1088/1361-6528/ac56f2
- Spalla, O. (2002). Nanoparticle interactions with polymers and polyelectrolytes. *Current Opinion in Colloid & Interface Science*, 7(3), 179-185. https://doi.org/https://doi.org/10.1016/S1359-0294(02)00045-6
- Steen, L. (2023). Percent Yield Formula | How to Calculate Yield.

 https://study.com/learn/lesson/percent-yieldformula.html#:~:text=We%20calculate%20the%20theoretical%20yield,leave%20grams%20in%20the%20end
- Stevie, F. A., & Donley, C. L. (2020). Introduction to x-ray photoelectron spectroscopy. *Journal of Vacuum Science & Technology A*, 38(6), 063204. https://doi.org/10.1116/6.0000412
- Struyf, J. (2009). Relating Functional Groups to the Periodic Table. *Journal of Chemical Education*, 86(2), 190. https://doi.org/10.1021/ed086p190
- Su, B., Wang, T., Wang, Z., Gao, X., & Gao, C. (2012). Preparation and performance of dynamic layer-by-layer PDADMAC/PSS nanofiltration membrane. *Journal of Membrane Science*, 423-424, 324-331. https://doi.org/https://doi.org/https://doi.org/10.1016/j.memsci.2012.08.041
- Su, Y., He, Y., Lu, H., Sai, L., Li, Q., Li, W., Wang, L., Shen, P., Huang, Q., & Fan, C. (2009). The cytotoxicity of cadmium based, aqueous phase Synthesized, quantum dots and its modulation by surface coating. *Biomaterials*, 30(1), 19-25. https://doi.org/https://doi.org/10.1016/j.biomaterials.2008.09.029
- Sun, D., Ban, R., Zhang, P.-H., Wu, G.-H., Zhang, J.-R., & Zhu, J.-J. (2013). Hair fiber as a precursor for synthesizing of sulfur- and nitrogen-co-doped carbon dots with tunable luminescence

- properties. *Carbon, 64,* 424-434. https://doi.org/https://doi.org/10.1016/j.carbon.2013.07.095
- Sun, R., Zhu, J., Wu, H., Wang, S., Li, W., & Sun, Q. (2021). Modulating layer-by-layer assembled sodium alginate-chitosan film properties through incorporation of cellulose nanocrystals with different surface charge densities. *International Journal of Biological Macromolecules*, 180, 510-522. https://doi.org/https://doi.org/10.1016/j.ijbiomac.2021.03.092
- Šupová, M., Suchy, T., Sucharda, Z., Filová, E., Kinderen, J., Steinerová, M., & Simha Martynková, G. (2018). The comprehensive in vitro evaluation of eight different calcium phosphates: Significant parameters for cell behavior. *Journal of the American Ceramic Society*, 102. https://doi.org/10.1111/jace.16110
- Szot, K., Lesniewski, A., Niedziolka, J., Jönsson, M., Rizzi, C., Gaillon, L., Marken, F., Rogalski, J., & Opallo, M. (2008). Sol–gel processed ionic liquid hydrophilic carbon nanoparticles multilayer film electrode prepared by layer-by-layer method. *Journal of Electroanalytical Chemistry*, 623(2), 170-176. https://doi.org/https://doi.org/10.1016/j.jelechem.2008.07.023
- Tang, K., & Besseling, N. A. M. (2016). Formation of polyelectrolyte multilayers: ionic strengths and growth regimes [10.1039/C5SM02118A]. *Soft Matter*, *12*(4), 1032-1040. https://doi.org/10.1039/C5SM02118A
- Tejwan, N., Saha, S. K., & Das, J. (2019). Multifaceted applications of green carbon dots synthesized from renewable sources. *Advances in Colloid and Interface Science*, 102046. https://doi.org/https://doi.org/10.1016/j.cis.2019.102046
- Tekkeli Evrim Kepekci, S., & Kiziltas Volkan, M. (2017). Current HPLC Methods for Assay of Nano Drug Delivery Systems. *Current Topics in Medicinal Chemistry*, *17*(13), 1588-1594. https://doi.org/http://dx.doi.org/10.2174/1568026616666161222112305
- Teng, X., Ma, C., Ge, C., Yan, M., Yang, J., Zhang, Y., Morais, P. C., & Bi, H. (2014). Green synthesis of nitrogen-doped carbon dots from konjac flour with "off—on" fluorescence by Fe3+ and I-lysine for bioimaging [10.1039/C4TB00368C]. *Journal of Materials Chemistry B, 2*(29), 4631-4639. https://doi.org/10.1039/C4TB00368C
- Thamilarasan, V., Sethuraman, V., Gopinath, K., Balalakshmi, C., Govindarajan, M., Mothana, R., Siddiqui, N., Khaled, J., & Benelli, G. (2018). Single Step Fabrication of Chitosan Nanocrystals Using Penaeus semisulcatus: Potential as New Insecticides, Antimicrobials and Plant Growth Promoters. *Journal of Cluster Science*, 29. https://doi.org/10.1007/s10876-018-1342-1
- Thermofisher. PrestoBlue Assays for Cell Viability Protocol, for Microplates.

 https://www.thermofisher.com/uk/en/home/references/protocols/cell-and-tissue-analysis/protocols/prestoblue-cell-viability-reagent-for-microplates-protocol.html?gclid=Cj0KCQjw0ruyBhDuARIsANSZ3woH6Kq1hmYXeKaWjBfPhgMmWJybqhn

 n AOmpJ1k7UmpAJNookKYGoQaApSQEALw wcB&ef id=Cj0KCQjw0ruyBhDuARIsANSZ3woH
 6Kq1hmYXeKaWjBfPhgMmWJybqhnn AOmpJ1k7UmpAJNookKYGoQaApSQEALw wcB:G:s&s
 kwcid=AL!3652!3!693106171610!p!!g!!prestoblue!2031782398!70575884383&cid=bid pca
 iva r01 co cp1359 pjt0000 bid000000 0se gaw bt pur con&gad source=1
- Thermofisher. (2023). Carbon X-ray photoelectron spectra, carbon electron configuration, and other elemental information. https://www.thermofisher.com/uk/en/home/materials-science/learning-center/periodic-table/non-metal/carbon.html
- Tian, L.-J., Zhou, N.-Q., Liu, X.-W., Liu, J.-H., Zhang, X., Huang, H., Zhu, T.-T., Li, L.-L., Huang, Q., Li, W.-W., Liu, Y.-Z., & Yu, H.-Q. (2017). A sustainable biogenic route to synthesize quantum dots with tunable fluorescence properties for live cell imaging. *Biochemical Engineering Journal*, 124, 130-137. https://doi.org/https://doi.org/10.1016/j.bej.2017.05.011
- Tian, X., Shi, A., Yin, H., Wang, Y., Liu, Q., Chen, W., & Wu, J. (2022). Nanomaterials Respond to Lysosomal Function for Tumor Treatment. *Cells*, *11*(21). https://doi.org/10.3390/cells11213348
- Tirtei E, C. A., Asaftei SD, Mareschi K, Cereda M, Fagioli F. (2021). Precision Medicine in Osteosarcoma: MATCH Trial and Beyond. *Cells*, *10*(2), 281. https://doi.org/https://doi.org/10.3390/cells10020281

- Tripathi, A. S., Zaki, M. E. A., Al-Hussain, S. A., Dubey, B. K., Singh, P., Rind, L., & Yadav, R. K. (2023). Material matters: exploring the interplay between natural biomaterials and host immune system. *Front Immunol*, *14*, 1269960. https://doi.org/10.3389/fimmu.2023.1269960
- Tsikourkitoudi, V., Karlsson, J., Merkl, P., Loh, E., Henriques-Normark, B., & Sotiriou, G. A. (2020). Flame-Made Calcium Phosphate Nanoparticles with High Drug Loading for Delivery of Biologics. *Molecules*, 25(7). https://doi.org/10.3390/molecules25071747
- Tuan Nguyen, H., Tuan Duong, A., & Lee, S. (2023). Fabrication and enhanced performance of LEDs based on multilayer CdSe@ZnS quantum dot films using layer-by-layer spin-coating with solid-state treatment. *Chemical Physics*, *572*, 111954. https://doi.org/https://doi.org/10.1016/j.chemphys.2023.111954
- Tung, M. S. (1998). Calcium Phosphates: Structure, Composition, Solubility, and Stability. In Z. Amjad (Ed.), *Calcium Phosphates in Biological and Industrial Systems* (pp. 1-19). Springer US. https://doi.org/10.1007/978-1-4615-5517-9 1
- Tungare, K., Bhori, M., Racherla, K. S., & Sawant, S. (2020). Synthesis, characterization and biocompatibility studies of carbon quantum dots from Phoenix dactylifera. *3 Biotech*, *10*(12), 540. https://doi.org/10.1007/s13205-020-02518-5
- Tuz Johra, F., Lee, J., & Jung, W.-G. (2014). Facile and safe graphene preparation on solution based platform. *Journal of Industrial and Engineering Chemistry*, *20*, 2883–2887. https://doi.org/10.1016/j.jiec.2013.11.022
- UKHealthSecurityAgency. *Culture Collections Saos-2*. Retrieved 03/10 from https://www.culturecollections.org.uk/nop/product/saos-2
- UKHealthSecurityAgency. *Culture collections U-2 OS*. https://www.culturecollections.org.uk/nop/product/u-2-os
- Ullal, N., Mehta, R., & Sunil, D. (2024). Separation and purification of fluorescent carbon dots an unmet challenge [10.1039/D3AN02134C]. *Analyst*, *149*(6), 1680-1700. https://doi.org/10.1039/D3AN02134C
- Urbaniak, T., Piszko, P., Kubies, D., Podgórniak, Z., Pop-Georgievski, O., Riedel, T., Szustakiewicz, K., & Musiał, W. (2023). Layer-by-layer assembly of poly-l-lysine/hyaluronic acid protein reservoirs on poly(glycerol sebacate) surfaces. *European Journal of Pharmaceutics and Biopharmaceutics*, 193, 274-284. https://doi.org/https://doi.org/10.1016/j.ejpb.2023.10.023
- Urch, H., Vallet-Regi, M., Ruiz, L., Gonzalez-Calbet, J. M., & Epple, M. (2009). Calcium phosphate nanoparticles with adjustable dispersability and crystallinity [10.1039/B810026H]. *Journal of Materials Chemistry*, *19*(15), 2166-2171. https://doi.org/10.1039/B810026H
- Venkatesan, S., Baloch, H. A., Jamro, I. A., & Rafique, N. (2022). Evaluation of the production of hydrochar from spent coffee grounds under different operating conditions. *Journal of Water Process Engineering*, 49, 103037. https://doi.org/https://doi.org/10.1016/j.jwpe.2022.103037
- Verma, A., Sharma, S., Gupta, P. K., Singh, A., Teja, B. V., Dwivedi, P., Gupta, G. K., Trivedi, R., & Mishra, P. R. (2016). Vitamin B12 functionalized layer by layer calcium phosphate nanoparticles: A mucoadhesive and pH responsive carrier for improved oral delivery of insulin. *Acta Biomaterialia*, 31, 288-300. https://doi.org/https://doi.org/10.1016/j.actbio.2015.12.017
- Vieira, R. S., Oliveira, M. L. M., Guibal, E., Rodríguez-Castellón, E., & Beppu, M. M. (2011). Copper, mercury and chromium adsorption on natural and crosslinked chitosan films: An XPS investigation of mechanism. *Colloids and Surfaces A: Physicochemical and Engineering Aspects*, 374(1), 108-114. https://doi.org/https://doi.org/10.1016/j.colsurfa.2010.11.022
- Vikash, & Kumar, V. (2020). Ultrasonic-assisted de-agglomeration and power draw characterization of silica nanoparticles. *Ultrasonics Sonochemistry*, *65*, 105061. https://doi.org/https://doi.org/10.1016/j.ultsonch.2020.105061
- Vishwakarma, A., Singh, M., Weclawski, B., Reddy, V. J., Kandola, B. K., Manik, G., Dasari, A., & Chattopadhyay, S. (2022). Construction of hydrophobic fire retardant coating on cotton fabric using a layer-by-layer spray coating method. *International Journal of Biological Macromolecules*, 223, 1653-1666.
 - https://doi.org/https://doi.org/10.1016/j.ijbiomac.2022.10.231

- Volpe, M., Messineo, A., Mäkelä, M., Barr, M. R., Volpe, R., Corrado, C., & Fiori, L. (2020). Reactivity of cellulose during hydrothermal carbonization of lignocellulosic biomass. *Fuel Processing Technology*, 206, 106456. https://doi.org/https://doi.org/10.1016/j.fuproc.2020.106456
- Wagner, A. M., Knipe, J. M., Orive, G., & Peppas, N. A. (2019). Quantum dots in biomedical applications. *Acta Biomaterialia*, *94*, 44-63. https://doi.org/https://doi.org/10.1016/j.actbio.2019.05.022
- Walling, A. M., Novak, A. J., & Shepard, J. R. E. (2009). Quantum Dots for Live Cell and In Vivo Imaging. *International Journal of Molecular Sciences*, *10*(2). https://doi.org/10.3390/ijms10020441
- Wang, B., Mu, Y., Zhang, H., Shi, H., Chen, G., Yu, Y., Yang, Z., Li, J., & Yu, J. (2019). Red Room-Temperature Phosphorescence of CDs@Zeolite Composites Triggered by Heteroatoms in Zeolite Frameworks. *ACS Central Science*, *5*(2), 349-356. https://doi.org/10.1021/acscentsci.8b00844
- Wang, C.-C., & Lu, S.-Y. (2015). Carbon black-derived graphene quantum dots composited with carbon aerogel as a highly efficient and stable reduction catalyst for the iodide/tri-iodide couple [10.1039/C4NR06118G]. *Nanoscale*, 7(3), 1209-1215. https://doi.org/10.1039/C4NR06118G
- Wang, C., Park, M. J., Yu, H., Matsuyama, H., Drioli, E., & Shon, H. K. (2022). Recent advances of nanocomposite membranes using layer-by-layer assembly. *Journal of Membrane Science*, 661, 120926. https://doi.org/https://doi.org/10.1016/j.memsci.2022.120926
- Wang, D. Z., Gao, J. F., Jing, S. F., Wei, H., Huang, X. Y., & Li, C. D. (2015). Antitumor Effect of Docetaxel in Osteosarcoma by the Inhibition of Wnt Signal Channel. *Drug Res (Stuttg)*, 65(11), 597-601. https://doi.org/10.1055/s-0034-1395597
- Wang, N., Wang, Y., Guo, T., Yang, T., Chen, M., & Wang, J. (2016). Green preparation of carbon dots with papaya as carbon source for effective fluorescent sensing of Iron (III) and Escherichia coli. *Biosensors and Bioelectronics*, 85, 68-75. https://doi.org/https://doi.org/10.1016/j.bios.2016.04.089
- Wang, Y., & Hu, A. (2014). Carbon quantum dots: synthesis, properties and applications [10.1039/C4TC00988F]. *Journal of Materials Chemistry C*, 2(34), 6921-6939. https://doi.org/10.1039/C4TC00988F
- Wang, Z., Liao, H., Wu, H., Wang, B., Zhao, H., & Tan, M. (2015). Fluorescent carbon dots from beer for breast cancer cell imaging and drug delivery. *Analytical methods.*, 7(20), 8911-8917. https://doi.org/10.1039/c5ay01978h
- Wang, Z., & Tang, M. (2021). The cytotoxicity of core-shell or non-shell structure quantum dots and reflection on environmental friendly: A review. *Environmental Research*, 194, 110593. https://doi.org/https://doi.org/10.1016/j.envres.2020.110593
- Wang, Z., Yu, J., Zhang, X., Li, N., Liu, B., Li, Y., Wang, Y., Wang, W., Li, Y., Zhang, L., Dissanayake, S., Suib, S. L., & Sun, L. (2016). Large-Scale and Controllable Synthesis of Graphene Quantum Dots from Rice Husk Biomass: A Comprehensive Utilization Strategy. *ACS Applied Materials & Interfaces*, 8(2), 1434-1439. https://doi.org/10.1021/acsami.5b10660
- Wareing, T., Phan, A., Gentile, P., & Cucinotta, F. (2023). Effect of Operating Parameters on the Properties of Carbon Dots from Spent Coffee Grounds. *Journal of Technical Education Science*(74), 56-64. https://doi.org/10.54644/jte.74.2023.1336
- Wareing, T. C., Gentile, P., & Phan, A. N. (2021). Biomass-Based Carbon Dots: Current Development and Future Perspectives. *ACS Nano*, *15*(10), 15471-15501. https://doi.org/10.1021/acsnano.1c03886
- Weast, R. C. (1975). CRC Handbook of Chemistry and Physics: A Ready-reference Book of Chemical and Physical Data. CRC Press. https://books.google.co.uk/books?id=hCwXNDAJizAC
- White, N. S. E., R J. . (2004). Fluorescence techniques for drug delivery research:
- theory and practice. Advanced Drug Delivery Reviews, 57, 17-42.
- Wicki, A., Witzigmann, D., Balasubramanian, V., & Huwyler, J. (2015). Nanomedicine in cancer therapy: Challenges, opportunities, and clinical applications. *Journal of Controlled Release*, 200, 138-157. https://doi.org/https://doi.org/10.1016/j.jconrel.2014.12.030

- Wilk, M., Śliz, M., Czerwińska, K., & Śledź, M. (2023). The effect of an acid catalyst on the hydrothermal carbonization of sewage sludge. *Journal of Environmental Management*, 345, 118820. https://doi.org/https://doi.org/10.1016/j.jenvman.2023.118820
- Wohl, B. M., & Engbersen, J. F. J. (2012). Responsive layer-by-layer materials for drug delivery. *Journal of Controlled Release*, 158(1), 2-14. https://doi.org/https://doi.org/10.1016/j.jconrel.2011.08.035
- Wolfbeis, O. S. (2015). An overview of nanoparticles commonly used in fluorescent bioimaging [10.1039/C4CS00392F]. *Chemical Society Reviews*, *44*(14), 4743-4768. https://doi.org/10.1039/C4CS00392F
- Wong, K.-L., Bünzli, J.-C. G., & Tanner, P. A. (2020). Quantum yield and brightness. *Journal of Luminescence*, 224, 117256. https://doi.org/https://doi.org/10.1016/j.jlumin.2020.117256
- Wu, S., Shi, S., Liu, R., Wang, C., Li, J., & Han, L. (2023). The transformations of cellulose after concentrated sulfuric acid treatment and its impact on the enzymatic saccharification. Biotechnology for Biofuels and Bioproducts, 16(1), 36. https://doi.org/10.1186/s13068-023-02293-4
- Wu, V. M., Mickens, J., & Uskoković, V. (2017). Bisphosphonate-Functionalized Hydroxyapatite Nanoparticles for the Delivery of the Bromodomain Inhibitor JQ1 in the Treatment of Osteosarcoma. ACS Applied Materials & Interfaces, 9(31), 25887-25904. https://doi.org/10.1021/acsami.7b08108
- Wu, Y., Ali, M. R. K., Chen, K., Fang, N., & El-Sayed, M. A. (2019). Gold nanoparticles in biological optical imaging. *Nano Today*, *24*, 120-140. https://doi.org/https://doi.org/10.1016/j.nantod.2018.12.006
- Xia, C., Zhu, S., Feng, T., Yang, M., & Yang, B. (2019). Evolution and Synthesis of Carbon Dots: From Carbon Dots to Carbonized Polymer Dots. *Advanced Science*, *6*(23), 1901316. https://doi.org/https://doi.org/10.1002/advs.201901316
- Xiao, D., Jiang, M., Luo, X., Liu, S., Li, J., Chen, Z., & Li, S. (2021). Sustainable Carbon Dot-Based AlEgens: Promising Light-Harvesting Materials for Enhancing Photosynthesis. *ACS Sustainable Chemistry & Engineering*, *9*(11), 4139-4145. https://doi.org/10.1021/acssuschemeng.0c09348
- Xiao, X., Teng, F., Shi, C., Chen, J., Wu, S., Wang, B., Meng, X., Essiet Imeh, A., & Li, W. (2022). Polymeric nanoparticles—Promising carriers for cancer therapy [Review]. *Frontiers in Bioengineering and Biotechnology*, 10. https://doi.org/10.3389/fbioe.2022.1024143
- Xie, H., Yu, W., Liu, X., Xie, W., Lv, G., Wang, F., & Ma, X. (2011). Basic properties of alginate/chitosan microcapsule surfaces and their interaction with proteins. *Journal of Controlled Release*, 152, e246-e248. https://doi.org/https://doi.org/10.1016/j.jconrel.2011.09.040
- Xie, M., Zhang, F., Peng, H., Zhang, Y., Li, Y., Xu, Y., & Xie, J. (2019). Layer-by-layer modification of magnetic graphene oxide by chitosan and sodium alginate with enhanced dispersibility for targeted drug delivery and photothermal therapy. *Colloids and Surfaces B: Biointerfaces, 176*, 462-470. https://doi.org/https://doi.org/10.1016/j.colsurfb.2019.01.028
- Xie, Y., Zheng, J., Wang, Y., Wang, J., Yang, Y., Liu, X., & Chen, Y. (2019). One-step hydrothermal synthesis of fluorescence carbon quantum dots with high product yield and quantum yield. *Nanotechnology*, *30*(8), 085406. https://doi.org/10.1088/1361-6528/aaf3fb
- Xin, Y., Yin, M., Zhao, L., Meng, F., & Luo, L. (2017). Recent progress on nanoparticle-based drug delivery systems for cancer therapy. *Cancer Biol Med*, *14*(3), 228-241. https://doi.org/10.20892/j.issn.2095-3941.2017.0052
- Xu, H., Huang, W.-p., Ren, K.-f., & Tang, Y.-m. (2021). Spraying layer-by-layer assembly of tannin-Fe3+ and polyethyleneimine for antibacterial coating. *Colloid and Interface Science Communications*, 42, 100422. https://doi.org/https://doi.org/10.1016/j.colcom.2021.100422
- Xu, H., Xie, L., & Hakkarainen, M. (2017). Coffee-Ground-Derived Quantum Dots for Aqueous Processable Nanoporous Graphene Membranes. *ACS Sustainable Chemistry & Engineering*, 5(6), 5360-5367. https://doi.org/10.1021/acssuschemeng.7b00663
- Xu, L., Chu, Z., Wang, H., Cai, L., Tu, Z., Liu, H., Zhu, C., Shi, H., Pan, D., Pan, J., & Fei, X. (2019). Electrostatically Assembled Multilayered Films of Biopolymer Enhanced Nanocapsules for on-

- Demand Drug Release. *ACS Applied Bio Materials*, 2(8), 3429-3438. https://doi.org/10.1021/acsabm.9b00381
- Xu, M., Xu, S. F., & Yu, X. C. (2014). Clinical analysis of osteosarcoma patients treated with high-dose methotrexate-free neoadjuvant chemotherapy. *Curr Oncol*, *21*(5), e678-684. https://doi.org/10.3747/co.21.1973
- Xu, N., Piao, M., Arkin, K., Ren, L., Zhang, J., Hao, J., Zheng, Y., & Shang, Q. (2019). Imaging of water soluble CdTe/CdS core-shell quantum dots in inhibiting multidrug resistance of cancer cells. *Talanta*, *201*, 309-316. https://doi.org/https://doi.org/10.1016/j.talanta.2019.04.021
- Xu, X., Ray, R., Gu, Y., Ploehn, H. J., Gearheart, L., Raker, K., & Scrivens, W. A. (2004). Electrophoretic Analysis and Purification of Fluorescent Single-Walled Carbon Nanotube Fragments. *Journal of the American Chemical Society*, 126(40), 12736-12737. https://doi.org/10.1021/ja040082h
- Xuan, M., Zhao, J., Shao, J., Du, C., Cui, W., Duan, L., Qi, W., & Li, J. (2017). Recent progresses in layer-by-layer assembled biogenic capsules and their applications. *Journal of Colloid and Interface Science*, 487, 107-117. https://doi.org/https://doi.org/10.1016/j.jcis.2016.10.018
- Xue, Y., & Chan, S. (2015). Layer-by-layer self-assembly of CHI/PVS-Nafion composite membrane for reduced methanol crossover and enhanced DMFC performance. *International Journal of Hydrogen Energy*, 40(4), 1877-1885. https://doi.org/https://doi.org/10.1016/j.ijhydene.2014.11.129
- Yamada, Y. (2020). Dimerization of Doxorubicin Causes Its Precipitation. *ACS Omega*, *5*(51), 33235-33241. https://doi.org/10.1021/acsomega.0c04925
- Yan, F., Jiang, Y., Sun, X., Bai, Z., Zhang, Y., & Zhou, X. (2018). Surface modification and chemical functionalization of carbon dots: a review. *Microchimica Acta*, 185(9), 424. https://doi.org/10.1007/s00604-018-2953-9
- Yan, M., Wang, R., Liu, B., Li, Y., Li, Y., & Jiang, M. (2023). Layer by layer assembly CS/PAA for high sensitivity detection of heavy metal ions using mode interference sensor. *Optics Communications*, *545*, 129725. https://doi.org/https://doi.org/10.1016/j.optcom.2023.129725
- Yan, S., Wang, M., Zhang, S., Tong, Z., Li, S., Yong, X., Zhang, X., & Zhou, J. (2023). Fe-doped hydrochar facilitating simultaneous methane production and pharmaceutical and personal care products (PPCPs) degradation in co-anaerobic digestion of municipal sludge and food waste. Chemical Engineering Journal, 474, 146001. https://doi.org/https://doi.org/10.1016/j.cej.2023.146001
- Yang, F., Chen, L., Cui, S., Yu, D., Zheng, S., Zhao, D., Yin, X., Lai, C., & Chen, J. (2024). Asymmetric chitosan-derivative/carboxymethylcellulose layer-by-layer film combining antimicrobial and vascular regeneration for the repair of infected wounds. *International Journal of Biological Macromolecules*, 269, 132031. https://doi.org/https://doi.org/10.1016/j.ijbiomac.2024.132031
- Yang, H., He, L., Pan, S., Liu, H., & Hu, X. (2019). Nitrogen-doped fluorescent carbon dots for highly sensitive and selective detection of tannic acid. *Spectrochimica Acta Part A: Molecular and Biomolecular Spectroscopy*, 210, 111-119. https://doi.org/https://doi.org/10.1016/j.saa.2018.11.029
- Yang, J., Fu, Q., Jiang, H., Li, Y., & Liu, M. (2022). Progress of phototherapy for osteosarcoma and application prospect of blue light photobiomodulation therapy [Review]. *Frontiers in Oncology*, 12. https://doi.org/10.3389/fonc.2022.1022973
- Yang, K., Zhang, F.-J., Tang, H., Zhao, C., Cao, Y.-A., Lv, X.-Q., Chen, D., & Li, Y.-D. (2011). In-vivo imaging of oral squamous cell carcinoma by EGFR monoclonal antibody conjugated near-infrared quantum dots in mice. *International journal of nanomedicine*, 6(null), 1739-1745. https://doi.org/10.2147/IJN.S23348
- Yang, L. (2015). *Nanotechnology-Enhanced Orthopedic Materials: Fabrications, Applications and Future Trends*. Woodhead Publishing.
- Yang, L., Liu, S., Quan, T., Tao, Y., Tian, M., Wang, L., Wang, J., Wang, D., & Gao, D. (2022). Sulfuricacid-mediated synthesis strategy for multi-colour aggregation-induced emission fluorescent carbon dots: Application in anti-counterfeiting, information encryption, and rapid

- cytoplasmic imaging. *Journal of Colloid and Interface Science*, *612*, 650-663. https://doi.org/https://doi.org/10.1016/j.jcis.2022.01.004
- Yang, L., Nazari, L., Yuan, Z., Corscadden, K., Xu, C., & He, Q. (2016). Hydrothermal liquefaction of spent coffee grounds in water medium for bio-oil production. *Biomass and Bioenergy*, *86*, 191-198. https://doi.org/https://doi.org/10.1016/j.biombioe.2016.02.005
- Yang, M., Yan, Y., He, F., Wang, Z., Liu, E., & Fan, J. (2024). Green synthesis of fluorescent carbon dots from discarded cigarette butts as an effective fluorescence probe for sensing iron ions. *Materials Letters*, 357, 135613. https://doi.org/https://doi.org/10.1016/j.matlet.2023.135613
- Yang, P., Zhu, Z., Li, X., Zhang, T., Zhang, W., Chen, M., & Zhou, X. (2020). Facile synthesis of yellow emissive carbon dots with high quantum yield and their application in construction of fluorescence-labeled shape memory nanocomposite. *Journal of Alloys and Compounds*, 834, 154399. https://doi.org/https://doi.org/10.1016/j.jallcom.2020.154399
- Yang, X., Peng, L., Zong, J., & Zhu, Y. (2013). Preparation of photoluminescent carbon dots-embedded polyelectrolyte microcapsules. *Particuology*, *11*(3), 334-339. https://doi.org/https://doi.org/10.1016/j.partic.2012.09.008
- Yang, Y., Liu, Y., Song, L., Cui, X., Zhou, J., Jin, G., Boccaccini, A. R., & Virtanen, S. (2023). Iron oxide nanoparticle-based nanocomposites in biomedical application. *Trends in Biotechnology*, 41(12), 1471-1487. https://doi.org/10.1016/j.tibtech.2023.06.001
- Yang, Y., Wu, D., Han, S., Hu, P., & Liu, R. (2013). Bottom-up fabrication of photoluminescent carbon dots with uniform morphology via a soft–hard template approach [10.1039/C3CC38815H]. *Chemical Communications*, 49(43), 4920-4922. https://doi.org/10.1039/C3CC38815H
- Yang, Z., Gao, M., Wu, W., Yang, X., Sun, X. W., Zhang, J., Wang, H.-C., Liu, R.-S., Han, C.-Y., Yang, H., & Li, W. (2019). Recent advances in quantum dot-based light-emitting devices: Challenges and possible solutions. *Materials Today*, 24, 69-93. https://doi.org/https://doi.org/10.1016/j.mattod.2018.09.002
- Yang, Z., Xu, M., Liu, Y., He, F., Gao, F., Su, Y., Wei, H., & Zhang, Y. (2014). Nitrogen-doped, carbon-rich, highly photoluminescent carbon dots from ammonium citrate [10.1039/C3NR05380F]. Nanoscale, 6(3), 1890-1895. https://doi.org/10.1039/C3NR05380F
- Yao, Y., Zhou, Y., Liu, L., Xu, Y., Chen, Q., Wang, Y., Wu, S., Deng, Y., Zhang, J., & Shao, A. (2020). Nanoparticle-Based Drug Delivery in Cancer Therapy and Its Role in Overcoming Drug Resistance [Review]. *Frontiers in Molecular Biosciences*, 7. https://doi.org/10.3389/fmolb.2020.00193
- Ye, Z., Tang, R., Wu, H., Wang, B., Tan, M., & Yuan, J. (2014). Preparation of europium complex-conjugated carbon dots for ratiometric fluorescence detection of copper(ii) ions [10.1039/C4NJ00966E]. *New Journal of Chemistry*, *38*(12), 5721-5726. https://doi.org/10.1039/C4NJ00966E
- Yeom, J.-H., Shin, E., Jin, H., Liu, H., Luo, Y., Nam, Y., Ryu, M., Song, W., Chi, H., Kim, J., Lee, K., & Bae, J. (2023). Aptamer-conjugated gold nanoparticles platform as the intracellular delivery of antibodies for cancer therapy. *Journal of Industrial and Engineering Chemistry*, *126*, 480-491. https://doi.org/https://doi.org/10.1016/j.jiec.2023.06.036
- Yifan, Z., Natalie, S., Taylor, T. C., Oleksandr, K., Rachel, L. B., Yusra, B. M., Haiyan, S. L., Eugenie, S. K., & Stephanie, S. W. (2020). Vaccine efficacy against primary and metastatic cancer with in vitro-generated CD103<sup>+</sup> conventional dendritic cells. *Journal for ImmunoTherapy of Cancer*, 8(1), e000474. https://doi.org/10.1136/jitc-2019-000474
- Yim, M. S., Hwang, Y. S., Bang, J. K., Jung, D.-W., Kim, J. M., Yi, G.-R., Lee, G., & Ryu, E. K. (2021). Morphologically homogeneous, pH-responsive gold nanoparticles for non-invasive imaging of HeLa cancer. *Nanomedicine: Nanotechnology, Biology and Medicine, 34*, 102394. https://doi.org/https://doi.org/10.1016/j.nano.2021.102394
- Yoncheva, K., Tzankov, B., Yordanov, Y., Spassova, I., Kovacheva, D., Frosini, M., Valoti, M., & Tzankova, V. (2020). Encapsulation of doxorubicin in chitosan-alginate nanoparticles improves its stability and cytotoxicity in resistant lymphoma L5178 MDR cells. *Journal of Drug Delivery Science and Technology*, 59, 101870. https://doi.org/https://doi.org/10.1016/j.jddst.2020.101870

- Yoshida, K., Okamoto, M., Sasaki, J., Kuroda, C., Ishida, H., Ueda, K., Ideta, H., Kamanaka, T., Sobajima, A., Takizawa, T., Tanaka, M., Aoki, K., Uemura, T., Kato, H., Haniu, H., & Saito, N. (2020). Anti-PD-1 antibody decreases tumour-infiltrating regulatory T cells. *BMC Cancer*, 20(1), 25. https://doi.org/10.1186/s12885-019-6499-y
- Yu, F., Ma, M., Wu, X., Li, Z., & Bi, H. (2023). Synthesis and bioimaging application of red-emissive carbon dots. *Mendeleev Communications*, *33*(3), 343-345. https://doi.org/https://doi.org/10.1016/j.mencom.2023.04.015
- Yuan, W., Weng, G.-M., Lipton, J., Li, C. M., Van Tassel, P. R., & Taylor, A. D. (2020). Weak polyelectrolyte-based multilayers via layer-by-layer assembly: Approaches, properties, and applications. *Advances in Colloid and Interface Science*, 282, 102200. https://doi.org/https://doi.org/10.1016/j.cis.2020.102200
- Yuan, Y., Guo, B., Hao, L., Liu, N., Lin, Y., Guo, W., Li, X., & Gu, B. (2017). Doxorubicin-loaded environmentally friendly carbon dots as a novel drug delivery system for nucleus targeted cancer therapy. *Colloids and Surfaces B: Biointerfaces*, 159, 349-359. https://doi.org/https://doi.org/10.1016/j.colsurfb.2017.07.030
- Yue, L., Wang, J., Dai, Z., Hu, Z., Chen, X., Qi, Y., Zheng, X., & Yu, D. (2017). pH-Responsive, Self-Sacrificial Nanotheranostic Agent for Potential In Vivo and In Vitro Dual Modal MRI/CT Imaging, Real-Time, and In Situ Monitoring of Cancer Therapy. *Bioconjugate Chemistry*, 28(2), 400-409. https://doi.org/10.1021/acs.bioconjchem.6b00562
- Zelikin, A. N., Quinn, J. F., & Caruso, F. (2006). Disulfide Cross-Linked Polymer Capsules: En Route to Biodeconstructible Systems. *Biomacromolecules*, 7(1), 27-30. https://doi.org/10.1021/bm050832v
- Zeng, J., & Matsusaki, M. (2019). Layer-by-layer assembly of nanofilms to control cell functions [10.1039/C9PY00305C]. *Polymer Chemistry*, 10(23), 2960-2974. https://doi.org/10.1039/C9PY00305C
- Zhai, Y., Peng, C., Xu, B., Wang, T., Li, C., Zeng, G., & Zhu, Y. (2017). Hydrothermal carbonisation of sewage sludge for char production with different waste biomass: Effects of reaction temperature and energy recycling. *Energy*, *127*, 167-174. https://doi.org/https://doi.org/10.1016/j.energy.2017.03.116
- Zhang, C., Li, C., Aliakbarlu, J., Cui, H., & Lin, L. (2022). Typical application of electrostatic layer-by-layer self-assembly technology in food safety assurance. *Trends in Food Science & Technology*, 129, 88-97. https://doi.org/10.1016/j.tifs.2022.09.006
- Zhang, C., Zhang, S., Gao, P., Ma, H., & Wei, Q. (2014). Superhydrophobic hybrid films prepared from silica nanoparticles and ionic liquids via layer-by-layer self-assembly. *Thin Solid Films*, *570*, 27-32. https://doi.org/https://doi.org/10.1016/j.tsf.2014.08.045
- Zhang, J., & Yu, S.-H. (2016). Carbon dots: large-scale synthesis, sensing and bioimaging. *Materials Today*, 19(7), 382-393. https://doi.org/https://doi.org/10.1016/j.mattod.2015.11.008
- Zhang, L., Zhang, Z.-Y., Liang, R.-P., Li, Y.-H., & Qiu, J.-D. (2014). Boron-Doped Graphene Quantum Dots for Selective Glucose Sensing Based on the "Abnormal" Aggregation-Induced Photoluminescence Enhancement. *Analytical Chemistry*, 86(9), 4423-4430. https://doi.org/10.1021/ac500289c
- Zhang, Q., Iwakuma, N., Sharma, P., Moudgil, B. M., Wu, C., McNeill, J., Jiang, H., & Grobmyer, S. R. (2009). Gold nanoparticles as a contrast agent for in vivo tumor imaging with photoacoustic tomography. *Nanotechnology*, 20(39), 395102. https://doi.org/10.1088/0957-4484/20/39/395102
- Zhang, Q., Tian, F., Zhou, Q., Zhang, C., Tang, S., Jiang, L., & Du, S. (2022). Targeted ginkgo kernel biomass precursor using eco-friendly synthesis of efficient carbon quantum dots for detection of trace nitrite ions and cell imaging. *Inorganic Chemistry Communications*, 140, 109442. https://doi.org/https://doi.org/10.1016/j.inoche.2022.109442
- Zhang, W., Dai, D., Chen, X., Guo, X., & Fan, J. (2014). Red shift in the photoluminescence of colloidal carbon quantum dots induced by photon reabsorption. *Applied Physics Letters*, 104(9). https://doi.org/10.1063/1.4867487
- Zhang, W., Taheri-Ledari, R., Ganjali, F., Mirmohammadi, S. S., Qazi, F. S., Saeidirad, M., KashtiAray, A., Zarei-Shokat, S., Tian, Y., & Maleki, A. (2023). Effects of morphology and size of nanoscale

- drug carriers on cellular uptake and internalization process: a review [10.1039/D2RA06888E]. *RSC Advances*, *13*(1), 80-114. https://doi.org/10.1039/D2RA06888E
- Zhang, X., Wang, H., Ma, C., Niu, N., Chen, Z., Liu, S., Li, J., & Li, S. (2018). Seeking value from biomass materials: preparation of coffee bean shell-derived fluorescent carbon dots via molecular aggregation for antioxidation and bioimaging applications [10.1039/C8QM00030A].

 Materials Chemistry Frontiers, 2(7), 1269-1275. https://doi.org/10.1039/C8QM00030A
- Zhang, X., Xu, Y., Zhang, X., Wu, H., Shen, J., Chen, R., Xiong, Y., Li, J., & Guo, S. (2019). Progress on the layer-by-layer assembly of multilayered polymer composites: Strategy, structural control and applications. *Progress in Polymer Science*, 89, 76-107. https://doi.org/https://doi.org/10.1016/j.progpolymsci.2018.10.002
- Zhang, Y.-P., Ma, J.-M., Yang, Y.-S., Ru, J.-X., Liu, X.-Y., Ma, Y., & Guo, H.-C. (2019). Synthesis of nitrogen-doped graphene quantum dots (N-GQDs) from marigold for detection of Fe3+ ion and bioimaging. *Spectrochimica Acta Part A: Molecular and Biomolecular Spectroscopy*, *217*, 60-67. https://doi.org/https://doi.org/10.1016/j.saa.2019.03.044
- Zhang, Y.-Q., Ma, D.-K., Zhuang, Y., Zhang, X., Chen, W., Hong, L.-L., Yan, Q.-X., Yu, K., & Huang, S.-M. (2012). One-pot synthesis of N-doped carbon dots with tunable luminescence properties [10.1039/C2JM32973E]. *Journal of Materials Chemistry*, 22(33), 16714-16718. https://doi.org/10.1039/C2JM32973E
- Zhang, Y., Qin, W., Tang, H., Yan, F., Tan, L., Xie, Q., Ma, M., Zhang, Y., & Yao, S. (2011). Efficient assembly of multi-walled carbon nanotube-CdSe/ZnS quantum dot hybrids with high biocompatibility and fluorescence property. *Colloids and Surfaces B: Biointerfaces*, 87(2), 346-352. https://doi.org/https://doi.org/10.1016/j.colsurfb.2011.05.038
- Zhang, Y., Song, T., Feng, T., Wan, Y., Blum, N. T., Liu, C., Zheng, C., Zhao, Z., Jiang, T., Wang, J., Li, Q., Lin, J., Tang, L., & Huang, P. (2020). Plasmonic modulation of gold nanotheranostics for targeted NIR-II photothermal-augmented immunotherapy. *Nano Today*, *35*, 100987. https://doi.org/https://doi.org/10.1016/j.nantod.2020.100987
- Zhang, Y., Wang, Y., Feng, X., Zhang, F., Yang, Y., & Liu, X. (2016). Effect of reaction temperature on structure and fluorescence properties of nitrogen-doped carbon dots. *Applied Surface Science*, *387*, 1236-1246. https://doi.org/https://doi.org/10.1016/j.apsusc.2016.07.048
- Zhang, Y., Yang, J., Zhao, N., Wang, C., Kamar, S., Zhou, Y., He, Z., Yang, J., Sun, B., Shi, X., Han, L., & Yang, Z. (2018). Progress in the chemotherapeutic treatment of osteosarcoma (Review).

 Oncol Lett, 16(5), 6228-6237. https://doi.org/10.3892/ol.2018.9434
- Zhao, D., Yuan, H., Yi, F., Meng, C., & Zhu, Q. (2014). Autophagy prevents doxorubicin-induced apoptosis in osteosarcoma. *Mol Med Rep*, *9*(5), 1975-1981. https://doi.org/10.3892/mmr.2014.2055
- Zhao, Q., Han, B., Wang, Z., Gao, C., Peng, C., & Shen, J. (2007). Hollow chitosan-alginate multilayer microcapsules as drug delivery vehicle: doxorubicin loading and in vitro and in vivo studies. *Nanomedicine: Nanotechnology, Biology and Medicine*, *3*(1), 63-74. https://doi.org/https://doi.org/10.1016/j.nano.2006.11.007
- Zhao, S., Caruso, F., Dähne, L., Decher, G., De Geest, B. G., Fan, J., Feliu, N., Gogotsi, Y., Hammond, P. T., Hersam, M. C., Khademhosseini, A., Kotov, N., Leporatti, S., Li, Y., Lisdat, F., Liz-Marzán, L. M., Moya, S., Mulvaney, P., Rogach, A. L., . . . Parak, W. J. (2019). The Future of Layer-by-Layer Assembly: A Tribute to ACS Nano Associate Editor Helmuth Möhwald. *ACS Nano*, *13*(6), 6151-6169. https://doi.org/10.1021/acsnano.9b03326
- Zhao, X., Zhang, J., Shi, L., Xian, M., Dong, C., & Shuang, S. (2017). Folic acid-conjugated carbon dots as green fluorescent probes based on cellular targeting imaging for recognizing cancer cells [10.1039/C7RA07002K]. *RSC Advances*, 7(67), 42159-42167. https://doi.org/10.1039/C7RA07002K
- Zhao, Y.-B., Liu, H.-P., Li, C.-Y., Chen, Y., Li, S.-Q., Zeng, R.-C., & Wang, Z.-L. (2018). Corrosion resistance and adhesion strength of a spin-assisted layer-by-layer assembled coating on AZ31 magnesium alloy. *Applied Surface Science*, 434, 787-795. https://doi.org/https://doi.org/10.1016/j.apsusc.2017.11.012
- Zhaparova, L. (2012). Synthesis of nanoparticles and nanocapsules for controlled release of the antitumor drug "Arglabin" and antituberculosis drugs. *Technische Universiteit Eindhoven*,

- [Phd Thesis 1 (Research TU/e / Graduation TU/e), Chemical Engineering and Chemistry]. https://doi.org/https://doi.org/10.6100/IR731636
- Zhi, S., Huang, M., & Cheng, K. (2024). Enzyme-responsive design combined with photodynamic therapy for cancer treatment. *Drug Discovery Today*, *29*(5), 103965. https://doi.org/https://doi.org/10.1016/j.drudis.2024.103965
- Zhou, H., Yi, W., Li, A., Wang, B., Ding, Q., Xue, L., Zeng, X., Feng, Y., Li, Q., Wang, T., Li, Y., Cheng, X., Tang, L., Deng, Z., Wu, M., Xiao, Y., & Hong, X. (2020). Specific Small-Molecule NIR-II Fluorescence Imaging of Osteosarcoma and Lung Metastasis. *Advanced Healthcare Materials*, *9*(1), 1901224. https://doi.org/https://doi.org/10.1002/adhm.201901224
- Zhou, J., Shan, X., Ma, J., Gu, Y., Qian, Z., Chen, J., & Feng, H. (2014). Facile synthesis of P-doped carbon quantum dots with highly efficient photoluminescence [10.1039/C3RA45294H]. *RSC Advances*, 4(11), 5465-5468. https://doi.org/10.1039/C3RA45294H
- Zhou, Y., Mintz, K. J., Sharma, S. K., & Leblanc, R. M. (2019). Carbon Dots: Diverse Preparation, Application, and Perspective in Surface Chemistry. *Langmuir*, *35*(28), 9115-9132. https://doi.org/10.1021/acs.langmuir.9b00595
- Zhu, B., Sun, S., Wang, Y., Deng, S., Qian, G., Wang, M., & Hu, A. (2013). Preparation of carbon nanodots from single chain polymeric nanoparticles and theoretical investigation of the photoluminescence mechanism [10.1039/C2TC00140C]. *Journal of Materials Chemistry C*, 1(3), 580-586. https://doi.org/10.1039/C2TC00140C
- Zhu, S., Meng, Q., Wang, L., Zhang, J., Song, Y., Jin, H., Zhang, K., Sun, H., Wang, H., & Yang, B. (2013). Highly Photoluminescent Carbon Dots for Multicolor Patterning, Sensors, and Bioimaging. *Angewandte Chemie International Edition*, 52(14), 3953-3957. https://doi.org/10.1002/anie.201300519
- Zhu, S., Song, Y., Zhao, X., Shao, J., Zhang, J., & Yang, B. (2015). The photoluminescence mechanism in carbon dots (graphene quantum dots, carbon nanodots, and polymer dots): current state and future perspective. *Nano Research*, 8(2), 355-381. https://doi.org/10.1007/s12274-014-0644-3
- Zong, J., Zhu, Y., Yang, X., Shen, J., & Li, C. (2011). Synthesis of photoluminescent carbogenic dots using mesoporous silica spheres as nanoreactors [10.1039/C0CC03092A]. *Chemical Communications*, 47(2), 764-766. https://doi.org/10.1039/C0CC03092A
- Zuo, P., Lu, X., Sun, Z., Guo, Y., & He, H. (2016). A review on syntheses, properties, characterization and bioanalytical applications of fluorescent carbon dots. *Microchimica Acta*, 183(2), 519-542. https://doi.org/10.1007/s00604-015-1705-3